# Mineralogical, geochemical and geochronological studies in the Uralides and Variscides – contributions to the understanding of dynamic processes in collisional orogens

Habilitationsschrift vorgelegt von

Sven Sindern

Fakultät für Georessourcen und Materialtechnik
Rheinisch-Westfälische Technische Hochschule Aachen

Im März 2014

Angenommen durch die Habilitationskommission am 22.10.2014

Diese Habilitationsschrift ist auf den Internetseiten der Universitätsbibliothek online verfügbar.

**Abstract**

This thesis presents mineralogical, geochemical and geochronological studies in the Variscides and Uralides to elucidate the petrochemical history of dynamic orogenic processes. In combination with published data the results highlight significant differences between both orogens.

Pre-orogenic (i.e. pre-Uralian) basement is incorporated to different degrees and in contrasting patterns in Variscides and Uralides. In the Variscides numerous different terranes were agglomerated in a complicated large scale bow-shaped pattern, whereas in the Uralides mainly the fragments of the longitudinally trending eastern margin of Baltica were incorporated. The Taratash Complex of the Middle Urals is an outstanding example of such fragments. This thesis delineates a succession of Palaeoproterozoic magmatic and amphibolite facies tectonometamorphic events (2.46 – 1.8 Ga) following Archean granulite facies metamorphism and granitoid formation (3.65 – 2.91 Ga) recorded in the rocks of the Taratash Complex. In the Uralides, pre-orogenic basement is restricted to the west of the Main Uralian Fault leading to a simple geometry compared to the Variscides.

In both orogens, pre-Neoproterozoic rocks are only preserved in basement slivers, whereas remnants of Neoproterozoic magmatism and tectonism are abundant. For the southern Urals this is shown in a study of detrital zircon. Isotope signatures (U/Pb) of detrital zircon serve as geochemical indicator for the dynamic process of terrane accretion and for the transition from a passive to an active continental margin around 620 Ma, which affected large parts of the eastern margin of Baltica.

The main suture lines and associated former subduction zones can well be traced in the Variscides (i.e. Rheic suture) and Uralides (i.e. Main Uralian Fault), although secondary suture lines in both orogens require further characterization for better understanding. Different to the Variscides, where high-pressure metamorphic rocks are known in all major terranes, such rocks are exclusively observed along the Main Uralian Fault in the Uralides. Lawsonite bearing mineral assemblages in rodingitized ultramafite of the Maksyutov Complex (Southern Urals) that are investigated in a part of this thesis are an example of such metamorphism related to the dynamic process of subduction.

In contrast to the Variscides, which are characterized by large scale lithospheric reequilibration, the Uralides were not affected by significant orogenic collapse and postorogenic extension. This is also reflected in the preservation of prograde high-

pressure/low-temperature metamorphic assemblages in the Maksyutov Complex (e.g. Lawsonite-bearing assemblages) and associated low-temperature pseudomorphs presented in this thesis. The lack of postorogenic extension highlights that the Uralides are characterized by a pronounced and isostatically equilibrated crustal root.

During the Variscan orogenesis existing continental crust was extensively recycled. In contrast to this, large amounts of juvenile crust, which formed in magmatic arcs, are a characteristic feature of the Uralian orogen. Here, data are presented for the Valerianovka arc in the Transuralian zone, which is rarely addressed in the literature. It is shown that granitoids formed by mixing of slab-derived melts and melts generated in the crust. This result supports the model of an Andean type setting.

Juvenile crust is particularly dominating in the Easturalian zone, where granitoids also formed after accretion of magmatic arcs. In this thesis it is demonstrated that the Borisov granite intruded in a first pulse of melt generation at 358 ± 23 Ma. Granitoid melt formation as well as high-temperature amphibolite facies metamorphic overprint of host rocks also reflect the dynamic process of crustal thickening during the Uralian orogeny.

Variscides and Uralides also vary with respect to their crustal architecture. Major crustal units of the Variscan orogen have a subhorizontal orientation, whereas crustal scale structural boundaries in the Uralides are high angle fault zones. Such structural differences are in line with the observation that the Variscides experienced significant crustal shortening, whereas the Uralides were affected by lower degrees of shortening. This can be demonstrated in a comparison of the Rhenohercynian (Variscan) and the Westuralian foreland fold and thrust belts.

Expulsion of hydrothermal fluids to the Variscan foreland during the dynamic process of orogenic compaction is investigated in this thesis applying various techniques. Enrichment of mobile components, such as Ba and $NH_4$, in sedimentary rocks studied in the RWTH-1 well in Aachen (Germany) serves as geochemical indicator for palaeo fluid-flow. Illite mineralogy, fluid inclusion petrography and microthermometry as well as isotope geochemistry of fluid inclusions and vein minerals suggest that expulsion of metamorphic fluids at the Variscan front was a short termed (approx. 5000 y) process , which was affected by fracture opening during episodic seismic activity and which occurred at depths between 4500 and 8000 m and temperatures close to 400 °C.

Both, Variscan and Uralian orogens were affected by post-Palaeozoic deformation, however Alpine reworking significantly obliterated Variscan structures, in particular in the southern part of the Variscides.

**Contents**

## 1. Introduction

This thesis presents the results of mineralogical, geochemical and geochronological studies to elucidate the petrochemical history of dynamic orogenic processes in the Variscides and Uralides.

Orogenies are the result of convergence of lithospheric plates, which perform relative movement related to the formation of oceanic lithosphere at constructive plate boundaries and to the reintegration of such lithosphere into the sub-lithospheric mantle at destructive plate boundaries. Orogens thus mainly form at destructive plate boundaries, either through collision of continents or through accretion at sites of subduction of oceanic crust (e.g. Frisch et al. 2011, Cawood et al. 2009). During plate convergence an accretionary stage often precedes a final collisional one leading to amalgamation of tectonic units. Consequently, accretional as well as collisional processes may be observed in one orogen. The terms “island-arc-type”, “Andean type” and “Alpine type” orogeny lay emphasis on specific settings and predominance of either accretionary or collisional events (Frisch et al. 2011). In addition to destructive plate boundaries orogens occasionally also form in intracratonic settings as a consequence of far-field stresses (Cawood et al. 2009).

Subduction and subduction-driven accretion and collision lead to crustal thickening and deformation. As a consequence thrusting, e.g. formation of nappe tectonics and foreland fold and thrust belts, is a characteristic structural feature. Syntectonic flysch-sediments also reflect such dynamic process. Changing p-T-conditions, controlled by depth of burial (defining lithostatic pressure and temperature) and tectonic stress result in metamorphism and finally magmatism. These, too, are characteristic orogenic processes (e.g. Frisch et al. 2011, Cawood et al. 2009, Condie 1997).

Fluid flow is an essential part of orogenic activity. Fluids released from a subducting slab cause arc magmatism, fluids are produced in prograde metamorphic reactions in deep crustal levels and fluids are expulsed from deformed sedimentary rocks in an orogenic wedge (Klemd 2013, Moore 1989, Oliver 1986). Fluid-rock interaction has an essential effect on the speed of metamorphic reactions and consequently is a controlling parameter for mechanical rock strength or lithosphere density (Jamtveit and Austrheim 2010, references therein), which significantly affects large-scale geodynamic processes.

Continental crust is characterised by lower density compared to oceanic crust or underlying lithospheric mantle. Thus, continental crust that may be thickened due to orogenic compression shows mass deficiency. Such mass deficiency in a thickened crust is compensated by isostatic uplift, which triggers erosion and transport of detritus. Uplift and transport of sediments, too, are dynamic processes during orogenic evolution. In lower levels a continental crust may respond to orogenic thickening by plastic flow causing gravitational collapse (Frisch et al. 2011).

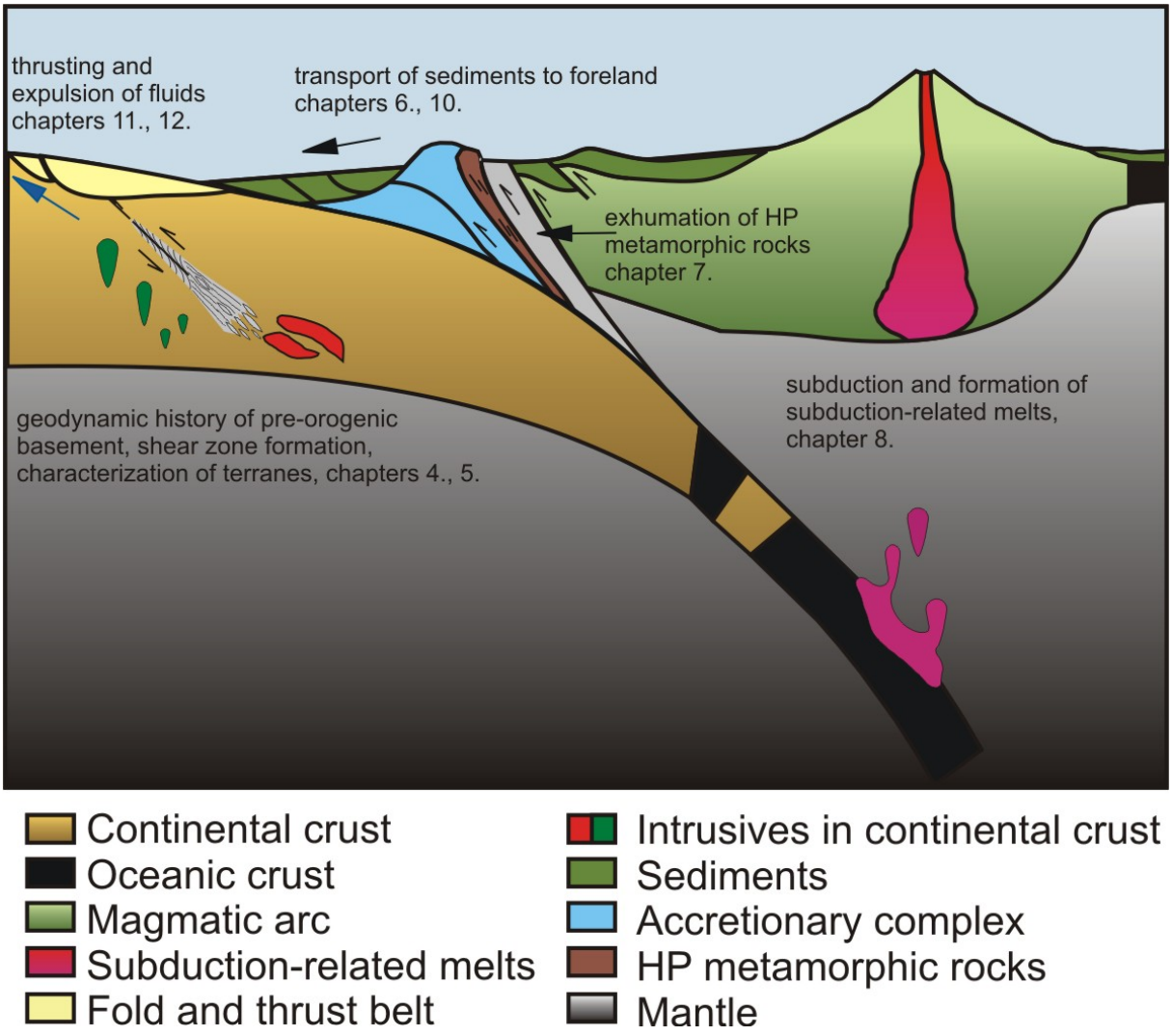


Fig. 1: Schematic sketch of an active continental margin and structural features that may form during different steps of an orogeny (adapted from Alvarez-Marrón 2002). The sketch illustrates dynamic processes occurring during orogenies, which are addressed in various chapters of this thesis. The process of crustal thickening (e.g. chapter 9) is not shown.

Therefore, orogens can be considered to form in a sequence of dynamic processes, which are reflected in tectonic patterns, rock textures, metamorphic mineral assemblages, occurrence and composition of magmatic intrusions, sedimentary facies and hydrothermal mineralisations (Fig. 1). The investigation of dynamic orogenic processes requires the evaluation of temporal and spatial variations of rock characteristics. Methods to unravel the kind and sequence of such processes are thus manifold and comprise petrological, structural, sedimentological, palaeontological, palaeomagnetic, seismic or numeric studies. In particular, mineralogical studies, including geochemical and geochronological techniques are a key to the understanding of dynamic processes in orogens.

For old and deeply eroded orogens, lacking faunal and palaeomagnetic information, geochemistry, including isotope geochemistry and geochronometry, provide valuable indicators and techniques to define tectonic setting, to show relative movement of rock units, to characterize the pre-orogenic status of crustal units and the adaption of their rocks to changing p-T-conditions during orogenic processes, to correlate different structural units also in complicated orogens or to characterize sedimentary sources and transport related to orogeny (e.g. Klemd et al. 2013, 2011, Zhang et al. 2012, Gao et al. 2011, 2009, Kisters et al. 2010, Kröner 2010, Pearce 1996).

This can perfectly be demonstrated using examples from the Variscides and Uralides. In the last years modern genetic concepts were developed for both orogens in large scientific programmes, such as the German seismic reflection programme (DEKORP), the priority programme “orogenic processes” (Orogene Prozesse – Ihre Simulation und Quantifizierung am Beispiel der Varisciden, 1992 – 1999) of the German Science foundation (DFG) as well as the major Europrobe programme of the European Science Foundation or IGCP 453 (Uniformitarianism revisited: a comparison between modern and ancient orogens, 1999 – 2004) and IGCP 497 (The Rheic ocean: its origin, evolution and correlatives, 2004 – 2008; Linnemann and Romer 2010, Murphy et al. 2009, Franke et al. 2000, Gee and Zeyen 1996).

The URSEIS project as part of the Europrobe Uralides programme and associated DFG funded studies have been in the focus of intensive research at RWTH Aachen University (Meyer et al. 1999). The investigations of the URSEIS project did not only reveal the lower crustal and mantle structure of the Urals, they also helped to set up a sequence of orogenic events, which are reflected by structures, magmatic and metamorphic rocks occurring at the surface. Significant parts of this thesis (chapters

4 to 9) are results of this work that supports the understanding of the Uralian orogen and that allows a comparison to other Palaeozoic orogens, such as the Variscides.
Further parts of this thesis are results of studies within the RWTH-1 DFG project package (DFG Bündel zur RWTH-1 Bohrung, 2004 – 2008). Research carried out at the RWTH-1 well in the city centre of Aachen addressed geothermal applications, the recent active stress field or natural seismicity (Trautwein-Bruns et al. 2010) but also focussed on an evaluation of existing concepts of orogenic structures and on an investigation of orogenic vein formation and palaeo-fluidflow in the Variscan orogenic front. This project, too, generated contributions to the understanding of dynamic processes within the Variscan orogen, which is presented in chapters 10 to 12 of this thesis.

## 2. Variscides and Uralides

### 2.1 Variscides and Uralides – structural categories

The Variscides and Uralides formed during late Palaeozoic convergence of Laurussia (consisting of Laurentia, Baltica and Avalonia) relative to Gondwana as well as to Siberia and Kazakhstan-Tarim (Görz and Hielscher 2010, Romer and Hahne 2010). Both orogens represent major continental structures, which together with the orogens of the Ouachita and the Alleghanian belt as well as the Mauretanides reflect the assembly of Pangaea (Nance et al. 2012, Kroner et al. 2010).
The complex successions of dynamic processes outlined in chapter 1 during both, the Variscan and Uralide orogenies, caused significant variation with respect to the following structural categories (also see Alvarez-Marrón 2002):

- occurrence and evolution of pre-orogenic basement
- characteristics and development of subduction zones
- occurrence and composition of island arcs accreted during orogeny
- development of the foreland fold and thrust belt

Mineralogical, geochemical and geochronological studies in the Variscides and Uralides characterizing the basement as well as dynamic processes will be presented in a comparison of both orogens within these four categories. This will be done on the basis of a literature review in this chapter as well as in selected examples based on own work in the following chapters 4 – 12.

## 2.2 Occurrence and evolution of pre-orogenic basement

### 2.2.1 Pre-Variscan and pre-Uralian crustal units

The Variscan fold belt represents a collage of formerly peri-Gondwanan Neoproterozoic terranes amalgamated during late Palaeozoic orogenic events and now exposed in the Variscan massifs of western and central Europe (Fig. 2). In a descriptive way one can distinguish East Avalonia, Iberia, Cadomia and Bohemia. Exact pre-Variscan plate tectonic constellations of these crustal fragments are a matter of an ongoing debate (e.g. Nance et al. 2012, 2008, Kroner and Romer 2010).

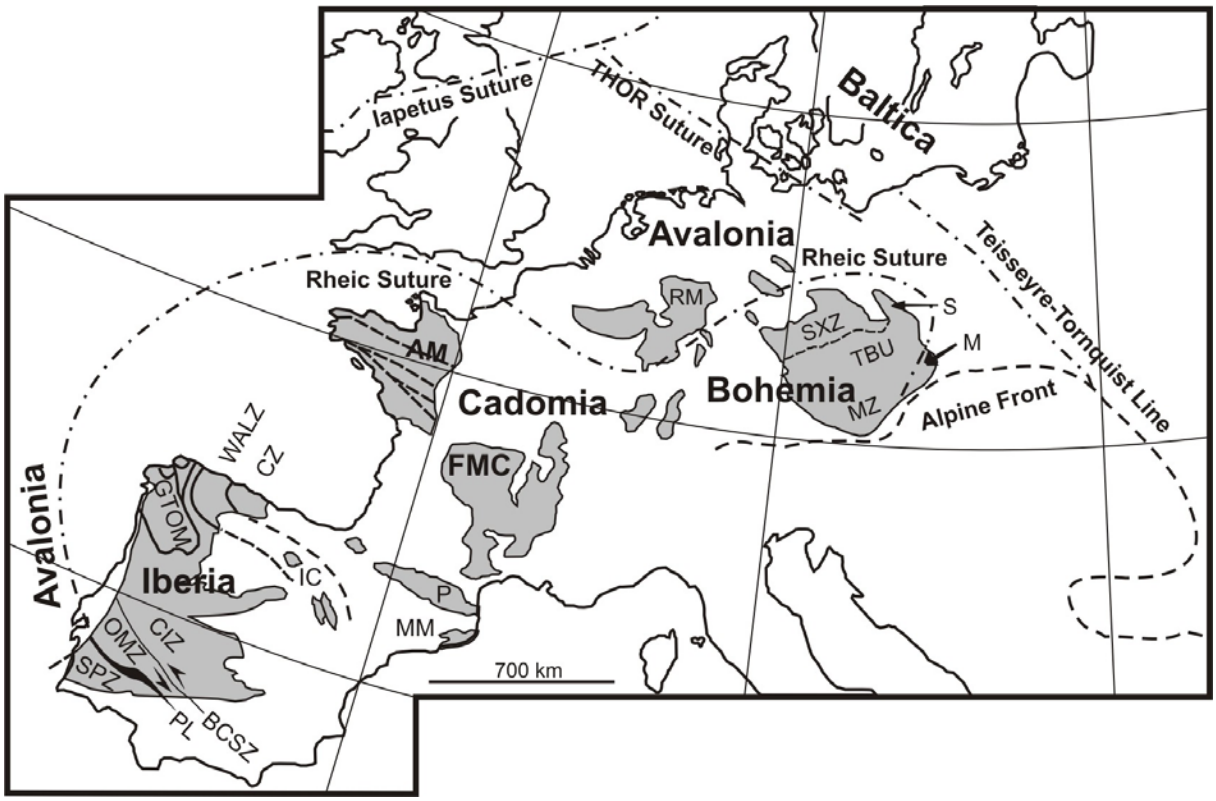


Fig. 2, Variscan massifs of southeastern and central Europe, modified from Linnemann et al. (2008a). AM – Armorican Massif, FMC – French Massif Central, RM – Rhenish Massif, SPZ – South Portuguese Zone, OMZ – Ossa-Morena Zone, CIZ – Central Iberian Zone, GTOM – Galicia-Trás os Montes Zone, WALZ – West Asturian Leonese Zone, CZ – Cantabrian Zone, PL – Pulo de Lobo oceanic units (black), IC – Iberian Chains, BCSZ – Badajoz-Cordoba Shear Zone, P – Pyrénées, MM – Maures Massif, SXZ – Saxo-Thuringian Zone, TBU – Teplá-Barrandian Unit, MZ – Moldanubian Zone, S – Sudetes, M – Moravo-Silesian Zone.

In contrast to the Variscides, which are characterised by re-organisation of existing crustal domains, the Uralides show a significant volume of juvenile crust formed in

intra-oceanic island arcs accreted to the eastern margin (current coordinates) of Baltica along the Main Uralian Fault zone (Fig. 3, Puchkov 2013, 2009a, 2009b, Alvarez-Marron 2002). Occurrences of pre-Uralian basement are therefore mainly confined to the area west of the Main Uralian Fault zone. As both, pre-Variscan as well as pre-Uralian crustal domains were affected by Neoproterozoic orogenic processes the description considers pre-Neoproterozoic and Neoproterozoic processes in separate sections.

### 2.2.2 Pre-Neoproterozoic basement

Within the Neoproterozoic terranes incorporated in the **Variscan orogen** pre-Neoproterozoic rocks, in which original mineral assemblages and textures are preserved, are rare. Archean mafic intrusives (2732 $^{+23}/_{-21}$ Ma, U-Pb zircon), which were later metamorphosed under amphibolite facies conditions at 2000 Ma without younger overprint occur in the Upper Silesian Block of SE Poland (see M in Fig. 2, Zelazniewicz et al. 2009), which is considered to be part of the Avalonian basement (Linnemann et al. 2008b). Archean acidic and basic magmatism dated at 2761 $^{+24}/_{-17}$ Ma and 2734 ± 2 Ma (U-Pb zircon), respectively (Guerrot et al. 1989) is recorded in granulites from the Bay of Biscay (Iberia). High grade metamorphism occurred in Palaeoproterozoic times with an age representing cooling after peak granulite facies conditions at 1865 $^{+23}/_{-25}$ Ma (U-Pb, monazite, Guerrot et al. 1989).

Several studies in the North Armorican Massif (Cadomia) yield U-Pb zircon ages ranging between 1790 ± 20 and 2061 ± 2 Ma that are interpreted to indicate intrusion of granitoids (Inglis et al. 2004, Samson and D'Lemos 1998, Vidal et al. 1981). Model ages ($T_{DM}$) of 2220 Ma show that the granitoids represent juvenile Palaeoproterozoic crust (Samson and D'Lemos 1998). However, mineral assemblages and textures in these occurrences from the North Armorican Massif broadly reequilibrated during Neoproterozoic (Cadomian) amphibolite facies metamorphism (Inglis et al. 2004, Samson and D'Lemos 1998, Vidal et al. 1981).

Similar to the North Armorican basement, granitoid magmatism is dated at 2104 ± 1 to 2048 ± 12Ma (U-Pb,zircon) in the basement of southern Bohemia. However, Variscan amphibolite facies metamorphism affected these crustal units at 355 +/- 2 Ma (U-Pb, sphene, Wendt et al. 1993).

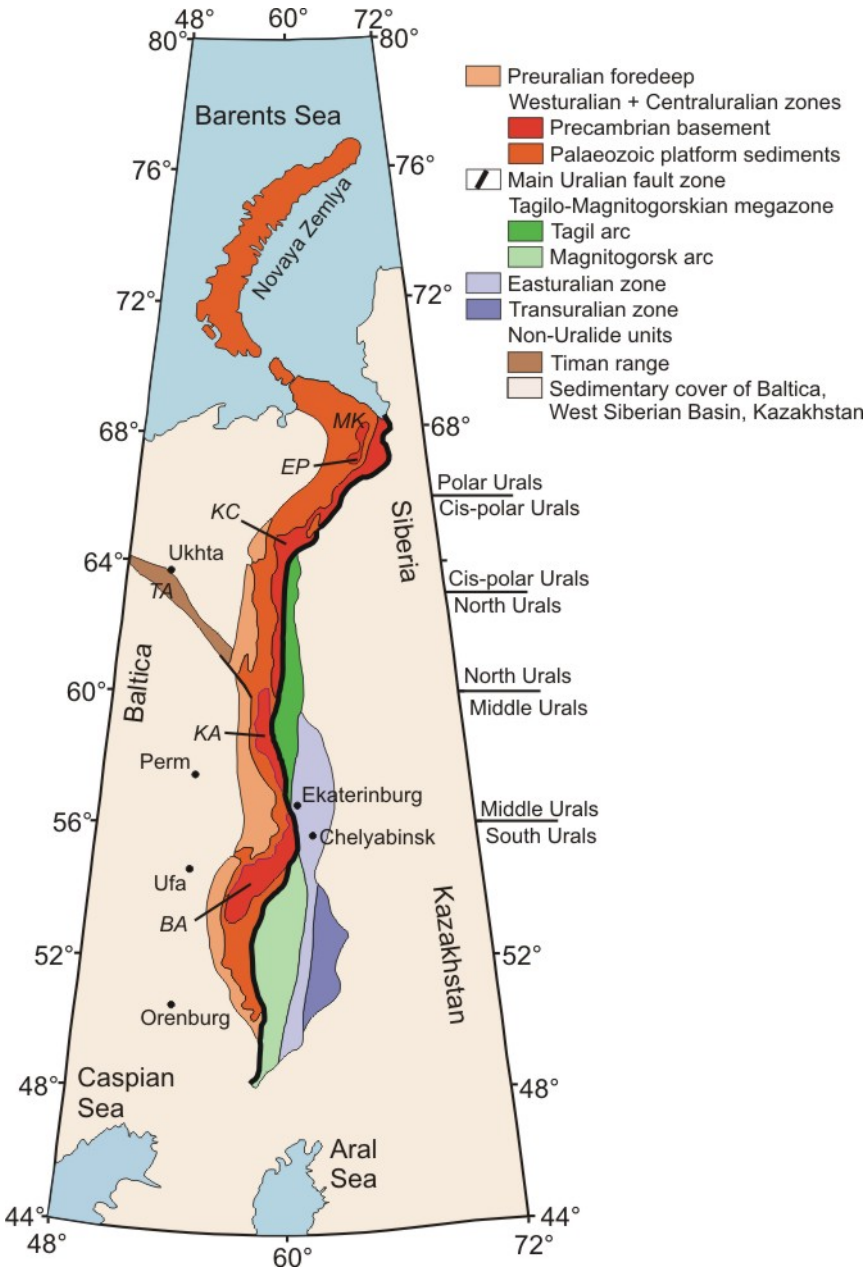


Fig. 3: Longitudinal zoning of the Uralian orogen, adapted from Brown et al. (2008), Gee and Pease (2004), Glasmacher et al. (2004). The Tagilo-Magnitogorskian Megazone as well as the East- and Transuralian zones are dominated by juvenile crust. Baltica, Siberia and Kazakhstan indicate relative position of the former continental plates. Major pre-Uralian occurrences: BA – Bashkirian Anticlinorium, EP - Engane-Pe Complex, KA – Kvarkush Anticlinorium, KC – Kozhim complex, MK – Marunkeu-Kharbey Anticlinorium, TA – Timan Anticlinorium.

Due to the high degree of Neoproterozoic to Palaeozoic metamorphic overprint pre-Neoproterozoic zircon ages may in some of these occurrences be considered as relicts. This is evident in the case of the Dobra orthogneiss (Bohemia), which may either be interpreted as a Mesoproterozoic (1380 Ma) granitoid metamorphosed at

ca. 600 Ma or a Neoproterozoic pluton derived from remelting of a Mesoproterozoic granitoid basement (Friedl et al. 2004).

While pre-Neoproterozoic mineral assemblages and textures are rarely preserved, inherited and detrital zircons provide broad evidence of the contribution of Archean to Proterozoic crust to Neoproterozoic and Palaeozoic magmatic and siliciclastic sedimentary rocks formed in the terranes composing the Variscan orogen (e.g. Hoffmann et al. 2013, Willner et al. 2013, Pereira et al. 2011, Sanchez-Martinez et al. 2011, Linnemann et al. 2010, 2008b, Chichorro et al. 2008, Nance et al. 2008, Solá et al. 2008, Friedl et al. 2004, de la Rosa et al. 2002, von Hoegen et al. 1990).

In addition to age data, Sm-Nd whole rock isotope data recalculated as ε Nd(t) values or average crustal residence ages (Nd $T_{DM}$) as well as ε Hf(t) zircon data indicate recycling of Archean to mainly Proterozoic crust during Neoproterozoic and Palaeozoic orogenic events (Gerdes and Zeh, 2006, Hegner and Kröner, 2000).

In the **Uralide orogen** pre-Neoproterozoic rocks are only exposed to the west of the Main Uralian Fault in the Bashkirian Anticlinorium (BA in Fig. 3, Maslov 2004). This structural unit was exhumed during the Uralian orogeny as part of a foreland fold and thrust belt. Crystalline basement, belonging to the Precambrian Volgo Uralia terrane, which is part of the eastern margin of Baltica (Bogdanova et al. 1996), forms the Taratash Complex. This complex is the largest and best exposed basement occurrence of the Uralides. The reconstruction of the pre-Neoproterozoic tectonometamorphic history of this crustal fragment, which is unaffected by Neoproterozoic or younger events, is in detail addressed in **chapter 4** of this thesis (Sindern et al. 2005).

The excellent preservation of these rocks allows the combined study of textural, mineralogical and isotopic data, which is a prerequisite for geochronological work. **Chapter 5** demonstrates the application of U-Pb monazite geochronology to dating of the dynamic process of shear zone formation in the Taratash Complex (Sindern et al. 2012a). In addition to data given in chapter 4, the results indicate a protracted structural and metamorphic evolution or a succession of tectonometamorphic events between 2030 and 2070 Ma at the eastern margin of Baltica. Data presented in chapters 4 and 5 as well as so far unpublished data define a detailed T-t-evolution path of this crustal fragment (Fig. 4).

The Taratash Complex is characterized by a succession of magmatic and amphibolite facies metamorphic events in Palaeoproterozoic times following Archean granulite facies metamorphism. This is a significant revision to the data set compiled by Scarrow et al. (2002), which was interpreted to indicate amphibolite facies metamorphism between 1.1 and 0.6 Ga.

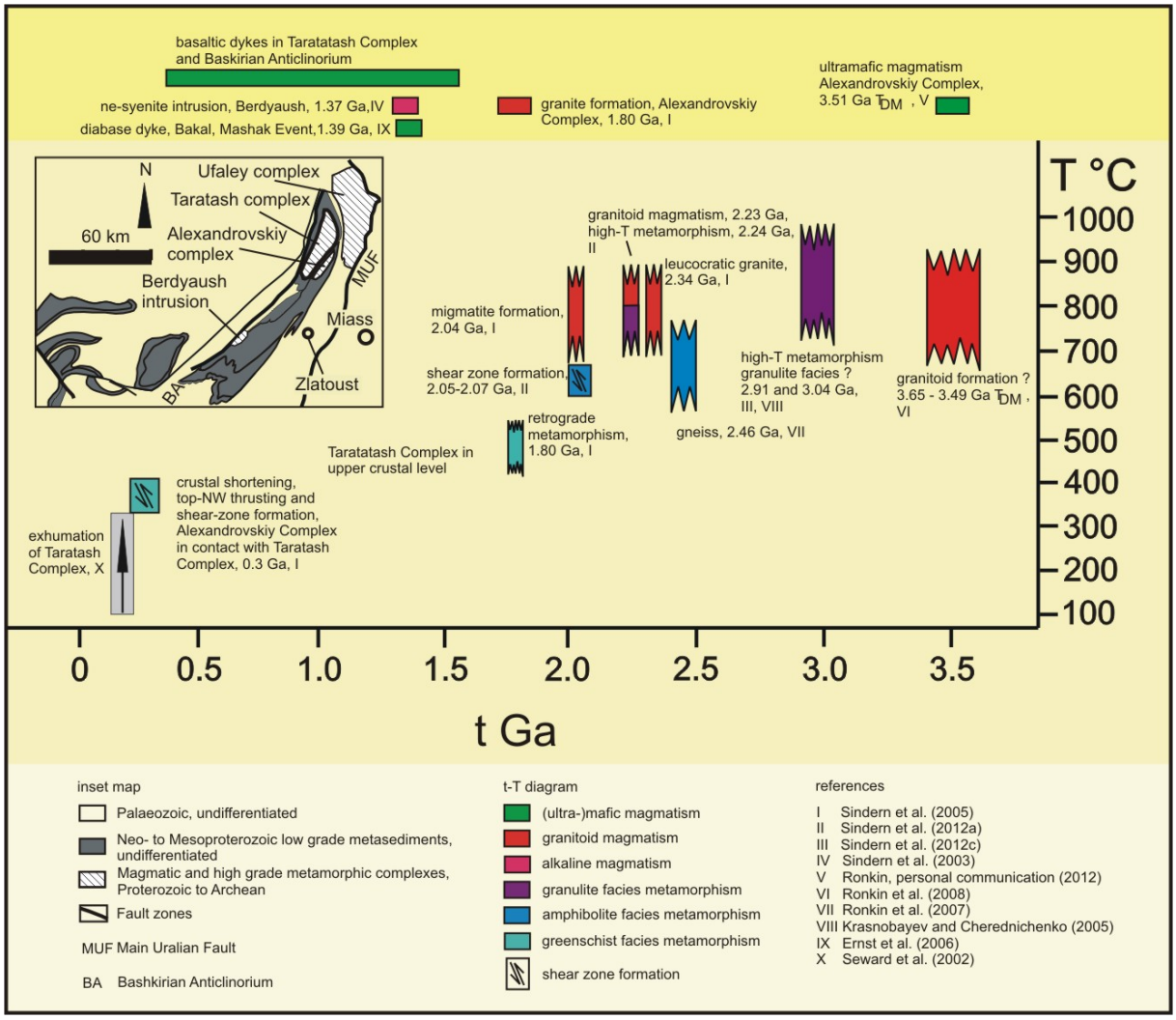


Fig. 4: t-T-diagram showing the evolution of the Taratash Complex. Inset map indicates the position of Proterozoic to Archean magmatic and metamorphic complexes in the northern Bashkirian Anticlinorium.

Other Precambrian basement domains, such as the Ufaley and Maksyutov Complexes are pervasively affected by Uralian HP and/or HT tectonometamorphism (e.g. Glodny et al. 2002, Hetzel 1999, Echtler et al. 1997). However, inherited U-Pb zircon ages as high as 1.4 Ga (Ufaley) and 1.8 Ga (Maksyutov) reflect pre-Neoproterozoic formation (Scarrow et al. 2002 and references therein). Contributions

of pre-Neoproterozoic crust to magmatic products of island arcs accreted to Baltica during the Uralian orogeny are indicated by rare observations of Palaeoproterozoic inherited zircon (e.g. Chelyabinsk pluton, Scarrow et al. 2002 and references therein).

In addition to high grade metamorphic and plutonic units also weak- to non-metamorphic pre-Neoproterozoic sedimentary successions are exposed in the Bashkirian Anticlinorium. Polycyclic detrital zircons have U-Pb isotope signatures indicative of crystallisation between 1.8 and 2.3 Ga, which is a characteristic age interval of the eastern Baltica margin, as shown also in chapters 4 and 5. This indicates the provenance of sediments and supports the idea of deposition along the passive margin of Baltica during Mesoproterozoic and early Neoproterozoic times. The lack of Mesoproterozoic ages sets constraints to palaeocontinental reconstructions as it precludes a position of the eastern Baltica margin opposite to Laurentia. The importance of U-Pb ages of detrital zircon for geodynamic discussions is shown in **chapter 6** (Willner et al. 2003).

At least two major Mesoproterozoic rifting events are recorded by angular unconformities in the sedimentary successions of the Bashkirian Anticlinorium (Maslov 2004) as well as by the occurrence of mafic dikes (Ernst et al. 2006) and alkaline granitic to nepheline syenitic intrusions, such as the Berdyaush pluton (1368 ± 6 Ma, Sindern et al. 2003, Fig. 4).

### 2.2.3 Neoproterozoic basement

Terranes amalgamated in the Variscan orogen as well as crustal domains forming the western Uralides have in common that all were part of a major Neoproterozoic to lower Palaeozoic active margin. This Timanian-Avalonian-Cadomian margin extended from the eastern margin of Baltica to an assembly of peri-Gondwanan terranes (Willner et al. 2013, Linnemann et al. 2010). In addition to petrologic, structural and geophysical information, element and isotope composition as well as geochronological data indicate magmatic arc activity and formation of juvenile crust next to reworking of pre-Neoproterozoic crust. Orogenic activity of that age is known as Cadomian stage in the Variscides and as Timanian stage at the eastern margin of Baltica (Puchkov 2013, Linnemann et al. 2010, 2008b, Gee and Pease 2004).

In the Avalonian terrane of the **Variscides** such rocks are exposed in the Midlands Microcraton of Southern Britain and Ireland, where a long-lived magmatic arc was accreted to Gondwana between 650 and 570 Ma (Linnemann et al. 2008b, and references therein). In Cadomia magmatic arc formation and convergent tectonics are reported for the Armorican Massif between 660 and 540 Ma (Ballèvre et al. 2001, Chantraine et al. 2001). Traces of the Cadomian orogeny are also preserved in Iberia in the Ossa Morena Zone and in the Central Iberian Zone, where arc magmatism was dated between 600 and 575 Ma (Bandres et al. 2002).

Extensive Cambro-Ordovician magmatism, mainly ranging between 510 to 470 Ma, is observed in all of the peri-Gondwanan terranes (e.g. Talavera et al. 2013, Zak et al. 2013, Melleton et al, 2010, Oberc-Dziedzic et al. 2010, Oggiano et al. 2010, Castineiras et al. 2008). This magmatism is considered to be related to the opening of the Rheic ocean (Talavera et al. 2013, Nance et al. 2012, 2010).

Numerous studies underline the importance of the analysis of detrital zircon to unravel the orogenic activity in these terranes (Brabant Massif, Willner et al. 2013, Von Hoegen et al. 1990, Gelnica terrane, Vozarova et al. 2012, Mid German Crystalline Zone, Gerdes and Zeh 2006, Saxothuringian zone, Bahlburg et al. 2010, Linnemann et al. 2007, 2008b, Cantabrian zone, Fernandez-Suarez et al. 2002).

At the eastern margin of Baltica the Neoproterozoic orogenic activity formed the Timanides extending along the western border of the Pechora basin from the northern Urals to the Kanin Peninsula in the Barents Sea (Fig. 3, Gee and Pease 2004). This orogeny also affected basement domains, which were later incorporated in the **Uralides**. Sedimentary successions reflecting the Timanian orogeny in angular unconformities and composition of detrital components, magmatic rocks with island arc affinity as well as HP/LT metamorphic rocks indicate late Neoproterozoic to early Cambrian subduction and arc-continent collision. These rocks are exposed in a series of Neoproterozoic to early Cambrian anticlinoria that extend from the Polar to the Southern Urals. The anticlinoria are: Marunkeu-Kharbey, Engane-Pe, Kolva-Khobeiz, Man'-Khambo, Kvarkush-Kamennogorsk and the Bashkirian anticlinorium, which is the largest of these structural units (Fig. 3, Beckholmen and Glodny 2004, Bogolepova and Gee 2004, Glasmacher et al. 2004, Glodny et al. 2004, Remizov and Pease 2004, Willner et al. 2004).

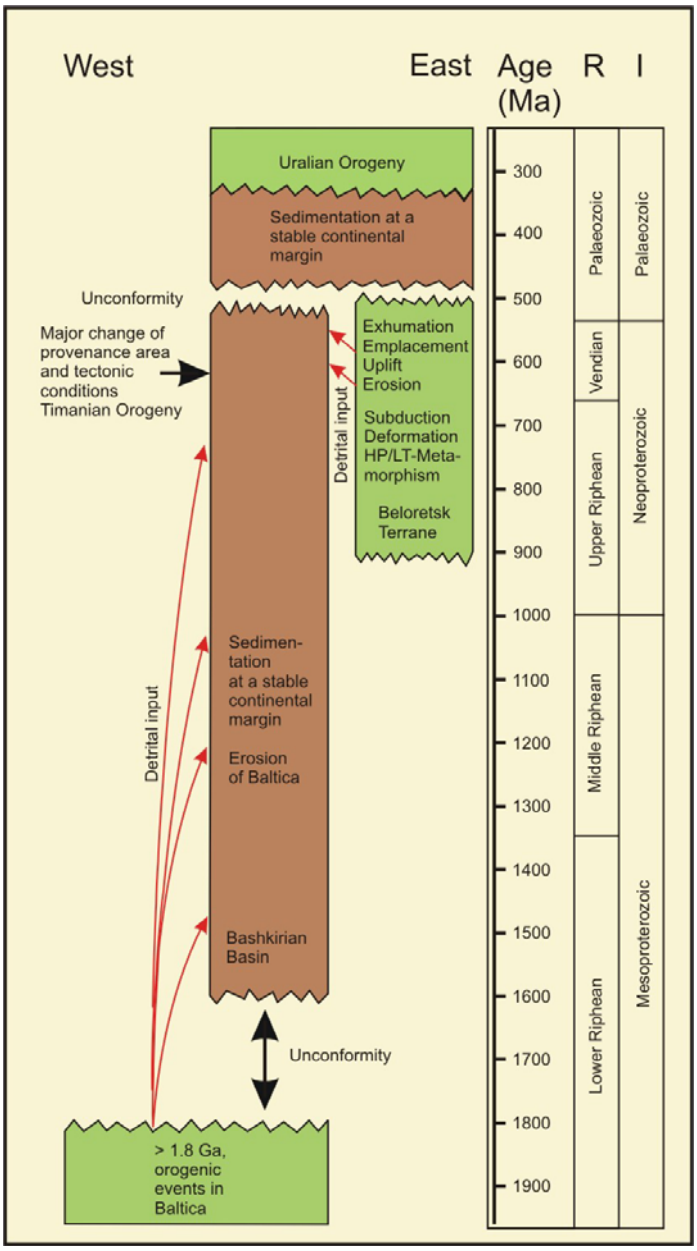


Fig. 5: Schematic presentation of the Proterozoic evolution in the Bashkirian basin and the Beloretsk terrane of the eastern margin of Baltica with russian (R) and international (I) stratigraphic subdivisions, see chapter 6, Willner et al. (2003). Orogenic events are marked in green, periods of stable continental margin sedimentation are marked in brown. Detrital zircon (red arrows) indicates a major change of sedimentary provenance areas as a consequence of the Timanian orogeny.

The accretion of the Beloretzk terrane to the eastern Baltica margin is a marked expression of Timanian orogenic activity in the Bashkirian anticlinorium. Detrital zircon analysed in Neoproterozoic sedimentary rocks of the region reflects final emplacement, exhumation and erosion of this terrane after 620 Ma (Fig. 5). The role of U/Pb isotope signatures of detrital zircon as a geochemical indicator to study the

dynamic process of accretion and to show the dynamic transition from a passive to an active continental margin in eastern Baltica is presented in chapter 6 (Willner et al. 2003).

### 2.3 Development of subduction zones

The convergence of two plates is compensated by subduction of oceanic or thin continental crust (Frisch et al. 2011, Cloos 1993). Thus, subduction is an important dynamic process in the evolution of an orogen. Traces of subduction in ancient orogens are: magmatic arcs, relics of ancient oceanic crust, which are obducted and tectonically incorporated in continental crust, as well as high-pressure/low-temperature metamorphic rocks such as eclogites (Klemd et al. 2013, 2011). Exhumation of the latter can be associated with accretion or collisional events but may also be related to late orogenic crustal reequilibration and can thus as well be indicative of a change in a plate tectonic constellation. Consequently, mineralogical and geochemical indicators for subduction and exhumation are important for the reconstruction of orogenic evolution.

Subduction of oceanic crust in Silurian and Devonian times as a response to the convergence of Gondwana with Laurussia is a crucial step in the development of the **Variscan orogen** (Nance et al. 2012, Kroner and Romer 2010). The ideas on the position of potential suture lines and details of geodynamic settings, however, are controversial (Nance et al. 2012, Kroner and Romer 2010, Murphy et al. 2009, von Raumer and Stampfli 2008, Stampfli et al. 2002, Matte 2001, Franke 2000).

Ophiolitic relics of the Rheic suture are preserved in the Galician nappes of Iberia and in the central sudetic ophiolites of Bohemia (Nance et al. 2012, Kryza and Pin 2010, Murphy et al. 2009, von Raumer and Stampfli 2008). These were deformed in a lower to middle Devonian subduction/collision orogenic channel (Puelles et al. 2012). Eclogites representative of Variscan convergence and subduction along the Rheic suture are exposed in the Odenwald (Mid German Crystalline Zone, Bohemia), in Saxothuringia and Moldanubia (Bohemia), in the Leon-Domain, in the Armorican Massif and the French Massif Central (Cadomia) or in the Galician nappes of Iberia (Faryad 2011, Klemd 2010, Kroner and Romer 2010, Zeh and Will 2010, Ballèvre et al. 2009, Murphy et al. 2009).

In addition to the Rheic suture further second order sutures are identified in the Variscan orogen, which are structurally independent of the Rheic suture and which also developed diachronously relative to the Rheic ocean (Matte 2001, Franke 2000). Examples of oceanic crust indicative of these zones are the ophiolites of the Vosges Klippen Belt (Skrzypek et al. 2012), the Iberian Beja-Acebuches ophiolite or the Lizard ophiolite (Murphy et al. 2009, Azor et al. 2008). The latter two may have formed in a back arc setting, i.e. the Lizard-Giessen-back arc basin, the Rhenohercynian basin and the Beja Acebuches back arc basin (Ribeiro et al. 2010, Zeh and Will 2010). Subduction along such sutures is reflected by HP metamorphism in the Central Iberian Zone, the French Massif Central, the South Armorican Zone or the Bohemian Massif/Marianske Lazne Complex (Faryad 2012, 2011, El Korh et al. 2012, Kroner and Romer 2010, Pitra et al. 2010, Ballèvre et al. 2009, Sintubin et al. 2008). Whether these sutures reflect (I) a constellation of different plates (e.g. Armorican Terrane Assemblage) separated by oceanic domains (Fig. 6, Frisch et al. 2011, Simancas et al. 2005, Franke 2000), (II) whether the pattern of sutures reflects duplication during complex amalgamation of a super terrane between a Rheic and a Palaeo Tethys ocean (Stampfli et al. 2002) or (III) whether the Rheic ocean is the exclusive oceanic domain and intracontinental subduction dominates in the second-order sutures (Kroner and Romer 2010) is an open debate.

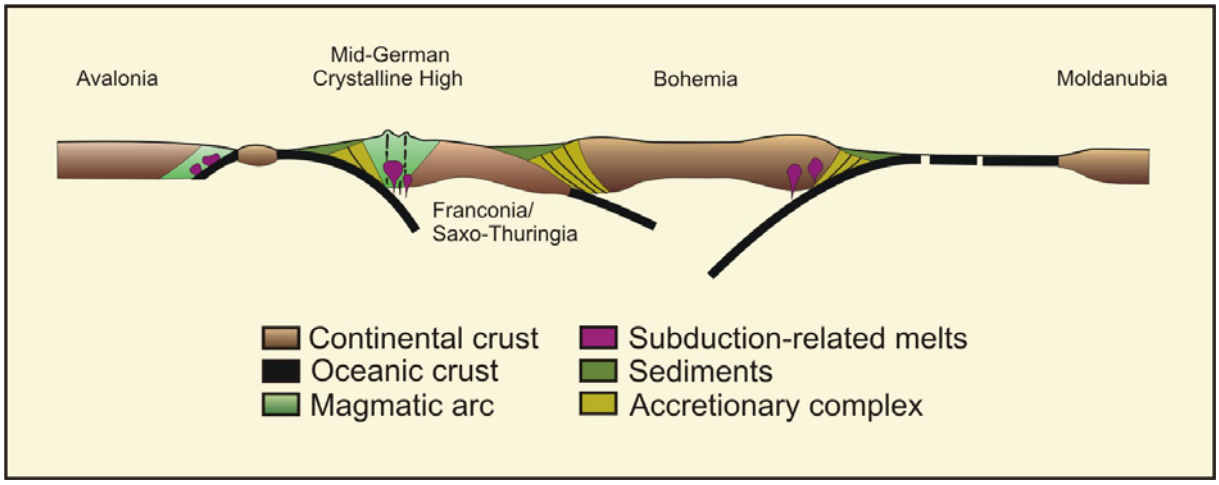


Fig. 6: Plate tectonic constellation of the Variscan orogen in the Frasnian (380 Ma) adapted from Franke (2000). Franconia/Saxo-Thuringia and Bohemia are considered to have formed part of an Armorican Terrane Assemblage (see text for further details).

Faryad (2011) discusses contrasting models to explain the constellations of suture lines in the Variscan orogen. The variation of ideas on potential geodynamic settings is due to intensive Variscan deformation combined with significant lateral displacement and rotation of terranes and in part later alpine reworking (Stampfli et al. 2002).

In contrast to the Variscides the exposures of ophiolites and mafic to ultramafic massifs are larger in the **Uralides**. Most of the massifs (i.e. Kempersay, Kraka, Mindyak, Nurali) are related to subduction of Ordovician to Silurian oceanic crust underneath the Magnitogorsk- and Tagil magmatic arcs. Other massifs (i.e. Tagil, Voykar-Syn'ya, Raiiz, Syumkeu) show a close genetic and structural relationship to these arcs, which were diachronously accreted to Baltica during the Middle Devonian to Early Carboniferous (Puchkov 2013, 2009b, 2002, Brown et al. 2008, Savelieva et al. 2002). The suture zone reflecting subduction of the former Uralian ocean and accretion of juvenile crust to Baltica is the Main Uralian Fault, which is a several km wide mélange zone with serpentinites, basalts, gabbros and metasediments. It is imaged in seismic sections as an east-dipping structure that extends from the surface into the middle crust (Fig. 7, Brown et al. 2002).

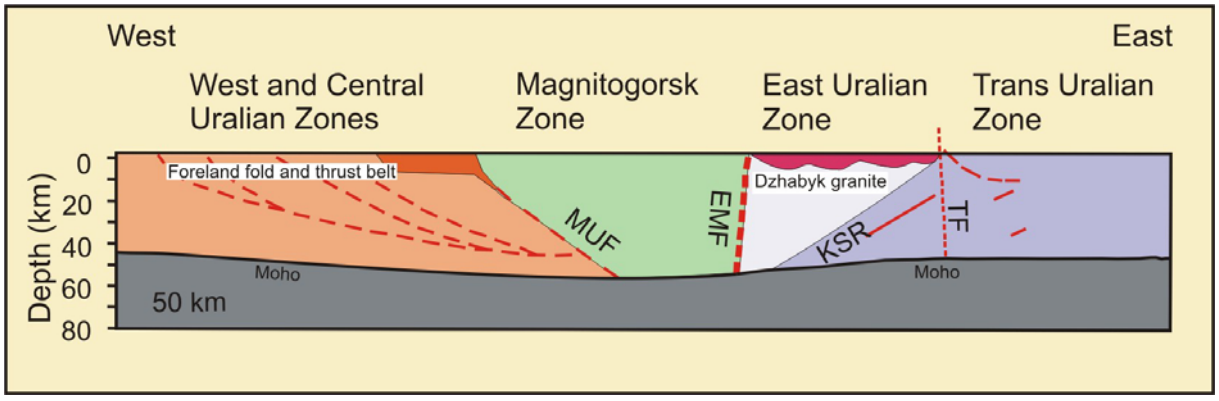


Fig. 7: West-East-section showing the major structures in the continental crust of the Uralides based on seismic data of the URSEIS project, adapted from Brown et al. (2008), MUF = Main Uralian Fault, EMF = East Magnitogorsk Fault, KSR = Kartaly Sequence of Reflectors, TF = Troitsk Fault.

To the east of the former Magnitogorsk-Tagil arcs remnants of oceanic crust are abundant but represent highly deformed and dismembered complexes occurring in anastomosing strike-slip fault zones (Brown et al. 2002, Savelieva et al. 2002). The

East-Magnitogorsk-, the Serov-Mauk- and the Troitsk-Faults are major structures along which accretion of mafic oceanic crust and magmatic island arc crustal material has taken place are (Brown et al. 2008, Alvarez-Marrón 2002).

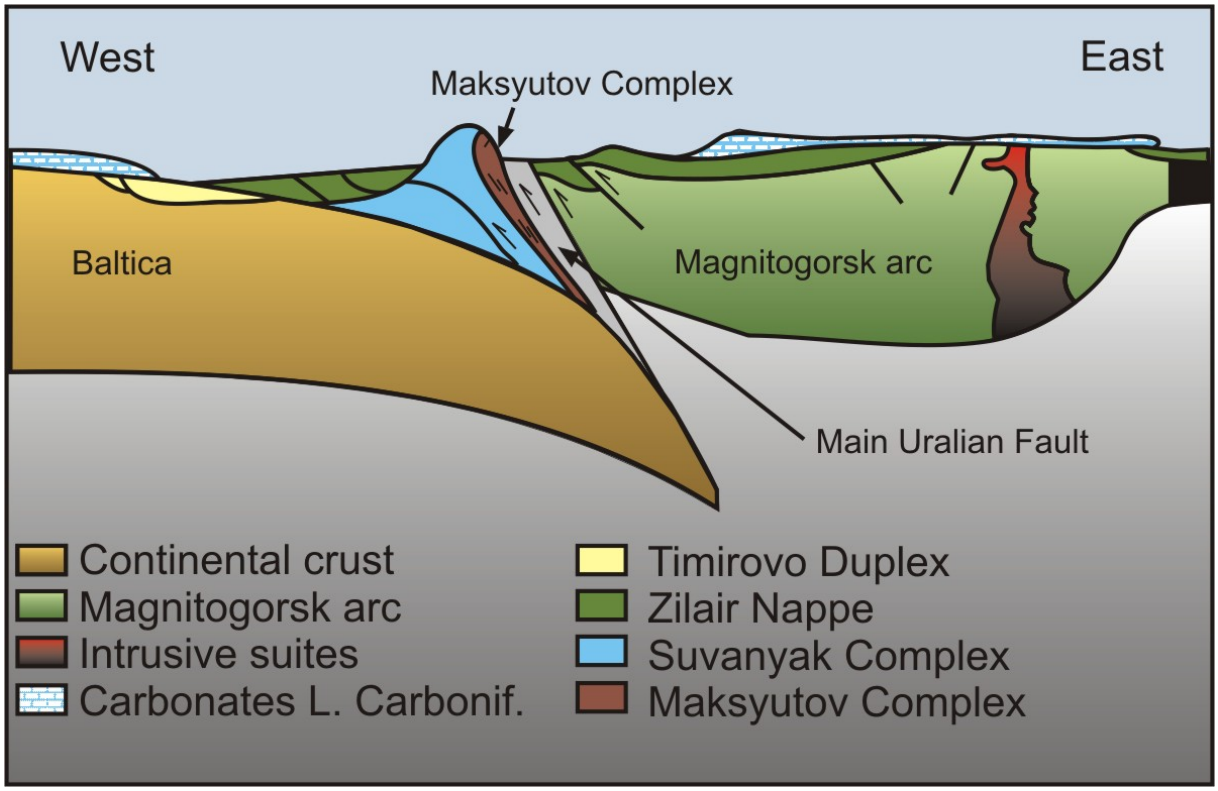


Fig. 8: Schematic sketch outlining the exhumation stage of the Maksyutov Complex in the Lower Carboniferous according to Brown et al. (2006), also see chapter 7 (Schulte and Sindern 2002) of this thesis.

Different to the Variscides where high pressure metamorphic rocks indicate subduction at second order sutures distinct from the main Rheic suture, high pressure metamorphic rocks in the Urals are only exposed close to the Main Uralian Fault and associated to the ophiolite complexes of the Polar Urals (Puchkov 2013, Glodny et al. 2004). They are not reported from the East- and Trans-Uralian zones.
The most prominent high pressure metamorphic occurrence in the southern Urals is the Maksyutov complex, which is composed of subducted continental and oceanic units of the former East-European continental margin. The eclogite facies lower unit of the complex shows peak metamorphic conditions of 550 – 650 °C and 15-23 kbar, which prevailed between 385 – 375 Ma (Glodny et al. 2002, 1999, Beane and Connelly 2000, Matte et al. 1993, Schulte and Blümel 1999). Pseudomorphs after lawsonite in ultramafite, exposed in km-sized serpentinite lenses, indicate high-

pressure metamorphism but also allow to characterize the exhumation path and to date this step. **Chapter 7** shows the application of combined mineralogical and geochronological work to unravel the stages between peak metamorphism and exhumation in the tectonometamorphic evolution of the Maksyutov Complex (Schulte and Sindern 2002). This supports existing exhumation models (Hetzel and Romer 2000, Hetzel 1999). The observations mirror the ongoing collision with the Magnitogorsk arc and termination of subduction along the most important subduction zone of the Urals.

### 2.4 Formation and accretion of magmatic arcs

Magmatic arcs reflect melt-production in the mantle due to release of fluids from a subducted plate. Consequently, they indicate the dynamic process of plate convergence as well as the transport process of large volumes of magmatic melts from mantle depths to middle and upper crustal levels.

In the **Variscides** intensive tectonic and metamorphic reworking during collisional stages of the Variscan orogeny but in part also during the Alpine stage may have obscured possible relics of magmatic arcs. Consequently, magmatic arcs are rarely identified in the Variscides (Nance et al. 2012). As structures and volcanosedimentary successions are not well preserved, evidence of arc-magmatism is mainly derived from geochemical signatures of magmatic rocks (e.g. Zeh and Will 2010, Altherr et al. 2000, Finger et al. 1997, Patocka 1987, see below). These data combined with geochronological information point to formation of magmatic arcs to both sides of the Rheic ocean as well as at the margins of peri-Gondwanan terranes.

A late Silurian to Early Devonian magmatic arc formed as a response to NW-directed subduction of the Rheic ocean along the southern margin of Baltica-Avalonia/Laurussia (Zeh and Will 2010, von Raumer and Stampfli 2008, Franke 2000). This arc is indicated by geochemical patterns of granitoids and metabasalts in different Variscan domains (Crystalline Complexes of Spessart, Ruhla and Trusetal Group of the Ruhla Crystalline Complex, Böllstein Odenwald, Saar-Nahe area, Zeh and Will 2010, von Raumer and Stampfli 2008, also see previous chapter 2.3).

The Late Devonian to Early Carboniferous Saxothuringian arc reflects subduction of the Rheic ocean to the south. Remnants of this arc are represented by granites in the Rhineland-Palatinate, by calc-alcaline magmatic rocks of the Bergsträsser Odenwald

and the Kyffhäuser Crystalline Complex, by metadiorites of the Brotterode Group (Ruhla Crystalline Complex) as well as by metabasites of the Hohnsdorf Crystalline Complex in Saxony-Anhalt (Zeh and Will 2010). Geochronological and geochemical data of calk-alkaline granitoids reported by Finger et al. (1997) and Altherr et al. (2000) may be interpreted to show that parts of the northern Vosges and northern Black Forest also formed part of the Saxothuringian arc (Zeh and Will 2010). An alternative model relating these granitoids to the Saxothuringian suture is given by Banka et al. (2002).

Devonian metabasites with chemical characteristics typical of island arcs are described by Patocka (1987) in the Jeseniky Mountains (Bohemian Massif) and may have been part of a late Silurian to lower Devonian magmatic arc at the active margin of Laurussia (Avalonia) to the Rheic ocean (Kroner and Romer 2010). Development of a magmatic arc due to closure of the Rheic ocean between the Iberian and South-Portuguese terranes in Lower and Middle Devonian times is inferred by Ribeiro et al. (2010).

Calc-alkaline plutonic rocks occurring to the south of the Rheic suture may have been generated due to subduction during closure of oceanic basins between the peri-Gondwanan terranes (e.g. Banka et al. 2002, Franke 2000, Pin 1990). Based on isotope- major- and trace element data Hann et al. (2003) conclude that the Rand granite in the southern Black Forest formed in a Variscan magmatic arc. This magmatic arc along an active continental margin of Cadomia in the north of the Moldanubian ocean is considered to have existed from Silurian to Early Carboniferous times (also see Fig. 6, Frisch et al. 2011). Further to the east, within the Moldanubian zone, the Central Bohemian Batholith, which intruded in early Carboniferous times (340 – 330 Ma) is also referred to as a product of a magmatic arc (Franke 2000, Finger et al. 1997). The complexity of data and contrasting interpretations on the Variscan evolution of Moldanubian crust is discussed by Finger et al. (2007).

Isotope and trace element data of the Devonian Brévenne suite of the north-eastern Massif Central are interpreted to show that its metavolcanics resulted from subduction of oceanic crust (Pin and Paquette 1997). Traces of a Silurian magmatic arc in the South Armorican Massif (Thieblemont et al. 1988) may have been part of the Ligerian cordillera, which extended to central France as indicated by Stampfli et al. (2002) who, however, relate this structure to subduction of the Rheic ocean.

These examples of possible magmatic arcs show that the identification of suprasubduction zone products is almost entirely based on isotope, major- and trace-element studies. Furthermore, it is evident that relics of magmatic arcs are rare and dispersed in the Variscan orogen, which hinders plate tectonic reconstructions as well as obliteration by later tectonic activity (e.g. Pin and Paquette 1997).

Different to the Variscides, well preserved magmatic arcs have a large volume in the **Uralides,** and their evolution is thoroughly studied (Fig. 3, Puchkov 2009b, Brown et al. 2008). The Ordovician-Silurian Tagil arc and the younger Middle to Upper Devonian Magnitogorsk arc were formed and attached to each other in an intraoceanic setting and diachronously collided with the eastern margin of Baltica (according to recent coordinates). The Magnitogorsk arc, which is exposed in the southern and middle Urals, was attached to Baltica in Upper Devonian times, whereas the collision of the Tagil arc in the Middle to Polar Urals took place in the Lower Carboniferous (Puchkov 2009b). Next to the Magnitogorsk-Tagil arcs the Carboniferous Valerianovka arc represents a second major magmatic arc (Fig. 9). According to Zonenshain et al. (1984) the latter structure is an Andean type arc formed on the margin of Kazakhstan. Parts of it are now amalgamated with former oceanic crust and Kazakhian continental fragments in the Transuralian Zone of the southern Urals (Görz et al. 2009, Puchkov 2009b, Herrington et al. 2005).
Recently, the existence of an Ordovician magmatic arc (Guberlya arc) and active continental margin in the southern Urals was hypothesized by Puchkov (2013). Due to intensive deformation during the Uralian orogeny, this structure is not as well preserved as the Tagil-, Magnitogorsk- and Valerianovka arcs.
**Chapter 8** presents major and trace element characteristics of magmatic rocks from the Valerianovka arc (Sindern et al., in prep.). The study shows that granitoids formed by mixing of slab-derived melts and melts generated in the crust. This result supports the model of an Andean type setting.
The Easturalian Zone, situated between the Magnitogorsk-Tagil arc in the west and remnants of the Valerianovka arc in the east, is a north-south extending strike-slip zone, resulting from an oblique NW-directed convergence of Kazakhstan-Tarim relative to Baltica (Görz and Hielscher 2010). This zone is composed of large granitoid massifs, which intruded into intensively sheared sedimentary and mafic

magmatic rocks of the former oceanic basin extending to the east of the Magnitogorsk-Tagil arc (Görz et al. 2009).

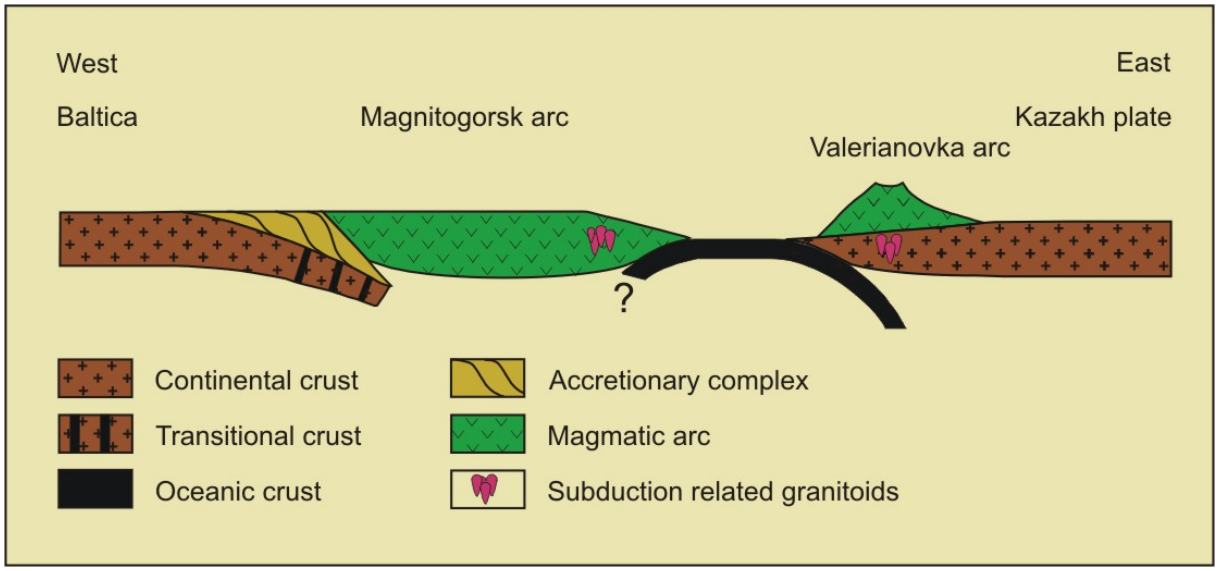


Fig. 9: Simplified profile depicting the tectonic constellation during the Uralian orogeny in Early Carboniferous times, adapted from Herrington et al. (2005) and Alvarez-Marrón (2002). The Devonian Magnitogorsk arc was affected by platform sedimentation during the Carboniferous. The accretionary complex formed during Devonian subduction underneath the Magnitogorsk arc and was later exhumed. Subduction-related granitoid magmatism in the Andean type Valerianovka arc on the continental margin of the Kazakh plate (now Transuralian zone) and in the oceanic zone to the west (now Easturalian zone) is indicated by the major- and trace-element signatures of rocks (see chapter 8 of this thesis) and points to contemporaneous subduction in both areas.

Granitoid melts formed in the southern and middle Urals in a first pulse between 365 and 315 Ma mainly after collision of the Magnitogorsk-Tagil arc with Baltica in the region (Görz et al. 2009, Bea et al. 2002, Gerdes et al. 2002, Hetzel and Romer 1999, Fershtater et al. 1997). The Borisov and Plast granitoids in the southern Urals belong to this stage. Granitoid melt formation as well as high-temperature amphibolite facies metamorphic overprint of host rocks reflect the dynamic process of crustal thickening during the Uralian orogeny. A mineralogical and geochemical characterization of the granitoids is given in **chapter 9** (Kolb et al. 2005). U-Pb data of zircon from the Borisov granite are discordant. The upper intercept of 358 ± 23 Ma is interpreted as crystallization age and confirms that this granite is formed during the first pulse of granitoid production, mentioned above (Fig. 10).

The region of the southern and middle Urals was affected by further compression after the collision of the Kazakhstan-Tarim continent with Baltica at c. 300 Ma (Görz and Hielscher 2010, Görz et al. 2009). Protracted crustal thickening and enhanced heat flow in that time caused further production of granitoid melts between 290 and 265 Ma (Bea et al. 2002, Gerdes et al. 2002). On the basis of trace element and isotope data Görz et al. (2009) conclude that granitoid melts in the Easturalian zone were produced by melting of island arc material in the Magnitogorsk-Tagil as well as Valerianovka zones, and that granitoid melts reached the Easturalian zone via lower crustal lateral channel flow.

Temporally limited enhanced heat flow in the Easturalian zone caused hydrothermal fluid flow, which also resulted in formation of major gold deposits (Kisters et al. 1999). Final hydrothermal gold mineralization under greenschist-facies conditions in the Kochkar region marking the end of this stage is dated at 265 ± 3 Ma (Fig. 10). This topic is also presented in chapter 9.

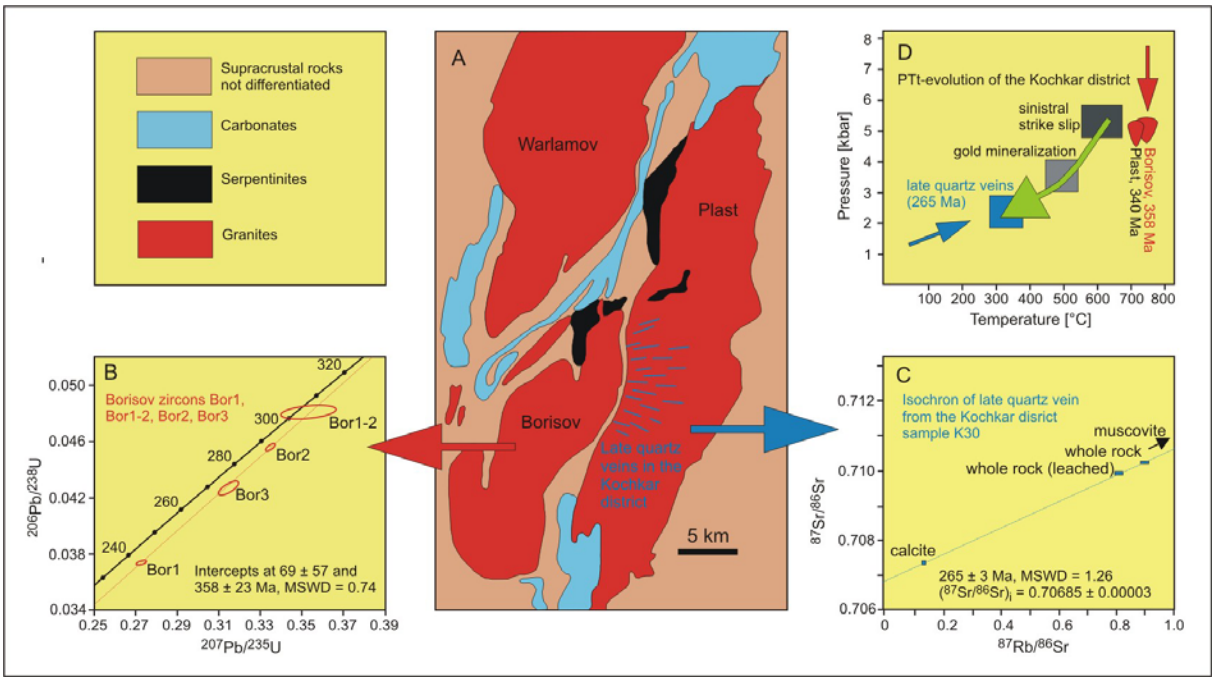


Fig. 10: Evolution of the Kochkar district (also see chapter 9). A, geological sketch map of the Kochkar district (Easturalian zone, southern Urals, adapted from Kolb et al. 2005). B, U-Pb isotope data of single zircons from the Borisov granite indicating the age of the first pulse of granitoid magmatism. C, Rb-Sr isochron of minerals and leached fraction of a late quartz vein reflecting the age of hydrothermal activity in a period of enhanced heat flow after compressive tectonism in the Kochkar district. D, PTt-evolution of the Kochkar district derived from mineralogical and geochronological data (adapted from Kolb et al. 2005, chapter 10).

The abundance of magmatic arcs and granitoid melts produced from such arcs in the Uralides makes clear that formation of juvenile continental crust is more important in the Uralian than in the Variscan orogen, in which reworking of older crust prevails (Alvarez-Marron 2002, Hegner and Kröner 2000).

### 2.5 Formation of foreland fold and thrust belts

Protracted convergence of terranes after collision is compensated by the formation of thin-skinned thrust sheets that propagate into foreland basins (Condie 1997). In the **Variscan orogen** the most extensive foreland fold and thrust belt is developed on the former margin of Avalonia (South Laurentia foreland fold and thrust belt, Pastor-Galan et al. 2011) extending from the South Portuguese zone over the south of Britain, the Westerns Ardennes thrust belt, the Rhenohercynian zone in Germany to the Variscan foreland basin of Poland (Mazur et al. 2010, Onézime et al 2002, Oncken et al. 2000). The well studied Rhenohercynian belt is characterized by thin- to thick-skinned orogenic domains, which formed in an up to 15 km thick sedimentary sequence. The latter was significantly shortened by 180 km (equivalent to 50 % of the former basin) during Variscan collision due to detachment at mid crustal levels (Oncken et al. 2000, 1999).

Orogenic events are also reflected by changes in sedimentary facies and sedimentological patterns in foreland sedimentary basins (Gray and Foster 1997, Stanistreet et al. 1991). Heavy mineral analysis as well as geochronology of detrital minerals in foreland sediments (e.g. zircon, white mica) are important indicators for the lithological composition and geodynamic evolution of the source areas (also see chapter 6). For the sediments exposed in the Variscan foreland fold and thrust belt heavy mineral studies were conducted by Mazur et al. (2010), Ganssloser (2000), Haverkamp (1991), Haverkamp et al. (1991) and Press (1986).

Major and trace element geochemical data of sedimentary rocks reflect provenance of detrital components and evolution of their sources (Veizer et al. 2003, McLennan et al. 1995, Cullers 1994, 1995, Condie 1993, Gibbs et al. 1986). A study of the geochemical characteristics of Devonian and Carboniferous foreland sediments of the Variscan orogen to the west of Rhine River sampled in the RWTH-1 well is presented in **chapter 10** (Sindern et al. 2008). These data support the idea of an ophiolite source in the NE of the Rhenohercynian Basin, reflect rapid uplift of the

Brabant Massif in Upper Devonian times and indicate resedimentation of Lower Devonian sediments in the foreland of the Variscan front.

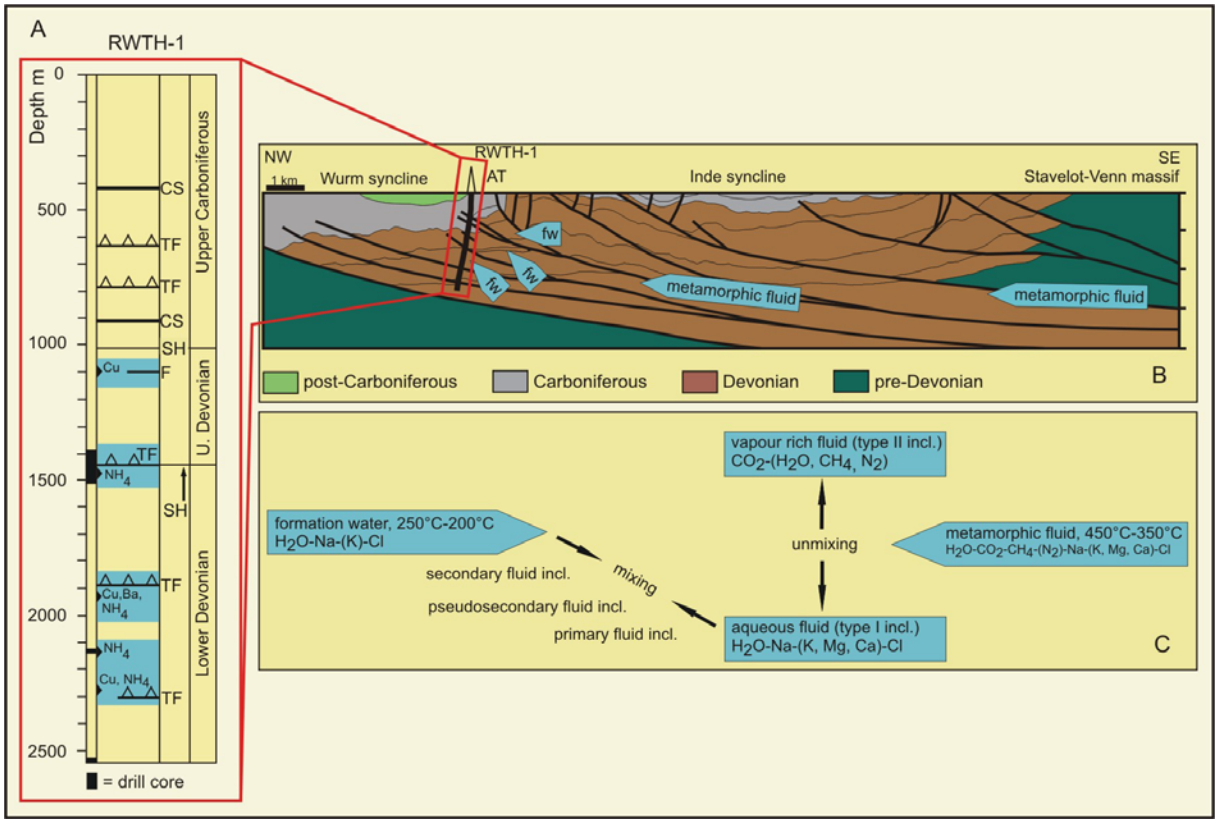


Fig. 11: Orogenic fluid flux in the Variscan fold and thrust belt (adapted from Sindern et al. 2008, 2012b, see chapters 11, 11, 12). A, geological profile of the RWTH-1 well. Black bars at left side indicate position of drill cores. Information on other sections is based on cuttings as well as on log data. Blue fields indicate sections along faults serving as pathways for hydrothermal fluids. Palaeofluid-flow is reflected by exceptional abundance of the components Ba, Cu and $NH_4$. Abbreviations CS = coal seam, SH = sedimentary hiatus, TF = thrust fault, F = fault with uncertain character of displacement. B, schematic cross section of the Variscan front zone near Aachen showing pathways for a metamorphic fluid released in the Stavelot-Venn massif from Lower Palaeozoic or older units and underlying Devonian strata. Mixing of metamorphic fluid with formation water (fw) occurs in the footwall of the Aachen thrust (AT). C, scheme of fluid evolution showing unmixing of the metamorphic fluid to an aqueous (type I) and a vapour rich (type II) fluid. Introduction of formation water and mixing with the aqueous metamorphic fluid causes the range of physicochemical fluid characteristics observed in primary, pseudosecondary and secondary fluid inclusions.

Orogenic compaction causes expulsion of hydrothermal fluids to the foreland (Duane and DeWit 1988, Oliver 1986). In particular, thrust faults may serve as fluid pathways along which mobile components, such as Ba or $NH_4$, can be enriched. In turn, these

may also serve as geochemical indicators for palaeo fluid-flow. This is also discussed in chapter 10 for sediments of the Variscan front zone near Aachen.

**Chaper 11** addresses the application of fluid inclusion microthermometry and of stable isotope geochemistry of fluid inclusions and vein minerals for the identification and characterization of metamorphic fluids expelled to the Variscan front zone in the vicinity of the Aachen thrust (Sindern et al. 2012b). Such fluid flux significantly affected the palaeotemperature field of the Variscan fold and thrust belt (Schroyen and Muchez 2000, Lünenschloß 1998, Lünenschloß et al. 1997). Reconstruction of the palaeotemperature field requires geothermometers, which yield temperature information in rocks of diagenetic to anchizonal grade.

In addition to fluid inclusion data, vitrinite reflectance, conodont alteration index as well as illite and chlorite “crystallinity” are commonly applied. **Chapter 12** (Sindern et al. 2007) shows that illite data in combination with additional temperature information help to constrain the maximum duration of a hydrothermal event.

In the south of the Variscan orogen foreland fold and thrust structures developed on the northern margin of Gondwana, as can be observed in the Cantabrian-Asturian arc (Pastor-Galan et al. 2011). Due to its position in the inner part of the Ibero-Armorican domain this arc was affected by significant bending and deformation in Upper Carboniferous times (Martinez-Catalan 1990).

Foreland sedimentation associated to the **Uralian orogeny** is recorded along the entire former margin of Baltica (Puchkov 1997). Orogenic flysch sedimentation started in the southern and middle Urals in the Upper Devonian, and in the northern and polar Urals in Lower Carboniferous times (Puchkov 1997). During Uralian orogenic compression flysch sedimentation was continuously extended towards western parts of the foredeep and terminated in the Permian with the onset of molasse deposition. With the end of Uralian foreland sedimentation in Triassic times up to 6000 m of flysch and molasse were deposited on top of 4000 to 7000 m of pre-orogenic Ordovician to Carboniferous sediments representing the passive margin stage of Baltica (Puchkov 1997). A mineralogical and geochronological characterization of foreland sediments indicating the dynamic process of exhumation of high-pressure rocks during the Uralian orogeny was performed by Willner et al. (2004).

Within the western Uralian orogenic wedge convergence was compensated by intensive thrusting and nappe structures close to the Main Uralian Fault leading to allochthonous units, such as the Taratash complex. Petrologic investigation and dating of the Aleksandrovskiy shear zone to the east of the Taratash complex at 302 ± 6 Ma, which is a weighted average of data presented in **chapter 4** (Sindern et al. 2005), shows that the Taratash complex, too, was exhumed and thrusted onto Devonian limestones during Upper Carboniferous to Permian compression.

Further to the west, a west-vergent fold and thrust belt (i.e. Westuralian Zone) was formed, which is best exposed in the southern Urals. This belt is characterized by the predominance of steep reverse faults (Giese et al. 1999). In line with such structures and contrasting to the Rhenohercynian fold and thrust belt tectonic shortening was low with a maximum value of 17 % (Brown et al. 1997, Perez-Estaun et al. 1997). Increased shortening of the foreland of c. 30 % can be expected in the Middle Urals, where an indenter of the former Baltica margin (Ufa amphitheatre) caused enhanced orogenic compression (Puchkov 2009a, Brown et al. 2002, Giese et al. 1999, Echtler et al. 1997). Shortening may even be higher in the Polar Urals, but is not quantified (Puchkov 2009a).

Remnants of the Valerianovka arc in the Transuralian zone (see chapter 8) are assumed to have formed on the margin of the Kazakhstan continent, which marks the eastern border of the Uralian orogen (Brown et al. 2008, Puchkov 2000, 1997). In this zone, which is only exposed in the southern Urals, thin-skinned tectonics similar to the Westuralian zone can not be observed. Nevertheless, the presence of west-dipping thrust-faults imaged in the URSEIS- and ESRU-profiles show the bi-vergent character of the Uralide orogen (Fig. 7, Puchkov 2009a). In contrast to the western foreland, a basin sedimentation recording the orogenic evolution is not documented. After the major stage of convergence, only lower amounts of molasse-like redbeds were deposited in graben structures in Upper Carboniferous to Permian times. Locally, final thrusting occurred in the Transuralian zone of the southern Urals and in the foredeep sediments of the Polar Urals at the end of the early Jurassic. This event, which marks the end of compressive orogenic activity in the Urals is followed by rapid uplift (Puchkov 2009a).

## 2.6 Comparison of Uralides and Variscides

The characteristics of Variscides and Uralides outlined so far reveal significant differences. **Pre-orogenic** basement is incorporated to different degrees and in contrasting patterns in both orogens. In the Variscides numerous different terranes were agglomerated in a complicated large scale bow-shaped pattern (Fig. 2), whereas in the Uralides mainly the fragments of the longitudinally trending eastern margin of Baltica were incorporated (see **chapters 2.2, 4, 5**). The latter are restricted to the west of the Main Uralian Fault leading to a simple geometry compared to the Variscides. In both orogens, pre-Neoproterozoic rocks are only preserved in basement slivers, whereas remnants of Neoproterozoic magmatism and tectonism are abundant (see **chapters 2.2, 6**).

The main **suture lines and associated former subduction zones** can be well traced in the Variscides (i.e. Rheic suture) and Uralides (i.e. Main Uralian Fault), although secondary suture lines in both orogens require further characterization for better understanding (see **chaper 2.3**). Different to the Variscides, where high-pressure metamorphic rocks are known in all structural units, such rocks are exclusively observed along the Main Uralian Fault in the Uralides (Puchkov 2013, Faryad 2011). The preservation of prograde high-pressure/low-temperature assemblages (e.g. Lawsonite-bearing assemblages and associated low-temperature pseudomorphs, **chapter 7**) is due to the fact that the Uralides were not affected by significant orogenic collapse and postorogenic extension (Echtler 1998). Such observation highlights that the Uralides are characterized by a pronounced and isostatically equilibrated crustal root (Puchkov 2013, Berzin et al. 1996). As a consequence, the Uralides show distinctly lower degrees of exhumation than other orogens (Alvarez-Marrón 2002, Giese et al. 1999). This is a marked difference to the Variscan orogen, which shows large scale late Carboniferous to Triassic lithospheric reequilibration and orogenic extension (Zeitlhofer et al. 2014, Puchkov 2013, Puchkov 2009a, Berzin et al. 1996).

The large amount of juvenile crust formed in **magmatic arcs** is a characteristic feature of the Uralides (see **chapters 2.4, 8, 9**). In contrast, in the Variscides existing continental crust is predominantly recycled (Alvarez-Marrón 2002).

Variscides and Uralides also vary with respect to their crustal architecture. Major crustal units of the Variscan orogen have a subhorizontal orientation, whereas crustal scale structural boundaries in the Uralides are high angle fault zones (Fig. 7, Alvarez-

Marrón 2002). Such structural differences are in line with the observation that the Variscides experienced significant crustal shortening of more than 1000 km (Kroner and Romer 2010). The Uralides were affected by a lower degree of shortening. The distinctly higher degree of shortening in the Variscan orogen is also reflected in the comparison of the Rhenohercynian and the Westuralian **fold and thrust belts** (**chapter 2.5**).

Both orogens are also characterized by contrasting histories. Active deformation started in the Variscides in Silurian times with first subduction and ended in final thrusting in the Rhenohercynian zone in Upper Carboniferous times (see **chapters 10, 11, 12** and references therein). First subduction indicating the onset of Uralian deformation is known already in the Ordovician and compressional deformation lasted until the end of the Permian (Puchkov 2013, 2009a) showing that the orogenic history of the Uralides is longer than that of the Variscides. Both orogens were affected by post-Palaeozoic deformation, however Alpine reworking significantly obliterated Variscan structures, in particular in the southern part of the Variscides.

## 3. References for chapters 1 and 2


Altherr, R., Holl, A., Hegner, E., Langer, C., Kreuzer, H. (2000) High-potassium, calc-alkaline I-type plutonism in the European Variscides: northern Vosges (France) and northern Schwarzwald (Germany). Lithos 50, 51 – 73.

Alvarez-Marrón, J. (2002) Tectonic processes during collisional orogenesis from comparison of the southern Uralides with the central Variscides. In: Brown, D., Juhlin, C., Puchkov, V. (eds.) Mountain building in the Uralides: Pangea to the present. Geophysical Monograph 132, American Geophysical Union, 83 – 99.

Azor, A. Rubatto, D., Simancas, J. F., González Lodeiro, F., Martínez Poyatos, D., Martín Parra, L. M., Matas, J. (2008) Rheic Ocean ophiolitic remnants in southern Iberia questioned by SHRIMP U-Pb zircon ages on the Beja-Acebuches amphibolites. Tectonics 27, TC5006

Bahlburg, H., Vervoort, J.D., DuFrane, S.A. (2010) Plate tectonic significance of Middle Cambrian and Ordovician siliciclastic rocks of the Bavarian Facies, Armorican Terrane assemblage, Germany; U-Pb and Hf isotope evidence from detrital zircons. Gondwana Research 17, 223 – 235.

Ballèvre, M., Bosse, V., Ducassou, C., Pitra, P. (2009) Palaeozoic history of the Armorican Massif: Models for the tectonic evolution of the suture zones. C. R. Geoscience 341, 174 – 201.

Ballèvre, M., Le Goff, E., Hébert, R. (2001) The tectonothermal evolution of the Cadomian belt of northern Brittany, France: a Neoproterozoic volcanic arc. Tectonophysics 331, 19 – 43.

Bandres, A., Eguíluz, L., Gil Ibarguchi, J. I., Palacios, T. (2002) Geodynamic evolution of a Cadomian arc region: the northern Ossa-Morena zone, Iberian massif. Tectonophysics 352, 105 – 120.

Banka, D., Pharaoh, T.C., Williamson, J.P. & TESZ Project Potential Field Core Group (2002) Potential field imaging of Palaeozoic orogenic structure in northern and central Europe. Tectonophysics 360, 23 – 45.

Bea, F., Fershtater, G.B., Montero, P. (2002) Granitoids of the Uralides : Implications for the Evolution of the Orogen. In: Brown, D., Juhlin, C., Puchkov, V. (eds.) Mountain building in the Uralides: Pangea to the present. Geophysical Monograph 132, American Geophysical Union, 211 – 232.

Beane, R.J., Connelly, J.N. (2000) $^{40}Ar/^{39}Ar$, U-Pb, and Sm-Nd constraints on the timing of metamorphic events in the Maksyutov Complex, Southern Ural Mountains. Journal of the Geological Society, London 157, 811 – 822.

Beckholmen, M., Glodny, J. (2004) Timanian blueschist-facies metamorphism in the Kvarkush metamorphic basement, Northern Urals, Russia. In: Gee, D. G., Pease, V. (eds.) The Neoproterozoic Timanide Orogen of eastern Baltica. Geol. Soc., London, Memoirs 30, 125 – 134.

Berzin, R., Oncken, O., Knapp, J.H., Pérez-Estaún, A., Hismatulin, T., Yunusov, N., Lipilin, A. (1996) Orogenic evolution of the Ural Mountains: Results from an integrated seismic experiment. Science 274, 220 – 221.

Bogdanova, S. V., Pashkevich, I. K., Gorbatschev, R., Orlyuk, M. I. (1996) Riphean rifting and major Palaeoproterozoic crustal boundaries in the basement of the East European Craton: geology and geophysics. Tectonophysics 268, 1 – 21.

Bogolepova, O. K., Gee, D. G. (2004) Early Palaeozoic unconformity across the Timanides, NW Russia. In Gee, D. G., Pease, V. (eds.) The Neoproterozoic Timanide Orogen of eastern Baltica. Geol. Soc., London, Memoirs 30, 145 – 157.

Brown, D., Juhlin, C., Ayala, C., Tryggvason, A., Bea, F., Alvarez-Marron, J., Carbonell, R., Seward, D., Glasmacher, U., Puchkov, V., Perez-Estaun, A. (2008) Mountain building processes during continent-continent collision in the Uralides. Earth Science Reviews 89, 177-195.

Brown, D., Padea, P., Puchkov, V., Alvarez-Marrón, J., Herrington, R., Willner, A.P., Hetzel, R., Gorozhanina, Y., Juhlin, C. (2006) Arc-continent collision in the southern Urals. Earth Science Reviews 79, 261 – 287.

Brown, D., Juhlin, C., Tryggvason, A., Steer, D., Ayarza, P., Beckholmen, M., Rybalka, A., Bliznetsov, M. (2002) The crustal architecture of the Southern and Middle Urals from the URSEIS, ESRU, and Alapaev reflection seismic surveys. In:

Brown, D., Juhlin, C., Puchkov, V. (eds.) Mountain building in the Uralides: Pangea to the present. Geophysical Monograph 132, American Geophysical Union, 33 – 48.

Brown, D., Alvarez-Marron, J., Perez-Estaun, A. (1997) Preservation of a subcritical wedge in the south Urals foreland thrust and fold belt. Journal of the Geological Society, London, 154, 593 – 596.

Castiñeiras, P., Navidad, M., Liesa, M., Carreras, J., Casas, J. M. (2008) U-Pb zircon ages (SHRIMP) for Cadomian and Early Ordovician magmatism in the Eastern Pyrenees: New insights into the pre-Variscan evolution of the northern Gondwana margin. Tectonophysics 461, 228 – 239.

Cawood, P.A., Kröner, A., Collins, W.J., Kusky, T.M., Mooney, W.D., Windley, B.F. (2009) Accretionary orogens through earth history. In: Cawood, P.A., Kröner, A. (eds.) Earth accretionary systems in space and time. The Geological Society, London, Special Publications 318, 1 – 36.

Chantraine, J., Egal, E., Thiéblemont, D., Le Goff, E., Guerrot, C., Ballévre, M., Guennoc, P. (2001) The Cadomian active margin (North Armorican Massif, France): a segment of the North Atlantic Panafrican belt. Tectonophysics 331, 1 – 18.

Chichorro, M., Pereira,M.F., Diaz-Azpiroz, M., Williams, I.S., Fernández, C., Pin,C., Silva,J.B. (2008) Cambrian ensialic rift-related magmatism in the Ossa-Morena Zone (Evora-Aracena metamorphic belt, SW Iberian Massif): Sm-Nd isotopes and SHRIMP zircon U-Th-Pb geochronology. Tectonophysics 461, 91 – 113.

Cloos, M. (1993) Lithospheric buoyancy and collisional orogenesis: Subduction of oceanic plateaus, continental margins, island arcs, spreading ridges, and seamounts. Geol. Soc. Of America Bulletin 105, 715 – 737.

Condie, K. C. (1997) Plate Tectonics and Crustal Evolution, 4$^{th}$ Edition, Butterworth Heinemann, Oxford.

Condie, K.C. (1993) Chemical composition and evolution of the upper continental crust: contrasting results from surface samples and shales. Chemical Geology, 104: 1–37, Amsterdam.

Cullers, R.L. (1995) The controls on the major- and trace-element evolution of shales, siltstones and sandstones of Ordovician to Tertiary age in the Wet Mountains region, Colorado, U.S.A.. Chemical Geology, 123: 107–131, Amsterdam.

Cullers, R.L. (1994) The chemical signature of source rocks in size fractions of Holocene stream sediments derived from metamorphic rocks in the Wet Mountains region, Colorado, U.S.A.. Chemical Geology, 113: 327–343, Amsterdam.

de la Rosa, J., Jenner, G.A., Castro, A. (2002) A study of inherited zircons in granitoid rocks from the South Portuguese and Ossa-Morena Zones, Iberian Massif: support for the exotic origin of the South Portuguese Zone. Tectonophysics 352, 245 – 256.

Duane, M.J., DeWit, M.J. (1988) Pb-Zn ore deposits of the northern Caledonides: Products of continental-scale fluid mixing and tectonic expulsion during continental collision. Geology 16, 999 – 1002.

Echtler, H.P. (1998) Das südliche Uralgebirge – Tektonik eines intakten paläozoischen Kollisionsorogens. Habilitationsschrift Universität Potsdam

Echtler, H.P., Ivanov, K.S., Ronkin, Yu.L., Karsten, L.A., Hetzel, R., Noskov, A.G. (1997) The tectonometamorphic evolution of gneiss complexes in the Middle Urals, Russia: A reappraisal, Tectonophysics 276, 229 – 251.

El Korh, A., Schmidt, S. Th., Ballèvre, M., Ulianov, A., Bruguier, O. (2012) Discovery of an albite gneiss from the Ile de Groix (Armorican Massif, France): geochemistry and LA-ICP-MS U-Pb geochronology of its Ordovician protolith. International Journal of Earth Sciences 101, 1169 – 1190.

Ernst, R.E., Pease, V., Puchkov, V.N., Kozlov, V.I., Sergeeva, N.D., Hamilton, M. (2006) Geochemical characterization of Precambrian magmatic suites of the southeastern margin of the East European Craton, Southern Urals, Russia. Geologichesky Sbornik (Geological Proceedings), 5. Ufimian Institute of Geology, Ufa, pp. 119–161.

Faryad, S. W. (2012) High-pressure polymetamorphic garnet growth in eclogites from the Mariánské Lázne Complex (Bohemian Massif). European Journal of Mineralogy 24, 483 – 497.

Faryad, S.W. (2011) Distribution and geological position of high-/ultrahigh-pressure units within the European Variscan Belt: a review, in Dobrzhinetskaya, L., Faryad, S.W., Wallis, S. Cuthbert, S. (eds.) ‘‘Ultrahigh pressure metamorphism: 25 years after the discovery of coesite and diamond’’, Elsevier, London, 361–397.

Fernández-Suárez, J., Gutiérrez-Alonso, G., Cox, R., Jenner, G. A. (2002) Assembly of the Armorica Microplate: A Strike-Slip Terrane Delivery? Evidence from U-Pb Ages of detrital Zircons. The Journal of Geology 110, 619 – 626.

Fershtater, G.B., Montero, P., Borodina, N.S., Pushkarev, E.V., Smirnov, V., Zinkova, E., Bea, F. (1997) Uralian magmatism: An overview. Tectonophysics 276, 87 – 102.

Finger, F., Gerdes, A., Janousek, V., René, M., Riegler, G. (2007) Resolving the Variscan evolution of the Moldanubian sector of the Bohemian Massif: the significance of the Bavarian and the Moravo-Moldanubian tectonometamorphic phases. Journal of Geosciences 52, 9 – 28.

Finger, F., Roberts, M.P., Haunschmid, B., Schermaier, A., Steyrer, H.P. (1997) Variscan granitoids of central Europe: their typology, potential sources and tectonothermal relations. Mineralogy and Petrology 61, 67 – 96.

Franke, W. (2000) The mid-European segment of the Variscides: tectonostratigraphic units, terrane boundaries and plate tectonic evolution. In: Franke, W., Haak, V., Oncken, O., Tanner, D. (eds.) Orogenic Processes: Quantification and Modelling in the Variscan Belt. Geological Society, London, Special publications 179, 35 – 61.

Franke, W., Haak, V., Oncken, O., Tanner, D. (2000) Orogenic processes: quantification and modelling in the Variscan belt. In: Franke, W., Haak, V., Oncken, O., Tanner, D. (eds.) Orogenic processes: quantification and modelling in the Variscan belt, Geological Society of London, Special Publications 179, 1 – 3.

Friedl, G., Finger, F., Paquette, J.L., von Quadt, A., McNaughton, M.J., Fletcher,I.R. (2004) Pre-Variscan geological events in the Austrian part of the Bohemian Massif deduced from U-Pb zircon ages. International Journal of Earth Sciences 93, 802 – 823.

Frisch, W., Meschede, M., Blakey, R. (2011) Plate Tectonics: Continental Drift and Mountain Building. Springer, Berlin Heidelberg, 212 p.

Ganssloser, M. (2000) Schwermineralanalytische Dokumentation rhenoherzynischer Grauwacken – ein Beitrag zur Liefergebiets-Interpretation. Zeitschrift der deutschen geologischen Gesellschaft 151, 127–170, Stuttgart.

Gao, J., Klemd, R., Qian, Q., Zhang, X., Li, J., Jiang, T., Yang, Y. (2011) The collision between the Yili and Tarim blocks of the southwestern Altaids: Geochemical and age constraints of a leucogranite dike crosscutting the HP-LT metamorphic belt in the Chinese Tianshan Orogen. Tectonophysics 499, 118 – 131.

Gao, J., Long, L., Klemd, R., Qian, Q., Liu, D., Xiong, X., Su, W., Liu, W., Wang, Y., Yang, F. (2009) Tectonic evolution of the South Tianshan orogen and adjacent regions, NW China: geochemical and age constraints of granitoid rocks. International Journal of Earth Sciences 98, 1221 – 1238.

Gee, D. G., Pease, V. (2004) The Neoproterozoic Timanide Orogen of eastern Baltica: introduction. In Gee, D. G., Pease, V. (eds.) The Neoproterozoic Timanide Orogen of eastern Baltica. Geol. Soc., London, Memoirs 30, 1 – 3.

Gee, D.G., Zeyen, H.J. (1996) EUROPROBE 1996 – Lithosphere dynamics: origin and evolution of continents. EUROPROBE Secretariate, Uppsala University, 138 p.

Gerdes, A., Zeh, A. (2006) Combined U-Pb and Hf isotope LA-(MC-)ICP-MS analyses of detrital zircons: Comparison with SHRIMP and new constraints for the provenance and age of an Armorican metasediment in Central Germany. Earth and Planetary Science Letters 249, 47 – 61.

Gerdes, A., Montero, P., Bea, F., Fershater, G., Borodina, N., Osipova, T., Shardakova, G. (2002) Peraluminous granites frequently with mantle-like isotope compositions: the continental-type Murzinka and Dzhabyk batholiths of the eastern Urals. International Journal of Earth Sciences 91, 3 – 19.

Gibbs, A.K., Montgomery, C.W., O'Day, P.A. , Erslev, E.A. (1986) The Archean-Proterozoic transition: Evidence from the geochemistry of metasedimentary rocks of Guyana and Montana. Geochimica Cosmochimica Acta 50, 2125–2141.

Giese, U., Glasmacher, U., Kozlov, V.I., Matenaar, I., Puchkov, V.N., Stroink, L., Bauer, W., Ladage, S., Walter, R. (1999) Structural framework of the Bashkirian anticlinorium, SW Urals. Geol. Rundschau 87, 526 – 544.

Glasmacher, U. A., Bauer, W., Clauer, N., Puchkov, V. N. (2004) Neoproterozoic metamorphism and deformation at the southeastern margin of the East European Craton, Urals, Russia. Int. J. Earth. Sci 93, 921 – 944.

Glodny, J., Pease, V., Montero, P., Austrheim, H., Rusin, A. I. (2004) Protolith ages of eclogites, Marun-Keu Complex, Polar Urals, Russia: implications for the pre- and early Uralian evolution of the northeastern European continental margin. In: Gee, D. G., Pease, V. (eds.) The Neoproterozoic Timanide Orogen of eastern Baltica. Geol. Soc., London, Memoirs 30, 87 – 105.

Glodny, J., Bingen, B., Austrheim, H., Molina, J.F., Rusin, A. (2002) Precise eclogitization ages deduced from Rb/Sr mineral systematics: The Maksyutov complex, Southern Urals, Russia. Geochimica et Cosmochimica Acta 66, 1221 – 1235.

Glodny, J., Austrheim, H., Bingen, B., Rusin, A., Scarrow, J.H. (1999) New age data for high-P rocks and ophiolites along the Main Uralian Fault, Urals, Russia: Implications for the Uralian orogeny. Terra Nostra 99, 89 – 90.

Görz, I., Hielscher, P. (2010) An explicit plate kinematic model for the orogeny in the southern Uralides. Tectonophysics 493, 1 – 26.

Görz, I., Buschmann, B., Kroner, U., Hauer, R., Henning, D. (2009) The Permian emplacement of granite-gneiss complexes in the East Uralian Zone and implications on the geodynamics of the Uralides. Tectonophysics 467, 119 – 130.

Gray, D.R., Foster, D.A. (1997) Orogenic concepts – application and definition: Lachlan Fold Belt, Eastern Australia. American Journal of Science 297, 859 – 891.

Guerrot, C., Peucat, J.J., Capdevila, R., Dosso, L. (1989) Archean protoliths within Early Proterozoic granulitic crust of the west European belt: Possible relics of the West African craton. Geology 17, 241 – 244.

Hann, H.P., Chen, F., Zedler, H., Frisch, W., Loeschke, J. (2003) The Rand Granite in the southern Schwarzwald and ist geodynamic significance in the Variscan belt of SW Germany. International Journal of Earth Sciences 92, 821 – 842.

Haverkamp, J. (1991) Detritusanalyse unterdevonischer Sandsteine des Rheinisch-Ardennischen Schiefergebirges und ihre Bedeutung für die Rekonstruktion der sedimentliefernden Hinterländer: 195 S., Aachen (Dissertation RWTH Aachen University, unpublished)

Haverkamp, J., von Hoegen, J., Kramm, U., Walter, R. (1991) Application of U-Pb-systems from detrital zircons for palaeogeographic reconstructions – a case-study from the Rhenohercynian. Geodinamica Acta, 5 (1991, 1992): 69–82, Paris.

Hegner, E., Kröner, A. (2000) Review of Nd isotopic data and xenocrystic and detrital zircon ages from the pre-Variscan basement in the eastern Bohemian Massif: speculations on palinspastic reconstructions. In: Franke, W., Haak, V., Oncken, O., Tanner, D. (eds.) Orogenic Processes: Quantification and Modelling in the Variscan Belt. Geological Society, London, Special publications 179, 113 – 129.

Herrington, R.J., Zaykov, V.V., Maslennikov, V.V., Brown, D., Puchkov, V.N. (2005) Mineral deposits of the Urals and links to geodynamic evolution. Economic Geology 100th Anniversary Volume, 1069 – 1095.

Hetzel, R., Romer, R.L. (2000) A moderate exhumation rate for the high-pressure Maksyutov Complex, southern Urals, Russia. Geological Journal 35, 327 -344.

Hetzel, R. (1999) Geology and geodynamic evolution of the high-P/low-T Maksyutov complex, southern Urals, Russia. Geologische Rundschau 87, 577 – 588.

Hetzel, R., Romer, R.L. (1999) U – Pb dating of the Verkniy Ufaley intrusion, middle Urals, Russia: a minimum age for subduction and amphibolite facies overprint of the East European continental margin. Geological Magazine 136, 593 – 597.

Hoffmann, U., Breitkreuz, C., Breiter, K., Sergeev, S., Stanek, K., Tichomirova, M. (2013) Carboniferous-Permian volcanic evolution in Central Europe – U/Pb ages of volcanic rocks in Saxony (Germany) and northern Bohemia (Czech Republic). Inernational Journal of Earth Sciences 102, 73 – 99.

Inglis, J.D., Samson, S.D., D'Lemos, R.S., Hamilton, M. (2004) U-Pb geochronological constraints on the tectonothermal evolution of the Palaeoproterozoic basement of Cadomia, La Hague, NW France. Precambrian Research 134, 293 – 315.

Jamtveit, B., Austrheim, H. (2010) Metamorphism: The role of fluids. Elements 6, 153 – 158.

Kisters, A.F.M., Belcher, R.W., Poujol, M., Dziggel, A. (2010) Continental growth and convergence-related arc plutonism in the Mesoarchean; evidence from the Barberton granitoid-greenstone terrain, South Africa. Precambrian Research 178, 15 – 26.

Kisters, A.F.M., Meyer, F.M., Seravkin, I.B., Znamensky, S.E., Kosarev, A.M., Ertl., R.G.W. (1999) The geological setting of lode-gold deposits in the central southern Urals: a review. Geologische Rundschau (International Journal of Earth Sciences) 87, 603 – 616.

Klemd, R., Hegner, E., Bergmann, H., Pfänder, J.A., Li, J.L., Hentschel, F. (2013) Eclogitization of continental crust of the Aktyuz Complex during Late Palaeozoic plate collisions in the Northern Tianshan of Kyrgyzstan. Gondwana Research, 2013, doi: 10.1016/j.gr.2013.08.018.

Klemd, R. (2013) Metasomatism during high-pressure metamorphism: Eclogites and blueschist facies rocks. In: Harlov, D.E., Austrheim, H. (eds.) Metasomatism and the chemical transformation of rocks. Lecture Notes in Earth System Sciences, Springer-Verlag, Berlin, Heidelberg, 351 – 413.

Klemd, R., John, T., Scherer, E.E., Rondenay, S., Gao, J. (2011) Changes in dip of subducted slabs at depth: Petrological and geochronological evidence from HP-UHP rocks (Tianshan, NW-China). Earth and Planetary Science Letters 310, 9 – 20.

Klemd, R. (2010) Early Variscan allochthonous domains: the Münchberg Complex, Frankenberg, Wildenfels, and Góry Sowie. In: Linnemann, U., Romer, R.L. (eds.) Pre-Mesozoic Geology of Saxo-Thuringia – From the Cadomian active margin to the Variscan Orogen. Schweizerbart, Stuttgart, 221 – 232.

Kolb, J., Sindern, S., Kisters, A.F.M., Meyer, M., Hoernes, S., Schneider, J. (2005) Timing of orogenic gold mineralization at Kochkar in the evolution of the East Uralian Granite-Gneiss terrane. Mineralium Deposita 40: 473 – 491.

Krasnobayev, A.A., Cherednichenko, N.V. (2005) The Archean in the Urals: evidence from zircon age. Doklady Earth Sciences 400 (1), 145–148.

Kröner, A. (2010) The role of geochronology in understanding continental evolution. In: Kusky, T.M., Zhai, M.-G., Xiao, W. (eds.) The Evolving Continents: Understanding Processes of Continental Growth. Geological Society, London, Special Publications 338, 179 – 196.

Kroner, U., Romer, R.L. (2010) The Saxo-Thuringian Zone – a tip of the Armorican Spur and part of the Gondwana plate. In: Linnemann, U., Romer, R.L. (eds.) Pre-Mesozoic Geology of Saxo-Thuringia – From the Cadomian active margin to the Variscan Orogen. Schweizerbart, Stuttgart, 371 – 394.

Kroner, U., Romer, R.L., Linnemann, U. (2010) The Saxo-Thuringian Zone of the Variscan Orogen as part of Pangea. In: Linnemann, U., Romer, R.L. (eds.) Pre-Mesozoic Geology of Saxo-Thuringia – From the Cadomian active margin to the Variscan Orogen. Schweizerbart, Stuttgart, 3 – 16.

Kryza, R., Pin, C. (2012) The central-sudetic ophiolites (SW Poland): petrogenetic issues, geochronology and palaeotectonic implications. Gondwana Research 17, 292 – 305.

Linnemann, U., Romer, R.L., Gerdes, A., Jeffries, T.E., Drost, K., Ulrich, J. (2010) The Cadomian orogeny in the Saxo-Thuringian Zone. In: Linnemann, U., Romer, R.L. (eds.) Pre-Mesozoic Geology of Saxo-Thuringia – From the Cadomian active margin to the Variscan Orogen. Schweizerbart, Stuttgart, 37 – 58.

Linnemann, U., Romer, R.L. (2010) Preface. In: Linnemann, U., Romer, R.L. (eds.) Pre-Mesozoic Geology of Saxo-Thuringia – From the Cadomian active margin to the Variscan Orogen. Schweizerbart, Stuttgart, preface.

Linnemann, U., Pereira, F., Jeffries, T.E., Drost, K., Gerdes, A. (2008a) The Cadomian orogeny and the opening of the Rheic Ocean: The diacrony of geotectonic processes constrained by LA-ICP-MS U-Pb zircon dating (Ossa-Morena and Saxo-Thuringian Zones, Iberian and Bohemian Massifs). Tectonophysics 461, 21 – 43.

Linnemann, U., Romer, R.L., Pin, C., Alexandrowski, P., Bula, Z., Geisler, T., Kachlik, V., Kreminska, E., Mazur, S., Motuza, G., Murphy, J.B., Namced, R.D., Pisarevsky, S.A., Schulz, B., Ulrich, J., Wisniewska, J., Zaba, J., Zeh, A. (2008b) The

Precambrian. In: McCann, T. (ed.) The Geology of Central Europe. Geol. Soc., London, 21 – 101.

Linnemann, U., Gerdes, A., Drost, K., Buschmann, B. (2007) The continuum between Cadomian orogenesis and opening of the Rheic ocean: Constraints from LA-ICP-MS U-Pb zircon dating and analysis of plate-tectonic setting (Saxo-Thuringian zone, northeastern Bohemian Massif, Germany). In: Linnemann, U., Nance, R.D., Kraft, P., Zulauf, G. (eds.) The evolution of the Rheic Ocean: From Avalonian-Cadomian active margin to Alleghenian-Variscan collision. Geological Society of America Special Paper 423, 61 – 96.

Lünenschloss, B. (1998): Modellierung der Temperatur- und Fluidgeschichte an der variszischen Front (Verviers-Synklinorium und Nordeifel). – Scientific Technical Report STR98/07: 132 p., Geoforschungszentrum Potsdam, Potsdam.

Lünenschloss, B., Bayer, U., Muchez, P. (1997): Coalification anomalies induced by fluid flow at the Variscan thrust front: a numerical model of the palaeotemperature field. Geol. Mijnbouw 76, 271–275, Dordrecht (Springer).

Martínez-Catalán, J. R. (1990) A non-cylindrical model for the northwest Iberian allochthonous terranes and their equivalents in the Hercynian belt of Western Europe. Tectonophysics 179, 253-272.

Maslov, A. V. (2004) Riphean and Vendian sedimentary sequences of the Timanides and Uralides, the eastern periphery of the East European Craton. In Gee, D. G., Pease, V. (eds.) The Neoproterozoic Timanide Orogen of eastern Baltica. Geol. Soc., London, Memoirs 30, 19 – 35.

Matte, P. (2001) The Variscan collage and orogeny (480 – 290 Ma) and the tectonic definition of the Armorica microplate: a review. Terra Nova 13, 122 – 128.

Matte, P., Maluski, H., Caby, R., Nicolas, A., Kepezhinskas, P., Sobolev, S. (1993) Geodynamic model and $^{40}Ar/^{39}Ar$ dating for the generation and emplacement of the high pressure (HP) metamorphic rocks in SW Urals. Comptes Rendus de l'Academie des Sciences, Serie 2, Mecanique, Physique, Chimie, Sciences de l'Univers, Sciences de la Terre 317, 1667 – 1674.

Mazur, S., Aleksandrowski, P., Turniak, K., Krzeminski, L., Mastalerz, K., Górecka-Nowak, A., Kurowski, L., Krzywiec, P., Zelazniewicz, A., Fanning, M. C. (2010) Uplift and late orogenic deformation of the Central European Variscan belt as revealed by sediment provenance and structural record in the Carboniferous foreland basin of western Poland. International Journal of Earth Sciences 99, 47 – 64.

McLennan, S.M., Hemming, S.R., Taylor, S.R., Eriksson, K.A. (1995) Early Proterozoic crustal evolution: Geochemical and Nd-Pb isotopic evidence from metasedimentary rocks, southwestern North America. Geochimica et Cosmochimica Acta, 59: 1153–1177, Amsterdam.

Melleton, J., Cocherie, A., Faure, M., Rossi, P. (2010) Precambrian protoliths and early Paleozoic magmatism in the French Massif Central; U-Pb data and the north Gondwana connection in the west European Variscan Belt. Gondwana Research 17, 13 – 25.

Meyer, F.M., Kisters, A.F.M., Stroink, L. (1999) Integrated geologic studies along the URSEIS ’95 transect: contributions to the understanding of the orogenic evolution of the southern Urals. Geologische Rundschau (International Journal of Earth Sciences) 87, 497 – 499.

Moore, J.C. (1989) Tectonics and hydrogeology of accretionary prisms: role of the décollement zone. Journal of Structural Geology 11, 95 – 106.

Murphy, J.B., Keppie, J.D., Hynes, A.J. (2009) Ancient orogens and modern analogues: an introduction. In: Murphy, J. B., Keppie, J. D., Hynes, A. J. (eds.) Ancient Orogens and Modern Analogues. Geol. Soc., London, Special Publications 327, 1 – 8.

Murphy, J. B., Gutiérrez-Alonso, G., Nance, R. D., Fernández-Suárez, J., Keppie, J. D., Quesada, C., Dostal, J., Braid, J. A. (2009) Rheic Ocean mafic complexes: overview and synthesis. In: Murphy, J. B., Keppie, J. D., Hynes, A. J. (eds.) Ancient Orogens and Modern Analogues. Geol. Soc., London, Special Publications 327, 343 – 369.

Nance, R.D., Gutiérrez-Alonso, G., Keppie, J.D; Linnemann, U., Murphy, J.B., Quesada, C., Strachan, R.A., Woodcock, N.H. (2012) A brief history of the Rheic Ocean. Geoscience Frontiers, doi:10.1016/j.gsf.2011.11.008.

Nance, R.D., Gutiérrez-Alonso, G., Keppie, J.D., Linnemann, U., Murphy, J.B., Quesada, C., Strachan R.A., Woodcock, N.H. (2010) Evolution of the Rheic Ocean. Gondwana Research 17, 194–222.

Nance, R.D., Murphy, J.B., Strachan, R.A., Keppie, J.D., Gutiérrez-Alonso, G., Fernández-Suárez, J., Quesada, C., Linnemann, U., D'Lemos, R., Pisarevsky, S.A. (2008) Neoproterozoic-early Palaeozoic tectonostratigraphy and palaeogeography of the peri-Gondwanan terranes: Amazonian v. West African connections. Geological Society, London, Special Publications 297, 345 – 383.

Oberc-Dziedzic, T., Kryza, R., Mochnacka, K., Larionov, A. (2010) Ordovician passive continental margin magmatism in the Central-European Variscides: U-Pb zircon data from the SE part of the Karkonosze-Izera Massif, Sudetes, SW Poland. International Journal of Earth Sciences 99, 27 – 46.

Oggiano, G., Gaggero, L., Funedda, A., Buzzi, L., Tiepolo, M. (2010) Multiple early Palaeozoic volcanic events at the northern Gondwana margin; U-Pb age evidence from the southern Variscan branch (Sardinia, Italy). Gondwana Research 17, 44 – 58.

Oliver, J. (1986) Fluids expelled tectonically from orogenic belts: Their role in hydrocarbon migration and other geological phenomena. Geology 14, 99-102.

Oncken, O., Plesch, A., Weber, J., Ricken, W., Schrader, S. (2000) Passive margin detachmend during arc-continent collision (Central European Variscides). In: Franke, W., Haak, V., Oncken, O. & Tanner, D. (eds.) Orogenic Processes: Quantification and Modelling in the Variscan Belt. Geol. Soc., London, Spec. Pub. 179, 179 – 216.

Oncken, O., von Winterfeld, C., Dittmar, U. (1999) Accretion of a rifted passive margin: The Late Palaeozoic Rhenohercynian fold and thrust belt (Middle European Variscides). Tectonics 18 (1), 75 – 91.

Onézime, J., Charvet, J., Faure, M., Chauvet, A., Panis, D. (2002) Structural evolution of the southernmost segment of the West European Variscides : the South Portuguese Zone (SW Iberia). Journal of Structural Geology 24, 451 – 468.

Pastor-Galán, D., Gutiérrez-Alonso, G., Weil, A. B. (2011) Orocline timing through joint analysis: Insights from the Ibero-Armorican Arc. Tectonophysics 507, 31 – 46.

Patocka, F. (1987) The geochemistry of mafic metavolcanics: implications for the origin of the Devonian massive sulphide deposits at Zlaté Hory, Czechoslovakia. Mineralium Deposita 22, 144 – 150.

Pereira,M.F., Chichorro, M., Sola, A.R., Silva, J.B., Sanchez Garcia, T., Bellido, F. (2011) Tracing the Cadomia magmatism with detrital/inherited zircon ages by in situ U/Pb SHRIMP geochronology (Ossa-Morena Zone, SW Iberian Massif). Lithos 123, 204 – 217.

Perez-Estaun, A., Alvarez-Marron, J., Brown, D., Puchkov, V., Gorozhanina, Y., Baryshev, V. (1997) Along-strike structural variations in the foreland thrust and fold belt of the southern Urals. Tectonophysics 276, 265 – 280.

Pin, C., Paquette, J.-L. (1997) A mantle-derived bimodal suite in the Hercynian belt: Nd isotope and trace element evidence for a subduction-related rift origin of the Late Devonian Brévenne metavolcanics, Massif Central (France). Contributions to Mineralogy and Petrology 129, 222 – 238.

Pin, C. (1990) Variscan oceans: Ages, origins and geodynamic implications inferred from geochemical and radiometric data. Tectonophysics 177, 215 – 227.

Pitra, P., Ballèvre, M., Ruffet, G. (2010) Inverted metamorphic field gradient towards a Variscan suture zone (Champtoceaux Complex, Armorican Massif, France). Journal of Metamorphic Geology 28 (2), 183 – 208.

Press, S. (1986) Detrital spinells from alpinotype source rocks in middle Devonian sediments of the Rhenish Massif. Geologische Rundschau 75, 333–340, Berlin.

Puchkov, V.N. (2013) Structural stages and evolution of the Urals. Mineralogy and Petrology 107, 3 – 37.

Puchkov, V.N. (2009a) The evolution of the Uralian orogen. In: Murphy, J.B., Keppie, J.D., Hynes, A.J. (eds.) Ancient orogens and modern analogues. Geological Society London, Special Publications 327, 161 – 195.

Puchkov, V. N. (2009b) The diachronous (step-wise) arc-continent collision in the Urals. Tectonophysics 479, 175 – 184.

Puchkov, V.N. (2000) Palaeogeodynamics of the Southern and Middle Urals. Dauria, Ufa, 146 p. (in Russian)

Puchkov, V.N. (1997) Structure and geodynamics of the Uralian orogen. In: Burg, J.P., Ford, M. (eds.) Orogeny through time. Geological Society Special Publication 121, 201 – 236.

Puelles, P., Gil Ibarguchi, J. I., Beranoaguirre, A., Ábalos, B. (2012) Mantle wedge deformation recorded by high-temperature peridotite fabric superposition and hydrous retrogression (Limo massif, Cabo Ortegal, NW Spain). International Journal of Earth Sciences 101, 1835 – 1853.

Remizov, D., Pease, V. (2004) The Dzela complex, Polar Urals, Russia: a Neoproterozoic island arc. In: Gee, D. G., Pease, V. (eds.) The Neoproterozoic Timanide Orogen of eastern Baltica. Geol. Soc., London, Memoirs 30, 107 – 123.

Ribeiro, A., Munhá, J., Fonseca, P. E., Araújo, A., Pedro, J. C., Mateus, A., Tassinari, C., Machado, G., Jesus, A. (2010) Variscan ophiolite belts in the Ossa-Morena Zone (Southwest Iberia): Geological characterization and geodynamic significance. Gondwana Research 17, 408 – 421.

Romer, R.L., Hahne, K. (2010) Baltica meets Gondwana – the isotope geochemical record. In: Linnemann, U., Romer, R.L. (eds.) Pre-Mesozoic Geology of Saxo-Thuringia – From the Cadomian active margin to the Variscan Orogen. Schweizerbart, Stuttgart, 363 – 370.

Ronkin, Yu.L., Sindern, S., Kramm, U., Lepikhina, O.P. (2008) Isotope geology of the most ancient formations of the Urals: U-Pb, Sm-Nd, Rb-Sr and $^{40}Ar$-$^{39}Ar$ systematics. The International Scientific Conference “The Structurally-Material Complexes and Problems of Geodynamics of the Precambrian Phanerozoic Orogens”, Ekaterinburg 2008, 117 – 120. (in Russian)

Ronkin, Yu.L., Maslov, A.V., Petrov, G.A., Matukov, D.I., Suslov, S.B., Sindern, S., Kramm, U., Lepikhina, O.P. (2007): In situ U-Pb (SHRIMP) dating of zircons from granosyenite of the Troitsk Pluton, Kvarkush-Kamennogorsk Anticlinorium, Central Urals. Doklady Earth Sciences 412, 11 – 16, Pleiades Publishing

Samson,S.D., D'Lemos, R.S. (1998) U-Pb geochronology and Sm-Nd isotopic composition of Proterozoic gneisses, Channel Islands, UK. Journal of the Geological Society, London, 155, 609 – 618.

Sánchez-Martínez, S., Arenas, R., Gerdes, A., Castineiras, P., Potrel, A., Fernández-Suárez, J. (2011) Isotope geochemistry and revised geochronology of the Purrido Ophiolite (Cabo Ortegal Complex, NW Iberian Massif): Devonian magmatism with mixed sources and involved Mesoproterozoic basement. Journal of the Geological Society, London 168, 733 – 750.

Savelieva, G.N., Sharaskin, A.Ya., Saveliev, A.A., Spadea, P., Pertsev, A.N., Babarina, I.I. (2002) Ophiolites and zoned mafic-ultramafic massifs of the Urals: A comparative analysis and some tectonic implications. In: Brown, D., Juhlin, C., Puchkov, V. (eds.) Mountain building in the Uralides: Pangea to the present. Geophysical Monograph 132, American Geophysical Union, 135 – 153.

Scarrow, J., Hetzel, R., Gorozhanin, V.M., Dinn, M., Glodny, J., Gerdes, A., Ayala, C., Montero, P. (2002) Four decades of geochronological work in the southern and middle Urals: A review. In: Brown, D., Juhlin, C., Puchkov, V. (eds.) Mountain building in the Uralides: Pangea to the present. Geophysical Monograph 132, American Geophysical Union, 233 – 255.

Schulte, B.A., Sindern, S. (2002) K-rich fluid metasomatism at high pressure metamorphic conditions: Lawsonite decomposition in rodingitized ultramafite of the Maksyutovo Complex, Southern Urals (Russia). Journal of metamorphic Geology 20, 1-13.

Schulte, B.A., Blümel, P. (1999) Metamorphic evolution of eclogite and associated garnet-mica schist in the high-pressure metamorphic Maksyutov complex, Ural, Russia. Geologische Rundschau 87, 561 – 576.

Schroyen K, Muchez P (2000) Evolution of metamorphic fluids at the Variscan fold-and-thrust belt in eastern Belgium. Sed Geol 131, 163–180.

Seward, D., Brown, D., Hetzel, R., Friberg, M., Gerdes, A., Petrov, G.A., Perez-Estaun, A. (2002) The syn- and post-orogenic low temperature events in the Southern and Middle Urals: evidence from fission-track analysis. In: Brown, D., Juhlin, Chr., Puchkov, V. (eds) Mountain Building in the Urals—Pangea to the present. Geophysical Monograph 132, American Geophysical Union, Washington, pp 257–272.

Simancas, J. F., Tahiri, A., Azor, A., González Lodeiro, F., Martínez Poyatos, D. J., El Hadi, H. (2005) The tectonic frame of the Variscan-Alleghanian orogen in Southern Europe and Northern Africa. Tectonophysics 398, 181 – 198.

Sindern, S., Gerdes, A., Ronkin, Y.L., Dziggel, A., Hetzel, R., Schulte, B.A. (2012a) Monazite stability, composition and geochronology as tracers of Proterozoic events at the eastern margin of the East European Craton (Taratash complex, Middle Urals). Lithos 132-133, 82-97.

Sindern, S., Meyer, F.M., Lögering, M.J., Kolb, J., Vennemann, T., Schwarzbauer, J. (2012b) Fluid evolution at the Variscan front in the vicinity of the Aachen thrust. International Journal of Earth Sciences (Geol Rundsch) 101:87–108.

Sindern, S.,Gerdes, A., Ronkin, Y., Dziggel, A., Schulte, B.A., Hetzel, R., Kramm, U. (2012c) Geochronology of the Archean to Proterozoic Taratash Complex (East European Craton) – evidence for a 1 billion years crustal evolution. European Mineralogical Conference Vol. 1, EMC2012-250.

Sindern, S., Warnsloh, J.M., Trautwein-Bruns, U., Chatziliadou, M., Becker, S., Yüceer, S., Hilgers, C., Kramm, U. (2008) Geochemical composition of sedimentary rocks and imprint of hydrothermal fluid flow at the Variscan front – an example from the RWTH-1 well (Germany). Zeitschrift der Deutschen Gesellschaft für Geowissenschaften 159, 623 – 640.

Sindern, S., Stanjek, H., Hilgers, C., Etoundi, Y. (2007) Short-term hydrothermal effects in the „crystallinities“ of illite and chlorite in the footwall of the Aachen-Faille

du Midi thrust fault – first results of the RWTH-1 drilling project. Clays and Clay Minerals 55, 200 – 212.

Sindern, S., Hetzel, R., Schulte, B.A., Kramm, U., Ronkin, YuL., Maslov, A.V., Lepikhina, O.P. (2005) Proterozoic magmatic and tectonometamorphic evolution of the Taratash complex, Central Urals, Russia, International Journal of Earth Sciences (Geologische Rundschau) 94, 319 – 335.

Sindern, S., Ronkin, Yu.L., Kramm, U., Maslov, A., Lepikhina, O.P. (2003) U-Pb dating of single zircon crystals from nepheline syenites of the Berdyaush Massif, Southern Urals, with application of a $^{205}Pb/^{233}U$ spike. II. Russian Conference on Geochronology, St. Petersburg, 461 – 465.

Sindern, S., Ronkin,Yu., Gronen, L., Winkler, R., Schulte, B.A., Kramm, U. (in prep.) Geochemistry of granitoid and mafic magmatic rocks of the south-eastern Urals, new data from the Mariinskiy and Nishniy Sanarskiy complexes.

Sintubin, M., van Noorden, M., Berwouts, I. (2008) Late Devonian – early Carboniferous contraction-dominated deformation in Central Armorica (Monts d'Arrée, Brittany, France) and its relationship with the closure of the Rheic Ocean. Tectonophysics 461, 343 – 355.

Skrzypek, E., Tabaud, A.-S., Edel, J.-B., Schulmann, K., Cocherie, A., Guerrot, C., Rossi, P. (2012) The significance of Late Devonian ophiolites in the Variscan orogen: a record from the Vosges Klippen Belt. International Journal of Earth Sciences 101, 951 – 972.

Solá, A.R., Pereira, M.F., Williams, I.S., Ribeiro, M.L., Neiva, A.M.R., Montero, P., Bea, F., Zinger, T. (2008) New insights from U-Pb zircon dating of Early Ordovician magmatism on the northern Gondwana margin: The Urra Formation (SW Iberian Massif, Portugal). Tectonophysics 461, 114 – 129.

Stampfli, G.M., von Raumer, J. F., Borel, G. D. (2002) Palaeozoic evolution of pre-Variscan terranes: From Gondwana to the Variscan collision. In: Martínez Catalán, J. R., Hatcher, R. D., Jr., Arenas, R., Díaz García, F. (eds) Variscan-Appalachian dynamics: The building of the late Paleozoic basement: Boulder, Colorado, Geol. Soc. Of America Special Paper 364, 263 – 280.

Stanistreet, I.G., Kukla, P.A., Henry, G. (1991) Sedimentary basinal responses to a Late Precambrian Wilson Cycle: the Damara Orogen and Nama Foreland, Namibia. Journal of African Earth Sciences 13, 141 – 156.

Talavera, C., Montero, P., Bea, F., González Lodeiro, F., Whitehouse, M. (2013) U-Pb zircon geochronology of the Cambro-Ordovician metagranites and metavolcanic rocks of central and NW Iberia. International Journal of Earth Sciences 102, 1 – 23.

Thieblemont, D., Triboulet, C., Godard, G. (1988) Mineralogy, petrology and P-T-t path of Ca-Na amphibole assemblages, Saint-Martin des Noyers formation, Vendeé, France. Journal of metamorphic Geology 6, 697 – 715.

Trautwein-Bruns, U., Schulze, K.C., Becker, S., Kukla, P.A., Urai, J.L. (2010) In situ stress variations at the Variscan deformation front – Results from the deep Aachen geothermal well. Tectonophysics 493, 196 – 211.

Veizer, J., Mackenzie, F.T. (2003) Evolution of sedimentary rocks. In: Mackenzie, F.T. (ed.) Sediments, diagenesis, and sedimentary rocks, 7: 369–407. In: Holland, H.D., Turekian, K.K. (eds.) Treatise on geochemistry, Oxford (Elsevier-Pergamon).

Vidal, P., Auvray, B., Charlot, R., Cogné, J. (1981) Precadomian relicts in the Armorican Massif: Their age and role in the evolution of the western and central European Cadomian-Hercynian Belt. Precambrian Research 14, 1-20.

Von Hoegen, J., Kramm, U., Walter, R. (1990) The Brabant Massif as part of Armorica/Gondwana: U-Pb isotopic evidence from detrital zircons. Tectonophysics 185, 37 – 50.

Von Raumer, J. F., Stampfli, G. M. (2008) The birth of the Rheic Ocean – Early Paleozoic subsidence patterns and subsequent tectonic plate scenarios. Tectonophysics 461, 9 – 20.

Vozarova, A., Sarinova, K., Rodionov, N., Laurinc, D., Paderin, I., Sergeev, S., Lepikhina, E. (2012) U-Pb ages of detrital zircons from Paleozoic metasandstones of the Gelnica Terrane (Southern Gemeric Unit, Western Carpathians, Slovakia): evidence for Avalonian-Amazonian provenance. International Journal of Earth Sciences 101, 919 – 936.

Wendt,J.I., Kröner, A., Fiala, J., Todt, W. (1993) Evidence from zircon dating for existence of approximately 2.1 Ga old crystalline basement of southern Bohemia, Czech Republic. Geologische Rundschau 82, 42 – 50.

Willner, A.P., Barr, S.M., Gerdes, A., Massonne, H.-J., White, C.E. (2013) Origin and evolution of Avalonia: evidence from U-Pb and Lu-Hf isotopes in zircon from the Mira terrane, Canada, and the Stavelot-Venn Massif, Belgium. Journal of the Geological Society, London. Doi: 10.1144/jgs2012-152, published online first

Willner, A. P., Wartho, J. –A., Kramm, U., Puchkov, V. N. (2004) Laser $^{40}Ar/^{39}Ar$ ages of single detrital white mica grains related to the exhumation of Neoproterozoic and Late Devonian high pressure rocks in the Southern Urals (Russia). Geol. Mag. 141 (2), 161 – 172.

Willner, A.P., Sindern, S., Metzger, R., Ermolaeva, T., Kramm, U., Puchkov, V., Kronz, A. (2003) Typology and single grain U/Pb ages of detrital zircon from Proterozoic sandstones in the SW Urals: early time marks at the eastern margin of Baltica. Precambrian Research 124, 1 – 20.

Zak, J., Kraft, P., Hajna, J. (2013) Timing, styles, and kinematics of Cambro-Ordovician extension in the Tepla-Barrandian Unit, Bohemian Massif, and its bearing on the opening of the Rheic Ocean. International Journal of Earth Sciences 102, 415 – 433.

Zeh, A., Will, T.M. (2010) The Mid-German Crystalline Zone. In: Linnemann, U., Romer, R.L. (eds.) Pre-mesozoic geology of Saxo-Thuringia – From the Cadomian Active margin to the Variscan orogeny. Schweizerbart, Stuttgart, 195 – 220.

Zeitlhofer, H., Schneider, D., Grasemann, B., Petrakakis, K., Thöni, M. (2014) Polyphase tectonics and late Variscan extension in Austria (Moldanubian Zone, Strudengau area). International Journal of Earth Sciences 103, 83 – 102.

Zelazniewicz, A., Bula, Z., Fanning, M., Seghedi, A., Zaba, J. (2009) More evidence on Neoproterozoic terranes in Southern Poland and southeastern Romania. Geological Quarterly 53, 93 – 124.

Zhang, X., Tian, J., Gao, J., Klemd, R., Dong, L., Fan, J., Jiang, T., Hu, Ch., Qian, Q. (2012) Geochronology and geochemistry of granitoid rocks from the Zhibo

syngenetic volcanogenic iron ore deposit in the Western Tianshan Mountains (NW-China): Constraints on the age of mineralization and tectonic setting. Gondwana Research 22, 585 – 596.

4.

Sindern, S., Hetzel, R., Schulte, B.A., Kramm, U., Ronkin, YuL., Maslov, A.V., Lepikhina, O.P. (2005) Proterozoic magmatic and tectonometamorphic evolution of the Taratash complex, Central Urals, Russia, International Journal of Earth Sciences (Geologische Rundschau) 94: 319 – 335.

With permission of Springer.

Re-use in thesis granted by Springer, Rights and Permissions, Tiergartenstrasse 17, 69121 Heidelberg, Germany, permission letter 14th of October 2015.

Int J Earth Sci (Geol Rundsch) (2005) 94: 319–335
DOI 10.1007/s00531-005-0489-9

ORIGINAL PAPER

S. Sindern · R. Hetzel · B. A. Schulte · U. Kramm
Yu. L. Ronkin · A. V. Maslov · O. P. Lepikhina

# Proterozoic magmatic and tectonometamorphic evolution of the Taratash complex, Central Urals, Russia

Received: 14 June 2004 / Accepted: 18 March 2005 / Published online: 13 May 2005
© Springer-Verlag 2005

**Abstract** The Taratash Complex (TC) in the northernmost Bashkirian Anticlinorium (Middle Urals) is unique among the pre-Uralian polymetamorphic complexes along the eastern margin of the East European Craton because it experienced granulite facies peak metamorphic conditions (850–900°C/10 kbar). Herein, we constrain the post-granulite facies polystage evolution of the complex, which records various increments of the geodynamic history of the East European continental margin. Formation of granite and migmatite associated with amphibolite facies events are dated at 2,344 ± 29 and 2,044 ± 8 Ma (U–Pb, zircon) in different structural units. At 1,810 ± 41 Ma, the TC was affected by a greenschist facies retrogressive metamorphism which was probably related to a stage of granite formation in the eastern part of the East European Craton. This is confirmed by a U–Pb–zircon age of 1,848 ± 8 Ma obtained from a sheared granite in the adjacent Alexandrovskiy Complex (AC). Greenschist facies shear zones which separate different structural units of the TC formed before 1,350 Ma. Partial re-equilibration of Rb–Sr- and K–Ar-isotope systems between 1,350 Ma and 1,200 Ma is attributed to fluid flow probably induced by anorogenic magmatism in the Bashkirian Anticlinorium. Meso- to Neoproterozoic basaltic dykes indicate that the TC had been exhumed to upper crustal levels at that time. Evidence for a Grenvillian event or for the Timanian orogeny which affected other pre-Uralian complexes in the Urals is lacking. Uralian orogenic shortening and thrusting on Devonian limestones is recorded by shear zones in the AC to the east of the TC and has been dated at 300 Ma (Rb–Sr, $^{40}Ar/^{39}Ar$).

**Keywords** Ural mountains · Taratash Complex · Alexandrovskiy Complex · U–Pb · Rb–Sr · Ar-Ar · Geochronology

S. Sindern · U. Kramm
Institute of Mineralogy and Economic Geology,
RWTH Aachen University, Wüllnerstr. 2,
52062 Aachen, Germany

R. Hetzel
Institute of Geology and Paleontology,
University of Münster, Corrensstraße 24,
48149 Münster, Germany

B. A. Schulte
Philipp-Röth-Weg 58, 64295 Darmstadt, Germany

Y. L. Ronkin · A. V. Maslov · O. P. Lepikhina
Institute of Geology and Geochemistry,
The Urals branch of Russian Academy of Sciences,
Pochtovy Per. 7, Yekaterinburg, 620151, Russia

S. Sindern (✉)
Mineralogical Institute, Zentrallabor für Geochronologie,
WWU-Münster, Corrensstr. 24,
48419 Münster, Germany
E-mail: sindern@rwth-aachen.de
Tel.: +49-241-8095778
Fax: +49-241-8092341

## Introduction

Paleogeographic reconstructions rely on accurate time constraints for well-defined geologic events recorded along the margins of continental blocks. For the Upper Proterozoic history of the East European Craton, different reconstructions exist placing its eastern margin (in present coordinates) either at the margin of Rodinia (e.g. Willner et al., 2003) or opposite of Laurentia (E-Greenland) (Hartz and Torsvik 2002). In order to better define the plate tectonic history of the East European Craton, *PTt* marks for metamorphic, magmatic and deformation events reflecting orogenic activity at the pre-Uralian margin of the East European Craton are needed.

The Ural orogen extends over more than 2,000 km from the Polar regions to near the Aral Sea in Kazakhstan. It resulted from the accretion of island arcs at the East European Craton in Devonian to Carboniferous times and crustal shortening during final collision of the East European Craton and the Siberian–Kazakhian terrane assemblage in Carboniferous to Permian times

(Brown et al. 2001; Hetzel 1999; Puchkov 1997, 2002; Zonenshain et al. 1990). The Main Uralian Fault (Fig. 1) represents the main suture between remnants of island arcs and possible microcontinental fragments to the east (Echtler et al. 1997; Friberg et al. 2000) and the pre-Uralian basement of the East European Craton and its Palaeozoic cover to the west. The western region of the Main Uralian Fault is conventionally divided into three domains: (1) the Central Uralian zone closest to the Main Uralian Fault, (2) the West Uralian zone, and (3) the Pre-Uralian foredeep (Puchkov 1997). The latter consists of Mesoproterozoic to Permian sediments of epizonal to diagenetic grade (Glasmacher et al. 1999; Matenaar et al. 1999; Anfimov 1997), whereas the West Uralian zone comprises folded Meso- to Neoproterozoic (Riphean to Vendian) metasediments (Puchkov 1997; Maslov et al. 1997; Maslov 2004). The most prominent structural features of this zone are the Bashkirian Anticlinorium (e.g. Brown et al. 1997; Giese et al. 1999) in the southern and the Kvarkush Anticlinorium in the northern Urals. Low- to high-grade metamorphic units form the Central Uralian zone. This heterogeneous group of units comprises parts of the continental margin of the East European Craton, which have been—at least some of them—subducted eastwards beneath Devonian island arcs. Devonian high-pressure metamorphism is documented in the Maksyutov Complex (Southern Urals; Matte et al. 1993; Dobretsov et al. 1996; Hetzel et al. 1998; Glodny et al. 2002) and in the East-Ufaley Complex (Middle Urals; Hetzel and Romer 1999; Echtler et al. 1997). Other occurrences are less overprinted by Uralian events but have recently come into the focus of interest because they preserve evidence for a Late Neoproterozoic orogeny (630–570 Ma, Puchkov 1997) along the eastern margin of the East European Craton. This Timanian orogeny can be correlated with the Cadomian events in western Europe (Puchkov 1997; Scarrow 2001; Willner et al. 2003). Occurrences reflecting Timanian magmatic and tectonometamorphic events are the Beloretzk complex (Southern Urals; Glasmacher et al. 1999, 2001, 2004), the Kvarkush Anticlinorium (Northern Urals, Beckholmen and Glodny 2004) and the Enganepe ophiolites and calc-alkaline magmatic rocks of the Polar Urals (Scarrow et al. 2001).

In the Central Uralian zone, the TC (Figs. 1, 2) is unique because of granulite facies metamorphic rocks which are absent in the Ufaley Complex and the Alexandrovskiy Complex (AC) (Fig. 1). The rocks of the TC reflect polyphase imprints of: (1) metamorphism ranging from granulite to greenschist facies conditions, (2) magmatism leading to the formation of migmatites and granites, (3) intensive shearing represented by mylonite zones and (4) mafic magmatism represented by diabase dykes (Lennykh et al. 1978, further references below). The TC thus represents a key locality for research on the Precambrian tectonometamorphic history of the eastern margin of the East European Craton. Existing isotopic age data point to Archean and Proterozoic events (see reviews of Ivanov et al. 1986; Scarrow et al. 2002). In many cases, the relevant publications as compiled in Scarrow et al. (2002) do not report petrographic descriptions or analytical details. This complicates an assessment of the geological significance of the data.

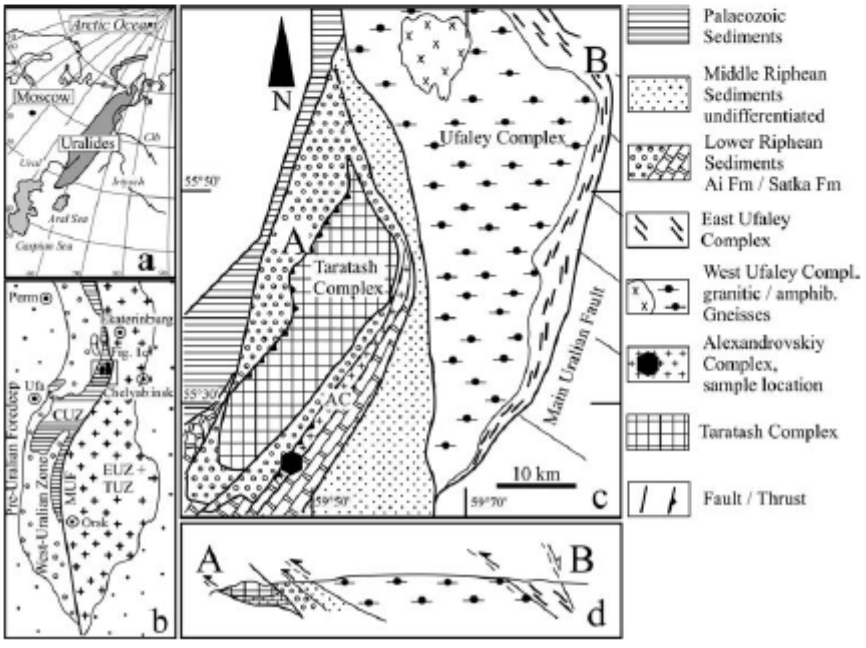


**Fig. 1** Schematic geological maps and profile. **a** overview of the Urals; **b** overview of the Middle and Southern Urals; *CUZ* Central Uralian Zone, *MUF* Main Uralian Fault, *EUZ* East Uralian Zone, *TUZ* Trans-Uralian Zone, box indicates position of Fig. 1c; **c** Geological sketch map of the Taratash Complex (TC), the Alexandrovskiy Complex (*AC*), and the Ufaley Complex, based on Kozlov (1990) and Echtler et al. (1997). The AC constitutes a deformed slice of rocks. Its western margin is a greenschist facies shear zone dipping SE that has a top-NW shear sense indicating that it was active as thrust. The fault on the eastern side is not exposed and has been adopted from Kozlov (1990); **d** schematic profile through points A and B in Fig. 1c, H.P. Echtler and R. Hetzel, unpublished data

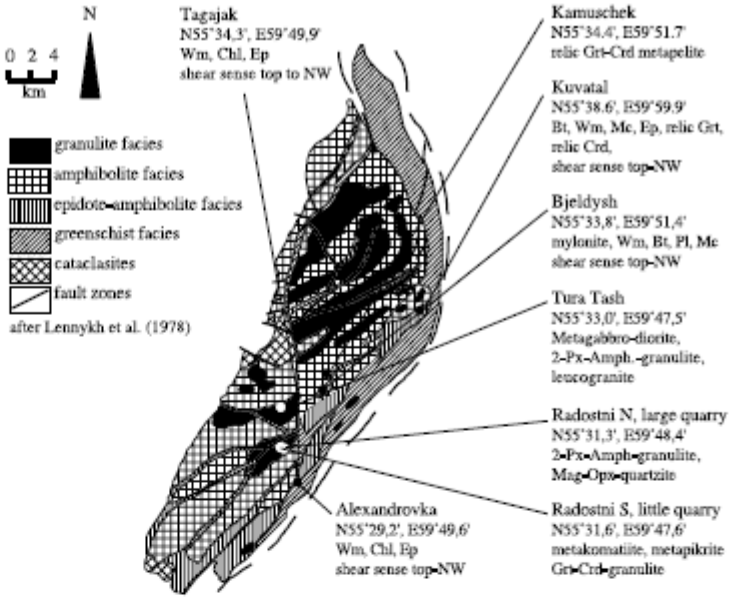


**Fig. 2** Metamorphic facies map of the Taratash Complex (TC), based on Lennykh et al. (1978), showing the different units characterized by granulite and amphibolite facies rocks which are separated by greenschist facies shear zones. *Names and positions* of the sample locations are indicated. See text for further explanation. Abbreviations of mineral names are given in Table 1

Our aim is to give an outline of the geological history of the TC by applying multi-system geochronology ($^{40}Ar/^{39}Ar$, Rb–Sr, U–Pb) combined with petrological and structural investigations. We will also address the small AC positioned 2 km SE of the TC because it gives further information on the Uralian structural overprint of the TC along its eastern border.

## Geological setting

The elongated TC is situated in the northernmost part of the Bashkirian Anticlinorium (Figs. 1, 2) and extends for 25 km NE–SW and 8 km NW–SE. Starting with Garan (1938, in Lennykh et al. 1978), the TC was intensely studied by Russian geologists. In map view, along its tectonic borders, the TC is almost entirely surrounded by Mesoproterozoic (Lower Riphean) metasediments of the Ai Formation (Alekseyev 1984). Drilling proved the existence of Devonian limestones at a depth of 593 m (borehole N 281, Malakhova et al. 1978) beneath the complex, indicating that the final emplacement of the TC by thrusting upon the Devonian limestones occurred during the Uralian orogeny. The AC is in map view surrounded by metasediments of the Ai Formation (Pystin 1978) and structurally separated from the TC by a SE-dipping shear zone.

## Geology of the TC and AC

The TC is composed of several granulite- to amphibolite facies units separated by greenschist facies shear zones. In particular, the eastern part of the complex is dominated by intensely sheared rocks (Fig. 2). A north–south striking greenschist facies shear zone separates the TC into a southwestern and a northeastern unit (Fig. 2). In the granulite- and amphibolite facies rocks, a SW–NE trending and 20–70°W dipping foliation dominates. Tight isoclinal folds with amplitudes of more than 100 m occur. On a metre to decametre scale metabasic layers alternate with metaacidic rocks. In all lithologies, garnet, pyroxene, amphibole and dark micas occur and locally define a cm-scale layering. Ultramafic rocks, metasedimentary (magnetite-) quartzites and metapelitic garnet-cordierite gneisses are rare and form lenses or band-like bodies within the metabasic and metaacidic layers. These contrasting rock-types have presumably been tectonically imbricated in the early history of the complex and are crosscut by sills and irregularly shaped leucosomes. Locally, several generations of leucosomes of granitic to tonalitic compositions cross each other. Some leucosomes contain garnet, amphibole as well as mesoperthitic alkalifeldspar. These leucosomes are bounded by garnet, biotite or amphibole-rich rims and lenses, which are interpreted as restites and thus confirm the anatectic-migmatic character of the leucosomes (Lennykh et al. 1978, this study). Magnetite-quartzites were mined from two large quarries at Radostniy (Fig. 2), which provide good exposure of the granulite to amphibolite facies rocks.

All these units are cut by basaltic dykes (alkalibasaltic to tholeiitic compositions, Lennykh and Petrov 1974). Dykes and volcanic equivalents of similar composition also occur in the Mesoproterozoic rocks surrounding the complex (Lennykh and Petrov 1974; Alekseyev 1984).

Lennykh et al. (1978) divide the rocks of the TC into four formations. Three of the four formations

(Kuwatal-, Schigir-, Radashnaya-Formation) have a similar lithological composition and represent the granulite to amphibolite facies rocks of the central and the western part of the TC. The fourth formation, Tagayak, comprises the greenschist facies shear zones. The shear zones of the TC are characterized by greenschist facies meta-acidic rocks which show intense dynamic recrystallization.

The AC consists of metapelites, metagranites and metadiorites as well as metabasites (amphibolites). The dominant foliation dips to the SSW and is cut by diabase dykes (Pystin 1978). The rocks of the AC as well as of the surrounding marbles (Ai Formation) are all deformed, however, shearing is most intense along the tectonic contacts of the AC.

## Previous geochronometric investigation

More than 100 isotopic age determinations on Taratash samples already exist, approximetely 60 of them are K–Ar ages summarized by Lennykh and Petrov (1974) and Lennykh and Krasnobayev (1978). Three Rb–Sr model ages of feldspar and muscovite are given by Ovchinnikov et al. (1964). Zircons have been dated using the Pb-alpha method (Krasnobayev et al. 1965), the U–Pb-isotope method (Tugarinov et al. 1970) and the "thermo-isochron" method (Krasnobayev and Sumin 1983), an evaporation technique based on the $^{207}Pb/^{206}Pb$ ratio (Sumin 1982) of Pb sequentially released from ca. 2 mg of zircon during heating from 300°C to 1,500°C. These data, which are repeatedly quoted in other publications (e.g. Ivanov et al. 1986; Krasnobayev 1986) and in part summarized by Scarrow et al. (2002), point to granulite facies metamorphism in an age range from >2,800 Ma to 1,800 Ma. Data for granites and migmatites fall between 2,300 Ma and 800 Ma and for mylonites between 2,300 Ma and 900 Ma. The K–Ar dates for basaltic dykes range from 2,052 Ma to 1,161 Ma (Lennykh and Petrov 1974). It has to be pointed out that all the ages, which exceed 2,400 Ma are produced by the Pb-alpha or by the "thermo-isochron" methods. Recently, Ronkin et al. (2003) derived $T_{DM}$ Nd-model ages between 2,030 and 2,560 Ma, from foliated metapelites of the Radostniy quarry. The Nd model ages point to a Palaeoproterozoic origin of the sedimentary precursor of the metapelites.

Within the AC, high K–Ar dates in the age range of 4,385–1,950 Ma on metabasites (whole rock samples) have been interpreted as anomalous due to the presence of excess Ar (Pystin 1978).

**Table 1** Short description of representative samples from the Taratash Complex (TC; see Fig. 2) and AC

| Sample | Locality | Peak metam. grade | Rock: assemblage |
|---|---|---|---|
| Metasediments | | | |
| 104 | Radostni S | Granulite | Grt–Crd granulite: Grt + Crd + Bt + Akf + Pl + Qtz – Wm |
| 124 | Radostni S | Granulite | Mag-quartzite: Opx + Grt + β-Qtz + Amp + Mag |
| 142 | Radostni S | Amphibolite | Metaclastite: Grt + $Bt_1$ + Pl + Qtz – Ep + Chl + $Bt_2$ + Wm + Mag |
| 175 | Radostni N | Granulite | Grt–Crd–granulite: Grt + Crd + Bt + Sil + Akf + Pl + β-Qtz – Wm |
| 26.6 | Radostni N | Amphibolite | Migmatite, leucosome: Pl + Akf + Qtz + Wm |
| 26A | Radostni N | Amphibolite to greenschist. | Amphibolite: Bt + Pl + Epi + Qtz |
| Leucogranite in metased. | | | |
| 34.4 | Tura Tash | Amphibolite | Pl + Qtz + Akf-Epi + Chl |
| Metabasites | | | |
| 145 | Radostni S | Granulite | Metabasic granulite: Opx + Amp + Pl + Qtz + opak – Grt + Bt |
| 179 | Tura Tash | Granulite | Metagabbro: Cpx + Opx + $Amp_1$ + $Pl_1$ + Qtz – $Amp_2$ + Bt + $Pl_2$ + $Qtz_2$ |
| Metaultrabasite | | | |
| 127 | Radostni N | Amphibolite | Talc + Carb + Grt + Ath |
| Mylonitized metagranitoids | | | |
| 78 | Bjeldysch | Epidote amphibolite | [Grt + perthite] - Mc + Pl + Wm + Bt + Qtz |
| 136 | Bjeldysch | Epidote amphibolite | [Grt + perthite]—Mc + Pl + Wm + Bt + Qtz |
| 191 | Kuvatal | Epidote amphibolite | [Grt + Akf] + Bt + Pl + Mc + Wm + Qtz |
| R85 | AC | Greenschist | [Bt]—Ab + Wm + Chl + Qtz |
| R86 | AC | Greenschist | [Bt]—Ab + Wm + Chl + Qtz |
| Mylonitized metasediment | | | |
| 83 | AC | Greenschist | [Bt]—Ab + Wm + Chl + Qtz |

*Akf* alkalifeldspar, *Ab* albite, *Amp* amphibole, *Adr* andradite, *Ath* anthophyllite, *Bt* biotite, *Carb* carbonate, *Chl* chlorite, *Cpx* clinopyroxene, *Crd* cordierite, *Di* diopside, *Ep* epidote, *Grt* garnet, *Mag* magnetite, *Mc* microcline, *Opx* orthopyroxene, *Phl* phlogopite, *Pl* plagioclase, *Qtz* quartz, *Sil* sillimanite, *Wm* white mica, [] resorbed

## Sampling and petrography

For this study, we selected representative samples of characteristic outcrops from the TC (Fig. 2, Table 1). Microprobe analyses (Table 2) for characterization of the metamorphic conditions of the TC were completed at Darmstadt University, Germany. A complete set of data is available from the first author on request. Analytical procedures of microprobe work and isotope analyses are given in the appendix.

### Granulite facies metamorphism

Granulite facies conditions in basic layered rocks (samples 145, 179) are characterized by (1) orthopyroxene + amphibole + (andesine + quartz) and (2) orthopyroxene ($X_{Mg}$ = 0.51–0.54) + clinopyroxene ($X_{Mg}$ = 0.65–0.69) + pargasitic to hastingsitic amphibole (Si p.f.u. = 6.1–6.4, $(Na + K)_A$ = 0.63–0.82, $Na_B$ = 0.02–0.10, $X_{Mg}$ = 0.47–0.56) + andesine + quartz. Small leucocratic layers of acidic composition are characterized by garnet + alkalifeldspar + plagioclase + quartz or

**Table 2** Representative analyses of orthopyroxene, clinopyroxene, garnet, amphibole and phengite of metabasites (sample 179), metasediments (sample 124) from the TC and of mylonitized metagranitoid (sample 86) from the Alexandrovskiy Complex (AC)

| Oxide | Orthopyroxene (179) | | Clinopyroxene (179) | | Oxide | Garnet (124) | | Oxide | Amphibole (179) | | Oxide | Phengite (86) | | |
|---|---|---|---|---|---|---|---|---|---|---|---|---|---|---|
| | No. 54 | No. 63 | No. 9 | No. 56 | | No. 34 | No. 37 | | No. 22 | No. 27 | | No. 11 | No. 20 | No. 21 |
| $SiO_2$ | 51.20 | 51.18 | 52.18 | 51.49 | $SiO_2$ | 37.84 | 37.65 | $SiO_2$ | 40.26 | 42.30 | $SiO_2$ | 49.94 | 50.03 | 49.63 |
| $TiO_2$ | 0.00 | 0.00 | 0.20 | 0.17 | $TiO_2$ | 0.02 | 0.01 | $TiO_2$ | 2.19 | 1.80 | $TiO_2$ | 0.15 | 0.11 | 0.15 |
| $Al_2O_3$ | 0.78 | 0.90 | 1.56 | 1.42 | $Al_2O_3$ | 20.78 | 20.55 | $Al_2O_3$ | 12.39 | 11.03 | $Al_2O_3$ | 30.29 | 30.65 | 30.34 |
| $Cr_2O_3$ | 0.00 | 0.00 | 0.00 | 0.02 | $Cr_2O_3$ | 0.00 | 0.00 | $Cr_2O_3$ | 0.11 | 0.00 | FeO | 4.30 | 3.99 | 3.81 |
| FeO | 29.34 | 27.87 | 11.58 | 10.69 | FeO | 35.81 | 36.86 | FeO | 18.42 | 17.73 | MnO | 0.01 | 0.00 | 0.02 |
| MnO | 0.80 | 0.83 | 0.29 | 0.42 | MnO | 0.39 | 0.36 | MnO | 0.10 | 0.13 | MgO | 1.56 | 1.45 | 1.40 |
| MgO | 16.95 | 17.84 | 12.26 | 12.64 | MgO | 3.36 | 2.70 | MgO | 8.85 | 9.66 | CaO | 0.08 | 0.26 | 0.05 |
| CaO | 0.56 | 0.57 | 21.45 | 22.08 | CaO | 2.34 | 2.25 | CaO | 11.78 | 11.32 | BaO | 0.25 | 0.23 | 0.38 |
| $Na_2O$ | 0.06 | 0.09 | 0.44 | 0.44 | | | | $Na_2O$ | 1.45 | 1.50 | $Na_2O$ | 0.15 | 0.17 | 0.13 |
| $K_2O$ | 0.00 | 0.00 | 0.00 | 0.00 | | | | $K_2O$ | 1.96 | 1.65 | $K_2O$ | 9.72 | 9.23 | 10.44 |
| Sum | 99.69 | 99.28 | 99.96 | 99.37 | Sum | 100.52 | 100.37 | Sum | 97.51 | 97.12 | Sum | 96.46 | 96.12 | 96.36 |

| Cations | Orthopyroxene (179) | | Clinopyroxene (179) | | Cations | Garnet (124) | | Cations | Amphibole (179) | | Cations | Phengite (86) | | |
|---|---|---|---|---|---|---|---|---|---|---|---|---|---|---|
| | 6 O | | 6 O | | | 12 O | | | 23 O | | | 11O | | |
| Si | 1.98 | 1.98 | 1.97 | 1.96 | Si | 3.02 | 3.03 | Si | 6.15 | 6.42 | Si | 3.31 | 3.31 | 3.30 |
| $Al^{IV}$ | 0.02 | 0.02 | 0.03 | 0.04 | $Al^{IV}$ | 0.00 | 0.00 | $Al^{IV}$ | 1.85 | 1.58 | $Al^{tot}$ | 2.36 | 2.39 | 2.38 |
| $Al^{VI}$ | 0.02 | 0.02 | 0.04 | 0.02 | $Al^{VI}$ | 1.96 | 1.95 | $Al^{VI}$ | 0.39 | 0.40 | Ti | 0.01 | 0.01 | 0.01 |
| $Fe^{3+}$ | 0.00 | 0.00 | 0.00 | 0.01 | $Fe^{3+}$ | 0.04 | 0.05 | $Fe^{3+}$ | 0.21 | 0.21 | Fe | 0.23 | 0.22 | 0.21 |
| Ti | 0.00 | 0.00 | 0.01 | 0.01 | Ti | 0.00 | 0.00 | Ti | 0.25 | 0.21 | Mn | 0.00 | 0.00 | 0.00 |
| Cr | 0.00 | 0.00 | 0.00 | 0.00 | Cr | 0.00 | 0.00 | Cr | 0.01 | 0.00 | Mg | 0.15 | 0.14 | 0.14 |
| Fe | 0.95 | 0.90 | 0.37 | 0.33 | Fe2+ | 2.35 | 2.43 | $Fe^{2+}$ | 2.14 | 2.05 | Ca | 0.01 | 0.02 | 0.00 |
| Mn | 0.03 | 0.03 | 0.01 | 0.01 | Mn | 0.03 | 0.03 | Mn | 0.01 | 0.02 | Ba | 0.01 | 0.01 | 0.01 |
| Mg | 0.98 | 1.03 | 0.69 | 0.72 | Mg | 0.40 | 0.32 | Mg | 2.02 | 2.19 | Na | 0.02 | 0.02 | 0.02 |
| Ca | 0.02 | 0.02 | 0.87 | 0.90 | Ca | 0.20 | 0.19 | Ca | 1.93 | 1.84 | K | 0.82 | 0.78 | 0.89 |
| Na | 0.01 | 0.01 | 0.03 | 0.03 | | | | $Na_A$ | 0.39 | 0.34 | | | | |
| K | 0.00 | 0.00 | 0.00 | 0.00 | | | | $Na_B$ | 0.04 | 0.10 | | | | |
| | | | | | | | | $K_A$ | 0.38 | 0.32 | | | | |
| Sum | 4.01 | 3.99 | 4.02 | 4.04 | | 8.00 | 8.00 | Sum | 7.77 | 7.68 | | | | |

| | Orthopyroxene (179) | | Clinopyroxene (179) | | | Garnet (124) | | | Amphibole (179) | | Phengite (86) | | |
|---|---|---|---|---|---|---|---|---|---|---|---|---|---|
| | No. 54 | No. 63 | No. 9 | No. 56 | | No. 34 | No. 37 | | No. 22 | No. 27 | No. 11 | No. 20 | No. 21 |
| $X_{Mg}$ | 0.51 | 0.53 | 0.65 | 0.69 | $X_{Mg}$ | 0.15 | 0.12 | $X_{Mg}$ | 0.48 | 0.52 | | | |
| | | | | | Alm | 0.79 | 0.82 | | | | | | |
| | | | | | Prp | 0.13 | 0.11 | | | | | | |
| | | | | | Sps | 0.01 | 0.01 | | | | | | |
| | | | | | Grs | 0.05 | 0.04 | | | | | | |
| | | | | | Adr | 0.02 | 0.03 | | | | | | |

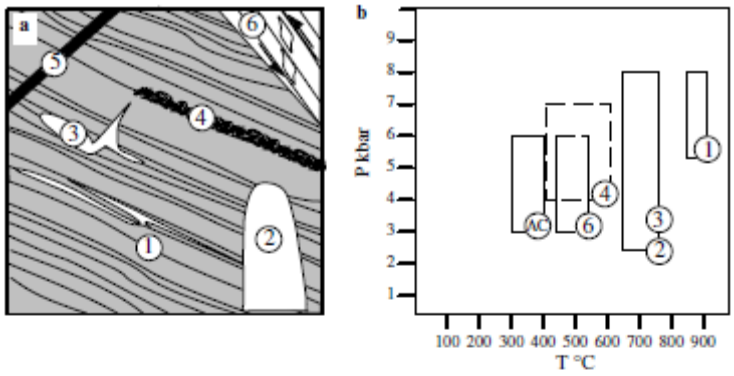


**Fig. 3** **a** Overview of the major rock types studied and their structural relationships in the TC: *1* foliated granulite facies rocks (metabasites, metagranites, rare metapelites, migmatites) with amphibolite facies overprint; *2* leucogranite of Tura Tash; *3* migmatite crosscutting metamorphic foliation; *4* retrograde amphibolite characterized by coarse grained biotite and plagioclase; *5* diabase dykes; *6* epidote-amphibolite facies shear zones of the Taratash Complex; **b** *P–T* conditions for the formation of different units indicated in Fig. 3a. AC denotes the shear zones studied in the Alexandrovskiy Complex

orthopyroxene + plagioclase + quartz. Garnetites at the rims of the leucosomes are interpreted as restites and together with the leucosomes point to the migmatic–granulitic origin of these acidic rocks (Schulte and Sindern 2001). Metapsammitic quartzite with garnet ($X_{Mg}$ = 0.10–0.15) + orthopyroxene ($X_{Mg}$ = 0.34–0.36) + β-quartz (sample 124) and metapelite with garnet + cordierite + alkalifeldspar + quartz + plagioclase (samples 104, 175) only occur locally as lenses or layers. *PT* calculations for the latter assemblages yield peak metamorphic conditions of 850–900°C/5.3–8.0 kbar (No. 1 in Fig. 3, Sindern et al. 2001). All granulite facies rocks are foliated indicating that deformation occurred during the granulite facies metamorphic event. Chessboard-like subgrains in quartz indicate that this foliation formed at granulite to high amphibolite facies conditions (Kruhl 1996, sample 104, Table 1). Deformation under peak metamorphic, i.e. granulite facies, conditions was followed by fast cooling as indicated by the preservation of growth zonation in metapelitic garnet (Sindern et al. 2001).

## Amphibolite facies metamorphism

In all outcrops, the granulite facies assemblages have been overprinted under amphibolite facies conditions. Overprinting caused recrystallization of plagioclase and quartz, resorption of garnet and alkalifeldspar in the metagranitic rocks as well as of pyroxene in the metabasites. The amphibolite facies metamorphism produced new biotite or sillimanite in the metagranitic and metapelitic rocks and new amphibole, garnet or biotite in the metabasic and ultrabasic rocks (sample 124). Locally, migmatites were formed as indicated by the assemblage white mica–alkalifeldspar—plagioclase–quartz in an undeformed leucosome crosscutting the metamorphic foliation in the Radostni quarry (sample 26.6, No. 3 in Fig. 3, Table 1). The latter observation supports the conclusion that the foliation formed predominantly during the granulite facies event. An undeformed and thus probably post-peak metamorphic (i.e. post-granulite facies) leucocratic granite was sampled at mountain Tura Tash (sample 34.4, No. 2 in Fig. 3). The rock is predominantly composed of slightly sericitized microcline and oligoclase as well as of quartz. Minor components are epidote and chlorite (Table 1).

Temperatures are constrained to be between 650°C and 750°C by eutectic granite melting temperatures and stability of muscovite at $P_{H_2O} = 1$ (Spear et al. 1999). The pressure interval is defined by the sillimanite stability that ranges between 2.5 and 8 kbar at 750°C (Spear et al. 1999).

## Shear zones in the TC and AC

In all shear zone outcrops of the TC (Fig. 2, No. 6 in Fig. 3) foliation dips 50–75°E to SE, and the stretching lineation plunges SE. Kinematic indicators such as S-C fabrics and σ-clasts show a consistent top-to-the NW shear sense. Sheared metapelitic to metagranitic rocks exhibit intense dynamic recrystallization. In these mylonites, white mica (< 400 μm) and biotite (< 800 μm) define the foliation, garnet (< 800 μm) is resorbed and K-feldspar and plagioclase recrystallize at their margins, thus forming core-and-mantle structures (samples 78, 136, 137, 191). Together with the recrystallization of biotite, these features indicate temperatures of 450–550°C (c.f. Pryer 1993) for this phase of deformation.

The shear zone exposed in the AC shows mylonitized granitoid rocks with S-C fabrics (samples 83, 85 and 86) and rare metapelites characterized by shear bands. Similar to the shear zones in the TC, foliation dips SE and shear sense indicators show a consistent top-to-the NW shear sense. Dominant modal components are

albite, dynamically recrystallized quartz and white mica. Biotite reacted syn-kinematically to chlorite as shown by chlorite aligned parallel to the foliation. This reaction and the dynamic recrystallization of quartz point to shear zone formation under lower greenschist facies conditions (300–400°C, e.g. Passchier and Trouw 1996). White mica (<200 μm) occurs in shear bands (samples 83 and 86) and as larger crystals (200–500 μm). Despite the different textural positions, white mica is chemically relatively homogeneous. The Si-contents vary between 3.24 and 3.33 (p.f.u.) indicating a minimum pressure of 3–6 kbar for a temperature range of 300–400°C (Massonne and Schreyer 1987).

### Local retrogression

Apart from the amphibolite facies metamorphism and the mylonitization mentioned so far, sericitization of feldspars as well as skarn and magnetite formation have been recognized (Table 1) as events subsequent to granulite facies metamorphism. In some parts of the Radostni quarry (Fig. 2), coarse grained biotite–plagioclase assemblages occur in the amphibolite facies metabasites (sample 26.A, No. 4 in Fig. 3). In order to explain the input of K and $H_2O$, these assemblages are interpreted to have formed by a fluid-driven retrogressive recrystallization event under lower amphibolite facies to greenschist facies conditions. In the metasediments, magnetite grows along grain boundaries and occurs along cracks together with quartz (sample 142).

## Isotope data

Petrographic evidence indicates that the rocks of the TC were affected by several tectonometamorphic events which renders isotopic age dating difficult. In the following, we line out geochronologic results for samples qualified by their comparatively simple and thus well-understood tectonometamorphic record.

### TC, early post-peak metamorphic HT events

Zircon from the Tura Tash granite (sample 34.4) is euhedral, short-prismatic and clear. Three zircon fractions of 2–3 grains (<250 μm) that were analysed for their U–Pb systematics define a discordia with an upper intercept of 2,344±29 Ma (Table 3, Fig. 4a), which is considered to date the crystallization of the granite. The undeformed nature of the rock implies that it is younger than the granulite facies metamorphism. Strictly speaking, this age thus provides a minimum age for the high-grade metamorphic event. However, since granite formation and granulite facies metamorphism are likely to be related, the granulite facies metamorphism is probably not much older. Such assumption is supported by the results of Ronkin et al. (2003) who derive maximum $T_{DM}$ Nd-model ages of 2,560 Ma for the sedimentary precursor of the metapelites.

The amphibolite facies leucosome from Radostniy (Sample 26.6) contains zircon characterized by milky disturbed cores with euhedral clear brownish overgrowths. The well-developed prism and pyramidal crystal faces of the overgrowths most probably formed in a magmatic melt. It is plausible to assume that this was the leucocratic melt formed during the migmatization event. The crystals (size fraction 250–355 μm) were crushed and fragments of the overgrowth fraction were separated. Fractions of the fragments yielded $^{206}Pb/^{235}U$- and $^{207}Pb/^{235}U$ ratios, which define a discordia intersecting the concordia at 2,044±8 Ma, which is interpreted as the age of the migmatite forming event (Fig. 4b).

**Table 3** Analytical data of the studied U–Pb systems in zircon from samples of the TC and AC, errors are absolute errors

| Sample | Pb[a] (ng) | U[b] (ng) | $^{206}Pb/^{204}Pb$ ratio[c] and 2σ error | $^{207}Pb/^{206}Pb$ ratio[d] and 2σ error | $^{207}Pb/^{235}U$ ratio[d] and 2σ error | $^{206}Pb/^{235}U$ ratio[d] and 2σ error | $^{207}Pb/^{206}Pb$ age (Ma) | $^{207}Pb/^{235}U$ age (Ma) | $^{206}Pb/^{235}U$ age (Ma) |
|---|---|---|---|---|---|---|---|---|---|
| Radostniy, TC, migmatite | | | | | | | | | |
| 26/6-B2 | 8.16 | 21.77 | 1877.0±6.8 | 0.12507±0.00061 | 5.737±0.250 | 0.3330±0.0140 | 2,030 | 1,937 | 1,851 |
| 26/6-B3 | 5.62 | 14.21 | 1,261.9±0.6 | 0.12477±0.00041 | 6.015±0.133 | 0.3496±0.0071 | 2,026 | 1,978 | 1,933 |
| 26/6-4 | 4.8 | 12.29 | 1,0206.6±0.6 | 0.12591±0.00020 | 6.289±0.026 | 0.3623±0.0014 | 2,042 | 2,017 | 1,993 |
| 26/6-5 | 0.02 | 2.43 | 1,876.3±0.53 | 0.12550±0.00030 | 5.872±0.031 | 0.3393±0.0016 | 2,036 | 1,957 | 1,883 |
| Tura Tash, TC, granite | | | | | | | | | |
| 34/4-1 | 1.67 | 4.1 | 1,640.9±0.6 | 0.14965±0.00029 | 7.425±0.0690 | 0.3598±0.0033 | 2,342 | 2,164 | 1,981 |
| 34/4-2 | 1.64 | 3.51 | 2,464.5±0.9 | 0.14962±0.00026 | 8.550±0.038 | 0.4144±0.0017 | 2,342 | 2,291 | 2,235 |
| 34/4-1/3[e] | 1.93 | 5.7 | 489.3±0.2 | 0.14039±0.00030 | 5.982±0.094 | 0.3091±0.0048 | 2,232 | 1,973 | 1,736 |
| 34/4-1/4 | 0.8 | 2.58 | 1,492.9±0.3 | 0.14892±0.00026 | 5.883±0.041 | 0.2865±0.0019 | 2,334 | 1,959 | 1,624 |
| AC, mylonite | | | | | | | | | |
| R85-3 | 1.8 | 6.62 | 4,147.8±0.4 | 0.10785±0.00018 | 3.781±0.020 | 0.2542±0.0013 | 1,763 | 1,589 | 1,460 |
| R85-4 | 3.82 | 10.61 | 3,814.7±0.3 | 0.11307±0.00017 | 5.210±0.044 | 0.3342±0.0028 | 1,849 | 1,854 | 1,859 |

[a] Amount of $^{207}Pb$, $^{206}Pb$ and $^{204}Pb$ in zircon
[b] Amount of U in zircon
[c] Corrected for spike and fractionation
[d] Atomic ratios corrected for blank, spike, fractionation and initial common Pb
[e] Not used for age calculation

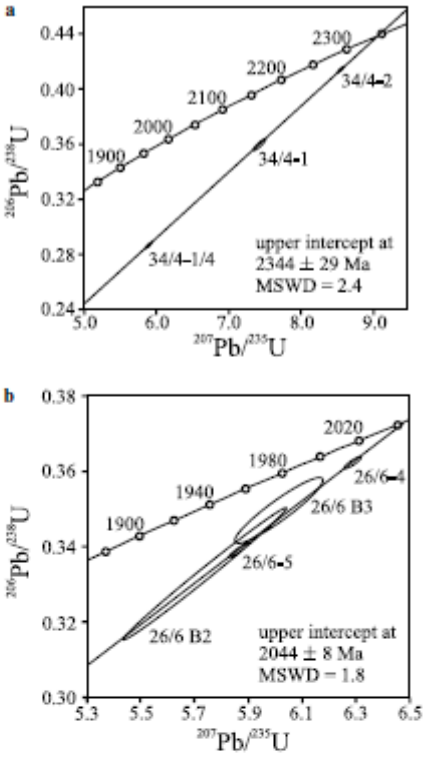


**Fig. 4** U–Pb Concordia diagrams for **a** zircons from the leucocratic granite from mountain Tura Tash, sample 34.4 and **b** migmatite leucosome from Radostniy quarry, sample 26.6

TC, lower amphibolite to greenschist facies event

The retrograde metamorphic event, which leads to the formation of coarse grained biotite-plagioclase assemblages in the amphibolites (sample 26A, Table 4, Fig. 5), has been dated using the Rb–Sr isochron method. Rb–Sr isotope signatures of the rock-forming minerals, biotite and plagioclase, define a two-point isochron yielding an age of 1,810 ± 41 Ma. Although the whole rock plots on the isochron, it was not used for age calculation because its isotopic composition is not independent of the two rock-forming minerals.

TC, shear zones

The mylonite samples 78 and 92 (Table 1) taken from the same outcrop are petrographically identical. Sample 78 was used for a study of spatial isotope homogenization using the thin slab technique (Table 4, Fig. 6, Hofmann 1979; Hradetzky and Lippolt 1993). The foliated mylonite was cut (perpendicular to foliation) into slices representing different laminae. Subsequently each slice (P2 to P8,) was analysed for its Rb–Sr isotope signatures (Table 4). Calculation of the former $^{87}Sr/^{86}Sr$ ratios of each slice, successively backward in time, indicates that there was no complete isotopic equilibration for any hypothetic age. This may indicate that either at the scale of the hand specimen isotopic homogenization by mylonitization was incomplete or that the isotopic signatures of the individual laminae were disturbed during a later event. Both alternatives do not exclude each other. Figure 6 shows that apparently Sr isotopic equilibrium was approached for the slices P2, P3, P5, P6 between 1,200 Ma and 1,350 Ma.

White mica and biotite from mylonites were also dated using the $^{39}Ar/^{40}Ar$ step heating technique. Detection of $^{37}Ar$, $^{38}Ar$ and $^{39}Ar$, produced by the irradiation of Ca, Cl and K, respectively, allows to calculate the abundance of these elements in each heating step. The ratios of these elements combined with the age information (calculated from the $^{40}Ar/^{39}Ar$ ratio) and the $^{36}Ar/^{40}Ar$ ratio (indicative of the proportion of atmospheric Ar) characterize each heating step (e.g. Villa et al. 2000). Thus, the distribution of these signatures helps to assess the homogeneity of the sample and degassing from crystal domains or impurities with different Ar reservoirs can be detected (e.g. Villa et al. 2000; De Gregorio et al. 2003).

**Table 4** Rb and Sr concentrations and isotope compositions for whole-rock samples and mineral fractions of samples from the TC and AC. Errors are within-run precisions (2σ-level)

| Sample | Rb (ppm) | Sr (ppm) | $^{87}Rb/^{86}Sr$ | $^{87}Sr/^{86}Sr$ |
|---|---|---|---|---|
| Diaphtorite, Radostniy, TC | | | | |
| 26-1, Whole rock | 112 | 271 | 1.2051 ± 0.0014 | 0.76881 ± 00.00002 |
| 26-2, Plagioclase | 3 | 405 | 0.0233 ± 00.00001 | 0.73820 ± 00.00002 |
| 26-4, Biotite | 565 | 7 | 695.2 ± 16.2 | 18.8379 ± 0.00027 |
| Mylonite, 78, Bjeldysh, TC | | | | |
| P2, Thin slab profile | 114 | 239 | 1.3920 ± 0.0020 | 0.76253 ± 0.000014 |
| P3 | 128 | 213 | 1.7539 ± 0.0015 | 0.76894 ± 0.000013 |
| P4 | 128 | 219 | 1.6999 ± 0.0050 | 0.76921 ± 0.000013 |
| P5 | 118 | 205 | 1.6687 ± 0.0104 | 0.76701 ± 0.000011 |
| P6 | 134 | 275 | 1.4148 ± 0.0024 | 0.76328 ± 0.000015 |
| P7 | 258 | 405 | 1.8575 ± 0.0048 | 0.77437 ± 0.000010 |
| P8 | 265 | 409 | 1.8897 ± 0.0121 | 0.77508 ± 0.000023 |
| Mylonite, AC | | | | |
| 83Wr, Whole rock | 35 | 236 | 0.4358 ± 0.0014 | 0.74331 ± 0.00002 |
| 83Hg1, White mica, 250–500 μm | 369 | 41 | 26.42 ± 0.37 | 0.85480 ± 0.00008 |
| 83Hg2, White mica, 80–125 μm | 338 | 32 | 31.419 ± 0.083 | 0.87589 ± 0.00002 |

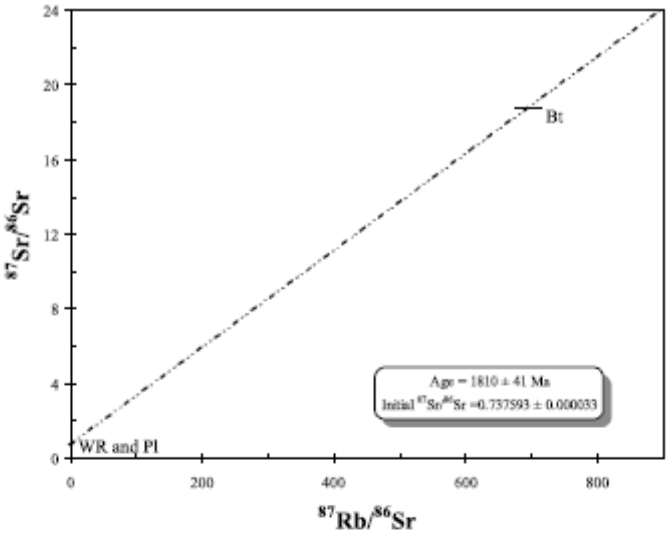


**Fig. 5** Rb–Sr-isochron diagram for the greenschist facies retrograde metabasite sample 26A from Radostniy quarry. Age calculation based on isotope signatures of biotite and plagioclase fractions

The $^{40}Ar/^{39}Ar$ spectra of white mica from the same sample (78) and of biotite from sample 92 have complex age patterns. Heating steps of white mica from sample 78 show a heterogeneous distribution of Cl/K ratios which do not correlate with the age information (Table 5, Figs. 7, 8). This indicates the presence of various Ar reservoirs with apparent ages ranging between 1,126 Ma and 1,301 Ma which is roughly in line with the Rb–Sr data of that sample mentioned above. The heating steps of biotite from mylonite sample 92 are also characterized by a complex pattern of age and Cl/K ratios. Heating steps 2, 3, 4, 7 and 8 of this analysis form a cluster in the Cl/K-age correlation plot (Cl/K $<0.015$) and are characterized by low $^{36}Ar/^{40}Ar$ ratios (Table 5). Though these steps do not define an inverse isochron, indicative of slightly different Ar reservoirs, the low scatter with respect to $^{36}Ar/^{40}Ar$ and $^{39}Ar/^{40}Ar$ ratios allows us to assign an age of 1,336 ± 25 Ma represented by 73.3% of the degassed $^{39}Ar$ to these steps. Thus, the Rb–Sr- and Ar–Ar data most probably point to a deformation event between ca. 1,200 Ma and 1,350 Ma, to be discussed below (Fig. 8).

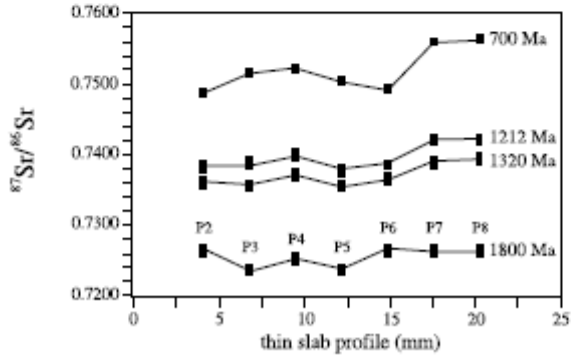


**Fig. 6** Calculated $^{87}Sr/^{86}Sr$ ratios for 700, 1,212, 1,320 and 1,800 Ma of the thin slab profile of mylonite sample 78. P2 to P8 denote the centres of thin slabs, the vertical extension of the symbols indicates the error due to uncertainty of the $^{87}Rb/^{86}Sr$ ratio

## AC, magmatic HT event

Two zircon fractions (size 125–250 µm, prismatic, clear, brownish) from the mylonite sample 85 from the AC were analysed for their U–Pb systematics. The concordant zircon age of 1,848 ± 8 Ma (Table 3) is considered to date the crystallization of the precursor granite of mylonite sample 85 (Fig. 9). The greenschist facies mylonitization obviously did not affect the U–Pb systems in zircon.

## AC, shear zones

The petrographic investigation of the mylonites from the AC (samples 83, 85, 86) shows pervasive recrystallization. Two white mica fractions from one sample (80–125 µm, 83A and 250–500 µm, 83B) have complex $^{40}Ar/^{39}Ar$ apparent age patterns and do not define isochrons (Fig. 10, Table 5). The Cl/K ratios show in both cases a contribution between lower ($<0.0005$) and higher values ($>0.0008$, Table 5). Using age information from heating steps with Cl/K $<0.0005$ one can assign ages of 304 ± 7 Ma (steps 2–8, representing 84% of total degassed $^{39}Ar$) to sample 83A and 306 ± 5 Ma (steps 3, 4, 5, 6, 8, representing 77% of total degassed $^{39}Ar$) to sample 83B.

The same white mica fractions define a two-point Rb–Sr isochron with an age of 296 ± 28 Ma. The

**Table 5** Analytical data of the $^{40}Ar/^{39}Ar$ analyses of biotite and white mica from samples of the Taratash and Alexandrovskiy Complexes. All Ar concentrations are given in picolitres per gram (pL/g); Cl/K ratios are calculated from the total $^{38}Ar$ and $^{39}Ar$, the production ratios and the irradiation time. Ages are given in Ma. Errors are 1σ. $J = 0.0044$

| Step | $T$ (°C) | $^{40}Ar_{tot}$ | $^{39}Ar$ | $^{38}Ar$ | $^{37}Ar$ | Cl/K | $^{36}Ar$ | Age ± 1s |
|---|---|---|---|---|---|---|---|---|
| Taratash Complex | | | | | | | | |
| 78, White mica, 125–250 μm, 1.58 mg | | | | | | | | |
| 1 | 679 | 17,475.0000 ± 0.0092 | 173.1595 ± 0.0005 | 4.9432 ± 0.0002 | 0.1206 ± 0.0004 | 0.0030 ± 0.0002 | 3.2766 ± 0.0002 | 587.0 ± 1.3 |
| 2 | 730 | 26,431.3291 ± 0.0025 | 184.9886 ± 0.0004 | 3.3018 ± 0.0003 | 1.2742 ± 0.0006 | 0.0011 ± 0.0002 | 1.3426 ± 0.0002 | 811.2 ± 1.2 |
| 3 | 751 | 105,251.8987 ± 0.0074 | 523.7829 ± 0.0008 | 9.4902 ± 0.0003 | 2.3976 ± 0.0010 | 0.0013 ± 0.0001 | 1.9739 ± 0.0002 | 1,066.5 ± 0.8 |
| 4 | 777 | 46,090.8228 ± 0.0036 | 230.8089 ± 0.0004 | 4.1662 ± 0.0002 | 1.5136 ± 0.0008 | 0.0011 ± 0.0002 | 2.1086 ± 0.0002 | 1,055.1 ± 1.0 |
| 5 | 804 | 32,082.0886 ± 0.0039 | 152.9949 ± 0.0004 | 2.6152 ± 0.0003 | 0.5711 ± 0.0005 | 0.0007 ± 0.0003 | 1.8331 ± 0.0002 | 1,091.8 ± 1.5 |
| 6 | 853 | 42,694.7468 ± 0.0027 | 199.2000 ± 0.0003 | 2.8319 ± 0.0002 | 0.0000 ± 0.0000 | 0.0002 ± 0.0002 | 1.5996 ± 0.0002 | 1,114.8 ± 1.1 |
| 7 | 919 | 51,237.7848 ± 0.0048 | 244.8759 ± 0.0004 | 4.9389 ± 0.0003 | 2.3778 ± 0.0006 | 0.0016 ± 0.0002 | 2.1651 ± 0.0002 | 1,093.7 ± 1.1 |
| 8 | 1,080 | 111,173.4177 ± 0.0067 | 471.6525 ± 0.0007 | 8.2204 ± 0.0002 | 3.8622 ± 0.0008 | 0.0010 ± 0.0001 | 3.7630 ± 0.0002 | 1,196.8 ± 0.9 |
| 9 | 1,394 | 58,701.5190 ± 0.0076 | 233.2994 ± 0.0004 | 5.9539 ± 0.0002 | 1.2944 ± 0.0008 | 0.0015 ± 0.0001 | 8.9644 ± 0.0002 | 1,222.5 ± 1.1 |
| 92, Biotite, 250–500 μm, 1.59 mg, assigned age 1,336 ± 25 Ma, steps 2, 3, 4, 7, 8, Cl/K < 0,015, $^{36}Ar/^{40}Ar$ < 0,000519 | | | | | | | | |
| 1 | 545 | 59,535.8491 ± 0.0017 | 265.9226 ± 0.0005 | 19.5027 ± 0.0002 | 0.91 ± 0.14 | 0.0136 ± 0.0001 | 3.6767 ± 0.0002 | 1,220.6 ± 1.1 |
| 2 | 628 | 79,586.7925 ± 0.0093 | 322.6830 ± 0.0005 | 22.6833 ± 0.0004 | 0.00 ± 0.00 | 0.0133 ± 0.0002 | 1.1311 ± 0.0002 | 1,321.8 ± 1.1 |
| 3 | 707 | 146,552.8302 ± 0.0110 | 581.1013 ± 0.0009 | 41.0330 ± 0.0002 | 0.80 ± 0.13 | 0.0134 ± 0.0000 | 1.9471 ± 0.0002 | 1,343.1 ± 0.9 |
| 4 | 777 | 48,454.3396 ± 0.0025 | 190.7635 ± 0.0004 | 13.1855 ± 0.0002 | 0.00 ± 0.00 | 0.0128 ± 0.0001 | 1.9377 ± 0.0001 | 1,342.3 ± 1.2 |
| 5 | 833 | 20,056.1635 ± 0.0013 | 80.9164 ± 0.0002 | 5.4003 ± 0.0002 | 0.00 ± 0.00 | 0.0118 ± 0.0003 | 1.5921 ± 0.0002 | 1,308.2 ± 2.3 |
| 6 | 890 | 26,506.7925 ± 0.0026 | 107.6654 ± 0.0002 | 8.6557 ± 0.0002 | 1.99 ± 0.15 | 0.0144 ± 0.0003 | 3.4598 ± 0.0002 | 1,287.5 ± 2.0 |
| 7 | 955 | 72,142.7673 ± 0.0120 | 288.4755 ± 0.0005 | 21.4549 ± 0.0002 | 1.95 ± 0.17 | 0.0138 ± 0.0001 | 3.7435 ± 0.0002 | 1,324.3 ± 1.0 |
| 8 | 1,011 | 91,478.6164 ± 0.0088 | 357.5748 ± 0.0005 | 25.1228 ± 0.0002 | 1.70 ± 0.25 | 0.0130 ± 0.0001 | 3.4858 ± 0.0002 | 1,349.6 ± 0.9 |
| 9 | 1,074 | 38,565.7233 ± 0.0026 | 146.6119 ± 0.0004 | 10.4875 ± 0.0002 | 0.00 ± 0.00 | 0.0124 ± 0.0002 | 4.4877 ± 0.0002 | 1,353.6 ± 1.9 |
| 10 | 1,221 | 7,172.0126 ± 0.0025 | 20.9048 ± 0.0003 | 3.0353 ± 0.0002 | 0.00 ± 0.00 | 0.0191 ± 0.0017 | 5.6417 ± 0.0002 | 1,388.2 ± 9.9 |
| 11 | 1,388 | 5,384.2075 ± 0.0022 | 10.9341 ± 0.0002 | 2.4962 ± 0.0002 | 1.16 ± 0.19 | 0.0154 ± 0.0032 | 8.7481 ± 0.0002 | 1,361.2 ± 14 |
| Alexandrovskiy Complex | | | | | | | | |
| 83A, White mica, 80–125 μm, 1.63 mg, assigned age 304 ± 7 Ma, steps 2–8, Cl/K < 0,0005 | | | | | | | | |
| 1 | 652 | 16,420.6748 ± 0.0060 | 355.4362 ± 0.0006 | 7.2298 ± 0.0003 | 0.00 ± 0.00 | 0.0012 ± 0.0001 | 6.4087 ± 0.0002 | 298.3 ± 0.6 |
| 2 | 694 | 13,299.3865 ± 0.0033 | 302.1049 ± 0.0006 | 4.1555 ± 0.0002 | 0.26 ± 0.16 | 0.0002 ± 0.0001 | 1.7368 ± 0.0001 | 308.1 ± 0.5 |
| 3 | 741 | 21,340.4908 ± 0.0026 | 495.2589 ± 0.0007 | 6.7535 ± 0.0002 | 0.00 ± 0.00 | 0.0003 ± 0.0001 | 1.9105 ± 0.0002 | 305.6 ± 0.5 |
| 4 | 772 | 13,959.5092 ± 0.0044 | 321.2018 ± 0.0005 | 4.2139 ± 0.0002 | 0.00 ± 0.00 | 0.0000 ± 0.0001 | 2.0212 ± 0.0002 | 303.2 ± 0.7 |
| 5 | 805 | 11,412.7607 ± 0.0018 | 258.9748 ± 0.0004 | 3.9347 ± 0.0001 | 1.43 ± 0.23 | 0.0004 ± 0.0001 | 2.4343 ± 0.0002 | 301.2 ± 0.9 |
| 6 | 850 | 11,367.9141 ± 0.0029 | 253.7429 ± 0.0005 | 3.8542 ± 0.0002 | 0.00 ± 0.00 | 0.0004 ± 0.0001 | 2.5682 ± 0.0002 | 304.6 ± 0.8 |
| 7 | 929 | 17,973.1902 ± 0.0018 | 411.9294 ± 0.0007 | 5.5923 ± 0.0003 | 0.00 ± 0.00 | 0.0001 ± 0.0001 | 3.5051 ± 0.0002 | 300.0 ± 0.7 |
| 8 | 1,079 | 13,152.0859 ± 0.0041 | 281.9828 ± 0.0005 | 4.6351 ± 0.0002 | 0.00 ± 0.00 | 0.0004 ± 0.0001 | 4.1512 ± 0.0002 | 307.9 ± 0.8 |
| 9 | 1,389 | 6,028.7669 ± 0.0016 | 83.9644 ± 0.0002 | 2.9244 ± 0.0003 | 0.55 ± 0.13 | 0.0010 ± 0.0004 | 8.3825 ± 0.0002 | 307.9 ± 2.4 |
| 83B, White mica, 250 – 500 μm, 1.80 mg, Assigned age 306 ± 5 Ma, steps 3–6, 8, Cl/K < 0.0005 | | | | | | | | |
| 1 | 661 | 5,417.9611 ± 0.0019 | 115.9106 ± 0.0003 | 2.3137 ± 0.0001 | 0.20 ± 0.15 | 0.0012 ± 0.0001 | 1.9323 ± 0.0002 | 304.7 ± 1.8 |
| 2 | 740 | 5,336.5944 ± 0.0020 | 119.4200 ± 0.0003 | 1.5506 ± 0.0003 | 0.00 ± 0.00 | 0.0000 ± 0.0000 | 1.5482 ± 0.0002 | 298.2 ± 1.9 |
| 3 | 740 | 28,090.8889 ± 0.0037 | 662.4222 ± 0.0011 | 9.3012 ± 0.0003 | 0.08 ± 0.16 | 0.0004 ± 0.0001 | 1.1682 ± 0.0002 | 305.2 ± 0.4 |
| 4 | 772 | 26,724.9444 ± 0.0031 | 628.7889 ± 0.0011 | 8.8501 ± 0.0003 | 0.52 ± 0.13 | 0.0005 ± 0.0001 | 0.9551 ± 0.0002 | 306.3 ± 0.4 |
| 5 | 807 | 11,906.0556 ± 0.0038 | 274.7339 ± 0.0005 | 3.7193 ± 0.0002 | 0.00 ± 0.00 | 0.0003 ± 0.0001 | 0.9715 ± 0.0002 | 307.9 ± 0.8 |
| 6 | 852 | 9,248.4444 ± 0.0030 | 209.8156 ± 0.0004 | 2.8531 ± 0.0002 | 0.69 ± 0.17 | 0.0001 ± 0.0001 | 1.7681 ± 0.0002 | 303.2 ± 1.0 |
| 7 | 930 | 12,143.5556 ± 0.0050 | 277.2039 ± 0.0005 | 4.6875 ± 0.0001 | 0.00 ± 0.00 | 0.0009 ± 0.0001 | 1.9019 ± 0.0002 | 304.4 ± 0.8 |
| 8 | 1,082 | 13,488.0556 ± 0.0031 | 299.2428 ± 0.0005 | 4.6242 ± 0.0002 | 0.42 ± 0.15 | 0.0005 ± 0.0001 | 2.5775 ± 0.0002 | 309.5 ± 0.6 |
| 9 | 1,391 | 6,225.5556 ± 0.0017 | 105.9539 ± 0.0002 | 2.8971 ± 0.0002 | 0.00 ± 0.00 | 0.0011 ± 0.0002 | 6.2105 ± 0.0002 | 302.1 ± 1.5 |

| | | | | | | | | | | | | |
|---|---|---|---|---|---|---|---|---|---|---|---|---|
| 86, White mica, 125–250 µm, 1.59 mg, assigned age | | | | 299 ± 4 Ma, steps 1,2,4,5,6, | $^{36}Ar/^{40}Ar - {}^{39}Ar/^{40}Ar$ isochron, MSWD = 0,24, | | | $^{40}Ar/^{36}Ar_0$ = 156 ± 23 | | | | |
| 1 | 661 | 33,097.9874 ± 0.0034 | | 770.4969 ± 0.0011 | 13.1249 ± 0.0002 | 0.29 ± 0.17 | | 0.0009 ± 0.0001 | | 5.2688 ± 0.0002 | | 298.8 ± 0.4 |
| 2 | 698 | 10,702.6415 ± 0.0019 | | 251.4195 ± 0.0004 | 3.4965 ± 0.0002 | 0.90 ± 0.16 | | 0.0003 ± 0.0001 | | 1.0005 ± 0.0002 | | 301.9 ± 0.8 |
| 3 | 741 | 14,076.0377 ± 0.0043 | | 332.5069 ± 0.0005 | 5.6344 ± 0.0002 | 1.78 ± 0.20 | | 0.0009 ± 0.0001 | | 1.9034 ± 0.0002 | | 296.8 ± 0.7 |
| 4 | 773 | 12,370.0629 ± 0.0060 | | 288.8767 ± 0.0005 | 4.3559 ± 0.0002 | 0.48 ± 0.11 | | 0.0005 ± 0.0001 | | 1.7804 ± 0.0002 | | 299.2 ± 1.0 |
| 5 | 806 | 10,477.2956 ± 0.0010 | | 243.6509 ± 0.0004 | 3.8392 ± 0.0003 | 2.26 ± 0.17 | | 0.0006 ± 0.0002 | | 1.7006 ± 0.0002 | | 298.8 ± 0.9 |
| 6 | 851 | 9,761.5723 ± 0.0013 | | 224.2824 ± 0.0004 | 3.7285 ± 0.0002 | 0.00 ± 0.00 | | 0.0007 ± 0.0002 | | 2.2953 ± 0.0002 | | 295.8 ± 0.9 |
| 7 | 933 | 12,449.3711 ± 0.0055 | | 283.4786 ± 0.0005 | 5.1140 ± 0.0003 | 1.00 ± 0.14 | | 0.0009 ± 0.0001 | | 3.4029 ± 0.0001 | | 295.0 ± 0.6 |
| 8 | 1,083 | 9,609.5597 ± 0.0035 | | 202.3673 ± 0.0004 | 4.0674 ± 0.0003 | 0.00 ± 0.00 | | 0.0010 ± 0.0002 | | 4.1624 ± 0.0001 | | 301.9 ± 0.7 |
| 9 | 1,387 | 4,932.8994 ± 0.0016 | | 56.9182 ± 0.0003 | 3.2080 ± 0.0002 | 1.25 ± 0.11 | | 0.0036 ± 0.0004 | | 8.7536 ± 0.0001 | | 300.7 ± 2.6 |

respective whole-rock plots on this isochron but was not included in the age calculation (Fig. 11).

The apparent age spectrum of white mica from sample 86 (125–250 µm fraction) shows a slight scatter of step ages around 299 Ma (Fig. 10). Heating steps 1, 2, 4–6 cluster in the Cl/K–age plot (Fig. 7) and define an $^{36}Ar/^{40}Ar$–$^{39}Ar/^{40}Ar$ inverse isochron (Table 5). These heating steps yield an age of 299 ± 4 Ma (representing 67% of the $^{39}Ar$ release).

All age data obtained from different isotope systems in different mineral fractions are concordant within limits of error. Dynamic recrystallization occurred at lower greenschist facies conditions (300–400°C), i.e. below the commonly accepted "closure" temperatures of the isotope systems in the different minerals analysed (c.f. Villa 1998). The data above are therefore interpreted to date the mylonitization event.

## Discussion

### Magmatic HT event, Paleoproterozoic

The U–Pb age determinations of zircon from two magmatic rocks the formation of which is attributed to HT events, most probably of amphibolite facies, following the granulite facies metamorphism of the TC, yield crystallization ages of 2,344 ± 29 and 2,044 ± 8 Ma, respectively (Fig. 4). The pronounced difference between

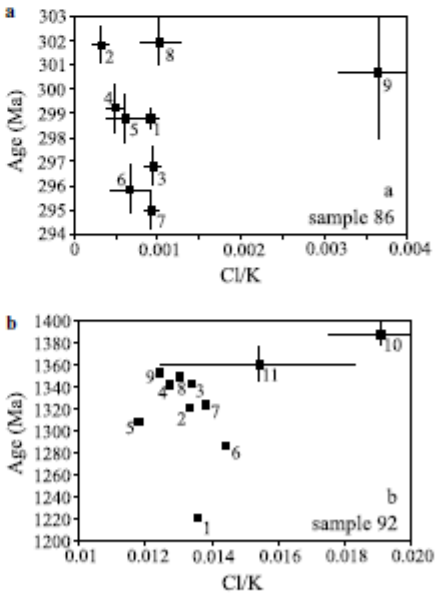


**Fig. 7** Cl/K age correlation diagrams of mylonite samples 86 (**a**) and 92 (**b**), the errors of age determination and Cl/K of most heating steps of sample 92 are lower than can be indicated at the scale of the figure. The *numbers* denote the heating steps during analysis

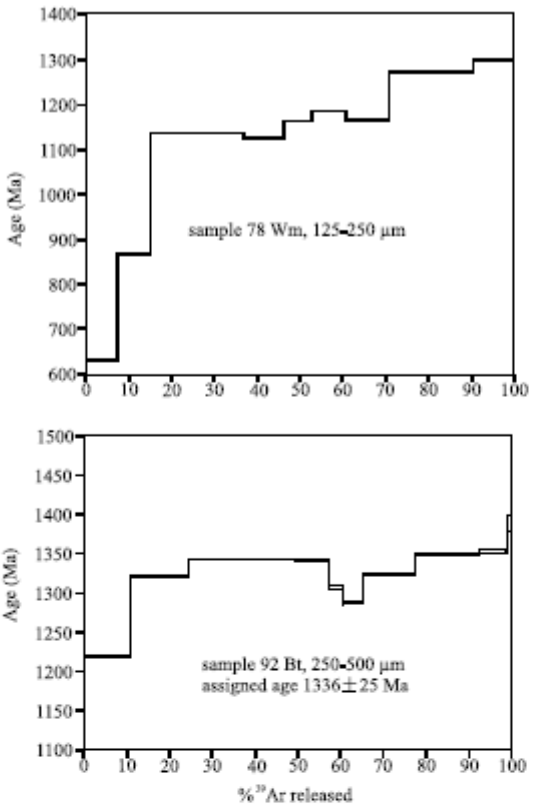


**Fig. 8** $^{40}Ar/^{39}Ar$ age spectra of white mica and biotite from mylonite samples 78 and −92, from the eastern shear zone in the TC. *Error assignments* are 1σ values taking into account the analytical error on each signal

the two ages of 300 Ma reveals that both events are not identical. As the two samples come from two different blocks of the TC (Fig. 2), separated by a greenschist facies shear zone it seems possible that both blocks record different *PT*-paths.

Ronkin et al. (2003) derived $T_{DM}$ Nd-model ages between 2,030 Ma and 2,560 Ma, from foliated metapelites of the Radostniy quarry where the 2,044 ± 8 Ma old migmatite leucosome sample 26.6 was taken. The Nd model ages point to a Palaeoproterozoic origin of the sedimentary precursor of the metapelites. Consequently, the granulite facies metamorphism must be older than 2,044 ± 8 Ma, although still of Palaeoproterozoic age in this part of the TC.

## HT event, early Paleoproterozoic

Fluid influx under lower amphibolite to greenschist facies conditions at 1,810 ± 41 Ma caused the retrograde event recorded in sample 26A from the Radostni quarry. Similar ages have been determined for several occurrences of the region. The granite precursor rock of the

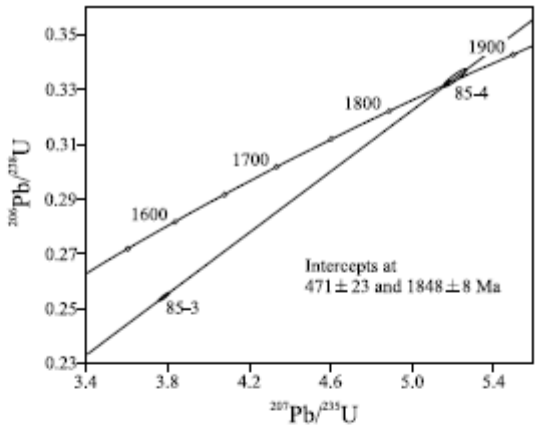


**Fig. 9** U–Pb Concordia diagram for zircon from mylonite sample 85

mylonites in the AC crystallized at 1,848 ± 8 Ma (sample 95, Fig. 9) and inherited zircons of the granitic to granodioritic Verkniy Ufaley intrusion located 40 km to the NE of the Taratash Complex in the East Ufaley Complex (Fig. 1) are considered to have a minimum age of about 1,780 Ma (Hetzel and Romer 1999). Both occurrences are situated to the west of the Main Uralian Fault and therefore might have been affected by the same granite forming thermal event at ~1,800 Ma within the East European Craton.

In this period, the TC was characterized by lower amphibolite to greenschist facies conditions and fluids released from lower crustal units caused recrystallization of amphibolite facies rocks as described in sample 26A (see No. 4 in Fig. 3).

## LT event, Mesoproterozoic

The shear zones of the TC indicate a top-to-the NW shear sense and in their present orientation, they reflect NW–SE directed crustal shortening. The mylonites are characterized by an incomplete isotopic re-equilibration between 1,350 Ma and 1,200 Ma. Whether this was the initial shear zone formation or a later re-equilibration, e.g. due to fluid flux through the shear zones, cannot be decided directly from the data. However, it is known that anorogenic alkaline magmatism related to extension and rifting occurred during the Mesoproterozoic in the southeastern parts of Baltica (Nikishin et al. 1996; Berdyaush nepheline syenite complex in the Bashkirian Anticlinorium, 1,350–1368 Ma, Koroteev et al. 1997; Sindern et al. 2003). The kinematics of the shear zones argues against the formation of shortening-related shear zones at that time. Partial isotope re-equilibration after shear zone formation due to fluid flow, possibly contemporaneous with anorogenic magmatism in the Bashkirian Anticlinorium, therefore seems to be the best explanation for the age data from

the amphibolite facies shear zone in the TC. Consequently, shear zone formation which reflects crustal shortening is bracketed between 1,350 Ma and 1,800 Ma. Crustal shortening and thickening might have caused granite formation. Therefore, the shear zones may have been active at about 1,800 Ma, the time at which heating and granite formation is documented in other parts of the region.

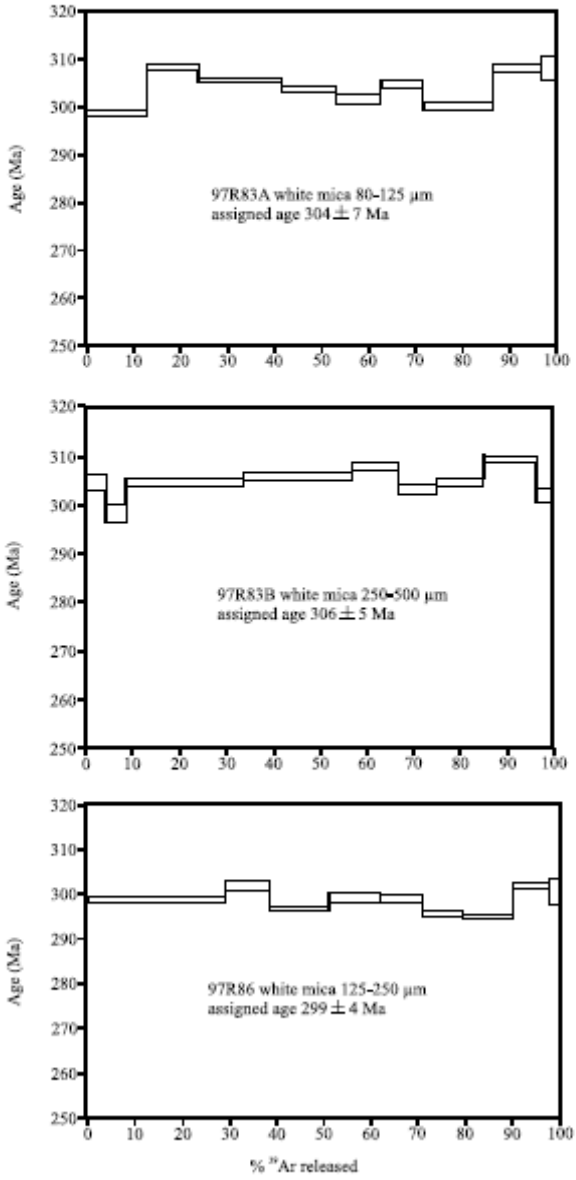


**Fig. 10** $^{40}Ar/^{39}Ar$ age spectra of white mica from mylonite samples 83 and –86 from the shear zone in the AC. *Error assignments* are 1σ values taking into account the analytical error on each signal

According to Nikishin et al. (1996) the entire East European Craton was affected by compressional deformation in the Mesoproterozoic (1,400–1,200 Ma). If the shear zones of the TC were formed during this stage and not during a stage of crustal thickening at about 1,800 Ma it must have been at the beginning of that time span. Whether the rifting and anorogenic magmatism at 1,350–1,368 Ma mark the onset of a ''Grenvillian'' orogenic activity cannot be deduced from this study.

For the Neoproterozoic times, Hartz and Torsvik (2002) proposed that the pre-Uralian eastern margin of the East European Craton was positioned close to Laurentia (E-Greenland). If that plate tectonic constellation was also established in the Mesoproterozoic one would expect more magmatic and metamorphic events between 1,870 Ma and 970 Ma in the pre-Uralian eastern margin of the East European Craton, as is typical for East Laurentia (Cawood and Nemchin 2001; Watt and Thrane 2001). From the data derived in this study, the magmatic event recorded in the AC (1,848 ± 8 Ma, Fig. 9) falls in this range.

## Meso- to Neoproterozoic events: < 1,600 Ma

Granulite and amphibolite facies rocks of the TC are cross-cut by mafic dykes, that partly have porphyric textures. Several generations of similar dykes in the Mesoproterozoic sediments of the Bashkirian Anticlinorium must be younger than 1,650 Ma (Lennykh and Petrov 1974) which is in part in line with the K–Ar dates for basaltic dykes from the TC. The youngest date reported by Lennykh and Petrov (1974) is 1,161 Ma. This indicates that the TC must already have been exhumed to an upper crustal level in the Neoproterozoic.

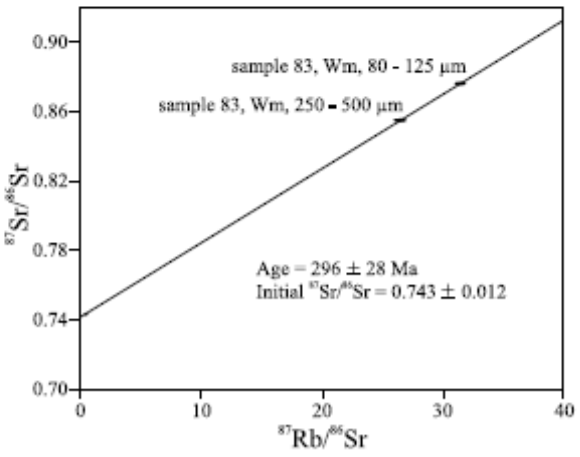


**Fig. 11** Rb–Sr-isochron diagram for white mica fractions of mylonite sample 83, shear zone of AC, the whole-rock fraction plots on the isochron but is not shown in this scale. Further explanation in the text

Evidence of the Neoproterozoic Timanian orogeny, which is reflected by geochronological data in several other metamorphic complexes in similar tectonic settings (e.g. Beloretzk Glasmacher et al. 2001, 2004; Kvarkush, Beckholmen and Glodny 2004) is not present in the TC and AC.

Carboniferous–Triassic

To the east of the TC, shear zones were active in the AC at lower greenschist facies conditions (3–6 kbar, 350–400°C) at 300 Ma (samples 83, 86). Despite their similar geometry and similar top-to-the NW sense of movement, the shear zones in both complexes are markedly different with respect to their syn-deformational *PT* conditions and their formation age. Shearing in the AC at ~300 Ma coincides with the main stage of Uralian crustal shortening in the Middle Urals (e.g. Puchkov 1997; Echtler et al. 1997). Similar ages are found in the East Ufaley complex (305 ± 6 and 296 ± 6 Ma, white mica, Eide et al. 1997). These ages have been interpreted as cooling ages which reflect the passage of the Ufaley Complex through the 450–500°C isotherm (Eide et al. 1997; Hetzel and Romer 1999) during exhumation. Consequently, the exhumation of the Ufaley Complex was compensated by thrusting and erosion of the AC, which is situated between the Ufaley Complex and the TC.

Relatively fast uplift and surface erosion of the Sysert complex E of the Main Uralian Fault between 280 Ma and 240 Ma was deduced by Hetzel and Glodny (2002) on the basis of Rb–Sr dating. At that time, the Sysert Complex was already in tectonic contact with the Ufaley Complex along the Main Uralian Fault. Rapid cooling of the TC below 110°C at a cooling rate > 20°C/Ma as a consequence of rapid exhumation between 300 Ma and 250 Ma is indicated by zircon and apatite fission-track dating (Seward et al. 2002). It seems plausible that during this stage, the TC was thrusted onto the underlying Devonian limestones and that Late Carboniferous to Early Permian thrusting was the last major deformation phase affecting the TC and AC.

## Conclusions

Although individual blocks of the TC might have slightly different evolutions, as recognized e.g. in the different magmatic zircon crystallization ages, the general *T*–*t* evolution of the complex is as follows (Fig. 12). Pervasively deformed granulite facies metamorphic rocks indicate peak conditions between 850°C and 900°C at 10 kbar and are overprinted by subsequent retrogressive stages of amphibolite facies and greenschist facies metamorphism. The age of this metamorphism is constrained to be Paleoproterozoic, although the precise age remains unclear. Magmatic activity, related to post-granulite facies overprints, is dated at 2,344 ± 29 Ma (leucocratic granite) and 2,044 ± 8 Ma (migmatite).

At 1,810 ± 41 Ma, the TC was affected by a lower amphibolite to greenschist facies retrogressive metamorphism which was probably related to a stage of crustal shortening and granite formation in the East European Craton as indicated by data from the adjacent AC and Ufaley Complexes. The shear zones of the TC might also have been formed at that stage. Partial re-equilibration of isotope systems disturbing original age information in these shear zones between 1,350 Ma and 1,200 Ma is attributed to fluid flow contemporaneous with anorogenic magmatism in the Bashkirian Anticlinorium. This means that the original shear zone for-

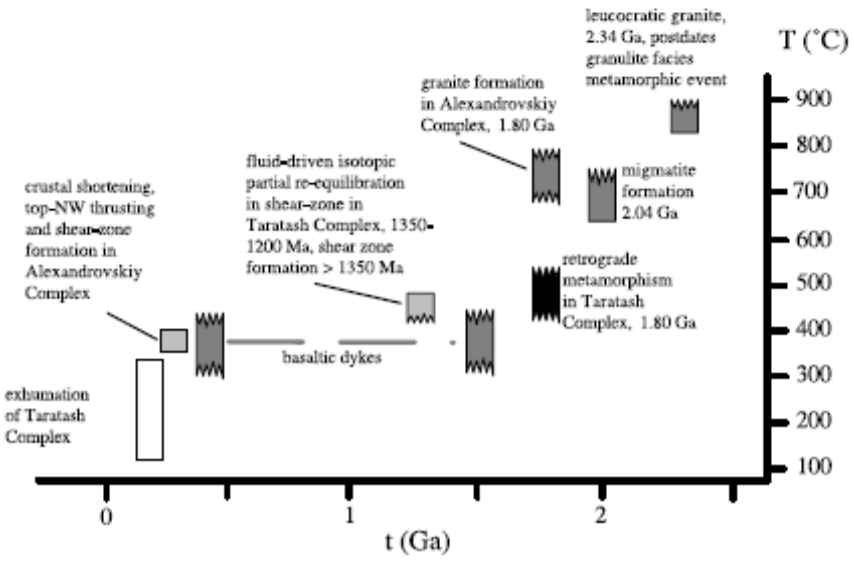


**Fig. 12** *T*–*t*-diagram illustrating the Proterozoic–Phanerozoic evolution of the TC and AC

mation is older than 1,350 Ma. The presence of Meso- to Neoproterozoic basaltic dykes in the TC documents its position in the upper crust at that time. The TC shows neither evidence of a Grenvillian orogenic event (indicative of a position of the eastern margin of the East European Craton opposite of East-Laurentia) nor of the Timanian orogeny which affected some metamorphic complexes in the Uralides. Thrusting on Devonian limestones is reflected in shear zones in the AC and has been dated at ~300 Ma.

**Acknowledgements** Logistic support and field guidance by V.I. Lennykh was invaluable for this study. Financial support by the Deutsche Forschungsgemeinschaft to UK, RH and BAS [grants KR 1195-4, EC 138/3-1/2] is gratefully acknowledged. Reviews by J. Glodny and an anonymous referee substantially improved the paper. We thank B. Grauert and K. Mezger for providing facilities at the Laboratory of Geochronology at the University of Münster. We are grateful for the support of H. Baier (Münster), J. Jakobi and G. Siebel during analytical work. S. Klebingat and D. Oellers (Aachen) are thanked for their help with the production of the figures. Y. and L. Etoundi provided translations of Russian publications. A. Rogers is thanked for proof reading the English manuscript.

## Appendix

### Analytical procedures

Rock-forming minerals in samples from the TC were analysed with a Cameca SX50 electron microprobe with wavelength-dispersive detection (LIF, TAP, PET crystals) and automated PAP correction at the Institute of Chemical Analytics at the Technical University in Darmstadt. The acceleration voltage was 15 kV, the beam current 10–20 nA, the beam size 2–7 µm. Peaks were detected for 10–30 s. The following standards were used for the major elements: Si, anorthite; Ti, rutile; Al, corund; Cr, chromite; Mn, rhodonite; Fe, hematite; Ca, wollastonite; Mg, diopside; K, K-feldspar; Na, albite. Repeated analyses of the standards ($n = 5$–12) result in $<0.1\%$ between 100 wt-% and 5 wt-% oxide, $<2\%$ between 2 wt-% and 5 wt-% oxide and $<30\%$ for concentrations $<2$ wt-% oxides ($2\sigma$ of all analyses).

Microprobe analyses of white mica from mylonites of the AC were performed at the GFZ Potsdam (Germany) on a Cameca SX 100 electron beam microprobe operating in wavelength-dispersive mode with the following conditions: 15 kV accelerating voltage, 20 nA beam current, 20 s peak counting time and 10 µm beam diameter. The Cameca standard set was used for calibration and the PAP programme for matrix correction.

For Rb/Sr isotope analyses mineral fractions were produced with the help of a magnetic separator, heavy liquids and finally hand-picking. Bulk samples and silicate mineral fractions were dissolved with a $HF$–$HNO_3$ mixture and HCl. Carbonate mineral fractions were leached from powdered samples in HCl. Elements were separated using standard cation exchange techniques. Rb–Sr isotope ratio measurements were performed on a VG Sector 54 solid source thermal ionization mass spectrometer (Mineralogisches Institut, Münster, Germany). For Sr, the mass fractionation corrections were based on $^{86}Sr/^{88}Sr = 0.1194$. Repeated analyses of the $^{87}Sr/^{86}Sr$ ratio of the NBS 987 Sr standard in the period of analytical work yielded $0.71028 \pm 0.00003$ ($n = 29$, $2\sigma$ of all analyses). Total blanks for Rb are $<60$ pg and for Sr $<100$ pg. All decay constants are taken from Steiger and Jäger (1977). Rb–Sr isochrons were calculated using $\lambda_{^{87}Rb} = 1.42 \times 10^{-11}\,a^{-1}$, an error estimate for $^{87}Rb/^{86}Sr$ of 1.0% and the $^{87}Sr/^{86}Sr$ precision ($2\sigma$-level) given by repeated analyses of the NBS-987 standard (0.00003, see above). In case the within-run precision of the $^{87}Sr/^{86}Sr$ ratio was lower than 0.00003, the actual within-run precision was used for age calculation.

Digestion of zircon crystals is performed in teflon liners designed for the dissolution of six single crystals simultaneously using 24 N HF at 180°C. The digestion is completed after 4–10 days and HF is evaporated on a heating plate. After spiking with a mixed $^{205}Pb$–$^{233}U$ solution, sample and spike are homogenized in 6 N HCl for 24 h at 80°C with all excess HCl being evaporated. The Pb standards as well as the spiked samples are loaded without element separation on single Re filaments into a silica gel bed with 2 µl of loading solution, containing 90 vol.% of 6 N HCl and 10 vol.% of 0.1 N $H_3PO_4$. Isotope measurements are performed on a VG sector 54 mass spectrometer at the Zentrallabor für Geochronologie, Münster University, equipped with a Daly multiplier. The Pb composition is determined at 1,300–1,400°C followed by the U measurement at 1,400–1,450°C. In most cases, signals are only analysed by the Daly multiplier leading to long times of analysis. The $2\sigma$ error margins obtained for $^{206}Pb/^{204}Pb$, $^{207}Pb/^{206}Pb$ and $^{233}U/^{235}U$ are better than 0.5, 0.5 and 0.1%, respectively. The obtained intensities range mostly at 1–2 mV for $^{206}Pb$ and 0.5–2 mV for $^{233}U$. Isotope ratios are corrected for mass fractionation ($0.11 \pm 0.02\%$/a.m.u.), blank ($<10$ pg total Pb, $^{206}Pb/^{204}Pb = 17.7 \pm 0.5$, $^{207}Pb/^{204}Pb = 15.5 \pm 0.1$, 1 pg U) and initial common Pb estimated after the model of Stacey and Kramers (1975). The isotope $^{208}Pb$ is not analysed. This has no impact on the U/Pb dating. However, the total amount of Pb in the sample solution cannot be calculated from the data. Only the sum of $^{204}Pb$, $^{206}Pb$ and $^{207}Pb$ can be given.

For $^{40}Ar/^{39}Ar$ dating, samples were crushed, sieved and white mica fractions were obtained by magnetic separation and frictional separation on paper. Final handpicking under the binocular resulted in high sample purities. White mica samples were washed in ethanol. Samples were irradiated in the Ford Michigan reactor, University of Michigan. The J-factor was estimated at a value of 0.00440 using duplicates of the Fish Canyon Sanidine standard with an age of $27.55 \pm 0.08$ Ma (Lanphere and Baadsgaard 1997). For age calculation, uncertainties of the monitor standard age, the decay constants as well as the *J*-factor, are not considered (see

also Villa et al. 2000). Samples were loaded in tin packets into a double vacuum furnace and step heated from usually 600–1,400°C. The gas was purified by means of SAES Al–Zr getters. The argon isotopic composition was measured in static mode on a MAT 215-50B rare gas mass-spectrometer at Mineralogical Institute, Isotope Geology, University Bern, Switzerland (I. Villa). Error assignments are 1σ values taking into account the analytical error on each signal and the error on the blank.

## References


Alekseyev AA (1984) Riphean and Vendian magmatism in the southern Urals. Nauka, Moscow, pp 1–136 (in Russian)

Anfimov LV (1997) Lithogenesis in the Riphean sedimentary series of the Bashkirian megaanticlinorium. Nauka, Urals Branch of Russian Academy of Sciences, Ekaterinburg, p 229 (in Russian)

Beckholmen M, Glodny J (2004) Early Cambrian blueschist facies metamorphism in the Kvarkush metamorphic basement, Northern Urals, Russia. In: Gee D, Pease V (eds) The Neoproterozoic Timanide orogen of Eastern Baltica. Geological Society, London Special Publications 30:125–134

Brown D, Alvarez-Marron J, Perez-Estaun A, Gorozhanina Y, Baryshev V, Puchkov VN (1997) Geometric and kinematic evolution of the foreland thrust and fold belt in the southern Urals. Tectonics 16:551–562

Brown D, Alvarrez-Marron J, Perez-Estaun A, Puchkov V, Ayarza P, Gorozhanina Y (2001) Structure and evolution of the Magnitogorsk forarc basin: Identifying upper crustal processes during arc-continent collision in the Southern Urals. Tectonics 20:364–375

Cawood PA, Nemchin AA (2001) Paleogeographic development of the east Laurentian margin: constraints from U-Pb dating of detrital zircons in the Newfoundland Appalachians. Geol Soc Amer Bull 113:1234–1246

De Gregorio S, Rotolo SG, Villa IM (2003) Geochronology of the medium to high-grade metamorphic units of the Peloritani Mts., Sicily. Int J Earth Sci 92:852–872

Dobretsov NL, Shatsky VS, Coleman RG, Lennykh VI, Valizer PM, Liou J, Zhang R, Beane RJ (1996) Tectonic setting and petrology of ultrahigh-pressure metamorphic rocks in the Maksyutov complex, Ural Mountains, Russia. Int Geol Rev 38:136–160

Echtler HP, Ivanov KS, Ronkin YuL, Karsten LA, Hetzel R, Noskov AG (1997) The tectono-metamorphic evolution of gneiss complexes in the Middle Urals, Russia: a reappraisal. Tectonophysics 276:229–251

Eide EA, Echtler HP, Hetzel R, Ivanov KS (1997) Cooling age diachroneity and Paleozoic orogenic processes in the Middle and Southern Urals. Terra Nova 9(Abstract Suppl 1):119

Friberg M, Larionov A, Petrov GA, Gee DG (2000) Paleozoic amphibolite-granulite facies magmatic complexes in the hinterland of the Uralide Orogen. Int J Earth Sci 89:21–39

Giese U, Glasmacher UA, Kozlov VI, Matenaar I, Puchkov VN, Stroink L, Bauer W, Ladage S, Walter R (1999) Structural framework of the Bashkirian Anticlinorium, SW Urals. Geol Rundsch 87:526–544

Glasmacher UA, Reynolds P, Alekseev AA, Puchkov VN, Taylor K, Gorozhanin V, Walter R (1999) $^{40}Ar/^{39}Ar$ thermochronology west of the Main Uralian fault, southern Urals, Russia. Geol Rundsch 87:515–525

Glasmacher UA, Bauer W, Giese U, Reynolds P, Kober B, Puchkov V, Stroink L, Alekseyev AA, Willner AP (2001) The metamorphic complex of Beloretzk, SW Urals, Russia—a terrane with a polyphase Meso- to Neoproterozoic thermodynamic evolution. Precamb Res 110:185–213

Glasmacher UA, Bauer W, Clauer N, Puchkov VN (2004) Neoproterozoic metamorphism and deformation at the southeastern margin of the East European Craton, Uralides, Russia. Int J Earth Sci 93:921–944

Glodny J, Bingen B, Austrheim H, Molina JF, Rusin A (2002) Precise eclogitization ages deduced from Rb/Sr mineral systematics: The Maksyutov complex, Southern Urals, Russia. Geochim Cosmochim Acta 66:1221–1235

Hartz EH, Torsvik TH (2002) Baltica upside down:a new plate tectonic model for Rodinia and the Iapetus Ocean. Geology 30:255–258

Hetzel R (1999) Geology and geodynamic evolution of the high-*P*/low-*T* Maksyutov Complex, southern Urals, Russia. Geol Rundsch 87:577–588

Hetzel R, Glodny J (2002) A crustal-scale, orogen-parallel strike slip fault in the Middle Urals: age, magnitude of displacement, and geodynamic significance. Int J Earth Sci 91:231–245

Hetzel R, Romer R (1999) U-Pb dating of the Verkhniy Ufaley intrusion, middle Urals, Russia: a minimum age for subduction and amphibolite facies overprint of the East European continental margin. Geol Mag 136:593–597

Hetzel R, Echtler HP, Seifert W, Schulte BA Ivanov KS (1998) Subduction- and exhumation-related fabrics in the Paleozoic high-pressure-low-temperature Maksyutov Complex, Antingan area, southern Urals, Russia. Geol Soc Am Bull 110:916–930

Hofmann AW (1979) Rb-Sr dating of thin slabs: an imperfect method to determine the age of metamorphism. In: Jäger E, Hunziker JC (eds), Lectures in isotope geology. Springer, Berlin Heidelberg New York, pp 27–29

Hradetzky H, Lippolt HJ (1993) Generation and distortion of Rb/Sr whole-rock isochrones—effects of metamorphism and alteration. Eur J Mineral 1993(5):1175–1193

Ivanov SN, Krasnobaev AA, Rusin AI (1986) Geodynamic regimes in the Precambrian of the Urals. Precamb Res 33:189–208

Koroteev VA, Ivanov KS, Echtler HP, Ronkin YuL (1997) Tectonic evolution of the Urals: complete geodynamic cycle during 1.6 – 0.2 Ga. Terra Abstracts 9:118

Kozlov VI (1990) On the stratigraphy of the Ai-suite, lower Riphean, southern Urals. In: Alekseev AA, Alekseeva GV, Harris MA, Larionov NN, Maslov AV (eds) Precambrian geology of the southern Urals and eastern Russian platform: selected contributions. Bashkirian Science Centre, Uro, Academy of Sciences, Ufa, pp 29–38 (in Russian)

Krasnobayev AA (1986) Zircons as indicator of geological processes. Acad. Nauka, Moscow, pp 1–148 (in Russian)

Krasnobayev AA, Sumin LV (1983) Geochemical and geochronological heterogeneity of zircons from polymetamorphic complexes. Geokhimiya 4:590–602 (in Russian)

Krasnobayev AA, Syashin IV, Trayanova MV, (1965) Absolute ages of the rocks of the Taratashskoi suite in the Urals using alpha-lead data. Methodic questions of isotope geology. Nauka, Moscow, pp 1–84 (in Russian)

Kruhl JH (1996) Prism- and basal-plane parallel subgrain boundaries in quartz: a micro-structural geothermobarometer. J Metamorph Geol 14:581–589

Lanphere MA, Baadsgaard H (1997) The fish canyon tuff: a standard for geochronology. In: AGU 1997 spring meeting. Eos, Transactions, American Geophysical Union 78; 17(Suppl):326

Lennykh VI, Krasnobayev AA (1978) Petrology and iron ore deposits of the Taratash Complex. Precambrian and Lower Paleozoic of the Urals. UNTs Akad Nauka USSR, Sverdlovsk, pp 69–76, (in Russian)

Lennykh VI, Petrov VI (1974) On the alkalibasaltoids in the surroundings of the Taratash complex. Volcanism of the southern Urals. Academy of Sciences USSR, Urals Science Centre, pp 146–164 (in Russian)

Lennykh VI, Pankov YuD, Petrov V (1978) Petrology and metamorphism of the migmatite complex. Petrology and iron ore deposits of the Taratash Complex. UNTs Akad Nauka, Sverdlovsk, pp 3–45 (in Russian)

Malakhova NP, Pankov YuD, Chebikin NY, Petrov VI (1978) New data on the age of thrust faulting along the western margin of the Taratash Complex. In: Year book of the Institute of Geology and Geochemistry Sverdlovsk 25: p 26 (in Russian)
Maslov AV (2004) Riphean and Vendian sedimentary sequences of the Timanides and Uralides, the eastern periphery of the East European Craton. In: Gee DG, Pease VL (eds) The Neoproterozoic Timanide Orogen of Eastern Baltica. Geological Society, London, Memoires 30:19 – 35
Maslov AV, Erdtmann BD, Ivanov KS, Ivanov SN, Krupenin MT (1997) The main tectonic events, depositional history, and the palaeogeography of the Southern Urals during the Riphean-Early Palaeozoic. Tectonophysics 276:313–335
Massonne HJ, Schreyer W (1987) Phengite geobarometry based on the limiting assemblage with K-feldspar, phlogopite, and quartz. Contrib Mineral Petrol 96:212–224
Matenaar I, Glasmacher UA, Pickel W, Giese U, Pazukhin VN, Puchkov VN, Kozlov VI, Stroink L (1999) Incipient metamorphism between Ufa and Beloretzk, western fold-and-thrust belt, southern Urals, Russia. Geol Rundsch 87:545–560
Matte P, Maluski H, Caby R, Nicolas A, Kepezhinskas P, Sobolev S (1993) Geodynamic model and $^{40}Ar/^{39}Ar$ dating for the generation and emplacement of the high pressure (HP) metamorphic rocks in SW Urals. Comptes Rendus de l'academie des Sciences, Paris, ser. II 317:1667–1674
Nikishin AM, Ziegler PA, Stephenson RA, Cloetingh SAPL, Furne AV, Fokin PA, Ershov AV, Bolotov SN, Korotaev MV, Alekseev AS, Gorbachev VI, Shipilov EV, Lankreijer A, Bembinova Eyu, Shalimov IV (1996) Late Precambrian to Triassic history of the East European Craton: dynamics of sedimentary basin evolution. Tectonophysics 268:23–63
Ovchinnikov LN (1964) Isotopic age of Precambrian formations of the Urals. In: Commission on Isotopic Age Determinations of Geological Formations, Moscow XI, pp 235 – 245 (in Russian)
Passchier CW, Trouw RAJ (1996) Microtectonics. Springer, Berlin Heidelberg New York, pp 1–304
Pryer LL (1993) Microstructures in feldspars from a major crustal thrust zone: the Grenville Front, Ontario, Canada. J Struct Geol 15:21–36
Puchkov VN (1997) Structure and geodynamics of the Uralian orogen. In: Burg JP, Ford M (eds) Orogeny through time. Geol Soc Spec Publ 121:201–196
Puchkov V (2002) Paleozoic evolution of the East European Continental Margin Involved in the Uralide Orogeny. In: Brown D, Juhlin Chr, Puchkov V (eds) Mountain building in the Urals—Pangea to the present. Geophysical Monograph 132, American Geophysical Union, pp 9–32
Pystin AM (1978) The Alexandrovskiy gneiss-amphibolite complex. In: Lennykh VI, Belkovskiy AI (eds) Volcanism, metamorphism and iron-quartzites of the Taratash complex. UNTs Akad Nauka USSR, Sverdlovsk, pp 3–32
Ronkin YuL, Sindern S, Kramm U, Lennykh VI, Maslov AV, Lepikhina OP (2003) Estimation of the degree of Sr and Nd isotopic homogenization of high grade metamorphic rocks by the thin slab method—an example from the Taratash complex, southern Urals. In: Proceedings of the 2nd Russian isotope geochronology conference: isotope geochronology in the solution of problems of geodynamics and ore-genesis, 25–27 November, St. Petersburg, Russia, pp 420–422 (in Russian)
Scarrow JH, Pease V, Fleutelot C, Dushin V (2001) The late Neoproterozoic Enganepe ophiolite, Polar Urals, Russia: an extension of the Cadomian arc? Precamb Res 110:255–275
Scarrow JH, Hetzel R, Gorozhanin VM, Dinn M, Glodny J, Gerdes A, Ayala C, Montero P (2002) Four decades of geochronological work in the southern and middle Urals: a review. In: Brown D, Juhlin Chr, Puchkov V (eds) Mountain Building in the Urals—Pangea to the present Geophysical Monograph 132, American Geophysical Union, pp 233–255
Schulte BA, Sindern S (2001) Multistage tectonometamorphic evolution of the Taratash complex, Middle Urals, Russia. J Conf Abstracts 6(1):584
Seward D, Brown D, Hetzel R, Friberg, M, Gerdes A, Petrov GA, Perez-Estaun A (2002) The syn- and post-orogenic low temperature events in the Southern and Middle Urals: evidence from fission-track analysis. In: Brown D, Juhlin Chr, Puchkov V (eds) Mountain Building in the Urals—Pangea to the present Geophysical Monograph 132, American Geophysical Union, Washington, pp 257–272
Sindern S, Schulte BA, Kramm U (2001) Die tektonometamorphe Entwicklung des Taratash Komplexes, Mittlerer Ural, Russland. Berichte der Deutschen Mineralogischen Gesellschaft – Beihefte zum. Eur J Miner 13:201
Sindern S, Ronkin YuL, Kramm U, Maslov AV, Lenikhina OP (2003) Application of the $^{205}Pb/^{233}U$-spike for the U–Pb dating of single zircons: an example of the Berdyaush nepheline syenites, southern Urals. In: Proceedings of the 2nd Russian isotope geochronology conference: isotope geochronology in the solution of problems of geodynamics and ore-genesis, 25–27 November, St. Petersburg, Russia, pp 461–465 (in Russian)
Sobolev ID (1986) Geological map of the northern, middle and northeastern part of the southern Urals. Scale 1:2500000. Geological Survey of the USSR and Ural Geology Commission (in Russian)
Spear FS, Matthew JK, Cheney JT (1999) *P–T* paths from anatectic pelites. Contrib Miner Petrol 134:17–32
Stacey JS, Kramers JD (1975) Approximation of terrestrial lead isotope evolution by a two stage model. Earth Planet Sci Lett 6:15–25
Steiger RH, Jäger E (1977) Subcommission on geochronology: Convention on the use of decay constants in geo- and cosmochronology. Earth Planet Sci Lett 26:359–362
Sumin LV (1982) The new thermoisochron method for radiological dating of zircons, Dokl. Akad. Nauka SSSR 263(4):959–964 (in Russian)
Tugarinov AI, Bibikova EV, Krasnobayev AA, Makarov VA (1970) Geochronology of the Precambrian of the Urals. Geokhimia 4:501 (in Russian)
Villa I (1998) Isotopic closure. Terra Nova 10:42–47
Villa IM, Hermann J, Müntener O, Trommsdorf V (2000) $^{39}Ar$ – $^{40}Ar$ dating of multiply zoned amphibole generations (Malenco, Italian Alps). Contrib Mineral Petrol 140:363–381
Watt GR, Thrane K (2001) Early Neoproterozoic events in East Greenland. Precamb Res 110:165–184
Willner AP, Sindern S, Metzger R, Ermolaeva T, Kramm U, Puchkov V, Kronz A (2003) Typology and single grain U/Pb ages of detrital zircons from Proterozoic sandstones in the SW Urals (Russia): early time marks at the eastern margin of Baltica. Precamb Res 124:1–20
Zonenshain LP, Kuzmin MI, Natapov LM (1990) Uralian foldbelt. Am Geophys Union Geodyn Ser 21:27–54

5.

Sindern, S., Gerdes, A., Ronkin, Y.L., Dziggel, A., Hetzel, R., Schulte, B.A. (2012a) Monazite stability, composition and geochronology as tracers of Proterozoic events at the eastern margin of the East European Craton (Taratash complex, Middle Urals). Lithos 132-133, 82-97.

Right of re-use in thesis for Elsevier journal author granted by Elsevier, confirmation by Elsevier Permissions Helpdesk, 1600 John F. Kennedy Boulevard, Suite 1800, Philadelphia, PA 19103-2899, USA, 23rd of October 2015.

Lithos 132-133 (2012) 82–97

Contents lists available at SciVerse ScienceDirect

Lithos

journal homepage: www.elsevier.com/locate/lithos

# Monazite stability, composition and geochronology as tracers of Paleoproterozoic events at the eastern margin of the East European Craton (Taratash complex, Middle Urals)

Sven Sindern [a,*], Axel Gerdes [b], Yuri L. Ronkin [c], Annika Dziggel [a], Ralf Hetzel [d], Bernd Aloys Schulte [e]

[a] Institute of Mineralogy and Economic Geology, RWTH Aachen University, Wüllnerstr. 2, 52056 Aachen, Germany
[b] Institute of Geosciences, Johann Wolfgang Goethe University, Altenhöferallee 1, 60438 Frankfurt a.M., Germany
[c] Institute of Geology and Geochemistry, Russian Academy of Sciences, Ekaterinburg, Russia
[d] Institut für Geologie und Paläontologie, Westfälische Wilhelms-Universität Münster, Corrensstr. 24, 48149 Münster, Germany
[e] Ruffinistr. 12, 80634 Munich, Germany

ARTICLE INFO

*Article history:*
Received 9 May 2011
Accepted 16 November 2011
Available online 01 December 2011

*Keywords:*
Ural mountains
Taratash complex
LA-ICP-MS
Geochronology
Monazite

ABSTRACT

The Precambrian Taratash complex (Middle Urals) is one of the rare windows into the Palaeoproterozoic and earlier history of the eastern margin of the East European Craton. Monazite from intensively deformed rocks within a major amphibolite-facies shear zone in the Taratash complex has been investigated by means of electron-probe microanalysis and laser-ablation SF-ICP-MS.

Metamorphic and magmatic cores of monazite from metasedimentary and metagranitoid rocks yield U–Pb ages of 2244±19 and 2230±22 Ma (±2 σ) and record a previously unknown pre-deformational HT-metamorphic event in the Taratash complex. Subsequent dissolution–reprecipitation of monazite, during shear zone formation under amphibolite-facies conditions, caused patchy zonation and chemical alteration of the recrystallised monazite domains, leading to higher cheralite and huttonite components. This process, which was mediated by a probable (alkali + OH)-bearing metamorphic fluid also caused a total resetting of the U–Pb-system. The patchy domains yield concordant U–Pb-ages between 2052±16 and 2066±22 Ma, interpreted as the age of the shear zone. In line with previously published ages of high grade metamorphism and migmatisation, the data may point to a Palaeoproterozoic orogenic event at the eastern margin of the East European Craton.

Post-deformational fluid-induced greenschist-facies retrogression caused partial to complete breakdown of monazite to fluorapatite, REE + Y-rich epidote, allanite and Th-orthosilicate.The retrograde assemblages either form coronas around monazite, or occur as dispersed reaction zones, indicating that the REE, Y, and Th were mobile at least on the thin section scale. The greenschist-facies metamorphic fluid was aqueous and rich in Ca. Monazite affected by advanced breakdown responded to the retrogression by incorporating the cheralite or huttonite components during a fluid-induced dissolution–reprecipitation process. This event did not reset the U–Pb-system but caused partial Pb loss reflected by discordant U–Pb-dates.

© 2011 Elsevier B.V. All rights reserved.

## 1. Introduction

Monazite is an abundant accessory mineral in many igneous and metamorphic rocks. Due to the incorporation of Th and U but not Pb during crystallisation, monazite is now used as a standard geochronometer (Harrison et al., 2002; Williams et al., 2007). Monazite has been shown to record magmatic (Broska et al., 2000; Kelts et al., 2008), metamorphic (Bingen et al., 1996; Fitzsimons et al., 2005; Foster et al., 2000, 2002; Franz et al., 1996; Krenn et al., 2009; Iizuka et al., 2010; Schulz, 2009; Spear and Pyle, 2002), and metasomatic or hydrothermal events (Ayers et al., 2006; Catlos et al., 2008; Kempe et al., 2008; Rasmussen et al., 2006; Schandl and Gorton, 2004).

Monazite is resistant to radioactive damage (Seydoux-Guillaume et al., 2004). Depending on the bulk rock chemistry, and the presence and composition of a fluid phase, it can be stable over a large PT-range (Budzyn et al., 2011; Harlov et al., 2011; Hetherington et al., 2010; Janots et al., 2008; Spear, 2010; Spear and Pyle, 2002; Wing et al., 2003). In rocks with complex P–T–t-histories, monazite growth is often reflected by the formation of distinct monazite generations or compositional subdomains within the monazite grains (Mahan et al., 2006a; Williams et al., 2007). Complex and irregularly distributed, chemically distinct monazite subdomains with sharp boundaries indicate that coupled dissolution–reprecipitation to be a common process

* Corresponding author. Tel. +49 241 8095778; fax: +49 241 8092341.
*E-mail address:* sindern@rwth-aachen.de (S. Sindern).

0024-4937/$ – see front matter © 2011 Elsevier B.V. All rights reserved.
doi:10.1016/j.lithos.2011.11.017

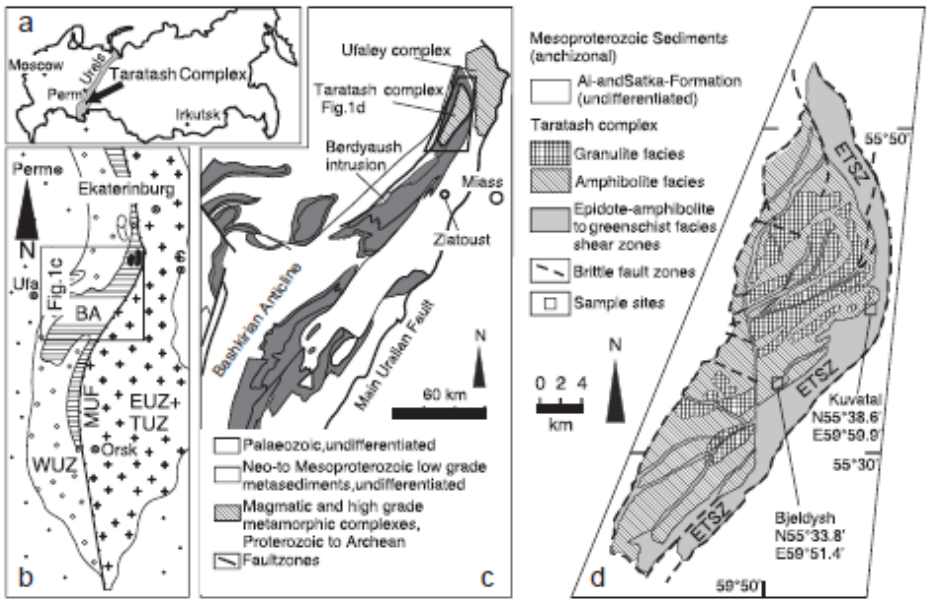


**Fig. 1.** Geographical and geological sketch maps. A, Simplified map of the Russian Federation, showing the position of the Urals and the Taratash Complex. B, Middle and Southern Urals showing the Bashkirian Anticline (BA). Further abbreviations: C Chelyabinsk, EUZ East-Uralian Zone, MUF Main Uralian Fault, TUZ Trans-Uralian Zone, WUZ West-Uralian Zone (Puchkov, 1997); box indicates position of Fig. 1c. C, Geology of the Bashkirian Anticline simplified after Ellries et al. (1999), box indicates position of Fig. 1d. D, Metamorphic facies map of the Taratash complex (Ivennykh et al., 1978), showing sample localities. ETSZ denotes East Taratash Shear Zone.

of monazite alteration (Ayers et al., 2006; Crowley and Ghent, 1999; Harlov et al., 2002, 2011; Hetherington and Harlov, 2008; Teufel and Heinrich, 1997; Williams et al., 2011). Due to low diffusion coefficients (Cherniak, 2010; Cherniak et al., 2004; Gardés et al., 2006, 2007), chemical changes caused by solid state volume diffusion within a stable monazite lattice are shown to be negligible under crustal P–T conditions, unless high grade metamorphic or magmatic temperatures prevail for long time period (Seydoux-Guillaume et al., 2004). Thus, monazite is often composed of domains, which give different ages (Braun et al., 1998; Cocherie et al., 2005; Kelts et al., 2008; Williams et al., 1999, 2007). Consequently, the mineral can be used to date events within rocks from repeatedly reactivated crustal domains such as shear zones (Catlos et al., 2004, 2007; Kohn et al., 2001; Mahan et al., 2006a,b; Williams and Jercinovic, 2002). However, this requires dating techniques with sufficient spatial resolution to obtain constraints on intracrystalline age distribution. The electron microprobe has become a common tool for dating monazite using the U–Th–Pb method, since the incorporation of common Pb, and partial Pb loss, are negligible (Cocherie and Albarède, 2001; Cocherie and Legendre, 2007; Montel et al., 1996; Spear et al., 2009; Williams et al., 2007). However, any disturbance in an isotope decay system can only be shown by assessment of concordancy with other decay systems, requiring isotope ratio determination (Williams et al., 2006). Beam techniques such as ion-probe or LA-ICP-MS assisted by high spatial resolution electron microprobe analysis appear to be the most suitable for a study of monazite (Catlos et al., 2002; Williams et al., 2006, 2007).

The eastern margin of the East European craton has been repeatedly affected by Archean, Palaeo- to Neoproterozoic, and Palaeozoic (Uralian) magmatic and tectonometamorphic events (Gee and Pease, 2004; Puchkov, 2002). In such geologically complex regions, shear zones have the potential to represent the focus of several deformation, hydrothermal, and even magmatic events (Alsop and Holdsworth, 2004). This study focuses on monazite from a major shear zone that is situated at the eastern margin of the Taratash complex in the northernmost Bashkirian Anticline (Fig. 1). The Taratash complex is one of the oldest crustal domains in the Middle Uralian orogen, and thus represents a window into the geologic past of the East European craton (Ronkin et al., 2007, 2008; Scarrow et al., 2002).

The aim of this study is to investigate the compositional and isotopic responses of monazite from this shear zone to a multistage geologic history and to explore the applicability of monazite for dating different geologic events. In order to do this, five mylonite samples from the two well-characterized shear zone outcrops were studied (Bjeldysh and Kuvatal, Fig. 1; Sindern et al., 2005). Monazite was carefully characterized by electron microprobe analysis. In total, 18 crystals were chosen for a detailed mineral-chemical investigation. Based on this, 61 U–Pb-isotope analyses on seven monazite crystals were performed by means of LA-SF-ICP-MS at the Goethe-University Frankfurt. The ages of protolith formation, deformation, and retrogression, recorded in monazite from the Taratash complex, are discussed within the framework of the Archean to Proterozoic tectonometamorphic history of the eastern margin of the East European Craton.

## 2. Geological setting of the Taratash complex

The Taratash complex is composed of several granulite- to amphibolite-facies crustal segments, which are dominated by strongly foliated metaacidic and metabasic rocks (Sindern et al., 2005). The individual crustal segments are separated by epidote-amphibolite- to greenschist-facies shear zones, which vary in thickness from several decametres to approximately 500 m (Fig. 1). A shear zone (up to 4 km wide), which is here referred to as the East Taratash Shear Zone (ETSZ), dominates the eastern margin of the complex. The foliation in the ETSZ dips 50–75° to the E or SE. The associated mineral stretching lineation plunges 42° to 63° to the SE. Kinematic indicators show a consistent top-to-the NW reverse sense of movement (Sindern et al., 2005). The samples investigated in this study include metagranitoid and

**Table 1**
Age data from the Taratash complex and the Bashkirian Anticline.

| Geologic event | Age (Ma) |
|---|---|
| Taratash complex | |
| Granulite facies metamorphism, zircon, U–Pb[1] | 3504 ± 210 |
| Granulite facies metamorphism, zircon, U–Pb[2] | 2913 ± 133 |
| HT metamorphism (gneiss), zircon, U–Pb[1] | 2461 ± 36 |
| Leucocratic granite formation, zircon, U–Pb[3] | 2344 ± 29 |
| HT metamorphism (migmatite, augen-gneisses), zircon, U–Pb[2] | 2127 ± 65 |
| Migmatite formation, zircon, U–Pb[3] | 2044 ± 8 |
| HT metamorphism (gneiss), zircon, U–Pb[4] | 2032 ± 27 |
| Retrograde biotite formation, biotite, Rb-Sr[3] | 1810 ± 41 |
| Partial resetting of Rb–Sr-, K–Ar-systems in shear zone [3] | 1350–1200 |
| Exhumation of Taratash complex, Rb-Sr, K-Ar[3] | 300 |
| Bashkirian anticline | |
| Granite formation, zircon, U–Pb[3] | 1848 ± 8 |
| Basaltic dyke intrusion, Baikal, baddeleyite, U–Pb[5] | 1385 ± 1.4 |
| Nepheline syenite formation, Berdyaush, zircon, U–Pb[6] | 1373 ± 21 |
| Nepheline syenite formation, Berdyaush, zircon, U–Pb[7] | 1368 ± 6 |

1 Ronkin et al. (2007), 2 Krasnobayev and Cherednichenko (2005), 3 Sindern et al. (2005), 4 Ronkin et al. (2008), 5 Ernst et al. (2006), 6 Ronkin et al. (2005), 7 Sindern et al. (2003).

metasedimentary rocks from two localities called Bjeldysh and Kuvatal (Fig. 1).

Details about the geology and geochronology of the Taratash complex are given by Sindern et al. (2005). In general, the currently available geochronological data suggest that the complex underwent a polyphase and prolonged tectono-metamorphic history between ca. 3500 and 1200 Ma (Sindern et al., 2005; Table 1). In the Palaeozoic, the Taratash complex was exhumed and thrusted towards the west over Devonian and Proterozoic strata of the Bashkirian Anticline during the Uralian orogeny (Alekseyev, 1984; Malakhova et al., 1978). However, the Uralian deformation, which is observed in the Bashkirian anticline (Brown et al., 2001; Hetzel, 1999; Puchkov, 2002), is not recorded in isotope geochronometers in the Taratash complex (Sindern et al., 2005). The same is true for the structural or metamorphic expressions of the Timanian orogeny between 850 and 560 Ma (Beckholmen and Glodny, 2004; Gee and Pease, 2004; Glasmacher et al., 1999, 2001, 2004; Puchkov, 1997; Willner et al., 2003). Therefore, the geologic evolution of the Taratash complex mainly reflects the earlier stages in the geologic history of the East European craton.

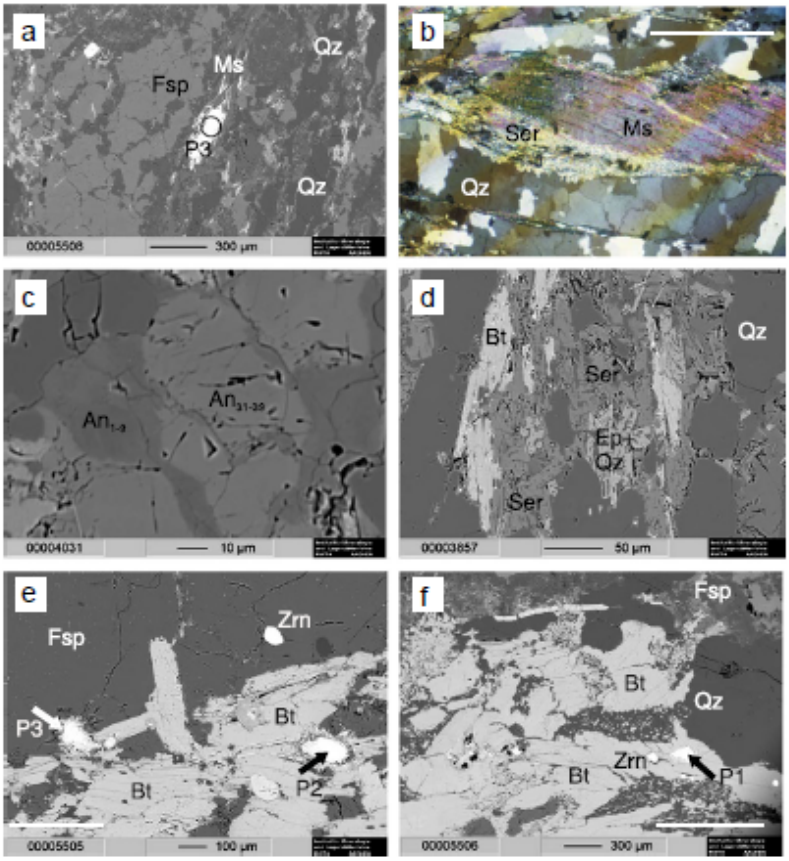


**Fig. 2.** Back-scattered electron (BSE) images and photomicrograph of samples from the Taratash shear zone, abbreviations according to Whitney and Evans (2010). Bt = biotite, Ep = epidote, Fsp = feldspar, Ms = muscovite, Qz = quartz, Ser = sericite, Zrn = zircon. A, BSE image of monazite grain P3 in metagranitoid sample 113. The foliation is defined by muscovite and quartz-ribbons. B, photomicrograph showing quartz-ribbons and mica porphyroclast with post-deformational sericite at edges (XPL), scale bar 1000 µm. C, BSE image (sample 116; Bjeldysh) of metagranitoid rock. Retrograde albite replaces plagioclase ($An_{31-39}$) formed during dynamic recrystallisation. D, BSE image of sample 116 (metagranitoid), showing the post-deformational replacement of feldspar by sericite, epidote and quartz. E, F, metasedimentary rock (sample 961; Kuvatal). Monazite grains P1–P3 are closely associated with biotite, which defines the foliation.

## 3. Analytical procedures

### 3.1. Electron microprobe analysis

Electron microprobe analyses were performed with a JEOL JXA 8900R microprobe at the Institute of Mineralogy and Economic Geology at RWTH Aachen University. The instrument, equipped with 5 spectrometers, was operated at an acceleration voltage of 20 kV, a probe current of 23.6 nA, and a focussed beam with a diameter of 1–2 μm (10 μm for fluorapatite). The X-ray lines used, in accordance with Pyle et al. (2002), were AlK$_\alpha$, SiK$_\alpha$, PK$_\alpha$, CaK$_\alpha$, FeK$_\alpha$, YL$_\alpha$, LaL$_\alpha$, CeL$_\alpha$, PrL$_\beta$, NdL$_\beta$, SmL$_\beta$, GdL$_\beta$, PbM$_\beta$, ThM$_\alpha$, and UM$_\beta$. The spectral interference of ThM$_\gamma$ on UM$_\beta$ was corrected offline. Calibration was carried out using natural and synthetic standards: Al, Si, Ca on plagioclase, P, La, Ce, Pr, Nd on monazite, Y, Sm, Gd, and U on synthetic glass, Fe on fayalite, Pb on galena, and Th on thorianite. ZAF matrix correction for element analyses was calculated by the JEOL JXA 8900R 3.02 software. Concentration contour maps showing the distribution of PbO, $ThO_2$ and $Y_2O_3$ were calculated by linear interpolation of concentration values between quantitative microprobe spot-analyses.

### 3.2. LA-ICP-MS analysis

In situ monazite U–Pb isotope analyses were carried out at Goethe-University Frankfurt (GUF), using a Thermo-Finnigan Element II sector field ICP-MS coupled to a New Wave UP213 UV laser with a teardrop low-volume cell following the method described in Gerdes and Zeh (2006, 2009). Monazite grains were analysed on polished thin sections after electron microprobe work. The laser was fired with 5 Hz repetition rate and an energy density of about 2 Jcm$^{-2}$. The spot size used was 16 μm with a typical depth penetration of about 8 to 10 μm during 21 s of ablation. Signal was tuned for maximum sensitivity while keeping oxide formation rate below 0.1% (UO/U). All data is corrected for common-Pb, based on the background and interference-corrected $^{204}$Pb signal (daily $^{204}$Hg = 245 ± 20 cps) and a model Pb composition (Stacey and Kramers, 1975). Within-run Pb/U fractionation was corrected for each analysis using a linear regression through all ratios. Subsequently instrumental mass bias and drift were corrected by normalisation to reference zircon GJ-1 (Gerdes and Zeh, 2006). A spot size of 60 μm was used for GJ-1 to achieve a signal strength and Pb/U fractionation behaviour similar to that of the monazites. Previous studies

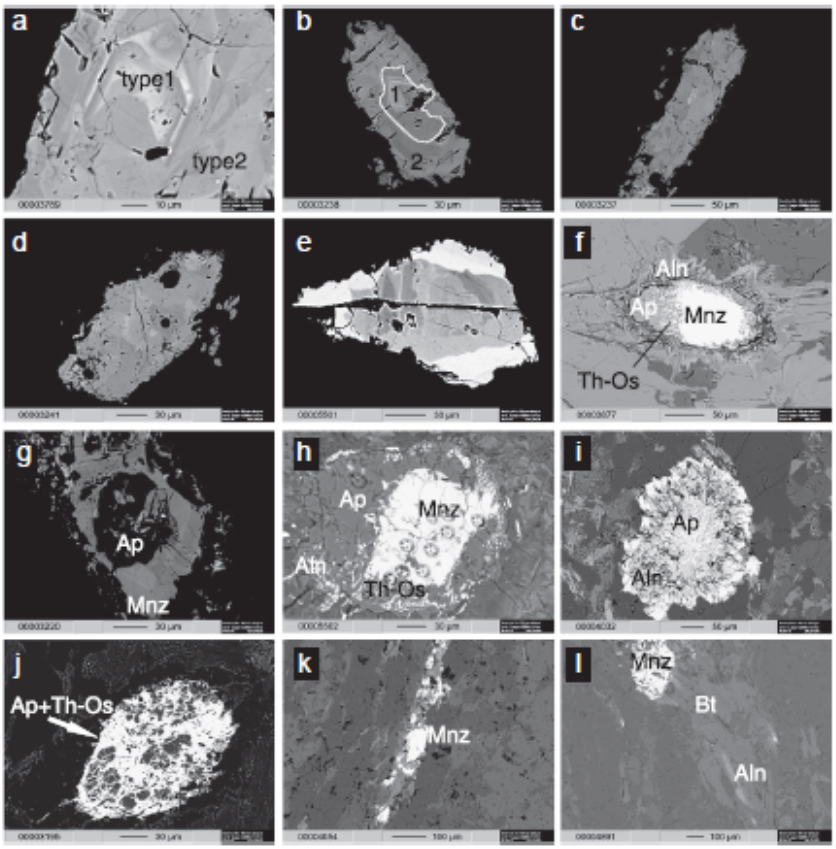


**Fig. 3.** Back-scattered electron (BSE) images of selected monazite grains and their breakdown-products, abbreviations according to Whitney and Evans (2010). A, B, euhedral oscillatory zonation, type 1 monazite grains 134 P2 and 133P4 (metagranitoid rock). Stippled line in B indicates contour of type 1 monazite core. C, D, anhedral type 2 monazite with patchy domains in metagranitoid rock, grains 133 P3 and 133 P5. E, patchy zoned monazite, metasediment sample 961, grain 961 P1. F, grain 961 P2 with corona composed of fluorapatite (Ap), REE- rich epidote, allanite (Aln), and Th-orthosilicate (Th-Os). Note that Th-Os appears larger in BSE image due to microprobe setting of contrast and brightness which was necessary to show apatite. G, monazite showing advanced breakdown with fluorapatite in centre, grain 132 P5 (metagranitoid rock). H, monazite showing advanced breakdown within a corona, grain 132 P1 (metagranitoid rock). I, J, reaction products of monazite, grains 116 A11 and 132 P3 (metagranitoid rock). K, grain R78 M3 (metagranitoid rock), characterized by advanced breakdown forming a dispersed reaction zone. L, Allanite, sample R78, forming along biotite cleavage planes distant from monazite.

**Table 2**
Representative analyses of monazite from metagranitoid (mg) and metasedimentary (ms) rocks of the East Taratash Shear Zone.

| | 133P4 | | 133P2 | | 133P3 | | | 134P2 | 961P2 | 132 P5 | |
|---|---|---|---|---|---|---|---|---|---|---|---|
| | type 1, core | | type 2, patchy domain | | | | | | | | |
| | 31mg | 34mg | 5mg | 14mg | 17mg | 21mg | 27mg | 2mg | 13ms | 7mg | 12mg |
| $P_2O_5$ | 24.92 | 25.35 | 26.39 | 27.94 | 27.54 | 26.37 | 27.24 | 26.88 | 28.07 | 25.55 | 24.52 |
| $SiO_2$ | 2.16 | 1.91 | 0.95 | 0.57 | 0.43 | 1.07 | 0.46 | 0.84 | 0.00 | 1.87 | 2.57 |
| $ThO_2$ | 12.78 | 12.61 | 12.42 | 10.17 | 11.66 | 10.82 | 10.16 | 10.73 | 5.59 | 11.72 | 14.65 |
| $UO_2$ | 0.27 | 0.16 | 0.36 | 0.36 | 0.32 | 0.47 | 0.52 | 0.23 | 0.39 | 0.05 | 0.14 |
| $Y_2O_3$ | 1.33 | 1.72 | 0.18 | 1.95 | 0.70 | 0.66 | 0.38 | 0.51 | 1.72 | 0.53 | 0.37 |
| $La_2O_3$ | 11.76 | 11.38 | 12.07 | 12.29 | 12.16 | 12.29 | 11.78 | 12.85 | 13.63 | 14.00 | 14.71 |
| $Ce_2O_3$ | 28.43 | 28.39 | 28.57 | 28.63 | 28.39 | 29.76 | 29.14 | 29.52 | 31.81 | 30.42 | 28.73 |
| $Pr_2O_3$ | 4.31 | 4.42 | 4.28 | 4.11 | 4.18 | 4.38 | 4.44 | 4.22 | 4.54 | 4.08 | 3.61 |
| $Nd_2O_3$ | 9.31 | 9.23 | 9.12 | 8.70 | 9.04 | 9.61 | 9.95 | 9.31 | 10.14 | 8.58 | 7.53 |
| $Sm_2O_3$ | 1.77 | 1.86 | 1.58 | 1.51 | 1.62 | 1.70 | 2.05 | 1.73 | 1.50 | 1.34 | 1.05 |
| $Gd_2O_3$ | 1.21 | 1.29 | 0.68 | 0.94 | 0.96 | 0.88 | 1.26 | 0.86 | 0.51 | 0.73 | 0.43 |
| CaO | 0.57 | 0.74 | 1.69 | 1.48 | 2.01 | 1.15 | 1.57 | 1.36 | 1.00 | 0.66 | 0.97 |
| PbO | 1.39 | 0.97 | 1.10 | 0.95 | 0.87 | 1.15 | 0.79 | 0.81 | 0.59 | 0.54 | 0.65 |
| Sum | 100.21 | 100.05 | 99.39 | 99.60 | 99.88 | 100.30 | 99.75 | 99.86 | 99.48 | 100.07 | 99.92 |
| | cations, 16 Ox | | | | | | | | | | |
| | **133P4** | **133P4** | **133P2** | **133P2** | **133P3** | **133P3** | **133P3** | **134P2** | **961P2** | **132P5** | **132P5** |
| | 31 | 34 | 5 | 14 | 17 | 21 | 27 | 2 | 13.00 | 7 | 12 |
| P | 3.51 | 3.56 | 3.70 | 3.82 | 3.79 | 3.68 | 3.78 | 3.73 | 3.85 | 3.58 | 3.46 |
| Si | 0.36 | 0.32 | 0.16 | 0.09 | 0.07 | 0.18 | 0.07 | 0.14 | 0.00 | 0.31 | 0.43 |
| Th | 0.48 | 0.48 | 0.47 | 0.37 | 0.43 | 0.41 | 0.38 | 0.40 | 0.21 | 0.44 | 0.56 |
| U | 0.01 | 0.01 | 0.01 | 0.01 | 0.01 | 0.02 | 0.02 | 0.01 | 0.01 | 0.00 | 0.01 |
| Y | 0.12 | 0.15 | 0.02 | 0.17 | 0.06 | 0.06 | 0.03 | 0.04 | 0.15 | 0.05 | 0.03 |
| La | 0.72 | 0.70 | 0.74 | 0.73 | 0.73 | 0.75 | 0.71 | 0.78 | 0.82 | 0.85 | 0.90 |
| Ce | 1.73 | 1.72 | 1.73 | 1.69 | 1.69 | 1.79 | 1.75 | 1.77 | 1.89 | 1.84 | 1.75 |
| Pr | 0.26 | 0.27 | 0.26 | 0.24 | 0.25 | 0.26 | 0.27 | 0.25 | 0.27 | 0.25 | 0.22 |
| Nd | 0.55 | 0.55 | 0.54 | 0.50 | 0.53 | 0.56 | 0.58 | 0.55 | 0.59 | 0.51 | 0.45 |
| Sm | 0.10 | 0.11 | 0.09 | 0.08 | 0.09 | 0.10 | 0.12 | 0.10 | 0.08 | 0.08 | 0.06 |
| Gd | 0.07 | 0.07 | 0.04 | 0.05 | 0.05 | 0.05 | 0.07 | 0.05 | 0.03 | 0.04 | 0.02 |
| Ca | 0.10 | 0.13 | 0.30 | 0.26 | 0.35 | 0.20 | 0.28 | 0.24 | 0.17 | 0.12 | 0.17 |
| Pb | 0.06 | 0.04 | 0.05 | 0.04 | 0.04 | 0.05 | 0.04 | 0.04 | 0.03 | 0.02 | 0.03 |
| Sum | 8.09 | 8.09 | 8.10 | 8.06 | 8.09 | 8.10 | 8.09 | 8.09 | 8.09 | 8.08 | 8.10 |

have shown that LA-SF-ICP-MS with non-matrix matched standardization can yield precise and accurate results (e.g. Dill et al., 2007; Meyer et al., 2006; Millonig et al., 2008)

Reported uncertainties ($\pm 2\sigma$) were propagated by quadratic addition of the external reproducibility (standard deviation) of the GJ-1 reference standard (1.1% and 1.4% for $^{207}Pb/^{206}Pb$ and $^{206}Pb/^{238}U$; $n=15$) of the day and the within-run statistics of each analysis (2 s.e., standard error). Accuracy and precision of the non-matrix matched standardization was checked by repeated analyses ($n=9$) of the Moacir monazite, which yielded a weighted mean $^{207}Pb/^{235}U$ and $^{208}Pb/^{232}U$ age of 506.3 ± 6.3 (MSWD = 1.3; S.D.: = 3.5%) and 505.3 ± 5.3 Ma (MSWD = 1.7; S.D. = 2.7%), respectively. This is in perfect agreement with recent ID-TIMS analyses of the Moacir monazite (Gasquet et al., 2010).

## 4. Petrography, textures and mineral reactions

### 4.1. Metagranitoid- and metasedimentary rocks

Samples taken from the outcrop at Bjeldysh are rich in feldspar and quartz, have a chemical composition similar to anatectic granites (Batchelor and Bowden, 1985), and are thus considered as metagranitoid rocks. The rocks are strongly mylonitic. The foliation is defined by muscovite, biotite, and quartz ribbons (Fig. 2a, b). The syntectonic mineral assemblage comprises K-feldspar, plagioclase ($An_{31-39}$, Fig. 2c), biotite, muscovite, quartz, ± garnet (rim), and monazite. Feldspars, garnet, and locally muscovite form porphyroclasts that reflect an earlier metamorphic event. The feldspar porphyroclasts show core and mantle structures, which point to minimum temperatures of ca. 450–550 °C (Pryer, 1993). Preliminary PT estimates for the syntectonic assemblage yield temperatures of 600–670 °C and c. 3.5 kbar (Sindern et al., 2005, 2009), indicating amphibolite-facies conditions during shear zone formation.

The metagranitoid rocks are variably overprinted by a posttectonic retrograde mineral assemblage made up of albite ($An_{1-9}$), chlorite, epidote, sericite, quartz, and locally fluorapatite, allanite and xenotime (Fig. 2c, d). The latter three minerals are restricted to reaction zones around monazite.

Albite ($An_{1-9}$) substitutes dynamically recrystallized syntectonic plagioclase ($An_{31-39}$) along grain boundaries (Fig. 2c). Locally, the plagioclase is also replaced by a fine-grained assemblage of epidote, quartz, and sericite (Fig. 2d). Epidote ($Ep_{0.41-0.54}$) replaces biotite along cleavage planes. Chlorite is a minor retrograde phase that locally replaces biotite. Sericite replaces syntectonic muscovite and feldspar porphyroclasts and overgrows the mylonitic foliation (Fig. 2b, d). It is therefore attributed to a greenschist-facies overprint associated with fluid influx subsequent to mylonitisation.

Samples taken from the outcrop at Kuvatal (Fig. 1) have a major element distribution characteristic of pelites and greywackes (Batchelor and Bowden, 1985; Sindern, unpublished data), and are therefore interpreted as metasedimentary rocks. The syntectonic mineral assemblage is biotite, K-feldspar, plagioclase ($An_{29-37}$), quartz, monazite, and, locally, fluorapatite. Similar to the metagranitoid rocks, the peak assemblage is locally overprinted by a greenschist-facies mineral assemblage of plagioclase, chlorite, epidote, sericite, quartz, titanite, fluorapatite, and allanite.

### 4.2. Monazite

Monazite predominantly occurs associated with biotite (Fig. 2e, f) within both metagranitoid and metasedimentary rocks. The grains are anhedral isometric to elongated and have a maximum size of

300 μm. However, most crystals are <100 μm (Fig. 3a–e). Monazite has highly embayed irregular grain boundaries, indicative of corrosion (Fig. 3b–h). In backscattered electron (BSE) images, two types of monazite grains or domains can be distinguished. Type 1 monazite occurs as rare, euhedral cores within monazite of the metagranitoid rocks. This type of monazite exhibits partly oscillatory zonation (Fig. 3a, b), a common feature of crystals grown in igneous rocks (Shore and Fowler, 1996).

Type 2 monazite is the dominant type of monazite. This type of monazite forms domains that surround the euhedral cores (Fig. 3a, b), or occurs as individual grains in both metagranitoid and metasedimentary rocks (Fig. 3c–h). The grains are characterized by patchy zonation, and the boundaries between patches are sharp and partly lobate (Fig. 3c–h). In monazite P4 of metagranitoid sample 133, the patchy-zoned domains are intergrown with the type 1 core (Fig. 3b).

### 4.3. Fluorapatite, allanite, REE-rich epidote, and Th-orthosilicate

Fluorapatite, allanite, and REE-rich epidote often form reaction zones or coronas around monazite in both metagranitoid and metasedimentary rocks. Irrespective of the position within the sample or the kind of neighbouring minerals, the coronas or irregular reaction zones replace monazite to different degrees, ranging from a partial replacement at the monazite rims to complete pseudomorphs after monazite (Fig. 3f–j). The coronas consist of an inner ring of fluorapatite and an outer zone of allanite and epidote (Fig. 3f, h). Allanite from the outer zone locally overgrows neighbouring phases such as biotite and quartz. Similar corona-textures, which are typical of monazite breakdown under various metamorphic conditions, have been described by Finger et al. (1998), Broska and Siman (1998), Broska et al. (2005), Krenn et al. (2008), Petrik and Konecny (2009), and Rasmussen and Muhling (2009).

In the irregular reaction zones (Fig. 3k, l), fluorapatite and allanite occur associated with monazite without forming a corona. Here, allanite grows along cleavage planes of biotite or epidote (Fig. 3l). Fluorapatite and allanite locally also occur as inclusions in monazite (Fig. 3g), or form anhedral isolated grains associated with epidote and biotite.

Within fluorapatite and allanite, tiny bright inclusions and/or networks of fracture fillings are visible in the BSE images (Fig. 3h–j). These phases consist primarily of Th and Si with minor amounts of

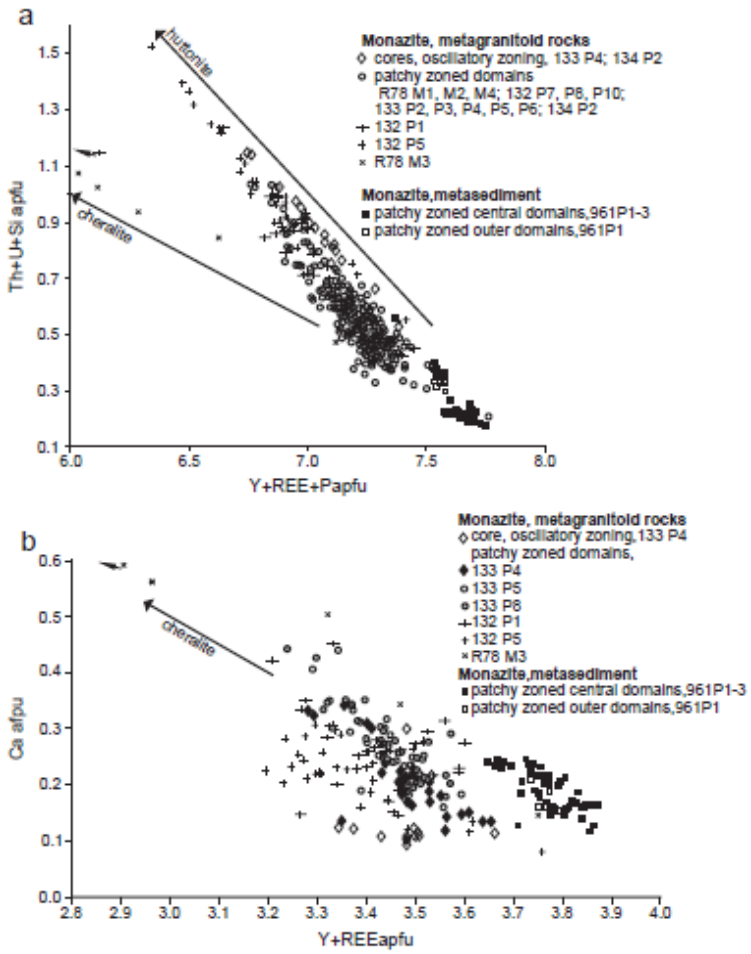


**Fig. 4.** A plot of Y + REE + P vs. Th + U + Si concentrations of monazite from metagranitoid and metasedimentary rocks. Monazite from metasedimentary rocks has the lowest cheralite and huttonite contents. Compositional data of euhedral magmatic cores (grains 133 P4, 134 P2) show marked variation along the huttonite substitution vector. Cheralite component increases in patchy-zoned grains. Highest huttonite and cheralite components occur in patchy-zoned monazite grains characterized by advanced breakdown (grains 132 P1, 132 P5, R78 M3). B, plot of Y + REE vs. Ca in monazite, showing increase of Ca and the cheralite component in patchy-zoned grains (metagranitoid samples).

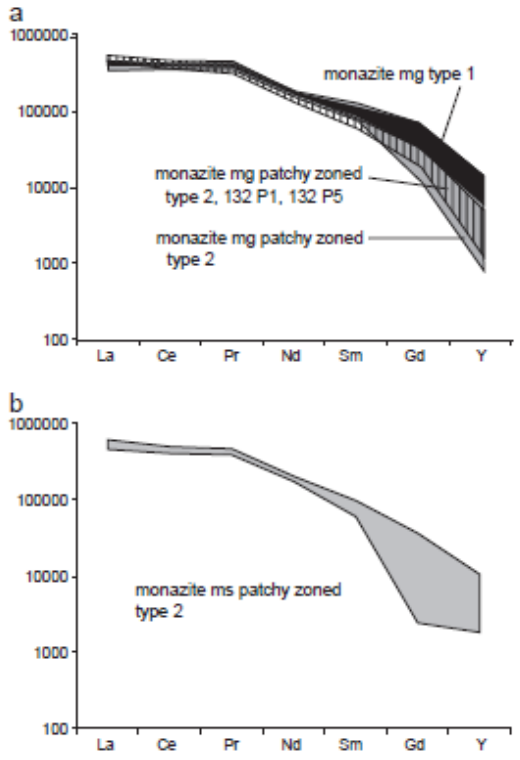


**Fig. 5.** Chondrite-normalized Y+REE patterns (chondrite according to McDonough and Sun, 1995). A, monazite from metagranitoid (mg) samples, compositional variation increases towards heavier REE (represented by Y) in patchy-zoned grains. The hatched field shows compositions of grains 132 P1 and P5 characterized by advanced breakdown. B, patchy monazite from metasedimentary (ms) samples, characterized by somewhat lower Gd values relative to monazite from metagranitoid sample.

Ca and P, which may be due to contamination from adjacent fluorapatite. This indicates that these phases are either tetragonal thorite or monoclinic huttonite. The small grain size (<3 μm) precludes quantitative microprobe analysis. In addition, tiny grains of xenotime are locally associated with both fluorapatite and allanite.

### 4.4. Mineral chemistry of monazite

The monazite grains are characterised by various amounts of Th + U + Si, which inversely covary with Y + REE + P (Table 2, Fig. 4a). This covariation is due to the substitution of the isostructural compositional endmembers monazite sensu stricto (Y + REE$PO_4$) and huttonite ($ThSiO_4$) or coffinite ($USiO_4$). It is most pronounced in the euhedral cores of metagranitoid monazite (Fig. 4a). Most electron microprobe analyses from the patchy domains in monazite from the metagranitoid rocks plot slightly below this trend. This is best explained by an admixture of cheralite ($CaTh(PO_4)_2$, Linthout, 2007) as another compositional endmember (Fig. 4a), consistent with the strong inverse covariation of Ca and Y + REE (Fig. 4b).

The incorporation of the cheralite component obviously is linked to the formation of the patchy domains. This is best illustrated by grain 133 P4 (Fig. 4b). Analyses of the oscillatory zoned type 1 monazite have the lowest Ca contents, whereas those from the outer patchy domains (type 2 monazite) follow the cheralite trend. This trend is also recorded by many other patchy-zoned grains, such as grains 133 P5 and 133 P8 (Fig. 4b). However, some patchy domains from metagranitoid monazite deviate from this trend, either by having a very pronounced cheralite- (e.g. R78 M3) or huttonite-component (e.g. 132 P5), or by displaying a significant scatter with respect to both components (e.g. 132 P1). In contrast to the other grains, these latter three grains are characterized by advanced breakdown either in a reaction zone (R78 M3, Fig. 3k) or a corona (132 P1, P5, Fig. 3g, h). In grain 132 P5, this breakdown even caused fluorapatite growth in the centre of the grain (Fig. 3g).

Crystals from the metasedimentary rocks (sample 961 P1–P3) have higher relative proportions of the monazite (s.s.) component, and plot in a field distinct from the monazite crystals from metagranitoid rocks (Fig. 4a). In these monazites, the patchy cores are enriched

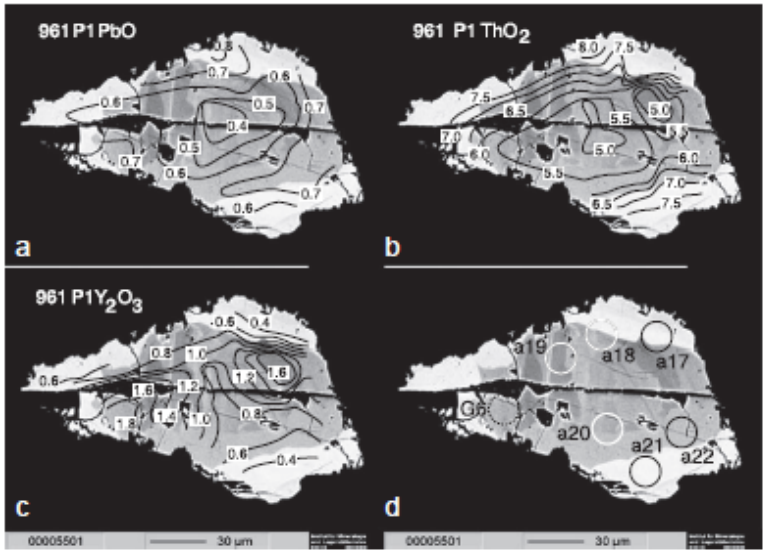


**Fig. 6.** Concentration contour maps of monazite grain 961 P1 (metasediment) showing the distribution of PbO (a), $ThO_2$ (b), and $Y_2O_3$ (c) in wt.% calculated from 22 quantitative analyses and spots analyzed by LA-ICP-SFMS (d). Solid lines in (d) indicate spots with concordant U–Pb dates, while stippled lines show spots with discordant dates. White circles in (d) indicate domains >2200 Ma, black circles those that are <2100 Ma (see Fig. 10f, Table 5).

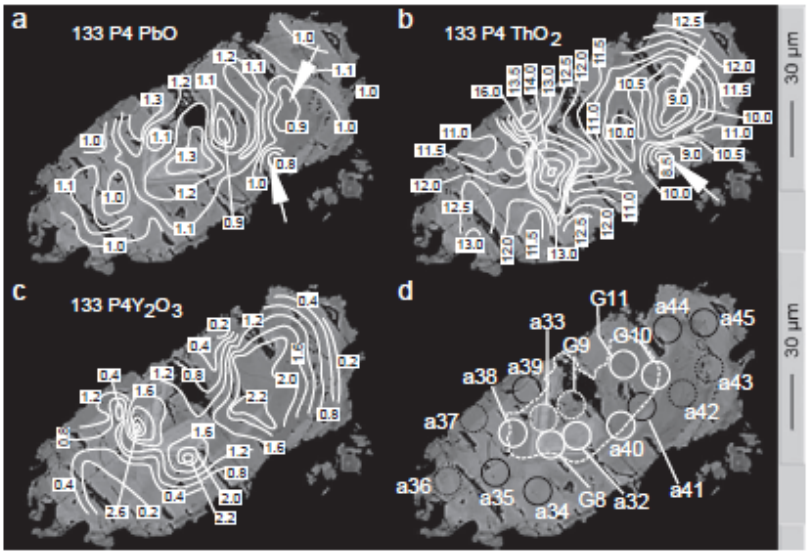


**Fig. 7.** Concentration contour maps of monazite grain 133 P4 (metagranitoid rock) with a euhedral core. Data as in Fig. 6, calculated from 45 quantitative analyses. Arrows in (a) and (b) point to correlating local minima in $ThO_2$ and PbO. Solid lines in (d) indicate spots with concordant U–Pb dates. Stippled lines show spots with discordant dates. Outline of type 1 core as in Fig. 3b. White circles in (d) indicate crystal domains with U–Pb dates of ca. 2230 ± 22 Ma. Black circles denote dates of ca. 2066 ± 22 Ma (Fig. 10a, b, Table 5).

in monazite (s.s.), whereas the outer domains are relatively enriched in the huttonite component.

The chondrite-normalised Y + REE patterns of all monazites show a strong enrichment in La, Ce, and Pr and a decrease from Nd to Y (Fig. 5a, b). Type 1 monazite is characterized by a lower scatter of concentration for Sm, Gd, and Y compared to type 2 monazite. The metasedimentary monazites have somewhat lower concentrations of Sm, Gd, and Y, and show large variations in their Gd contents (Fig. 5b). Low Gd and Y concentrations predominate in domains close to the edges.

Concentration contour maps for PbO, $ThO_2$, and $Y_2O_3$ are shown in Figs. 6–8. In grain 961 P1 (metasedimentary rock), the Th and Pb

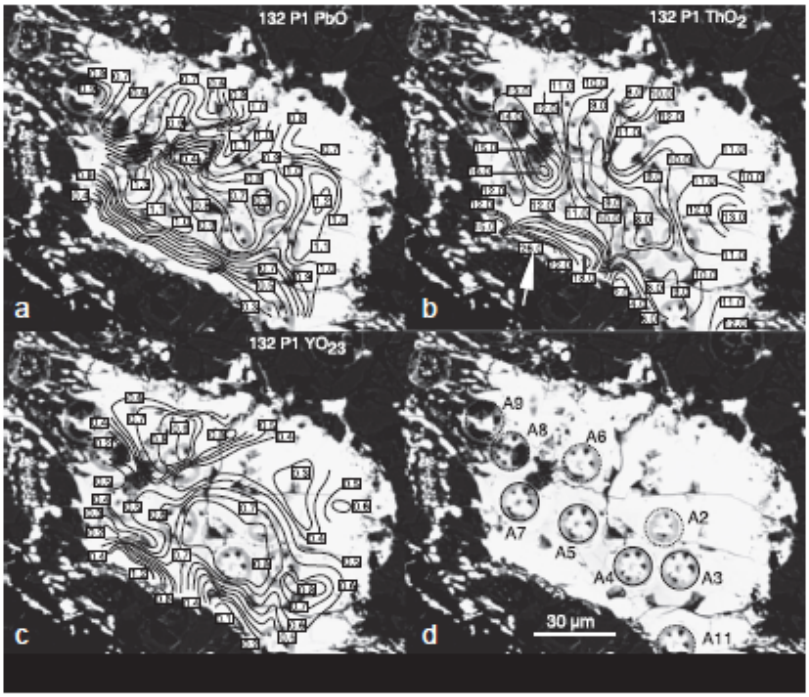


**Fig. 8.** Concentration contour maps of patchy-zoned monazite grain characterized by advanced breakdown, 132 P1 (metagranitoid rock). Data as in Fig. 6, calculated from 54 quantitative analyses. Solid lines in (d) indicate spots with concordant U–Pb dates, stippled lines show spots with discordant dates (data shown in Fig. 10d, Table 5).

**Table 3**
Representative chemical analyses from apatite of metagranitoid (mg) and metasedimentary (ms) rocks of the East Taratash Shear Zone, rz denotes apatite in reaction zones around monazite.

| | 29/1 P1–4 | 29/1 P7-24 | 29/1 P7-25 | 29/1 P8a-38 | 29/1 P8a-40 | 29/1 P12-1 | 29/1 P13-27 | 37/1 6 | 37/1 12 | 97R10 5 51 | 97R10 5 70 |
|---|---|---|---|---|---|---|---|---|---|---|---|
| | mg rz | mg rz | mg rz | mg rz | mg rz | mg rz | mg rz | ms | ms | ms | ms |
| $P_2O_5$ | 38.68 | 39.32 | 39.03 | 40.10 | 39.24 | 39.80 | 41.54 | 40.78 | 41.02 | 40.55 | 41.35 |
| $SiO_2$ | 2.44 | 0.91 | 0.92 | 1.20 | 1.19 | 0.93 | 0.44 | 0.10 | 0.03 | 0.04 | 0.05 |
| $ThO_2$ | 1.83 | 3.53 | 3.03 | 0.87 | 2.20 | 1.89 | 0.68 | 0.04 | <0.01 | <0.01 | <0.01 |
| $UO_2$ | n.d. | n.d. | n.d. | n.d. | n.d. | n.d. | n.d. | <0.01 | <0.01 | <0.01 | <0.01 |
| $Y_2O_3$ | 0.05 | 0.14 | 0.19 | 0.08 | 0.20 | 0.04 | 0.04 | 0.11 | 0.06 | 0.02 | 0.03 |
| $La_2O_3$ | 0.04 | 0.41 | 0.15 | 0.04 | 0.06 | 0.07 | 0.03 | 0.04 | <0.01 | 0.02 | <0.01 |
| $Ce_2O_3$ | 0.27 | 0.99 | 0.64 | 0.24 | 1.13 | 0.52 | 0.20 | 0.05 | 0.06 | 0.06 | 0.04 |
| $Pr_2O_3$ | n.d. | n.d. | n.d. | n.d. | n.d. | n.d. | n.d. | <0.01 | <0.01 | <0.01 | <0.01 |
| $Nd_2O_3$ | n.d. | n.d. | n.d. | n.d. | n.d. | n.d. | n.d. | 0.02 | 0.07 | 0.03 | <0.01 |
| PbO | n.d. | n.d. | n.d. | n.d. | n.d. | n.d. | n.d. | <0.01 | <0.01 | <0.01 | <0.01 |
| FeO* | 0.45 | 0.12 | 0.12 | 0.12 | 0.23 | 0.08 | 0.10 | 0.17 | 0.16 | 0.13 | 0.15 |
| SrO | 0.05 | 0.07 | 0.07 | 0.04 | 0.09 | 0.09 | 0.06 | n.d. | n.d. | n.d. | n.d. |
| CaO | 52.16 | 52.72 | 53.26 | 54.41 | 53.02 | 53.47 | 53.21 | 56.26 | 56.38 | 55.74 | 55.81 |
| F | 3.65 | 2.70 | 3.03 | 3.77 | 3.32 | 3.81 | 3.73 | 2.91 | 2.94 | 3.83 | 3.69 |
| Cl | 0.05 | 0.02 | 0.02 | 0.02 | 0.01 | 0.05 | 0.08 | 0.10 | 0.07 | 0.09 | 0.08 |
| −O = F | 1.55 | 1.14 | 1.28 | 1.59 | 1.40 | 1.62 | 1.57 | 1.23 | 1.24 | 1.61 | 1.55 |
| Total | 98.12 | 99.79 | 99.18 | 99.30 | 99.29 | 99.13 | 98.54 | 99.36 | 99.55 | 98.90 | 99.66 |
| | | | | | | | | | | | |
| Cations | O,F,Cl | = 26 | | | | | | | | | |
| P | 5.68 | 5.83 | 5.79 | 5.80 | 5.78 | 5.81 | 6.00 | 5.73 | 5.75 | 5.64 | 5.71 |
| Si | 0.42 | 0.16 | 0.16 | 0.20 | 0.21 | 0.16 | 0.08 | 0.02 | 0.01 | 0.01 | 0.01 |
| Th | 0.07 | 0.14 | 0.12 | 0.03 | 0.09 | 0.07 | 0.03 | 0.00 | 0.00 | 0.00 | 0.00 |
| U | | | | | | | | 0.00 | 0.00 | 0.00 | 0.00 |
| Y | 0.00 | 0.01 | 0.02 | 0.01 | 0.02 | 0.00 | 0.00 | 0.01 | 0.01 | 0.00 | 0.00 |
| La | 0.00 | 0.03 | 0.01 | 0.00 | 0.00 | 0.00 | 0.00 | 0.00 | 0.00 | 0.00 | 0.00 |
| Ce | 0.02 | 0.06 | 0.04 | 0.02 | 0.07 | 0.03 | 0.01 | 0.00 | 0.00 | 0.00 | 0.00 |
| Pr | | | | | | | | 0.00 | 0.00 | 0.00 | 0.00 |
| Nd | | | | | | | | 0.00 | 0.00 | 0.00 | 0.00 |
| Pb | | | | | | | | 0.00 | 0.00 | 0.00 | 0.00 |
| Fe | 0.07 | 0.02 | 0.02 | 0.02 | 0.03 | 0.01 | 0.01 | 0.02 | 0.02 | 0.02 | 0.02 |
| Sr | 0.01 | 0.01 | 0.01 | 0.00 | 0.01 | 0.01 | 0.01 | | | | |
| Ca | 9.69 | 9.89 | 10.00 | 9.95 | 9.88 | 9.88 | 9.73 | 10.01 | 10.00 | 9.82 | 9.75 |
| F | 2.00 | 1.37 | 1.68 | 2.04 | 1.83 | 2.08 | 2.01 | 1.53 | 1.54 | 1.99 | 1.90 |
| Cl | 0.01 | 0.01 | 0.01 | 0.01 | 0.00 | 0.01 | 0.02 | 0.03 | 0.02 | 0.03 | 0.02 |
| Total | 17.98 | 17.80 | 17.84 | 18.08 | 17.91 | 18.08 | 17.90 | 17.35 | 17.35 | 17.51 | 17.41 |

concentrations increase from the centre of the grain towards the rim. Yttrium is heterogeneously distributed, but shows the highest values in the patchy central part and lower values in the outer domains (Fig. 6a–c).

In the metagranitoid rocks, type 1 monazite has higher Th and Pb contents than the patchy-zoned type 2 domains (Fig. 7a, b). The latter are also characterized by low concentration gradients, and local concentration minima of PbO correlate with minima in $ThO_2$ (arrows in Fig. 7a, b, see also ES1 in the electronic supplement). The Y concentration is highly variable (Fig. 7c). However, it is generally higher in the euhedral core than in the type 2 domains.

Type 2 monazite grains, characterised by advanced breakdown, display strong concentration gradients. In grain 132 P1 (Fig. 8), the Th concentration varies between 2 and 26 wt.%, and the PbO content also varies more strongly than in other monazite grains (< 0.3–1.3 wt.%; Fig. 8a, b). However, the steady decrease of PbO towards the rim is not mirrored by $ThO_2$. Instead, the maximum value of 26 wt.% $ThO_2$ (arrow in Fig. 8b) corresponds to the lowest PbO concentration (<0.3 wt.%). This is in marked contrast to the centre of the grain, where local maxima in PbO correlate with maxima in $ThO_2$ (Fig. 8a, b). This indicates that the distribution of both elements is decoupled towards the rim. Similar to $ThO_2$, $Y_2O_3$ shows marked concentration gradients towards the rim (Fig. 8c).

### *4.5. Mineral chemistry of fluorapatite, REE-rich epidote and allanite associated with monazite*

Chemical analyses of fluorapatite, allanite, and REE-rich epidote from reaction zones around monazite and metamorphic fluorapatite, which is texturally unrelated to monazite, are given in Tables 3 and 4. Fluorapatite, that formed by breakdown of monazite, shows variable but generally higher concentrations of Th, Si, and Ce in comparison to metamorphic fluorapatite. The latter two elements point to a significant britholite component ($(Ca, REE)_5(SiO_4)_3(F, OH)$), which has also been observed in fluorapatite derived from monazite breakdown elsewhere (Broska et al., 2005; Finger et al., 1998).

Allanite from the coronas as well as from lamellae within epidote, is chemically heterogeneous. REE contents are in the range of several wt.% (Table 4), and Th-concentrations vary up to ca. 2.3 wt.% $ThO_2$. As the cation-sum of Y + REE + Th (p.f.u., 12.5 oxygen) in some domains is > 0.5 and <0.5 in others, their composition varies between that of allanite *sensu stricto* and that of REE-rich epidote (Gieré and Sorensen, 2004).

## 5. U–Pb isotope data

Seven grains from three different samples were chosen for LA-SF-ICP-MS U–Pb dating (Table 5, Fig. 10). The analysis of monazite grain 133 P4 with the euhedral core (type 1) reveals two growth episodes (Fig. 10a, b). Dates obtained from the euhedral core of the monazite (8 analyses) are concordant or near-concordant, and define a discordia line with an upper intercept date of 2230 ± 24 Ma. The second group, from the patchy-zoned (type 2) part of the grain (10 analyses), gives a considerably younger upper intercept date of 2066 ± 22 Ma (Fig. 10b).

Analyses of the remaining patchy-zoned type 2 monazite grains from the metagranitoid rocks are concordant to variably discordant. The data define two discordia lines with upper intercepts of 2058 ± 22 Ma and

**Table 4**
Representative analyses of epidote, REE-rich epidote and allanite from coronas and dispersed reaction zones (rz) around monazite.

| | −116 Al1 | 97R78 | 97R78 | 97R78 | −116 Al1 | −116 Al1 | −116 Al2 | 97R78 | 97R78 |
|---|---|---|---|---|---|---|---|---|---|
| | 10 corona | 17 rz | 23 rz | 24 rz | 7 corona | 8 corona | 4 corona | 20 rz | 22 rz |
| | Epidote | Epidote | Epidote | Epidote | Allanite | REE-ep.[c] | Allanite | REE-ep.[c] | REE-ep.[c] |
| $SiO_2$ | 38.87 | 38.38 | 38.33 | 38.85 | 36.60 | 37.83 | 40.07 | 35.01 | 35.53 |
| $TiO_2$ | 0.14 | 0.01 | 0.01 | 0.02 | 0.18 | 0.12 | 0.24 | 0.02 | 0.00 |
| $Al_2O_3$ | 27.84 | 27.30 | 26.69 | 27.49 | 21.83 | 22.99 | 19.57 | 22.91 | 24.54 |
| FeO | 6.65 | 8.02 | 9.04 | 7.79 | 8.71 | 7.14 | 6.89 | 9.92 | 8.50 |
| $La_2O_3$ | 0.00 | 0.08 | 0.00 | 0.00 | 3.84 | 2.83 | 5.38 | 2.69 | 2.65 |
| $Ce_2O_3$ | 0.01 | 0.24 | 0.00 | 0.06 | 8.02 | 6.59 | 9.87 | 5.78 | 5.14 |
| $Pr_2O_3$ | 0.02 | 0.12 | 0.00 | 0.05 | 1.25 | 1.22 | 1.28 | 0.82 | 0.65 |
| $Nd_2O_3$ | 0.00 | 0.06 | 0.00 | 0.04 | 2.48 | 2.42 | 2.22 | 1.66 | 1.59 |
| $Sm_2O_3$ | 0.02 | 0.02 | 0.02 | 0.02 | 0.25 | 0.31 | 0.10 | 0.10 | 0.15 |
| $Gd_2O_3$ | 0.03 | 0.08 | 0.06 | 0.06 | 0.07 | 0.17 | 0.03 | 0.08 | 0.16 |
| $Y_2O_3$ | 0.00 | 0.43 | 0.08 | 0.82 | 0.13 | 0.19 | 0.08 | 0.33 | 0.53 |
| $ThO_2$ | 0.01 | 0.01 | 0.00 | 0.00 | 1.24 | 2.32 | 2.20 | 0.01 | 0.00 |
| $UO_2$ | 0.00 | 0.00 | 0.00 | 0.01 | 0.01 | 0.03 | 0.06 | 0.00 | 0.01 |
| MnO | 0.09 | 0.17 | 0.11 | 0.20 | 0.10 | 0.16 | 0.15 | 0.11 | 0.27 |
| CaO | 24.17 | 23.26 | 23.76 | 22.86 | 11.96 | 11.88 | 8.41 | 17.40 | 18.22 |
| MgO | 0.02 | 0.03 | 0.00 | 0.02 | 0.36 | 0.30 | 0.55 | 0.06 | 0.04 |
| $Na_2O$ | 0.00 | 0.00 | 0.00 | 0.00 | 0.11 | 0.14 | 0.09 | 0.00 | 0.00 |
| Total | 97.88 | 98.21 | 98.10 | 98.28 | 97.14 | 96.64 | 97.16 | 96.91 | 97.97 |
| Cations[a] | O = 12.5 | | | | | | | | |
| Si | 3.024 | 3.004 | 3.000 | 3.033 | 3.216 | 3.272 | 3.519 | 3.011 | 2.989 |
| Ti | 0.008 | 0.001 | 0.001 | 0.001 | 0.012 | 0.008 | 0.016 | 0.001 | 0.000 |
| Al | 2.553 | 2.519 | 2.462 | 2.529 | 2.261 | 2.343 | 2.025 | 2.322 | 2.433 |
| $Fe_{tot}$ | 0.433 | 0.525 | 0.591 | 0.509 | 0.640 | 0.517 | 0.506 | 0.713 | 0.598 |
| $Fe^{II}$ | 0.009 | 0.042 | 0.000 | 0.107 | 0.640 | 0.517 | 0.506 | 0.392 | 0.323 |
| $Fe^{III}$ | 0.382 | 0.435 | 0.532 | 0.362 | 0.000 | 0.000 | 0.000 | 0.289 | 0.247 |
| La | 0.000 | 0.002 | 0.000 | 0.000 | 0.124 | 0.090 | 0.174 | 0.085 | 0.082 |
| Ce | 0.000 | 0.007 | 0.000 | 0.002 | 0.258 | 0.209 | 0.317 | 0.182 | 0.158 |
| Pr | 0.001 | 0.004 | 0.000 | 0.001 | 0.040 | 0.039 | 0.041 | 0.026 | 0.020 |
| Nd | 0.000 | 0.002 | 0.000 | 0.001 | 0.078 | 0.075 | 0.070 | 0.051 | 0.048 |
| Sm | 0.001 | 0.001 | 0.001 | 0.001 | 0.008 | 0.009 | 0.003 | 0.003 | 0.004 |
| Gd | 0.001 | 0.002 | 0.002 | 0.001 | 0.002 | 0.005 | 0.001 | 0.002 | 0.004 |
| Y | 0.000 | 0.018 | 0.003 | 0.034 | 0.006 | 0.009 | 0.004 | 0.015 | 0.024 |
| Th | 0.000 | 0.000 | 0.000 | 0.000 | 0.025 | 0.046 | 0.044 | 0.000 | 0.000 |
| U | 0.000 | 0.000 | 0.000 | 0.000 | 0.000 | 0.001 | 0.001 | 0.000 | 0.000 |
| Mn | 0.006 | 0.011 | 0.007 | 0.013 | 0.007 | 0.012 | 0.011 | 0.008 | 0.019 |
| Ca | 2.014 | 1.950 | 1.992 | 1.912 | 1.126 | 1.101 | 0.792 | 1.604 | 1.643 |
| Mg | 0.002 | 0.004 | 0.000 | 0.003 | 0.047 | 0.038 | 0.072 | 0.008 | 0.005 |
| Na | 0.000 | 0.000 | 0.000 | 0.000 | 0.018 | 0.024 | 0.015 | 0.001 | 0.000 |
| Total | 8.000 | 8.001 | 8.000 | 8.000 | 7.868 | 7.796 | 7.610 | 8.000 | 8.000 |
| $X_{ep}$[b] | 0.41 | 0.46 | 0.54 | 0.41 | | | | | |

[a] electron microprobe analyses balanced for $Fe^{III}$ by normalization to 12.5 oxygen and 8 cations.
[b] $X_{ep}$ denotes molecular proportion of epidote in the binary epidote-clinozoisite mixing.
[c] REE-ep. indicates REE-rich epidote.

2062 ± 26 Ma, respectively (Fig. 10c,d). The dates are, within error, indistinguishable from the date of the patchy-zoned monazite of grain 133 P4. While the dates from monazite grain 133 P3 and the central parts of 132 P1 are mostly concordant (Fig. 10c, d), the two grains affected by advanced breakdown (i.e. the outer domains of grain 132 P1 and 132 P5) are variably discordant (Fig. 10d, e). This is most pronounced in grain 132 P5, which yields an upper intercept date of 2073 ± 47 Ma (Fig. 10e). In grain 132 P1, the monazite domains in the central part of the grain that show only minor variations in Th, Pb and Y yield concordant U–Pb dates, whereas domains with marked chemical gradients yield discordant dates (Figs. 8 and 10d).

Similar to sample 133, monazite from metasediment sample 961 records two growth episodes (Fig. 10f). The Y-rich domains yield slightly reverse discordant dates, with a pooled mean $^{207}Pb/^{235}U$ date of 2244 ± 19 ma ($n = 9$), which is within the uncertainty of the apparent $^{207}Pb/^{206}Pb$ date of 2219 ± 21 Ma. The other group has an upper intercept date of 2052 ± 16 Ma, which is, within error, indistinguishable from the dates of type 2 monazite from metagranitoid rocks.

## 6. Discussion

### 6.1. Formation of type 1 and type 2 monazite

The geochronological data outlined above suggest that monazite from the ETSZ records two distinct growth episodes. An early growth period is indicated by 1) a $^{207}Pb/^{206}Pb$ date of 2230 ± 22 Ma for type 1 monazite from metagranitoid rocks, and 2) a pooled mean $^{207}Pb/^{235}U$ date of 2244 ± 19 Ma for a Y-rich core of type 2 monazite in metasedimentary rocks. Based on the euhedral shape and oscillatory zoning of type 1 monazite, we interpret the date of 2230 ± 22 Ma as the age of magmatic crystallisation of the precursor of the metagranitoid rock. The 2244 ± 19 Ma date of the older monazite generation, which is preserved in type 2 monazite from the metasedimentary rocks correlates time wise with this igneous activity. Similar to the younger age domains of type 2 monazite, this early monazite generation shows patchy domains, with sharp boundaries and irregular size, shape, and orientation, indicative of monazite grown in a dissolution–reprecipitation process (Harlov et al., 2011; Hetherington et al., 2010;

**Table 5**
Results of U–Pb monazite LA-ICP-MS dating.

| Grain | | $^{207}Pb^{a}$ | $U^{b}$ | $Pb^{b}$ | $Th^{b}$ | $^{206}Pb^{c}$ | $^{206}Pb^{d}$ | ±2 s | $^{207}Pb^{d}$ | ±2 s | rho[e] | $^{207}Pb^{d}$ | ±2 s | $^{206}Pb$ | ±2 s | $^{207}Pb$ | ±2 s |
|---|---|---|---|---|---|---|---|---|---|---|---|---|---|---|---|---|---|
| | | (cps) | (ppm) | (ppm) | U | $^{204}Pb$ | $^{238}U$ | (%) | $^{235}U$ | (%) | | $^{206}Pb$ | (%) | $^{238}U$ | (Ma) | $^{235}U$ | (Ma) |
| 27132 P1 | A2 | 28742 | 1651 | 6653 | 44.9 | 18013 | 0.3036 | 5.8 | 5.177 | 6.0 | 0.97 | 0.1237 | 1.5 | 1709 | 87 | 1849 | 52 |
| 27132 P1 | A3 | 46475 | 2722 | 9043 | 37.6 | 6618 | 0.3759 | 2.4 | 6.588 | 2.7 | 0.88 | 0.1271 | 1.3 | 2057 | 42 | 2058 | 24 |
| 27132 P1 | A4 | 51887 | 2771 | 10408 | 39.3 | 4526 | 0.3753 | 2.7 | 6.610 | 2.9 | 0.91 | 0.1277 | 1.2 | 2054 | 47 | 2061 | 26 |
| 27132 P1 | A5 | 53822 | 2802 | 10133 | 39.8 | 4449 | 0.3721 | 2.7 | 6.428 | 2.8 | 0.96 | 0.1253 | 0.8 | 2039 | 47 | 2036 | 25 |
| 27132 P1 | A6 | 47321 | 2483 | 7562 | 39.6 | 3577 | 0.3200 | 2.4 | 5.492 | 3.0 | 0.79 | 0.1245 | 1.8 | 1790 | 37 | 1899 | 26 |
| 27132 P1 | A7 | 48789 | 2559 | 12170 | 52.7 | 4413 | 0.3704 | 2.2 | 6.489 | 2.4 | 0.92 | 0.1271 | 1.0 | 2031 | 38 | 2044 | 21 |
| 27132 P1 | A8 | 34105 | 1792 | 6411 | 53.3 | 869 | 0.3404 | 2.9 | 6.025 | 3.9 | 0.76 | 0.1283 | 2.5 | 1889 | 48 | 1979 | 34 |
| 27132 P1 | A9 | 37374 | 1475 | 6941 | 74.7 | 209 | 0.2572 | 2.5 | 4.361 | 3.7 | 0.66 | 0.1230 | 2.8 | 1476 | 33 | 1705 | 31 |
| 27132 P1 | A11 | 47501 | 2793 | 9050 | 51.0 | 860 | 0.2296 | 3.7 | 3.616 | 4.4 | 0.85 | 0.1142 | 2.3 | 1332 | 45 | 1553 | 36 |
| 27132 P5 | A19 | 63074 | 1657 | 7453 | 84.9 | 182 | 0.3283 | 3.3 | 5.699 | 5.2 | 0.63 | 0.1259 | 4.0 | 1830 | 52 | 1931 | 46 |
| 27132 P5 | A20 | 40969 | 1636 | 7494 | 76.1 | 792 | 0.3492 | 2.5 | 6.057 | 4.5 | 0.55 | 0.1258 | 3.7 | 1931 | 41 | 1984 | 40 |
| 27132 P5 | A21 | 101157 | 2798 | 13809 | 82.9 | 166 | 0.2651 | 2.6 | 4.374 | 6.6 | 0.39 | 0.1197 | 6.1 | 1516 | 35 | 1708 | 56 |
| 27132 P5 | A22 | 25263 | 173 | 1147 | 187.1 | 176 | 0.3337 | 4.9 | 5.866 | 6.6 | 0.74 | 0.1275 | 4.4 | 1856 | 80 | 1956 | 59 |
| 27132 P5 | A23 | 43845 | 3664 | 16149 | 79.1 | 505 | 0.2221 | 3.9 | 3.396 | 4.4 | 0.89 | 0.1109 | 2.0 | 1293 | 46 | 1503 | 35 |
| 27132 P5 | A24 | 57778 | 4698 | 15684 | 66.9 | 354 | 0.1956 | 3.1 | 2.889 | 4.3 | 0.72 | 0.1071 | 3.0 | 1152 | 33 | 1379 | 33 |
| 27132 P5 | A25 | 133537 | 4518 | 20912 | 66.4 | 319 | 0.3050 | 3.6 | 4.974 | 5.5 | 0.66 | 0.1183 | 4.2 | 1716 | 55 | 1815 | 48 |
| 27132 P5 | A26 | 285969 | 3239 | 18417 | 101.9 | 110 | 0.2894 | 5.9 | 4.953 | 8.9 | 0.67 | 0.1241 | 6.6 | 1639 | 87 | 1811 | 78 |
| 27132 P5 | A27 | 223694 | 3456 | 18616 | 95.4 | 69 | 0.2761 | 3.6 | 4.544 | 4.9 | 0.74 | 0.1194 | 3.3 | 1572 | 51 | 1739 | 42 |
| 27133 P4 | a32 | 37363 | 2302 | 10227 | 36.4 | 6188 | 0.4197 | 3.8 | 8.173 | 4.4 | 0.87 | 0.1412 | 2.2 | 2259 | 73 | 2250 | 41 |
| 27133 P4 | a33 | 34399 | 2631 | 8240 | 29.2 | 20545 | 0.3798 | 3.2 | 7.177 | 3.6 | 0.90 | 0.1371 | 1.6 | 2075 | 58 | 2134 | 33 |
| 27133 P4 | G8 | 32725 | 2170 | 9269 | 34.7 | 12461 | 0.4296 | 2.9 | 8.409 | 3.6 | 0.81 | 0.1419 | 2.1 | 2304 | 57 | 2276 | 33 |
| 27133 P4 | G9 | 21572 | 1553 | 6146 | 39.7 | 5972 | 0.3337 | 2.9 | 5.874 | 3.8 | 0.76 | 0.1277 | 2.5 | 1856 | 47 | 1957 | 34 |
| 27133 P4 | G10 | 26504 | 2061 | 8267 | 32.9 | 14159 | 0.3937 | 2.7 | 7.574 | 3.5 | 0.75 | 0.1395 | 2.3 | 2140 | 49 | 2182 | 32 |
| 27133 P4 | a34 | 16785 | 1425 | 7901 | 51.8 | 7302 | 0.3818 | 3.2 | 6.700 | 3.9 | 0.84 | 0.1273 | 2.1 | 2085 | 58 | 2073 | 35 |
| 27133 P4 | a35 | 22741 | 1522 | 8341 | 55.3 | 1363 | 0.3846 | 3.5 | 6.759 | 5.3 | 0.66 | 0.1275 | 4.0 | 2098 | 64 | 2080 | 48 |
| 27133 P4 | a36 | 21089 | 1767 | 7370 | 43.0 | 1224 | 0.3469 | 2.7 | 5.996 | 3.2 | 0.83 | 0.1254 | 1.8 | 1920 | 45 | 1975 | 29 |
| 27133 P4 | a37 | 60155 | 2297 | 7757 | 30.7 | 174 | 0.3097 | 3.0 | 5.241 | 5.0 | 0.59 | 0.1228 | 4.0 | 1739 | 45 | 1859 | 43 |
| 27133 P4 | a38 | 27579 | 1995 | 9318 | 40.3 | 10437 | 0.4170 | 3.5 | 7.997 | 4.2 | 0.84 | 0.1391 | 2.2 | 2247 | 67 | 2231 | 38 |
| 27133 P4 | a39 | 20599 | 1507 | 8668 | 55.0 | 817 | 0.3963 | 2.7 | 7.172 | 3.4 | 0.79 | 0.1313 | 2.1 | 2152 | 50 | 2133 | 31 |
| 27133 P4 | a40 | 24758 | 1759 | 8410 | 40.6 | 1481 | 0.4129 | 3.4 | 7.876 | 3.8 | 0.91 | 0.1384 | 1.6 | 2228 | 65 | 2217 | 35 |
| 27133 P4 | a41 | 41908 | 3593 | 7259 | 16.7 | 4980 | 0.3763 | 3.5 | 6.508 | 3.8 | 0.91 | 0.1254 | 1.6 | 2059 | 61 | 2047 | 34 |
| 27133 P4 | a42 | 28781 | 2755 | 7991 | 28.9 | 115899 | 0.3518 | 3.6 | 6.042 | 4.1 | 0.89 | 0.1246 | 1.9 | 1943 | 61 | 1982 | 36 |
| 27133 P4 | a43 | 26941 | 2709 | 8397 | 30.0 | 4033 | 0.3147 | 4.3 | 5.460 | 5.0 | 0.87 | 0.1258 | 2.5 | 1764 | 67 | 1894 | 44 |
| 27133 P4 | a44 | 27286 | 2330 | 9543 | 35.4 | 14285 | 0.3776 | 3.1 | 6.587 | 3.7 | 0.83 | 0.1265 | 2.1 | 2065 | 55 | 2058 | 33 |
| 27133 P4 | a45 | 29709 | 2638 | 9102 | 29.4 | 32148 | 0.4012 | 2.5 | 7.189 | 3.0 | 0.84 | 0.1300 | 1.7 | 2174 | 47 | 2135 | 27 |
| 27133 P4 | G11 | 30546 | 2417 | 8984 | 29.0 | 11500 | 0.4091 | 3.4 | 7.924 | 3.7 | 0.91 | 0.1405 | 1.6 | 2211 | 63 | 2222 | 34 |
| 27133 P3 | a50 | 32711 | 3117 | 10931 | 31.7 | 127101 | 0.3898 | 3.7 | 6.985 | 4.2 | 0.88 | 0.1300 | 2.0 | 2122 | 68 | 2110 | 38 |
| 27133 P3 | a51 | 26272 | 2419 | 11730 | 44.8 | 11681 | 0.3882 | 3.7 | 6.905 | 4.3 | 0.86 | 0.1290 | 2.2 | 2114 | 66 | 2099 | 39 |
| 27133 P3 | a52 | 39121 | 3884 | 11158 | 26.2 | 16252 | 0.3871 | 3.4 | 6.727 | 3.8 | 0.90 | 0.1260 | 1.6 | 2110 | 62 | 2076 | 34 |
| 27133 P3 | a53 | 36817 | 3835 | 11692 | 27.6 | 11029 | 0.3783 | 4.4 | 6.968 | 5.0 | 0.87 | 0.1336 | 2.4 | 2069 | 78 | 2107 | 45 |
| 27133 P3 | a55 | 61210 | 3126 | 10075 | 35.5 | 1733 | 0.2345 | 6.0 | 3.544 | 7.9 | 0.77 | 0.1096 | 5.0 | 1358 | 74 | 1537 | 64 |
| 27133 P3 | G12 | 22523 | 2275 | 10093 | 44.4 | 8278 | 0.3757 | 3.9 | 6.556 | 5.0 | 0.79 | 0.1265 | 3.0 | 2056 | 69 | 2053 | 45 |
| 27133 P3 | a1 | 19172 | 4198 | 6672 | 24.5 | 1608 | 0.2024 | 3.5 | 2.921 | 4.7 | 0.76 | 0.1047 | 3.0 | 1188 | 39 | 1387 | 36 |
| 27133 P3 | a3 | 47601 | 4920 | 10904 | 20.1 | 1437 | 0.3673 | 3.7 | 6.286 | 4.0 | 0.91 | 0.1241 | 1.7 | 2017 | 64 | 2017 | 36 |
| 27133 P3 | a4 | 41706 | 4525 | 11130 | 21.6 | 6211 | 0.4006 | 4.3 | 7.237 | 4.7 | 0.93 | 0.1310 | 1.7 | 2172 | 81 | 2141 | 43 |
| 27133 P3 | a5 | 62547 | 7028 | 10870 | 14.3 | 5191 | 0.3678 | 3.4 | 6.428 | 4.0 | 0.85 | 0.1268 | 2.1 | 2019 | 59 | 2036 | 36 |
| 27961 P2 | a11 | 60304 | 5185 | 11064 | 10.4 | 28662 | 0.4262 | 4.0 | 8.155 | 4.3 | 0.93 | 0.1388 | 1.6 | 2289 | 78 | 2248 | 40 |
| 27961 P2 | a12 | 46120 | 4289 | 8223 | 15.2 | 9493 | 0.4288 | 2.9 | 8.331 | 3.4 | 0.84 | 0.1409 | 1.8 | 2300 | 56 | 2268 | 32 |
| 27961 P2 | a13 | 45909 | 4539 | 7707 | 14.6 | 6630 | 0.4114 | 2.8 | 7.840 | 3.6 | 0.77 | 0.1382 | 2.3 | 2221 | 53 | 2213 | 33 |
| 27961 P2 | G4 | 84783 | 7534 | 10516 | 8.8 | 52647 | 0.4249 | 2.8 | 8.226 | 3.3 | 0.85 | 0.1404 | 1.8 | 2283 | 54 | 2256 | 30 |
| 27961 P2 | G5 | 19760 | 1788 | 8915 | 39.8 | 68163 | 0.4296 | 2.9 | 8.478 | 3.5 | 0.82 | 0.1431 | 2.0 | 2304 | 56 | 2284 | 32 |
| 27961 P3 | a14 | 19504 | 1766 | 8120 | 38.4 | 71257 | 0.4247 | 3.0 | 8.091 | 3.9 | 0.78 | 0.1382 | 2.4 | 2282 | 59 | 2241 | 36 |
| 27961 P3 | a15 | 8790 | 1049 | 7860 | 73.3 | 34817 | 0.3767 | 2.7 | 6.593 | 3.4 | 0.80 | 0.1269 | 2.0 | 2061 | 48 | 2058 | 30 |
| 27961 P3 | a16 | 13912 | 1592 | 9656 | 58.9 | 56137 | 0.3809 | 2.9 | 6.533 | 4.1 | 0.71 | 0.1244 | 2.9 | 2081 | 52 | 2050 | 37 |
| 27961 P1 | a17 | 36143 | 4026 | 7361 | 16.3 | 22717 | 0.3862 | 2.7 | 6.832 | 2.9 | 0.94 | 0.1283 | 1.0 | 2105 | 49 | 2090 | 26 |
| 27961 P1 | a18 | 8004 | 766 | 5992 | 75.4 | 28472 | 0.4278 | 2.6 | 8.297 | 2.9 | 0.88 | 0.1407 | 1.3 | 2296 | 50 | 2264 | 27 |
| 27961 P1 | a19 | 57555 | 6057 | 8170 | 10.1 | 211893 | 0.4195 | 2.5 | 7.882 | 2.8 | 0.91 | 0.1363 | 1.1 | 2258 | 48 | 2218 | 25 |
| 27961 P1 | a20 | 16661 | 1841 | 6093 | 29.4 | 60859 | 0.4189 | 2.7 | 7.929 | 2.9 | 0.91 | 0.1373 | 1.2 | 2255 | 51 | 2223 | 27 |
| 27961 P1 | a21 | 10051 | 1297 | 7336 | 62.4 | 40208 | 0.3747 | 2.2 | 6.469 | 2.6 | 0.86 | 0.1252 | 1.4 | 2051 | 39 | 2042 | 23 |
| 27961 P1 | a22 | 51328 | 6145 | 8240 | 10.7 | 19234 | 0.3883 | 2.3 | 6.887 | 2.6 | 0.88 | 0.1286 | 1.2 | 2115 | 41 | 2097 | 23 |
| 27961 P1 | G6 | 48452 | 6777 | 8472 | 10.8 | 30199 | 0.3473 | 3.0 | 5.937 | 3.1 | 0.96 | 0.1240 | 0.8 | 1922 | 50 | 1967 | 27 |
| Moacir[f] | $n=9$ | 16380 | 10066 | 13594 | 62 | 3325 | 0.08246 | 2.7 | 0.6482 | 4.4 | 0.58 | 0.05701 | 3.9 | 511 | 13 | 507 | 18 |

[a] Within run background-corrected mean $^{207}Pb$ signal.
[b] U and Pb content and Th/U ratio were calculated relative to GJ-1 reference.
[c] Measured ratio corrected for background and $^{204}Hg$ interference.
[d] Corrected for background and within-run Pb/U fractionation and normalised to GJ-1 (ID-TIMS value/measured value); $^{207}Pb/^{235}U$ calculated using $^{207}Pb/^{206}Pb/(^{238}U/^{206}Pb*1/137.88)$.
[e] Rho is the $err^{206}Pb/^{238}U$ / $err^{207}Pb/^{235}U$ correlation coefficient.
[f] Accuracy and reproducibility was checked by repeated analyses ($n=9$) of reference monazite Moacir; data given as mean with 2 standard deviation uncertainties.

Putnis, 2009; Williams et al., 2011). We therefore interpret this age to record a major pre-deformational HT-metamorphic event that was associated with granitoid magmatism.

The second stage of monazite growth occurred between ca. 2058 ± 22 Ma and 2066 ± 22 Ma, and was associated with renewed alteration of the monazite again via coupled dissolution–reprecipitation.

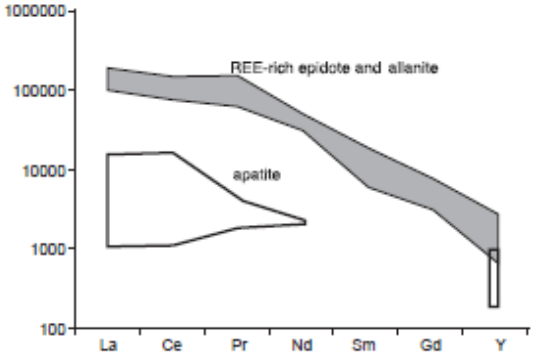


**Fig. 9.** Chondrite-normalized Y+REE patterns (chondrite according to McDonough and Sun, 1995) of REE-rich epidote and allanite as well as apatite from coronas and dispersed reaction zones around monazite. Sm and Gd in apatite <detection limit (see Table 3).

Type 2 monazite thus replaced magmatic monazite in the metagranitoid rocks and a metamorphic precursor in the metasedimentary rocks. In the metagranitoid rocks, type 2 monazite shows an increase in the cheralite component, a common feature of metamorphic monazite (Kim et al., 2009; Spear and Pyle, 2002). Although we cannot rule out that this second metamorphic event pre-dates the formation of the ETSZ, several lines of evidence suggest that monazite growth occurred during ductile shearing. First, in both types of rocks, the mylonitic fabric is defined by amphibolite-facies mineral assemblages, and monazite is aligned along the foliation (e.g. Fig. 2a). This suggests that type 2 monazite formed during amphibolite-facies metamorphism and ductile shearing. Second, the dissolution–reprecipitation process requires the presence of a fluid phase acting as a catalyst to increase rates of dissolution and reprecipitation of the monazite, and to provide a medium enhancing transfer of elements from and to the solids (Putnis, 2009). However, HT-metamorphic rocks (especially granitoids) are relatively dry and their permeability is typically too low to allow fluids to infiltrate (Brace, 1980). Shear zones often represent major fluid pathways in the crust, as the interplay between ductile shearing and fluid–rock interaction may significantly increase the permeability (e.g., Dziggel et al., 2009). It is therefore inferred that both metasedimentary and metagranitoid rocks were affected by fluids during shear zone formation between 2052 ± 16 and 2066 ± 22 Ma and that this represents the formation age of the ETSZ.

### 6.2. Fluid composition

The fluid phase and its composition also play a crucial role in the nature of monazite-producing reactions, as indicated by recent experimental work (e.g. Harlov et al., 2011). Formation of distinct, and chemically different, monazite domains, and the development of micropores were observed in monazite after experiments with $Na_2Si_2O_5 + H_2O$ or NaOH fluids at temperatures between 450 and 600 °C (Budzyn et al., 2011; Harlov et al., 2011; Hetherington et al., 2010). It was shown that patchy monazite forms in a reaction with (alkali + OH)-bearing fluids with negligible Cl (Harlov et al., 2011). In contrast, aqueous brines with NaCl or KCl components induce no or limited reactions in monazite. Acid and brine fluids including components such as $CaF_2$, HCl, $H_2SO_4$, $CaCl_2$ rather cause monazite dissolution and new nucleation of secondary monazite or other phases (Budzyn et al., 2011; Hetherington et al., 2010).

Experiments have also shown the removal of Pb to levels below detection limit from domains altered by (alkali + OH)-bearing fluids, suggesting total resetting of the U–Pb decay system during such alteration (Harlov et al., 2011; Williams et al., 2011). These data are consistent with our interpretation that the concordant U–Pb dates of patchy monazite domains reflect the age of a fluid-mediated dissolution–reprecipitation process, which was triggered by metamorphism and ductile shearing.

### 6.3. Monazite breakdown

Corroded edges, truncated outer domains, as well as dispersed reaction zones or corona structures reflect an event to which monazite responded by dissolution and formation of secondary phases such as fluorapatite, allanite, REE-epidote and Th-orthosilicate. Among the secondary phases, fluorapatite accommodated P, Y+REE and Th. The higher concentrations of Y+REE in allanite and REE-epidote compared to fluorapatite (Tables 3, 4, Fig. 9) indicate that these are the main sinks for Y+REE released by monazite. Thorium is not only incorporated in fluorapatite and allanite/REE-epidote, but also forms Th-orthosilicate. Replacement of biotite and quartz by coronas suggests input of Si, Al, and Fe to form Th-orthosilicate, REE-epidote and allanite. Biotite also provides F, enhancing the mobility of REE and Th as an effective complexing agent (Haas et al., 1995; Langmuir and Herman, 1980; Wood, 1990). A potential source for Ca is the anorthite component of the plagioclase. Formation of albite, at the expense of syntectonic plagioclase ($An_{31-39}$) and epidote along cleavage plains in biotite, indicate mobility of Ca in the rock. Monazite breakdown is therefore best-explained by post-deformational greenschist-facies retrogression. This is in line with the observation that the coronas are undeformed showing that this event postdated shearing of the rock. Similar textures and secondary minerals formed during greenschist- or amphibolite-facies metamorphism have been described in nature by Finger et al. (1998), Broska et al. (2005), Krenn et al. (2008), Petrik and Konecny (2009), Yi and Cho (2009), and Rasmussen and Muhling (2009). These studies and Janots et al. (2011) highlight the importance of a fluid for monazite breakdown and transport of elements. Mobility of Y+REE and Th, at least in a range of several 100 μm, is indicated by the occurrence of allanite or REE-epidote at this distance from the source monazite (e.g. Fig. 3l). Formation of hydrous minerals and evidence of element mobility thus show that monazite breakdown occurred during influx of a metamorphic aqueous fluid.

Similar to monazite-forming reactions, recent experimental work underlines the crucial role of the fluid composition for monazite dissolution (Budzyn et al., 2011; Harlov et al., 2011; Hetherington et al., 2010; Tropper et al., 2011). The effects observed here, i.e. monazite dissolution and formation of fluorapatite, REE-epidote or allanite were partly reproduced in experiments using $Ca(OH)_2$, $CaCl_2 + H_2O$ or $CaCO_3 + H_2O$ at T = 450–500 °C and P = 450–600 MPa (Budzyn et al., 2011). In that study, the fluid also caused precipitation of a Th-phase (i.e. thorianite). In conclusion, petrographic observations in these rocks coupled with experimental work show that monazite dissolution and replacement by secondary minerals occurred during retrograde greenschist-facies metamorphism, and was promoted by an aqueous Ca-rich fluid in a post-deformational stage. The concentric corona textures point to diffusion-controlled growth of secondary minerals (Finger et al., 1998). The dispersed reaction zones may then be interpreted to reflect enhanced, possibly advection-controlled, transport properties. Considering the importance of a fluid for element mobility, the occurrence of coronas and dispersed reaction zones could be interpreted to indicate areas of different permeability within the rock, i.e. coronas were formed in areas of low permeability, dispersed reaction zones surrounded by areas of higher permeability.

### 6.4. Retrograde effects on monazite chemistry

Monazite grains showing advanced breakdown differ from other patchy type 2 domains in that they are enriched in huttonite or cheralite components (Fig. 4a), and display strong concentration gradients of Th and Pb (Fig. 8, ES2 in the electronic supplement).

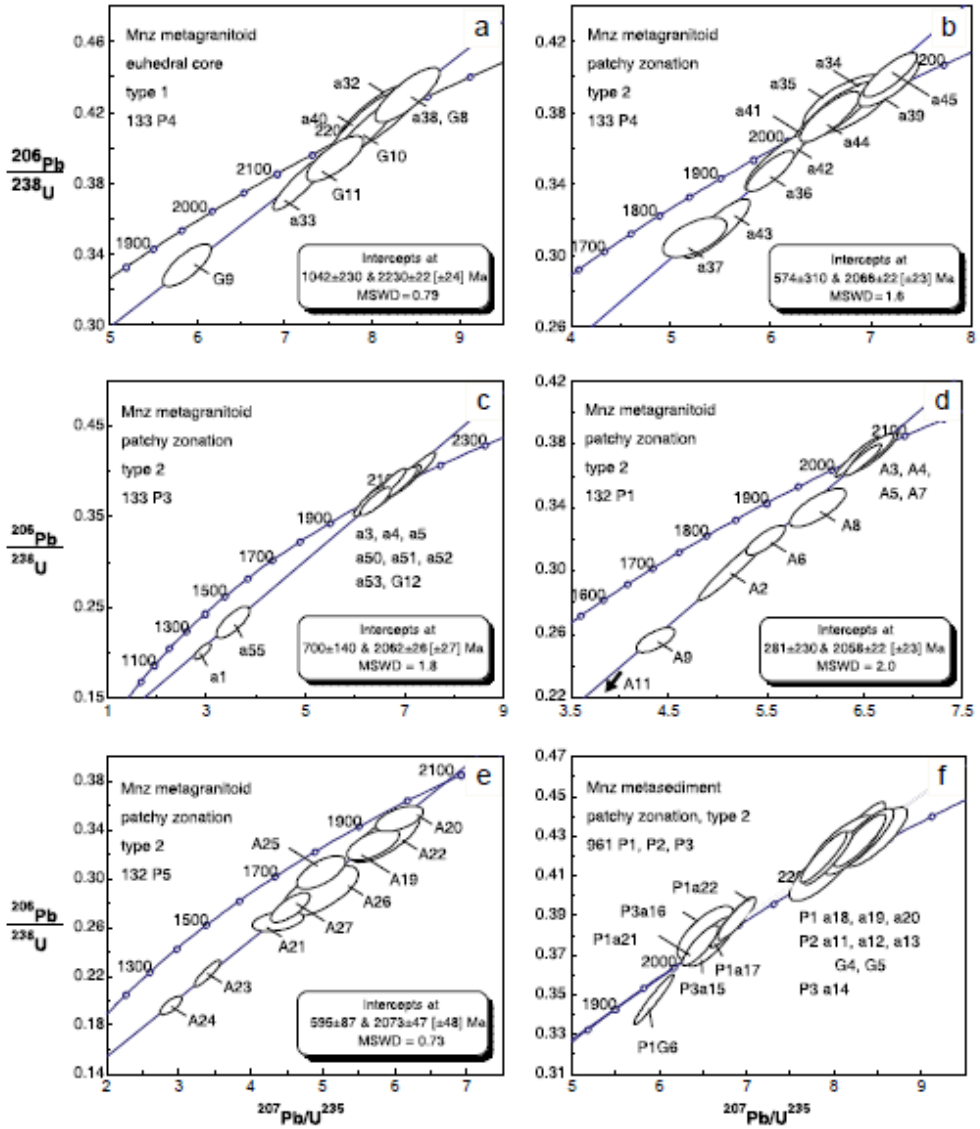


**Fig. 10.** Concordia diagrams showing U–Pb data of monazite domains from metagranitoid and metasedimentary samples. Numbers of spots analysed shown in Figs. 6–8. Intercept ages calculated using Isoplot 3.00 (Ludwig, 2003). A, B, Type 1 and type 2 monazite (Mnz) of grain 133 P4 (metagranitoid rock). C, Type 2 monazite of grain 133 P3 (metagranitoid rock), Fig. 3c, spots are displayed in the electronic supplement 1. D, Type 2 monazite of grain 132 P1 (metagranitoid rock), is characterised by advanced breakdown. E, Type 2 monazite of grain 132 P5 (metagranitoid rock) is characterised by advanced breakdown, Fig. 3g, spots are displayed in electronic supplement 2. F, Type 2 monazite of grains P1, P2, and P3 are from sample 961 (metasedimentary rock). The Y-rich domains are slightly reverse discordant, with a pooled mean $^{207}Pb/^{235}U$ date of 2244 ± 19 ma ($n = 9$), which is within uncertainty of the apparent $^{207}Pb/^{206}Pb$ age of 2219 ± 21 Ma. The other group ($n = 6$), analysed in outer domains has an upper intercept date of 2052 ± 16 Ma.

Diffusion of these elements cannot explain the observed changes in monazite chemistry, given the low diffusion coefficients of Th and Pb under low grade conditions (Cherniak, 2010; Cherniak and Pyle, 2008; Cherniak et al., 2004; Gardés et al., 2006, 2007). The observation of these characteristics in domains close to the edge, which is affected by solution, suggests the influence of fluids on the monazite breakdown reaction. Thorium-Si-enriched (i.e. huttonite-rich) domains, as shown here, have also been observed in experiments partly dissolving monazite (Harlov et al., 2011; Hetherington et al., 2010).

The fact that different element enrichment occurs in distinct grains or even domains of one grain (e.g. 132 P1, Fig. 8) points to local equilibria in distinct parts of the sample. Thus, we infer that the outer domains of grains affected by advanced breakdown represent a stage of local monazite stabilisation during retrogression. High Ca-activities in a fluid promote monazite breakdown to fluorapatite, REE-epidote or allanite (e.g., Budzyn et al., 2011). If growth of fluorapatite and REE-epidote or allanite consume Ca faster than Ca is transported to the reaction front of the dissolving crystal, monazite could locally be stabilised due to local undersaturation in Ca. Formation of secondary monazite in response to changing saturation limits of ions in a fluid is also proposed by Hetherington et al. (2010) and Budzyn et al. (2011). These monazite domains could thus represent "frozen" stages of local

equilibration during a dissolution–reprecipitation process. Possible factors explaining such local equilibration include the generally low temperatures, changes in fluid chemistry, and a low fluid–rock-ratio and/or permeability, reducing reaction rates (Harlov et al., 2011; Putnis, 2009).

In contrast to monazite domains formed during amphibolite-facies metamorphism, domains affected by the local re-equilibration are discordant (e.g., Figs. 8 and 10). For example, monazite 132 P5 (Fig. 3g), which is characterised by advanced breakdown, shows strongly discordant U–Pb isotope ratios (Fig. 10e and ES2). However, the upper intercept date of 2073 ± 47 Ma is, within error, similar to the age of the amphibolite-facies event. Hence, local re-equilibration did not reset the U–Pb system but caused only partial loss of Pb. This is consistent with experimental results showing that removal of Pb from a reacting monazite is a function of fluid chemistry (Harlov and Hetherington, 2010; Harlov et al., 2011; Williams et al., 2011). Whether Pb is retained within nanometer-sized domains in the re-equilibrated monazite, as described by Seydoux-Guillaume et al. (2003), cannot be resolved.

### 6.5. Implications for the Pre-Uralian margin of the East European Craton

The data presented in this study also add new information to the tectonometamorphic history of the eastern continental margin of the East European Craton. The ages of 2244 ± 19 Ma for metamorphic monazite and 2230 ± 22 Ma for igneous monazite provide the first evidence for a HT tectono-magmatic event of that age in the Taratash complex. Slightly older and younger ages (Table 1) have been reported from a leucocratic granite (2344 ± 29 Ma, Sindern et al., 2005), a gneiss (2461 ± 36 Ma, Ronkin et al., 2007) and a migmatite/augen-gneiss (2127 ± 65 Ma, Krasnobayev and Cherednichenko, 2005) from other parts of the Taratash complex, supporting the idea that the complex is an amalgamation of different crustal domains with a prolonged and probably polyphase tectonic history (Sindern et al., 2005).

The time interval from 2052 ± 16 to 2066 ± 22 Ma reflects shear zone formation. Similar ages (Table 1) have been reported for metamorphic zircon (2032 ± 27 Ma, Ronkin et al., 2007) and zircon in migmatite (2044 ± 8 Ma, Sindern et al., 2005) from granulite- to amphibolite-facies domains of the Taratash complex. The data indicate that high-grade metamorphism and ductile shearing affected and possibly amalgamated the different crustal domains of the Taratash complex. This may point to a Palaeoproterozoic orogenic event at the eastern margin of the East European Craton.

Supplementary materials related to this article can be found online at doi:10.1016/j.lithos.2011.11.017.

## Acknowledgements

We are grateful for the logistic support as well as field guidance by V.I. Lennykh. We thank R. Klinghardt (Aachen) for the patient help with electron microprobe analyses and Th. Derichs (Aachen) for preparation of polished thin sections. B. Schulz and associate editor Daniel Harlov are thanked for their constructive reviews and rewrite of the text.

## References

Alekseyev, A.A., 1984. Riphean and Vendian magmatism in the southern Urals. Nauka, Moscow, pp. 1–136 (in Russian).
Alsop, G.I., Holdsworth, R.E., 2004. Shear zones – an introduction and overview. In: Alsop, G.I., Holdsworth, R.E., McCaffrey, K.J.W., Hand, M. (Eds.), Flow processes in faults and shear zones: Geological Society, London, Special publications, 224, pp. 1–9.
Ayers, J.C., Loflin, M., Miller, C.F., Barton, M.D., Coath, C.D., 2006. In situ oxygen isotope analysis of monazite as a monitor of fluid infiltration during contact metamorphism: Birch Creek Pluton aureole, White Mountains, eastern California. Geology 34, 653–656.
Batchelor, R.A., Bowden, P., 1985. Petrogenetic interpretation of granitoid rock series using multicationic parameters. Chemical Geology 48, 43–55.
Beckholmen, M., Glodny, J., 2004. Early Cambrian blueschist facies metamorphism in the Kvarkush metamorphic basement, Northern Urals, Russia. In: Gee, D.G., Pease, V. (Eds.), The Neoproterozoic Orogen of Eastern Baltica: Geological Society Memoirs 30, London, pp. 125–134.
Bingen, B., Demaiffe, D., Hertogen, J., 1996. Redistribution of rare earth elements, Th and U over accessory minerals in the course of amphibolite to granulite facies metamorphism: the role of apatite and monazite in orthogneisses from SW Norway. Geochimica et Cosmochimica Acta 60, 1341–1354.
Brace, W.F., 1980. Permeability of crystalline and argillaceous rocks. International Journal of Rock Mechanics and Mining Sciences 17, 241–251.
Braun, I., Montel, J.M., Nicollet, Chr., 1998. Electron microprobe dating of monazites from high-grade gneisses and pegmatites of the Kerala Khondalite Belt, southern India. Chemical Geology 146, 65–85.
Broska, I., Siman, P., 1998. The breakdown of monazite in the West-Carpathian Veporic orthogneisses and Tatric granites. Geologica Carpathica 49, 161–167.
Broska, I., Petrík, I., Williams, C.T., 2000. Coexisting monazite and allanite in peraluminous granitoids of the Tribec Mountains, Western Carpathians. American Mineralogist 85, 22–32.
Broska, I., Williams, C.T., Janák, M., Nagy, G., 2005. Alteration and breakdown of xenotime-(Y) and monazite-(Ce) in granitic rocks of the Western Carpathians, Slovakia. Lithos 82, 71–83.
Brown, D., Alvarrez-Marron, J., Perez-Estaun, A., Puchkov, V., Ayarza, P., Gorozhanina, Y., 2001. Structure and evolution of the Magnitogorsk forarc basin: identifying upper crustal processes during arc-continent collision in the Southern Urals. Tectonics 20, 364–375.
Budzyn, B., Harlov, D.E., Williams, M.L., Jercinovic, M.J., 2011. Experimental determination of stability relations between monazite, fluorapatite, allanite, and REE-epidote as a function of pressure, temperature, and fluid composition. American Mineralogist 96, 1547–1567.
Catlos, E.J., Gilley, L.D., Harrison, T.M., 2002. Interpretation of monazite ages obtained via in situ analysis. Chemical Geology 188, 193–215.
Catlos, E.J., Dubey, C.S., Harrison, T.M., Edwards, M.A., 2004. Late Miocene movement within the Himalayan main central thrust shear zone, Sikkim, north-east India. Journal of Metamorphic Geology 22, 207–226.
Catlos, E.J., Dubey, C.S., Marston, R.A., Harrison, T.M., 2007. Geochronologic constraints across the main central thrust shear zone, Bhagirathi River (NW India): implications for Himalayan tectonics. In: Cloos, M., Carlson, W.D., Gilbert, M.C., Liou, J.G., Sorensen, S.S. (Eds.), Convergent margin terranes and associated regions; a tribute to W.G. Ernst: Special Paper – Geological Society of America 2007, vol. 419, pp. 135–151.
Catlos, E.J., Dubey, C.S., Sivasubramanian, P., 2008. Monazite ages from carbonatites and high grade assemblages along the Kambam Fault (Southern Granulite Terrane, South India). American Mineralogist 93, 1230–1244.
Cherniak, D.J., 2010. Diffusion in accessory minerals: zircon, titanite, apatite, monazite and xenotime. Reviews in Mineralogy and Geochemistry 72, 827–869.
Cherniak, D.J., Pyle, J.M., 2008. Th diffusion in monazite. Chemical Geology 256, 52–61.
Cherniak, D.J., Watson, E.B., Grove, M., Harrison, T.M., 2004. Pb diffusion in monazite : a combined RBS/SIMS study. Geochimica et Cosmochimica Acta 68, 829–840.
Cocherie, A., Albarède, F., 2001. An improved U–Th–Pb age calculation for electron microprobe dating of monazite. Geochimica et Cosmochimica Acta 65, 4509–4522.
Cocherie, A., Legendre, O., 2007. Potential minerals for determining U–Th–Pb chemical age using electron microprobe. Lithos 93, 288–309.
Cocherie, A., Be Mezeme, E., Legendre, O., Fanning, C.M., Faure, M., Rossi, P., 2005. Electron microprobe dating as a tool for determining the closure of Th–U–Pb systems in migmatitic monazites. American Mineralogist 90, 607–618.
Crowley, J.L., Ghent, E.D., 1999. An electron microprobe study of the U–Th–Pb systematics of metamorphosed monazite: the role of Pb diffusion versus overgrowth and recrystallization. Chemical Geology 157, 285–302.
Dill, H., Gerdes, A., Weber, B., 2007. Cu-Fe-U phosphate mineralization of the Hagendorf–Pleystein pegmatite province, Germany: With spezial reference to Laser-Ablation-Inductive-Coupled-Plasma Mass Spectrometry (LA-ICP-MS) of iron-cored torbernite. Mineralogical Magazine 71, 423–439.
Dziggel, A., Wulff, K., Kolb, J., Meyer, F.M., Lahaye, Y., 2009. Significance of oscillatory and bell-shaped growth zoning in hydrothermal garnet: evidence from the Navachab gold deposit, Namibia. Chemical Geology 262, 278–292.
Ellmies, R., Voigtländer, G., Germann, K., Krupenin, M.T., Möller, P., 1999. Origin of giant stratabound deposits of magnesite and siderite in Riphean carbonate rocks of the Bashkir mega-anticline, western Urals. Geologische Rundschau 87, 589–602.
Ernst, R.E., Pease, V., Puchkov, V.N., Kozlov, V.I., Sergeeva, N.D., Hamilton, M., 2006. Geochemical characterization of Precambrian magmatic suites of the southeastern margin of the East European Craton, southern Urals, Russia. Geologicheskiy Sbornik 5, 119–161.
Finger, F., Broska, I., Roberts, M.P., Schermaier, A., 1998. Replacement of primary monazite by apatite-allanite-epidote coronas in an amphibolite facies granite gneiss from the eastern Alps. American Mineralogist 83, 248–258.
Fitzsimons, I.C.W., Kinny, P.D., Wetherley, S., Hollingsworth, D.A., 2005. Bulk chemical control on metamorphic monazite growth in pelitic schists and implications for U–Pb age data. Journal of Metamorphic Geology 23, 261–277.
Foster, G., Kinny, P., Vance, D., Prince, C., Harris, N., 2000. The significance of monazite U–Th–Pb age data in metamorphic assemblages; a combined study of monazite and garnet chronometry. Earth and Planetary Science Letters 181, 327–340.
Foster, G., Gibson, H.D., Parrish, R., Horstwood, M., Fraser, J., Tindle, A., 2002. Textural, chemical and isotopic insights into the nature and behaviour of metamorphic monazite. Chemical Geology 191, 183–207.

Franz, G., Andrehs, G., Rhede, D., 1996. Crystal chemistry of monazite and xenotime from Saxothuringian–Moldanubian metapelites, NE Bavaria, Germany. European Journal of Mineralogy 8, 1097–1118.

Gardés, E., Jaoul, O., Montel, J.-M., Seydoux-Guillaume, A.-M., Wirth, R., 2006. Pb diffusion in monazite : an experimental study of $Pb^{2+} + Th^{4+} \leftrightarrow 2Nd^{3+}$ interdiffusion. Geochimica et Cosmochimica Acta 70, 2325–2336.

Gardés, E., Montel, J.-M., Seydoux-Guillaume, A.-M., Wirth, R., 2007. Pb diffusion in monazite : New constraints from the experimental study of $Pb^{2+} \leftrightarrow Ca^{2+}$ interdiffusion. Geochimica et Cosmochimica Acta 71, 4036–4043.

Gasquet, D., Bertrand, J.M., Paquette, J.L., Lehmann, J., Ratzov, G., De Ascenção Guedes, R., Tiepolo, M., Boullier, A.M., Scaillet, S., Nomade, S., 2010. Miocene to Messinian deformation and hydrothermalism in the Lauzière massif (French Western Alps): new U–Th–Pb and Ar ages. Bulletin de la Société Géologique de France 2010 (181), 227–241.

Gee, D.G., Pease, V., 2004. The Neoproterozoic Timanide Orogen of Eastern Baltica: introduction. In: Gee, D.G., Pease, V. (Eds.), The Neoproterozoic Orogen of Eastern Baltica: Geological Society Memoirs 30, London, pp. 1–3.

Gerdes, A., Zeh, A., 2006. Combined U–Pb and Hf isotope LA-(MC)ICP-MS analyses of detrital zircons: Comparison with SHRIMP and new constraints for the provenance and age of an Armorican metasediment in Central Germany. Earth and Planetary Science Letters 249, 47–61.

Gerdes, A., Zeh, A., 2009. Zircon formation versus zircon alteration – new insights from combined U–Pb and Lu–Hf in-situ LA-ICP-MS analyses, and consequences for the interpretation of Archean zircon from the Limpopo Belt. Chemical Geology 261, 230–243.

Gieré, R., Sorensen, S.S., 2004. Allanite and other REE-rich epidote-group minerals. In: Liebscher, A., Franz, G. (Eds.), Epidotes. : Reviews in Mineralogy and Geochemistry, 56. Mineralogical Society of America, pp. 431–493.

Glasmacher, U.A., Reynolds, P., Alekseev, A.A., Puchkov, V.N., Taylor, K., Gorozhanin, V., Walter, R., 1999. $^{40}Ar/^{39}Ar$ thermochronology west of the Main Uralian fault, southern Urals, Russia. Geologische Rundschau 87, 515–525.

Glasmacher, U.A., Bauer, W., Giese, U., Reynolds, P., Kober, B., Puchkov, V., Stroink, L., Alekseyev, A.A., Willner, A.P., 2001. The metamorphic complex of Beloretzk, SW Urals, Russia – a terrane with a polyphase Meso- to Neoproterozoic thermodynamic evolution. Precambrian Research 110, 185–213.

Glasmacher, U.A., Bauer, W., Clauer, N., Puchkov, V.N., 2004. Neoproterozoic metamorphism and deformation at the southeastern margin of the East European Craton, Uralides, Russia. International Journal of Earth Sciences 93, 921–944.

Haas, J.R., Shock, E.L., Sassani, D.C., 1995. Rare earth elements in hydrothermal systems: estimates of standard partial molal thermodynamic properties of aqueous complexes of rare earth elements at high pressures and temperatures. Geochimica et Cosmochimica Acta 58, 4329–4359.

Harlov, D.E., Hetherington, C.J., 2010. Partial high-grade alteration of monazite using alkali-bearing fluids: experiment and nature. American Mineralogist 95, 1105–1108.

Harlov, D.E., Förster, H.J., Nijland, T.G., 2002. Fluid-induced nucleation of (Y+REE)-phosphate minerals within apatite: nature and experiment. Part I. Chlorapatite. American Mineralogist 87, 245–261.

Harlov, D.E., Wirth, R., Hetherington, C.J., 2011. Fluid-mediated partial alteration in monazite: the role of coupled dissolution–reprecipitation in element redistribution and mass transfer. Contributions to Mineralogy and Petrology 162, 329–348.

Harrison, T.M., Catlos, E.J., Montel, J.-M., 2002. U–Th–Pb dating of phosphate minerals. In: Kohn, M.J., Rakovan, J., Hughes, J.M. (Eds.), Phosphates: geochemical, geobiological, and materials importance. : Reviews in Mineralogy and Geochemistry, 48. Mineralogical Society of America, pp. 523–558.

Hetherington, C.H., Harlov, D.E., 2008. Metasomatic thorite and uraninite inclusions in xenotime and monazite from granitic pegmatites, Hidra anorthosite massif, southwestern Norway: mechanics and fluid chemistry. American Mineralogist 93, 806–820.

Hetherington, C.J., Harlov, D.E., Budzyn, B., 2010. Experimental metasomatism of monazite and xenotime: mineral stability, REE mobility and fluid composition. Mineralogy and Petrology 99, 165–184.

Hetzel, R., 1999. Geology and geodynamic evolution of the high-P/low-T Maksyutov Complex, southern Urals, Russia. Geologische Rundschau 87, 577–588.

Iizuka, T., McCulloch, M.T., Komiya, T., Shibuya, T., Ohta, K., Ozawa, H., Sugimura, E., Collerson, K.D., 2010. Monazite geochronology and geochemistry of metasediments in the Narryer Gneiss Complex, Western Australia: constraints on the tectonothermal history and provenance. Contributions to Mineralogy and Petrology 160, 803–823.

Janots, E., Engi, M., Berger, A., Allaz, J., Schwarz, J.-O., Spandler, C., 2008. Prograde metamorphic sequence of REE minerals in pelitic rocks of the Central Alps: implications for allanite-monazite-xenotime phase relations from 250 to 610 °C. Journal of Metamorphic Geology 26, 509–526.

Janots, E., Berger, A., Engi, M., 2011. Physico-chemical control on the REE minerals in chloritoid-grade metasediments from a single outcrop (Central Alps, Switzerland). Lithos 121, 1–11.

Kelts, A.B., Ren, M., Anthony, E.Y., 2008. Monazite occurrence, chemistry, and chronology in the granitoid rocks of the Lachlan Fold Belt, Australia: an electron microprobe study. American Mineralogist 93, 373–383.

Kempe, U., Lehmann, B., Wolf, D., Rodionov, N., Bombach, K., Schwengfelder, U., Dietrich, A., 2008. U–PbSHRIMP geochronology of Th-poor, hydrothermal monazite, an example from the Llallagua tin-porphyry deposit, Bolivia. Geochimica et Cosmochimica Acta 72, 4352–4366.

Kim, Y., Yi, K., Cho, M., 2009. Paragenesis and Th-U distributions among allanite, monazite, and xenotime in Barrovian-type metapelites, Imjingang belt, central Korea. American Mineralogist 94, 430–438.

Kohn, M.J., Catlos, E.J., Ryerson, F.J., Harrison, T.M., 2001. Pressure-temperature-time path discontinuity in the main central thrust zone, central Nepal. Geology 29, 571–574.

Krasnobayev, A.A., Cherednichenko, N.V., 2005. The Archean in the Urals: evidence from zircon age. Doklady Earth Sciences 400 (1), 145–148.

Krenn, E., Ustaszewski, K., Finger, F., 2008. Detrital and newly formed metamorphic monazite in amphibolite-facies metapelites from the Motajica Massif, Bosnia. Chemical Geology 254, 164–174.

Krenn, E., Janák, M., Finger, F., Broska, I., Konecný, P., 2009. Two types of metamorphic monazite with contrasting La/Nd, Th, and Y signatures in an ultrahigh-pressure metapelite from the Pohorje Mountains, Slovenia: Implications for pressure-dependent REE exchange between apatite and monazite ? American Mineralogist 94, 801–815.

Langmuir, D., Herman, J.S., 1980. The mobility of thorium in natural waters at low temperatures. Geochimica et Cosmochimica Acta 44, 1753–1766.

Lennykh, V.I., Pankov, Yu.D., Petrov, V., 1978. Petrology and metamorphism of the migmatite complex. Petrology and iron ore deposits of the Taratash complex. UNTs Akad. Nauka, Sverdlovsk, pp. 3–45 (in Russian).

Linthout, K., 2007. Tripartite division of the system $2REEPO_4 - CaTh(PO_4)_2 - 2ThSiO_4$ discreditation of brabantite, and recognition of cheralite as the name for members dominated by $CaTh(PO_4)_2$. The Canadian Mineralogist 45, 503–508.

Ludwig, K.R., 2003. isoplot 3.00. A Geochronological Toolkit for Microsoft Excel. : Berkeley Geochronological Center Special Publication No 4, Berkeley, CA. 70 pp.

Mahan, K.H., Goncalves, P., Williams, M.L., Jercinovic, M.J., 2006a. Dating metamorphic reactions and fluid flow: application to exhumation of high-P granulites in a crustal-scale shear zone, western Canadian Shield. Journal of Metamorphic Geology 24, 193–217.

Mahan, K., Williams, M., Flowers, R., Jercinovic, M., Baldwin, J., Bowring, S., 2006b. Geochronological constraints on the Legs Lake shear zone with implications for regional exhumation of lower continental crust, western Churchill Province, Canadian Shield. Contributions to Mineralogy and Petrology 152, 223–242.

Malakhova, N.P., Pankov, Yu.D., Chebikin, N.Y., Petrov, V.I., 1978. New data on the age of thrust faulting along the western margin of the Taratash Complex. Year book of the Institute of Geology and Geochemistry Sverdlovsk, 25, p. 26 (in Russian).

McDonough, W.F., Sun, S.-S., 1995. The composition of the earth. Chemical Geology 120, 223–253.

Meyer, F.M., Kolb, J., Sakellaris, G.A., Gerdes, A., 2006. New ages from the Mauretanides: recognition of Archean IOCG mineralization at Guelb Moghrein, Mauritania. Terra Nova 18, 345–352.

Millonig, L., Zeh, A., Gerdes, A., Klemd, R., 2008. Neoarchean high-grade metamorphism in the Central Zone of the Limpopo Belt (South Africa): combined petrological and geochronological evidence from the Bulai Pluton. Lithos 103, 333–351.

Montel, J.M., Foret, S., Veschambre, M., Nollet, Chr, Provost, A., 1996. Electron microprobe dating of monazite. Chemical Geology 131, 37–53.

Petrik, I., Konecny, P., 2009. Metasomatic replacement of inherited metamorphic monazite in a biotite–garnet granite from the Nízke Tatry Mountains, Western Carpathians, Slovakia: Chemical dating and evidence for disequilibrium melting. American Mineralogist 94, 957–974.

Pryer, L.L., 1993. Microstructures in feldspars from a major crustal thrust zone: the Grenville Front, Ontario, Canada. Journal of Structural Geology 15, 21–36.

Puchkov, V.N., 1997. Structure and geodynamics of the Uralian orogen. In: Burg, J.P., Ford, M. (Eds.), Orogeny through time: Geological Society Special Publication, 121. 201–196.

Puchkov, V., 2002. Paleozoic evolution of the East European Continental Margin Involved in the Uralide Orogeny. In: Brown, D., Juhlin, Chr., Puchkov, V. (Eds.), Mountain Building in the Urals – Pangea to the present. : Geophysical Monograph, 132. American Geophysical Union, pp. 9–32.

Putnis, A., 2009. Mineral replacement reactions. In: Oelkers, E.H., Schott, J. (Eds.), Thermodynamics and kinetics of water-rock interaction. : Reviews in Mineralogy and Geochemistry, 70. Mineralogical Society of America, Washington DC, pp. 87–124.

Pyle, J.M., Spear, F.S., Wark, D.A., 2002. Electron microprobe analysis of REE in apatite, monazite and xenotime: protocols and pitfalls. In: Kohn, M.J., Rakovan, J., Hughes, J.M. (Eds.), Phosphates – Geochemical, geobiological and material importance. : Reviews in Mineralogy and Geochemistry, 48. Mineralogical Society of America, Washington DC, pp. 337–362.

Rasmussen, B., Muhling, J.R., 2009. Reactions destroying detrital monazite in greenschist-facies sandstones from the Witwatersrand basin, South Africa. Chemical Geology 264, 311–327.

Rasmussen, B., Sheppard, S., Fletcher, I.R., 2006. Testing ore deposit models using in situ U–Pb geochronology of hydrothermal monazite: Palaeoproterozoic gold mineralization in northern Australia. Geology 34, 77–80.

Ronkin, Yu.L., Matukov, D.I., Presnyakov, S.L., Lepyokhina, E.N., Lepikhina, O.P., Popova, O.Y., 2005. "In situ" U–Pb SHRIMP dating of the zircons from nepheline syenites of the Berdyaush Massif, Southern Urals. Lithosphere 1, 135–142.

Ronkin, Yu.L., Sindern, S., Maslov, A.V., Matukov, D.I., Kramm, U., Lepikhina, O.P., 2007. Oldest (3.5 Ga) zircons in the Urals: U-Pb (SHRIMP II) and $T_{DM}$ constraints. Doklady Earth Sciences 415A, 860–865.

Ronkin, Yu.L., Sindern, S., Kramm, U., Lepikhina, O.P., 2008. Isotope geology of the most ancient formations of the Urals: U-Pb, Sm-Nd, Rb-Sr and $^{40}Ar-^{39}Ar$ systematics. Proceedings of the International Scientific Conference "The structural and geodynamic Problems of Precambrian of the Phanerozoic orogens". Ekaterinburg, pp. 117–120.

Scarrow, J.H., Hetzel, R., Gorozhanin, V.M., Dinn, M., Glodny, J., Gerdes, A., Ayala, C., Montero, P., 2002. Four decades of geochronological work in the southern and middle Urals: A Review. In: Brown, D., Juhlin, Chr., Puchkov, V. (Eds.), Mountain

Building in the Urals – Pangea to the present Geophysical Monograph, 132. American Geophysical Union, pp. 233–255.
Schandl, E.S., Gorton, M.P., 2004. A textural and geochemical guide to the identification of hydrothermal monazite: criteria for selection of samples for dating epigenetic hydrothermal ore deposits. Economic Geology 99, 1027–1035.
Schulz, B., 2009. EMP-monazite age controls on P–T paths of garnet metapelites in the Variscan inverted metamorphic sequence of La Sioule, French Massif Central. Bulletin de la Société Géologique de France 180, 271–282.
Seydoux-Guillaume, A.M., Goncalves, P., Wirth, R., Deutsch, A., 2003. Transmission electron microprobe study of polyphase and discordant monazites: site-specific specimen preparation using the focused ion beam technique. Geology 31, 973–976.
Seydoux-Guillaume, A.M., Wirth, R., Deutsch, A., Schärer, U., 2004. Microstructure of 24–1928 Ma concordant monazites; implications for geochronology and nuclear waste deposits. Geochimica et Cosmochimica Acta 68, 2517–2527.
Shore, M., Fowler, A.D., 1996. Oscillatory zoning in minerals: a common phenomenon. The Canadian Mineralogist 34, 1111–1126.
Sindern, S., Ronkin, Yu.L., Kramm, U., Maslov, A.V., Lepikhina, O.P., 2003. Application of the $^{205}Pb/^{235}U$-spike for the U–Pb dating of single zircons: An example of the Berdyaush nepheline syenites, southern Urals. Isotope geochronology in geodynamics and ore genesis. II Russ. Conf. on geochronology, Conference proceedings, St. Petersburg, pp. 461–465. in Russian.
Sindern, S., Hetzel, R., Schulte, B.A., Kramm, U., Ronkin, Yu.L., Maslov, A.V., Lepikhina, O.P., 2005. Proterozoic magmatic and tectonometamorphic evolution of the Taratash complex, Central Urals, Russia. International Journal of Earth Sciences 94, 319–335.
Sindern, S., Gerdes, A., Dziggel, A., Ronkin, Yu., Hetzel, R., 2009. Metamorphic conditions and age of Proterozoic shearing at the eastern margin of the East European Craton. Hallesches Jahrbuch für Geowissenschaften 31, 235.
Spear, F.S., 2010. Monazite–allanite phase relations in metapelites. Chemical Geology 279, 55–62.
Spear, F.S., Pyle, J.M., 2002. Apatite, monazite, and xenotime in metamorphic rocks. In: Kohn, M.J., Rakovan, J., Hughes, J.M. (Eds.), Phosphates – Geochemical, geobiological and material importance. : Reviews in Mineralogy and Geochemistry, 48. Mineralogical Society of America, Washington DC, pp. 293–335.
Spear, F.S., Pyle, J.M., Cherniak, D., 2009. Limitations of chemical dating of monazite. Chemical Geology 266, 218–230.
Stacey, J.S., Kramers, J.D., 1975. Approximation of terrestrial lead isotope evolution by a two-stage model. Earth and Planetary Science Letters 26, 207–221.
Teufel, S., Heinrich, W., 1997. Partial resetting of the U–Pb isotope system in monazite through hydrothermal experiments: an SEM and U–Pb isotope study. Chemical Geology 137, 273–281.
Tropper, P., Manning, C.E., Harlov, D.E., 2011. Solubility of $CePO_4$ monazite and $YPO_4$ xenotime in $H_2O$ and $H_2O$–NaCl at 800 °C and 1GPa: implications for REE and Y transport during high-grade metamorphism. Chemical Geology 282, 58–66.
Whitney, D.L., Evans, B.W., 2010. Abbreviations for names of rock-forming minerals. American Mineralogist 95, 185–187.
Williams, M.L., Jercinovic, M.J., 2002. Microprobe monazite geochronology: putting absolute time into microstructural analysis. Journal of Structural Geology 24, 1013–1028.
Williams, M.L., Jercinovic, M.J., Terry, M.P., 1999. Age mapping and dating of monazite on the electron microprobe: deconvoluting multi stage tectonic histories. Geology 27, 1023–1026.
Williams, M.L., Jercinovic, M.J., Goncalves, P., Mahan, K., 2006. Format and philosophy for collecting, compiling, and reporting microprobe monazite ages. Chemical Geology 225, 1–15.
Williams, M.L., Jercinovic, M.J., Hetherington, C.J., 2007. Microprobe monazite geochronology: understanding geologic processes by integrating composition and chronology. Annual Review of Earth and Planetary Sciences 35, 137–175.
Williams, M.L., Jercinovic, M.J., Harlov, D.E., Budzyn, B., Hetherington, C.J., 2011. Resetting monazite ages during fluid-related alteration. Chemical Geology 283, 218–225.
Willner, A.P., Sindern, S., Metzger, R., Ermolaeva, T., Kramm, U., Puchkov, V., Kronz, A., 2003. Typology and single grain U/Pb ages of detrital zircons from Proterozoic sandstones in the SW Urals (Russia): early time marks at the eastern margin of Baltica. Precambrian Research 124, 1–20.
Wing, B.A., Ferry, J.M., Harrison, T.M., 2003. Prograde destruction and formation of monazite and allanite during contact and regional metamorphism of pelites: petrology and geochronology. Contributions to Mineralogy and Petrology 145, 228–250.
Wood, S.A., 1990. The aqueous geochemistry of rare-earth elements and yttrium 2. Theoretical predictions of speciation in hydrothermal solutions to 350 °C at saturation water pressure. Chemical Geology 88, 99–125.
Yi, K., Cho, M., 2009. SHRIMP geochronology and reaction texture of monazite from a retrogressive transitional layer, Hwacheon Granulite Complex, Korea. Geosciences Journal 13, 293–304.

6.

Willner, A.P., Sindern, S., Metzger, R., Ermolaeva, T., Kramm, U., Puchkov, V., Kronz, A. (2003) Typology and single grain U/Pb ages of detrital zircon from Proterozoic sandstones in the SW Urals: early time marks at the eastern margin of Baltica. Precambrian Research 124, 1 – 20.

Right of re-use in thesis for Elsevier journal author granted by Elsevier, confirmation by Elsevier Permissions Helpdesk, 1600 John F. Kennedy Boulevard, Suite 1800, Philadelphia, PA 19103-2899, USA, 23rd of October 2015.

Available online at www.sciencedirect.com
SCIENCE DIRECT®
Precambrian Research 124 (2003) 1–20
Precambrian Research
www.elsevier.com/locate/precamres

# Typology and single grain U/Pb ages of detrital zircons from Proterozoic sandstones in the SW Urals (Russia): early time marks at the eastern margin of Baltica

A.P. Willner[a,*], S. Sindern[b,c], R. Metzger[b,c], T. Ermolaeva[b], U. Kramm[b], V. Puchkov[d], A. Kronz[e]

[a] Institut für Geologie, Mineralogie und Geophysik, Ruhr-Universität, D-44795 Bochum, Germany
[b] Institut für Mineralogie und Lagerstättenlehre, RWTH, Wüllnerstr. 2, D-52056 Aachen, Germany
[c] Zentrallaboratorium für Geochronologie, Corrensstraße 24, D-48149 Münster, Germany
[d] Ufimian Geoscience Centre, Russian Academy of Science, K. Marx Street 16/2, 450000 Ufa, Russia
[e] Institut für Geochemie, Goldschmidtstr. 1, D-37077 Göttingen, Germany

Received 13 November 2001; accepted 18 January 2003

**Abstract**

In the SW Urals a change of tectonic conditions occurred at around 620 Ma leading to a detrital input from contrasting provenance areas. Fifty-seven detrital zircons were separated from Proterozoic sandstones of this setting to study their typologies and pattern of U–Pb systematics.

Detritus from Riphean sandstones (1.63–0.65 Ga) contains three populations of zircon: (1) completely rounded fragmental grains with complicated, but weak internal fabrics derived from high grade metamorphic areas with multistage reworking; (2) long-prismatic zircon grains with rounded edges and weakly preserved growth zoning from S-type granites; (3) types 1 and 2, but cloudy due to intense alteration (hydration of metamict areas). Zircons from Upper Vendian sandstones (0.62–0.54 Ga) comprise two groups: (1) zircons similar to those of Riphean populations 1, 2 and 3; (2) perfectly euhedral zircons with preserved magmatic growth zoning from potassic alkaline as well as acid magmas.

Age signatures of polycyclic zircons from both Riphean and Upper Vendian detritus are compatible with crystallization in the interval of 1.8–2.3 Ga. This appears to be the significant age signature for the largely covered basement of the East European Platform, the presumed source region in the W. The pattern of U–Pb systems shows evidence of at least two events leading to lead loss. Data clusters in the concordia diagram confined to single samples show a remarkably strong influence of local sources. Alteration during diagenesis was an important factor of lead loss.

Upper Vendian detrital zircons have two sources: (1) The majority of the polycyclic rounded zircons also has a Paleoproterozoic crystallization age consistent with that of the Riphean detrital zircons. However, a few zircon grains point to a later anorogenic event which does not match with known events in the Riphean basin and hence underline an allochthonous character of the source area. (2) The data of the euhedral zircon would reflect a source age between 643 and 512 Ma.

The latter age signature is compatible with a local magmatic event concomitant with exhumation and emplacement of the allochthonous Beloretzk Terrane after 620 Ma. This eastern source area for the Upper Vendian detritus had partly been affected by high-pressure/low temperature metamorphism. The change of tectonic conditions reflected by the detritus composition

* Corresponding author. Fax: +49-234-32-14433.
*E-mail address:* arne.willner@ruhr-uni-bochum.de (A.P. Willner).

represents a change from a passive continental margin along the Rodinia supercontinent persisting during the Riphean to a convergent continental margin during the Upper Vendian within a transpressional setting.
© 2003 Elsevier Science B.V. All rights reserved.

*Keywords:* Zircon typology; Detrital zircon; Single grain U/Pb systematics; Timanide orogeny; Riphean sandstone; Vendian sandstone; Rodinia; SW-Urals

## 1. Introduction

During the past decade U–Pb-dating of single zircon crystals from all rock types combined with better imaging of their internal structures has provided a foundation to better understand many processes in general. Here we try to apply this combination of methods to detrital zircon crystals from the relatively well known Precambrian sedimentary basins in the Southern Urals.

The Urals represent a Variscan collisional orogen between the Baltica, Kazakhstanian and Siberian protocontinents with an intervening magmatic arc. At the eastern margin of Baltica a remarkably long Precambrian history of this margin can be detected below its Paleozoic cover (Fig. 1; Puchkov, 1997; Maslov et al., 1997). This early evolution is especially important in the light of recent efforts in understanding the formation and break up of the Late Precambrian supercontinent of Rodinia (e.g. Torsvik et al., 1996; Weil et al., 1998). The record is found in siliciclastic sediments from two contrasting, long persisting basins (Riphean and Vendian) between about 1.63 and 0.54 Ga. This period of time covers the entire history of assembly and dispersal of the Rodinia supercontinent.

The provenance signal of the detritus changes at around 620 Ma, which is consistent with the pre-Uralian Timanide orogeny (Puchkov, 1997; Maslov et al., 1997) representing a transition from a passive to an active continental margin (Willner et al., 2001). A similar history during the Neoproterozoic is observed, at least partly, along the entire length of the Urals on the western side of the suture zone, but it is definitely missing on the eastern (Siberian) side (Maslov et al., 1997; Puchkov, 1997).

Applying typological characterization and U–Pb systematics of single detrital zircon from siliciclastic rocks of the two different sedimentary piles with contrasting provenance areas, we attempt to answer the following methodological and regional issues:

- Does a systematic correlation exist between the internal structure and U–Pb isotope signature of the investigated zircon crystals?
- How does the internal structure and isotope information of the zircon crystals differ between the two contrasting types of detritus and how does this reflect different geological histories in the source areas?
- Is lead loss also caused by the process of diagenesis? Can we distinguish between isotope information of the source area and isotope disturbances from diagenetic processes ?
- Is the U–Pb isotope signature of the zircon crystals indicative for a specific protocontinent source?

From the stratigraphic sequence six zircon-rich samples of medium-grained non-metamorphosed sandstones were selected, four Riphean samples (8c, 32, 37, 40) and two Upper Vendian samples (18/19, 29). A thorough light and heavy mineral study of those samples has been performed previously (Willner et al., 2001).

## 2. Geological setting and evolution

The geological evolution at the eastern margin of Baltica starts within a Paleoproterozoic crystalline basement underlying the East European platform. Age information from these rocks, which are exposed e.g. in the Taratash Complex of the SW Urals (Fig. 1), was compiled by Lennykh and Krasnobaev (1978), Bogdanova (1986) and Ivanov et al. (1986). These data suggest a major Paleoproterozoic orogenic cycle between about 2.3 and 1.8 Ma based on U–Pb zircon data. This broad age pattern is confirmed by new data of Sindern et al. (2001) ranging between 2.34 and 1.8 Ga that can be correlated to specific geological processes. Granites (1.61–1.57; U–Pb) and diabase dykes (1.6 Ga; Rb–Sr) cutting the basement

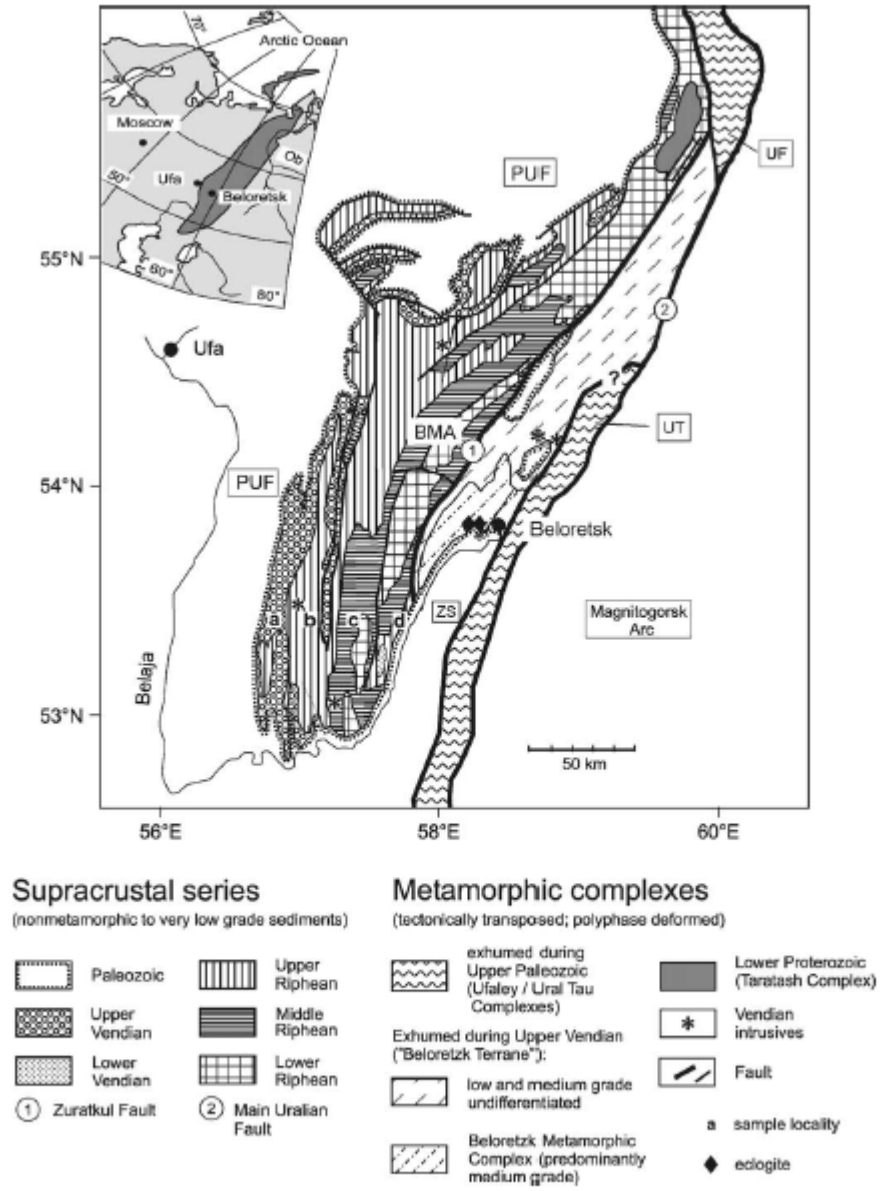


Fig. 1. Geological sketch map of the southwestern Urals. PUF Pre-Uralian Foredeep; BMA Bashkirian Megaanticlinorium; ZS Zilair Syncline; UT Ural Tau Antiform; BMC Metamorphic Complex of Beloretsk; UF Ufaley Metamorphic Complex. Samples studied for this paper were taken from the following localities: (a) 18/19, 22, 23, 28, 29; (b) 32; (c) 40; (d) 8c.

in the Taratash Complex are interpreted to be related to a younger rift event (Keller and Krasnobaev, 1983).

In the SW-Urals the overlying unmetamorphosed Proterozoic sediments are exposed in the Bashkirian Megaanticlinorium (Fig. 1). The 12–15 km thick, mainly siliciclastic sequence of the Riphean basin is subdivided by extrusions and intrusions of bimodal igneous rocks, which are related to three major rift events providing rough time markers around 1.65, 1.35 and 1.0 Ga (see Krasnobaev, 1986 and Maslov et al., 1997; Fig. 2). These ages are based on combined U/Pb dating on zircons and Rb/Sr whole rock isochrons. Sedimentation was partially under terrestrial conditions grading into shallow marine deposits towards the east (Maslov et al., 1997). The detrital components of the Riphean sandstones are characterized by a "continental platform provenance" in accordance to its derivation from the basement of the East European Platform (Willner et al., 2001). Supposed source rocks were granitoids and high grade metamorphic rocks as well as siliciclastic sediments and acid volcanic rocks reworked within the basin during episodic block faulting. The limited heavy mineral spectrum (zircon, tourmaline, rutile) provides evidence for polycyclic sedimentation.

The Riphean sediments are conformably overlain by Vendian siliciclastic sediments with a thickness of 2000–3000 m. While Lower Vendian sediments include glacial deposits, the Upper Vendian detritus was discharged from a proximal high-relief area in the east (Maslov et al., 1997; Willner et al., 2001) and deposited within a foredeep basin on the western flank of a pre-Uralian orogen (Puchkov, 1997) comprising mainly turbiditic sandstones and siltstones. Absolute ages of sedimentation of the Vendian siliciclastic rocks were mainly estimated from K/Ar and Rb/Sr-data from glauconites (see review of Maslov et al., 1997).

The provenance signal of the Upper Vendian sediments indicates a drastic change of tectonic conditions around 620 Ma (Willner et al., 2001). It has a "recycled orogenic provenance" including mineral and lithic clasts of mainly low grade siliciclastic metasediments and mylonites containing phengites with a high pressure signature as well as clasts of bimodal volcanic rocks and siliciclastic sediments derived from intrabasinal reworking. The heavy mineral spectrum is dominated by epidote, while the rest is rather reduced (zircon, tourmaline, rutile, apatite) suggesting polycyclic sedimentation and similarity to the Riphean heavy mineral spectrum.

The source area for the Upper Vendian detritus is still preserved between the Zuratkul Fault in the west and the Main Uralian Fault in the east (Fig. 1). This Beloretsk Terrane is characterized by low to medium grade metamorphic rocks, the latter dominating in its southern part (Metamorphic Complex of Beloretsk; Glasmacher et al., 1999, 2001; Fig. 1). Local lenses of eclogite occur within this complex. The country rocks contain phengite, which also implies high pressure during crystallization. White mica Ar–Ar cooling ages between 543 and 597 Ma (Glasmacher et al., 1999, 2001) suggest concomitant exhumation, surface uplift and emplacement of this complex during Vendian. A local granite gneiss has a protolith age of 950 Ma (zircon; Pb–Pb evaporation method; Glasmacher et al., 2001). In contrast to the interpretation of Glasmacher et al. (2001), we consider that this gneiss was deformed and metamorphosed along with the nearby eclogites between 950 and 718 Ma. The latter lower age limit of metamorphism is given by an Ar–Ar age of amphibole (Glasmacher et al., 2001). At that time there was ongoing sedimentation within the Bashkirian basin indicating an allochthonous derivation of the Beloretsk Terrane. Neoproterozoic deformation in Riphean sediments west of the Zuratkul fault is limited to weak folding, which decreases further west.

Small plutons, dykes and (sub)volcanic equivalents of a partly alkaline suite (alkali gabbro, essexite, syenite, monzonite, granite, rhyolite) represent a Vendian magmatic event according to Alekseev and Alekseeva (1980), because they cut Riphean, but not Upper Vendian sediments and have K–Ar ages between 602 and 670 Ma. Ar–Ar ages of 590–630 Ma for detrital orthoclase in the Upper Vendian given by Glasmacher et al. (1999) may also be attributed to cooling immediately following this magmatic event.

Ordovician sediments overlie the pre-Uralian basement east of the Zuratkul Fault and the Riphean basin further west with a pronounced angular unconformity (Puchkov, 1997). Later the entire area was incorporated into a westverging foreland fold-and-thrust belt during the Uralian orogeny.

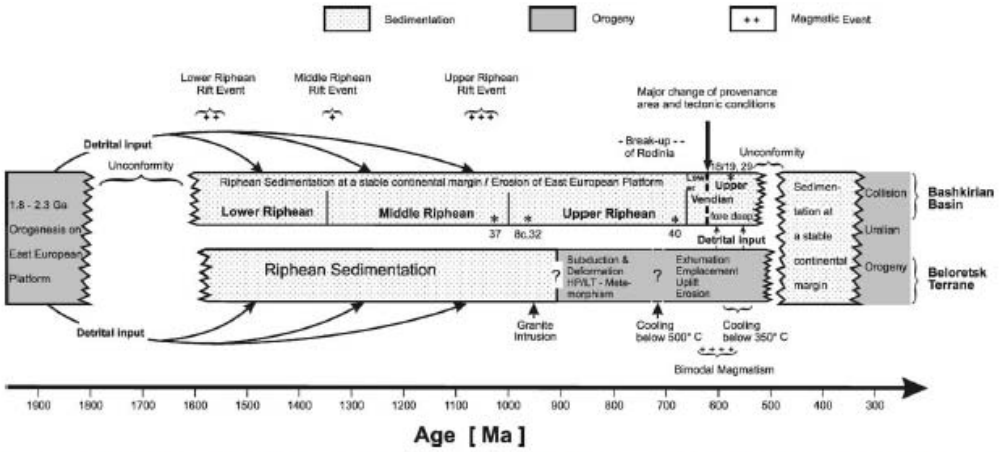


Fig. 2. Summary of Precambrian geological events in the SW Urals compatible with the results of this paper; the lithostratigraphic subdivision of Maslov et al. (1997) with the approximate stratigraphic position of the analysed samples (asterisk) is included.

## 3. Analytical methods

### 3.1. Sample selection and qualitative image analysis

Zircon crystals from Riphean and Vendian sandstones were selected from the spectrum of heavy minerals by magnetic separation and panning after dissolving of Fe stainings from the heavy minerals using 5N HCl during 5 min in an ultrasonic bath. A final selection and separation into colour, shape and transparency fractions was performed by hand-picking under the binocular microscope.

After a prior comprehensive study of light and heavy minerals in the Riphean and Vendian detritus (Willner et al., 2001) zircon crystals (grain size fraction 63–125 μm) were separated from those samples which show a typologically variable zircon population. Morphological studies on these populations were performed with a Zeiss scanning electron microscope at Aachen University. The typological classification scheme of Pupin (1980) was used.

Ninety two selected grains were embedded in epoxy resin, mostly cut parallel to {1 0 0} prism zones and polished. Backscattered electron images, cathodoluminescence images, element distribution maps and qualitative energy-dispersive analysis of inclusions and alteration zones were performed with a Jeol JXA 8900 RL microprobe at Göttingen University and a Cameca SX 50 microprobe at Bochum University. A complete set of images can be obtained upon request from the senior author.

### 3.2. Zircon preparation for isotope analysis

Fifty to hundred transparent, colourless and inclusion free crystals per zircon fraction were cleaned in $H_2O$, heated for 30 min at 80 °C and washed finally four times with acetone. All reagents were of ultrapure grade.

The marginal shells of part of the selected crystals were partly abraded in a mill as described by KROGH (1982) using pyrite as an abrasive. These zircon crystals were cleaned from adhesive pyrite by washing with 7.5N $HNO_3$ for 30 min at 50 °C and rinsing with $H_2O$ and acetone. The weight of the single zircons was not determined because of their size, hence, the concentrations of Pb and U cannot be calculated from the isotopic data.

Digestion of original and abraded zircon crystals was performed in teflon liners designed for the dissolution of six single crystals simultaneously using 24N HF at 180 °C (vapour digestion technique according to Wendt, 1993). The digestion was completed after 4 days. After spiking with a mixed $^{205}Pb$–$^{233}U$ solution sample and spike were homogenized in 6N HCl for 24 h at 80 °C. The excess HCl was evaporated finally.

### 3.3. Mass spectrometry

The Pb standards as well as the spiked samples were loaded without element separation on single Re filaments (Wendt, 1993) into a silica gel bed with 2 μl of a loading solution containing 90 vol.% of 6N HCl and 10 vol.% of 0.1N $H_3PO_4$.

Isotope measurements were performed on a VG sector 54 mass spectrometer at the Zentrallabor für Geochronologie, Münster University, equipped with a Daly multiplier. The Pb composition was determined at 1300–1400 °C followed by the U measurement at 1400–1450 °C. At maximum the $2\sigma_m$ errors obtained for $^{206}Pb/^{204}Pb$, $^{207}Pb/^{206}Pb$, and $^{233}U/^{238}U$ were 3.0, 0.05, and 0.1%, respectively (see Table 1 for individual absolute errors). The isotope $^{208}Pb$ was not analysed. Isotope ratios were corrected for mass fractionation (0.11% ± 0.02/amu), blank (<10 pg total Pb, $^{206}Pb/^{204}Pb = 17.7 \pm 0.5$, $^{207}Pb/^{204}Pb = 15.5 \pm 0.1$, 1 pg U) and initial common Pb estimated after the model of Stacey and Kramers (1975). The $^{206}Pb/^{204}Pb$ and $^{207}Pb/^{204}Pb$ ratios were deduced from the latter model using the apparent $^{207}Pb/^{206}Pb$ ages. Uncertainties of the $^{206}Pb/^{204}Pb$ and $^{207}Pb/^{204}Pb$ ratios were assumed to be 2 and 0.3%, respectively. Decay constants are taken from Jaffey et al. (1971).

## 4. Typology of zircon

### 4.1. Detrital zircons from Riphean sandstones

Among zircon grains separated from four Riphean sandstones (8c, 32, 37, 40; see appendix for petrography) three groups can be distinguished based on morphology and type of internal zoning:

Table 1
Analytical data of the studied U–Pb systems

| Sample | Zircon group | Pb[a] (pg) | U[b] (pg) | $^{206}Pb/^{204}Pb$ ratio[c] and $2\sigma_m$ error | $^{207}Pb/^{206}Pb$ ratio[d] and $2\sigma_m$ error | $^{207}Pb/^{235}U$ ratio[d] and $2\sigma_m$ error | $^{206}Pb/^{238}U$ ratio[d] and $2\sigma_m$ error | $^{207}Pb/^{206}Pb$ age (Ma) | $^{207}Pb/^{235}U$ age (Ma) | $^{206}Pb/^{238}U$ age (Ma) |
|---|---|---|---|---|---|---|---|---|---|---|
| Riphean | | | | | | | | | | |
| 40Z1-0 | I | 56 | 216 | 264.3 ± 0.2 | 0.09216 ± 0.00058 | 2.853 ± 0.027 | 0.2246 ± 0.0014 | 1471 | 1370 | 1306 |
| 40Z1-1 | I | 56 | 214 | 248.5 ± 0.2 | 0.09141 ± 0.00057 | 2.838 ± 0.029 | 0.2251 ± 0.0017 | 1455 | 1366 | 1309 |
| 40Z1-2 | I | 39 | 189 | 294.3 ± 0.3 | 0.09023 ± 0.00060 | 2.258 ± 0.023 | 0.1815 ± 0.0013 | 1430 | 1199 | 1075 |
| 40Z1-3 | I | 35 | 146 | 276.7 ± 0.3 | 0.09723 ± 0.00058 | 2.820 ± 0.027 | 0.2104 ± 0.0015 | 1572 | 1361 | 1231 |
| 40Z1-4 | II | 26 | 111 | 211.4 ± 0.2 | 0.09002 ± 0.00063 | 2.525 ± 0.027 | 0.2034 ± 0.0014 | 1426 | 1279 | 1194 |
| 40Z1-5 | II | 33 | 137 | 273.5 ± 0.1 | 0.08873 ± 0.00044 | 2.560 ± 0.019 | 0.2092 ± 0.0010 | 1398 | 1289 | 1225 |
| 32Z3r-0 | I | 22 | 68 | 104.9 ± 0.8 | 0.12760 ± 0.00179 | 4.307 ± 0.119 | 0.2448 ± 0.0056 | 2065 | 1695 | 1411 |
| 32Z3r-1 | I | 78 | 215 | 275.0 ± 0.2 | 0.12292 ± 0.00048 | 5.214 ± 0.036 | 0.3076 ± 0.0016 | 1999 | 1855 | 1729 |
| 32Z3r-2 | I | 92 | 259 | 331.3 ± 0.3 | 0.12639 ± 0.00073 | 5.264 ± 0.049 | 0.3021 ± 0.0021 | 2048 | 1863 | 1701 |
| 32Z3r-3 | I | 77 | 222 | 145.7 ± 0.5 | 0.12834 ± 0.00117 | 4.842 ± 0.058 | 0.2736 ± 0.0018 | 2075 | 1792 | 1559 |
| 32Z3r-5/1 | I | 44 | 121 | 175.9 ± 1.1 | 0.12327 ± 0.00245 | 4.995 ± 0.127 | 0.2939 ± 0.0041 | 2004 | 1818 | 1661 |
| 32Z3r-5/2 | I | 44 | 121 | 179.5 ± 0.9 | 0.12792 ± 0.00156 | 5.252 ± 0.081 | 0.2978 ± 0.0022 | 2070 | 1861 | 1680 |
| 32Z3r-0 | I | 94 | 240 | 693.5 ± 0.1 | 0.12186 ± 0.00040 | 5.763 ± 0.035 | 0.3430 ± 0.0017 | 1984 | 1941 | 1901[e] |
| 32Z3-1 | I | 97 | 245 | 686.1 ± 0.3 | 0.12009 ± 0.00057 | 5.748 ± 0.040 | 0.3471 ± 0.0016 | 1958 | 1939 | 1921[e] |
| 32Z3-2 | I | 98 | 245 | 562.1 ± 0.1 | 0.12171 ± 0.00034 | 5.814 ± 0.034 | 0.3465 ± 0.0017 | 1981 | 1949 | 1918[e] |
| 32Z3-3 | I | 98 | 246 | 479.7 ± 0.2 | 0.12223 ± 0.00041 | 5.820 ± 0.035 | 0.3453 ± 0.0017 | 1989 | 1949 | 1912[e] |
| 32Z3r-4 | I | 97 | 242 | 441.2 ± 0.2 | 0.12094 ± 0.00044 | 5.761 ± 0.039 | 0.3455 ± 0.0019 | 1970 | 1941 | 1913[e] |
| 32Z3-5 | I | 95 | 239 | 506.9 ± 0.2 | 0.12075 ± 0.00039 | 5.729 ± 0.033 | 0.3441 ± 0.0016 | 1967 | 1936 | 1906[e] |
| 8cZ1-0 | II | 108 | 336 | 1512.5 ± 0.1 | 0.11369 ± 0.00022 | 4.485 ± 0.019 | 0.2861 ± 0.0011 | 1859 | 1728 | 1622 |
| 8cZ1-1 | II | 61 | 257 | 987.3 ± 0.1 | 0.09475 ± 0.00027 | 2.814 ± 0.013 | 0.2154 ± 0.0008 | 1523 | 1359 | 1258 |
| 8cZ1-2 | II | 179 | 693 | 2062.0 ± 0.1 | 0.10681 ± 0.00019 | 3.418 ± 0.017 | 0.2321 ± 0.0011 | 1746 | 1509 | 1345 |
| 8cZ1-3 | II | 196 | 778 | 2524.0 ± 0.1 | 0.10866 ± 0.00018 | 3.385 ± 0.015 | 0.2260 ± 0.0009 | 1777 | 1501 | 1313 |
| 8cZ1-4 | II | 214 | 853 | 2881.6 ± 0.1 | 0.10665 ± 0.00019 | 3.329 ± 0.016 | 0.2264 ± 0.0010 | 1743 | 1488 | 1315 |
| 8cZ1-5 | II | 175 | 605 | 2496.7 ± 0.1 | 0.10898 ± 0.00017 | 3.906 ± 0.016 | 0.2600 ± 0.0010 | 1782 | 1615 | 1490 |
| 37bZ1-1 | I | 69 | 186 | 681.8 ± 0.3 | 0.13667 ± 0.00050 | 6.067 ± 0.044 | 0.3220 ± 0.0019 | 2185 | 1986 | 1799 |
| 37bZ1-2 | I | 33 | 85 | 380.5 ± 0.9 | 0.13198 ± 0.00138 | 6.078 ± 0.083 | 0.3340 ± 0.0022 | 2124 | 1987 | 1858 |

Table 1 (*Continued*)

| Sample | Zircon group | Pb[a] (pg) | U[b] (pg) | $^{206}Pb/^{204}Pb$ ratio[c] and $2\sigma_m$ error | $^{207}Pb/^{206}Pb$ ratio[d] and $2\sigma_m$ error | $^{207}Pb/^{235}U$ ratio[d] and $2\sigma_m$ error | $^{206}Pb/^{238}U$ ratio[d] and $2\sigma_m$ error | $^{207}Pb/^{206}Pb$ age (Ma) | $^{207}Pb/^{235}U$ age (Ma) | $^{206}Pb/^{238}U$ age (Ma) |
|---|---|---|---|---|---|---|---|---|---|---|
| Upper vendian | | | | | | | | | | |
| 18/19Z3r-0 | I | 143 | 431 | 173.8 ± 0.2 | 0.11947 ± 0.00071 | 5.128 ± 0.045 | 0.3113 ± 0.0017 | 1948 | 1841 | 1747 |
| 18/19Z3r-1 | I | 140 | 375 | 206.6 ± 0.2 | 0.11826 ± 0.00058 | 5.027 ± 0.051 | 0.3083 ± 0.0026 | 1930 | 1824 | 1732 |
| 18/19Z3r-2 | I | 54 | 137 | 180.6 ± 0.1 | 0.11877 ± 0.00062 | 5.280 ± 0.044 | 0.3224 ± 0.0019 | 1938 | 1866 | 1802 |
| 18/19Z3r-3 | I | 71 | 169 | 129.3 ± 0.4 | 0.11918 ± 0.00106 | 5.358 ± 0.064 | 0.3261 ± 0.0022 | 1944 | 1878 | 1819 |
| 18/19Z3r-5 | I | 92 | 243 | 183.0 ± 0.2 | 0.11792 ± 0.00061 | 5.020 ± 0.049 | 0.3087 ± 0.0024 | 1925 | 1823 | 1734 |
| 18/19Z1r-0 | I | 79 | 223 | 1135.5 ± 0.1 | 0.11841 ± 0.00031 | 5.128 ± 0.030 | 0.3141 ± 0.0016 | 1932 | 1841 | 1761 |
| 18/19Z1r-1 | I | 42 | 160 | 586.1 ± 0.2 | 0.09276 ± 0.00123 | 3.018 ± 0.042 | 0.2360 ± 0.0010 | 1483 | 1412 | 1366 |
| 18/19Z1r-2 | I | 72 | 201 | 1152.6 ± 0.1 | 0.11293 ± 0.00053 | 4.974 ± 0.032 | 0.3195 ± 0.0014 | 1847 | 1815 | 1787 |
| 18/19Z1r-4 | I | 43 | 120 | 602.6 ± 0.1 | 0.10930 ± 0.00070 | 4.702 ± 0.037 | 0.3120 ± 0.0013 | 1788 | 1768 | 1750 |
| 18/19Z1r-5 | I | 19 | 68 | 331.1 ± 0.3 | 0.09061 ± 0.00059 | 3.108 ± 0.027 | 0.2488 ± 0.0012 | 1438 | 1435 | 1432 |
| 18/19Z3rb2 | I | 72 | 189 | 323.3 ± 0.2 | 0.11810 ± 0.00050 | 5.290 ± 0.040 | 0.3249 ± 0.0019 | 1928 | 1867 | 1814 |
| 18/19Zrb3 | I | 92 | 189 | 73.5 ± 1.7 | 0.12711 ± 0.00330 | 5.939 ± 0.183 | 0.3389 ± 0.0033 | 2058 | 1967 | 1881 |
| 18/19Zrb4 | I | 71 | 189 | 335.9 ± 0.2 | 0.11798 ± 0.00042 | 5.283 ± 0.033 | 0.3248 ± 0.0016 | 1926 | 1866 | 1813 |
| 18/19Z3ra0 | I | 72 | 190 | 291.3 ± 0.2 | 0.11814 ± 0.00051 | 5.283 ± 0.040 | 0.3244 ± 0.0019 | 1928 | 1866 | 1811 |
| 18/19Z3ra-1 | I | 74 | 189 | 239.2 ± 0.2 | 0.11863 ± 0.00050 | 5.336 ± 0.040 | 0.3263 ± 0.0018 | 1936 | 1875 | 1820 |
| 18/19Z3ra5 | I | 74 | 189 | 213.5 ± 0.1 | 0.11738 ± 0.00055 | 5.268 ± 0.039 | 0.3255 ± 0.0017 | 1917 | 1864 | 1817 |
| 18/19-Z4-0 | IIa | 14 | 462 | 132.4 ± 0.6 | 0.05902 ± 0.00132 | 0.898 ± 0.023 | 0.1103 ± 0.0010 | 568 | 650 | 675 |
| 18/19-Z4-1 | IIa | 14 | 354 | 113.0 ± 0.4 | 0.06109 ± 0.00118 | 0.916 ± 0.020 | 0.1087 ± 0.0006 | 643 | 660 | 665 |
| 18/19-Z4-4 | IIa | 15 | 181 | 98.2 ± 0.4 | 0.05917 ± 0.00130 | 0.824 ± 0.021 | 0.1010 ± 0.0007 | 573 | 610 | 620 |
| 18/19-Z4-5 | IIa | 15 | 505 | 134.8 ± 0.6 | 0.05815 ± 0.00125 | 0.874 ± 0.021 | 0.1090 ± 0.0006 | 535 | 638 | 667 |
| 18/19Z4-0 | IIa | 14 | 105 | 64.9 ± 0.7 | 0.06055 ± 0.00215 | 0.777 ± 0.031 | 0.0931 ± 0.0009 | 623 | 584 | 574 |
| 18/19Z4-1 | IIa | 15 | 104 | 60.5 ± 0.5 | 0.06044 ± 0.00203 | 0.776 ± 0.029 | 0.0931 ± 0.0008 | 619 | 583 | 574 |
| 18/19Z4-3 | IIa | 14 | 104 | 69.3 ± 0.3 | 0.05869 ± 0.00156 | 0.754 ± 0.023 | 0.0931 ± 0.0007 | 556 | 570 | 574 |
| 18/19Z4-4 | IIa | 15 | 104 | 53.0 ± 0.3 | 0.05754 ± 0.00209 | 0.743 ± 0.030 | 0.0936 ± 0.0008 | 512 | 564 | 577 |
| 18/19Z4-5 | IIa | 16 | 105 | 52.8 ± 1.0 | 0.06043 ± 0.00330 | 0.780 ± 0.047 | 0.0936 ± 0.0009 | 619 | 585 | 577 |
| 29Z1-1 | I | 96 | 226 | 103.7 ± 0.2 | 0.11725 ± 0.00094 | 5.180 ± 0.060 | 0.3204 ± 0.0023 | 1915 | 1849 | 1792 |
| 29Z1-4 | I | 87 | 227 | 183.2 ± 0.2 | 0.11736 ± 0.00066 | 5.074 ± 0.045 | 0.3136 ± 0.0019 | 1916 | 1832 | 1758 |
| 29Z1-5 | I | 93 | 228 | 123.8 ± 1.0 | 0.12104 ± 0.00195 | 5.271 ± 0.103 | 0.3158 ± 0.0024 | 1972 | 1864 | 1769 |
| 29Z10 | I | 85 | 229 | 234.8 ± 0.2 | 0.11615 ± 0.00051 | 4.962 ± 0.040 | 0.3098 ± 0.0019 | 1898 | 1813 | 1740 |
| 29Z12 | I | 84 | 226 | 244.3 ± 0.2 | 0.11737 ± 0.00059 | 5.022 ± 0.043 | 0.3103 ± 0.0020 | 1917 | 1823 | 1742 |
| 29Z13 | I | 85 | 228 | 213.8 ± 0.3 | 0.11716 ± 0.00064 | 5.027 ± 0.043 | 0.3112 ± 0.0018 | 1913 | 1824 | 1746 |

[a] Amount of $^{207}Pb$, $^{206}Pb$ and $^{204}Pb$ in zircon.
[b] Atomic ratios corrected for blank, spike, fractionation and initial common Pb.
[c] Amount of U in zircon.
[d] Corrected for spike and fractionation.
[e] Further abraded.

A.P. Willner et al. / Precambrian Research 124 (2003) 1–20

Zircon *group I* (19 grains) comprises clear, colourless, generally perfectly rounded fragments of larger crystals (Fig. 3(1 and 2)) suggesting multistage reworking. The surfaces are mostly rough and pitted. The degree of fracturing and filling of fractures is variable. The type of internal zoning also varies considerably, but is always faint and cathodoluminescence is usually very weak. Some grains even appear unzoned in back scatter electron images. Apart from some former well-developed, concentric growth zonation partly with traces of round dissolution surfaces, relict zoning is generally hazy and diffuse (Fig. 3(1)). Also blurred former oscillatory zoning without distinct borders occurs. Internal unconformities due to overgrowth phenomena are frequent. Patchy zoning with sharp and curved sectoral boundaries, planar and non-planar sectoral overgrowth as well as some older inherited cores are observed. Two grains show fir-tree sector zoning in overgrowth rims (Fig. 3(2)) as described by Vavra et al. (1996). Tiny, round inclusions of apatite and quartz are abundant. In one grain inclusions of Cl-rich apatite were observed.

Group I internal fabrics are rather similar to zircon from amphibolite and granulite facies terranes as described by Vavra et al. (1996, 1999) and Schaltegger et al. (1999). The low contrasts between adjacent individual growth bands are inferred to be due to small chemical differences and may be interpreted as gradual erasing of primary zoning either by diffusion under elevated temperatures or by annealing effects within strained lattice domains as suggested by Schaltegger et al. (1999). Inherited zircon can occur as xenocrysts or detrital cores that are overgrown in a complex manner. Observed patchy, sector or fir-tree zones and thin overgrowths at the rims are due to subsolidus crystallisation.

Zircon *group II* (11 grains) comprises clear, colourless and long prismatic grains (S11, S12 and S17 type after Pupin, 1980) that are edge rounded to variable degrees (Fig. 3(3 and 4)). The crystals are partly broken at one end along fresh cracks. The surfaces are generally rough and pitted, but a few grains are euhedral with smooth surfaces. Filled cracks are always developed. Round inclusions of magnetite, Fe-rich biotite, K-feldspar, quartz, xenotime and apatite needles were observed.

A perfect concentric, narrowly spaced, oscillatory growth zoning pattern is generally developed. The grains can display cores with traces of round dissolution surfaces (Fig. 3(3)) and planar overgrowth. Three grains contain a round inherited core. Small filled dissolution embayments can also occur at the edges of the grains. Most grains show outer planar overgrowth zones at the edges.

Group II typically comprises magmatic zircon. Morphology, typical inclusions as well as some occurrence of inherited cores point to (at least partly S-type) granitoids as source rocks. Resorption during zircon growth can be due to the onset of anatexis or changing PTAX conditions in a magma (Vavra et al., 1996, 1999). Edge rounding points to less abrasive transport compared to group I zircon. The coincidence of features indicating less transport with specific zoning, morphology and inclusion types suggests a rather local and more restricted detritus information compared to the more variable group I zircon with longer transport.

Zircon *group III* (21 grains) includes groups I and II type grains characterised by alteration as a prominent additional feature (Fig. 3(5 and 6)). These grains are typically cloudy and coloured (brownish, yellowish or reddish).

Irregular patches of alteration (darker in BSE images than the surroundings and with spotted appearance) are bound to specific growth zones that can also be entirely affected. Alteration zones are mostly located near the edges of the zircon grains or can even affect the entire zircon except an outer overgrowth (Fig. 3(6)). Abundant prominent filled cracks propagate from the rims and end in alteration zones (Fig. 3(5)) or can be confined to individual growth zones being oriented perpendicular to growth surfaces and radial to the centre. In larger zones alteration forms irregular halos or fronts around crack terminations. Alteration starts along cracks that are widened and first affects specific narrow crystallographic zones. If the net of cracks becomes denser, more alteration occurs. In extreme cases alteration also affects previously unaltered zones changing finally the entire crystal with some remaining unaltered islands.

In BSE images two different types of alteration can be distinguished that can even occur within a single grain: dark zones being relatively enriched in Ca and Al compared to the unaltered zones, while slightly brighter zones are relatively enriched in Fe with few Ca and no Al. Relative enrichment of these elements as well as of Y and P prove alteration.

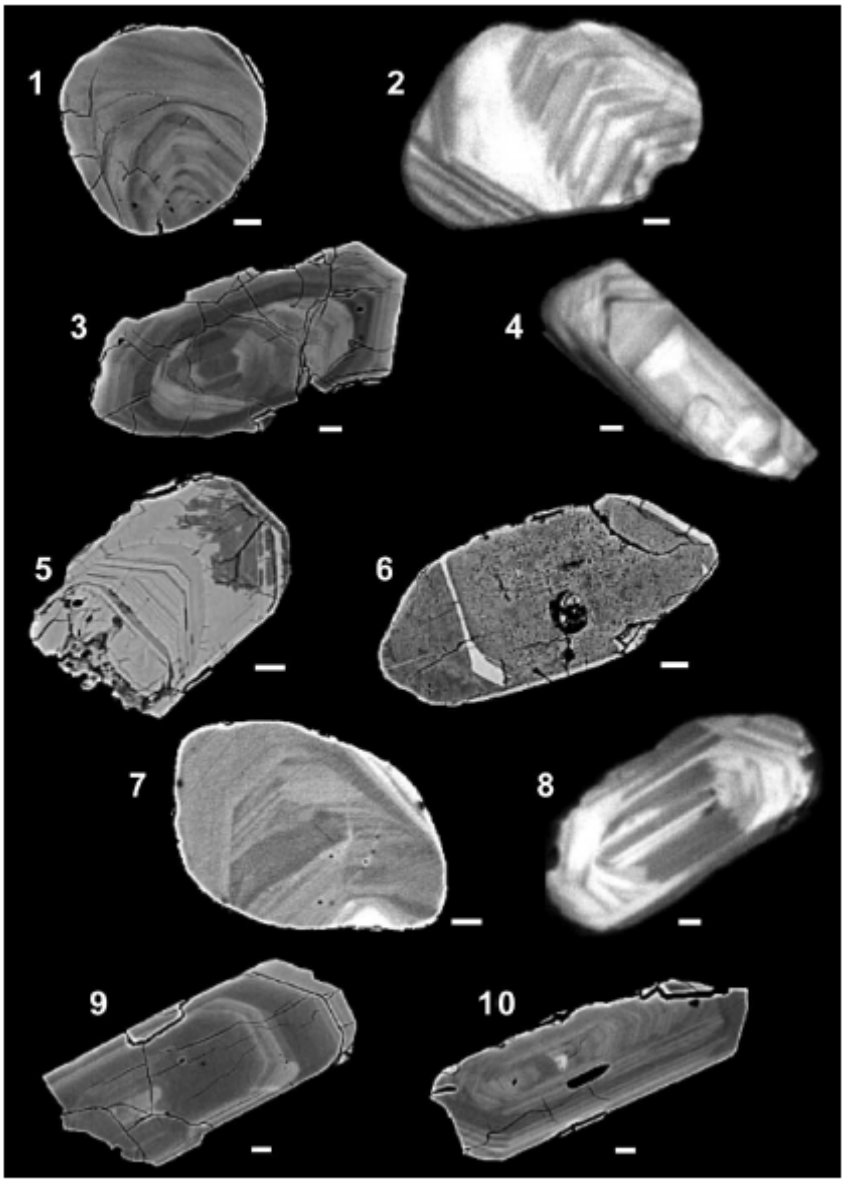


Fig. 3. Images of polished zircon crystals (for explanation see text): *Riphean zircon*: 1, 2 group I; 3, 4 group II; 5, 6 group III; *Vendian zircon*: 7 subgroup Ia; 8 subgroup Ib; 9 subgroup IIa; 10 subgroup IIb 1, 3 5, 6, 7, 9, 10 BSE images; 2, 4, 8 CL images; all scales are 10 μm.

Lee and Tromp (1995) pointed out that microcracks as potential fluid pathways for alteration can be induced by metamictisation. This process leads to lattice expansion due to high local radiation damage which also weakens certain zircon zones locally that can be preferably altered. Alteration is presumably an effect of hydration in metamict areas as was suggested by Medenbach (1976). Kurz (2000) altered zircon experimentally with hydrothermal Ca-rich fluids proving the observed effects and a considerable U and Pb mobility. Clear zircon became cloudy.

Yet it is not clear whether alteration happened in the source rock during a specific hydrothermal event or enclosed in the sandstone either due to continuous exposure to sedimentary brines or a more time-restricted hydrothermal event. However, if we regard the very long exposure of the Riphean zircon to formation water in the Bashkirian basin and also the fact that nearly all Riphean zircon show at least some effects of alteration, sedimentation and diagenesis are the most probable alteration processes.

### 4.2. Detrital zircons from Upper Vendian sandstones

Two major groups of zircon may be distinguished in the Vendian sandstones (see appendix for petrography), rounded recycled (Vendian group I) and fresh euhedral individuals (Vendian group II).

*Group I* contains rounded, i.e. recycled and older zircon grains that allow a further subdivision into three subtypes:

*Subgroup Ia* zircons (17 grains) are clear, partly colourless and partly coloured (yellowish, brownish), but well rounded with rough and pitted surfaces. Most are nearly ball-shaped, some slightly elongated, but always fragments of bigger original crystals. Zoning is generally diffuse, hazy or patchy, irregular rather than concentric, with extremely faint differences between the zones and mostly blurred transitions (Fig. 3(7)). Some faint relict concentric zoning may still be visible with catodoluminescence. Boundaries of patchy sectors are planar or curved. Four grains show fir-tree zoning. One grain contains a discordant core. Small non-planar concentric overgrowth at the rims occurs sometimes. The degree of filled cracks varies. Very small round inclusions dominate over rare larger inclusions of plagioclase, quartz, euhedral apatite as well as Fe- and Ti-rich biotite.

*Subgroup Ib* zircons (8 grains) consist of long-prismatic, but moderately rounded grains with rough and pitted surfaces. They seem to have a S-type morphology after Pupin (1980). They show faint former concentric magmatic growth zoning with rather narrowly spaced zones parallel to the prism planes (Fig. 3(8)). Sectoral zoning and discordant cores are rare as well as filled cracks. Sometimes slight planar and nonplanar overgrowth is observed at the rims. Tiny inclusions of quartz and K-feldspar are always round.

Five *subgroup Ic* grains are similar to those of Ib subtype, but are cut by abundant filled cracks terminating in narrow patchy alteration zones parallel to former growth zones. Strong alteration in the outermost zones is characteristic.

All group I subtypes show most features also observed in groups I-III of Riphean zircon. This includes similar S-type typologies, inclusion minerals and occurrence of inherited cores within long-prismatic edge-rounded varieties that point to granitoid source rocks of crustal origin as well as zoning pattern typical for zircon from high grade metamorphic areas. Alteration appears to be much less frequent.

Among the euhedral zircon grains (*group II*) two subtypes can be distinguished that derived from two different magmatic rocks as constrained by their morphology and their inclusion types:

*Group IIa* (12 grains) consists of perfectly euhedral, columnar grains that are clear, slightly yellowish-greenish and contain abundant inclusions. Surfaces are perfectly smooth. P-type zircon (P2, P3, P4; P5 after Pupin, 1980) dominates, more rarely S-type grains are found (S19, S24). All sections parallel {1 0 0} show perfect igneous concentric, strongly oscillatory and sometimes slight sectoral zoning (Fig. 3(9)). Round or concave traces of unconformably overgrown dissolution surfaces occur in some. Xenocryst cores were not observed. Incipient alteration in the outermost growth zone was only observed in two grains. Among very abundant inclusions are Ti- and Fe-rich biotite, K-feldspar, Cl-rich apatite, Mn-rich ilmenite and very small round monazite grains.

Zircon morphology and the type of inclusions point to Si-undersaturated potassic alkaline magmas such as

syenite as the most probable source. Pebbles of syenite are abundant in the immediately overlying Kukkarauk conglomerate. The perfect euhedral shape and the high concentration of group IIa zircons with respect to other Upper Vendian sandstones indicates a nearby local source for group IIa zircon grains as for the conglomerate pebbles.

Three further long-prismatic grains (*subgroup IIb*; Fig. 3(10)) show similar features (P2; P4 type), but contain quartz, magnetite, Mn-free ilmenite and K-feldspar as inclusions. Also incipient alteration in an outermost zone is observed in two zircon grains. This evidently less abundant group of zircon resembles zircon from a Si-saturated melt. Rhyolite that also occurs among pebbles in the conglomerate of the Upper Vendian Kukkarauk Formation is a possible source rock.

## 5. Geochronological results

For the U–Pb isotope determinations we tried to use clear and colourless zircon crystals only to avoid alteration as far as possible as an additional process modifying the U–Pb-systematics. Nevertheless, due to the random occurrence of this feature even at a small scale, no exclusive avoidance is possible.

### 5.1. Riphean samples

All U–Pb systems analysed in all samples are discordant (Figs. 4 and 5). Due to the low amount of radiogenic Pb in some analyses relatively large errors occur (Table 1). Surprisingly, the U–Pb-data of the Riphean samples show separation into four distinctly different clusters in the U–Pb-concordia diagram for

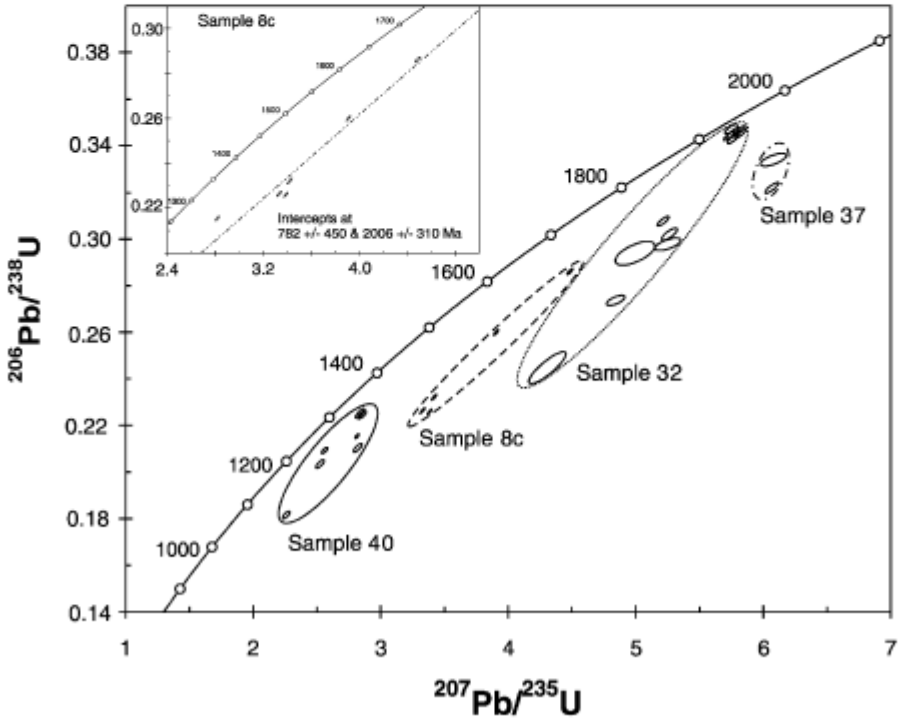


Fig. 4. Synoptic concordia diagram showing single grain U–Pb data of detrital zircons in all analysed Riphean samples (8c, 32, 37, 40). Inset shows the best fit reference line for data of sample 8c.

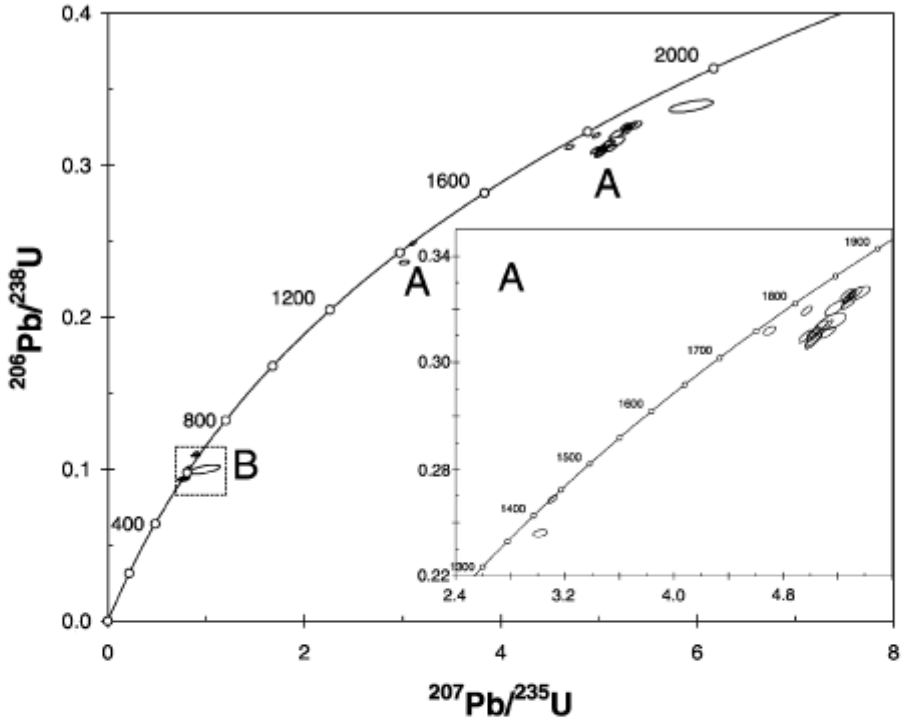


Fig. 5. Synoptic concordia diagram showing single grain U–Pb data of detrital zircons in all analysed Upper Vendian samples (18/19, 29). (A) Data of rounded detrital zircons (group I). (B) Data of euhedral detrital zircon (group IIa). Box around group IIa zircons indicates the area of uncertainty derived from initial lead correction using the maximum variation of $^{206}Pb/^{204}Pb$ and $^{207}Pb/^{204}Pb$ signatures in alkaline magmas (Wilson, 1996).

each sample population instead of having an overall uniform random scatter (Fig. 4). Thus, the zircon grains from the four samples appear to represent local age information related to the individual geological history of the original host rocks. All four clusters have elongate shapes oriented in an "en echelon" pattern subparallel to each other. However, they do not define distinct discordias.

### 5.2. Sample 8c

The population of six grains in this sample includes only those of group II (edge rounded prismatic grains). After correction for blank Pb and initial lead the $^{207}Pb/^{206}Pb$ apparent ages range from 1523 to 1859 Ma (Table 1). Assuming a young Pb loss event these apparent ages represent minimum ages for the crystallisation of the zircon. If older or several such events occurred, the age of crystallisation would definitely be higher.

Compared to the shapes of clusters of the other Riphean zircon populations (Fig. 4) that of sample 8c zircon rather resembles a discordia-like alignment of U–Pb-data. Under the presumption that the zircon grains have similar primary ages of crystallisation they must have suffered similar processes leading to discordancy. This concurs with the fact that all grains represent edge rounded euhedral zircon from S-type granites (group II; see above) indicating a similar source and less transport than group I zircons.

The upper intercept of the best fit reference line shows a value around 2006 Ma. This illustrates the

possible range of crystallization ages of granitic magmas in the source area. Yet due to the given pattern it is too speculative to give a reasonable interpretation for the lower intercept near the presumable age of sedimentation of the enclosing sandstone.

### 5.3. Sample 32

Twelve grains only of group I type were analysed from sample 32 (Fig. 4) showing a narrow range of $^{207}Pb/^{206}Pb$ apparent ages between 1958 and 2075 Ma (Table 1), but a wide scatter of U–Pb-data, because this population invariably contains rounded zircon fragments with multiple overprints, which is also reflected by the extremely low $^{206}Pb/^{204}Pb$ ratios. However, six more abraded grains show a much more reduced range of $^{207}Pb/^{206}Pb$ apparent ages between 1958 and 1989 Ma and a clustering near the concordia. This again is taken to point to an age of zircon crystallisation near 2000 Ma. Apparently improved results with more abraded zircons suggest strong influence by alteration subsequent to crystallisation regarding the strong discordancy of the other zircon grains in the population.

### 5.4. Samples 37 and 40

$^{207}Pb/^{206}Pb$ apparent ages of two grains (group I type) from sample 37 (Fig. 4) are the oldest (2124–2185 Ma) of the analysed Riphean zircon grains, those of six grains (groups I and II type) from sample 40 (Fig. 4) the youngest (1399–1572 Ma). The cluster of sample 40 shows that groups I and II zircons of its population have similar apparent ages suggesting similar histories. A derivation from a Riphean magmatic event, which might be suggested for sample 40 zircons with the lowest apparent $^{207}Pb/^{206}Pb$ ages, can be excluded on the basis of the observed zonation patterns and relatively low $^{206}Pb/^{204}Pb$ ratios. Such features point to a metamorphic origin of the zircons. A metamorphic event with $T > 150\,^{\circ}C$ between 1.8 and 0.65 Ma is not known yet for the Riphean sedimentary basin or for the source area for its sediments. Hence, the protolith ages of sample 40 zircons probably are in the same range as for the other Riphean samples.

The scatter of the U–Pb data in all four samples means that the U–Pb systems definitely experienced two or more effective geological processes. Internal features within the zircon grains suggest that the following effects could have led to discordancy:

(A) Effects in the source area: (1) magmatic growth on inherited cores as well as (2) metamorphic overgrowth and (3) annealing effects of strained lattices under high grade conditions.
(B) Effects of alteration in the sedimentary basin including diagenesis. All Riphean zircon crystals are more or less affected by alteration along cracks.

All age signatures are consistent with derivation from the pre-Riphean basement of the East European Platform (U–Pb age cluster of 1.8–2.3 Ga related to a Paleoproterozoic orogenic cycle; see above) representing high grade metamorphism and granite intrusion.

Two possibilities exist for the en echelon pattern of the U–Pb data of the Riphean samples:

1. Varying primary ages between 1.8 and 2.3 Ga, then at least two different events of lead loss (in the source area and the sedimentary basin).
2. Uniform primary ages, but variable lead loss after a first event followed by overprint during a second event.

Knowing that the zircon grains must have been affected by formation waters in the Riphean basin for at least the duration of the Upper Riphean one could assume a strong effect on lead loss. Such a mechanism would be rather likely in view of the fact that all Riphean zircon grains are at least slightly altered along cracks. Showing distinct U–Pb isotopic patterns for all samples the zircon crystals nevertheless reflect distinct events of lead loss as well as distinct source region signature.

### 5.5. Upper Vendian samples

The U–Pb systems of 31 Upper Vendian zircon crystals (samples 18/19, 29) were analysed (Fig. 5). Of these, four have $^{206}Pb/^{204}Pb$ ratios >500. These four all belong to the Vendian Group I zircon crystals. All Vendian Group II zircon crystals have remarkably low $^{206}Pb/^{204}Pb$ ratios (Table 1).

The four zircon crystals of *Vendian Group I type* which are characterized by higher amounts of radiogenic Pb have apparent $^{207}Pb/^{206}Pb$ ages of 1932,

1847, 1788 and 1483 Ma. Most other, but lower radiogenic Group I zircons (apparent $^{207}Pb/^{206}Pb$ ages 1898–2058 Ma, samples 18/19, 29) are within this range. Thus most of these data are certainly consistent with the assumption of a Paleoproterozoic origin of the Group I zircons. This is compatible with the presumed age of the Riphean detrital zircon and the major orogenic imprint in the East European Platform.

The zircons with lower apparent $^{207}Pb/^{206}Pb$ ages around 1439 and 1483 Ma (Fig. 5; sample 18/19) evidently did not suffer the same type or intensity of overprint as did the majority of the Vendian Group I zircons with higher apparent $^{207}Pb/^{206}Pb$ ages. These values might point to a later magmatic event within the Riphean basin. However, our data do not match with the 1350 Ma Mashak rift event in the Riphean basin presumed by Maslov et al. (1997; see Fig. 2). This would give further evidence for the allochthonous nature of the Beloretsk terrane, where the zircon grains are inferred to have been eroded.

Inspite of differences in zircon typologies the indication of a Paleoproterozoic origin suggests a common provenance from the eastern margin of the East European Platform for all Riphean and the Vendian Group I detrital zircons. This is also proved by the similarity of the Riphean and Upper Vendian heavy mineral spectrum (Willner et al., 2001).

Upper Vendian *Group IIa zircon crystals* (sample 18/19), which are classified as euhedral magmatic zircon without overprint and without rounding by their morphology and internal structures, were presumably delivered from one source, as can be assumed owing to their perfect pristine character and the coherence of zircon inclusions and detritus composition. The source can be identified as syenite as has been deduced above from mineral inclusions and the geological situation.

However, the content of radiogenic Pb and in consequence also the Pb-concentration are remarkably low in these zircon grains (Table 1). Apparent $^{207}Pb/^{206}Pb$ ages range from 643 to 512 Ma with a clustering of ages near the concordia around 580 Ma. However, in view of the low $^{206}Pb/^{204}Pb$ ratios the uncertainty of the isotope ratios used for the correction of the initial lead component becomes a crucial parameter for these data. We used the Stacey & Kramers model for common lead correction in Table 1. Using the maximum variation of $^{206}Pb/^{204}Pb$ and $^{207}Pb/^{204}Pb$ signatures in alkaline magmas (Wilson, 1996) which could also serve to derive the initial lead ratios in the zircons a larger range of uncertainty results (Fig. 5).

Despite the large errors resulting the U–Pb isotope data of the Vendian Group IIa zircon crystals do not contradict to age constraints given by Alekseev and Alekseeva (1980) and Glasmacher et al. (1999; see above) and with the presumed age of deposition of the Upper Riphean Kukkarauk-Formation (around 580 Ma, Maslov et al., 1997), from which the sandstone sample 18/19 was derived. The alkaline magmatic event would also be concomitant with the final exhumation of the Beloretsk terrane after 620 Ma.

## 6. Conclusions and implications for paleocontinental reconstructions

The following conclusions can be derived from the data presented:

- U–Pb-isotopic patterns as well as typological features of detrital zircon from Riphean and Upper Vendian sandstones are different. This gives further evidence for a change in detritus composition at around 620 Ma, when Upper Vendian sedimentation started.
- Clusters in the concordia diagram confined to single samples show remarkably strong influence of local sources on the composition of the detritus in spite of the large areas of discharge of detritus.
- Polycyclic rounded zircons with multiple overprint in the Riphean and Upper Vendian detritus show evidence of at least two events leading to lead loss. Alteration during diagenesis has been an important factor of lead loss.
- It can be confirmed that the age interval 1.8–2.3 Ga seems to be the significant age signature for the eastern margin of the Baltica protocontinent reflecting a major orogenic event. Both types of polycyclic zircon in the Riphean and Upper Vendian detritus first crystallized during this interval. Typological features show that they originally derived from high grade metamorphic rocks and granites.
- Zircon from the Upper Vendian detritus has two further sources apart from the majority of polycyclic zircon:
  - A few zircon grains with apparent $^{207}Pb/^{206}Pb$ ages around 1439 and 1483 Ma point to a later magmatic event, which is unknown in the

adjacent Riphean basin and underlines the allochthonous character of the source area.
- Euhedral zircons define a magmatic intrusion event of bimodal, partly alkaline magmas concomitant with the exhumation of the source area after 620 Ma.

The data match the Precambrian evolution in the Southern Urals as follows (Fig. 2):

Major constraints for the Neoproterozoic evolution of the Southern Urals are provided by Ar–Ar amphibole and white mica cooling ages between 720 and 540 Ma (Glasmacher et al., 1999, 2001) in the metamorphic complex of Beloretsk which contains high pressure rocks and is part of the supposed source area for the Upper Vendian detritus. Concomitant with this long history of exhumation, cooling, surface uplift, erosion and final emplacement of this complex bimodal, partly alkaline intrusions occurred that show no sign of overprint. During burial and early exhumation of the Beloretsk terrane, however, there was ongoing sedimentation in the Bashkirian basin further east. Upper Vendian foredeep sedimentation of detritus from the Beloretzk terrane started after 620 Ma and marks its final emplacement. Evidently the Beloretsk Terrane is an exotic continental block, but presumably also derived from Baltica as proved by the zircon age signatures in this study and by its heavy mineral spectra, which is similar to those of the Riphean sandstones (Willner et al., 2001).

A reasonable model explaining these major constraints would be a "Carribean-type" transpressional convergent margin setting. A good analog is the northern margin of South America that was originally a passive margin until the early Mesozoic and converted into a convergent one during displacement of high pressure rocks over a thousand km from the west along a major transcurrent fault system (Pindell and Barrett, 1990; Stöckhert et al., 1995). This also causes a major uplift within narrow high relief areas undergoing rapid erosion providing major detrital input into small foredeeps. Also alkaline magmatism is known from this setting (Lewis and Draper, 1990).

Many other features of a Neoproterozoic active continental margin have been detected along the entire length of the Urals and beyond represented by relics of the so-called Timanide orogen (Puchkov, 1997). These include HP/LT-rocks (Kvarkush Anticline of the Middle Urals, Puchkov, 1989), ophiolites (in the Polar Urals, Puchkov, 1997, Scarrow et al., 2001) and calc-alkaline magmatism (in the Polar Urals, Scarrow et al., 2001).

Prior to the existence of this Timanide active margin, the Riphean basin must have been situated at a stable continental margin. Such a geodynamic environment is compatible with numerous current paleocontinental reconstructions of different approaches such as those by Torsvik et al. (1996), Weil et al. (1998) or Rainbird et al. (1998). During the existence of the Rodinia supercontinent and its break-up, i.e. in the time of 1100–700 Ma, the entire eastern margin of Baltica was a stable margin of that continent continuing along its length into Siberia and Amazonia.

Furthermore we concur with recent reconstructions of Nance and Murphy (1994), Weil et al. (1998), Torsvik et al. (1996) and particularly with the suggestion of Scarrow et al. (2001) that the active Timanide margin of Baltica was a lateral extension of the Cadomian arc, which represented a collage of terranes in front of the W-African and Amazonian protocontinents that were still connected with Baltica (Fig. 6). The change to active margin conditions in the Southern Urals occurred after the Lower Vendian glaciation and lasted until the end of the Precambrian, when Baltica and West Gondwana separated.

It must also be noted that a similar history of zircon formation was detected in the continuation of the margin along the presumably neighbouring continental fragments of Amazonia and the Cadomian terranes. This history is characterized by a pronounced gap between Paleo- and Neoproterozoic zircon-forming orogenic events: Da Silva et al. (2000) report 2.0–2.2 Ga zircon ages from high grade gneisses in Southern Brazil overprinted by a 590 Ma event, Von Hoegen et al. (1990) show >2050 and 545 Ma zircon ages in detritus of the Belgian Brabant Massif (part of the "East Avalonia" terrane), and Tichomirowa et al. (2001) provide a comprehensive collection of zircon ages from gneisses in the East German Erzgebirge (part of the "Armorica" terrane) including 540–700 Ma and 2.1–2.2 Ga zircon-forming events. Evidently, this long history of coherent continental margins is characterized by a lack of Mesoproterozoic, especially "Grenvillian" events and a change to active margin conditions after a remarkably long orogenic silence.

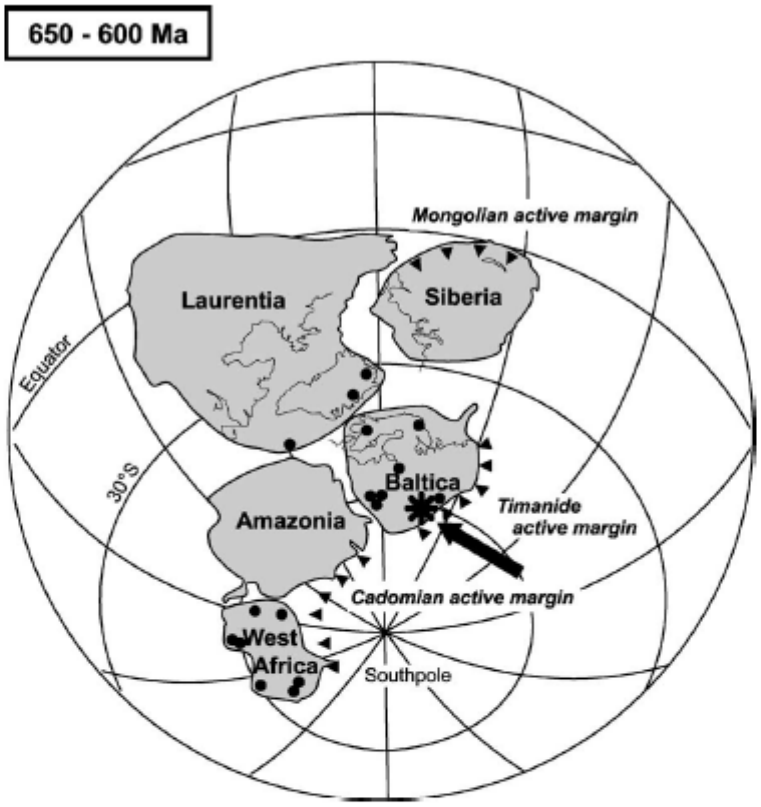


Fig. 6. Paleocontinental situation of the Southern Urals (asterisk/arrow) at the Eastern border of Baltica shortly after Lower Vendian glaciations (dots—glacial deposits). The reconstruction is of Torsvik et al. (1996) with the orientation of Siberia changed after Kravchinsky et al. (2001). The chain of active margins along this continental collage was formed between about 750 and 600 Ma and converted from a prior passive continental margin of the Rodinia supercontinent.

This is rather important, because Hartz and Torsvik (2002) recently questioned the mentioned reconstructions and alternatively place the eastern margin of Baltica opposite of Laurentia (E-Greenland) before 750 Ma. However, in this intracontinental position the Uralian Proterozoic detritus should show influence of the more variable East Laurentian age spectra as well, which predominantly contain 0.97–1.87 Ga age groups (Cawood and Nemchin, 2001; Watt and Thrane, 2001) including signatures of orogenic events in this period. There is neither an extension of the Riphean basin with continuous sedimentation from 1.63 to 0.65 Ga in Greenland nor any evidence of the 0.95 Ga orogen perpendicular to the Greenland continental margin (Watt and Thrane, 2001) in East Baltica.

After denudation of the Beloretsk Terrane during Cambrian, major extension occurred again (Puchkov, 1997) and from Ordovician until Late Devonian the western part of the Urals again became a stable continental margin along the entire eastern margin of Baltica.

## Acknowledgements

Financial support by the Deutsche Forschungsgemeinschaft [grant Wi 875-6/1, 2] is gratefully

acknowledged. Perfect logistic support by the Ufa crew and invaluable field guidance by V.I. Kozlov and A.A. Alekseev during the 1999 field leg made this work possible. We also thank K. Mezger for providing facilities at the Laboratory of Geochronology at the University of Münster. Reviews particularly by P. Cawood and also by an anonymous referee substantially improved the paper. This paper is a contribution to EUROPROBE [URALIDES]. Europrobe is coordinated within the International Lithosphere Program and sponsored by the European Science Foundation. The paper is also a contribution to IGCP 440: Assembly and Breakup of Rodinia.

## Appendix A. Petrographic characteristics of the samples

### A.1. Riphean samples

*Sample 8c* (Upper Riphean Zilmerdak Formation) is a red laminated feldspathic sandstone with mm-thick laminae containing heavy mineral concentrations (mainly magnetite, ilmenite and zircon, but also tourmaline and rutile). Light minerals in the sandstone are composed of well rounded grains of predominantly monocrystalline quartz, both feldspars, white mica and abundant lithic clasts (chert, siltstone, acidic tuff). Quartz is the cement mineral.

*Sample 32* (Upper Riphean Zilmerdak Formation) is a white, fine-grained, pure quartz arenite with primary well rounded quartz grains still detectable by minute inclusions along the original grain boundary against the quartzose matrix overgrown with optical continuity. Monocrystalline quartz clasts with abundant fluid inclusion trails are predominant, while perfectly round heavy minerals (tourmaline, rutile, zircon) and lithic fragments (quartz mylonite, chert, acidic tuff) occur as accessories.

*Sample 37* (Middle Riphean Avzyan Formation) is a fine grained quartz arenite. The rock is well sorted and has a homogeneous grain size. Grains are moderately to well rounded with prominent quartz overgrowth. Undulous monocrystalline quartz is dominant. Plagioclase and K-feldspar is observed as well as few white mica, chlorite, opaques and tourmaline.

*Sample 40* (Uppermost Riphean Krivoluk Formation) is a white quartz arenite, which shows similar characteristics as sample 32.

### A.2. Upper Vendian samples

*Sample 18/19* (Upper Vendian Kukkarauk Formation) is a coarse grained red quartzose sandstone. The sandstone contains mainly subrounded to rounded mono- and polycrystalline quartz, quartz mylonites, red chert, some quartz phyllite and rhyolite clasts. The heavy mineral spectrum is strongly reduced to about 80% zircon and some tourmaline and rutile. Conglomerates from the same locality contain abundant pebbles of quartz sandstone and quartz vein material, but also of abundant syenite and some rhyolite that are missing at other localities suggesting a rather local nearby source.

Four *samples* (*22, 23, 28, 29*; Upper Vendian Basa Formation) were investigated as one sample group (29), because rocks are petrographically identical, from the same sedimentary environment and were collected in close proximity of about 100 m along road outcrops. Furthermore, zircon is relatively rare in these horizons and hence, some concentration is necessary. All four samples are greenish medium grained litharenites from monotonous proximal grain flow deposits. They contain abundant angular to subangular, mono- and polycrystalline quartz and some feldspar clasts, detrital white mica and chlorite. Lithoclasts contain siliciclastic sedimentary material and low-grade metamorphic clasts in similar abundance. Acid and basic volcanic material is relatively rare. The heavy mineral spectrum is dominated by about 70% epidote, 5% apatite, 10% tourmaline, 10% rutile and only 5% zircon.

## References

Alekseev, A.A., Alekseeva, G., 1980. Vendian alkaligabbros and their potassic suite in the SW Urals. Doklady Akad. Nauk USSR 255, 954–957 (in Russian).

Bogdanova, S.V., 1986. The Earth crust of the Russian platform in the Early Precambrian. Acad. Sci. USSR (Nauka) Moskow, 219 p. (in Russian).

Cawood, P.A., Nemchin, A.A., 2001. Paleogeographic development of the east Laurentian margin: constraints from U–Pb dating of detrital zircons in the Newfoundland Appalachians. Geol. Soc. Amer. Bull. 113, 1234–1246.

Da Silva, L.C., Hartmann, L.A., Mc Naughton, N.J., Fletcher, I., 2000. Zircon U–Pb SHRIMP dating of a Neoproterozoic overprint in Paleoproterozoic granitic-gneissic terranes, Southern Brazil. Am. Mineral. 85, 649–667.

Glasmacher, U.A., Reynolds, P., Alekseev, A.A., Puchkov, V.N., Taylor, K., Gorozhanin, V., Walter, R., 1999. $^{40}Ar/^{39}Ar$ thermochronology west of the Main Uralian fault, southern Urals, Russia. Geol. Rundsch. 87, 515–525.

Glasmacher, U.A., Bauer, W., Giese, U., Reynolds, P., Kober, B., Puchkov, V., Stroink, L., Alekseev, A.A., Willner, A.P., 2001. The metamorphic complex of Beloretzk, SW Urals, Russia—a terrane with a polyphase Meso- to Neoproterozoic tectonothermal evolution. Precambrian Res. 110, 185–213.

Ivanov, S.N., Krasnobaev, A.A., Rusin, A.I., 1986. Geodynamic regimes in the Precambrian of the Urals. Precambrian Res. 33, 189–208.

Jaffey, A.H., Flynn, K.F., Glendenin, L.E., Bentley, W.C., Essling, A.M., 1971. Precision measurement of half lives and specific activities of $^{235}U$ and $^{238}U$. Phys. Rev. Sec. C Nucl. Phys. 4, 1889–1906.

Hartz, E.H., Torsvik, T.H., 2002. Baltica upside down: a new plate tectonic model for Rodinia and the Iapetus Ocean. Geology 30, 255–258.

Keller, B.M., Krasnobaev, A.A., 1983. Late Precambrian geochronology of the European part of the USSR. Geol. Mag. 120, 381–389.

Krasnobaev, A.A., 1986. Zircon as indicator of geological processes. Acad. Sci. USSR (Nauka) Moskow 145 p. [in Russian].

Kravchinsky, V.A., Konstantinov, K.M., Cogné, J.P., 2001. Paleomagnetic study of Vendian and Early Cambrian rocks of South Siberia and Central Mongolia: was the Siberian platform assembled at this time? Precambrian Res. 110, 61–92.

Kurz, S., 2000. Alterationsprozesse in Zirkon—Isotopengeologische und geochemische Implikationen. Doctoral thesis Univ. Göttingen/Germany [unpublished], 112 p.

Lee, J.K.W., Tromp, J., 1995. Self-induced fracture generation in zircon. J. Geophys. Res. 100/B9, 17753–17770.

Lennykh, W.I. , Krasnobaev, A.A., 1978. Absolute ages of metamorphic rocks. In: Petrology and iron ore deposits of the Taratash Complex. Acad. Sci. USSR Sverdlovsk, pp. 69–76 [in Russian]

Lewis, J.F., Draper, G., 1990. Geology and tectonic evolution, northern Caribbean margin. In: Dengo, G., Case, J.E. (Eds.), The Caribbean region—vol. H, The Geology of North America. Boulder, Geological Society of America, pp. 77–140.

Maslov, A.V., Erdtmann, B.D., Ivanov, K.S., Krupenin, M.T., 1997. The main tectonic events, depositional history and the paleogeography of the southern Urals during the Riphean-early Palezoic. Tectonophysics 276, 313–335.

Medenbach, O., 1976. Geochemie der Elemente in Zirkon und ihre räumliche Verteilung.-Eine Untersuchung mit der EMS. doctoral thesis, Univ. Heidelberg/Germany, 58 p. [unpublished].

Nance, R.D., Murphy, J.B., 1994. Contrasting basement isotopic signatures and the palinspastic restoration of peripheral orogens: example from the Neoproterozoic Avalonian-Cadomian belt. Geology 22, 617–620.

Pindell, J.L., Barrett, S.F., 1990. Geological evolution of the Caribbean region; a plate-tectonic perspective. In: Dengo, G., Case, J.E. (Eds.), The Caribbean Region—vol. H. The Geology of North America, Boulder, Geological Society of America. pp. 405–432.

Puchkov, V.N., 1989. The collisional origin of the eclogite-glaucophane-schist belt of the Urals. Ofioliti 14, 213–220.

Puchkov, V.N., 1997. Structure and geodynamics of the Uralian orogen. In: Burg, J.-P., Ford, M. (Eds.), Orogeny Through Time. Geol. Soc. Am. Spec. Publ. 121, 201–236.

Pupin, J.P., 1980. Zircon and granite petrology. Contrib. Mineral Petrol. 73, 207–220.

Rainbird, R.H., Stern, R.A., Khudoley, A.K., Kropachev, A.P., Heaman, L.M., Sukhorukov, V.I., 1998. U–Pb geochronology of Riphean sandstone and gabbro from southeast Siberia and ist bearing on the Laurentia-Siberia connection. Earth Planet. Sci. Lett. 164, 409–420.

Scarrow, J.H., Pease, V., Fleutelot, C., Dushin, V., 2001. The late Neoproterozoic Enganepe ophiolite, Polar Urals, Russia: an extension of the Cadomian arc? Precambrian Res. 110, 255–275.

Schaltegger, U., Fanning, C.M., Günther, D., Maurin, J.C., Schulmann, K., Gebauer, D., 1999. Growth, annealing and recrystallisation of zircon and preservation of monazite in high-grade metamorphism: conventional and in-situ U–Pb isotope, cathodoluminescence and microchemical evidence. Contrib. Mineral. Petrol. 134, 186–201.

Sindern, S., Schulte, B., Kramm, U., 2001. Die tektonometamorphe Entwicklung des Taratash-Komplexes Mittlerer Ural Rußland. Eur. J. Min. 13 (Beiheft 1), 174.

Stacey, J.S., Kramers, J.D., 1975. Approximation of terrestrial lead isotope evolution by a two stage model. Earth. Planet. Sci. Lett. 6, 15–25.

Stöckhert, B., Maresch, W.V., Brix, M., Kaiser, C., Toetz, A., Kluge, R., Krückhans-Lueder, G., 1995. Crustal history of Margarita Island (Venezuela) in detail: constraint on the Carribean plate-tectonic scenario. Geology 23, 787–790.

Tichomirowa, M., Berger, H.J., Koch, E.A., Belyatski, B.V., Götze, J., Kempe, U., Nasdala, L., Schaltegger, U., 2001. Zircon ages of high-grade gneisses in the Eastern Erzgebirge (Central European Variscides)—constraints on the origin of the rocks and Precambrian to Ordovician magmatic events in the Variscan fold belt. Lithos 56, 303–332.

Torsvik, T.H., Smethurst, M.A., Meert, J.G., Van der Voo, R., McKerrow, W.S., Brasier, M.D., Sturt, B.A., Walderhaug, H.J., 1996. Continental break-up and collision in the Neoproterozoic and Paleozoic—a tale of Baltica and Laurentia. Earth Sci. Rev. 40, 229–258.

Vavra, G., Gebauer, D., Schmid, R., Compston, W., 1996. Multiple zircon growth and recrytallisation during polyphase Late Carboniferous to Triassic metamorphism in granulites of the Ivrea Zone (Southern Alps): an ion microprobe (SHRIMP) study. Contrib. Mineral. Petrol. 122, 337–358.

Vavra, G., Schmid, R., Gebauer, D., 1999. Internal morphology, habit and U–Th–Pb microanalysis of amphibolite-to-granulite facies zircons: geochronology of the Ivrea Zone (Southern Alps). Contrib. Mineral. Petrol. 134, 380–404.

Von Hoegen, J., Kramm, U., Walter, R., 1990. The Brabant Massif as part of Armorica/Gondwana: U–Pb isotopic evidence from detrital zircons. Tectonophysics 185, 37–50.

Watt, G.R., Thrane, K., 2001. Early Neoproterozoic events in East Greenland. Precambrian Res. 110, 165–184.

Weil, A.B., Van der Voo, R., Niocaill, C.M., Meert, J.G., 1998. The Proterozoic supercontinent Rodinia: paleomagnetically derived reconstructions for 1100–800 Ma. Earth Planet. Sci. Lett. 154, 13–24.

Wendt, J.I., 1993. Early Archean crustal evolution in Swaziland, southern Africa, as revealed by combined use of zircon geochronology, Pb–Pb and Sm-Nd systematics. Unpublished doctoral thesis, Univ. Mainz, Germany, 123 S.

Willner, A.P., Ermolaeva, T., Stroink, L., Glasmacher, U.A., Giese, U., Puchkov, V.N., Kozlov, V.I., Walter, R., 2001. Contrasting provenance signals in Riphean and Vendian sandstones in the SW Urals (Russia): constraints for a change from passive to active continental margin conditions in the Late Precambrian. Precambrian Res. 110, 185–213.

Wilson, M., 1996. Igneous Petrogenesis. Chapman & Hall, London, 466 p.

7.

Schulte, B.A., Sindern, S. (2002) K-rich fluid metasomatism at high pressure metamorphic conditions: Lawsonite decomposition in rodingitized ultramafite of the Maksyutovo Complex, Southern Urals (Russia). Journal of Metamorphic Geology 20, 1-13. © Blackwell Science Inc., 0263-4929/02/$15.00

With permission of Wiley.

Re-use in thesis granted by John Wiley & Sons Ltd, The Atrium, Southern Gate, Chichester, West Sussex, PO19 8SQ, UK, permission 5th of November 2015.

J. metamorphic Geol., 2002, 20, 529–541

# K-rich fluid metasomatism at high-pressure metamorphic conditions: Lawsonite decomposition in rodingitized ultramafite of the Maksyutovo Complex, Southern Urals (Russia)

B. SCHULTE[1] AND S. SINDERN[2]
[1]Philipp-Roeth-Weg 58, 64295 Darmstadt, Germany, (bernd.aloys.schulte@gmx.de)
[2]Institut für Mineralogie und Lagerstättenlehre, Rheinisch-Westfälische Technische Hochschule Aachen, 52056 Aachen, Wüllnerstr. 2, Germany

**ABSTRACT** Fine grained rodingite-like rocks containing epidote, clinozoisite, garnet, chlorite, phengite and titanite occur within antigorite serpentinite boudins from the high-pressure metamorphic Maksyutovo Complex in the Southern Urals. Pseudomorphs after lawsonite, resorption of garnet by chlorite and phengite and stoichiometry suggest the reaction lawsonite + garnet + K-bearing fluid → clinozoisite + chlorite + phengite, and define a relic assemblage of lawsonite + garnet + chlorite + titanite ± epidote as well as a later post-lawsonite assemblage of clinozoisite + phengite + chlorite + titanite. The reaction lawsonite + titanite → dinozoisite + rutile + pyrophyllite + $H_2O$ delimits the maximum stability of former lawsonite + titanite to pressures > 13 kbar. *P–T* conditions of 18–21 kbar/520–540 °C result, if the average chlorite, Mg-rich garnet rim and average epidote compositions are used as equilibrium compositions of the former lawsonite assemblage. These estimates indicate a similar depth of formation but lower temperatures to those recorded in nearby eclogites. The metamorphic conditions of the lawsonite assemblage are considerably higher than previously suggested and, together with published structural data, support a model in which a normal fault within the Maksyutovo complex acted as the major transport plane of eclogite exhumation.The maximum Si content of phengite and minimum Fe content in clinozoisite constrain the metamorphic conditions of the later pseudomorph assemblage to be > 4.5 kbar and < 440 °C. Rb–Sr isotopic dating of the pseudomorph assemblage results in a formation age of 339 ± 6 and 338 ± 5 Ma, respectively. These results support the recent exhumation models for this complex.

**Key words:** garnet, lawsonite, Maskyutovo Complex, phengite, rodingite, titanite.

## INTRODUCTION

The Maksyutovo Complex in the Southern Urals, Russia, is subdivided into an eclogite facies, structurally lower unit, and a greenschist facies, structurally upper unit (Lennykh, 1977). Serpentinite lenses, up to a kilometre in diameter, occur at the base of the upper unit. They have fine grained centres of epidote, clinozoisite, garnet, chlorite, phengite and titanite. Garnet, epidote, clinozoisite and chlorite are modally dominant and indicate an unusual rock composition rich in Ca and Mg, classified between rodingitic and (ultra)basic. The most spectacular feature of the rock is centimetre sized pseudomorphs after lawsonite which clearly indicate an earlier high-pressure/low-temperature metamorphism (Lennykh & Valizer, 1986). Therefore the rock is defined as a lawsonite fels.

The aim of this paper is to establish the *P–T* conditions of this earlier metamorphism, its relation to the main pseudomorph forming metamorphic event, the age of the pseudomorph formation and the origin of the unusual protolith type. In addition we examine the significance of the relic metamorphism to the tectonometamorphic evolution of the complex.

## GEOLOGICAL SETTING

The Maksyutovo Complex of the Central Uralian zone in the Southern Urals formed during Devonian subduction and collision of the continental units of the East European Platform with a Silurian/Devonian island arc (Magnitogorsk island arc, Fig. 1) (Ivanov *et al.*, 1975; Hetzel, 1999). The east-dipping Main Uralian Normal Fault (MUNF) separating the Maksyutovo Complex from the island arc (Fig. 2), is a several kilometres wide mélange zone with serpentinites, basalts, gabbros and various Palaeozoic lithologies. West of the Maksyutovo Complex the Central Uralian zone consists of the greenschist facies Suvanjak Complex, the Upper Devonian Zilair Flysch sedimentary rocks and ophiolitic nappes (Fig. 1). The Maksyutovo Complex is subdivided into two major tectonometamorphic units (Dobretsov *et al.*, 1974; Lennykh *et al.*, 1995; Dobretsov *et al.*, 1996; Hetzel, 1999; Hetzel *et al.*, 1998). The lower unit consists of

© Blackwell Science Inc., 0263-4929/02/$15.00

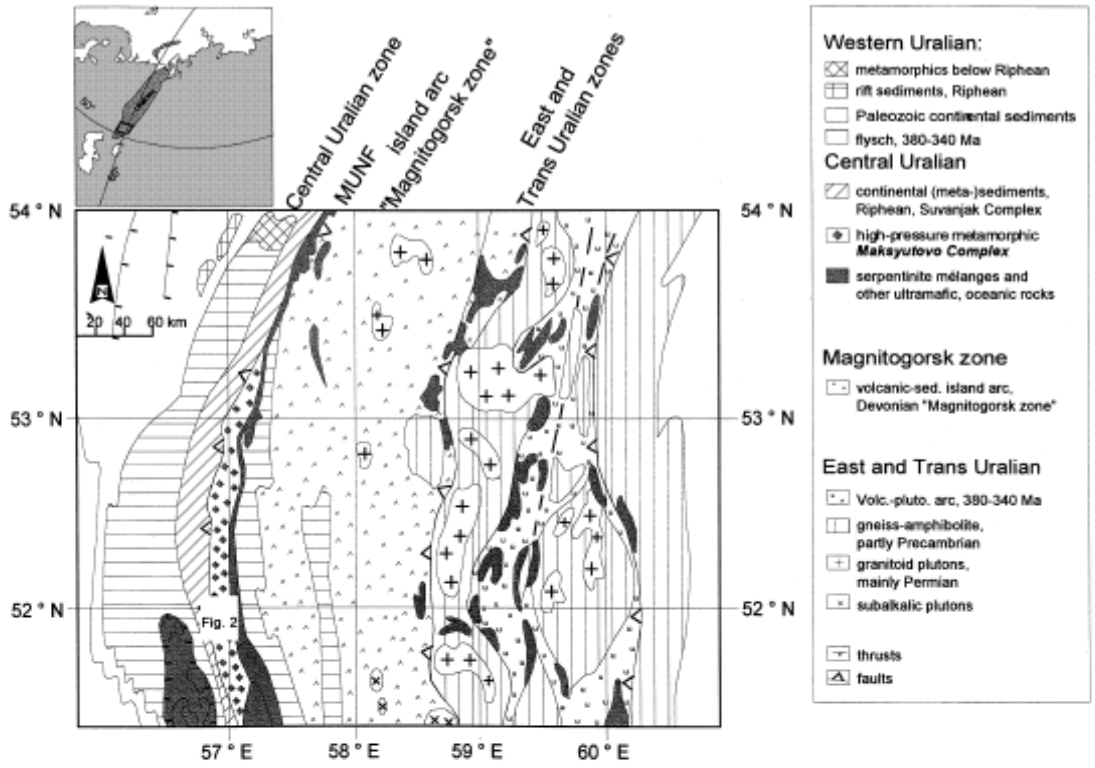


**Fig. 1.** Southern Urals and the position of the Urals in Eurasia, modified after Lennykh (1977). The position of Fig. 2 is shown in the central Maksyutovo Complex. Inlet shows position of Fig. 1 in Eurasia.

garnet-mica schist, quartzite and local occurrences of eclogite. The upper unit mainly consists of stilpnomelane quartzite. Metabasic greenschist, metachert and a few marble occurrences can be found predominantly close to the base of this unit. Antigorite serpentinite lenses which include the studied lawsonite fels are exclusively present at the base of this unit.

Mineral assemblages of eclogite and garnet-mica schist of the lower unit indicate metamorphic conditions of 550–650 °C and 15–23 kbar (Beane *et al.*, 1995; Lennykh *et al.*, 1995; Dobretsov *et al.*, 1996; Schulte & Blümel, 1999). Isotopic dating of the eclogites using Sm–Nd and Rb–Sr mineral isochrons, U–Pb on rutile and Ar–Ar on phengite gives an age of 385–375 Ma for the eclogite facies metamorphism (Matte *et al.*, 1993; Lennykh *et al.*, 1995; Shatsky *et al.*, 1997; Glodny *et al.*, 1999; Beane & Connelly, 2000). Rb–Sr whole rock and U–Pb zircon dating of eclogites indicate Riphean and Vendian protolith ages (Dobretsov, 1974; Sobolev *et al.*, 1986; Valizer & Lennykh, 1988). The protolith ages and range of lithologies suggest that the lower unit is a relic of the East European passive continental margin (Ivanov *et al.*, 1975 and references therein; Hetzel, 1999 and references therein). The metamorphic conditions of the upper unit are not constrained in detail, but the regional distribution of stilpnomelane + phengite metaclastites (Miyano & Klein, 1989) and metabasites with the assemblage clinozoisite + actinolite + albite + titanite (Frey *et al.*, 1991) indicate greenschist facies conditions. In addition local spessartine quartzites and pumpellyite + chlorite + quartz schists imply temperatures of $<400$ °C (Coombs *et al.*, 1996; Frey *et al.*, 1991). The pseudomorphs after lawsonite in rodingitized (ultra)mafite (Lennykh & Valizer, 1986) demonstrate that a high-pressure metamorphic event affected at least the serpentinite lenses containing the pseudomorphs. The greenschist facies metamorphism is probably Tournaisian–Viséan in age (Beane, 1997; Beane & Connelly, 2000) and the protolith age of the upper unit is probably Silurian to Ordovician, based on conodont fossils in marbles (Zakharov & Puchkov, 1994). The upper unit is interpreted as a fragment of the palaeo-ocean between the East European platform and the island arc, based mainly on the occurrence of serpentinite and local conodont marble (Ivanov *et al.*, 1975; Dobretsov *et al.*, 1996; Hetzel, 1999).

Structural and regional observations (Echtler & Hetzel, 1997; Puchkov, 1997 and references therein;

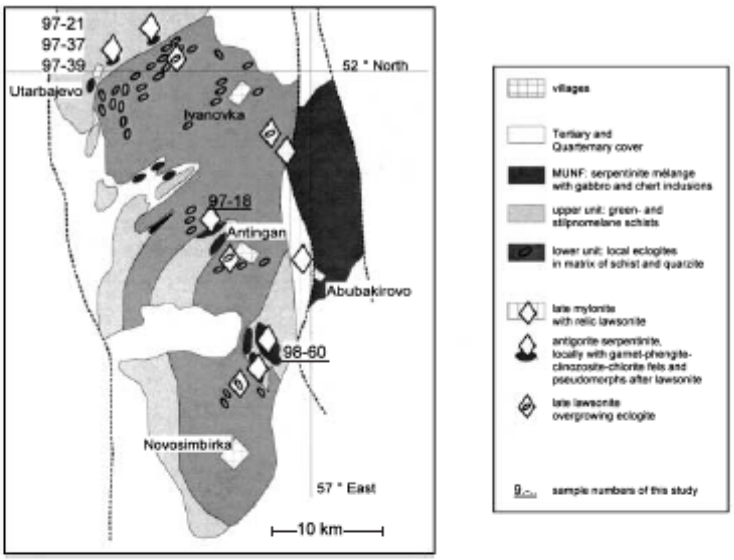


**Fig. 2.** Simplified geological map of the Central Maksyutovo Complex with samples used in chemical and isotopic analysis, modified after Lennykh (1977).

Hetzel *et al.*, 1998) indicate a south-eastward dip of the subduction zone during the eclogite metamorphism. North–south striking structures, defined at map scale, are representative of a later deformation stage at greenschist facies conditions.

## FIELD RELATIONS AND PETROGRAPHY

The lawsonite fels occurs as metre scale blocks within the up to kilometre sized antigorite serpentinite boudins (Fig. 2, Table 1). The structural relations between the lawsonite fels and serpentinite are not exposed, but detailed mapping places the lawsonite fels in the centre of the serpentinite boudins (Lennykh & Valizer, 1986) which in turn are rimmed by strongly sheared talc schists, greenschists, marbles, metacherts and stilpnomelane quartzites of the upper unit of the Maksyutovo Complex.

The lawsonite fels consists of centimetre sized, rhombic shaped, bright, polycrystalline aggregates— interpreted as pseudomorphs after lawsonite porphyro- blasts—and a dark matrix (Fig. 3). The pseudomorphs consist of clinozoisite + phengite + garnet + titanite (Fig. 4). The rhombic outline of the pseudomorphs is typical of lawsonite, which is verified by the occurrence of fresh, millimetre sized lawsonite in late, quartzitic mylonite (Fig. 2) and partly pseudomorphosed, relic lawsonite in eclogite (Fig. 2, Lennykh, 1977; Beane *et al.*, 1995; Schulte & Blümel, 1999). The dark matrix of the lawsonite fels consists of chlorite + epidote + garnet + titanite ± phengite (Fig. 4).

**Table 1.** Localities with pseudomorphs after lawsonite in metarodingite.

| Latitude | Longitude | Locality | Number | Investigations |
|---|---|---|---|---|
| 51°48,53′ | 57°53,41′ | Novosimbirka | 1 | |
| 51°49,54′ | 57°55,15′ | Abubakirovo | 2 | 98–60 (*P–T*) |
| 51°53,90′ | 57°51,42′ | Antingan | 6 | 97–18 (age) |
| 51°59,90′ | 57°45,70′ | Utarbajevo | 14 | 97–21, 97–37, 97–39 (age, *P–T*) |
| 52°19,19′ | 57°47,11′ | Maksyutova* | 2 | |
| 52°22,35′ | 57°46,44′ | Yuldybaevo* | 6 | |

* Not in Fig. 2 but in the north of the Maksyutovo Complex.

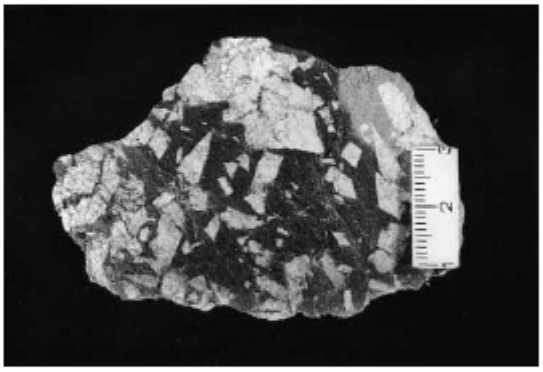

**Fig. 3.** Photograph of metarodingite with rhombic shaped, white pseudomorphs after lawsonite in a dark, chlorite rich matrix. Scale in cm.

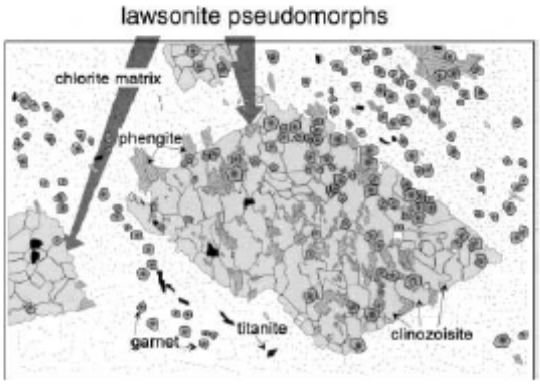


**Fig. 4.** Thin section sketch of pseudomorph after lawsonite. Length of sketch 1 cm.

Hypidioblastic garnet is surrounded by chlorite in the matrix and, locally, by phengite within the pseudomorphs, indicating partial resorption (Fig. 4). Yellow epidote with metamict core only occurs in the matrix, whereas colourless clinozoisite aggregates are part of the pseudomorphs after lawsonite. Phengite is concentrated along the pseudomorph rim and thus clearly is involved in the lawsonite breakdown reaction. Titanite is the only Ti bearing mineral in the rock and occurs as hypidioblastic grains in the matrix and in the pseudomorphs or as inclusions in the garnet core. Late stage pumpellyite grew in fractures which cut all minerals.

## METHODS

Minerals were analysed with an automated CAMECA SX 50 electron microprobe and Rb–Sr isotope ratios were analysed with a FINNIGAN MAT 261 mass spectrometer. For technical data see Appendix. The program THERMOCALC (Powell & Holland, 1988) was used together with the recommended thermodynamic data sets and activity models of Holland & Powell (1996, 1998) for the *P–T* estimates.

## MINERAL CHEMISTRY

Garnet in the pseudomorphs and in the matrix has a spessartine-rich core and a spessartine-poor rim (Fig. 5a-f, Table 2) and this zonation is interpreted as a result of prograde metamorphism (Tracy, 1982). There is no difference in zoning style between garnet in the pseudomorphs and in the matrix, but zoning varies between different samples. The zonation in sample 97–39 (Fig 5a,d) is simple, Fe ↔ Mn in the core and Mn ↔ Mg in the rim, while Ca is more or less constant throughout the profile. In the garnet core of samples 97–37 (Fig 5b,e) and 98–60 (Fig 5c,f) Mn decreases at the expense of Fe and Ca, while Mg is almost constant and in the garnet rim Fe decreases at the expense of Ca and Mg. The yellow colour of epidote supports the relatively high Fe content analysed, while the colourless clinozoisite has a lower Fe content (Fig. 6, Table 2). An inverse relationship between grossular content in garnet and Fe content in epidote–clinozoisite points to the interdependence between the mineral and rock composition in this multivariant assemblage (compare Figs 5a–f & 6). The phengite and chlorite compositions vary, but no systematic relations are recognised (Figs 7 & 8, Table 2). Titanite only has low Al contents (Table 2) and late pumpellyite is Al-rich with intermediate Fe–Mg ratios (Table 2).

## EQUILIBRIUM ESTIMATES AND LAWSONITE-OUT REACTION

The metamict core of epidote indicates long standing radioactivity and therefore either is part of the lawsonite assemblage or even a prelawsonite relic. The resorption of garnet by chlorite and phengite points to the coexistence of former lawsonite with garnet, while phengite and clinozoisite clearly crystallized during the pseudomorph formation. Chlorite is abundant and thus it coexisted with lawsonite and with clinozoisite of the pseudomorphs. The lack of any other Ti-phase beside titanite shows, that titanite also coexisted with lawsonite and clinozoisite. Pumpellyite, filling fractures, is a very late phase, therefore it is not considered further. Thus the petrographic observations indicate two equilibrium assemblages: a former lawsonite assemblage of lawsonite + garnet + chlorite + titanite ± epidote, and a pseudomorph assemblage of clinozoisite + phengite + chlorite + titanite.

The model system believed to be most applicable to the lawsonite-out reaction is at least trivariant, because there are 10 system components with eight phases ($SiO_2$, $TiO_2$, $AlO_{1.5}$, $FeO_{1.5}$, FeO, MgO, MnO, CaO, $KO_{0.5}$, $HO_{0.5}$/lawsonite, fluid, phengite, clinozoisite, garnet, chlorite, titanite, epidote). Therefore three system components have to be reduced if an univariant lawsonite-out reaction is to be written. As Fe, Mg and Mn have similar crystal chemical characteristics they are taken as one component, so the system is reduced to eight components. Although ferric iron occurs in chlorite, phengite and epidote, there is no microprobe means to distinguish between $Fe^{2+}$ and $Fe^{3+}$ and so they combine to a 'mafic component – FFMM', giving a 7 × 7 Matrix ($SiO_2$, $TiO_2$, $AlO_{1.5}$, FFMM, CaO, $KO_{0.5}$, $HO_{0.5}$/aqueous potassium-bearing fluid, phengite, clinozoisite, garnet, chlorite, titanite, epidote) to solve for lawsonite. But the 7 × 7 matrix is not consistent in that clinozoisite does not coexist with lawsonite. Therefore another approach and further simplification is necessary. Titanite is stable in the lawsonite- as well as in the pseudomorph-assemblage, and thus does not take part in the reaction and may be ignored. Epidote might not have been part of the lawsonite-out reaction because its metamict core possibly implies a prelawsonite growth. Thus the major ferric iron mineral and $Fe^{3+}$ as system component may be omitted. The new matrix – six system components and five phases ($SiO_2$, $AlO_{1.5}$, 'FMM', CaO, $KO_{0.5}$, $HO_{0.5}$/aqueous potassium-bearing fluid, phengite, clinozoisite, garnet, chlorite) – is not a square matrix. However, a system should be described by the minimum number of necessary system components and in this case K and Si may be combined in the form of a $KSi_{3.3}O_{7.1}$ component indicative of the average K and Si content of phengite giving a 5×5 matrix ($KSi_{3.3}O_{7.1}$, $AlO_{1.5}$, FMM, CaO, $HO_{0.5}$/aqueous-potassium bearing fluid, phengite, clinozoisite, garnet, chlorite) to solve for lawsonite (Table 3). This simplification is believed to be justified, because phengite is the most K and Si rich phase in the system and approximately represents the K and Si concentration of the fluid associated with phengite formation or lawsonite consumption. This in turn means that all other phases—garnet, clinozoisite, chlorite and lawsonite—are free of $KSi_{3.3}O_{7.1}$.

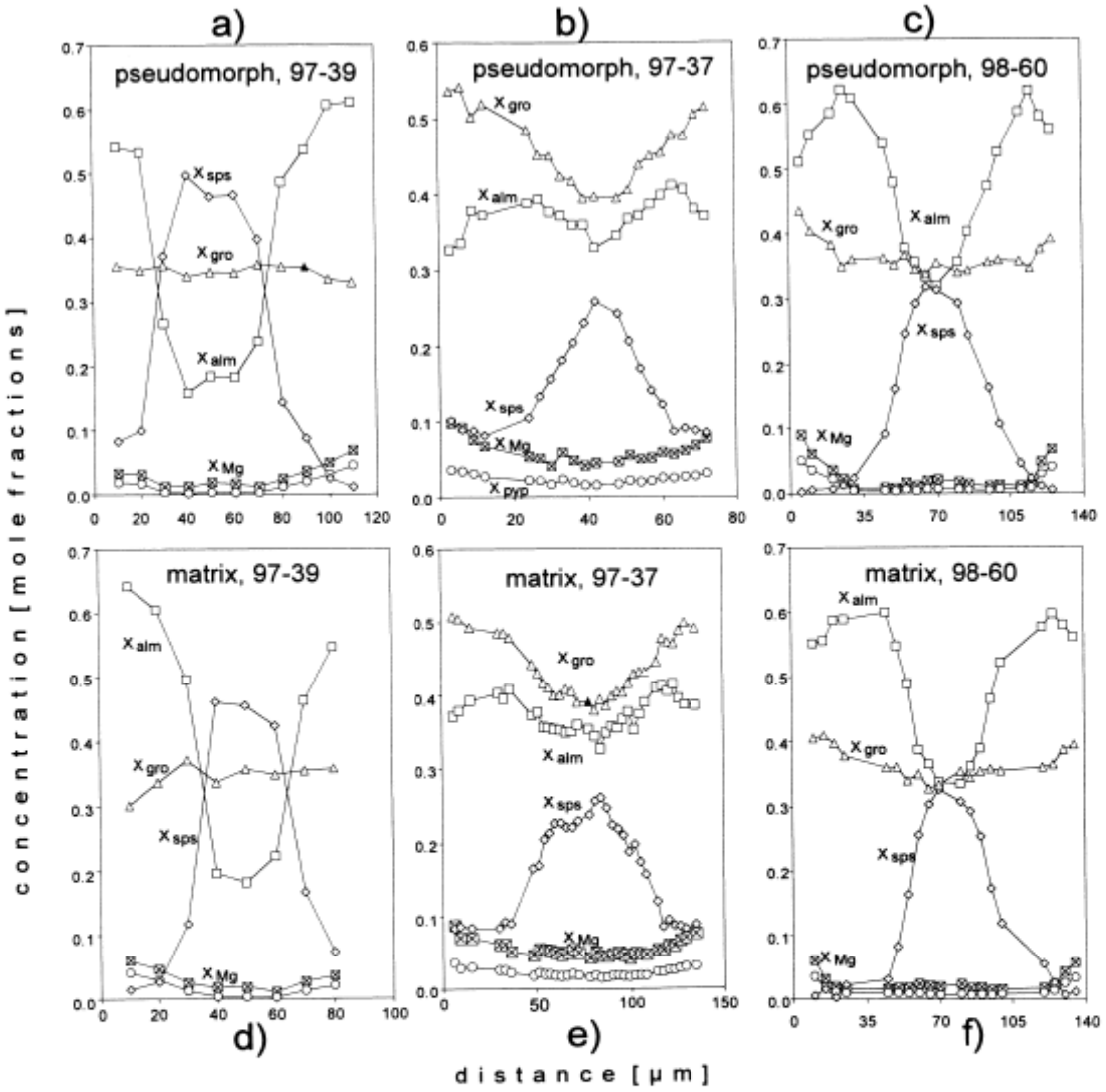


**Fig. 5.** (a)–(c), garnet compositional zonation in pseudomorphs after lawsonite; (d)–(f), garnet compositional zonation in matrix.

The 5×5 matrix results in

(I): 100 lawsonite + 0.3 garnet + 2 fluid → 2 phengite + 50 clinozoisite + 9 chlorite

in sample 97 – 39,

(II): 100 lawsonite + 0.4 garnet + 2 fluid → 2 phengite + 50 clinozoisite + 9 chlorite

in sample 97 – 37 and

(III): 100 lawsonite + 0.4 garnet + 2 fluid → 2 phengite + 50 clinozoisite + 9 chlorite

in sample 98–60. The stoichiometric relation of 100 lawsonite/0.3–0.4 garnet in reactions (I)–(III) explains the penetrative replacement of lawsonite in contrast to the persistence of garnet.

The system can be graphically displayed in a tetrahedron constructed with the components $AlO_{1.5}$-CaO-(FeO + MgO-MnO)-$KSi_{3.3}O_{7.1}$. The fifth component, $HO0_{.5}$, has to be visualised in a position opposite and central to the $AlO_{1.5}$-CaO-(FeO-MgO-MnO) plane behind the $KSi_{3.3}O_{7.1}$ apex and therefore the $KSi_{3.3}O_{7.1}$-apex represents the fluid composition. Accordingly phengite is projected onto

**Table 2.** Average compositions of chlorite, clinozoisite and phengite of the pseudomorph assemblage. Garnet rim composition, titanite and epidote of the lawsonite assemblage and average composition of late pumpellyite.

| | Epidote | | | Clinozoisite | | | Titanite | | Garnet | | |
|---|---|---|---|---|---|---|---|---|---|---|---|
| | 97-37 | 97-39 | 98-60 | 97-37 | 97-39 | 98-60 | 97-39 | | 97-37 | 97-39 | 98-60 |
| Oxides | 10* | 15* | 8* | 7* | 25* | 22* | 8* | Oxides | Rim | Rim | Rim |
| $SiO_2$ | 38.57 | 38.75 | 38.48 | 38.67 | 38.57 | 38.51 | 30.42 | $SiO_2$ | 37.92 | 37.16 | 37.42 |
| $TiO_2$ | 0.10 | 0.07 | 0.00 | 0.08 | 0.18 | 0.01 | 39.17 | $TiO_2$ | 0.07 | 0.06 | 0.02 |
| $Al_2O_3$ | 31.21 | 28.72 | 29.17 | 32.47 | 29.65 | 30.18 | 1.01 | $Al_2O_3$ | 21.47 | 21.76 | 21.39 |
| $Cr_2O_3$ | 0.04 | 0.04 | 0.05 | 0.05 | 0.03 | 0.04 | 0.00 | $Cr_2O_3$ | 0.04 | 0.00 | 0.05 |
| $Fe_2O_3^1$ | 2.58 | 6.13 | 4.92 | 0.87 | 4.50 | 3.82 | 0.27 | FeO[1] | 16.94 | 28.37 | 24.19 |
| MgO | 0.04 | 0.01 | 0.01 | 0.00 | 0.02 | 0.01 | 0.00 | MgO | 0.93 | 0.96 | 1.31 |
| MnO | 0.51 | 0.15 | 0.39 | 0.18 | 0.33 | 0.58 | 0.02 | MnO | 3.77 | 0.80 | 0.11 |
| CaO | 24.13 | 24.00 | 24.33 | 24.57 | 24.08 | 24.51 | 29.00 | CaO | 18.03 | 11.59 | 15.64 |
| $Na_2O$ | – | – | – | – | – | – | – | $Na_2O$ | – | – | – |
| $K_2O$ | – | – | – | – | – | – | – | $K_2O$ | – | – | – |
| Total | 97.18 | 97.87 | 97.35 | 96.89 | 97.36 | 97.66 | 99.89 | Total | 99.17 | 100.70 | 100.13 |
| Cations | 12.5 O | | | 12.5 O | | | 4 Si | Cations | 12 O | | |
| Si | 2.98 | 2.99 | 2.99 | 2.98 | 2.98 | 2.97 | 4.00 | Si | 2.99 | 2.95 | 2.96 |
| Ti | 0.01 | 0.00 | 0.00 | 0.00 | 0.01 | 0.00 | 3.87 | Ti | 0.00 | 0.00 | 0.00 |
| Al | 2.84 | 2.61 | 2.67 | 2.94 | 2.70 | 2.75 | 0.16 | Al | 2.00 | 2.04 | 1.99 |
| Cr | 0.00 | 0.00 | 0.00 | 0.00 | 0.00 | 0.00 | 0.00 | Cr | 0.00 | 0.00 | 0.00 |
| $Fe^{3+}$ | 0.16 | 0.39 | 0.32 | 0.06 | 0.29 | 0.24 | 0.03 | $Fe^{2+}$ | 1.12 | 1.88 | 1.59 |
| Mg | 0.00 | 0.00 | 0.00 | 0.00 | 0.00 | 0.00 | 0.00 | Mg | 0.11 | 0.11 | 0.15 |
| Mn | 0.03 | 0.01 | 0.03 | 0.01 | 0.02 | 0.04 | 0.00 | Mn | 0.25 | 0.05 | 0.01 |
| Ca | 1.99 | 1.99 | 2.02 | 2.02 | 2.00 | 2.03 | 4.09 | Ca | 1.53 | 0.99 | 1.32 |
| Na | – | – | – | – | – | – | – | Na | – | – | – |
| K | – | – | – | – | – | – | – | K | – | – | – |
| Total | 8.01 | 7.99 | 8.03 | 8.01 | 8.00 | 8.03 | 12.15 | Total | 8.00 | 8.02 | 8.02 |
| Si + Al + $Fe^3$ | 5.98 | 5.99 | 5.98 | 5.98 | 5.97 | 5.96 | | $X_{Mg}$ | 0.09 | 0.06 | 0.09 |
| Fe/(Fe + Al-1)[2] | 0.08 | 0.20 | 0.16 | 0.03 | 0.14 | 0.12 | | Alm | 0.37 | 0.62 | 0.51 |
| | | | | | | | | Prp | 0.04 | 0.04 | 0.05 |
| | | | | | | | | Sps | 0.08 | 0.02 | 0.00 |
| | | | | | | | | Grs | 0.51 | 0.33 | 0.44 |

**Table 2.** (*Cont'd*).

| | Chlorite | | | Phengite | | | Pumpellyite |
|---|---|---|---|---|---|---|---|
| | 97-37 | 97-39 | 98-60 | 97-37 | 97-39 | 98-60 | 97-37 |
| Oxides | 8* | 11* | 12* | 11* | 46* | 27* | 39* |
| $SiO_2$ | 28.94 | 28.75 | 28.85 | 48.81 | 49.29 | 49.00 | 37.58 |
| $TiO_2$ | 0.04 | 0.02 | 0.05 | 0.06 | 0.08 | 0.05 | 0.09 |
| $Al_2O_3$ | 21.12 | 20.78 | 19.96 | 32.60 | 31.65 | 30.39 | 26.41 |
| $Cr_2O_3$ | 0.06 | 0.03 | 0.03 | 0.03 | 0.04 | 0.05 | 0.04 |
| FeO[1] | 15.42 | 22.00 | 21.91 | 1.29 | 1.76 | 2.48 | 1.91 |
| MgO | 21.79 | 17.61 | 17.46 | 2.03 | 1.87 | 2.81 | 3.40 |
| MnO | 0.84 | 0.57 | 0.47 | 0.07 | 0.04 | 0.05 | 1.29 |
| CaO | 0.20 | 0.06 | 0.10 | 0.05 | 0.07 | 0.06 | 23.39 |
| $Na_2O$ | 0.08 | 0.03 | 0.02 | 0.44 | 0.33 | 0.27 | 0.29 |
| $K_2O$ | 0.04 | 0.03 | 0.25 | 10.45 | 10.27 | 10.60 | 0.03 |
| Total | 88.53 | 89.88 | 89.10 | 95.83 | 95.40 | 95.76 | 94.43 |
| Cations | 14 O | | | 11 O | | | 12.5 O |
| Si | 5.72 | 5.77 | 5.85 | 3.22 | 3.27 | 3.26 | 3.03 |
| Ti | 0.01 | 0.00 | 0.01 | 0.00 | 0.00 | 0.00 | 0.01 |
| $Al^{IV}$ | 2.28 | 2.23 | 2.15 | 0.78 | 0.73 | 0.74 | – |
| $Al^{VI}$ | 2.63 | 2.68 | 2.62 | 1.76 | 1.74 | 1.65 | 2.51 |
| Cr | 0.01 | 0.00 | 0.00 | 0.00 | 0.00 | 0.00 | 0.00 |
| $Fe^{2+}$ | 2.55 | 3.69 | 3.71 | 0.07 | 0.10 | 0.14 | 0.13 |
| Mg | 6.42 | 5.27 | 5.28 | 0.20 | 0.18 | 0.28 | 0.41 |
| Mn | 0.14 | 0.10 | 0.08 | 0.00 | 0.00 | 0.00 | 0.09 |
| Ca | 0.04 | 0.01 | 0.02 | 0.00 | 0.01 | 0.00 | 2.02 |
| Na | 0.03 | 0.01 | 0.01 | 0.06 | 0.04 | 0.03 | 0.05 |
| K | 0.01 | 0.01 | 0.06 | 0.88 | 0.87 | 0.90 | 0.00 |
| Total | 19.84 | 19.77 | 19.79 | 6.97 | 6.94 | 7.00 | 8.25 |
| $X_{Mg}$ | 0.72 | 0.59 | 0.59 | 0.74 | 0.64 | 0.67 | |
| $y = Al^{IV}/4$ | 0.57 | 0.56 | 0.54 | | | | |

* Number of analyses on which mean is based.
Ave = average; $X_{Mg}$ = Mg/(Fe + Mg); Alm = mole fraction of almandine; Prp = mole fraction of pyrope;
Sps = mole fraction of spessartine; Grs = mole fraction of grossular; $Al^{IV}$ = tetrahedral aluminium; $Al^{VI}$ = octahedral aluminium.
[1] Total Fe.
[2] Mole fractions.

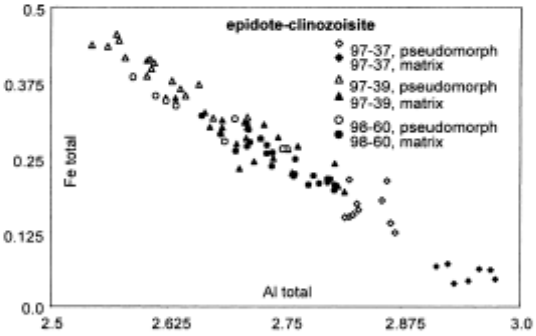


**Fig. 6.** Fe-Al relationships of epidote-clinozoisite from samples 97–37, 97–39 & 98–60.

the $AlO_{1.5}$-(FeO-MgO-MnO) edge and all other phases plot onto the $AlO_{1.5}$-CaO-(FeO-MgO-MnO) plane (Fig. 9).

In summary, analyses of the petrographic and chemographic data indicate the following four conclusions about the metamorphic evolution: (1) Mg-rich garnet rim + lawsonite + titanite + chlorite (± epidote) define a relic lawsonite assemblage (2) the compositional zonation of garnet implies prograde growth (3) lawsonite broke down by fluid controlled reactions like I–III and (4) chlorite + phengite + clinozoisite + titanite define the pseudomorph assemblage.

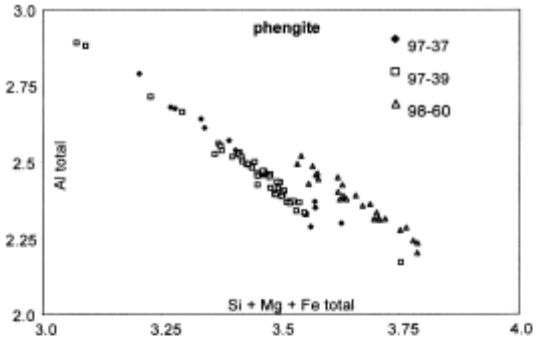


**Fig. 7.** Phengite $Al_{(tot)}$ v (Si + Mg + $Fe_{(tot)}$) composition in samples 97–37, 97–39 & 98–60.

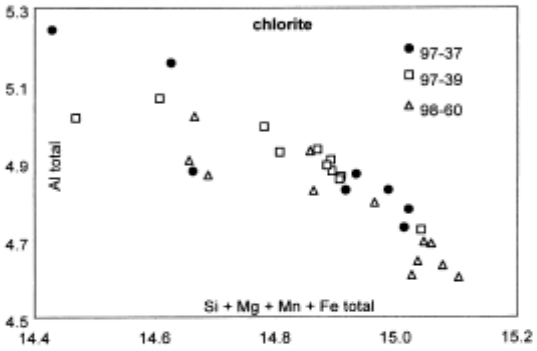


**Fig. 8.** Al v (Si + Mg + Fe + Mn) of chlorite from samples 97–37, 97–39 & 98–60.

**Table 3.** A 5 × 5 matrix to solve for lawsonite.

| | grt | phg | chl | czo | fluid | lws |
|---|---|---|---|---|---|---|
| $KSi_{3.3}O_{7.1}$ | 0 | 1 | 0 | 0 | 1 | 0 |
| $AlO_{1.5}$ | 2 | 2.4 | 4.9 | 3 | 0 | 2 |
| CaO | 1.5–1* | 0 | 0 | 2 | 0 | 1 |
| FeMgMnO | 2–1.5* | 0.3 | 9 | 0 | 0 | 0 |
| $H_2O$ | 0 | 1 | 16 | 1 | 1 | 1 |

* Depends on sample, all other values are average or ideal values.

## PRESSURE AND TEMPERATURE ESTIMATES

### Lawsonite assemblage

The maximum stability of lawsonite + titanite is given by reaction

(IV) lawsonite + titanite → clinozoisite + rutile + pyrophyllite + $H_2O$.

Different clinozoisite compositions ($X_{epidote}$ = 0–0.5) were used to simulate the epidote component. Within this compositional range the reaction is stable up to 30 kbar and more. The most Fe-rich clinozoisite in the

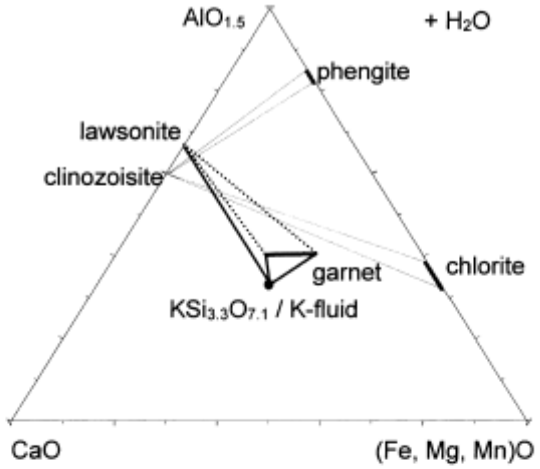


**Fig. 9.** Al-Ca-($Fe^{2+}$ + Mg + Mn) diagram, projected from $KSi_{3.3}O_{7.1}$ and $H_2O$: Garnet-lawsonite tie line crosscuts clinozoisite-chlorite tie line. The phengite projection plots on the $AlO_{1.5}$-(FMM)O side and the fluid is placed in the centre of the triangle.

pseudomorphs of each sample delimits the maximum stability of the former lawsonite and titanite coexistence to temperatures < 400 °C at 10 kbar and < 580 °C at 20 kbar (Fig. 10a).

The *P–T* conditions of the lawsonite assemblage may be constrained further: the six system components CaO-MgO-FeO-$AlO_{1.5}$-$SiO_2$-$HO_{0.5}$ with the four phases, garnet rim + lawsonite + chlorite + $H_2O$ is a good approximation to the real system, because phengite was not present in the lawsonite assemblage. Titanite may be omitted because it is the only Ti-phase. As the spessartine content in garnet is low (1–8 mole%) and probably mixes in close to ideal conditions with almandine it is added to the almandine component. A minimum temperature of > 460 °C at minimum pressures of > 13 kbar is estimated for the quadrivalent assemblage garnet rim + lawsonite + chlorite (of any composition) + $H_2O$ (Fig. 10a). This estimate takes into account, that neither the exact chlorite composition, nor the coexistence of epidote in the lawsonite assemblage is known.

In order to derive a *P–T* estimate it is necessary to make three assumptions namely that: (i) epidote is part of the lawsonite assemblage and (ii) chlorite and (iii) epidote compositions in the lawsonite assemblage are specified. Chlorite is modally abundant and thus it's composition in the lawsonite assemblage might be similar to the existing composition. Epidote is quite resistant to re-equilibration (Franz & Selverstone, 1992) and thus its composition might also be unchanged. However, no systematic relations are recognised for chlorite and epidote compositions and therefore the existing average values are used for

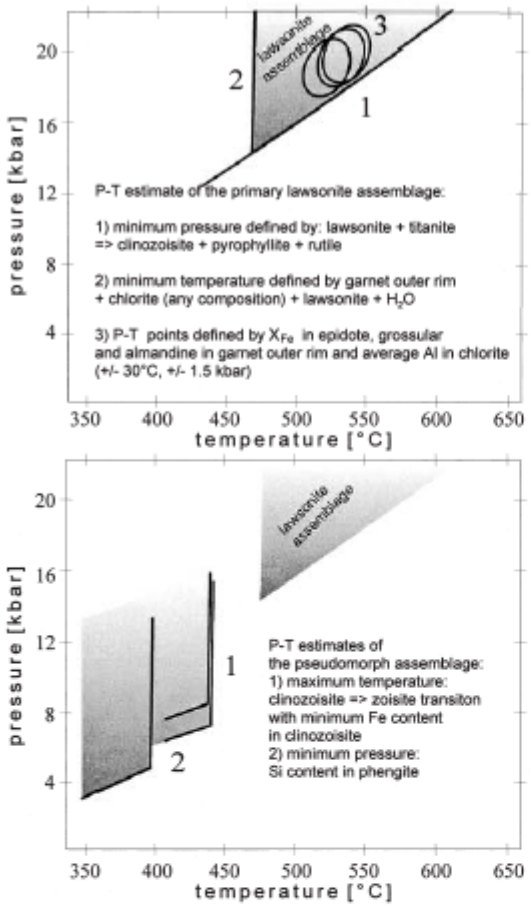


**Fig. 10. (a)–(b).** (a) Stability of the lawsonite assemblage is defined by maximum stability of lawsonite + titanite and the minimum stability of garnet + chlorite + lawsonite + $H_2O$. Additional estimates, shown by ovals are based on average chlorite and epidote compositions (see Table 4). (b) Maximum stability of the pseudomorph assemblage is defined by the clinozoisite = > zoisite transition with minimum Fe content in clinozoisite and by maximum Si content in phengite.

the *P–T* calculation. Now seven system components with five phases (CaO-FeO-$Fe_2O_3$-MgO-$AlO_{1.5}$-$SiO_2$-$HO_{0.5}$/garnet, chlorite, lawsonite, epidote, $H_2O$) indicate again quadrivalency and the four phase components grossular, almandine, $X_{epidote}$ (Fe/(Fe + Al-1) and $y_{chlorite}$ ($Al^{IV}$/4) have to be fixed. Using the garnet rim, average chlorite and epidote compositions for samples 97–37, 97–39 and 98–60 (Table 4, Fig. 10a) estimates of 20.3 kbar/540 °C, 18.3 kbar/518 °C and 20.7 kbar/543 °C are derived.

In summary, despite the unknown equilibrium composition of chlorite and epidote and the uncertainty if epidote coexisted with lawsonite, the *P–T* calculations reveal that the assemblage was formed at

**Table 4.** Mineral compositions used to estimate *P–T* of lawsonite and pseudomorph assemblage.

| Sample | 97–37 | 97–39 | 98-60 |
|---|---|---|---|
| *lawsonite assemblage* | | | |
| almandine + spessartine (outer rim) | 0.45 | 0.63 | 0.51 |
| grossular (outer rim) | 0.51 | 0.33 | 0.45 |
| average $X_{Fe}$ epidote = (Xep) | 0.08 | 0.2 | 0.16 |
| average $Al^{IV}$/4 chlorite = y(chl) | 0.57 | 0.56 | 0.54 |
| *P* (kbar) | 20.3 | 18.3 | 20.7 |
| *T* (°C) | 540 | 518 | 543 |
| *pseudomorph assemblage* | | | |
| $X_{Fe}$ minimum clinozoisite | 0.02 | 0.1 | 0.1 |
| Si p.f.u. maximum phengite | 3.27 | 3.44 | 3.36 |
| minimum pressure (kbar) | > 4.5 | > 7.5 | > 6.0 |
| maximum temperature (°C) | < 386 | < 433 | < 433 |

pressures > 13 kbar and temperatures between 460 and 550 °C. The lack of any indication for pressure as high as 13 kbar in the upper unit of the Maksyutovo Complex leads to the interpretation that the serpentinite lenses containing the pseudomorphs after lawsonite were incorporated into the base of the upper unit subsequent to high-pressure metamorphism.

### Pseudomorph assemblage

Any precise estimate of *P–T* conditions of the pseudomorph assemblage clinozoisite + phengite + chlorite + $H_2O$ is strongly hampered by the variability of mineral compositions and the unknown $Fe^{3+}$ content in phengite and chlorite. However, maximum temperatures may be derived from the clinozoisite to zoisite transition using the minimum Fe content in clinozoisite (Holland & Powell, 1998), and minimum pressures from the highest Si content in phengite (Massone, 1991; Massonne & Schreyer, 1987). For samples 97–37, 98–60 and 97–39 the derived values are > 4.5 kbar/< 400 °C, > 6 kbar/< 440 °C, and > 7.5 kbar/ < 440 °C, respectively (Table 4, Fig. 10b). The temperature of the pseudomorph formation is obviously lower than that of the lawsonite assemblage, indicating that the pseudomorph-forming event was not isofacial with the lawsonite assemblage. The minimum pressure for the pseudomorph assemblage is near or above the maximum pressure stability of stilpnomelane + phengite in metasiliclastic rocks (Miyano & Klein, 1989), indicating that the pseudomorph formed during exhumation. Assuming that the upper unit never reached depths greater than those defined by the stilpnomelane stability field (see above; Fig. 12), it is concluded that the pseudomorph formed prior to incorporation of the pseudomorph-containing-serpentinite lenses into the base of the upper unit.

### Rb–Sr dating

For samples 97–18 and 97–21, fractions of all modal components have been used for isotopic analyses using the Rb–Sr system (Table 5), which is

appropriate for dating the pseudomorphs that are modally dominated by clinozoisite + phengite. Both samples have Sr concentrations that are low in the matrix (70 and 134 p p m) and high in the pseudomorphs (2987 and 3440 p p m). The Rb concentrations and Rb/Sr ratios are generally rather low, except for white mica (Table 5). In addition pseudomorphs of metarodingites from the north of the Maksyutovo Complex (sample 97–3) also show these Rb/Sr characteristics (Table 5) which seems to be a regional phenomenon (see Discussion). The breakdown of the lawsonite porphyroblasts by the fluid-controlled reaction (I)– (III) explains the cogenetic origin of clinozoisite and phengite as indicated by the textural observations. Thus the isotopic data from these two minerals were used for isochron calculation (Table 5, Fig. 11) and the two samples

**Table 5.** Rb–Sr isotope data of pseudomorphs after lawsonite.

| | $Rb_{(p.p.m.)}$ | $Sr_{(p.p.m.)}$ | $^{87}Rb/^{86}Sr$ | $^{87}Sr/^{86}Sr$ |
|---|---|---|---|---|
| sample 97–18 | | | | |
| phengite* | 224 | 150 | 4.33 ± 0.05 | 0.72909 ± 0.00005 |
| c-zoisite* | 1.4 | 5289 | 0.00078 ± 0.00002 | 0.70822 ± 0.00005 |
| garnet | 0.3 | 29 | 0.031 ± 0.0007 | 0.70832 ± 0.00005 |
| pseudom. | 12 | 3540 | 0.0096 ± 0.0001 | 0.70821 ± 0.00005 |
| matrix 1 | 1 | 134 | 0.0115 ± 0.0002 | 0.70850 ± 0.00005 |
| matrix 2 | 0.2 | 110 | 0.004 ± 0.0015 | 0.70835 ± 0.00005 |
| isochron | age(Ma) | $^{87}Sr/^{86}Sr$ | | |
| calculation | 339 ± 6 | initial: | | 0.70822 ± 0.00005 |
| sample 97–21 | | | | |
| phengite* | 109 | 170 | 1.86 ± 0.02 | 0.71787 ± 0.00005 |
| c-zoisite* | 5 | 3539 | 0.0042 ± 0.0001 | 0.70895 ± 0.00005 |
| pseudom. | 28 | 2987 | 0.0274 ± 0.0003 | 0.70908 ± 0.00005 |
| matrix | 1 | 70 | 0.0612 ± 0.0014 | 0.70919 ± 0.00005 |
| isochron | age(Ma) | $^{87}Sr/^{86}Sr$ | | |
| calculation | 338 ± 5 | initial: | | 0.70893 ± 0.00005 |
| sample 97–3 | | | | |
| pseudomorph | 26 | 3340 | 0.0222 ± 0.0003 | 0.70936 ± 0.00005 |

* Used for isochron calculation sample 97–18.

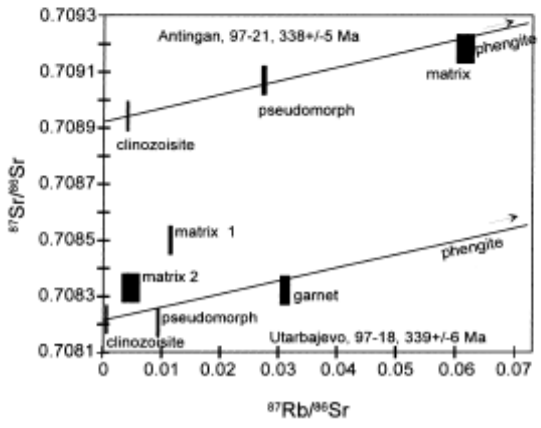


**Fig. 11.** $^{87}Rb/^{86}Sr$-$^{87}Sr/^{86}Sr$-isochron diagram for samples 97–18 and 97–21. The size of symbols indicates 2σ errors of the analyses.

yield ages of 339 ± 6 and 338 ± 5 Ma, which are identical within error. The $^{87}Sr/^{86}Sr$ – $^{87}Rb/^{86}Sr$ ratio of garnet in sample 97–18, within its limits of error, lies on the isochron although garnet – at least the core – is not part of the pseudomorph forming assemblage. This indicates either that the garnet + lawsonite assemblage did not differ isotopically in a significant way from the pseudomorph assemblage, or that garnet equilibrated isotopically with clinozoisite and phengite.

Two matrix parts from sample 97–18 have markedly different Rb/Sr isotope signatures (Fig. 11) and deviate from the isochron of the pseudomorph components. Comparing these data with those from the matrix of sample 97–21 indicates that the isotopic heterogeneity in the matrix of 97–18 is best explained by an episodic loss of Rb in various parts of the matrix during different stages of the isochron development after initial equilibration at *c.* 339 Ma. This might have caused a shift from a position with high $^{87}Rb/^{86}Sr$-ratio on the isochron to one with lower $^{87}Rb/^{86}Sr$ ratios above the isochron.

## DISCUSSION

### Lawsonite assemblage, rock composition

The deduction of the lawsonite assemblage is based on garnet resorption by chlorite and phengite and the stoichiometry of reaction (I)–(III). In addition Fe-Mg exchange between garnet/chlorite and garnet/phengite gives temperatures of < 350 °C, which are interpreted as disequilibrium, because garnet with up to 5 mole percentage pyrope and 1 mole percentage spessartine is not stable at < 350 °C, at least in Si saturated compositions (Mahar *et al.*, 1997). Another indicator of the coexistence of garnet + lawsonite is that the decomposition of lawsonite to clinozoisite is always associated with grossular on the lawsonite side in a CASH system with grossular, lawsonite, pyrophyllite, kyanite, margarite, anorthite, laumontite, that is a simplified model for rocks of rodingitic composition at subgreenschist to blueschist facies conditions. Lawsonite coexisting with garnet is described in various rocks at different high-pressure metamorphic conditions (Black, 1977; Caron & Pecquinot, 1986; Okay, 1980; Helmstaedt & Schulze, 1988). However, it is a rare assemblage that is restricted to geological settings with very low temperature gradients and lithologies rich in Ca and Al.

Rodingites are metasomatic rocks rich in Ca-Al-silicate minerals and are commonly associated with serpentinites. They occur at contacts between serpentinite and country rock or as dykes, sills and boudins within serpentinite (Bloxam, 1955; Bilgrami & Howie, 1960; Dubinska, 1995; O'Hanley *et al.*, 1992) as do the presently described rocks. Rodingites mostly derive from mafic rocks (e.g. gabbro, diabase) but sedimentary protoliths have also been described (Rice, 1983).

**Table 6.** Rock Composition of sample 97–39 from Utarbajewo (oxide wt%).

| $SiO_2$ | $TiO_2$ | $Al_2O_3$ | $Fe_2O_3$ | MnO | MgO | CaO | $Na_2O$ | $K_2O$ | $P_2O_5$ | S |
|---|---|---|---|---|---|---|---|---|---|---|
| 35.3 | 1.39 | 24.4 | 14.7 | 1.31 | 6.48 | 11.2 | 0.12 | 1.19 | 0.01 | < 0.02 |

The rodingitization of the mafic rocks and the serpentinization of the ultramafic rocks are probably cogenetic processes (Schandl *et al.*, 1989; Thayer, 1966) that lead to the addition of Ca, Al, OH- and removal of Si and alkalis (Na, K) from the mafic rocks (Harper *et al.*, 1988; Staudigel *et al.*, 1981). Rodingites are known from oceanic fracture zones (Honnorez & Kirst, 1975) as well as in re-equilibrated rocks in alpine-type ophiolites (e.g. Deutsch, 1979; Evans *et al.*, 1979; Evans *et al.*, 1981; Rösli *et al.*, 1991). In all the settings there is a wide range of rock compositions ($SiO_2$: 52–33 wt%, $Al_2O_3$: 10–25 wt%, CaO: 20–30 wt%, rest: < 37 wt%). Sample 97–39 plots within the published range of (meta-)rodingite compositions, except for CaO (CaO = 11.2 wt%) (Table 6), and so is better termed as a rodingitized (ultra)mafic rock, rather than a (meta)rodingite.

### Pseudomorph formation

The pseudomorph assemblage formed by the infiltration of a K-bearing fluid into the rock via reactions (I)-(III) and the Rb–Sr ages are interpreted to date the isotopic equilibration between the pseudomorph minerals clinozoisite and phengite. In principle, the isotopic equilibration between clinozoisite and phengite could also have occurred after the formation of the pseudomorphs due to subsequent heating or an influx of fluids, but the following two lines of evidence suggest that this is not the case. First, the temperature in the pseudomorphs did not exceed 440 °C (see *P–T* estimate), and so re-equilibration due to heating seems unlikely. Second, Rb–Sr ages obtained from mylonites, quartzites and mica schist in the central Maksyutovo Complex cluster at *c.* 360 Ma (Beane & Connelly, 2000) and preclude a regional resetting of the Rb–Sr system by fluids at 339–338 Ma. In consequence, it is most plausible that the isotopic equilibration dates the crystallization of the pseudomorph minerals at a point between the $^{40}Ar/^{39}Ar$ ages of 338–331 Ma from phengite of the upper unit and 365–358 Ma from phengite of the lower unit (Beane & Connelly, 2000). The high Sr concentrations and low $^{87}Rb/^{86}Sr$ ratios of the pseudomorphs raise the question if they are products of a crystallization event at 339–338 Ma, or whether they are features of the precursor lawsonite. If the former was true, the regional occurrence of the high Sr concentrations in the lawsonite fels would require an influx of appreciable amounts of Sr and probably elements with similar transport characteristics such as Ca, Eu or Ba for which there is no evidence. Extremely low $^{87}Rb/^{86}Sr$ ratios and high Sr concentrations of more than 1400 p p m are characteristic of lawsonite (Domanik *et al.*, 1993; Miyajima *et al.*, 1999). It is thus probable that the Rb–Sr characteristics of the pseudomorphs are inherited from the precursor lawsonite and that the fluid, responsible for lawsonite break-down, was not Sr rich. The exact origin of the fluid remains obscure so far, but it seems obvious, that the normal fault between the lower unit and upper unit may have triggered the fluid influx and the abundance of metasiliclastic rocks in both units is a potential source for the K-bearing fluid.

### Tectonometamorphic significance

Pressures of > 13 kbar and temperatures of < 550 °C are estimated for the lawsonite assemblage, which is a similar pressure but lower temperature to the eclogites of the lower unit (Beane *et al.*, 1995; Dobretsov *et al.*, 1996; Schulte & Blümel, 1999). The same relationship is also recognised if the lawsonite + titanite stability of the lawsonite fels is compared with the lawsonite + jadeite stability of the eclogites (Fig. 12). Both stabilities have a similar slope and values in *P–T* space, but the lawsonite + jadeite formation in eclogite is a late process that post-dates the peak metamorphic temperatures (Beane *et al.*, 1995; Lennykh *et al.*, 1995;

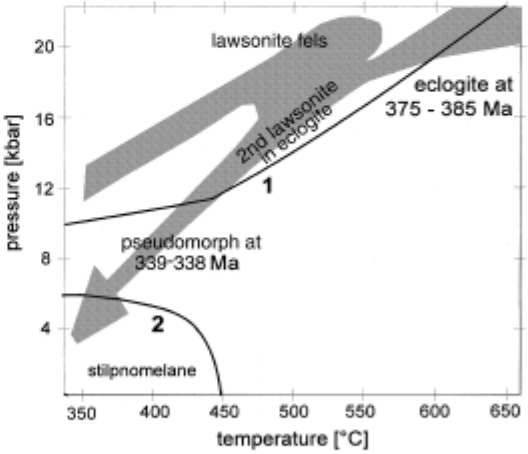


**Fig. 12.** (1) Stability of secondary lawsonite in eclogite in lower unit and stilpnomelane metaclastites in upper unit. Stability of lawsonite is limited by the reactions lawsonite + jadeite ($X_{Jd} = 0.43$) => clinozoisite ($X_{Fe} = 0.5$) + paragonite and jadeite ($X_{Jd} = 0.43$) + quartz => albite. (2) Stability of stilpnomelane after Miyano & Klein (1989).(3) P–T-t path interpretation of the lawsonite fels and eclogite. Oceanic and continental crust, represented by lawsonite fels and eclogite of the lower unit meet at a minimum of 13 kbar/470 °C, are exhumed together and partially re-equilibrate in the stability field of stilpnomelane. The formation of the lawsonite fels predates 339 Ma and post-dates the formation of eclogites (375–385 Ma, Matte *et al.*, 1993; Shatsky *et al.*, 1997).

Schulte & Blümel, 1999), whereas the lawsonite + titanite stability characterises the peak metamorphic conditions of the lawsonite fels. It is noted that thermal modelling and field studies of subduction settings (Peacock, 1993; Ernst & Peacock, 1996; Trouw *et al.*, 1998) also show strong temperature variations with 'cold' margins and 'hot' centres in an horizontal section through a subduction zone. Thus the present distribution of 'high temperature eclogite' and 'low temperature lawsonite fels' in the central Maksyutovo Complex (Fig. 2) resembles such a horizontal section through a relic south-east dipping subduction zone and might have persisted further transposition and re-equilibration.

The ultramafic rocks with lawsonite fels are boudins with undeformed cores and strongly foliated rims, which can be attributed to rigid, exotic blocks, within fault zones. This type of structural arrangement can be interpreted as the boudins being constitutional parts of the fault zone at the base of the upper unit that separates the lower from the upper unit (Dobretsov *et al.*, 1996; Hetzel *et al.*, 1998; Leech & Ernst, 2000). If this is correct then it indicates (1) the width of the fault zone between the lower unit and the upper unit increases upwards (2) the close association of ultramafic rock, lawsonite fels, marble and metachert, and thus all rocks with 'oceanic affinity', are part of this normal fault (3) the derived *P–T* estimate of the lawsonite fels demonstrates that this fault zone became active at low-temperature eclogite facies conditions and (4) the upper unit is not necessarily of oceanic origin but restricted to the greenschist facies metamorphosed stilpnomelane-phengite metaclastites. These conclusions strongly support the exhumation model of Hetzel *et al.* (1998), that stresses the significance of this internal normal fault zone in the Maksyutovo Complex as a major transport plane of exhumation for the eclogites.

## CONCLUSIONS

The eclogite facies lower unit of the Maksyutovo Complex is separated by a normal fault zone from the greenschist facies upper unit. Included in the fault zone are ultramafic boudins that enclose blocks of lawsonite fels. The *P–T* estimate of the assemblage lawsonite + titanite + garnet + chlorite ± epidote in this rock points to similar depths but lower temperatures of formation as the eclogites of the lower unit (Fig. 12). This pressure estimate suggests that the fault zone was active at low-temperature eclogite facies conditions and supports the significance of the fault zone as a major plane of eclogite exhumation (Hetzel *et al.*, 1998). The *P–T* conditions and age (339–338 Ma) of the pseudomorph formation either correlate with the greenschist facies metamorphism in the upper unit or with a late exhumation stage of the lower unit, respectively, the activity of the normal fault zone.

## ACKNOWLEDGEMENTS

Our thanks to V. I. Lennykh for two excellent field trips through the Maksyutovo Complex and fruitful discussions in the summers of 1997 and 1998. Additionally we thank the reviewers and the editor for constructive criticism, P. Blümel (TU Darmstadt), U. Kramm, A. Rogers (RWTH Aachen) and A. Willner (Ruhr-University Bochum) for discussions on the subject and K. Richter (University Würzburg) and H. Ortner (TU Darmstadt) who provided analytical facilities. We are grateful to U. Haack and J. Schneider (University Gießen) who made the isotope analyses possible. J. Kolb and B. Thybusch (TU Darmstadt) prepared samples and helped during analytical work. Most of this study was financed by the Deutsche Forschungs Gemeinschaft.

## REFERENCES

Beane, R. J., 1997. Ar/Ar evidence for Paleozoic high-pressure metamorphism in the South Urals. In: *Annual Meeting of the Geological Society of America, (EOS EI)* (Suppl.) Salt Lake City, pp. BTH-35.

Beane, R. J. & Connelly, J. N., 2000. $^{40}Ar/^{39}Ar$, U-Pb, and Sm-Nd constraints on the timing of metamorphic events in the Maksyutov Complex, southern Ural Mountains. *Journal of the Geological Society of London*, **157**, 811–822.

Beane, R. J., Liou, J. G., Coleman, R. G. & Leech, M. L., 1995. Petrology and retrograde *P-T* path for eclogites of the Maksyutov Complex, South Ural Mountains, Russia. *Island Arc*, **4**, 254–266.

Bilgrami, S. A. & Howie, R. A., 1960. The Mineralogy and the Petrology of a Rodingite Dike, Hindubagh, Pakistan. *American Mineralogist*, **45**, 791–801.

Birck, J. L. & Allègre, C. J., 1978. Chronology and chemical history of the parent body of basaltic achondrites studied by the $^{87}Rb/^{86}Sr$ method. *Earth and Planetary Science Letters*, **39**, 37–51.

Black, P. A. M., 1977. Regional high-pressure metamorphism in New Caledonia: Phase equilibria in the Ouéga district. *Tectonophysics*, **43**, 59–107.

Bloxam, T. W., 1955. Rodingite from the Girvan-Ballantrae complex, Ayrshire. *Mineralogical Magazine*, **30**, 525–528.

Caron, J. M. & Pecquinot, G., 1986. The transition between blueschists and lawsonite-bearing eclogites based on observations from Corsican metabasalts. *Lithos*, **19**, 205–218.

Coombs, D. S., Kawachi, Y. & Ford, B. P., 1996. Porphyroblastic manganaxinite metapelagites with incipent garnet in prehnite-pumpellyite facies, near Meyers Pass, Torless Terrane, New Zealand. *Journal of Metamorphic Geology*, **14**, 125–142.

Deutsch, A., 1979. Serpentinite und Rodingite der Cima Sgiu (NW Aduladecke, Ticino). *Schweizerische Mineralogische Petrographische Mitteilungen*, **59**, 319–347.

Dobretsov, N. L., 1974. *Glaucophane Schists and. Eclogite-Glaucophane-Schist complexes in the USSR*. Nauka press, Novosibirsk (in Russian).

Dobretsov, N. L., Shatsky, V. S., Coleman, R. G., Lennykh, V. I., Valizer, P. M., Liou, J., Zhang, R. & Beane, R. J., 1996. Tectonic setting and Petrology of Ultrahigh-Pressure Metamorphic Rocks in the Maksyutov Complex, Ural Mountains, Russia. *International Geology Review*, **38**, 136–160.

Dobretsov, N. L., Sobolev, V. S., Sobolev, N. V. & Khlestov, V. V., 1974. *The Facies of Regional Metamorphism at High pressure*. Moscov (English Translation by DA Brown 1975. ANU Press, Canberra.

Domanik, K. J., Hervig, R. L. & Peacock, S. M., 1993. Beryllium and boron in subduction zone minerals: An ion microprobe study. *Geochimica et Cosmochimica Acta*, **57,** 4997–5010.

Dubinska, E., 1995. Rodingites of the Eastern Part of the Jordanów – Gogolów Serpentinite Massif, Lower Silesia, Poland. *Canadian Mineralogist*, **33,** 585–608.

Echtler, H. P. & Hetzel, R., 1997. Main Uralian Thrust and Main Uralian Normal Fault: non-extensional Paleozoic high-P rock exhumation, oblique collision, and normal faulting in the Southern Urals. *Terra Nova*, **9,** 158–162.

Ernst, W. G. & Peacock, S. M., 1996. A thermotectonic model for preservation of ultrahigh-pressure phases in metamorphosed continental crust. In: *Subduction, Top to Bottom.* (eds Bebout, G. E., Scholl, D. W., Kirby, S. H. & Platt, J. P.) *Geophysical Monograph.* 96, 171–178.

Evans, B. W., Trommsdorf, V. & Goles, G. G., 1981. Geochemistry of High-Grade Eclogites and Metarodingites from the Central Alps. *Contributions to Mineralogy and Petrology*, **76,** 301–311.

Evans, B. W., Trommsdorf, V. & Richter, W., 1979. Petrology of an eclogite-metarodingite suite at Cima di Gagnone, Ticino, Switzerland. *American Mineralogist*, **64,** 15–31.

Franz, G. & Selverstone, J., 1992. An empirical phase diagram for the clinozoisite-zoisite transformation in the system $Ca_2Al_3Si_3O_{12}$ (OH)-$Ca_2Al_2Fe^{3+}Si_3O_{12}$ (OH). *American Mineralogist*, **77,** 631–642.

Frey, M., de Capitani, C. & Liou, J. G., 1991. A new petrogenetic grid for low-grade metabasites. *Journal of Metamorphic Geology*, **9,** 497–509.

Glodny, J., Austrheim, H., Bingen, B., Rusin, A. & Scarrow, J. H., 1999. New age data for high-P rocks and ophiolites along the Main Uralian Fault, Urals, Russia: Implications for the Uralian orogeny. *Terra Nostra*, **99/1,** 89–90.

Harper, G. D., Bowman, J. R. & Kuhns, R., 1988. A Field, Chemical and Stable Isotope Study of Subseafloor Metamorphism of the Josephine Ophiolite, California-Oregon. *Journal of Geophysical Research*, **93,** 4625–4656.

Helmstaedt, H. & Schulze, D. J., 1988. Eclogite facies ultramafic xenoliths from Colorado Plateau diatreme breccias: Comparison with eclogites in crustal environments, evaluation of the subduction zone hypothesis and implications for eclogite xenoliths from Diamandoferous kimberlites. In: *Eclogites and Eclogite Facies Rocks* (ed. Smith, D.C.), 387–450 Elsevier, New York.

Hetzel, R., 1999. Geology and geodynamic evolution of the high-pressure/low-temperature metamorphic Maksyutov Complex, Southern Urals, Russia. *Geologische Rundschau*, **87,** 577–588.

Hetzel, R., Echtler, H. P., Seifert, W., Schulte, B. A. & Ivanov, K. S., 1998. Subduction- and exhumation-related fabrics in the Paleozoic high-pressure/low-temperature Maksyutov complex, Antingan area, Southern Urals, Russia. *Geological Society of America Bulletin*, **110,** 916–930.

Holland, T. J. B. & Powell, R., 1996. Thermodynamics of order-disorder in minerals. II. Symmetric formalism applied to solid solutions. *American Mineralogist*, **81,** 1425–1437.

Holland, T. J. B. & Powell, R., 1998. An internally consistent thermodynamic data set for phases of petrological interest. *Journal of Metamorphic Geology*, **16,** 309–343.

Honnorez, J. & Kirst, P., 1975. Petrology of Rodingites from the Equatorial Mid-Atlantic Fracture Zones and Their Geotectonic Significance. *Contributions to Mineralogy and Petrology*, **49,** 233–257.

Ivanov, S. N., Perfiliev, A. S., Efimov, A. A., Smirnov, G. A., Necheukhin, V. M. & Fershtater, G. B., 1975. Fundamental features in the structure and evolution of the Urals. *American Journal of Science*, **254A,** 107–136.

Leech, M. L. & Ernst, W. G., 2000. Petrotectonic evolution of the high- to ultrahigh-pressure Maksyutov Complex, Karayanova area, south Ural Mountains: structural and oxygen isotopic constraints. *Lithos*, **52,** 235–252.

Lennykh, V. I., 1977. Eclogite–glaucophaneschist of the South Urals. Akademii Nauka, Moskau (in Russian).

Lennykh, V. I. & Valizer, P. M., 1986. Lawsonite rodingite of the Maksyutov eclogite–glaucophane complex. Sverdlovsk, Nauka Press, 73–76 (in Russian).

Lennykh, V. I., Valizer, P. M., Beane, R. J., Leech, M. & Ernst, W. G., 1995. Petrotectonic Evolution of the Maksyutov Complex, Southern Urals, Russia: Implications for Ultrahigh-Pressure Metamorphism. *International Geology Review*, **37,** 584–600.

Mahar, E. M., Baker, J. M., Powell, R., Holland, T. J. B. & Howell, N., 1997. The effect of Mn on mineral stability in metapelites. *Journal of Metamorphic Geology*, **15,** 223–238.

Massone, H. J., 1991. *High-Pressure, Low-Temperature Metamorphism of Pelitic and Other Protoliths Based on Experiments in the System* $K_2O$-MgO-$Al_2O_3$-$Sio_2$-$H_2O$ Unpublished Habilitation, Ruhr-Universität Bochum, Germany.

Massonne, H. J. & Schreyer, W., 1987. Phengite geobarometry based on the limiting assemblage with K-feldspar, phlogopite, and quartz. *Contributions to Mineralogy and Petrology*, **96,** 212–224.

Matte, P., Maluski, H., Caby, R., Nicolas, A., Kepezhinskas, P. & Sobolev, S., 1993. Geodynamic model and Ar/Ar dating for the generation and emplacement of the High Pressure (HP) metamorphic rocks in SW Urals. *Comptée Rendue Academie Science*. **317/** II, 1667–1674.

Miyajima, H., Matsubara, S., Miyawaki, R. & Ito, K., 1999. Itoigawaite, a new mineral, the Sr-analogue of lawsonite in jadeitite from the Itoigawa-Ohmi district, central Japan. *Mineralogical Magazine*, **63,** 909–916.

Miyano, T. & Klein, C., 1989. Phase equilibria in the system $K_2O$-FeO-MgO-$Al_2O_3$-$SiO_2$-$H_2O$-$CO_2$ and the stability limit of stilpnomelane in metamorphosed Precambrian iron-formations. *Contributions to Mineralogy and Petrology*, **102,** 478–491.

O'Hanley, D. S., Schandl, E. S. & Wicks, F. J., 1992. The origin of rodingites from Cassiar, British Columbia, and their use to estimate T and P ($_{H2O}$) during serpentinization. *Geochimica et Cosmochimica Acta*, **56,** 97–108.

Okay, A. I., 1980. Mineralogy, Petrology and Phase Relations of Glaucophane-Lawsonite Zone Blueschists from the Tavsanli Region, Northwest Turkey. *Contributions to Mineralogy and Petrology*, **72,** 243–255.

Peacock, S. M., 1993. The importance of blueschist => eclogite dehydration reactions in subducting oceanic crust. *Geological Society of America Bulletin of the*, **105,** 684–694.

Powell, R. & Holland, T. J. B., 1988. An internally consistent thermodynamic dataset with uncertainties and correlations: 3. Application methods, worked examples and a computer program. *Journal of Metamorphic Geology*, **6,** 173–204.

Puchkov, V. N., 1997. Structure and geodynamics of the Uralian orogen. In: *Orogeny Through Time, Geological Society Special Publications 121,* (eds Burg, J. P. & Ford, M.) pp. 201–236, Geological Society, London.

Rice, J. M., 1983. Metamorphism of rodingites: Part I. Phase relations in a portion of the system CaO-MgO-$Al_2O_3$-$SiO_2$-$CO_2$-$H_2O$. *American Journal of Science*, **238,** 121–150.

Rösli, U., Hoernes, S. & Köppel, V., 1991. Isotope data of metarodingites and associated rocks from the Lanzo and the Bracco ophiolitic massifs: Indications on the evolution of the Alpine-type ultramafic-mafic complexes. *Schweizerische Mineralogische und Petrographische Mitteilungen*, **71,** 125–141.

Schandl, E. S., O'Hanley, D. S. & Wicks, F. J., 1989. Rodingites in the serpentinized ultramafic rocks of the Abitibi Greenstone Belt, Ontario. *Canadian Mineralogist*, **27,** 579–591.

Schulte, B. A. & Blümel, P., 1999. Metamorphic evolution of eclogite and associated garnet-mica schist in the high-pressure metamorphic Maksyutov Complex, Ural, Russia. *Geologische Rundschau*, **87,** 561–577.

Shatsky, V. S., Jagoutz, E. & Koz'Menko, O. A., 1997. Sm-Nd dating of the high-pressure metamorphism of the Maksyutov complex, Southern Urals. *Transactions Russian Academy of Science (Translated from Doklady Akademii Nauk)*, **353**, 285–288.

Sobolev, N. V., Dobretsov, N. L., Bakirov, A. B. & Shatsky, V. S., 1986. Eclogites from various types of metamorphic complexes in the USSR and the problems of their origins. In: *Blueschists and Eclogites Memoirs of the Geological Society, 164*, (eds Evans, B. W. & Brown, E. H.), pp. 349–364, Geological Society of America, Boulder.

Staudigel, H., Hart, S. R. & Richardson, S. H., 1981. Alteration of the Oceanic Crust: Processes and timing. *Earth and Planetary Science Letters*, **52**, 311–327.

Thayer, T. P., 1966. Serpentinization Considered as a Constant-Volume Metasomatic Process. *American Mineralogist*, **51**, 685–710.

Tracy, R. J., 1982. Compositional zoning and inclusions in metamorphic minerals. In: *Characterization of Metamorphism Through Mineral Equilibria* (ed. Ferry, J. M.), pp. 355–397. Mineralogical Society America, Washington DC.

Trouw, R. A. J., Simoes, L. S. A. & Valladares, C. S., 1998. Metamorphic evolution of a subduction complex, South Shetland Islands, Antarctica. *Journal of Metamorphic Geology*, **16**, 475–490.

Valizer, P. M. & Lennykh, V. I., 1988. *Amphiboles of Blueschists of the Urals*. Nauka press, Moscov (in Russian).

Zakharov, O. A. & Puchkov, V. N., 1994. On the tectonic nature of the Maksyutovo complex of the Ural-Tau zone. Ufimian. Science Centre, Russian Academy of Science, Ufa (in Russian).

*Received 15 November 2000; revision accepted 13 January 2002.*

## APPENDIX

Mineral compositions were analysed by wavelength dispersive X-ray analyses with an CAMECA SX 50 electron microprobe at the Institute of Chemical Analytics with automated PAP correction at the Technical University Darmstadt. Rb–Sr isotope compositions were analysed with a FINNIGAN MAT 261 solid source mass spectrometer at the Institute of Geowissenschaften und Lithosphärenforschung, University Gießen and the bulk rock composition was analysed by X-ray fluorescence at the Institute of Mineralogy, University of Würzburg.

For the separation of mineral fractions the samples have been crushed to pieces of the minimum diameter of the pseudomorphs. This fraction has been used for handpicking of pseudomorph parts free of matrix material which were then ground again to smaller fractions and separated conventionally to pure mineral fractions. Bulk samples and mineral fractions were dissolved in a HF-$HNO_3$ mixture and Rb and Sr were separated by cation exchange techniques using SrSpec of EichromIndustries and according Birck & Allègre (1978). Rb–Sr isotopic ratio measurements were made on a multi-collector Finnigan MAT 261 solid source mass spectrometer. Repeated analyses ($n = 23$) of the $^{87}Sr/^{86}Sr$ ratio of the NBS 987 Sr standard during the period of analytical activity yielded 0.71023 ± 0.00003 (2σ of all analyses).

**Table A1.** Technical data and standards used for automatic WDX analyses.

| | Qualitative analyses | Quantitative analyses |
|---|---|---|
| High voltage | 15 kv | 15 kv |
| Beam current | 10–40 nA | 10–20 nA |
| Beam size | 1–5 µ | 2–7 µ |
| Resolution | 256 × 256 or 512 × 512 pixel | |
| Measuring time (peak) | 200–400 µ s | 10–30 s |
| Background | + – peak/2 | |
| Crystals | LIF, TAP, PET | LIF, TAP, PET |
| Standards: | | |
| Anorthite | $CaAl_2Si_2O_8$, Si kα on PET | |
| Albite | $NaAlSi_3O_8$, Na kα on TAP | |
| Chromite | $Cr_2O_3$, Cr kα on LIF | |
| corundum | $Al_2O_3$, Al kα on TAP | |
| diopside | $CaMgSi_2O_6$, Mg kα on TAP | |
| hematite | $Fe_2O_3$, Fe kα on LIF | |
| orthoclase | $KAlSi_3O_8$, K kα on PET | |
| rhodonite | $MnSiO_3$, Mn kα on LIF | |
| rutile | $TiO_2$, Ti kα on LIF | |
| wollastonite | $CaSiO_3$, Ca kα on PET | |

Repeated analyses of the standards ($n = 5$–12) results in < 0.1% between 100 and 5 wt% oxide, > 2% between 5 and 2 wt% oxide and > 30% < 2% wt% oxides (2σ of all analyses).

8.

Sindern, S., Ronkin,Yu., Gronen, L., Winkler, R., Schulte, B.A., Kramm, U. (in prep.) Geochemistry of granitoid and mafic magmatic rocks of the south-eastern Urals, new data from the Mariinskiy and Nishniy Sanarskiy complexes.

Geochemistry of granitoid and mafic magmatic rocks of the south-eastern Urals, new data from the Mariinskiy and Nishniy Sanarskiy complexes

Sindern, S., Ronkin,Yu., Gronen, L., Winkler, R., Schulte, B.A., Kramm, U.

Abstract

New data on the major and trace element geochemistry of granitoid and basaltic intrusive rocks of the Mariinskiy and Nishniy Sanarskiy complexes to the east of the Troitsk fault (western Transuralian zone) are presented. The granitoids are magnesian, calcic to calc-alkalic and metaluminous to mildly peraluminous. Their mineralogical as well as major and trace element characteristics indicate formation by mixing of slab-derived melts and melts generated in the crust, which is most consistent with an Andean type magmatic arc setting. This and compositional characteristics of subalkaline basaltic rocks support ideas that the Transuralian zone contains remnants of the Valerianovka Andean type magmatic arc along the margin of the Kazakh continent. In age and composition the granitoids of the western Transuralian zone are similar to subduction-related intrusives of the Magnitogorsk and Easturalian zone to the west of the study area. This points to contemporaneous subduction of the Uralian ocean underneath the Magnitogorsk arc as well as the Kazakh continent in late Devonian to early Carboniferous times.

Key words

Geochemistry, granitoid, basalt, Transuralian zone

## Introduction

The geochemical composition of magmatic rocks reflects processes of magma generation, magma diversification and magma sources. Such factors are correlated with tectonic environment, in which the parental melts are formed (Pearce 1996, Pearce and Cann 1973, Vermeesch 2006, see compilation in Rollinson 1993). Geochemistry allows to distinguish between oceanic and continental origin of magmas as well as to identify magmatic arcs and consequently active continental margins.

A geochemical characterisation of magmatic rocks may thus also serve to unravel the evolution of crustal domains, which are now amalgamated in an orogen and it may yield valuable information in addition to structural data and sedimentary record.
Magmatic rocks, in particular granitoids, predominate in the eastern parts of the Urals and have intensively been studied in the Easturalian zone (Bea et al. 2002, Gerdes et al. 2002, Montero et al. 2000, Bea et al. 1997, Fershtater et al. 1997).
Despite of these studies, the geochemistry of magmatic rocks in the zone to the east of the Troitsk fault in the southern Urals (Fig. 1) has not been addressed in detail in the international literature. This zone, which is conventionally termed Transuralian zone, represents the most poorly exposed and least studied eastern front of the Uralian orogen (Puchkov 1997).
Puchkov (2009a) points to the accretionary nature of the Transuralian zone, which is composed of various continental as well as oceanic domains and which are considered to be amalgamated to the Valerianovka magmatic arc at the former active continental margin of the Kazakh plate (Brown et al. 2008, Herrington et al. 2005).
While detailed information is given on marine and terrigenous sedimentary and volcano-sedimentary successions (e.g. Puchkov 1997, Puchkov 2000), geochemical data are very rare (e.g. Mamayev 1965). This study presents a characterisation of the major and trace element composition of three larger granitoid intrusions and of four mafic volcanic and subvolcanic occurrences. The data are used to set constraints to the geotectonic environment of magma formation and to compare these data with the existing information – in particular – on the voluminous granitoid intrusions of the eastern Urals to the west of the Troitsk fault. The results are discussed within the framework of the existing ideas on the eastern part of the Uralian orogen.

## Geology

The Uralian orogen is composed of several longitudinal zones (Fig. 1), representing:
- a foreland sedimentary basin (Preuralian foredeep, Puchkov 1997),
- a foreland fold- and thrust-belt (Westuralian megazone, Giese et al. 1999, Brown et al. 1997),
- a complex and highly shortened zone consisting of different metamorphic crystalline domains derived from the Baltica margin as well as of other provenance, e.g. Beloretzk terrane (Centraluralian Zone, Echtler et al. 1997, Glasmacher et al. 2001)

- accreted oceanic crust and island arc complexes (Tagilo-Magnitogorskian megazone, Puchkov 2009b)
- a wrench zone consisting of highly deformed oceanic crust and major granitoid-gneiss complexes, which mainly formed due to partial melting of island-arc material and of Palaeozoic to Proterozoic metasediments (Easturalian zone, Görz et al. 2009, Gerdes et al. 2002)
- a heterogeneous zone composed of low- to high-grade metamorphic, different magmatic as well as sedimentary rocks (Transuralian zone).

The easternmost of these zone, the Transuralian zone, is only exposed in the southern Urals (Puchkov 2009a). Conventionally, the Troitsk fault zone (Fig. 1) is considered as eastern border of the Transuralian to the Easturalian zone (e.g. Puchkov 2009a, Brown et al. 2008, Herrington et al. 2005). In contrast, according to other authors, this border is situated further to the east (e.g. Görz and Hielscher 2010). Hence, western parts of the Transuralian zone would belong to the Easturalian zone.

The region to the east of the Troitsk fault does not show significant elevations and natural outcrops are restricted to river banks. This zone shows Ordovician to Carboniferous successions consisting of volcanic, volcano-sedimentary and sedimentary sequences with thicknesses generally exceeding 3000 m (Puchkov 1997, Mamayev 1965). In part, these rocks were affected by greenschist- to amphibolite-facies metamorphism (Mamayev 1965).

The Mariinskiy complex is a dominant structure to the east of the Troitsk fault (Fig. 1). It is composed of high grade metamorphic rocks of the Mariinskiy suite, lower Palaeozoic greenschist-facies metasediments with basaltic subvolcanic bodies and dikes, serpentinites and granitoid plutons (Mamayev 1965). The Mariinskiy suite comprises biotite-rich and quartzitic gneisses, amphibolites and migmatites (Keilmann 1974). Uranium-Pb ages of 1850 and 2054 +/- 35 Ma of zircon from (biotite-garnet gneiss) point to a Proterozoic protolith (A.A. Krasnobayev, personal communication). Recently, Gronen (2013) has shown that migmatite formation has a Uralian age of 353 +/- 6 Ma (U-Pb zircon). In the northern part of the complex granitoids predominate. A tonalitic pluton, which crops out near the villages of Mariinskiy (Mariinskiy pluton), a granodiorite near the village of Andreevka (Andreevka pluton) and a gabbro near the village of Atamanovskiy are studied here (Fig. 1).

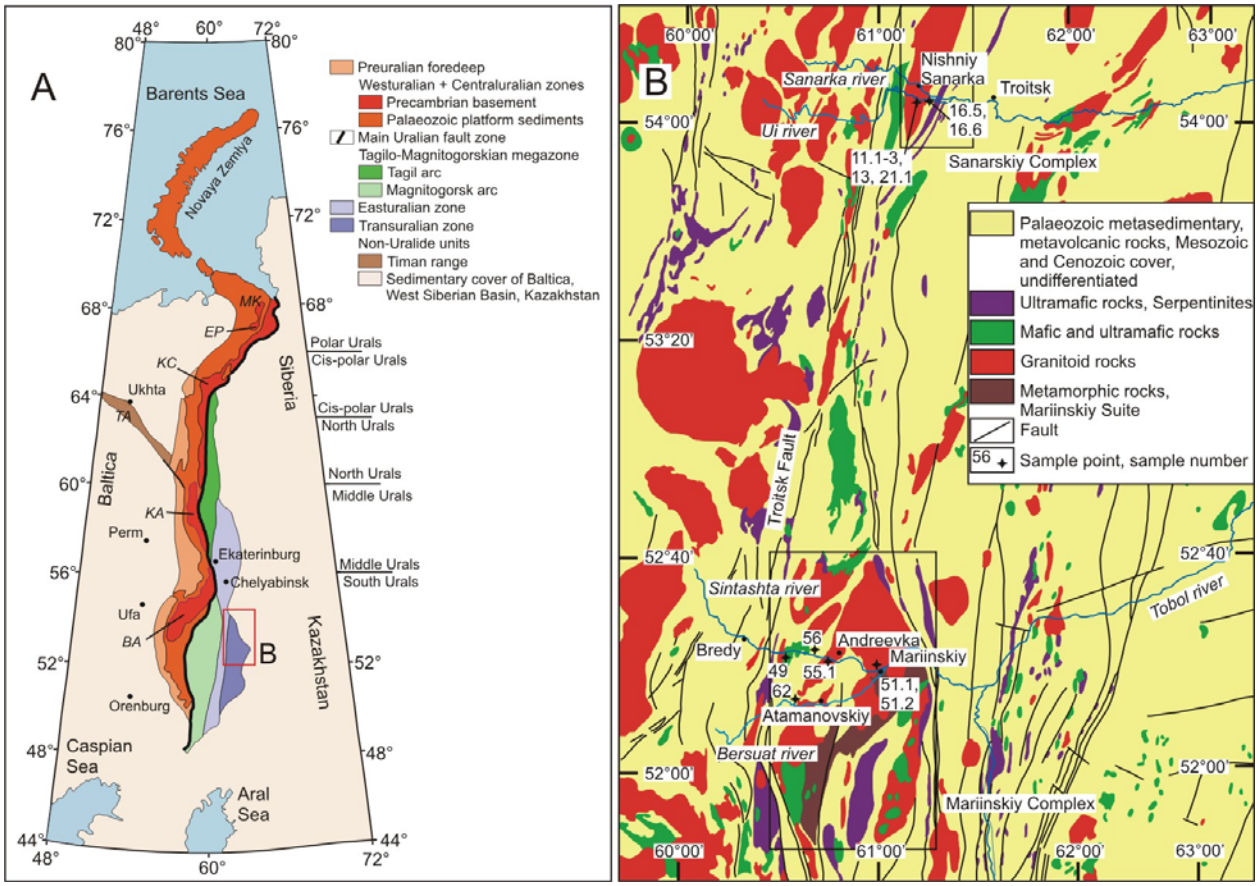


Fig. 1: Sketch maps, A, longitudinal zonation of Urals, adapted from Brown et al. (2008), B, simplified geological map of the western Transuralian zone adapted from Nalivkin (1965) with study reas around the Mariinskiy and Sanarskiy Complexes and sample points.

The Nishniy Sanarskiy pluton crops out along the rivers Sanarka and Ui (Fig. 1, Mamayev 1965). It is surrounded by intensively sheared gneisses, which are also host of basaltic rocks. All, the granitoid and its host rocks, are referred to as Nishniy Sanarskiy complex in this study.

For the plutons of Mariinskiy and Nishniy Sanarskiy Gronen (2013) determined zircon dates of 364 ± 14 and 357 ± 6 Ma, respectively, which are considered to indicate magmatic crystallisation ages. The ages of granitoid magmatism and migmatite formation fall at the lower limit of a range of K-Ar dates (525 to 360 Ma) for magmatic and metamorphic amphiboles and micas from the Mariisnkiy complex given by Ovchinnikov et al. (1969). Younger Rb-Sr ages were obtained for magnetite-garnet-biotite-amphibole-gneisses from the Mariinskiy complex. An isochron calculation of

Rb-Sr-isotope data of biotite-, amphibole-and quartz-feldspar-fractions yields a date of 254 ± 1.2 Ma (2 δ, MSWD = 1.7, Ronkin unpublished data). This is interpreted as age of late metamorphism, which is widely observed in geological formations of the Urals (e.g. Echtler et al. 1997).

Mafic and ultramafic rocks are abundant in the study area. These are strongly deformed serpentinites as well as gabbros and diabases, which form irregular bodies or dykes cutting the metasedimentary and volcanosedimentary sequences.

Due to the bad outcrop conditions contact relationships between different lithologic units are not constrained. In addition, all lithologic units are partly affected by intensive strike-slip deformation, which also obliterates primary structural features (Schulte and Sindern, unpublished data).

Samples

The Nishniy Sanarskiy pluton was sampled in a quarry and along river Ui (samples 11.1 – 3, 13, 21.1, Fig. 1). It is formed by a medium- to coarse-grained plagioclase-quartz-biotite ± hornblende ± K-feldspar granitoid rock. Plagioclase is subhedral, complexely twinned and shows oscillatory zonation. Hornblende forms euhedral grains but is often replaced by biotite, which is more abundant than hornblende. Minor flame-perthitic K-feldspar can also be present. Accessory minerals are zircon, apatite and opaques. Locally, epidote, chlorite replacing biotite and sericite grown in plagioclase can be observed.

The Mariinskiy pluton was sampled near river Sintashta (samples 51.1 – 2, Fig. 1). It is composed of a medium- to coarse-grained plagioclase-quartz-biotite rock with a panxenomorphic texture. Plagioclase, which is rarely sericitised, displays polysynthetic twinning and weak irregular zonation. Biotite is the only mafic magmatic mineral, and is locally replaced by chlorite. In contrast to the other granitoids, aggregates of anhedral to subhedral garnet, with irregular lobate grain boundaries can be found. Accessory minerals are opaques and zircon.

The Andreevskiy pluton crops out along river Sintashta and along the street between Andreevskiy and Bredy (sample 55.1, Fig. 1). It is a medium- to coarse-grained panxenomorphic granitoid rock composed of plagioclase, quartz, biotite and minor film-perthitic K-feldspar as well as minor muscovite, which is distinct to the other granitoids. In plagioclase twinning can be observed but no zonation. Chlorite, epidote and sericite can occur locally.

A medium-grained gabbro (sample 62) occurs in a small intrusive body that crops out near river Bersuat close to the village of Atamanovskiy (Fig. 1). Its contacts to Lower Palaeozoic metasediments are not exposed. It is dominated by euhedral to semihedral plagioclase and amphibole, which are affected by sericitisation and chloritisation, respectively. Quartz is a minor phase, epidote and opaques are accessories.

All granitoid samples display serrated grain boundaries of quartz and less abundant of plagioclase due to bulging. Quartz is often characterized by undulose and patchy extinction. Such features, which are indicative of dynamic recrystallisation (e.g. Passchier and Trouw 1996), show that the plutons have pervasively been affected by low degrees of plastic deformation.

Basaltic rocks occur in all regions of the Western Transuralian zone (Fig. 1) and were sampled in the southern part of the study area (samples 49, 56) as well as in the north at the banks of river Ui (samples 16.5, 16.6).

A dolerite dyke (sample 56), which cross cuts Lower Palaeozoic metasediments, was sampled in an outcrop of a dyke near the village Komsomolskiy. It is a holocrystalline fine- to medium-grained rock with an intergranular texture. Laths of plagioclase, which are zoned and partially sericitised, predominate. Euhedral to semihedral amphibole, which is partially replaced by actinolite, is present in interstitial positions. Opaque phases are minor. Locally, calcite, chlorite, epidote and muscovite formed.

Sample 49 is a porphyric basalt with a microcrystalline groundmass and euhedral, partially sericitised, plagioclase phenocrysts (≤ 7 mm), which are more abundant than phenocrysts of clinopyroxene. This sample represents a larger basaltic body with unclear contact relations to the surrounding rocks (Fig. 1).

The dykes occurring close to river Ui (samples 16.5, 16.6, Fig. 1) are formed by microcrystalline basalts with a groundmass dominated by plagioclase exhibiting a trachytic texture. They contain clinopyroxene as most abundant phenocrysts followed by sericitized plagioclase and rare amphibole. Opaques are also present. Vugs filled with carbonate can rarely be observed.

The occurrence of secondary sericite, actinolite, epidote and chlorite indicates retrograde greenschist facies metamorphic overprint of the basaltic rocks.

## Methods

Major elements were analyzed by XRF after determination of loss on ignition (24h at 1000 °C) and fusion with Li-tetraborate/metaborate (Merck Spectromelt A12 mixed with sample at a ratio of 10:1). Determination of samples 11.1, 13, 21.1 and Zr in all samples was carried out by XRF on pressed powder pellets. Analyses of most samples were performed on a Philipps PW 1400 spectrometer at RWTH Aachen University, equipped with a Rh-tube operated at 40 to 90 kV. Samples 11.1, 13 and 21.1 were analysed using a Spectro XLab 2000 (RWTH Aachen University), see Sindern et al. (2008) for details on analytical procedures. For both procedures precision was better than 0.5 % for the major and 5 % for the trace elements. All other trace element analyses were determined by SF-HR-ICP-MS (Element2) at the Institute of Geology and Geochemistry of the Urals branch of the Russian Academy of Sciences, Ekaterinburg, Russia, see Ronkin et al. (2005) for details on the analytical procedures.

## Results

All granitoids are magnesian, calcic to calc-alkalic and metaluminous to mildly peraluminous rocks according to the classification of Frost et al. (2001). In addition to this, Tabel 1 also depicts the classifications of Debon and LeFort (1980), De la Roche et al. (1980) and Cox (1979), which show slight variations.

Samples of the Nishniy Sanarskiy pluton are variable (e.g. $SiO_2$ 59.74 – 69.98, $K_2O$ 0.75 – 2.55 wt.-%) with $Na_2O > K_2O$ and have dioritic, granodioritic to tonalitic compositions (Table 1). They show a systematic decrease in $TiO_2$, MgO, $Fe_2O_3^t$ and CaO with increasing $SiO_2$ (Fig. 2 ). The Sanarka granitoids are characterized by high Sr- and Ba-concentration but also slightly elevated U-, P- and Li-values, whereas a marked Nb-depletion cannot be observed (Fig. 3a). The chondrite-normalized REE patterns display moderate LREE/HREE fractionation ($La_N/Lu_N$ = 9.78 – 10.06) and a positive Eu-anomaly (Eu/Eu* = 1.41 – 2.54, Table 1).

Table 1: Major[1] and trace element[2] composition of granitoid and basaltic rocks of the western Transuralian zone.

| Sample location | Nishniy Sanarskiy pluton | | | Marlinskiy complex | | | | | | N. Sanarskiy | | Marlinskiy complex | |
|---|---|---|---|---|---|---|---|---|---|---|---|---|---|
| rock | Granitoids | | | | | | | | | Basaltic rocks | | | |
| sample No. | 11.1[3] | 11.2 | 11.3 | 13[3] | 21.1[3] | 51.1 | 51.2 | 55.1 | 62 | 16.5 | 16.6 | 49 | 56 |
| $SiO_2$ | 60,06 | 69,98 | 66,39 | 59,74 | 62,26 | 67,50 | 62,52 | 74,15 | 52,25 | 49,18 | 47,90 | 48,09 | 52,44 |
| $TiO_2$ | 0,71 | 0,13 | 0,26 | 0,58 | 0,57 | 0,33 | 0,48 | 0,16 | 0,79 | 0,97 | 1,15 | 1,08 | 1,77 |
| $Al_2O_3$ | 17,33 | 15,48 | 18,97 | 17,12 | 16,12 | 17,03 | 18,84 | 14,60 | 18,78 | 17,30 | 17,22 | 20,76 | 15,36 |
| $Fe_2O_3^{tot}$ | 6,19 | 1,29 | 2,14 | 5,98 | 5,30 | 2,83 | 3,99 | 1,78 | 7,70 | 9,62 | 10,49 | 6,60 | 10,70 |
| MnO | 0,12 | 0,03 | 0,04 | 0,12 | 0,11 | 0,03 | 0,06 | 0,07 | 0,13 | 0,18 | 0,18 | 0,09 | 0,20 |
| MgO | 2,47 | 0,22 | 0,83 | 3,02 | 2,22 | 1,14 | 1,69 | 0,26 | 4,54 | 5,17 | 5,28 | 5,08 | 4,25 |
| CaO | 5,55 | 2,82 | 5,38 | 6,39 | 5,64 | 4,20 | 4,46 | 2,35 | 7,87 | 8,12 | 7,07 | 10,58 | 8,07 |
| $Na_2O$ | 3,29 | 4,21 | 4,06 | 3,24 | 3,10 | 3,93 | 4,27 | 4,14 | 3,39 | 2,65 | 3,50 | 2,37 | 4,31 |
| $K_2O$ | 2,31 | 2,55 | 1,57 | 1,23 | 0,75 | 1,38 | 1,80 | 2,12 | 1,63 | 1,47 | 2,71 | 2,43 | 1,05 |
| $P_2O_5$ | 0,21 | 0,03 | 0,12 | 0,15 | 0,15 | 0,13 | 0,20 | 0,07 | 0,19 | 0,21 | 0,17 | 0,16 | 0,33 |
| $SO_3$ | 0,50 | 0,00 | 0,19 | 0,01 | 0,01 | 0,28 | 0,09 | 0,08 | 0,18 | 0,31 | 0,34 | 0,00 | 0,14 |
| LOI | 0,36 | 3,60 | 0,15 | 1,37 | 1,90 | 0,23 | 0,53 | 0,27 | 1,60 | 4,86 | 4,07 | 2,63 | 1,53 |
| Sum | 99,09 | 100,35 | 100,10 | 98,94 | 98,12 | 99,01 | 98,92 | 100,05 | 99,04 | 100,03 | 100,08 | 99,87 | 100,17 |
| Li | nd | 8,9 | 10,4 | nd | nd | 11,4 | 14,1 | 24,4 | 6,7 | 21,5 | 18,7 | 15,4 | 3,7 |
| Rb | 58 | 49,3 | 32,5 | 34 | 17 | 40,9 | 58,9 | 50,6 | 37,1 | 40,8 | 100,0 | 51,2 | 15,1 |
| Cs | nd | 2,0 | 1,1 | nd | nd | 0,6 | 0,9 | 1,9 | 0,7 | 0,5 | 0,4 | 0,5 | 0,2 |
| Be | nd | 2,2 | 2,2 | nd | nd | 2,0 | 2,4 | 2,1 | 0,8 | 0,6 | 0,7 | 0,7 | 1,3 |
| Sr | 326 | 518 | 441 | 571 | 434 | 770 | 780 | 325 | 486 | 309 | 361 | 281 | 278 |
| Ba | 570 | 775 | 575 | 514 | 585 | 539 | 814 | 592 | 320 | 361 | 593 | 277 | 187 |
| Sc | nd | 1,9 | 2,6 | nd | nd | 1,7 | 9,3 | 2,0 | 24,6 | 24,4 | 29,0 | 20,0 | 31,6 |
| Ga | nd | 14,8 | 17,5 | 20 | 22 | 18,8 | 22,2 | 14,7 | 18,0 | 16,6 | 16,3 | 15,4 | 18,7 |
| Y | 18 | 5,7 | 7,0 | < 20 | < 20 | 2,3 | 7,0 | 6,7 | 21,9 | 22,9 | 22,7 | 21,6 | 40,9 |
| Nb | < 10 | 6,4 | 3,9 | < 10 | 13 | 6,7 | 12,4 | 6,7 | 4,9 | 4,9 | 5,5 | 7,4 | 11,0 |
| Zr (RFA) | 133 | 84 | 74 | 86 | 142 | 111 | 149 | 105 | 77 | 91 | 84 | 97 | 169 |
| Hf | nd | 1,9 | 0,9 | nd | nd | 1,9 | 3,1 | 2,4 | 1,5 | 1,9 | 2,0 | 2,0 | 4,2 |
| Tl | nd | 0,30 | 0,20 | nd | nd | 0,25 | 0,37 | 0,31 | 0,22 | 0,27 | 0,71 | 0,24 | 0,07 |
| Pb | 12 | 32,4 | 19,8 | 12 | 19 | 14,0 | 13,1 | 16,9 | 9,7 | 3,5 | 5,4 | 1,2 | 4,4 |
| U | nd | 1,69 | 1,49 | nd | nd | 0,49 | 0,82 | 1,50 | 1,95 | 0,35 | 0,31 | 0,31 | 0,63 |
| Th | nd | 2,65 | 1,76 | nd | nd | 3,55 | 8,97 | 4,35 | 4,21 | 1,10 | 0,99 | 0,86 | 2,37 |
| La | nd | 8,75 | 8,50 | 17 | 26 | 14,76 | 34,95 | 16,21 | 15,51 | 7,62 | 7,78 | 5,35 | 13,83 |
| Ce | nd | 17,6 | 14,9 | nd | nd | 27,4 | 64,9 | 29,9 | 35,3 | 18,7 | 18,5 | 14,3 | 34,2 |
| Pr | nd | 1,75 | 1,63 | nd | nd | 2,84 | 6,96 | 2,95 | 4,42 | 2,55 | 2,51 | 2,11 | 4,65 |
| Nd | nd | 6,3 | 6,4 | nd | nd | 9,8 | 24,0 | 9,8 | 19,0 | 11,5 | 11,5 | 10,1 | 20,8 |
| Sm | nd | 1,18 | 1,34 | nd | nd | 1,46 | 3,67 | 1,53 | 4,06 | 2,98 | 2,99 | 2,79 | 5,33 |
| Eu | nd | 0,51 | 1,10 | nd | nd | 0,76 | 1,06 | 0,48 | 1,14 | 1,01 | 0,97 | 0,96 | 1,77 |
| Gd | nd | 0,99 | 1,25 | nd | nd | 0,94 | 2,54 | 1,17 | 3,76 | 3,25 | 3,36 | 3,17 | 6,01 |
| Tb | nd | 0,15 | 0,19 | nd | nd | 0,11 | 0,30 | 0,17 | 0,58 | 0,54 | 0,57 | 0,54 | 1,00 |
| Dy | nd | 0,83 | 1,13 | nd | nd | 0,48 | 1,45 | 1,00 | 3,56 | 3,56 | 3,69 | 3,48 | 6,46 |
| Ho | nd | 0,17 | 0,23 | nd | nd | 0,08 | 0,24 | 0,20 | 0,75 | 0,76 | 0,79 | 0,73 | 1,37 |
| Er | nd | 0,49 | 0,63 | nd | nd | 0,19 | 0,54 | 0,56 | 2,10 | 2,17 | 2,23 | 2,01 | 3,81 |
| Tm | nd | 0,08 | 0,09 | nd | nd | 0,02 | 0,06 | 0,09 | 0,30 | 0,33 | 0,33 | 0,29 | 0,56 |
| Yb | nd | 0,56 | 0,60 | nd | nd | 0,16 | 0,37 | 0,65 | 2,02 | 2,12 | 2,15 | 1,83 | 3,61 |
| Lu | nd | 0,09 | 0,09 | nd | nd | 0,03 | 0,06 | 0,11 | 0,29 | 0,32 | 0,32 | 0,27 | 0,53 |
| Mg# | 0,44 | 0,25 | 0,43 | 0,50 | 0,45 | 0,44 | 0,46 | 0,22 | 0,54 | 0,52 | 0,50 | 0,60 | 0,44 |
| Fe* | 0,56 | 0,75 | 0,57 | 0,50 | 0,55 | 0,56 | 0,54 | 0,78 | 0,46 | 0,48 | 0,50 | 0,40 | 0,56 |
| MALI | 0,05 | 3,94 | 0,25 | -1,92 | -1,79 | 1,11 | 1,61 | 3,91 | -2,85 | -4,00 | -0,85 | -5,78 | -2,71 |
| ASI | 0,98 | 1,05 | 1,05 | 0,95 | 1,01 | 1,10 | 1,12 | 1,10 | | | | | |
| $(Al/Na+K)_{molar}$ | 2,19 | 1,60 | 2,26 | 2,57 | 2,73 | 2,14 | 2,10 | 1,60 | 2,56 | 2,91 | 1,98 | 3,18 | 1,87 |
| Nd/Th | | 2,37 | 3,61 | | | 2,75 | 2,68 | 2,25 | | | | | |
| Sr/Y | 18,11 | 90,37 | 63,07 | | | 338,96 | 111,93 | 48,87 | | | | | |
| $La_N/Lu_N$ | | 9,78 | 10,06 | | | 59,90 | 62,82 | 15,82 | 5,47 | 2,44 | 2,54 | 2,09 | 2,69 |
| $La_N/Yb_N$ | | 10,63 | 9,63 | | | 62,28 | 64,12 | 16,88 | 5,23 | 2,44 | 2,45 | 1,98 | 2,60 |
| Eu/Eu* | | 1,41 | 2,54 | | | 1,84 | 1,00 | 1,05 | 0,87 | 0,98 | 0,93 | 0,98 | 0,95 |
| Q[4] | 112 | 164 | 140 | 125 | 162 | 169 | 118 | 205 | 52 | 60 | 11 | 13 | 33 |
| P[4] | -156 | -132 | -194 | -192 | -185 | -173 | -179 | -130 | -215 | -199 | -181 | -213 | -261 |
| Debon & LeFort[5] | granod. | granod. | tonalite | tonalite | tonalite | tonalite | tonalite | tonalite | monzog. | | | | |
| R1 De la Roche (1980) | 2119 | 2532 | 2552 | 2377 | 2723 | 2698 | 2115 | 2923 | 1683 | 1725 | 1021 | 1601 | 1402 |
| R2 De la Roche (1980) | 1056 | 617 | 989 | 1169 | 1030 | 840 | 930 | 551 | 1436 | 1464 | 1356 | 1792 | 1376 |
| De la Roche[6] | diorite | granod. | tonalite | diorite | tonalite | granod. | tonalite | granod. | gabbro | | | | |
| TAS C[7] | diorite | granite | granod. | diorite | diorite | granod. | diorite | granite | gabbro | | | | |

[1] determined by XRF

[2] determined by ICP-MS unless otherwise indicated

[3] all elements determined by XRF

[4] P = K-(Na+Ca), Q = Si/3-(K+Na+2Ca/3), Debon and Le Fort (1982)

[5] Classification according to Debon and LeFort (1982), granod. = granodiorite, monzog. = monzogabbro

[6] Classification according to De la Roche et al. (1980), in Batchelor and Bowden (1985)

[7] Classification according to Cox et al. (1979)

nd = not determined

The samples of the Mariinskiy complex are gabbroic to granitic in composition. The gabbro (sample 62) and the granodiorite of Andreevskiy (sample 55.1) are moderately enriched in the LREE ($La_N/Lu_N$ = 5.47 – 15.82) whereas samples 51.1

and 51.2 show a more pronounced LREE/HREE fractionation. Except for 51.1 the samples of the Mariinskiy complex do not display a Eu-anomaly (Table 1).

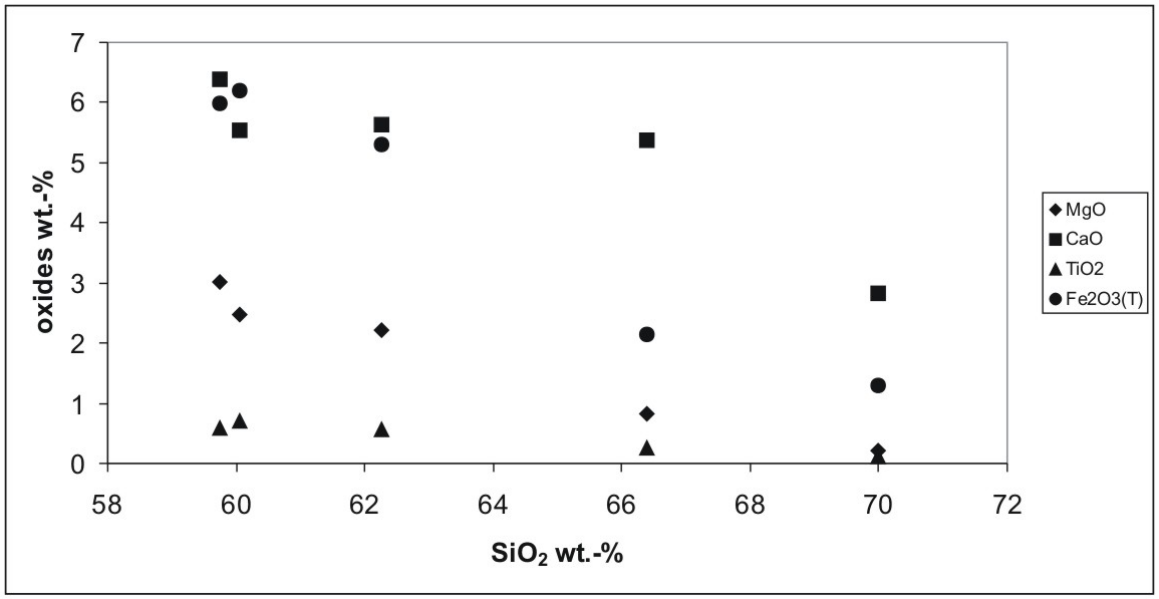


Fig. 2: $SiO_2$ vs. $TiO_2$, MgO, CaO, $Fe_2O_3^t$ (wt.-%) in granitoid samples of the Nishniy-Sanarskiy pluton.

In the basaltic rocks MgO is ≤ 5.28 wt.-% and the Mg# is relatively low ranging between 0.44 and 0.60, which indicates an evolved magma composition. In contrast to some of the granitoids LOI is between 1.53 and 4.86 wt.-% reflecting the presence of secondary hydrous minerals. Their formation may have caused mobilisation of alkalis. Accordingly, methods of classification (TAS, LeMaitre 1989) or discrimination (e.g. Verma et al. 2006) based entirely on major elements are not applied. Rather, HFSE that are immobile during alteration are preferentially used for discrimination (Table 2). The subalkaline basaltic composition of all samples (16.5, 16.6, 49 and 56) is shown by Nb/Y < 0.7 and Zr/(TiO2 * 10000) < 0.01 (Winchester and Floyd 1977). They have variable U- and Th-concentrations, and in general show slightly negative Nb- and Ti-anomalies in the primitive mantle-normalized plot (Fig. 3b). Except for sample 56 the basaltic rocks have positive Sr-anomalies. Positive Pb-anomalies can be observed in all samples, except sample 49. They all have flat REE patterns with only weak enrichment of the LREE ($La_N/Lu_N$ = 2.09 – 2.69, Table 1).

Table 2: Minor and trace element criteria used for classification and for indication of tectonic setting of basaltic rocks of the western Transuralian zone

| Criteria | Samples | | | |
|---|---|---|---|---|
| | 49 (Mariinskiy) | 56 (Mariinskiy) | 16.5 (N. Sanarskiy) | 16.6 (N. Sanarskiy) |
| Zr/TiO2 vs. Nb/Y, Winchester and Floyd (1977) | Basalt | Basalt | Basalt | Basalt |
| Zr-Ti-Y, Pearce and Cann (1973) | All: calc-alcali basalts, island arc tholeiites, MORB | | | |
| Zr/Y vs. Ti/Y, Pearce and Gale (1977) | All: plate margin basalts | | | |
| Zr-Y, Pearce (1983) | All: continental arc | | | |
| Ti/Zr vs. Nb/Y, Pearce (1982) | All: volcanic arc basalts | | | |
| Ti-Zr, Pearce (1982) | Volcanic arc | Within-plate | Volcanic arc | Volcanic arc |
| $MnO_2$-$TiO_2$-$P_2O_5$, Mullen (1983) | Oceanic island basalt, seamount alk. basalt | Island arc tholeiite | Island arc tholeiite | Island arc tholeiite |
| La-Y-Nb, Cabanis and Lecolle (1989) | Enriched MORB | Continental basalt | Continental basalt | Continental basalt |
| La/Nb, Condie (2003) | < 1.4, no subduction signature | < 1.4, no subduction signature | > 1.4, subduction signature | > 1.4, subduction signature |
| Zr-Nb-Y, Meschede (1986) | Within plate tholeiite, volcanic arc basalt | Within plate tholeiite, volcanic arc basalt | Within plate tholeiite, N-type MORB, volcanic arc basalt | Within plate tholeiite, N-type MORB, volcanic arc basalt |
| Classification tree, Vermeesch (2006) | All: island arc basalts | | | |

## Discussion

The petrographic and geochemical characteristics of the magmatic rocks from the western Transuralian zone yield information on origin of magmas as well as on magmatic diversification.

## Granitoids

The mineralogical and geochemical variation (i.e. decrease in $TiO_2$, MgO, $Fe_2O_3^t$ and CaO with increasing $SiO_2$) observed in samples 11.1 – 11.3, 13 and 21.1 indicates that fractionation of hornblende is an important factor of magmatic diversification in the Nishniy Sanarskiy pluton. Despite of such process and despite of the differences between the various granitoids of the study area, their magnesian, calcic to calc-alkaline character is consistent with a formation in a cordilleran or island-arc setting (Frost et al. 2001). Derivation of melts from descending oceanic crust may also be supported by trace element composition. All samples from the four granitoid and gabbro occurrences show arc signatures like negative Nb- and Ti- , as well as positive Sr-anomalies in the primitive mantle normalized element plot (Fig. 3a) (Zhang et al. 2009, references therein). The latter is in line with Sr > 300 ppm, Sr/Y > 20, low Nb (< 11 ppm) as well as enriched LREE in most of these samples (Table 1). These criteria are also considered as characteristic of slab derived Al-rich granitoid melts (Drummond and Defant 1990). In a Rb vs. Nb+Y-plot all granitoid and gabbro samples, including those with LOI < 0.53 wt.-%, for which later transport of alkalis is

considered as negligible, also plot in the “volcanic arc granite” field (Fig. 4, Table 1, Pearce et al. 1984, Pearce 1996).

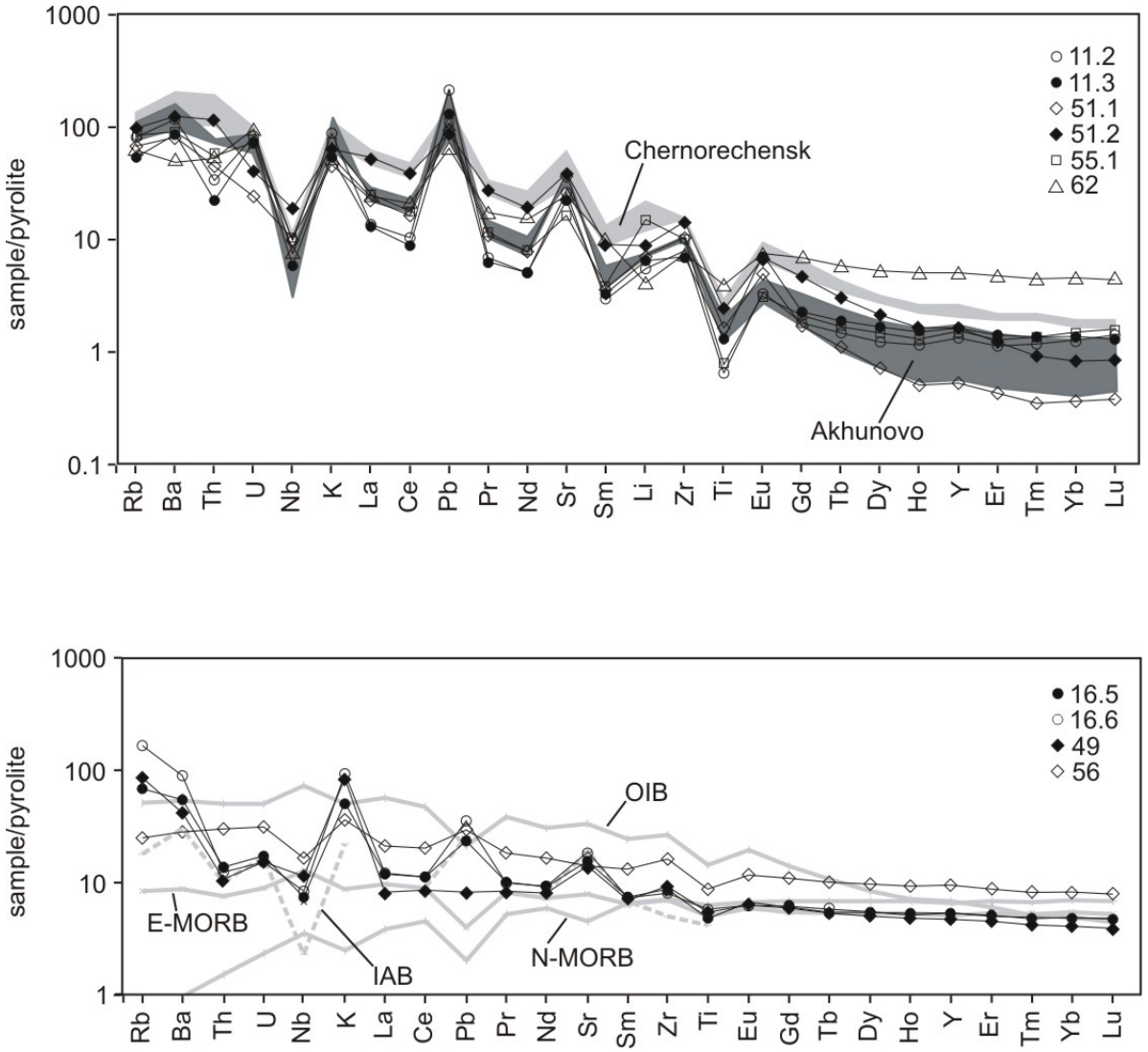


Fig. 3: Primitive mantle normalized plots (relative to pyrolite of McDonough and Sun 1995), A, plot for granitoid samples of the Nishniy Sanarskiy (11.2, 11.3) and Mariinskiy complexes (51.1, 51.2, 55.1, 62). Light and dark grey fields are compositional ranges of the granitoids of Chernorechensk and Akhunovo from the Easturalian and Magnitogorsk zone, respectively (Bea et al. 2002).
B, plot of basaltic samples of the Nishniy Sanarskiy (16.5, 16.6) and Mariinskiy complexes (49, 56).Grey lines denote representative oceanic magmatic products from Sun and McDonough (1989), E-MORB = enriched mid ocean ridge basalt, N-MORB = normal mid ocean ridge basalt, OIB = ocean island basalt, IAB = island arc basalt.

In contrast to this, the granitoids show other features, which are characteristic of melts formed in the continental crust, such as strongly positive Pb-anomalies of high Ba values (Fig. 3a). A positive U-anomaly in the plutons of Nishniy Sanarskiy and

Andreevskiy are also indicative of melt contribution from crustal sources, as well as a positive Li-anomaly in the latter pluton.

Influence of crustal sources is also indicated by Nd/Th ratios of all granitoids clustering around a value of Nd/Th = 2.6 (Table 1), which is considered to show control of trace element abundance by monazite in the source (Bea and Montero 1999).

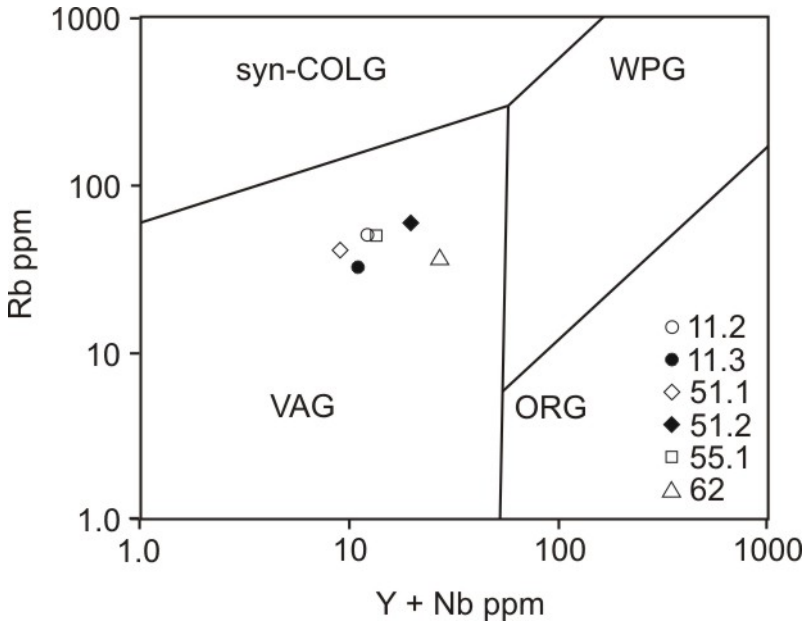


Fig. 4: Rb vs. Nb + Y plot for granitoid and gabbro samples of the western Transuralian zone (Nishniy Sanarskiy complex 11.2, 11.3, Mariinskiy complex 51.1, 51.2, 55.1, 62, VAG = volcanic arc granites, ORG = ocean ridge granites, WPG= within-plate granite, syn-COLG = syn-collision granites, Pearce et al. 1984)

In the Mariinskiy pluton garnet forms anhedral grains with irregular lobate grain boundaries, which are indicative of dissolution. Growth of these crystals in the melt as phenocrysts appears as unlikely. Though mineral chemical data of garnet, which could help to identify the origin of garnet more precisely, are not available, it can be inferred that they represent relics of xenocrysts entrained from a metamorphic rock or peritectic garnet formed during dehydration melting of biotite in the source of the granitoid melt. In both cases, the observation of garnet points to the contribution of aluminous metamorphic rocks to the tonalite of Mariinskiy.

Geochemical data thus support the idea that the granitoids reflect mixing of slab derived melts and melts generated in the continental crust. This is also well constrained in the $R_1$-$R_2$-plot (Batchelor and Bowden 1985, Fig. 5). Sample 55.1,

which shows most affinity to crustal melts, plots in the field of anatectic melts, while most other samples fall in the field of destructive plate margins. Deviations from this field may best be explained by contributions from metasedimentary sources. All compositional characteristics are most consistent with a formation in an Andean type magmatic arc.

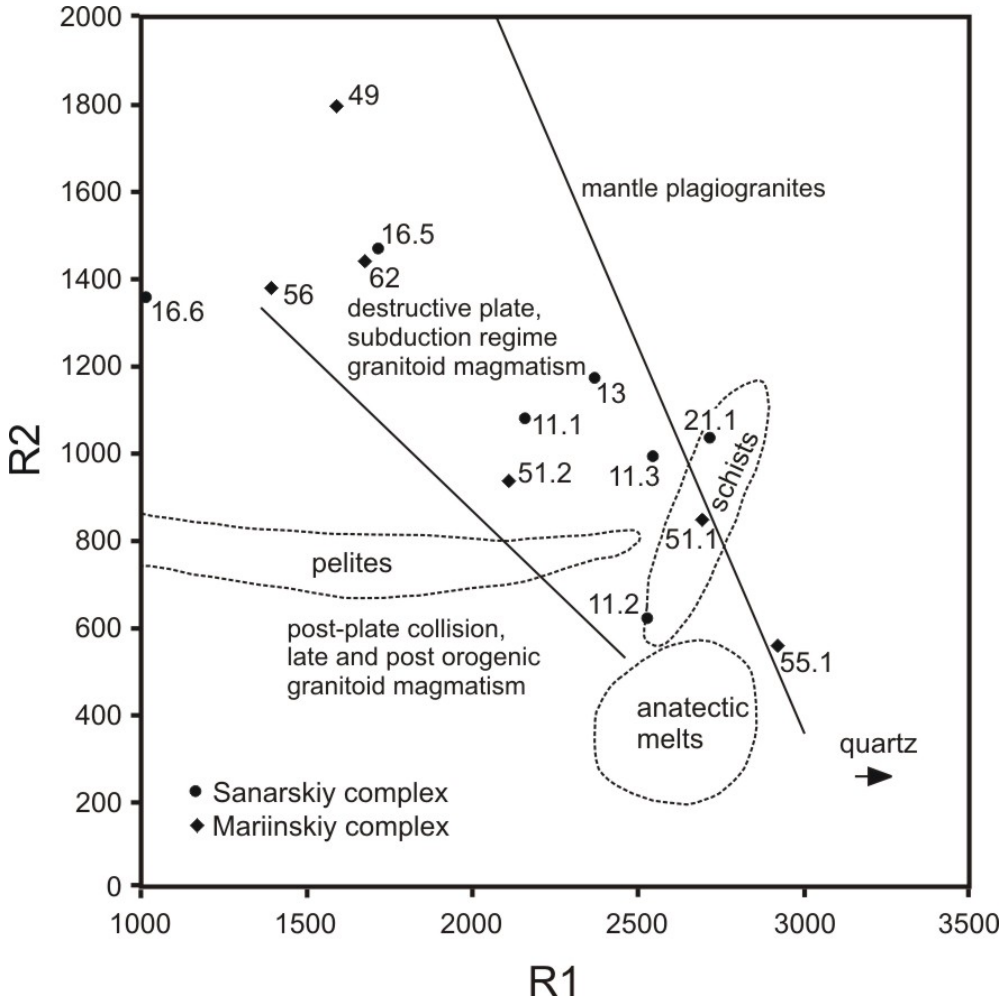


Fig. 5: De la Roche R1-R2 multicationic diagram adapted from Batchelor and Bowden (1985) displaying compositions of granitoids (Nishniy Sanarskiy complex 11.1, 11.2, 11.3, 13, 16.5, 16.6, 21.1, Mariinskiy complex 49, 51.1, 51.2, 55.1, 62) of potential metasedimentary sources and of anatectic melts. The fields of mantle plagiogranites, subduction regime granitoid magmatism, late and post orogenic granitoid magmatism are according to the tectonometamorphic divisions postulated by Pitcher (1979, 1982).

The granitoids of the Mariinskiy complex as well as of the Nishniy Sanarskiy pluton have a tendency towards lower K-concentrations (Fig. 6) but in general show element patterns, which are similar to those of the Akhunovo or Chernorechensk

complex in the Easturalian zone (Fig. 3a). Granitoids of these plutons are characterized as subduction-related as well (Bea et al. 2002). Their ages (i.e. Akhunovo 365 ± 3, 365 ±9 Ma, Chernorechensk 354 ± 7 Ma, Bea et al. 2002) are within error identical to the ages determined for the plutons of Nishniy Sanarskiy (357 ± 6 Ma) and Mariinskiy (364 ± 14 Ma, Gronen 2013).

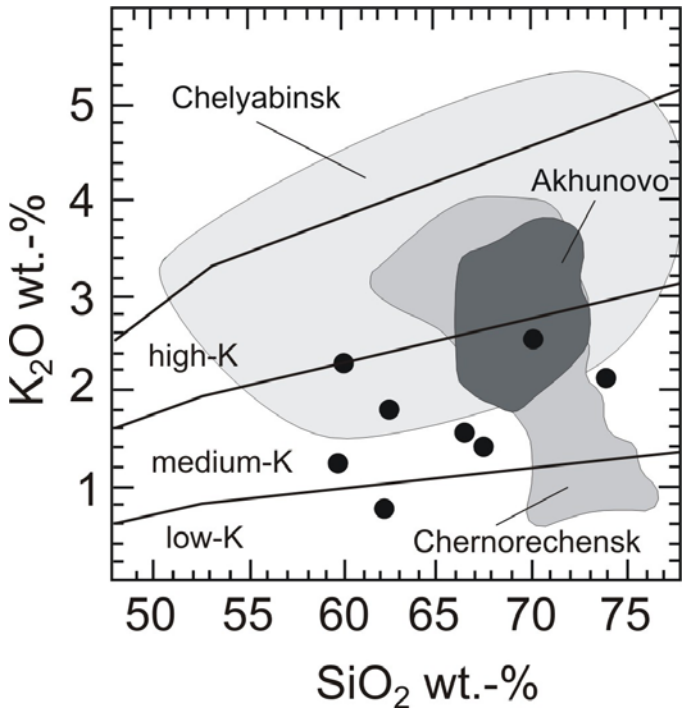


Fig. 6: $K_2O$ vs. $SiO_2$ plot (LeMaitre 1989), comparison of compositions of granitoids from the western Transuralian zone (Nishniy Sanarskiy and Mariinskiy complexes, this study), the Easturalian (Chelyabinsk, Chernorechensk) and the Magnitogorsk zone (Akhunovo) in the southern Urals (Bea et al. 2002).

Basalts

Primitive mantle normalized element patterns can be used to discuss potential sources of the basaltic rocks. Exceptionally high values of Rb and K in all basalt samples could be due to metamorphic growth of hydrous minerals and will not be used for discrimination of the data set. Apart from that, most patterns are similar to volcanic arc basalts (Fig. 3b). A dominant contribution of slab derived melts to these rocks, in particular to the dyke samples 16.5 and 16.6, is also indicated by other minor- and trace element criteria (Table 2). Due to a weak Nb- and lack of a Pb-anomaly sample 49 shows least similarity to volcanic arc basalts. Rather, the data are more consistent with other settings, such as MOR or within plate settings (Fig. 3b, Table 2). It should be noted that this sample is from an occurrence, which is not a

dyke but has uncertain contact relationships. Possibly, the basalt body represented by sample 49 is a domain of former oceanic crust.

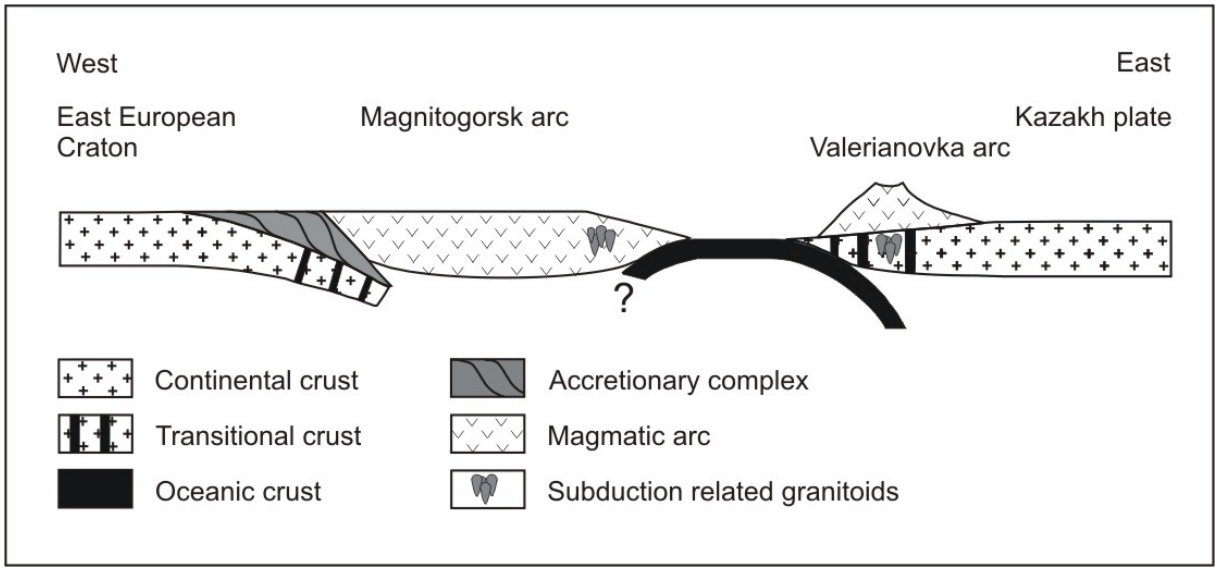


Fig. 7: Simplified profile depicting the tectonic constellation during the Uralian orogeny in Early Carboniferous times, adapted from Herrington et al. (2005) and Alvarez-Marrón (2002). The Devonian Magnitogorsk arc was affected by platform sedimentation during the Carboniferous. Subduction-related granitoid magmatism in the Andean type Valerianovka arc on the continental margin of the Kazakh plate (now Transuralian zone) and in the oceanic zone to the west (now Easturalian zone) points to contemporaneous subduction in both areas.

Tectonic Setting

The association of basalts formed in an oceanic setting with basalts and granitoids typical of a magmatic arc setting supports the idea that the Transuralian zone represents the former active margin of the Kazakh plate (Brown et al. 2002, Puchkov 2000, Herrington et al. 2005, Görtz and Hielscher 2010). In such setting, transitional oceanic crust may have existed, which could explain the existence of different types of basalts (Fig. 7). The subduction-related rocks of the western Transuralian zone can then be considered to be plutonic and subvolcanic parts of the Valerianovka magmatic arc, which is also represented by volcanosedimentary successions of the Valerianovka zone in the eastern Transuralian zone (Puchkov 1997, 2000, Herrington et al. 2005). These successions record mainly Carboniferous volcanic activity in the Valerianovka zone (Puchkov 1997). If this reflects the lifetime of the Valerianovka arc, the granitoids of the western Transuralian zone (Nishniy Sanarskiy,

357 ± 6 Ma and Mariinskiy, 364 ± 14 Ma, Gronen 2013) belong to the earlier products in the history of the arc.

The pervasive, though low, degree of deformation reflected in textures of all granitoid samples studied here points to a pre- to syntectonic origin. In line with the ages known for the granitoids, strike slip deformation observed in the Transuralian zone must have a maximum age of c. 360 Ma. This is compatible with a recent model by Görtz and Hielscher (2010) who state that strike slip tectonism took place in Permian times as response to a relative plate motion of the Kazakh plate and the East-European Craton.

## Conclusions

The compositional variability of the Nishniy Sanarskiy pluton is mainly caused by fractionation of hornblende, which is an important factor of magmatic diversification. Despite of their close spatial association, the plutons of Andreevskiy and Mariinskiy witin the Mariinskiy complex have different sources. Crustal melts contribute to a larger degree to the pluton of Andreevskiy.

The mineralogical as well as major and trace element characteristics of all granitoids in the Mariinskiy and Nishniy Sanarskiy complexes indicate formation by mixing of subduction-related melts and melts generated in the crust, which is most consistent with an Andean type magmatic arc setting. This and compositional characteristics of subalkaline basaltic rocks support ideas that the western Transuralian zone contains remnants of the Valerianovka Andean type magmatic arc along the margin of the Kazakh continent. In age and composition the granitoids of the western Transuralian zone are similar to subduction-related intrusives of the Magnitogorsk and Easturalian zone to the west of the study area. This points to contemporaneous subduction of the Uralian ocean underneath the Magnitogorsk arc as well as the Kazakh continent in late Devonian to early Carboniferous times. Similar to the evolution of the Easturalian zone, the western Transuralian zone was affected by intensive post-magmatic strike-slip tectonism.

References

Alvarez-Marrón, J. (2002) Tectonic processes during collisional orogenesis from comparison of the southern Uralides with the Central Variscides. In: Brown, D., Juhlin, C., Puchkov, V. (eds.) Mountain building in the Uralides: Pangea to the present. Geophysical Monograph 132, American Geophysical Union, 83 – 99.

Batchelor, R.A., Bowden, P. (1985) Petrogenetic interpretation of granitoid rock series using multicationic parameters. Chemical Geology 48, 43–55.

Bea, F., Montero, P. (1999) Behavior of accessory phases and redistribution of Zr, REE, Y, Th, and U during metamorphism and partial melting of metapelites in the lower crust: An example from the Kinzigite formation of Ivrea-Verbano, NW Italy. Geochimica et Cosmochimica Acta 63, 1133 – 1153.

Bea, F., Fershtater, G., Montero, P., Smirnov, V., Zinkova, E. (1997) Generation and evolution of subduction-related batholiths from the central Urals: Constraints on the P-T history of the Uralian orogen: Tectonophysics 276, 103 – 116.

Bea, F., Fershtater, G.B., Montero, P. (2002) Granitoids of the Uralides : Implications for the Evolution of the Orogen. In: Brown, D., Juhlin, C., Puchkov, V. (eds.) Mountain building in the Uralides: Pangea to the present. Geophysical Monograph 132, American Geophysical Union, 211 - 232

Brown, D., Alvarez-Marrón, J., Perez-Estaun, A., Gorozhanina, Y., Baryshev, V., Puchkov, V. (1997) Geometric and kinematic evolution of the foreland thrust and fold belt in the Southern Urals. Tectonics 16, 551 – 562.

Brown, D., Juhlin, C., Tryggvason, A., Steer, D., Ayarza, P., Beckholmen, M., Rybalka, A., Bliznetsov, M. (2002) The crustal architecture of the southern and middle Urals from the URSEIS, ESRU and Alapaev reflection seismic surveys. In: Brown, D., Juhlin, C., Puchkov, V. (eds.) Mountain building in the Uralides: Pangea to the present. Geophysical Monograph 132, American Geophysical Union, 33 – 48.

Brown, D., Juhlin, C., Ayala, C., Tryggvason, A., Bea, F., Alvarez-Marron, J., Carbonell, R., Seward, D., Glasmacher, U., Puchkov, V., Perez-Estaun, A. (2008) Mountain building processes during continent-continent collision in the Uralides. Earth Science Reviews 89, 177-195.

Cabanis, B., Lecolle, M. (1989) Le diagramme La/10 – Y/15 – Nb/8: un outil pour la discrimination des series volcaniques et la mise en evidence des processus de melange et/ou de contamination crustale. C.R. Acad. Sci. Ser. II 309, 2023 – 2029.

Condie, K.C. (2003) Incompatible element ratios in oceanic basalts and komatiites: tracking deep mantle sources and continent growth rates with time. Geochemistry, Geophysics, Geosystems 4, no. 1, 1005, doi: 10.1029/2002GC000333.

Cox, K.G., Bell, J.D., Pankhurst, R.J. (1979) The interpretation of igneous rocks. George, Allen and Unwin, London.

Debon, F., LeFort, P. (1982) A chemical-mineralogical classification of common plutonic rock association. Transactions of the Royal Society of Edinburgh: Earth Sciences 73,135 – 149.

De la Roche, H., Leterrier, J., Grande Claude, P., Marchal, M. (1980) A classification of volcanic and plutonic rocks using R1 – R2 diagrams and major element analyses – its relationship and current nomenclature. Chemical Geology 29, 183 – 210.

Drummond, M.S., Defant, M.J. (1990) A model for trondhjemite-tonalite-dacite genesis and crustal growth via slapb melting: Archean to modern comparisons. Journal of Geophysical Research 95 (No. B13), 21503 – 21521.

Echtler HP, Ivanov KS, Ronkin YuL, Karsten LA, Hetzel R, Noskov AG (1997) The tectono-metamorphic evolution of gneiss complexes in the Middle Urals, Russia: a reappraisal. Tectonophysics 276: 229-251

Fershtater, G.B., Montero, P., Borodina, N.S., Pushkarev, E.V., Smirnov, V., Zinkova, E., Bea, F. (1997) Uralian magmatism: An overview. Tectonophysics 276, 87 – 102.

Frost R.B., Barnes, C.G., Collins, W.J., Arculus, R.J., Ellis, D.J., Frost, C.D. (2001) A geochemical classification for granitic rocks. Journal of Petrology 42, 2033 – 2048.

Gerdes, A., Montero, P., Bea, F., Fershater, G., Borodina, N., Osipova, T., Shardakova, G. (2002) Peraluminous granites frequently with mantle-like isotope compositions: the continental-type Murzinka and Dzhabyk batholiths of the eastern Urals. International Journal of Earth Sciences 91, 3 – 19.

Giese U, Glasmacher UA, Kozlov VI, Matenaar I, Puchkov VN, Stroink L, Bauer W, Ladage S, Walter R (1999) Structural framework of the Bashkirian Anticlinorium, SW Urals. Geologische Rundschau 87, 526-544.

Glasmacher, U.A., Bauer, W., Giese, U., Reynolds, P., Kober, B., Puchkov, V.N., Stroink, L., Alekseev, A., Willner, A. (2001) The metamorphic complex of Beloretzk, SW Urals, Russia: a terrane with a polyphase Meso- to Neoproterozoic thermo-dynamic evolution. Precambrian Research 110: 185 – 213.

Görz, I., Buschmann, B., Kroner, U., Hauer, R., Henning, D. (2009) The Permian emplacement of granite-gneiss complexes in the East Uralian Zone and implications on the geodynamics of the Uralides. Tectonophysics 467, 119 – 130.

Görz, I., Hielscher, P. (2010) An explicit plate kinematic model for the orogeny in the southern Uralides. Tectonophysics 493, 1 -26.

Gronen. L. (2013) U-Pb-Altersbestimmung von metamorphen und magmatischen Prozessen in der Transuralzone, Russland, unpublished MSc-thesis RWTH Aachen University, 64 p., (in German)

Herrington, R.J., Zaykov, V.V., Maslennikov, V.V., Brown, D., Puchkov, V.N. (2005) Mineral deposits of the Urals and links to geodynamic evolution. Economic Geology 100th Anniversary Volume, 1069 – 1095.

Keilman, G.A. (1974) Migmatite complexes of mobile belts. Nedra, 200 p. (in Russian)

LeMaitre, R.W. (1989) A classification of igneous rocks and glossary of terms. Oxford: Blackwell, 193 pp.

Mamayev, N.F. (1965) Geological structure and history developed of the eastern slope of the South-Urals. Sverdlovsk, The Urals branch of Academy of Sciences of the USSR, 169 p. (in Russian)

McDonough, W.F., Sun, S.-s. (1995) The composition of the earth. Chemical Geology 120, 223 - 253

Meschede, M. (1986) A method of discriminating between different types of mid-ocean ridge basalts and continental tholeiites with the Nb-Zr-Y diagram. Chemical Geology 56, 207 - 218

Montero, P., Bea, F., Gerdes, A., Fershtater, G., Zinkova, E., Borodina, N., Osipova, T., Smirnov, V. (2000) Single-zircon evaporation ages and Rb-Sr dating of four major Variscan batholiths of the Urals: A perspective on the timing of deformation and granite generation. Tectonophysics 317, 93 – 108.

Mullen, E.D. (1983) $MnO/TiO_2/P_2O_5$: a minor element discriminant for basaltic rocks of oceanic environments and its implications for petrogenesis. Earth and Planetary Science Letters 62, 53 - 62

Nalivkin, D.V. (1965) Geological Map 1:2500000. The Ministry of Geology of the USSR (in Russian)

Ovchinnikov, L.N., Stepanov, A.I., Krasnobaev, A.A., Dunaev, W.A. (1969) Review of absolute age data for geological formations of the Urals. In: Trans. 2nd Ural. Petrogr. Meet., 173 – 204, Sverdlovsk (in Russian).

Passchier, C.W., Trouw, R.A.J. (1996) Microtectonics. Springer, Berlin Heidelberg New York, 304 p..

Pearce, J.A. (1996) Sources and settings of granitic rocks. Episodes 19, 120 – 125.

Pearce, J.A. (1983) Role of the sub-continental lithosphere in magma genesis at active continental margins. In: Hawkesworth, C.J., Norry, M.J. (eds.) Continental basalts and mantle xenoliths. Shiva, Nantwich, 230 – 249.

Pearce, J.A. (1982) Trace element characteristics of lavas from destructive plate boundaries. In: Thorpe, R.S. (ed.) Andesites. Wiley, Chichester, 525 – 548.

Pearce, J.A., Cann, J.R. (1973) Tectonic setting of basic volcanic rocks determined using trace element analyses. Earth and Planetary Science Letters 19, 290 – 300.

Pearce, J.A., Gale, G.H. (1977) Identification of ore-deposition environment from trace element geochemistry of associated igneous host rocks. Geol. Soc. Spec. Publ. 7, 14 – 24.

Pearce, J.A., Harris, N.B.W., Tindle, A.G. (1984) Trace element discrimination diagrams for the tectonic interpretation of granitic rocks. Journal of Petrology 25, 956 – 983.

Pitcher, W.S. (1979) Comments on the geological environments of granites. In: Atherton, M.P., Tarney, J. (eds.) Origin of granite batholiths – geochemical evidence. Shiva, Orpington, 1 – 8.

Pitcher, W.S. (1982) Granite type and tectonic environment. In: Hsu, K.J. (ed.) Mountain building processes. Academic press, London, 19 – 40.

Puchkov, V.N. (1997) Structure and geodynamics of the Uralian orogen, in: Burg, J.P., Ford, M., (Eds.), Orogeny through time. Geolical Society Special Publication 121 , pp. 201-196.

Puchkov, V.N. (2000) Palaeogeodynamics of the central and southern Urals: Pauria, Ufa, 145 p. (in Russian)

Puchkov, V.N. (2009a) The evolution of the Uralian orogen. In: Murphy, J.B., Keppie, J.D., Hynes, A.J. (eds.) Ancient orogens and modern analogues. Geological Dociety, London, Special Publications 327, 161 – 195.

Puchkov, V. N. (2009b) The diachronous (step-wise) arc-continent collision in the Urals. Tectonophysics 479, 175 – 184.

Rollinson, H. (1993) Using geochemical data: evaluation, presentation, interpretation. Longman, UK, 352 p..

Ronkin Yu.L., Lepikhina O. P., Golik S.V., Zhuravlyov D. Z., Popova O. Yu. (2005) The multielement analysis of geological samples by acid decomposition and finished by HR ICP-MS Element2. Information collection of scientific works of Institute of Geology and Geochemistry. Year-book-2004. IGG URO Russian Academy of Sciences. Yekaterinburg. 423 – 433. (in Russian)

Sindern, S., Warnsloh, J.M., Trautwein-Bruns, U., Chatziliadou, M., Becker, S., Yüceer, S., Hilgers, C., Kramm, U. (2008) Geochemical composition of sedimentary rocks and imprint of hydrothermal fluid flow at the Variscan front – an example from the RWTH-1 well (Germany). Zeitschrift der Deutschen Gesellschaft für Geowissenschaften 159, 623 – 640.

Sun, S.-s., McDonough, W.F. (1989) Chemical and isotopic systematics of oceanic basalts: implications for mantle composition and processes. In: Saunders, A.D:,

Norry, M.J. (eds.) Magmatism in the Ocean Basins, Geological Society Special Publications No. 42, 313 – 345.

Verma, S.P., Guevara, M., Agrawal, S. (2006) Discriminating four tectonic settings: Five new geochemical diagrams for basic and ultrabasic volcanic rocks based on log-ratio transformation of major-element data. J. Earth Syst. Sci 115, 485 – 528.

Vermeesch, P. (2006) Tectonic discrimination of basalts with classification trees. Geochimica et Cosmochimica Acta 70, 1839 – 1848.

Winchester, J.A., Floyd, P.A. (1977) Geochemical discrimination of different magmaseries and their differentiation products using immobile elements. Chemical Geology 20, 325 – 343.

Zhang, S-H., Zhao, Y., Kröner, A., Liu, X-M., Xie, L-W., Chen, F-K. (2009) Early Permian plutons from the northern North China Block: constraints on continental arc evolution and convergent margin magmatism related to the Central Asian Orogenic Belt. International Journal of Earth Sciences 98, 1441 – 1467.

9.

Kolb, J., Sindern, S., Kisters, A.F.M., Meyer, M., Hoernes, S., Schneider, J. (2005) Timing of orogenic gold mineralization at Kochkar in the evolution of the East Uralian Granite-Gneiss terrane. Mineralium Deposita 40, 473 – 491.

With permission of Springer.

Re-use in thesis granted by Springer, Rights and Permissions, Tiergartenstrasse 17, 69121 Heidelberg, Germany, permission letter 14th of October 2015.

Mineralium Deposita (2005) 40: 473–491
DOI 10.1007/s00126-005-0020-z

ARTICLE

Jochen Kolb · Sven Sindern · Alexander F. M. Kisters
F. Michael Meyer · Stephan Hoernes · Jens Schneider

# Timing of Uralian orogenic gold mineralization at Kochkar in the evolution of the East Uralian granite-gneiss terrane

Received: 3 December 2004 / Accepted: 27 July 2005 / Published online: 11 October 2005
© Springer-Verlag 2005

**Abstract** Gold mineralization at Kochkar (Urals, Russia) is hosted mainly by quartz lodes, which developed at lithological contacts between mafic dikes and granitoids of the Plast massif during late Carboniferous to early Permian, regional E–W compression in the East Uralian Zone (EUZ). The alteration mineralogy in mafic dikes comprises biotite, actinolite, albite, K-feldspar, quartz, epidote, tourmaline, sericite, pyrite, arsenopyrite, chalcopyrite, sphalerite, fahlores, galena, bismuthinite, and gold, and in Plast granitoids quartz, sericite, calcite, epidote, and ore minerals. Geochemically, an enrichment of Si, K, Rb, Ba, S, base metals, W, and Au can be observed. The ore fluid had $\delta^{18}O$ values between 8.2‰ and 9.5‰ typical for metamorphic or deep magmatic fluids. The tectonometamorphic evolution of the EUZ is marked by peak metamorphic conditions at 635 ± 40°C and 5–6 kbar through 500 ± 20°C during gold mineralization, and 300–350°C and 2–3 kbar. The last event was dated on a late, barren quartz vein formed during greenschist facies metamorphism at 265 ± 3 Ma by the Rb–Sr method. Fluids related to this overprint had a $\delta^{18}O$ value of 5.2‰ and an initial $^{87}Sr/^{86}Sr$ ratio of 0.70685 indicating that they are largely equilibrated with metamorphic lithologies of the EUZ. The Plast granitoids and the adjacent Borisov granite, which was dated at 358 ± 23 Ma (U–Pb zircon age), have an adakitic character. This, together with the arc-signature of the mafic dikes, supports the setting of the EUZ within the Valerianovsky continental arc. Eastward subduction of the Uralian Ocean below this arc began during the late Devonian to early Carboniferous. Between 320 and 265 Ma, the oblique closure of the ocean resulted in doming of granitoid massifs in a sinistral transpressional regime, subsequent retrograde gold mineralization during E–W compression and a later greenschist facies overprint. This long-lasting retrograde evolution of the EUZ was caused by the lack of postcollisional collapse. Heat for a "deep-later" type of metamorphism and triggering the auriferous fluid system was supplied by radiogenic heating of an overthickened crust. The greenschist facies overprint at Kochkar and coeval crustal melting in the EUZ was additionally initiated by local external heating of the terrane. This could have been caused by syn- to postcollisional slab rollback or delamination resulting in magmatic underplating of the EUZ, which postdates orogenic gold mineralization at Kochkar. The tectonic interpretation of the EUZ indicates that gold mineralization at Kochkar formed in a mid-crustal environment of a continental magmatic arc at the cessation of active subduction predating post orogenic plutonism.

**Keywords** Kochkar · Orogenic gold · Ural · East Uralian Zone

Editorial handling: A. Boyce

J. Kolb (✉) · S. Sindern · F. Michael Meyer
Institute of Mineralogy and Economic Geology,
RWTH Aachen University,
Wüllnerstr. 2, 52056 Aachen, Germany
E-mail: kolb@rwth-aachen.de
Tel.: +49-241-8095773
Fax: +49-241-8092153

S. Sindern
Institute for Mineralogy, Münster University,
Corrensstr. 24, 48149 Münster, Germany

A. F. M. Kisters
Department of Geology, University of Stellenbosch,
Private Bag X1, Matieland 7602, South Africa

S. Hoernes
Institute for Mineralogy and Petrology, Bonn University,
Poppelsdorfer Schloß, 53115 Bonn, Germany

J. Schneider
Institute for Geoscience, Giessen University,
Senckenbergstraße 3, 35390 Gießen, Germany

## Introduction

Historical gold mining in the late-Paleozoic Uralides started 250 years ago with about 400 t gold produced to

date (Anonymous 1996). The majority of the gold was mined from placer deposits and orogenic gold deposits. Gold deposits are irregularly distributed with respect to tectonic units such as the Main Uralian Fault (MUF) and the East Uralian Zone (EUZ) (Kisters et al. 1999; Sazonov et al. 2001). The MUF controls the distribution of important orogenic gold districts hosted by lower- to middle-Paleozoic island arc and ophiolite complexes (Kisters et al. 1999). This is a typical setting for Phanerozoic orogenic gold deposits (Goldfarb et al. 2001) and was used to define a geodynamic model for these deposits, typified by transpressive accretion of allochthonous terranes to one another or a continental margin, emphasizing Cordilleran style tectonics (Kerrich et al. 2000). Gold mineralization in general is related to active subduction late in the orogenic evolution and is associated with terrane exhumation (Goldfarb et al. 1998; Bierlein and Crowe 2000). A thermal anomaly triggering the auriferous fluid plumbing system is suggested by contemporaneous emplacement of granitoids and metamorphism, which was possibly formed by a change in the subduction regime, by either slab rollback, delamination of the mantle lithosphere, or subduction of a slab window (Goldfarb et al. 1998). Structurally controlled fluid flow in major shear zones during orogenic gold mineralization coincides with the shift from convergent thrust to transcurrent tectonics (Goldfarb et al. 1991; Kisters et al. 1999; Kolb and Meyer 2001). Phanerozoic orogenic gold mineralization is, in most cases, postpeak metamorphic and predates granitoid intrusions by around 10 m.y. (Bierlein and Crowe 2000; Goldfarb et al. 2001).

In the EUZ, large orogenic gold deposits such as Kochkar are hosted in granite-gneiss complexes that have intruded supracrustal rocks (Seravkin et al. 1992; Kisters et al. 2000). Although these deposits share many similarities with other orogenic gold deposits worldwide, they are not directly associated with transcrustal shear zones (Kisters et al. 2000). The emplacement of voluminous Permian granitoids in the EUZ is interpreted as an Ural-wide melting event (Fershtater et al. 1997; Bea et al. 1997, 2002; Gerdes et al. 2002), which was possibly responsible for triggering fluid plumbing systems (Kisters et al. 1999; Kolb and Meyer 2001).

In this paper, we use geochemical, petrological, and isotope data to describe the magmatic and tectonometamorphic evolution of the EUZ. The main aim is to define the position of gold mineralization in Kochkar in a model for the orogenic evolution of the Urals and compare this to the typical setting of Phanerozoic orogenic gold deposits, associated with transcrustal shear zones.

## Regional geology

The Urals form a bivergent fold-and-thrust belt wedged between the East European Platform in the west and a complex of microplates and terranes of the Siberian and Kazakhstan cratons in the east. This linear, N–S trending orogenic belt formed during convergence and final E–W collision during the late Paleozoic (Zonenshain et al. 1984, 1990; Echtler et al. 1996; Puchkov 1997). Its southern part (south of 56°N) can be subdivided from west to east into four tectonic units (Brown et al. 2002): the foreland thrust and fold belt, the Magnitogorsk and Tagil volcanic arcs, the EUZ, and the Trans-Uralian Zone (TUZ) (Fig. 1). The foreland thrust and fold belt is separated from the Magnitogorsk and Tagil volcanic arcs by the 2,500 km long MUF, which is generally regarded as the principal suture zone. In the southern Urals, subduction towards the east commenced in the Devonian beneath the Magnitogorsk volcanic arc (Puchkov 1997; Echtler et al. 1997). The NW–SE accretion of the Magnitogorsk volcanic arc and the East European Platform occurred along the MUF in Late Devonian to Early Carboniferous times (Echtler et al. 1997; Brown et al. 1998; Hetzel et al. 1998; Sazonov et al. 2001). Intrusion of a post tectonic batholith, dated at 327 ± 2 Ma, into the MUF marks the end of tectonic activity in that region (Montero et al. 2000). Subsequently, closure of the Uralian Ocean occurred to the east of the Magnitogorsk volcanic arc with E–W accretion of various terranes of the EUZ and TUZ (Puchkov 1997; Brown et al. 1998; Friberg et al. 2000). The EUZ is separated in the west from the Magnitogorsk volcanic arc by a serpentinitic mélange zone referred to as East Magnitogorsk Fault, and in the east from the TUZ by the Troitsk Fault (Fig. 1; Puchkov 1997; Ayarza et al. 2000). Some authors have suggested westward subduction at the boundary between EUZ and TUZ based on a west dipping seismic reflector (i.e. the Kartaly reflection sequence: Echtler et al. 1997; Kimbell et al. 2002). In contrast to this view, Zonenshain et al. (1990) and Bea et al. (2002) proposed that eastward subduction occurred beneath an Andean-type arc on the Siberian and Kazakhstan cratons, namely the Valerianovsky arc, which is represented by lithologies of the EUZ and the TUZ. Final closure occurred at ~300 Ma with the reactivation of terrane-bounding faults as strike-slip faults and the intrusion of Permian late- to post-orogenic granitoids (Bea et al. 2002). The post tectonic Dzhabyk granite intruded the Troitsk fault at 291 ± 4 Ma. This age is thought to mark the end of tectonic activity in the southern Urals (Montero et al. 2000).

### Geology of the EUZS

In the EUZ, most of the large orogenic gold deposits such as Kochkar are hosted by granite-gneiss complexes that are intrusive into mafic- to intermediate metavolcanic, metavolcanoclastic and metasedimentary rocks (Seravkin et al. 1992). The supracrustal rocks strike N–S and are subvertical, parallel to the overall trend of the EUZ as a result of shortening during the upper-Paleozoic assembly of the southern Urals. The granite-gneiss

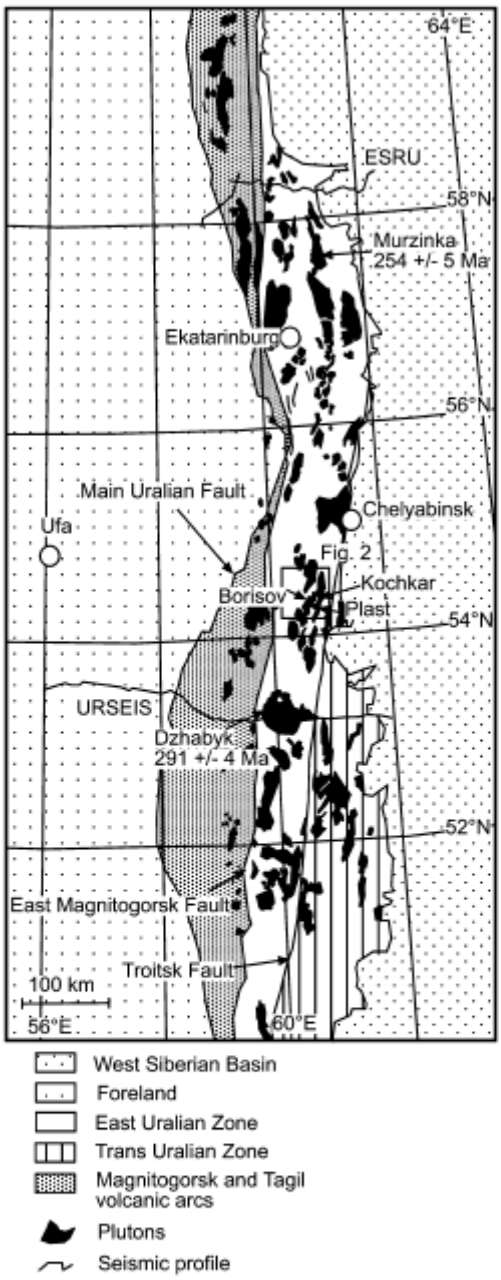


**Fig. 1** Geological map of the southern and middle Urals showing the main structural units (modified after Kimbell et al. 2002; ages: Murzinka, Gerdes et al. 2002; Dzhabyk, Montero et al. 2000). Note the area at ca. 56°N where the Magnitogorsk and Tagil volcanic arcs become narrow, which is interpreted to be the result of oblique indenter tectonics (Sazonov et al. 2001)

complexes are attributed to long-lived orogenic magmatism (Samarkin and Samarkina 1988; Fershtater et al. 1997; Bea et al. 2002) that commenced at 370–350 Ma with the intrusion of subduction-related, I–type granitoids in the eastern part of the EUZ. These plutons crystallized at 5–6 kbar and are considered to be coeval with late Paleozoic regional metamorphism and sinistral transcurrent deformation along the major N–S trending shear zones such as the East Magnitogorsk and the Troitsk faults (Fershtater et al. 1997; Puchkov 1997). Permian (292–250 Ma), "calc-alkaline" and "biotite granites" intruded into shallow crustal levels (2–3 kbar), postdating regional metamorphism and deformation. They form oval-shaped bodies surrounded by contact metamorphic halos (Fershtater et al. 1997). This later suite is considered to be the product of partial melting of Paleozoic island arc material as well as of Proterozoic to Paleozoic metasedimentary sources during a large scale, postorogenic melting event in the EUZ (Fershtater et al. 1997; Bea et al. 1997; Gerdes et al. 2002). Two batholiths of the latter suite, namely Murzinka and Dzhabyk, have been dated by zircon single-crystal stepwise-evaporation at 254 ± 5 Ma and 291 ± 4 Ma, respectively (Montero et al. 2000). The age difference is interpreted to be the result of the northward migration of continent–continent collision and subsequent granite magmatism from the late Carboniferous at Dzhabyk in the south to the late Permian at Murzinka in the north (Montero et al. 2000).

## Geology of the Kochkar district

In the Kochkar district in the south central Urals (Fig. 2), a number of gold deposits are hosted by the Plast massif. Gneissic granitoids of this massif intruded at 341 ± 20 Ma (Sazonov et al. 2001) into a sequence of N–S trending, steeply inclined, tightly folded and foliated, upper-greenschist to mid-amphibolite facies metavolcanic rocks and less abundant metasediments. The stratigraphically youngest supracrustal unit consists of limestones of Carboniferous age ($C_u$–$C_0$; Puchkov 1997). Intrusive relationships are indicated by the presence of variably sized supracrustal xenoliths within the Plast massif. Contacts between the plutonic rocks and the surrounding supracrustal rocks are sharp and dip steeply outward from the center of the massif (Kisters et al. 2000). The Plast massif itself is distinctly elongated in an N–S direction and is about 50 km in length with a maximum width of ca. 10 km in its central parts (Fig. 2). The marginal zones are strongly foliated giving the overall impression of an elongated gneiss dome. Fabric development and crosscutting relationships between different intrusive phases point to a synkinematic emplacement of the granitoids during regional transpression and sinistral transcurrent shearing along the regionally developed N–S trending shear zones that bound the EUZ (Bankwitz et al. 1997; Puchkov 1997).

The Borisov granitoid, to the west of the Plast massif (Fig. 2), is of unknown age. In the center of the Borisov complex, which is 8 km wide and 25 km long in N–S direction, yellowish to reddish, fine- to medium-grained

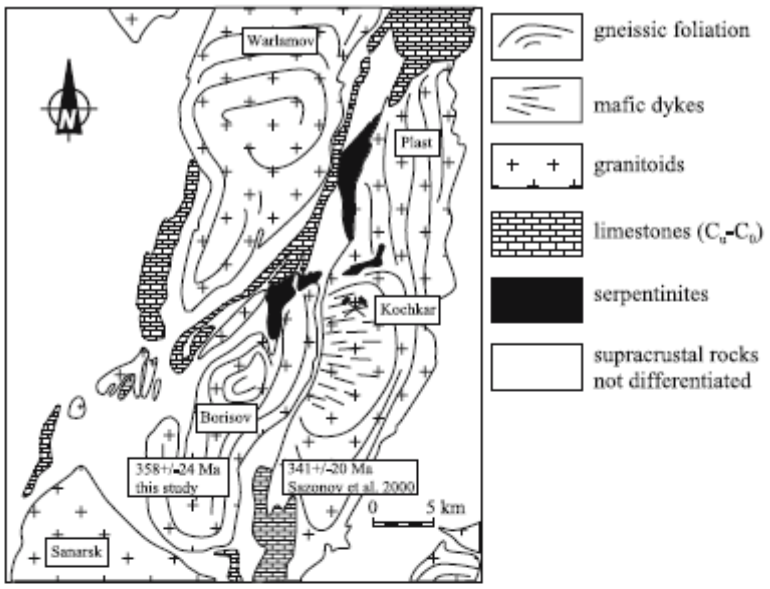


**Fig. 2** Geological map of the Kochkar region showing the Borisov and Plast massifs (modified after Borodaevsky 1952; Kisters et al. 2000). Gold mineralization is hosted by quartz lodes, which developed at the mafic dikes-Plast granitoid contacts

granitoids dominate. Towards the contact with the supracrustal rocks, the foliation of the granitoids increases, leading to an augen-texture and an increase in the biotite and muscovite content (Kisters et al. 2000). The contact between the Borisov granitoids and the surrounding supracrustal rocks is sharp and dips steeply outward from the center of the massif, similar to the outcrop pattern described for the Plast massif.

Numerous, steeply dipping mafic dikes intruded at about 320 Ma (Sazonov et al. 2001) into the Plast massif, describing an overall ENE–WSW to ESE–WNW trending radial pattern (Fig. 2). The width of the dikes ranges from a few cm to >20 m and strike lengths vary from several tens of meters to >1.5 km (Kisters et al. 2000). The mafic dikes are crosscut by numerous generations of later dikes. While some of the later dikes are subparallel to mafic dikes, the majority of crosscutting dikes shows northerly trends.

Economic-grade gold mineralization in the Plast massif is hosted by steeply-inclined, ENE–WSW trending quartz-sulfide lodes developed in a N–S extended, 15 km long and 5 km wide area around the town of Plast. The lodes are spatially associated with the northern, ENE–WSW trending mafic dikes and occur mostly parallel and directly adjacent to these dikes (Kisters et al. 2000). The massive and/or laminated, grayish to milky quartz veins are, on average, 0.2–1 m wide and show distinctly tabular geometries. They contain, on average, 4–6 g/t Au with locally high-grade ore shoots carrying ≥30 g/t Au, whereas mafic dikes and alteration zones surrounding the quartz lodes are subeconomic (< 1 g/t Au). Prominent quartz lodes can be traced along strike for over 500 m with similar subvertical extents.

Fluid infiltration during hydrothermal gold mineralization and quartz veining was promoted particularly along the contact between mafic dikes and granitoids. Repeated dilation normal to dike walls readily explains the dike-parallel laminated or ribbon textures of gold-quartz lodes. Mafic dikes acted as weak layers during regional-scale E–W directed horizontal shortening related to the Permian terrane amalgamation in the Uralides (Kisters et al. 2000).

## Petrology of intrusive rocks from the Kochkar area

The various intrusive rocks from the Kochkar area were studied for their mineralogical inventory in order to obtain information about the relative timing of magmatism, metamorphism, and alteration and to define mineral parageneses. Electronprobe microanalyses (EPMA) were performed on suitable parageneses to calculate *P*–*T* data for the metamorphic evolution.

### Borisov and Plast massifs

Intrusive rocks of the *Borisov* massif are variably foliated and comprise microcline, plagioclase, quartz, and biotite as main constituents, and subordinate muscovite, apatite, and zircon (Fig. 3a). A concentric $S_1$ foliation is developed in the massif outlined by the alignment of biotite and muscovite (Fig. 2). Microcline, with typical crosshatched twinning, is recrystallized at its rims where myrmekitic microcline and zoned plagioclase has formed. These second generation feldspars have straight grain boundaries that form triple junctions (Fig. 3a).

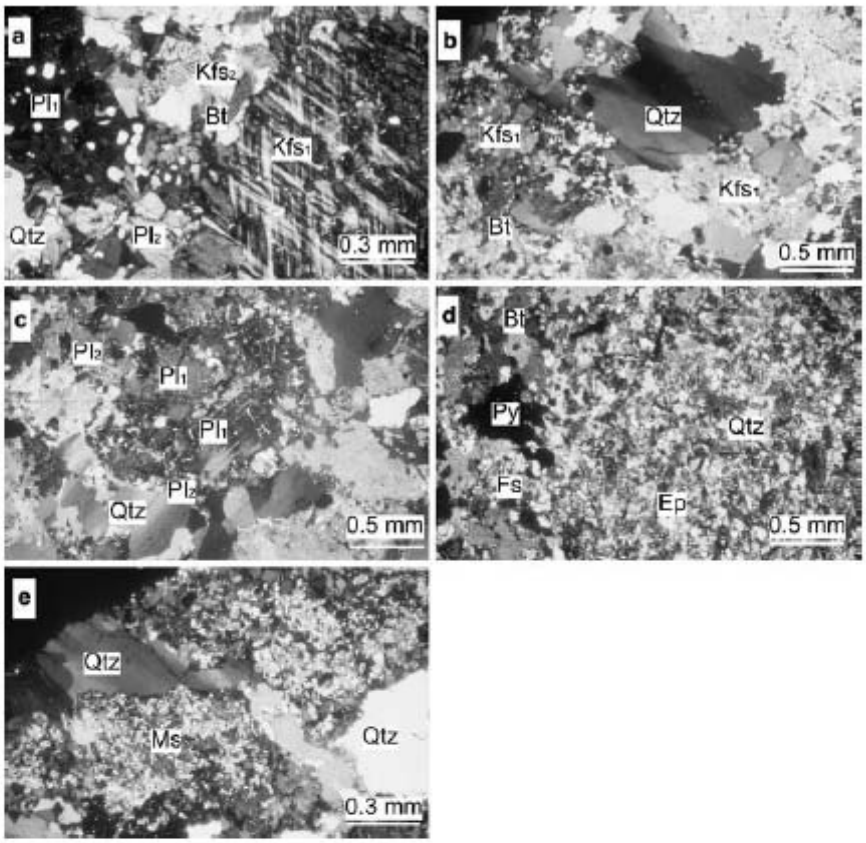


**Fig. 3** Photomicrographs of the Borisov and Plast granitoids (*crossed polarized light*). **a** Plagioclase (*Pl*) and K-feldspar (*Kfs*) of the typical Borisov granite mineral assemblage that are recrystallized to $Pl_2$ and $Kfs_2$, including quartz (*Qtz*) and biotite (*Bt*). Locally, myrmekitic textures are developed indicating mid-amphibolite facies conditions during recrystallization. **b** Typical assemblage of Kfs, Qtz, and Bt of the Plast granitoid. Kfs has a characteristic patchy decomposition texture. Note the pronounced subgrain formation in Qtz indicative of intracrystalline deformation. **c** Microstructure of a Plast granitoid showing dynamic recrystallization of Pl and strongly sutured grain boundaries of Qtz and $Pl_1$, which are indicative of amphibolite facies deformation. **d** Alteration assemblage of the Plast granitoids including biotite, epidote (*Ep*), and pyrite (*Py*). Note the fine recrystallized matrix of quartz and feldspar. **e** Plast granitoid with intense greenschist facies overprint showing nearly complete replacement of feldspar by muscovite (*Ms*)

Larger quartz is recrystallized to smaller grains with straight grain boundaries and triple junctions. Locally subgrain formation is prominent in the larger quartz grains.

The *Plast* massif is characterized by schollen- and raft migmatites together with variably deformed granitoids. The main constituents of the granitoids are perthitic feldspar, plagioclase, quartz, microcline, biotite, and muscovite in decreasing order of abundance (Fig. 3b). Accessories are titanite, apatite, zircon, rutile, monazite, and ilmenite. The $S_1$ foliation is developed by the alignment of biotite and the migmatitic banding. This fabric is concentric with respect to the outline of the massif (Fig. 2). The perthitic feldspar shows a stained texture and is recrystallized at its rims forming smaller plagioclase and microcline with straight grain boundaries, which form triple junctions. Larger plagioclase with albite twinning is also recrystallized at its rims (Fig. 3c). Quartz displays various recrystallization fabrics including subgrain formation, grain boundary migration, and undulose extinction (Fig. 3b). Biotite and muscovite occur in random orientation or form a weak, ENE–WSW trending $S_2$ foliation. $S_2$ foliated rocks are also characterized by the recrystallization of feldspar and quartz, which is restricted to the lithological contact zones of granitoids and mafic dikes. Feldspars are locally affected by saussuritization and sericitization, and mafic minerals are locally replaced by chlorite and rutile (Fig. 3d, e). In these rocks, sericite and chlorite define a $S_3$ foliation.

## Mafic dikes

The mafic dikes display highly variable textures ranging from fine-grained, massive, to porphyritic or strongly foliated. In general, the development of an ENE–WSW trending $S_2$ foliation is more pronounced in the mafic dikes compared to the granitoids. They are black to dark greenish in color and consist of biotite, hornblende, actinolite, plagioclase, K-feldspar, quartz, apatite, epidote, tourmaline, sericite, and sulfides together with chlorite, calcite, and sphene (Fig. 4). Amphiboles are mainly relics in the dikes displaying a poikiloblastic texture with plagioclase forming the inclusions (Fig. 4b). The amphibole grains have a characteristic zoning with tschermakitic hornblende compositions in the center and actinolitic compositions at the rims (Fig. 5a; Table 1). Feldspar inclusions in amphibole display a zoning from oligoclase in the center to andesine at the rims (Fig. 5b;

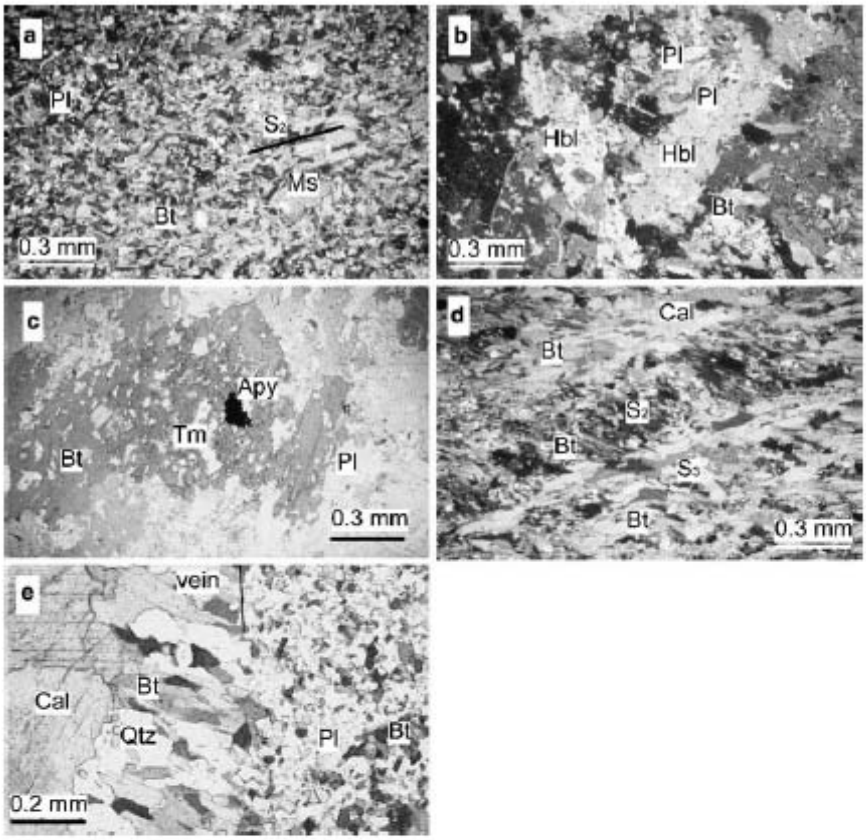


**Fig. 4** Photomicrographs of the mafic dikes. **a** Typical (alteration) mineral assemblage comprising biotite (*Bt*), plagioclase (*Pl*), and muscovite (*Ms*). The micas are aligned parallel to the penetrative $S_2$ foliation (*crossed polarized light*). **b** Least altered mafic dike showing poikiloblastic hornblende (*Hbl*) with inclusions of plagioclase (*crossed polarized light*). This assemblage was used for geothermometry. Locally, hornblende is replaced by biotite. **c** Biotite-tourmaline (*Tm*) alteration assemblage used for geothermometry (*plain polarized light*). Note, the arsenopyrite (*Apy*) grain associated with tourmaline. **d** $S_2$–$S_3$ asymmetric crenulation cleavage formed during greenschist facies deformation and retrogression (calcite: *Cal; crossed polarized light*). **e** Barren calcite, green biotite, quartz vein (*plain polarized light*). Biotite in the adjacent mafic dike lithology has also the green color. A similar vein was used to date the greenschist facies event

Table 1). In the matrix, plagioclase is strongly zoned and has an andesine core followed by an oligoclase seam and an andesine rim. Locally, where amphiboles are absent, a continuous zoning from oligoclase to labradorite compositions can be observed.

## Mineralization and alteration

Auriferous quartz lodes are made up of predominantly quartz with minor amounts of calcite, sericite, scheelite, biotite, tourmaline, and actinolite together with opaques. Sulfides comprise 2–7 vol.% and are generally aligned parallel to wall-rock laminae or they form irregular clots within quartz veins. The sulfide assemblage includes mainly pyrite and arsenopyrite with subordinate chalcopyrite, sphalerite, fahlores, galena, and bismuthinite. Gold is fine-grained ($< 20$ μm) and commonly occurs as specks of free gold in quartz.

A biotite-K-feldspar alteration assemblage that replaces the peak metamorphic hornblende-plagioclase paragenesis almost invariably characterizes mafic dikes bordering or enveloping the auriferous quartz lodes. The alteration mineralogy comprises biotite, actinolite, albite, K-feldspar, quartz, epidote, tourmaline, sericite, and a sulfide-gold assemblage similar to that described for the mineralized veins. Biotite, muscovite, and tourmaline outline the $S_2$ foliation, which is developed parallel to the auriferous quartz lodes (Fig. 4a). S–C and S–C′ fabrics are locally developed indicating dextral strike-slip shearing (Kisters et al. 2000). In places, the $S_2$ foliation is overgrown by biotite, muscovite, tourmaline, and epidote.

By contrast, wall-rock alteration in the Plast granitoids is less pronounced and commonly consists of quartz as well as sericite, calcite, and epidote, which replace original feldspar (Fig. 3d).

A set of late, barren quartz veins crosscut the Plast granitoids, the mafic dikes, and the auriferous quartz lodes. The late veins comprise quartz, muscovite, calcite, chlorite, and green biotite (Fig. 4e) and are easily distinguishable from the auriferous veins by their white, milky appearance. They are invariably associated with fault gouges of regional, NE–SW and NW–SE trending faults and a chlorite alteration halo that replaces the biotite-K-feldspar alteration paragenesis with chlorite, sphene, calcite, and sericite. Biotite has either changed color to a greenish appearance or is replaced by chlorite and sphene. The green biotite also varies in composition from the biotite of the earlier biotite-K-feldspar alter-

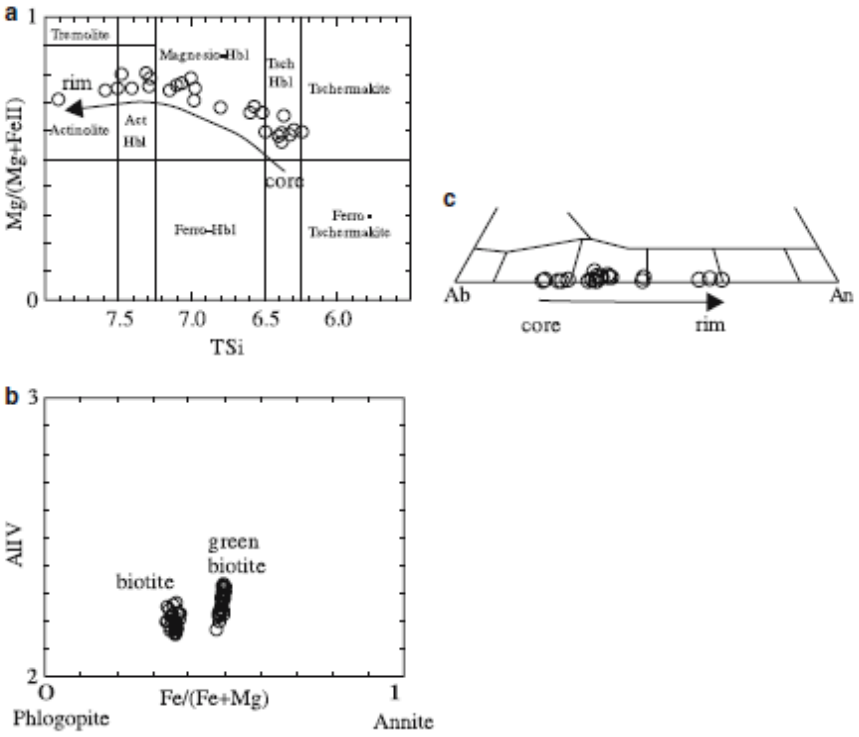


**Fig. 5** Mineral discrimination diagrams for amphibole, plagioclase and biotite in mafic dikes. Representative analyses are given in Table 1. **a** Typical retrograde zoning from tschermakitic hornblende in the crystal core to actinolite at the rims. Core compositions were used to calculate peak metamorphic conditions. **b** Prograde zoning recorded by plagioclase from oligoclase compositions in the core to labradorite at the rims. **c** Biotite of the alteration paragenesis and retrogressive green biotite vary significantly in their Fe/Fe+Mg ratio

ation (Fig. 5c; Table 1). The retrograde overprint is characterized by the development of a crenulation cleavage, where green biotite and chlorite define the $S_3$ foliation. If $S_2$–$S_3$ is developed as an asymmetrical crenulation cleavage, dextral strike-slip shearing is indicated (Fig. 4d). In case the late veins crosscut Plast granitoids, alteration is characterized by the almost complete sericitization of feldspars and the replacement of biotite by chlorite (Fig. 3e).

## Textural development and *P*–*T* conditions

*P*–*T* conditions were calculated using critical mineral parageneses of the least altered mafic dikes and the biotite-K-feldspar alteration paragenesis (Table 2). Amphibole and plagioclase are zoned in the least altered mafic dikes, with the amphiboles displaying a characteristic retrograde zoning, whereas plagioclase grains show a complex zoning. Plagioclase included in the poikiloblastic amphiboles has andesine (ca. $An_{40}$) compositions in contact with tschermakitic hornblende (Table 1). Using these compositions, metamorphic conditions were estimated at 635 ± 40°C after the method of Holland and Blundy (1994) (Table 2). Higher An contents are only developed in plagioclase in the matrix or in samples, where amphibole is absent. Amphibolite facies conditions are also in agreement with gneissic textures of the Borisov and Plast granitoids where the $S_1$ foliation is developed and the original minerals are recrystallized (Fig. 3a, b). Recrystallization of microcline to myrmekite in the Borisov massif is a typical amphibolite facies process (Simpson 1985; Simpson and Wintsch 1989). In the Plast granitoids, the decomposition of K-feldspar and probably the formation of migmatites can be assigned to peak metamorphic conditions in the amphibolite facies.

Biotite and tourmaline are minerals of the biotite-K-feldspar alteration assemblage in mafic dikes, which is closely intergrown with the sulfide-gold assemblage and developed in the $S_2$ foliation parallel to the auriferous lodes (Fig. 4c). EPMA yields a relative uniform composition of both minerals with no internal zoning indicating that biotite and tourmaline are in textural and compositional equilibrium (Table 1). The biotite-tourmaline Fe–Mg exchange thermometer of Colopietro and Friberg (1987), was applied to calculate the temperature of the biotite-K-feldspar alteration and gold mineralization, which revealed conditions of 500 ± 20°C (Table 2).

These retrograde conditions can be correlated with retrograde zoning of the amphiboles to actinolitic hornblende and the occurrence of epidote in least altered mafic dikes, which suggests metamorphic conditions of the amphibolite-epidote facies. At the mafic dike-granitoid contact, the $S_2$ foliation is also developed in the Plast granitoids with a weak alteration zone. In these

**Table 1** Representative mineral analyses used for geothermometry and discrimination (cf., Table 2, Fig. 5)

| Sample | Hbl 9 | Hbl 4 | Hbl 7 | | Pl 6 | Pl 4 | Pl 11 | | Bt 7 | Bt 37 | | Tm 29 |
|---|---|---|---|---|---|---|---|---|---|---|---|---|
| Description | Tschermakitic hornblende | Magnesio hornblende | Actinolitic hornblende | | Andesine | Labradorite | Oligoclase | | Biotite | Green biotite | | Tourmaline |
| $SiO_2$ | 42.35 | 47.00 | 51.31 | $SiO_2$ | 59.11 | 51.54 | 62.26 | $SiO_2$ | 37.22 | 35.81 | $SiO_2$ | 35.82 |
| $TiO_2$ | 0.28 | 0.43 | 0.20 | $Al_2O_3$ | 26.11 | 31.15 | 23.81 | $Al_2O_3$ | 17.35 | 17.81 | $TiO_2$ | 0.33 |
| $Al_2O_3$ | 14.43 | 8.12 | 3.79 | FeO | 0.08 | 0.15 | 0.09 | $TiO_2$ | 1.95 | 1.90 | $Al_2O_3$ | 30.81 |
| FeO | 14.39 | 11.34 | 9.96 | CaO | 7.26 | 13.23 | 4.49 | FeO | 14.17 | 19.12 | $Cr_2O_3$ | < 0.02 |
| MnO | 0.27 | 0.33 | 0.34 | $Na_2O$ | 6.95 | 3.69 | 8.37 | MgO | 14.10 | 10.66 | FeO | 5.17 |
| MgO | 9.77 | 14.26 | 16.70 | $K_2O$ | < 0.01 | 0.16 | < 0.01 | MnO | 0.19 | 0.18 | MnO | < 0.02 |
| CaO | 11.51 | 11.93 | 12.33 | BaO | < 0.03 | < 0.03 | < 0.03 | CaO | < 0.02 | 0.04 | MgO | 8.59 |
| $Na_2O$ | 1.43 | 0.90 | 0.43 | Total | 99.58 | 99.93 | 99.10 | $Na_2O$ | 0.10 | 0.03 | CaO | 1.10 |
| $K_2O$ | 0.27 | 0.13 | < 0.01 | Si | 10.57 | 9.36 | 11.09 | $K_2O$ | 10.15 | 10.21 | $Na_2O$ | 2.13 |
| Total | 94.70 | 94.44 | 95.06 | Al | 5.50 | 6.66 | 4.99 | Total | 95.23 | 95.76 | $K_2O$ | < 0.01 |
| T Si | 6.40 | 6.98 | 7.48 | $Fe^{2+}$ | 0.01 | 0.02 | 0.01 | Si | 5.80 | 5.70 | F | 0.13 |
| T Al | 1.60 | 1.02 | 0.52 | Ba | 0 | 0 | 0 | Al IV | 2.20 | 2.30 | $B_2O_3$ | 12.90 |
| Sum T | 8 | 8 | 8 | Ca | 1.39 | 2.58 | 0.86 | Al VI | 0.98 | 1.03 | $H_2O$ | 3 |
| C Al | 0.97 | 0.40 | 0.13 | Na | 2.41 | 1.30 | 2.89 | Ti | 0.23 | 0.23 | Total | 99.95 |
| C $Fe^{3+}$ | 0.23 | 0.36 | 0.30 | K | 0.01 | 0.04 | 0.02 | $Fe^{2+}$ | 1.85 | 2.54 | B | 3 |
| C Ti | 0.03 | 0.05 | 0.02 | Cations | 19.89 | 19.96 | 19.86 | Mn | 0.03 | 0.02 | Si | 5.97 |
| C Mg | 2.20 | 3.16 | 3.63 | Ab | 63.2 | 33.2 | 76.8 | Mg | 3.27 | 2.53 | Ti | 0.04 |
| C $Fe^{2+}$ | 1.54 | 1.02 | 0.90 | An | 36.5 | 65.8 | 22.8 | Ca | 0 | 0.01 | Al | 6.05 |
| C Mn | 0.02 | 0.02 | 0.02 | Or | 0.3 | 0.9 | 0.4 | Na | 0.03 | 0.01 | $Fe^{2+}$ | 0.72 |
| C Ca | 0 | 0 | 0 | | | | | K | 2.02 | 2.07 | Mn | 0 |
| Sum C | 5 | 5 | 5 | | | | | Cations | 16.40 | 16.44 | Mg | 2.13 |
| B Mg | 0 | 0 | 0 | | | | | O | 24 | 24 | Ca | 0.20 |
| B $Fe^{2+}$ | 0.05 | 0.03 | 0.01 | | | | | Fe/(Fe + Mg) | 0.36 | 0.50 | Na | 0.69 |
| B Mn | 0.02 | 0.02 | 0.02 | | | | | Mg/(Mg + Fe) | 0.64 | 0.50 | K | 0 |
| B Ca | 1.87 | 1.90 | 1.93 | | | | | | | | Total | 18.80 |

**Table 2** Results of geothermometry calculations

| Mineral pair | *n* | Calibration | Temperature (°C) |
|---|---|---|---|
| Tschermakitic hornblende – andesine | 7 | Holland and Blundy (1994) | 635 ± 40 |
| Biotite – tourmaline | 20 | Colopietro and Friberg (1987) | 500 ± 20 |

zones, the dynamic recrystallization of feldspar indicates temperatures > 450°C for $D_2$ deformation (Fig. 3c; Voll 1976; Tullis 1983; Stünitz and FitzGerald 1993). Similar temperatures are suggested by the polygonal fabric of recrystallized quartz (cf., Stipp et al. 2002).

These deformation-recrystallization textures are absent in the Plast lithologies farther than about 3 m from the contact with the mafic dikes. In the Borisov lithologies, these textures are conspicuous by their absence. Hence, the retrograde stage in the lower amphibolite facies and associated fluid infiltration is only observed in a narrow zone surrounding the mafic dikes, which spatially control the distribution of the gold-quartz veins.

The formation of the late, barren quartz veins is related to a second retrograde overprint. This overprint is constrained by strongly retrogressed rocks of the chlorite alteration zone, spatially associated with fault zones and a locally developed $S_3$ foliation, which crosscut the gold-quartz veins (Kisters et al. 2000). The replacement of previous mineral assemblages by chlorite, green biotite, and sericite points to lower to mid greenschist facies conditions for this metamorphic stage.

## Geochemistry

In order to constrain the chemical characteristics of the Kochkar deposit we analyzed ten samples from the Plast and Borisov granitoids, 13 samples of mafic dikes, and 12 quartz lodes. Notably, the Plast granitoid and mafic dike samples were affected by various degrees of geochemical modification during the two alteration stages. The least altered samples are given in italics in Table 3. Due to restricted exposure, only one sample from the Borisov granitoid was available. Whole rock major and trace element analyses were performed by X-ray fluorescence analysis, instrumental neutron activation analysis and inductively coupled plasma mass spectrometry. Stable isotope analyses were carried out on hydrothermal quartz from the auriferous quartz lodes and a late, barren quartz vein (sample K30). For radiogenic isotope investigations, three samples (least altered Plast granitoid, altered Plast granitoid, and a late, barren quartz vein) were used for Rb–Sr analyses and one sample of the Borisov granitoid was dated with the help of U–Pb analyses of zircon.

### Granitoid geochemistry

The modal variation of the *Plast* granitoids is reflected by their major element composition. They are medium to high-K, calc-alkaline (Peacock Index = 57), and $SiO_2$

**Table 3** Major and trace element data for Plast granitoids, mafic dikes, and quartz lodes

| | Plast granitoids | | | | | | | | | Borisov granite | Mafic dikes | | | | | | | | | | | | Quartz lodes | | | | | | | | | | |
|---|---|---|---|---|---|---|---|---|---|---|---|---|---|---|---|---|---|---|---|---|---|---|---|---|---|---|---|---|---|---|---|---|---|
| Sample No. | K5 | K8 | K13 | *K16* | K18 | *K22* | *K26* | K39 | K40 | BOR | K1 | K3 | *K4* | *K9* | K13 | *K15* | K21 | *K23* | K24 | *K25* | *K29* | *K30b* | K37 | K2 | K6 | K12 | K14 | K15 | K17 | K19 | K20 | K27 | K34 | K36 | K71 |
| wt % | | | | | | | | | | | | | | | | | | | | | | | | | | | | | | | | | | | |
| $SiO_2$ | 70.40 | 65.66 | 69.63 | 71.31 | 70.46 | 71.01 | 72.00 | 68.47 | 71.57 | 71.08 | 62.48 | 47.71 | 56.37 | 52.65 | 69.63 | 44.21 | 53.83 | 52.42 | 48.76 | 54.31 | 49.47 | 58.54 | 49.32 | 92.97 | 95.72 | 87.05 | 86.75 | 97.50 | 92.49 | 97.66 | 98.36 | 99.01 | 85.97 | 95.41 | 96.07 |
| $TiO_2$ | 0.27 | 0.18 | 0.14 | 0.23 | 0.27 | 0.17 | 0.15 | 0.19 | 0.15 | 0.20 | 0.63 | 0.90 | 0.75 | 0.73 | 0.14 | 1.37 | 0.91 | 1.05 | 0.97 | 1.06 | 0.96 | 0.10 | 0.94 | 0.01 | 0.01 | 0.02 | 0.29 | 0.01 | 0.01 | b.d.l. | 0.01 | 0.01 | 0.01 | 0.01 | 0.01 |
| $Al_2O_3$ | 13.31 | 14.31 | 16.43 | 15.22 | 15.32 | 16.64 | 15.18 | 16.76 | 15.46 | 14.57 | 15.98 | 17.60 | 18.51 | 14.59 | 16.43 | 15.99 | 16.73 | 14.90 | 14.01 | 15.01 | 18.12 | 22.90 | 12.38 | 0.81 | 0.24 | 2.23 | 2.70 | 0.16 | 0.31 | 0.37 | 0.56 | b.d.l. | 0.23 | 0.48 | 0.68 |
| $Fe_2O_3$ | 3.27 | 2.48 | 1.24 | 1.17 | 1.73 | 1.10 | 0.81 | 1.59 | 1.23 | 2.14 | 5.06 | 9.78 | 6.21 | 8.26 | 1.24 | 14.56 | 8.45 | 7.52 | 7.30 | 7.35 | 10.82 | 1.85 | 6.66 | 0.95 | 0.82 | 4.61 | 3.69 | 1.15 | 2.69 | 0.09 | 0.08 | 0.03 | 10.55 | 0.87 | 0.15 |
| MnO | 0.04 | 0.05 | 0.01 | 0.04 | 0.05 | 0.01 | 0.02 | 0.03 | 0.02 | 0.05 | 0.08 | 0.17 | 0.11 | 0.17 | 0.01 | 0.47 | 0.10 | 0.10 | 0.16 | 0.09 | 0.14 | 0.03 | 0.18 | 0.02 | 0.01 | 0.01 | 0.07 | b.d.l. | 0.01 | b.d.l. | b.d.l. | b.d.l. | b.d.l. | 0.02 | 0.01 |
| MgO | 1.08 | 0.99 | 0.43 | 0.40 | 0.58 | 0.45 | 0.43 | 1.14 | 0.37 | 0.46 | 2.30 | 5.77 | 3.52 | 5.13 | 0.43 | 10.90 | 5.65 | 5.98 | 5.93 | 6.73 | 5.28 | 0.70 | 4.99 | 0.45 | 0.11 | 0.15 | 1.81 | 0.03 | b.d.l. | b.d.l. | b.d.l. | b.d.l. | b.d.l. | 0.12 | b.d.l. |
| CaO | 3.28 | 4.26 | 1.38 | 2.09 | 2.89 | 2.14 | 1.78 | 2.28 | 1.78 | 1.66 | 3.59 | 5.83 | 5.06 | 6.91 | 1.38 | 0.66 | 3.61 | 6.27 | 9.78 | 5.26 | 4.03 | 2.27 | 10.68 | 1.75 | 1.11 | 0.86 | 0.98 | 0.17 | 1.19 | 0.40 | 0.20 | 0.37 | 0.02 | 1.12 | 0.61 |
| $Na_2O$ | 3.02 | 3.45 | 5.83 | 2.96 | 2.54 | 5.76 | 5.27 | 3.15 | 4.97 | 3.49 | 1.57 | 3.09 | 4.60 | 2.76 | 5.83 | 0.72 | 1.97 | 2.36 | 1.62 | 2.75 | 2.76 | 4.84 | 1.08 | 0.23 | 0.25 | 0.48 | 0.26 | b.d.l. | 0.22 | 0.23 | 0.23 | 0.20 | 0.24 | 0.25 | 0.24 |
| $K_2O$ | 3.80 | 2.89 | 1.70 | 4.06 | 3.89 | 1.36 | 2.48 | 4.35 | 2.82 | 4.61 | 5.94 | 4.40 | 3.12 | 3.17 | 1.70 | 8.78 | 5.39 | 4.70 | 4.07 | 4.27 | 5.97 | 4.76 | 2.37 | 0.07 | b.d.l. | 0.65 | 0.33 | 0.05 | 0.05 | b.d.l. | b.d.l. | b.d.l. | 0.02 | 0.02 | 0.06 |
| $P_2O_5$ | 0.19 | 0.08 | 0.08 | 0.10 | 0.11 | 0.08 | 0.06 | 0.08 | 0.09 | 0.08 | 0.23 | 0.27 | 0.28 | 0.20 | 0.08 | 0.26 | 0.41 | 0.40 | 0.36 | 0.43 | 0.31 | 0.07 | 0.25 | 0.02 | b.d.l. | b.d.l. | 0.14 | 0.03 | b.d.l. | b.d.l. | b.d.l. | b.d.l. | b.d.l. | b.d.l. | 0.02 |
| LOI | 1.51 | 4.36 | 2.00 | 1.64 | 1.17 | 0.91 | 1.06 | 0.92 | 0.65 | 0.32 | 1.05 | 3.79 | 1.45 | 4.81 | 2.00 | 1.32 | 1.46 | 4.52 | 7.55 | 3.06 | 2.32 | 4.06 | 11.20 | 0.96 | 0.36 | 2.68 | 1.57 | 0.78 | 1.65 | 0.02 | 0.08 | 0.32 | 2.78 | 0.67 | 0.19 |
| Total | 100.18 | 98.71 | 98.86 | 99.21 | 99.01 | 99.64 | 99.24 | 98.96 | 99.11 | 98.66 | 98.90 | 99.30 | 99.98 | 99.38 | 98.86 | 99.23 | 98.51 | 100.22 | 100.50 | 100.32 | 100.18 | 100.12 | 100.04 | 98.24 | 98.63 | 98.74 | 98.58 | 99.88 | 98.61 | 98.77 | 99.52 | 99.93 | 99.83 | 98.97 | 98.04 |
| S | 0.60 | 0.46 | 0.46 | 0.04 | 0.01 | 0.13 | 0.02 | 0.24 | 0.02 | ND | 0.55 | 0.48 | 0.12 | 0.27 | 0.46 | 0.02 | 0.30 | 0.04 | 0.15 | 0.03 | 0.05 | 0.02 | 0.18 | 0.29 | 0.50 | 3.70 | 0.83 | 1.11 | 2.28 | 0.03 | 0.07 | 0.01 | 5.83 | 0.41 | 0.06 |
| $CO_2$ | 0.57 | 1.37 | 0.96 | 0.96 | 0.36 | ND | 0.94 | ND | ND | ND | 0.26 | 1.95 | 0.79 | 3.01 | 0.96 | 0.12 | 0.39 | ND | ND | ND | ND | ND | 7.85 | 1.53 | 0.26 | 0.74 | 0.72 | ND | 0.91 | 0.29 | 0.20 | 0.26 | 0.21 | 4.26 | ND |
| $H_2O$ | 0.01 | b.d.l. | 0.02 | 0.75 | 0.55 | ND | 0.73 | ND | ND | ND | 0.66 | 1.89 | 0.14 | 1.95 | 0.02 | 1.30 | 0.31 | ND | ND | ND | ND | ND | 3.36 | 0.02 | 0.78 | 0.73 | 1.05 | ND | 0.13 | 0.06 | 0.06 | b.d.l. | 0.17 | 1.15 | ND |
| ppm | | | | | | | | | | | | | | | | | | | | | | | | | | | | | | | | | | | |
| Rb | 51 | 67.8 | 68 | 110 | 112.5 | 29.6 | 57 | 83 | 74 | 149.8 | 140 | 139 | 91 | 99 | 68 | 454 | 196 | 165.6 | 134.4 | 144.5 | 241.4 | 101.1 | 60 | ND | ND | 20 | 17 | ND | 6 | ND | ND | ND | ND | ND | ND |
| Cs | ND | 2 | 2 | 3 | 4 | 1.4 | ND | 3 | 1 | 7 | 3 | 6 | 4 | 5 | 2 | 43 | 13 | 19.7 | 14.8 | 30.9 | 17.3 | 2.7 | 2 | ND | ND | ND | 2 | ND | ND | ND | ND | ND | ND | ND | ND |
| Be | ND | 2 | ND | ND | 3 | 2 | ND | ND | ND | 2 | ND | ND | ND | ND | ND | ND | ND | 2 | 2 | 2 | 3 | 2 | ND | ND | ND | ND | ND | ND | ND | ND | ND | ND | ND | ND | ND |
| Sr | 284 | 299 | 292 | 299 | 259 | 508 | 232 | 288 | 481 | 237 | 81 | 255 | 364 | 347 | 292 | 46 | 151 | 549 | 319 | 948 | 276 | 216 | 228 | 26 | 20 | 32 | 26 | 4 | 36 | 9 | 9 | 10 | 3 | 22 | 31 |
| Ba | 1,600 | 1,109 | 190 | 850 | 747 | 524 | 410 | >1,200 | 570 | 860 | >1,200 | >1,200 | >1,200 | 770 | 190 | 620 | 930 | 914 | 597 | 548 | 1,123 | 712 | 560 | 53 | 40 | 120 | 78 | 6 | 48 | 34 | 35 | 34 | 55 | 39 | 52 |
| Sc | 6.2 | 3 | 2 | 2.9 | 4 | 3 | 2 | 2.5 | 2.2 | 3 | 11 | 30 | 26 | 31 | 2 | 27 | 19 | 20 | 22 | 19 | 29 | 5 | 15 | 0.6 | 0.5 | 0.3 | 4.9 | ND | 0.4 | ND | 0.3 | 0.3 | 0.4 | 0.2 | 0.2 |
| V | ND | 43 | ND | ND | 27 | 13 | ND | ND | ND | 14 | ND | ND | ND | ND | ND | ND | ND | 158 | 158 | 149 | 227 | 22 | ND | ND | ND | ND | ND | ND | ND | ND | ND | ND | ND | ND | ND |
| Cr | ND | 6 | ND | ND | ND | ND | ND | ND | ND | ND | ND | 180 | 28 | 95 | ND | 890 | 240 | 260.9 | 242.9 | 300.3 | ND | ND | 160 | ND | ND | ND | ND | ND | 12 | 7 | ND | ND | ND | ND | ND |
| Co | 12 | 2 | 3 | 2 | 1 | b.d.l. | b.d.l. | 3 | b.d.l. | 1.2 | 9 | 32 | 15 | 25 | 3 | 26 | 25 | 23.9 | 22.8 | 26.1 | 18.1 | b.d.l. | 14 | 10 | 5 | 19 | 9 | 10.6 | ND | ND | 1 | 1 | 40 | 7 | ND |
| Ni | ND | 4.0 | ND | ND | ND | 1.3 | ND | ND | b.d.l. | b.d.l. | <20 | 22 | < 20 | 19 | < 20 | 332 | 120 | 133.6 | 147.3 | 159.1 | 8.0 | <20 | 69 | ND | ND | ND | ND | 6.8 | ND | ND | ND | ND | 19 | ND | ND |
| Cu | 78 | 96.8 | ND | ND | 5.98 | 23.7 | ND | ND | ND | b.d.l. | 73 | 75 | 21 | 49 | < 20 | < 20 | 46 | 17.0 | 55.9 | b.d.l. | 2.9 | <20 | <20 | 31 | 15 | 423 | 8 | 28.7 | 32 | ND | ND | ND | 716 | 44 | ND |
| Zn | 30 | 34.0 | 34 | 33 | 32.6 | 3.6 | 28 | 13 | 32 | 20.8 | 52 | 120 | 79 | 93 | 34 | 340 | 53 | 48.8 | 48.2 | 76.3 | 126.0 | 10.1 | 58 | 12 | ND | 47 | 146 | 1.1 | ND | ND | ND | ND | 11 | 11 | ND |
| Ga | 13 | 19.4 | 17 | 17 | 23.3 | 22.6 | 18 | 18 | 17 | 16 | 17 | 21 | 17 | 15 | 17 | 53 | 25 | 26.4 | 20.1 | 24.1 | 23.0 | 27.7 | 19 | ND | ND | ND | ND | 1.1 | ND | ND | ND | ND | ND | ND | ND |
| Ge | ND | 1.1 | ND | ND | 1.1 | 1.3 | ND | ND | ND | 1.0 | ND | ND | ND | ND | ND | ND | ND | 2.3 | 1.5 | 2.4 | 1.5 | 1.1 | ND | ND | ND | ND | ND | 1.0 | ND | ND | ND | ND | ND | ND | ND |
| As | 11 | 5.0 | 6.3 | 1.4 | 2.9 | 13.1 | 3.9 | 21 | 7.1 | b.d.l. | 4.2 | 3.9 | ND | 2.3 | 6.3 | 3.7 | 11 | 6.9 | 41.7 | 9.1 | ND | 11.5 | 43 | 10 | 37 | 39 | 18 | 13.2 | 26 | 3.8 | 11 | 9.5 | 69 | 19 | 2.1 |
| Se | ND | ND | ND | ND | ND | ND | ND | ND | ND | ND | ND | ND | ND | ND | ND | ND | ND | ND | ND | ND | ND | ND | ND | ND | ND | 16 | 5 | ND | ND | ND | ND | ND | 30 | ND | 4 |
| Y | ND | 5.7 | ND | b.d.l. | 9.1 | 4.7 | ND | ND | ND | 12.1 | 16 | 17 | 21 | 17 | ND | ND | 15 | 16.1 | 16.0 | 19.7 | 15.5 | 6.6 | ND | ND | ND | ND | ND | 0.6 | ND | ND | ND | ND | ND | ND | ND |
| Nb | ND | 5.3 | ND | 10 | 8.0 | 5.3 | ND | ND | ND | 9.8 | ND | ND | ND | ND | ND | 24 | ND | 10.7 | 9.3 | 11.7 | 7.9 | 6.1 | ND | ND | ND | ND | ND | 2.5 | ND | ND | ND | ND | ND | ND | ND |
| Ta | ND | 0.3 | 0.6 | 1.6 | 0.9 | 0.3 | 0.9 | ND | 0.9 | 0.8 | ND | ND | ND | ND | 0.6 | ND | 2 | 0.6 | 0.5 | 0.7 | 0.4 | 0.5 | ND | ND | ND | ND | ND | ND | ND | ND | ND | ND | ND | ND | ND |
| Zr | 90 | 85 | 87 | 94 | 125 | 94 | 95 | 135 | 92 | 155 | 117 | 103 | 127 | 94 | 87 | 110 | 154 | 176 | 165 | 191 | 103 | 66 | 154 | 17 | 22 | 26 | 20 | 17 | 20 | 24 | 14 | 15 | 18 | 12 | 15 |
| Hf | 3 | 2.5 | 2 | 2 | 3.2 | 2.4 | 3 | 3 | 2 | 3.4 | 3 | 3 | 4 | 2 | 2 | 3 | 5 | 3.9 | 3.3 | 4.2 | 2.2 | 2.0 | 4 | ND | ND | ND | ND | ND | ND | ND | ND | ND | ND | ND | ND |
| Mo | ND | ND | ND | 5 | 7 | ND | ND | 2 | ND | ND | 2 | ND | ND | ND | ND | ND | 6 | ND | ND | ND | ND | ND | 5 | 21 | 108 | 2 | ND | ND | 15 | 6 | 8 | 5 | 54 | ND | 10 |
| W | 30 | 11.3 | 7 | 10 | 78.4 | 3.4 | ND | 10 | ND | 0.8 | 64 | ND | ND | ND | 7 | ND | 12 | 2.7 | 61.1 | 1.3 | 2.3 | 1.2 | 63 | 35 | 3,000 | 15 | 7 | 78.3 | 2,000 | 2,200 | 49 | 230 | 4 | 6 | 1,900 |
| Ag | b.d.l. | b.d.l. | b.d.l. | b.d.l. | b.d.l. | ND | b.d.l. | b.d.l. | b.d.l. | ND | b.d.l. | b.d.l. | b.d.l. | b.d.l. | b.d.l. | b.d.l. | b.d.l. | ND | ND | ND | ND | ND | b.d.l. | b.d.l. | b.d.l. | b.d.l. | b.d.l. | ND | 7 | b.d.l. | b.d.l. | b.d.l. | b.d.l. | b.d.l. | b.d.l. |
| ppb | | | | | | | | | | | | | | | | | | | | | | | | | | | | | | | | | | | |
| Au | 94 | 541 | 35 | 19 | 1,850 | ND | 62 | 807 | b.d.l. | ND | 3,920 | 63 | 27 | 22 | 35 | 39 | 29 | ND | ND | ND | ND | ND | 1,200 | 434 | 46,300 | 2,120 | 201 | ND | 75,000 | 15,800 | 35,800 | 1,010 | 11,300 | 2,970 | 56,200 |
| ppm | | | | | | | | | | | | | | | | | | | | | | | | | | | | | | | | | | | |
| Sb | 0.2 | 0.5 | 0.3 | b.d.l. | 0.3 | 0.3 | b.d.l. | 0.3 | 0.5 | 0.5 | 0.4 | b.d.l. | b.d.l. | 0.3 | 0.3 | 1.1 | 0.9 | 0.7 | 0.3 | 0.4 | b.d.l. | 1.6 | 0.9 | ND | 0.9 | 0.3 | 1.4 | 0.7 | 1.2 | 0.2 | 0.8 | 0.2 | 1.2 | 0.2 | 0.5 |
| Pb | 24 | 64 | ND | 52 | 27.7 | 6.5 | 52 | 10 | 18 | 24.7 | 10 | 18 | 15 | 14 | ND | ND | ND | ND | ND | 30.9 | ND | 4.5 | ND | ND | 41 | 45 | 91 | 8.1 | 299 | 22 | 91 | ND | ND | ND | 87 |
| Bi | ND | 0.5 | ND | ND | 1.5 | 0.6 | ND | ND | ND | 0.4 | 27 | ND | ND | ND | ND | ND | ND | 0.4 | 0.4 | 0.9 | 0.8 | 0.2 | ND | ND | 316 | 175 | 307 | 1.4 | 420 | 55 | 172 | ND | 27 | ND | 451 |
| U | 2.9 | 1.9 | 1.2 | 6 | 3.5 | 1.7 | 1.7 | 1.8 | 3.2 | 1.5 | 1.9 | 1.5 | 3 | 1.6 | 1.2 | 1.7 | 3.6 | 2.0 | 1.7 | 2.1 | 1.2 | 2.6 | 1.8 | ND | ND | 0.8 | 4.2 | 0.0 | 2.3 | ND | ND | ND | ND | ND | ND |
| Th | 5.5 | 6.1 | 5.6 | 7.3 | 8.8 | 6.2 | 6.1 | 7.5 | 6.3 | 11.9 | 6 | 4.7 | 7.7 | 4.7 | 5.6 | 6.7 | 11 | 6.3 | 6.2 | 6.9 | 1.9 | 4.8 | 4.7 | ND | ND | 0.7 | 0.3 | ND | ND | ND | ND | ND | ND | ND | 0.9 |

**Table 3** (Contd.)

| | Plast granitoids | | | | | | | | | | Borisov granite | Mafic dikes | | | | | | | | | | Quartz lodes | | | | | | | | | |
|---|---|---|---|---|---|---|---|---|---|---|---|---|---|---|---|---|---|---|---|---|---|---|---|---|---|---|---|---|---|---|---|
| Sample No. | K5 | K8 | K13 | K16 | K18 | K22 | K26 | K39 | K40 | BOR | K1 | K3 | K4 | K9 | K13 | K15 | K21 | K23 | K24 | K25 | K29 | K30b | K37 | K2 | K6 | K12 | K14 | K15 | K17 | K19 | K20 | K27 | K34 | K36 | K71 |
| La | 19 | 11.8 | 8.3 | 21 | 25.7 | 18.7 | 17 | 26 | 17 | 22.6 | 19 | 19 | 25 | 17 | 8.3 | 29 | 67 | 38.4 | 40.3 | 41.0 | 8.1 | 8.2 | 25 | 1 | 1.9 | 2 | 4 | 0.6 | 2.6 | 0.6 | 1.6 | 0.7 | 1.1 | 0.6 | 1.9 |
| Ce | 34 | 22.5 | 16 | 37 | 50.2 | 35.0 | 30 | 43 | 27 | 40.6 | 31 | 36 | 46 | 33 | 16 | 48 | 120 | 76.5 | 79.2 | 81.9 | 16.1 | 15.1 | 46 | ND | ND | ND | 7 | 1.3 | 7 | ND | ND | ND | ND | ND | 4 |
| Pr | ND | 2.6 | ND | ND | 4.7 | 3.2 | ND | ND | ND | 3.5 | ND | ND | ND | ND | ND | ND | ND | 7.6 | 7.8 | 8.1 | 1.7 | 1.6 | ND | ND | ND | ND | ND | 0.2 | ND | ND | ND | ND | ND | ND | ND |
| Nd | 12 | 8.9 | 6 | 11 | 19.7 | 13.0 | 9 | 13 | 12 | 13.4 | 12 | 17 | 18 | 11 | 6 | 19 | 43 | 33.0 | 33.6 | 35.2 | 8.0 | 6.5 | 17 | ND | ND | ND | b.d.l. | 0.6 | 10 | ND | ND | ND | ND | ND | ND |
| Sm | 2.4 | 1.6 | 1.2 | 2.7 | 3.5 | 2.2 | 1.9 | 2.5 | 1.6 | 2.3 | 2.6 | 3.5 | 3.9 | 3.1 | 1.2 | 3.6 | 7.9 | 5.6 | 5.8 | 6.2 | 1.9 | 1.3 | 2.9 | 0.2 | 0.3 | 0.3 | 0.3 | 0.1 | 0.2 | ND | ND | 0.2 | 0.1 | ND | 0.2 |
| Eu | 0.9 | 0.5 | 0.4 | 0.6 | 0.8 | 0.6 | 0.5 | 0.7 | 0.4 | 0.5 | 0.9 | 1 | 1.3 | 0.9 | 0.4 | 1.2 | 2.3 | 1.7 | 1.6 | 1.8 | 0.6 | 0.4 | 1.1 | ND | ND | ND | 0.3 | b.d.l. | ND | ND | ND | ND | ND | ND | 0.2 |
| Gd | ND | 1.2 | ND | ND | 2.8 | 1.6 | ND | ND | ND | 2.1 | ND | ND | ND | ND | ND | ND | ND | 4.9 | 5.1 | 5.3 | 2.0 | 1.4 | ND | ND | ND | ND | ND | 0.1 | ND | ND | ND | ND | ND | ND | ND |
| Tb | 0.5 | 0.2 | ND | ND | 0.4 | 0.2 | ND | ND | ND | 0.3 | b.d.l. | 0.6 | b.d.l. | b.d.l. | b.d.l. | b.d.l. | b.d.l. | 0.7 | 0.7 | 0.7 | 0.4 | 0.2 | b.d.l. | ND | ND | ND | ND | b.d.l. | ND | ND | ND | ND | ND | ND | 0.9 |
| Dy | ND | 1.0 | ND | ND | 1.8 | 0.8 | ND | ND | ND | 2.0 | ND | ND | ND | ND | ND | ND | ND | 3.3 | 3.3 | 3.6 | 2.3 | 1.2 | ND | ND | ND | ND | ND | 0.1 | ND | ND | ND | ND | ND | ND | ND |
| Ho | ND | 0.2 | ND | ND | 0.3 | 0.1 | ND | ND | ND | 0.4 | ND | ND | ND | ND | ND | ND | ND | 0.6 | 0.6 | 0.6 | 0.5 | 0.2 | ND | ND | ND | ND | ND | b.d.l. | ND | ND | ND | ND | ND | ND | ND |
| Er | ND | 0.6 | ND | ND | 0.8 | 0.4 | ND | ND | ND | 1.3 | ND | ND | ND | ND | ND | ND | ND | 1.6 | 1.6 | 1.8 | 1.6 | 0.6 | ND | ND | ND | ND | ND | b.d.l. | ND | ND | ND | ND | ND | ND | ND |
| Tm | ND | 0.1 | ND | ND | 0.1 | 0.1 | ND | ND | ND | 0.2 | ND | ND | ND | ND | ND | ND | ND | 0.2 | 0.2 | 0.2 | 0.2 | 0.1 | ND | ND | ND | ND | ND | b.d.l. | ND | ND | ND | ND | ND | ND | ND |
| Yb | 0.8 | 0.6 | 0.6 | 0.6 | 0.7 | 0.3 | 0.4 | 0.4 | 0.3 | 1.4 | 1.4 | 1.9 | 2 | 1.8 | 0.6 | 0.9 | 2.2 | 1.5 | 1.5 | 1.6 | 1.7 | 0.6 | 1.1 | ND | ND | ND | 0.7 | b.d.l. | 0.7 | ND | ND | ND | ND | ND | ND |
| La | 0.2 | 0.1 | 0.1 | 0.1 | 0.1 | 0.0 | 0.1 | 0.1 | 0.1 | 0.2 | 0.3 | 0.3 | 0.3 | 0.3 | 0.1 | 0.2 | 0.3 | 0.2 | 0.2 | 0.2 | 0.3 | 0.1 | 0.2 | ND | ND | ND | 0.12 | b.d.l. | 0.11 | ND | ND | ND | ND | ND | ND |
| $La_N/Lu_N$ | 12.3 | 9.8 | 9.5 | 21.6 | 31 | 42.6 | 26.7 | 39.1 | 25.2 | 10.7 | 7.3 | 7.04 | 7.6 | 5.3 | 9.6 | 16.7 | 24.7 | 20.3 | 19.1 | 18.6 | 2.98 | 10.1 | 13.6 | ND | ND | 3.4 | 10.8 | 2.5 | ND | ND | ND | ND | ND | ND | ND |

ND not determined, b.d.l. below detection limit

The least altered granitoid and mafic dike samples are in *italics*

ranges between 65 and 72 wt.% (Table 3). The aluminum-saturation-index (ASI) varies between 0.9 and 1.2, indicating a metaluminous to slightly peraluminous character. Plast granitoids are classified as trondhjemites, granodiorites, and granites after Barker (1979). $Na_2O/K_2O$ ratios are highly variable between 0.7 and 4.2 but are not correlated with LOI or S suggesting that the $Na_2O/K_2O$ ratios are not systematically affected by alteration. Slight enrichments of S, base metals, W, and Au are explained by a weak gold-sulfide mineralization, which correlates well with the only weakly developed alteration and mineralization assemblages.

Plast granitoids with elevated Au contents have similar trace element characteristics compared to least altered samples, which points to a minor modification by alteration. Low Yb (0.3 – 0.8 ppm), Y (4.7 – 9.1 ppm) and relatively high Al contents give the Plast lithologies an adakitic character (Table 3). The average continental crust normalized pattern (Weaver and Tarney 1984) has a slightly negative slope except for the HFSE (Fig. 6a). Relatively unaltered Plast granitoids are enriched in U and partly in Sr, and depleted in Nb and Ti. Chondrite (C1) normalized REE patterns (McDonough and Sun 1995) have a negative slope from La to Dy and are flat or show a weak negative slope from Ho to Lu (Fig. 6b). In general, the LREE/HREE fractionation is low to moderate with $La_N/Lu_N$ varying between 9.5 and 42.6. Plast granitoids with a strong greenschist facies overprint show variable compositions in P, Ba, and LREE.

Geochemically, the *Borisov* granitoid (BOR) is similar to the Plast granitoids, but is enriched in Rb, K, Zr, Hf, HREE, and shows a slightly negative Eu anomaly (Fig. 6a, b).

The major and trace element data of the calc-alkaline granitoid rocks of the Plast and Borisov massifs are consistent with a formation in a magmatic arc setting. The relatively high U contents indicate input from a continental source, possibly pointing to an Andean-type arc setting. However, a contribution by hydrothermal alteration cannot be ruled out.

## Geochemistry of mafic dikes

The mafic dikes are chemically heterogeneous ($SiO_2$ 44.2 – 69.6 wt.%) but in general have an alkaline character (Table 3). Elevated Si, K, Rb, Ba, and variable Sr concentrations can be attributed to the strong alteration of the mafic dikes by quartz, biotite, K-feldspar, and sericite of the biotite-K-feldspar alteration. Enrichments of S, base metals, W, and Au are related to gold-sulfide mineralization.

Trace elements are highly enriched relative to primitive mantle compositions (Fig. 6c). Incompatible elements such as Rb and K show most pronounced enrichments due to biotite-K-feldspar alteration, whereas Nb, Ta, and Ti are depleted. Sr displays a pronounced spread in the composition data, which is

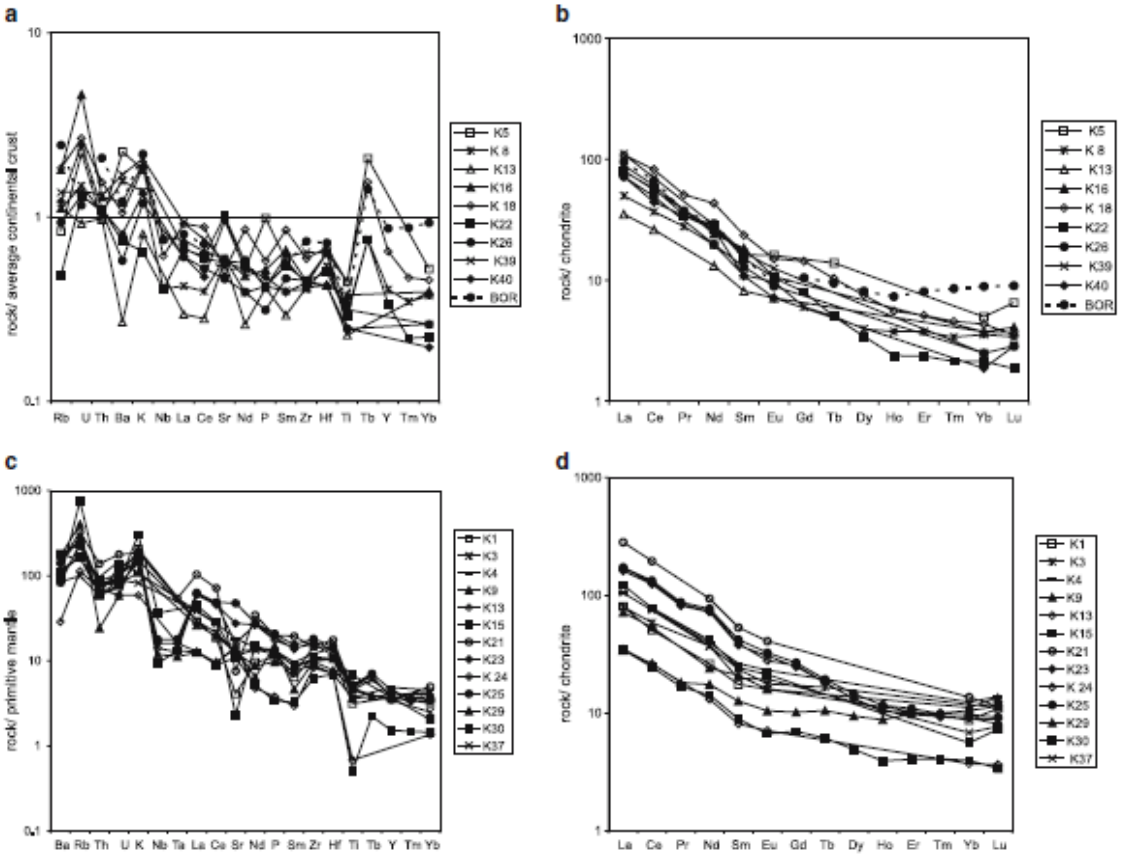


**Fig. 6** Geochemistry of the wall rocks. **a** Spider diagram of the granitoids normalized to average continental crust. Plast granitoids are enriched in U and depleted in Nb and Ti. Note that compositions of least altered (K16, K22, K26, K40: *filled symbols*) and altered samples overlap. The Borisov granite (*Bor*) is enriched in Rb, K, Zr, Hf. **b** Chondrite-normalized REE pattern of the granitoids. Note the similar pattern for all samples. The Borisov granite (*Bor*) is enriched in the HREE and has a negative Eu anomaly. **c** Spider diagram of the mafic dikes normalized to primitive mantle. Rb and K are enriched, whereas Nb, Ta, and Ti are depleted and Sr compositions are variable. Note that compositions of least altered (K4, K9, K15, K23, K25, K29, K30: *filled symbols*) and altered samples overlap. **d** Chondrite-normalized REE pattern of the mafic dikes. Note the similar pattern for all samples

most probably related to the two alteration stages overprinting the mafic dikes.

A chondrite (C1) normalized REE plot (McDonough and Sun 1995) of the mafic dikes displays a negative slope up to Dy and flat patterns in the region of the HREE with $La_N/Lu_N$ ranging between 3.0 and 24.7 (Fig. 6d). Samples with elevated Au concentrations (K1, K3, K37) are characterized by a relatively narrow range of normalized REE values, suggesting that alteration processes related to gold mineralization did not significantly affect trace elements. Mafic dikes with an intense greenschist facies overprint show no significant differences in geochemical composition. The REE pattern together with the depleted nature of generally immobile elements Ti, Nb, and Ta point to the formation of the mafic dikes in a magmatic arc setting.

## Geochemistry of gold-sulfide lodes

The auriferous quartz lodes contain some Al, Mg, Ca, Na, Ba, and Sr largely due to the low contents of calcite, sericite, biotite, and tourmaline (Table 3). High Fe contents correlate with high S or LOI, which is explained by a higher sulfide concentration in the lodes. These samples also contain higher amounts of Co, Cu, Pb, Zn, and As, which are incorporated into the sulfides. High Au concentrations of up to 75 ppm coincide with high Bi and W, suggesting that gold occurs together with bismuthinite and scheelite in the lodes. The chondrite (C1) normalized REE values (McDonough and Sun 1995) of the quartz lodes show a slight LREE enrichment with $La_N/Lu_N$ ratios ranging between 2.5 and 10.8 similar to those from mafic dikes and Plast granitoids (Table 3).

## Stable isotopes

Quartz separates from five quartz lodes have variable $\delta^{18}O$ values between 10.5‰ and 11.8‰. The barren later quartz vein is characterized by a $\delta^{18}O$ value of 10.5‰ (Table 4). The values for the mineralized and barren veins overlap in the lighter isotopic range, possibly indicating that quartz lodes were reactivated and their $\delta^{18}O$ value was influenced by the later, retrograde event during the formation of the barren veins. Using the isotope data from the quartz lodes and a temperature of 500°C, the isotopic composition of the water component of the ore fluid was calculated to $\delta^{18}O$ values between 8.2‰ and 9.5‰ (after Clayton et al. 1972). These $\delta^{18}O$ values lie well within the range for metamorphic and deep magmatic fluids (cf., Taylor 1979; Shephard 1986; Ridley and Diamond 2000). Taking the maximum temperature of 350°C for the formation of the barren late quartz vein, the $\delta^{18}O$ value of the hydrothermal fluid was calculated to 5.2‰ (after Clayton et al. 1972). This lighter isotopic composition of the later fluid is consistent with an overprint of the auriferous quartz lodes by this hydrothermal event and the modification of their composition to lower $\delta^{18}O$ values.

## Radiogenic isotope data

Zircon from the *Borisov* granitoid was analyzed for U/Pb isotope systematics. Three fractions can be distinguished in the zircon population. The grains of fractions Bor1 and Bor2 are euhedral, clear and colorless with length to width ratios of 8:1. Zircons of fraction Bor3 are anhedral and cloudy with brownish color. Four separates, each consisting of two grains, were used for analysis. These are discordant, but define an upper intercept at 358 ± 23 Ma, with a low MSWD (0.74) (Table 5; Fig. 7). This age is interpreted to mark the crystallization of the Borisov granite, which is within errors similar to the 341 ± 20 Ma age of the Plast massif reported by Sazonov et al. (2001).

Rb–Sr isotope data was collected for muscovite, calcite, and two whole rock fractions from a barren, late quartz vein (sample K30) crosscutting a mafic dike. All mineral and whole rock fraction data define an isochron yielding an age of 265 ± 3 Ma (Fig. 8a, Table 6). Due to the perfect definition of the isochron, the age is interpreted to mark the formation of the late, greenschist facies quartz veins. The initial $(^{87}Sr/^{86}Sr)_I$ ratio is determined at 0.70685 ± 0.00003.

Mineral fractions of a weakly altered Plast granitoid (sample K16) show isotopic disequilibrium (Fig. 8b, c; Table 6). Muscovite and whole rock fractions insoluble in HCl lie on one line. This "isochron" would give a date of 323 Ma. However, calcite plots markedly above that line, which suggests that the Rb/Sr isotope data represents at least two events. Therefore, the data are not used for age calculation. Retrospective calculation of the decay of $^{87}Rb$ to an age spectrum between 260 and 320 Ma, shows the calcite fraction to vary between initial $(^{87}Sr/^{86}Sr)_I$ values of 0.7076 and 0.7069, respectively (Fig. 8d). These signatures are slightly higher than the initial $(^{87}Sr/^{86}Sr)_I$ of sample K30. Therefore, either calcite in sample K16 formed earlier than calcite in K30, or, more likely, the signature in K16 indicates enhanced input from higher radiogenic mineral phases during the formation of calcite in the chlorite alteration zone.

**Table 4** $\delta^{18}O$ values for quartz of five different quartz lodes and one late, barren quartz vein, and calculated values for the fluid composition (after Clayton et al. 1972)

| No. | K6 | K15 | K20 | K34 | K36 | K30 |
|---|---|---|---|---|---|---|
| Sample | Quartz lode | Quartz lode | Quartz lode | Quartz lode | Quartz lode | Late quartz vein |
| $\delta^{18}O$ | 10.8 | 11.3 | 10.5 | 11.8 | 11.7 | 10.5 |
| Temperature (°C) | 500 | 500 | 500 | 500 | 500 | 350 |
| $\delta^{18}O$ for $H_2O$ in fluid | 8.5 | 9.0 | 8.2 | 9.5 | 9.4 | 5.2 |

**Table 5** Results of U–Pb isotope analyses of Borisov zircons

| Sample | Zircon characteristics | Pb[a] (pg) | U[b] (pg) | $^{206}Pb/^{204}Pb$ ratio[c] | $^{207}Pb/^{206}Pb$ ratio[d] | $^{207}Pb/^{235}U$ ratio[d] | $^{206}Pb/^{238}U$ ratio[d] | $^{207}Pb/^{206}Pb$ age (Ma) | $^{207}Pb/^{235}U$ age (Ma) | $^{206}Pb/^{238}U$ age (Ma) |
|---|---|---|---|---|---|---|---|---|---|---|
| Bor 1 | eu, l:w = 8:1 | 248 | 5,867 | 509.4 ± 0.3 | 0.05288 ± 0.00032 | 0.2727 ± 0.0020 | 0.0374 ± 0.0001 | 324 | 245 | 237 |
| Bor 1-2 | | 126 | 2,073 | 152.7 ± 0.3 | 0.0533 ± 0.0015 | 0.353 ± 0.022 | 0.0481 ± 0.0004 | 340 | 307 | 303 |
| Bor 2 | | 683 | 13,487 | 595.0 ± 0.2 | 0.05329 ± 0.00019 | 0.3349 ± 0.0019 | 0.0456 ± 0.0002 | 341 | 293 | 287 |
| Bor 3 | | 253 | 5,183 | 557.8 ± 0.4 | 0.05344 ± 0.00043 | 0.3146 ± 0.0041 | 0.0427 ± 0.0004 | 348 | 278 | 270 |

Errors are 2$\sigma$ errors
[a] Amount of $^{207}Pb$, $^{206}Pb$ and $^{204}Pb$ in zircon
[b] Amount of U in zircon
[c] Corrected for spike and fractionation
[d] Atomic ratios corrected for blank, spike, fractionation and initial common Pb
*eu* euhedral, *l:w* length to width ratio

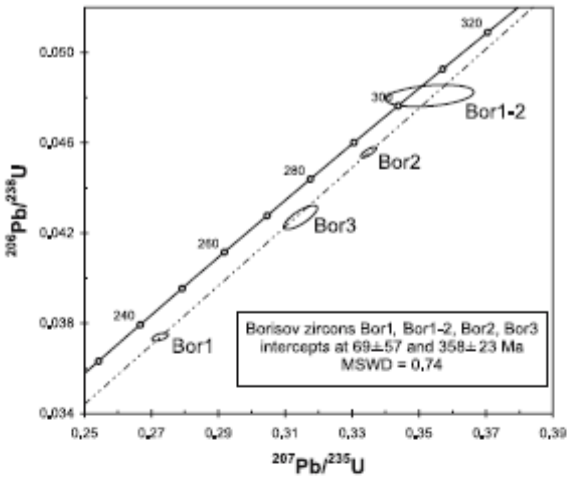


**Fig. 7** Concordia diagram showing the position of zircon separates Bor1, Bor1-2, Bor2 and Bor3 from granite of the Borisov massif. The upper intercept of 358 ± 23 Ma is interpreted as the intrusion age of the Borisov massif

The Plast granitoid (sample K40), which does not show mineralogical evidence of alteration, is also characterized by disequilibrium of its Rb–Sr systematics (Fig. 8e, Table 6). A two-point "isochron" for biotite and feldspar fractions yields a date of 271 ± 2 Ma, whereas muscovite lies markedly above that line. Biotite and feldspar are more easily affected by Rb- and Sr-diffusion during later hydrothermal alteration and metamorphism than muscovite. Most probably, partial resetting of plagioclase and biotite occurred during the greenschist facies stage and chlorite alteration at 265 ± 3 Ma.

The results show that the Plast lithologies have been affected by at least two stages of alteration after their intrusion at ca. 340 Ma leading to Rb–Sr disequilibria. These stages most probably correlate with lower amphibolite facies gold mineralization/biotite-K-feldspar alteration and greenschist facies chlorite alteration between 320 and 265 Ma.

## Discussion

The Urals represent an intact Paleozoic mountain belt with a preserved crustal root and a lack of postcollisional collapse (e.g., Bea et al. 2002; Brown et al. 2002). This makes it a favored target for comparative studies of Paleozoic orogenic gold mineralization and terrane evolution. Paleozoic orogenic gold deposits are invariably spatially associated with translithospheric compressional to transpressional-transtensional shear zones (Bierlein and Crowe 2000). Such crustal-scale first-order structures are interpreted as representing the fluid conduits for the hydrothermal fluids forming orogenic gold deposits, but only rarely directly host the deposits (e.g., Colvine et al. 1988; Eisenlohr et al. 1989; Groves 1993; Groves et al. 2003). Although the Kochkar deposit shares many similarities with other orogenic gold deposits worldwide, it is not spatially associated with a major shear zone (this study; Kisters et al. 2000). On a more regional scale, Sazonov et al. (2001) suggested that a NW–SE trending transcrustal sidewall ramp has activated plumbing systems for hydrothermal fluids forming the Kochkar deposit. This sidewall ramp is interpreted from regional magnetic data and is thought to have formed during NW–SE directed oblique convergence and indenter tectonics during collision in the central Urals (cf., ca. 56°N in Fig. 1). In the following, we discuss the alteration characteristics of the Kochkar deposit together with the terrane evolution and the plate tectonic configuration of the EUZ.

### Geodynamic setting and evolution of the granite-gneiss terrane

To the west of the EUZ, final accretion of the Magnitogorsk volcanic arc and the East European Platform occurred in late Devonian to early Carboniferous times (Brown et al. 1998). The coeval intrusion of the arc-related Borisov (358 ± 23 Ma; this study) and Plast (341 ± 20 Ma; Sazonov et al. 2001) granitoids into the EUZ suggests a shift of the subduction to the east at that time (Table 7). The mafic dikes, which intruded the Plast granitoids, also show geochemical characteristics of a magmatic arc and, therefore, possibly represent feeder dikes of arc-related mafic volcanism. This situation in the Kochkar region is in agreement with regional observations in the EUZ, which suggest eastward subduction beneath the Andean-type Valerianovsky arc (Zonenshain et al. 1990; Bea et al. 2002). Based on geophysical data, Echtler et al. (1997) and Kimbell et al. (2002) postulated a flip from eastward subduction at the MUF to westward subduction to the east of the EUZ. This model, however, is disputed by the data of Bea et al. (2002) as it contradicts the geochemistry of the arc-related magmas, which suggests contamination by old crustal material that could only be provided by the Siberian and Kazakhstan cratons.

The Plast and Borisov massifs have a rim characterized by a concentric $S_1$ foliation and dynamically recrystallized quartz and feldspar, which is interpreted to be related to a peak metamorphic overprint of the intrusive rocks at 635 ± 40°C and 5–6 kbar (Fig. 9). These gneissic fabrics formed during synkinematic ($D_1$) doming and sinistral transcurrent shearing along the major shear zones bounding the EUZ to the adjacent terranes. The change from E–W compressional to NW–SE transpressional tectonics along the East Magnitogorsk and Troitsk faults is coeval with the final closure of the Uralian Ocean and accretion at about 300 Ma (Table 7; Montero et al. 2000; Bea et al. 2002), which possibly coincides with indenter tectonics and changes in the regional stress field (Sazonov et al. 2001). Our data

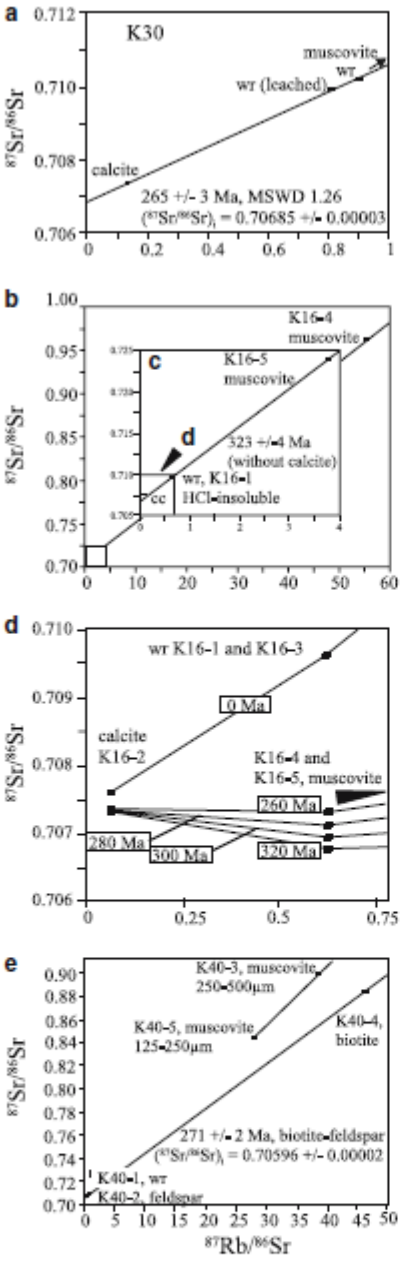


◀ **Fig. 8** **a** $^{87}Rb/^{86}Sr$–$^{87}Sr/^{86}Sr$ isochron diagram of muscovite, calcite, and two whole rock fractions (*wr*, leached with 0.1 N HCl and not leached) from a barren, late quartz vein (sample K30). **b** $^{87}Rb/^{86}Sr$–$^{87}Sr/^{86}Sr$ isotope diagram of the weakly altered Plast granitoid (K16), the inset **c** shows an enlargement of the lower left of the main diagram. The whole rock and muscovite data define a line giving a date of 323 ± 4 Ma. Calcite (*cc*) plots above that line indicating isotopic disequilibrium. **d** Recalculated $^{87}Sr/^{86}Sr$ ratios of calcite K16-2, whole rock and insoluble whole rock samples (K16-1, K16-3). The decay of $^{87}Rb$ was calculated for hypothetic ages between 260 and 320 Ma using the $^{87}Rb/^{86}Sr$ ratio of each sample. The signatures are slightly higher than the initial $(^{87}Sr/^{86}Sr)_I$ composition of sample K30 (see text for discussion). **e** $^{87}Rb/^{86}Sr$–$^{87}Sr/^{86}Sr$ characteristics of mineral fractions and whole rock powder of the Plast granitoid (K40). Whole rock, biotite, and feldspar define a line pointing to a date of 271 ± 2 Ma. The muscovite fractions fall above this line, suggesting isotopic disequilibrium

suggests that this was followed by a long-lasting (~50 m.y.) cooling history, recorded at Kochkar, until 265 ± 3 Ma (Fig. 9). The proposed *P*–*T* conditions during the retrograde path are typical for a HT/LP type of metamorphism of the EUZ (this study; Echtler et al. 1997; Puchkov 1997; Kroner et al. 2002).

Gold mineralization and $D_2$ deformation of granitoids and mafic dikes in a regional E–W compressional regime occurred during retrogression at lower amphibolite facies conditions (500 ± 20°C), postdating $D_1$ granitoid doming. This contradicts that gold mineralization at Kochkar is controlled by extension related to oblique indenter tectonics as suggested by Sazonov et al. (2001). Instead, the structural reactivation of the ENE–WSW trending mafic dike-granitoid contacts by dextral strike-slip deformation is in agreement with a regional E–W directed stress field (this study; Kisters et al. 1999, 2000), which possibly correlates with E–W shortening during the second collisional phase in the Urals during early Permian until early Triassic time (Brown et al. 1997; Puchkov 1997; Giese et al. 1999).

The end of the tectonometamorphic activity recorded at Kochkar is marked by greenschist facies veining and chlorite alteration during $D_3$ at a temperature of about 350°C, dated at 265 ± 3 Ma. This age is in agreement with the age of the final posttectonic plutonic activity, which progressed from 290 Ma (Dhzabyk) in the south to 254 Ma (Murzinka) in the north within the EUZ (Fig. 1; Table 7). These plutons, interpreted as partial melts of arc material, intruded into the EUZ at 2–3 kbar (Fershtater et al. 1997; Puchkov 1997).

The tectonothermal history of the EUZ at Kochkar postdating terrane collision is consistent with internal heat production by radiogenic elements of an overthickened crust (Bea et al. 2002). Especially, the voluminous Carboniferous granitoid magmatism contributed to the elevated heat production and the typical retrograde HT/LP path during $D_1$ doming.

The Permian granites were emplaced about 50 m.y. after collision by partial melting of the deeper crust (Puchkov 1997; Montero et al. 2000; Bea et al. 2002). This cannot be explained by internal heating and a "deep-later" type of metamorphism alone (Bea et al. 2002), which involve prograde heating of deep crustal levels whereas the upper crust undergoes a retrograde path (Stüwe et al. 1993). In this case, an external heat supply by magmatic underplating of the EUZ and accumulation of heat by fluid circulation is required (Bea et al. 1997, 2002; Gerdes et al. 2002). This external

**Table 6** Results of Rb–Sr isotope analyses of the weakly altered Plast granitoid sample K16, the greenschist facies vein sample K30, and the not altered Plast granitoid sample K40

| Sample | Lithology | Fraction | $^{87}Rb/^{86}Sr$ | $^{87}Sr/^{86}Sr$ |
|---|---|---|---|---|
| K16-1 | Weakly altered Plast granitoid | Whole rock, powdered | 0.6229 ± 0.0021 | 0.70960 ± 0.00001 |
| K16-2 | | Calcite, dissolved in 0.1 N cold HCl | 0.0667 ± 0.0003 | 0.70762 ± 0.00001 |
| K16-3[a] | | Whole rock, insoluble in 0.1 N HCl | 0.6279 ± 0.0013 | 0.70964 ± 0.00001 |
| K16-4[a] | | Muscovite, 250–500 µm | 55.20 ± 0.27 | 0.96237 ± 0.00002 |
| K16-5[a] | | Muscovite, 150–180 µm | 3.771 ± 0.003 | 0.72406 ± 0.00002 |
| "isochron" date 325 ± 4 Ma, MSWD 0.93 | | | $(^{87}Sr/^{86}Sr)_i$ = 0.70673 ± 0.00005 | |
| K30-1[a] | Late quartz vein | Muscovite, 250–500 µm | 53.26 ± 0.65 | 0.90753 ± 0.00007 |
| K30-2[a] | | Whole rock, insoluble in 0.1 N HCl | 0.8112 ± 0.0102 | 0.70993 ± 0.00005 |
| K30-3[a] | | Calcite, dissolved in 0.1 N cold HCl | 0.1334 ± 0.0025 | 0.70735 ± 0.00005 |
| K30-4 | | Whole rock, powdered | 0.9023 ± 0.0114 | 0.71022 ± 0.00005 |
| isochron age 265 ± 3 Ma, MSWD 1.26 | | | $(^{87}Sr/^{86}Sr)_i$ = 0.70685 ± 0.00003 | |
| K40-1 | Plast granitoid | Whole rock, powdered | 0.5114 ± 0.0007 | 0.70795 ± 0.00002 |
| K40-2[a] | | Feldspar | 0.3576 ± 0.0014 | 0.70733 ± 0.00001 |
| K40-3 | | Muscovite, 250–500 µm | 38.543 ± 0.025 | 0.89792 ± 0.00002 |
| K40-4[a] | | Biotite | 46.091 ± 0.057 | 0.88363 ± 0.00002 |
| K40-5 | | Muscovite, 125–250 µm | 27.948 ± 0.039 | 0.84366 ± 0.00003 |
| "isochron" date 271 ± 2 Ma | | | $(^{87}Sr/^{86}Sr)_i$ = 0.70596 ± 0.00002 | |

samples K16 and K40 analyzed at University of Münster, sample K30 analyzed at University of Gießen
[a]Used for isochron calculation

heating of the EUZ must have been a local feature, because coeval prograde heating is not recorded by metamorphic assemblages at Kochkar and the Permian plutons have contact metamorphic aureoles (Fershtater et al. 1997; Bea et al. 2002; Kroner et al. 2002). This tectonothermal evolution is consistent with a postcollisional slab rollback or delamination of the lithosphere, possibly providing the heat source for the Permian melting event in the EUZ.

## Fluid system and gold mineralization

The early Carboniferous Plast massif of the EUZ hosts the Kochkar deposit, which is structurally controlled at the boundary between the granitoids and mafic dikes by ENE–WSW trending, auriferous lodes. Non-coaxial deformation was partitioned into rheologically weak mafic dikes and coaxial deformation into the more competent Plast lithologies during regional E–W com-

**Table 7** Compilation of the timing of various tectonomagmatic events at the MUF and in the EUZ around Kochkar

| Timing | Main Uralian Fault (MUF) | East Uralian Zone (EUZ) |
|---|---|---|
| Late Devonian – Early Carboniferous | End of eastward subduction; collision of the East European Platform and the Magnitogorsk terrane; postcollisional transcurrent tectonics[a] | Onset of eastward subduction at the East Magnitogorsk Fault; intrusion of arc related magmas[c] |
| 358 ± 23 Ma | | Borisov granite[d] |
| 341 ± 20 Ma | | Plast granitoid[e] |
| 327 ± 2 Ma | End of tectonic activity in the southern Urals[b] | |
| Late Carboniferous – Early Permian | | Closure of the Uralian ocean at ~300 Ma; transcurrent tectonics at the East Magnitogorsk and Troitsk faults[c]; granitoid doming during the retrograde *P–T* evolution and subsequent gold mineralization at Kochkar[d] |
| 290 – 255 Ma | | End of tectonic activity at the Troitsk Fault and postorogenic plutonism, younging northward and postdating collision by about 50 m.y.[c, f] |
| 291 ± 4 Ma | | Dzhabyk batholith[f] |
| 265 ± 3 Ma | | Greenschist facies retrogression at Kochkar[d] |
| 254 ± 5 Ma | | Murzinka batholith[b] |

[a]Brown et al. (1998)
[b]Montero et al. (2000)
[c]Fershtater et al. (1997); Bea et al. (2002)
[d]this study
[e]Sazonov et al. (2001)
[f]Gerdes et al. (2002)

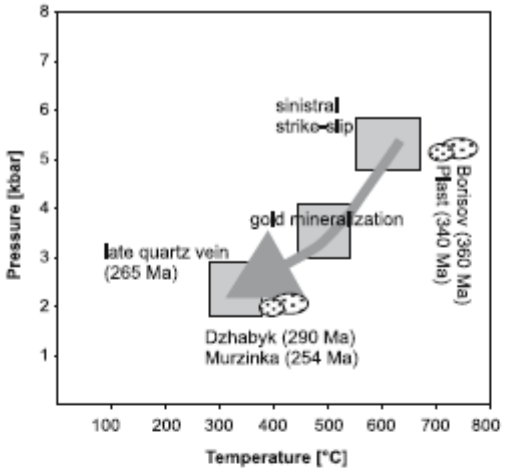


**Fig. 9** *P–T–t–D* path for the EUZ at Kochkar including major plutonic events

pression (Kisters et al. 2000). At the estimated temperatures of gold mineralization (~500°C), however, the quartz-feldspar-rich rocks of the Plast massif should be rheologically weaker than mafic dikes, which is supported by the fact that the $S_2$ foliation and the recrystallized fabric of granitoids is best developed close to the contact with mafic dikes. In the mafic dikes, deformation was concentrated in the plagioclase matrix, whereas hornblende formed porphyroclasts. Under the proposed *P–T* conditions, feldspar deformation has a significant contribution by microfracturing (Tullis 1983; Tullis and Yund 1985; Kruse et al. 2001), which possibly provides conduits for initial fluid flow (Kolb et al. 2004). This caused pervasive alteration of the hornblende-plagioclase assemblage to the biotite-K-feldspar alteration paragenesis and, thus, rheological weakening of the mafic dikes (Fig. 4a).

The alteration mineralogy of biotite, actinolite, albite, K-feldspar, quartz, epidote, tourmaline, sericite, pyrite, and arsenopyrite is typical for lower amphibolite facies conditions at about 500°C for mafic host rocks in other hypozonal gold deposits (cf., Eilu et al. 1999; Ridley et al. 2000). Au-bearing mafic dikes have the same trace element patterns as less altered mafic dikes, however, they show less spread in the normalized trace element patterns. This feature is less pronounced for the Plast granitoid samples (Fig. 6). From this, it is concluded that the ore fluid at least partly equilibrated with the host rocks and alteration was pervasive through the proposed microfracture porosity system. The equilibrated nature and the $\delta^{18}O$ values of the ore fluid is characteristic for the proposed deep source and long migration path of typical orogenic gold fluids (Ridley and Diamond 2000). The auriferous fluid system was possibly initiated by prograde metamorphism at deeper crustal levels due to crustal thickening in the EUZ. This resulted in gold mineralization on the retrograde *P–T* path of the terrane evolution (cf., Stüwe et al. 1993). Gold mineralization at Kochkar postdates active subduction and granitoid doming, and is not spatially associated with a transcrustal shear zone. This situation for gold mineralization differs markedly from other Phanerozoic orogenic gold settings. The thermal evolution of the EUZ was strongly influenced by the lack of postcollisional collapse, leading to a slow exhumation and a long-lasting cooling history, which probably triggered an intense fluid plumbing system responsible for gold mineralization in the minor shear zones at Kochkar. The west dipping Kartaly seismic reflector, situated only 5 km below Kochkar, may represent a transcrustal structure, which contributed in focusing auriferous fluids, however, its tectonic significance is still largely unclear (Echtler et al. 1996; Brown et al. 2002; Kimbell et al. 2002).

Gold mineralization was overprinted by a greenschist facies chlorite alteration paragenesis comprising quartz, muscovite, calcite, green biotite, and chlorite (Figs. 3e, 4e). Whole rock data show that geochemical changes were minor and only Ba, LREE, P, and Sr were mobilized. This redistribution of Sr has, however, a marked effect on the Rb–Sr-isotope systematics. The initial $(^{87}Sr/^{86}Sr)_I$ ratio of the greenschist facies related fluid is 0.70685. Calculation of the initial $^{87}Sr/^{86}Sr$ ratio of granites from Dzhabyk south of the Plast massif at the age of 265 Ma using the data of Montero et al. (2000) and Gerdes et al. (2002) yield $(^{87}Sr/^{86}Sr)_{265}$ ratios between 0.7046 and 0.7055, which is slightly lower than the isotopic signature of the greenschist facies fluid. This suggests that this fluid was not derived from the Permian granites, but possibly from older metamorphic rocks of the EUZ. Nevertheless, it should be mentioned that higher radiogenic initial Sr ratios (0.7093) occur in younger granites (Murzinka: Gerdes et al. 2002) to the north of the Plast massif and, therefore, a contribution from granitoid sources cannot be ruled out. The regional setting indicates that this fluid system was coeval with posttectonic plutonism and, therefore, triggered by prograde metamorphism in deep crustal parts of the EUZ and possible external heating of the terrane. This, however, clearly postdates gold mineralization at Kochkar.

## Conclusions

The hypozonal (~500°C) orogenic gold mineralization at Kochkar is hosted by quartz lodes, which developed in minor shear zones at mafic dike-granitoid contacts. The mafic dike and granitoid rocks were affected by two stages of hydrothermal activity (gold mineralization and greenschist facies retrogression) during the retrograde *P–T* path of the EUZ. The greenschist facies event was dated at 265 ± 3 Ma, which, together with other radiometric age data, indicates that gold mineralization occurred during terrane exhumation between 320 and 265 Ma, and predates postorogenic granitoid emplace-

ment. However, gold mineralization postdates active subduction and the intrusion of continental arc related felsic and mafic magmas emphasized by the Borisov granitoid that was dated at 358 ± 23 Ma. Active eastward subduction of the Uralian Ocean was followed by doming of the Plast and Borisov granitoids in a sinistral transpressional setting and a long-lasting retrograde tectonometamorphic history, which was caused by the lack of postcollisional collapse. This has triggered the fluid plumbing system responsible for gold mineralization at Kochkar. Later postorogenic plutonism and hydrothermal activity was due to additional external heating of the EUZ. Kochkar, therefore, represents a Paleozoic orogenic gold deposit, which formed in a mid-crustal section of an Andean-type volcanic arc that postdates active subduction and granitoid doming.

**Acknowledgements** SS is grateful to the late Vladimir Lennykh for his support during fieldwork. We thank U. Haack (Gießen), K. Mezger, H. Baier (Münster), and J. Jakobi (Aachen) for assistance with analytical work. Comments by R. Herrington and P. Weihed are greatly appreciated. The German Science Foundation (DFG), grants Kr 1195/4 and Me 1425/2, financially supported this study.

## Appendix

### Analytical procedure

The composition of amphibole, plagioclase, biotite, and tourmaline was determined by a JEOL JXA-8900R electron microprobe on polished thin sections. Operating conditions were 15 kV and 2 mA. Amphibole, plagioclase, and tourmaline were measured with a focused beam, whereas biotite was analyzed by a defocused beam of 10 µm diameter.

Handpicked quartz from five quartz lodes and one late quartz vein were analyzed for their $^{18}O/^{16}O$ ratios in order to obtain information on the fluid source and characteristic variations in $\delta^{18}O$ values. The data are given in the usual $\delta$-notation versus SMOW (Table 4). Mass spectrometric measurements have been performed on a SIRA 9 triple collector instrument of VG-Isogas at the University of Bonn, Germany. Ni-autoclaves were loaded with 8–10 mg of powdered samples, which subsequently reacted with $F_2$ at 2 bars and a temperature of 650°C. Reaction usually occurred overnight within 12-15 h. The fluorine was cleaned according to the method described by Asprey (1976). The rest of the analytical procedure (conversion to $CO_2$) is adapted from the classical method described by Clayton and Mayeda (1963). The $CO_2$ pressure was used to determine reaction yields, which were between 98 and 100% in most cases. Since sulfide contamination in silicate samples is known to cause fractionation in oxygen isotope compositions, several samples had to be treated with diluted HCl prior to isotope analysis. The data presented in Table 3 are mean values of at least two analyses of the same sample. The accuracy for the analyses lies within ±0.2‰.

For Rb–Sr isotope analyses mineral fractions were produced with the help of a magnetic separator, heavy liquids, and final handpicking. Bulk samples and silicate mineral fractions were dissolved with a HF–$HNO_3$ mixture and HCl (Table 6). Carbonate mineral fractions were leached from powdered samples in HCl. Elements were separated using standard cation exchange techniques. Rb–Sr-isotope ratio measurements were performed on a multicollector Finnigan MAT 261 (Institut für Geowissenschaften und Lithosphärenforschung, Gießen, Germany) and a VG Sector 54 (Mineralogisches Institut, Münster, Germany) solid source mass spectrometer (Table 6). For Sr the mass fractionation corrections were based on $^{86}Sr/^{88}Sr = 0.1194$. Repeated analyses of the $^{87}Sr/^{86}Sr$ ratio of the NBS 987 Sr standard in the period of analytical activity yielded $0.71023 \pm 0.00003$ ($n = 23$, $2\sigma$ of all analyses) in Gießen and $0.71028 \pm 0.00003$ ($n = 29$, $2\sigma$ of all analyses) in Münster. Total blanks are Rb < 60 pg and Sr < 100 pg. All decay constants are taken from Steiger and Jäger (1977).

Digestion of zircon crystals is performed in Teflon liners designed for the dissolution of six single crystals simultaneously using 24 N HF at 180°C. The digestion is completed after 4–10 days. HF is evaporated on a heating plate. After spiking with a mixed $^{205}Pb$–$^{233}U$ solution, sample and spike are homogenized in 6 N HCl for 24 h at 80°C. The excess HCl is evaporated finally. The Pb standards as well as the spiked samples are loaded without element separation on single Re filaments into a silica gel bed with 2 µl of a loading solution containing 90 vol.% of 6 N HCl and 10 vol.% of 0.1 N $H_3PO_4$. Isotope measurements are performed on a VG sector 54 mass spectrometer at the Zentrallabor für Geochronologie, Münster University, equipped with a Daly multiplier (Table 5). The Pb composition is determined at 1,300 – 1,400°C followed by the U measurement at 1,400 – 1,450°C. In most cases signals are only analyzed by the Daly multiplier leading to long times of analysis. At maximum the $2\sigma$ error margin obtained for $^{206}Pb/^{204}Pb$, $^{207}Pb/^{206}Pb$, and $^{233}U/^{238}U$ is 0.5, 0.5, and 0.1%, respectively. The obtained intensities range mostly at 1 – 2 mV for $^{206}Pb$ and 0.5 – 2 mV for $^{233}U$. Isotope ratios are corrected for mass fractionation (0.11% ±0.02/a.m.u.), blank (< 10 pg total Pb, $^{206}Pb/^{204}Pb = 17.7 \pm 0.5$, $^{207}Pb/^{204}Pb = 15.5 \pm 0.1$, 1 pg U) and initial common Pb estimated after the model of Stacey and Kramers (1975). The isotope $^{208}Pb$ is not analyzed. This has no impact on the U–Pb dating. However, the total amount of Pb in the sample solution cannot be calculated from the data. Only the sum of $^{204}Pb$, $^{206}Pb$ and $^{207}Pb$ can be given.

## References

Anonymous (1996) Russia. Eng Mining J 197(11):18–20
Asprey L (1976) The preparation of very pure fluorine gas. J Fluorine Chem 7:359–361

Ayarza P, Brown D, Alvarez-Marron J, Juhlin C (2000) Contrasting tectonic history of the arc-continent suture in the southern and middle Urals: implications for the evolution of the orogen. J Geol Soc Lond 157:1065–1076
Bankwitz P, Bankwitz E, Ivanov KS (1997) Schertektogen Südural. Freiberger Forschungshefte 470:1–17
Barker F (1979) Trondhjemite: Definition, environment and hypothesis of origin. In: Barker F (ed) Throndhjemites, dacites and related rocks. Elsevier, Amsterdam, pp 1–12
Bea F, Fershtater GB, Montero P, Smirnov VN, Zin'kova E (1997) Generation and evolution of subduction-related batholiths from the central Urals: constraints on the *P–T* history of the Uralian orogen. Tectonophysics 276:103–117
Bea F, Fershtater GB, Montero P (2002) Granitoids of the Uralides: implications for the evolution of the orogen. In: Brown D, Juhlin C, Puchkov VN (eds) Mountain building in the Uralides: Pangea to the present. Geophysical Monograph, Washington DC, pp 211–232
Bierlein FP, Crowe DE (2000) Phanerozoic orogenic lode gold deposits. In: Hagemann SG, Brown PE (eds) Gold in 2000. Rev Econ Geol, pp 103–139
Borodaevsky NI (1952) The gold deposits of the Kochkar district. Russian Academy of Science, Nauka, Moscow, pp 269–413
Brown D, Alvarez-Marron J, Perez-Estaun A, Gorozhanina Y, Baryshev V, Puchkov VN (1997) Geometric and kinematic evolution of the foreland thrust and fold belt in the southern Urals. Tectonics 16:551–562
Brown D, Juhlin C, Alvarez-Marron J, Pérez-Estaún A, Oslianski A (1998) Crustal-scale structure and evolution of an arc-continent collision zone in the southern Urals. Russia. Tectonics 17:158–170
Brown D, Juhlin C, Tryggvason A, Steer D, Ayarza P, Beckholmen M, Rybalka A, Bliznetsov M (2002) The crustal architecture of the southern and middle Urals from the URSEIS, ESRU, and Alapaev reflection seismic surveys. In: Brown D, Juhlin C, Puchkov VN (eds) Mountain building in the Uralides: Pangea to the present. Geophysical Monogr, Washington DC, pp 33–48
Clayton RN, Mayeda TK (1963) The use of bromine pentafluoride in the extraction of oxygen from oxides and silicates for isotopic analysis. Geochim Cosmochim Acta 27:43–52
Clayton RN, O'Neil JR, Mayeda TK (1972) Oxygen isotope exchange between quartz and water. J Geophys Res 77:3057–3067
Colopietro MR, Friberg LM (1987) Tourmaline-biotite as a potential geothermometer for metapelites, Black Hills, South Dakota. Geol Soc Am Abstr 19:624
Colvine AC, Fyon JA, Heather KB, Marmont S, Smith PM, Troop DG (1988) Archean lode gold deposits in Ontario: Part I. A depositional model; Part II. A genetic model. In: Keays RR, Ramsay WHR, Groves DI (eds) Ontario Geological Survey Miscellaneous. Econ Geol Monogr, p 136
Echtler HP, Stiller M, Steinhoff F, Krawczyk CM, Suleimanov A, Spiridonov V, Knapp JH, Menshikov Y, Alvarez-Marron J, Yunusov N (1996) Preserved collisional structure of the southern Urals revealed by Vibroseis profiling. Science 274:224–226
Echtler HP, Ivanov KS, Ronkin YL, Karsten LA, Hetzel R, Noskov AG (1997) The tectono-metamorphic evolution of gneiss complexes in the Middle Urals, Russia: a reappraisal. Tectonophysics 276:229–251
Eilu PK, Mathison CI, Groves DI, Allardyce WJ (1999) Atlas of alteration assemblages, styles and zoning in orogenic lode-gold deposits in a variety of host rock and metamorphic settings. Geology and Geophysics Department (Centre for Strategic Mineral Deposits) and University of Western Australia Extension. The University of Western Australia Publication, p 50
Eisenlohr BN, Groves DI, Partington GA (1989) Crustal-scale shear zones and their significance to Archaean gold mineralization in Western Australia. Mineral Deposita 24:1–8
Fershtater GB, Montero P, Borodina NS, Pushkarev EV, Smirnov VN, Bea F (1997) Uralian magmatism: an overview. Tectonophysics 276:87–103
Friberg LM, Larionov A, Petrov GA, Gee DG (2000) Paleozoic amphibolite-granulite facies magmatic complexes in the hinterland of the Uralide Orogen. Int J Earth Sci 89:21–39
Gerdes A, Montero P, Bea F, Fershtater GB, Borodina NS, Osipova T, Shardakova G (2002) Peraluminous granites frequently with mantle-like isotope compositions: the continental-type Murzinka and Dzhabyk batholiths of the eastern Urals. Int J Earth Sci 91:3–19
Giese U, Glasmacher UA, Kozlov VI, Matenaar I, Puchkov VN, Stroink L, Bauer W, Ladage S, Walter R (1999) Structural framework of the Bashkirian Anticlinorium, SW Urals. Geol Rundsch 87:526–544
Goldfarb RJ, Newberry RJ, Pickthorn WJ, Gent CA (1991) Oxygen, hydrogen, and sulphur isotope studies in the Juneau gold belt, southeastern Alaska: constraints on the origin of hydrothermal fluids. Econ Geol 86:66–80
Goldfarb RJ, Phillips GN, Nokleberg WJ (1998) Tectonic setting of synorogenic gold deposits of the Pacific Rim. Ore Geol Rev 13:185–218
Goldfarb RJ, Groves DI, Gardoll S (2001) Orogenic gold and geologic time: a global synthesis. Ore Geol Rev 18:1–75
Groves DI (1993) The crustal continuum model for late-Archaean lode-gold deposits of the Yilgarn Block, Western Australia. Mineral Deposita 28:366–374
Groves DI, Goldfarb RJ, Robert F, Hart CJR (2003) Gold deposits in metamorphic belts: overview of current understanding, outstanding problems, future research, and exploration significance. Econ Geol 98:1–29
Hetzel R, Echtler HP, Seifert W, Schulte AB, Ivanov KS (1998) Subduction- and exhumation-related fabrics in the Paleozoic high-pressure/low-temperature Maksyutov Complex, Antingan area, southern Urals, Russia. Geol Soc Am Bull 110:916–930
Holland TJB, Blundy J (1994) Non-ideal interactions in calcic amphiboles and their bearing on amphibole-plagioclase thermometry. Contrib Mineral Petrol 116:433–447
Kerrich R, Goldfarb RJ, Groves DI, Garwin S (2000) The geodynamics of world-class gold deposits: characteristics, space-time distribution, and origins. In: Hagemann S, Brown PE (eds) Gold in 2000. Rev Econ Geol, pp 501–551
Kimbell GS, Ayala C, Gerdes A, Kaban MK, Shapiro VA, Menshikov YP (2002) Insights into the architecture and evolution of the Southern and Middle Urals from gravity and magnetic data. In: Brown D, Juhlin C, Puchkov VN (eds) Mountain building in the Uralides: Pangea to the present. Geophysical Monogr, Washington DC, pp 49–65
Kisters AFM, Meyer FM, Seravkin IB, Znamenski SN, Kosarev AM, Ertl RGW (1999) The geological setting of lode-gold deposits in the central south Urals: a review. Geologische Rundschau 87:603–616
Kisters AFM, Meyer FM, Znamenski S, Seravkin I, Ertl RGW, Kosarev A (2000) Structural controls of lode-gold mineralization by mafic dykes in late-Paleozoic granitoids of the Kochkar district, southern Urals, Russia. Mineral Deposita 53:157–168
Kolb J, Meyer FM (2001) Tektonik Orogener Goldlagerstätten. Erzmetall 52:491–505
Kolb J, Rogers A, Meyer FM, Vennemann TW (2004) Development of fluid conduits in the auriferous shear zones of the Hutti Gold Mine, India: evidence for spatially and temporally heterogeneous fluid flow. Tectonophysics 378:65–84
Kroner U, Görz I, Henning D, Ruttloff K, Ivanov KS, Juminov A, Brőcker M (2002) Die Granit-Gneisdome des Osturals-Juvenile kontinentale Kruste in einem steckengebliebenen Kollisionsorogen. Erlanger Geologische Abhandlungen Sonderband 3:55–56
Kruse R, Stünitz H, Kunze K (2001) Dynamic recrystallization processes in plagioclase porphyroclasts. J Struct Geol 23:1781–1802
McDonough WF, Sun S-S (1995) The composition of the earth. Chemical Geol 120:223–253
Montero P, Bea F, Gerdes A, Fershtater GB, Zin'kova E, Borodina NS, Osipova T, Smirnov VN (2000) Single-zircon evaporation ages and Rb-Sr dating of four major Variscan batholiths

of the Urals: a perspective on the timing of deformation and granite generation. Tectonophysics 317:93–108
Puchkov VN (1997) Structure and geodynamics of the Uralian orogen. In: Burg J-P, Ford M (eds) Orogeny through time. Geol Soc Lond Spec Pub, London, pp 201–237
Ridley JR, Diamond LW (2000) Fluid chemistry of orogenic lode gold deposits and implications for genetic models. Rev Econ Geol 13:141–162
Ridley JR, Groves DI, Knight JT (2000) Gold deposits in amphibolite and granulite facies terranes of the Archean Yilgarn craton, Western Australia: evidence and implications of synmetamorphic mineralization. Rev Econ Geol 11:265–290
Samarkin GI, Samarkina YE (1988) Granitoids from southern Urals and the origin of granitic belts in folded regions (in Russian). Nauka, Moscow, p 209
Sazonov VN, van Herk AH, de Boorder H (2001) Spatial and temporal distribution of gold deposits in the Urals. Econ Geol 96:685–703
Seravkin IB, Kosarev AM, Salikhof DN, Znamenski SE, Rykus Y, Rodicheva ZI (1992) Volcanism in the southern Urals (in Russian). Nauka, Moscow, p 195
Shephard SMF (1986) Characterization and isotope variations in natural waters. In: Valley JW, Taylor HP Jr, O'Neil JR (eds) Stable isotopes in high temperature geological processes. Mineral Soc America, Washington, pp 165–183
Simpson L (1985) Deformation of granitic rocks across the brittle-ductile transition. J Struct Geol 7:503–511
Simpson L, Wintsch RP (1989) Evidence for deformation-induced K-feldspar replacement by myrmekite. J Metamorphic Geol 7:261–275
Stacey JS, Kramers JD (1975) Approximation of terrestrial lead isotope evolution by a two stage model. Earth Planet Sci Lett 6:15–25
Steiger HJ, Jäger E (1977) Subcommission on geochronology: convention on the use of decay constants in geo- and cosmochronology. Earth Planet Sci Lett 36:359–362
Stipp M, Stünitz H, Heilbronner R, Schmid SM (2002) The eastern Tonale fault zone: a 'natural laboratory' for crystal plastic deformation of quartz over a temperature range from 250 to 700°C. J Struct Geol 24:1861–1884
Stünitz H, FitzGerald JD (1993) Deformation of granitoids at low metamorphic grade II: granular flow in albite-rich mylonites. Tectonophysics 221:269–297
Stüwe K, Will TH, Zhou S (1993) On the timing relationship between fluid production and metamorphism in metamorphic piles: some implications for the origin of post-metamorphic gold mineralisation. Earth Planet Sci Lett 114:417–430
Taylor HP (1979) Oxygen and hydrogen isotope relationships in hydrothermal mineral deposits. In: Barnes (ed) Geochemistry of hydrothermal ore deposits, 2nd edn. Wiley, New York, pp 236–277
Tullis J (1983) Deformation of feldspars. In: Ribbe PH (ed) Feldspar mineralogy. Mineral Soc America, Washington, pp 259–277
Tullis J, Yund RA (1985) Dynamic recrystallization of feldspar: a mechanism for ductile shear zone formation. Geology 13:238–241
Voll G (1976) Recrystallization of quartz, biotite and feldspars from Erstfeld to the Leventina Nappe, Swiss Alps, and its geological significance. Schweizerische Mineralogisch Petrograpghische Mitteilungen 56:641–647
Weaver B, Tarney J (1984) Empirical approach to estimating the composition of the continental crust. Nature 310:575–579
Zonenshain LP, Korinevski VG, Kazmin VG, Pechersky GM, Khain VV, Matveenkov VV (1984) Plate tectonic model of the south Urals development. Tectonophysics 109:95–135
Zonenshain LP, Kuzmin LM, Natapov LM (1990) Uralian foldbelt. In: Page BM (ed) Geology of the USSR: a plate tectonic synthesis. American Geophysical Union Geodynamics Series, pp 27–54

10.

Sindern, S., Warnsloh, J.M., Trautwein-Bruns, U., Chatziliadou, M., Becker, S., Yüceer, S., Hilgers, C., Kramm, U. (2008) Geochemical composition of sedimentary rocks and imprint of hydrothermal fluid flow at the Variscan front – an example from the RWTH-1 well (Germany). Zeitschrift der Deutschen Gesellschaft für Geowissenschaften 159, 623 – 640. (www.schweizerbart.de)

With permission of E. Schweizerbart'sche Verlagsbuchhandlung OHG.

Re-use in thesis granted by E. Schweizerbart'sche Verlagsbuchhandlung OHG (Nägele u. Obermiller), Science Publishers, Johannesstr. 3A, 70176 Stuttgart, Germany, permission 14th of October 2015.

Z. dt. Ges. Geowiss., 159/4, p. 623–640, 9 figs., 3 tabs., Stuttgart, December 2008 **Article**

# Geochemical composition of sedimentary rocks and imprint of hydrothermal fluid flow at the Variscan front – an example from the RWTH-1 well (Germany)

Sven Sindern, Jens Martin Warnsloh, Ute Trautwein-Bruns, Maria Chatziliadou, Stephan Becker, Sükran Yüceer, Christoph Hilgers & Ulrich Kramm*

Sindern, S., Warnsloh, J.M., Trautwein-Bruns, U., Chatziliadou, M., Becker, S., Yüceer, S., Hilgers, C. & Kramm, U. (2008): Geochemical composition of sedimentary rocks and imprint of hydrothermal fluid flow at the Variscan front – an example from the RWTH-1 well (Germany). [Sedimentgeochemie und hydrothermaler Einfluss an der variszischen Front – am Beispiel der Bohrung RWTH-1 (Deutschland).] – Z. dt. Ges. Geowiss., 159: 623–640, Stuttgart.

**Abstract:** The mineralogical and chemical characteristics of Palaeozoic rocks in the northern Eifel Mountains provide information on the sedimentary provenance in the NW Rhenohercynian Basin and on the mineralogical and hydrothermal control of trace element abundance. Elements mainly bound to illite (i.e. V, Ni, Rb, Sr, Cu, Ba) can be distinguished from elements predominantly controlled by chromite (Cr) and zircon (Zr). Lower Devonian and Upper Carboniferous units have similar chemical characteristics indicating similar sources of detritus and in part resedimentation of Lower Devonian detritus during Upper Carboniferous times. Their high Chemical Index of Alteration points to intensive weathering in the source area and/or recycling during transport. The existence of an ophiolitic source of detritus situated in the NE of the Rhenohercynian Basin can be supported in this study by the abundance of Cr and Ni. A marked change of the sedimentary input is recorded in the Upper Devonian Famennian shales and Condroz Beds. Here, chemically unweathered rocks with felsic composition of the Brabant Massif dominate the source rocks.

Chemical evidence for fluid flow is observed at fault zones indicated in the RWTH-1 well. Input of Cu, Ba and $NH_4$ is attributed to Variscan hydrothermal fluid flow. Fluid flow was caused by dewatering of sedimentary rocks during the Variscan compressive deformation and was focussed along larger thrust faults within the footwall of the Aachen Thrust.

**Kurzfassung:** Paläozoische Gesteine der nördlichen Eifel werden mineralogisch und geochemisch charakterisiert. Damit ergeben sich Rückschlüsse auf Liefergebiete für das Nordwest-Rhenoherzynische Becken sowie auf Stoffeinträge durch hydrothermale Prozesse. Die Spurenelemente V, Ni, Rb, Sr, Cu und Ba werden vor allem durch die Häufigkeit von Illit kontrolliert, Cr und Zr durch die Schwerminerale Chromit und Zirkon. Unterdevonische und oberkarbonische Einheiten haben chemische Charakteristika, die auf ähnliche Sediment-Provenienz sowie Resedimentation von unterdevonischem Detritus im Oberkarbon hinweisen. Der „Chemical Index of Alteration" belegt intensive Verwitterung im Liefergebiet und/oder Aufarbeitung während des Transports. Die Cr- und Ni-Konzentrationen bestätigen das Vorkommen von ultramafischen Gesteinen im NE des Rhenoherzynischen Beckens. Die Condroz-Schichten stellen einen markanten Wechsel dar. Chemisch nahezu unverwitterte felsische Gesteine des Brabanter Massivs dominieren die Schüttung. Erhöhte Werte von Cu, Ba und $NH_4$ im Umfeld von Störungen in der Bohrung RWTH-1 belegen den strukturell fokussierten variszischen hydrothermalen Fluss, der während der variszischen Kompression durch Entwässerung von Sedimentgesteinen erzeugt wurde.

**Keywords:** Variscides, Rhenohercynian, geochemistry, ammonium, sedimentary rocks, Devonian, Carboniferous, hydrothermal, Brabant Massif, provenance

**Schlüsselwörter:** Variziden, Rhenoherzynikum, Geochemie, Ammonium, Sedimentgesteine, Devon, Karbon, hydrothermal, Brabanter Massiv, Provenanz

*Addresses of the authors:
Dr. Sven Sindern (sindern@rwth-aachen.de), Dr. Jens Martin Warnsloh (warnsloh@iml.rwth-aachen.de), Dipl.-Min. Maria Chatziliadou (chatziliadou@iml.rwth-aachen.de), Cand. Min. Sükran Yüceer (sukranyuceer@yahoo.com), Prof. Dr. Ulrich Kramm (Kramm@rwth-aachen.de), Institut für Mineralogie und Lagerstättenlehre, RWTH Aachen University, Wüllnerstrasse 2, D-52056 Aachen, Germany;
Dr. Ute Trautwein-Bruns (trautwein@geol.rwth-aachen.de), Cand. Geol. Stephan Becker (Stephan.Becker@rwth-aachen.de), Geologisches Institut Aachen, RWTH Aachen University, Wüllnerstrasse 2, D-52056 Aachen, Germany;
PD Dr. Christoph Hilgers (c.hilgers@ged.rwth-aachen.de), Lehrstuhl für Fertigungsmesstechnik und Qualitätsmanagement, Steinbachstrasse 52, D-52074 Aachen, Germany.

**DOI:** 10.1127/1860-1804/2008/0159-0623

1860-1804/0159-0623 $ 8.10
© 2008 E. Schweizerbart'sche Verlagsbuchhandlung, D-70176 Stuttgart

## 1. Introduction

Chemical signatures of clastic sediments represent the provenance as well as the kind of detrital components (Gibbs et al. 1986, Condie 1993, Cullers 1994, 1995, McLennan et al. 1995, Veizer & McKenzie 2003). The chemical composition of sediments is also affected by post-depositional processes, such as diagenetic and hydrothermal fluid flux (Milliken 2003). The latter has caused numerous Pb-Zn mineralisations in the Rhenohercynian (Behr et al. 1987, Redecke 1992, Krahn & Baumann 1996). It may also control the abundance of elements which are highly mobile in hydrous fluids, such as N or Cl.

Nitrogen, mainly released by breakdown of organic matter (Mingram et al. 2005) during diagenetic and metamorphic events (Meyer & Ridgway 1991) becomes mobile in a hydrothermal fluid. Depending on the temperature (Williams & Ferrell 1991, Williams et al. 1992, Mingram et al. 2005) it can again be incorporated into minerals as ammonium during fluid/rock interaction. Increased concentration of ammonium bound to mineral phases may therefore be indicative of former fluid flow.

Geochemical data of sedimentary rocks can also serve as an indicator of clastic components and their provenance which is well studied for the eastern part of the Rhenohercynian Basin (Schulz-Dobrick & Wedepohl 1983, Press 1986). However, not many data exist from the NW part of the Rhenohercynian Basin to the west of the Rhine River (Haverkamp 1991).

This study characterizes the geochemical composition of the Devonian and Carboniferous sediments sampled in the RWTH-1 well and in surface outcrops in the NW Rhenohercynian close to Aachen (Fig. 1). The results are compared with the well-studied occurrences east of Rhine River (Schulz-Dobrick & Wedepohl 1983) and mineralogical parameters controlling chemical characteristics are discussed. In addition the data are used to define the elements enriched by a fluid phase which can thus be used to identify zones of hydrothermal fluid flow.

The RWTH-1 well was drilled in the city of Aachen between July and December 2004 and reached a depth of 2544 m. Serving as a deep heat exchanger it will be used for heating and cooling of the new students service centre "SuperC" of RWTH Aachen University. Technical aspects are described by Lundershausen et al. (2005). A comprehensive DFG funded geoscientific research program carried out by RWTH Aachen University in cooperation with the Geological Survey of North Rhine-Westphalia (GD-NRW) aims at providing new information on recent and palaeo stress field as well as hydrothermal fluid and material transport (Trautwein-Bruns et al. 2007).

## 2. General geological setting

The Devonian to Carboniferous sedimentary rocks of the NW Rhenohercynian were deposited in a shallow marine to littoral environment at the passive continental margin of the southern Brabant Massif (Fig. 1; Oncken et al. 1999, 2000, Stets & Schäfer 2004). In this part of the basin, the predominantly siliciclastic sedimentary succession is interrupted by carbonates of a wide shelf lagoon during the Middle Devonian and lower Upper Devonian (Kasig & Wilder 1983, Grabert 1998).

In the Lower and Middle Devonian source areas for clastic sediments were mainly situated in the north which can be derived from facies characteristics (e.g. Knapp 1980, Walter 1992, Grabert 1998), heavy minerals (Press 1986) and Pb-isotope signatures of detrital zircon (Haverkamp 1991, Haverkamp et al. 1991). With beginning closure of the Rhenohercynian Basin in the Upper Devonian, sediments in most parts of the basin predominantly originated from southern source areas, formed from a tectonic flysch wedge and an emerging magmatic arc, i.e. the Mid-German Crystalline Rise (Engel et al. 1983, Haverkamp et al. 1991, Ganssloser 2000, Oncken et al. 2000). However, in the NW Rhenohercynian Basin the Brabant Massif constitutes a more significant source of detritus (Walter 1992, Meyer 1994). In Upper Carboniferous times sediments were again derived from northern, as well as from southern source areas (Haverkamp et al. 1991).

During Variscan foreland compression the Rhenohercynian Basin was shortened by app. 50 %. A fold and thrust belt formed which represents the northernmost domain of the Variscan orogenic belt (Hollmann 1997, Hollmann & Winterfeld 1999, Oncken et al. 1999, 2000). The Faille du Midi and its NE prolongation, the Aachen Thrust, is the frontal thrust of the Rhenohercynian domain (Oncken et al. 1999, 2000). Along the SE dipping Aachen Thrust Devonian to Carboniferous carbonaceous and siliciclastic units of the Aachen imbrication zone and the Venn-Weser-Inde-Nappe are placed on top of the Wurm Syncline (Fig. 1). The RWTH-1 well samples rocks in the footwall of the Variscan front a few hundred metres NW of the Aachen Thrust (Fig. 1). It represents a zone that is partially intensively deformed and highly affected by syn-deformational Variscan hydrothermal fluid flow (Lõgering et al. 2006, Sindern et al. 2007).

The compressive Variscan deformation, subsequent metamorphism, cleavage formation in the Venn-Weser-Inde-Nappe and hydrothermal fluid flow were dated between 336 and 300 Ma (Nierhoff 1994, Glasmacher et al. 2001). In the immediate vicinity of the Aachen Thrust, represented in the RWTH-1 well, the onset of hydrothermal activity was syntectonic (Lõgering et al. 2006, Sindern et al. 2007) which is in line with the idea that hydrothermal fluid flow was caused by fluid mobilisation along the Aachen Thrust due to thrusting and thrust loading during the Variscan orogeny (Winterfeld 1994).

Significant fluid discharge along the Aachen Thrust into the Wurm Syncline is also assumed by Lünenschloss et al. (1997) and Lünenschloss (1998) which is in line with markedly high vitrinite temperatures close to the Aachen Thrust relative to the northern Wurm and southern Inde Synclines (Winterfeld 1994, Oncken et al. 1999).

In the RWTH-1 well, based on a study of fluid-inclusions and mineral equilibria, Lõgering et al. (2006) determine tem-

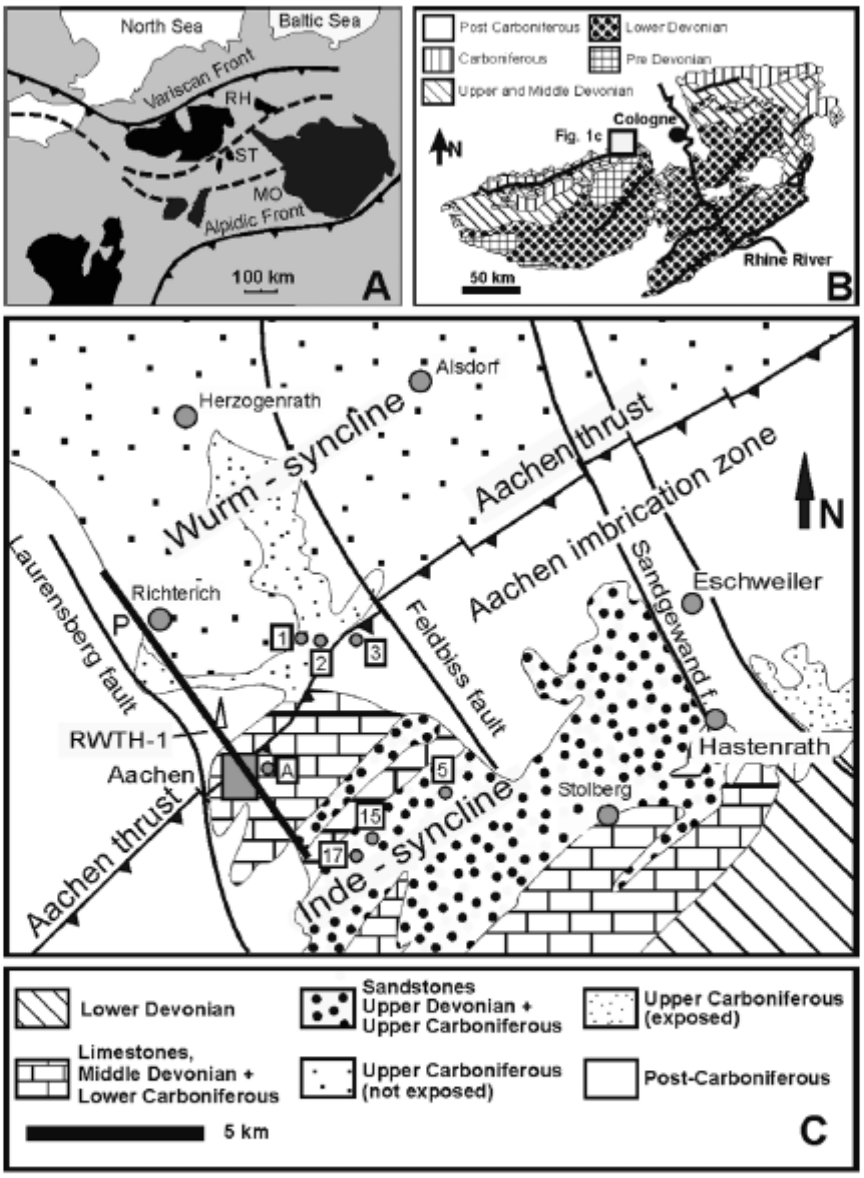


Fig. 1: Geological sketch maps. (A) Overview of the Middle European Variscan zones (according to Oncken et al. 2000); MO = Moldanubian, RH = Rhenohercynian, ST = Saxothuringian. (B) Simplified geological map of the NW Rhenohercynian domain; modified from Stroetmann-Heinen (1999). (C) Location of the RWTH-1 well and northern Eifel region around Aachen. Numbers and letters in white squares indicate sample locations, 1–3 = YWT1–3; A = AK1; 5, 15, 17 = IM5–17; see table 2 for further information on samples; map modified from Steingrobe (1990).

Abb. 1: Geologische Kartenskizzen. (A) Überblick über die mitteleuropäischen Varisziden (nach Oncken et al. 2000); MO = Moldanubikum, RH = Rhenoherzynikum, ST = Saxothuringikum. (B) Vereinfachte geologische Karte des NW-Rhenoherzynikums (modifiziert nach Stroetmann-Heinen 1999). (C) Position der Bohrung RWTH-1 und nördliche Eifel-Region in der Umgebung von Aachen. Zahlen und Buchstaben in den weißen Feldern geben Probenpunkte an, 1–3 = YWT1–3; A = AK1; 5, 15, 17 = IM5–17; siehe auch Tabelle 2 zu weiteren Informationen zu den Proben; Karte modifiziert nach Steingrobe 1990).

peratures of 280–370 °C for minerals formed in hydrothermal veins. Such temperatures as well as low salinities revealed in fluid inclusions (< 9 wt.-%, Lögering et al. 2006) are considered similar to those of Variscan tectonic brines (Behr et al. 1987). In a study of illite and chlorite crystallinities Sindern et al. (2007) conclude that the Variscan hydrothermal fluid flux probably lasted less than 10 000 years.

In post-Variscan times the region was affected by Pb-Zn mineralisation at temperatures below 150 °C which was also controlled by major fracture zones (Friedrich et al. 1993, Muchez et al. 1994). Schneider et al. (2007) published an age of 134 ± 2 Ma for the non-economic Pb-Zn-mineralisation of Hastenrath in the Inde Syncline (Fig. 1).

## 3. Stratigraphy of the RWTH-1 well

The upper 1012 m of the RWTH-1 well consist of Upper Carboniferous Namurian to Westphalian strata composed of shales and sandstones with intercalated coal seams (Fig. 2; Oesterreich & Lundershausen 2002, Lundershausen et al. 2005, Oesterreich et al. 2005, Ribbert 2006). Lower Carboniferous stratigraphic units are missing in the well. Such hiatus in the Lower Carboniferous is also described in other profiles near Aachen (Kasig & Wilder 1983). The Upper Carboniferous rocks are underlain by Upper Devonian (Famennian) strata down to 1438 m. Within the Famennian, the section from 1012 to 1260 m is dominated by silt- and sandstones considered as equivalent to the Evieux and Montfort Formations of the Condroz Beds, whereas shales mainly compose the succession from 1260 to 1407 m (Pechnig 2005, Ribbert 2006). Stratigraphically, the latter unit represents the Upper Famennian shales. Between 1407 and 1438 m nodular limestones occur which belong to the Famennian crepida-zone (based on conodonts; Ribbert 2006), and possibly Lower Famennian shales. The depth of 1438 m marks a lithological change and lies in the centre of a thrust fault zone. The detailed stratigraphy of the Lower Devonian sand-siltstones and shales below 1438 m down to the end at 2544 m has not fully been worked out. Age determination by spores indicates that the rocks at 1490 m are Upper Siegenian (Wrede, pers. comm.) and are thus considered as part of the Lower Devonian Zweifall Beds. Within the Lower Devonian rocks red and green colours dominate between 1438 to 1895 m and 2250 to 2515 m. Between 1895 to 2250 m the silt-sandstones and shales mainly have grey to green colours (Oesterreich et al. 2005). This segmentation corresponds to geophysical log data (Pechnig 2005).

It has to be stated that Lower Famennian to Givetian units are missing. This can be explained by sedimentary hiatus levels which occur in other areas of the western Rhenohercynian as well (Ribbert 2006).

Cores were cut at the depth intervals 1392–1515 m, 2128–2143 m and 2536–2544 m. The first interval is characterized by intensive deformation and hydrothermal vein formation (Lögering et al. 2006, Sindern et al. 2007) especially in the thrust fault zone around 1438 m. Further fault zones with thrust-faulting character are identified between 660–

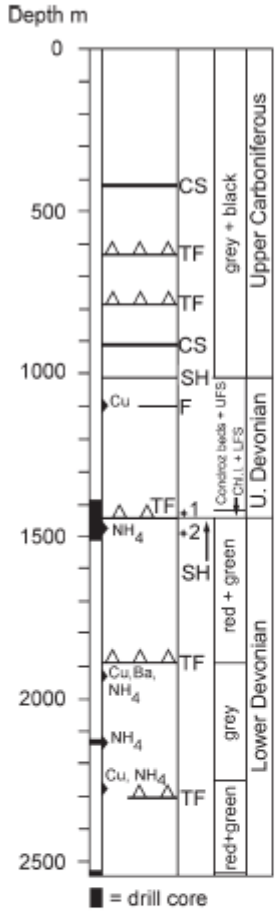


Fig. 2: Geological profile of the RWTH-1 well. Black bars at left side indicate position of drill cores. Information on other sections is based on cuttings as well as on log data (Oesterreich et al. 2005, Ribbert 2006, Trautwein-Bruns unpublished data). Filled triangular marks indicate exceptional abundance of the components Ba, Cu and $NH_4$, see text for discussion. CS = coal seam, SH = sedimentary hiatus, TF = thrust fault, F = fault with uncertain character of displacement, Chl.l. = Cheiloceras Limestone, LFS = Lower Famennian Shale, UFS = Upper Famennian Shale; 1: marks a level indicated as belonging to the Famennian crepida zone by conodonts (Ribbert 2006), 2: level characterized by spores as part of Upper Siegenian (Wrede, pers. comm.).

Abb. 2: Geologische Profildarstellung der Bohrung RWTH-1. Schwarze Balken an der linken Seite geben die gekernten Strecken an. Angaben zu den anderen Bohrstrecken basieren auf der Untersuchung von Bohrklein und Log-Daten (Oesterreich et al. 2005, Ribbert 2006, Trautwein-Bruns unveröff.). Gefüllte Dreiecke geben erhöhte Gehalte von Ba, Cu und $NH_4$ an, siehe Text für weitere Diskussion. Abkürzungen: CS = Kohleflözchen, SH = Sedimentärer Hiatus, TF = Überschiebung, F = Störung mit nicht spezifiziertem Versatz, Chl.l. = Cheiloceras-Kalk, LFS = Untere Famenne-Schiefer, UFS = Obere Famenne-Schiefer; 1: Niveau, das durch den Fund von Conodonten der crepida-Zone zugeordnet werden kann (Ribbert 2006), 2: Niveau, das durch Sporenfunde den oberen Siegener Schichten zugewiesen wird (Wrede, pers. Mitt.).

720 m, 900–960 m, 1880–1942 m and 2220–2310 m (Fig. 2). This is based on dipmeter and image data, shear wave anisotropy measurements determined by geophysical logging (Pechnig 2005, Trautwein-Bruns unpublished data) and the interpretation of a seismic profile shot close to the RWTH-1 site (Becker unpublished data). The repeated occurrence of thrust faults underlines the generally compressive character of the footwall of the Aachen Thrust. In the RWTH-1 well the degree of shear wave anisotropy correlates with fracture density which is increased in fault zones. This is in line with general observations in well log data (Armstrong et al. 1994). An exception to this correlation can be seen between 400 m and 535 m. Here, steeply inclined bedding planes are the main cause for the high formation anisotropy. Euhedral quartz crystals of up to 5 mm length are also observed in drill cuttings in the Upper Devonian section indicating the presence of open fractures during hydrothermal activity.

## 4. Analytical techniques and methods

Drill cuttings were washed repeatedly in an ultrasonic cleaner for more than 20 minutes to guarantee removal of adhering drilling mud according to Chatziliadou et al. (2005), occasionally followed by a step of hand-picking to remove artificial plastic material from the drilling and vein fillings. Field and drill core samples were cleaned, weathered parts were cut off if necessary and crushed to cm-sized pieces in a polyethylene bag. All samples were ground in a tungsten-carbide disk swing mill. Thus W, Co and Ta are not considered.

Major and trace elements were determined by energy dispersive x-ray fluorescence (Spectro XLab2000, Institute of Mineralogy and Economic Geology, RWTH Aachen University) equipped with a Pd-tube operated at acceleration voltages between 15 and 53 kV and currents between 1.5 and 12.0 mA. Major elements were analysed on fused discs (diluted 1:10 with a Li-tetraborate/Li-metaborate mixture, FX-X65, Fluxana, Kleve, Germany) using Co, Ti and Al as secondary targets. Data computation was performed using a fundamental parameter procedure. Pressed powder pellets were used for trace element determination. For these elements best excitation was achieved by Mo, $Al_2O_3$, Pd and Co targets. Chlorine was excited using Pd L of the tube reflected on the sample by a graphite target. For matrix correction the Mo-Compton peak was taken. Precisions are < 0.5 % for the major and < 5 % for the trace elements, except for Ba (precision < 10 %). Loss on ignition was determined by heating the powdered sample for 120 min at 1000 °C. Lower limits of determination are 10 ppm for Cu, Zn, Sr; 20 ppm for V, Cr, Ni, As, Rb, Zr, Pb, and 50 ppm for Ba and Cl.

Carbon analyses were carried out using a RC-412 (Leco) analyser at T < 500 °C (organic carbon, $C_{org}$) and T > 500 °C (inorganic carbon, $C_i$) with oxygen gas. Carbon-dioxide produced by combustion was detected by IR absorption. Nitrogen and S were analysed at the Department of Geography RWTH Aachen University (analyst M. Dohms) on a Eurovektor EA3000 (Hekatech) with element separation after combustion at 1000 °C by gas-chromatography and detection by a thermal conductivity detector. Precision for C and N analyses was better than 4 %.

X-ray powder diffraction analyses were performed using a Siemens D500 x-ray diffractometer with the following instrumental parameters: Cu Kα radiation ($\lambda$ = 1.5406 for Cu $K\alpha_1$) with Ni filter, tube conditions: 45 kV and 35 mA, curved graphite monochromator on diffracted beam, detector: scintillation, scan range 3–72° (2Θ), scanning speed 0.4°/min. The pulverized rock samples were filled into conventional top-loading holders (25 mm opening diameter) and spinned around the Z-axis during analysis. Data were processed with the software kit "DIFFRACPLUS EVA 3" (Bruker AXS) for mineral identification and the Rietveld-software "BGMN" (4th revised edition 2006 by Jörg Bergmann, Dresden, Germany) for quantitative phase analysis.

## 5. Results

Mineralogical and chemical data were derived from sediments sampled in the RWTH-1 well (drill core and rock cuttings) and in surface outcrops in the NW Rhenohercynian. The volume of shale ($V_{SH}$; Tab. 1) was calculated from gamma ray data (Th radiation) according to Larionov (1969).

The mineral composition of representative samples and literature data for comparison is also displayed in table 1. The predominating mineral in all rocks is quartz, followed by white mica (i.e. illite of late diagenetic grade in matrix and subordinate detrital mica; Sindern et al. 2007), chlorite and feldspars.

Highest quartz abundances are observed in Lower Devonian units at depths > 1770 m. Complementary to the increase in quartz these rocks are characterized by a decrease in white mica and chlorite. This is also reflected by a decrease in $V_{SH}$. Chlorite reaches maximum abundances at c. 1556 and 2500 m. In the Lower Devonian K-feldspar is insignificant, whereas albite reaches abundances of 8–10 wt.-% at 1949 and 2540 m. Highest contents of both, albite and K-feldspar, are encountered in the Upper Devonian section.

Highest carbonate contents occur in the Famennian zone between 1407 and 1438 m (e.g. sample 10-1; Tab. 2) which consists of nodular limestone. The inorganic carbon, $C_i$, increases in the Upper Famennian Shales and Condroz Beds from low values (# 0.35 %, > 1296 m) to 1.84 % at 1096 m.

When the abundance of carbonate bearing sand-siltstones in the Condroz Beds of the northern Eifel Mountains (Knapp 1980, Meyer 1994) is taken into account, it can be assumed that the increase of $C_i$ mirrors the succession from the Upper Famennian Shales (1407 to approx. 1260 m) to the Montfort and Evieux Formations of the Condroz Beds (approx. 1260 to 1012 m). This is in line with the finding of sand- and siltstone in cuttings between 1260 to 1012 m and shales between 1260 and 1407 m (Oesterreich et al. 2005).

Pyrite was detected by XRD in the Upper Devonian sample 1255 (Tab. 1) but can be seen in Upper Devonian cuttings as well as in the Upper Devonian part of the first core section (1438–1392 m). The Upper Carboniferous rocks are rela-

Tab. 1:Mineralogical composition (wt.-%) of samples from the RWTH-1 drill hole calculated by Rietveld analysis (250 to EK1) and literature data from the Rhenohercynian (UCF83, UDF83, SiegF83). White mica mainly represents illite but also detrital muscovite.

| sample | strat. unit | depth (m) | $V_{sh}$[7] | quartz | albite | K-fsp | white mica | chlorite | dolomite | calcite | ankerite |
|---|---|---|---|---|---|---|---|---|---|---|---|
| 250 | UC | 285.40 | 50 | 43.1 | 4.8 | 1.1 | 46.6 | 4.3 | 0.1 | | |
| 302 | UC | 338.05 | 54 | 47.5 | 2.2 | 1.1 | 38.7 | 3.7 | | 4.2 | 2.6 |
| 550 | UC | 593.50 | 48 | 39.2 | 3.3 | 0.5 | 32.0 | 9.3 | | 9.5 | 6.1 |
| 799 | UC | 844.00 | 62 | 49.0 | 2.5 | 1.2 | 37.6 | 5.0 | | 1.2 | 3.8 |
| 1100 | UD[5] | 1146.98 | 33 | 42.0 | 8.9 | 22.7 | 5.8 | 7.9 | 12.7 | | |
| 1146 | UD[5] | 1193.95 | 22 | 42.7 | 11.7 | 18.7 | 10.6 | 8.1 | 8.2 | | |
| 1255[1] | UD[6] | 1301.40 | 42 | 38.7 | 11.5 | 12.1 | 26.6 | 9.0 | 1.9 | | |
| 1346 | UD[6] | 1392.00 | 51 | 30.1 | 7.8 | 4.0 | 46.2 | 9.6 | 2.3 | | |
| 1477 | LD | 1556.00 | 63 | 40.8 | | 1.8 | 41.0 | 16.0 | 0.4 | | |
| 1688 | LD | 1774.00 | 47 | 56.1 | 2.4 | 1.4 | 30.0 | 8.6 | 0.9 | 0.5 | |
| 1873 | LD | 1949.00 | 11 | 63.8 | 9.1 | | 18.2 | 8.3 | 0.6 | | |
| 2130 | LD | 2194.05 | 7 | 73.2 | 3.5 | 0.6 | 15.7 | 6.9 | 0.2 | | |
| 2239 | LD | 2302.03 | 39 | 69.6 | 2.0 | 2.4 | 15.0 | 8.9 | 2.1 | | |
| 2470 | LD | 2536.01 | nd | 58.9 | 9.6 | 0.5 | 19.9 | 11.2 | | | |
| EK1 | LD | 2543.90 | nd | 41.3 | 8.5 | 0.7 | 33.8 | 15.7 | | | |
| | | | | | | | | | | carbon. | |
| UCF83[2] | UC | | | 31–61 | 3–7 | | 25–49 | 3–9 | | 1.6–2.4 | |
| UDF83[3] | UD | | | 33–52 | 4–6 | 0.2–3 | 26–45 | 10–15 | | 1.4–2 | |
| SiegF83[4] | LD | | | 38–61 | 3–4 | 0.2–0.3 | 26–44 | 8–14 | | 0–0.8 | |

[1] contains 0.19 wt-% pyrite, [2] Average Upper Carboniferous shales and silty shales, [3] Average Upper Devonian shales and silty shales; [4] Average Siegenian (Lower Devonian) shales and silty shales, [2] to [4] data from Flehmig (1983) representative of the Rhenohercynian to the east of Rhine river, white mica represents illite, carbon. – carbonates not distinguished, [5] Assigned to Montfort/Evieux formation of Condroz beds, [6] Assigned to Upper Famennian Shales, [7] $V_{sh}$ denotes the volume of shale (wt.-%) calculated from log data (Th radiation) according to Larionov (1969).
UC – Upper Carboniferous, UD – Upper Devonian, LD – Lower Devonian, K-fsp – K-feldspar, nd – not determined

tively uniform with regard to the major phases quartz and white mica. However, at 590 m relatively high chlorite and carbonate (calcite, ankerite) contents are observed.

The major element composition mirrors and confirms in greater detail the mineralogical composition trends described so far (Fig. 3). The Upper Devonian samples, especially those from the depth interval 1012–c. 1260 m show a trend towards arkosic compositions and the tendency towards higher quartz abundances in the Lower Devonian rocks in the depth interval > 2000 m (Tab. 1) is shown by trend towards sublitharenite lithologies (Fig. 3). Most Lower Devonian and Upper Carboniferous rocks, as well as Upper Devonian in the depth interval 1407–c. 1300 m, plot into the shale and wacke fields of the diagram (Fig. 3).

The abundance of the light rock forming minerals (quartz, plagioclase, K-feldspar) of Lower Devonian and Upper Carboniferous rocks quantified in this study (Tab. 1) roughly corresponds to the values determined by Haverkamp (1991) for the same stratigraphic units of the western Rhenohercynian within the hangingwall of the Aachen Thrust. Compared to the average modal compositions of rocks of the Rhenohercynian Belt sampled to the east of Rhine River (Flehmig 1983) the samples from the RWTH-1 well differ slightly although they generally show similar modal characteristics. The Lower Devonian rocks of the well exhibit similar quartz abundances as corresponding stratigraphic units studied by Flehmig (1983), but are characterized by slightly higher abundances of albite, K-feldspar and less illite. Similar to the overall trend (Flehmig 1983, Rottke & Stroink 1999) K-feldspar is more abundant in the Upper Devonian unit of the RWTH-1 well but clearly exceeds the average amounts of the Rhenohercynian (Flehmig 1983).

The high quartz amounts in the average Rhenohercynian compositions relative to the rocks of the RWTH-1 well are also reflected in higher average $SiO_2/Al_2O_3$ ratios (Fig. 3) determined by Schulz-Dobrick & Wedepohl (1983) for the Rhenohercynian. In addition, the Upper Devonian rocks of the RWTH-1 well tend to lower $Fe_2O_3/K_2O$ ratios (Fig. 3) in accordance with their high K-feldspar abundance mentioned before.

In the Upper Carboniferous and Lower Devonian the Chemical Index of Alteration (CIA; Nesbitt & Young 1982) varies between 72 and 83 (Tab. 2) whereas the Upper Devonian rocks are characterized by lower values (43–74). The CIA which was originally developed for soils formed on a particular kind of rock (Nesbitt & Young 1982) is used here as a rough indicator for the total of sources and for the degree of transport and recycling related compositional maturity of

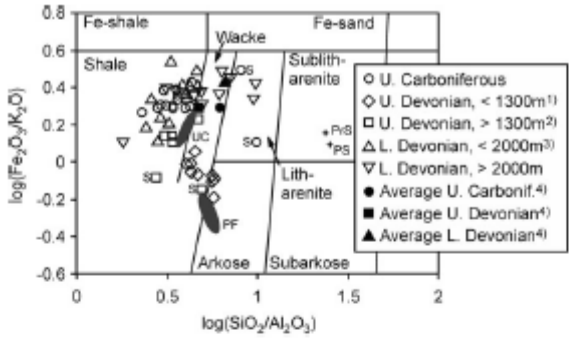


Fig. 3: Diagramm for terrigenous sandstones and shales according to Herron (1988). 1) Upper Devonian samples from depth intervals 1012 to 1300 m approximately equivalent to the Montfort and Evieux Formations of the Condroz Beds. 2) Upper Devonian samples from depth intervals 1300 to 1438 m (Famenne shales to Esneux Formation of Condroz Beds, undistinguished). 3) Representative Lower Devonian samples from depth interval 1438 to 2000 m; not all sample data from table 2 are plotted. 4) Average compositions of equivalent rocks of the Rhenohercynian to the east of river Rhine (Schulz-Dobrick & Wedepohl 1983). PF = Average Palaeozoic felsic volcanics and Phanerozoic granites (Condie 1993), PrS = average Proterozoic cratonic sandstones, PS = average Phanerozoic cratonic sandstone, S = surface samples taken in the northern Eifelian Mountains, UC = average upper crust (Rudnick & Gao 2005, Wedepohl 1995).

Abb. 3: Diagramm für terrigene siliziklastische Sedimentgesteine nach Herron (1988). 1) Oberdevonische Proben aus dem Teufenintervall 1012 bis 1300 m, annähernd äquivalent zu den Montfort- und Evieux-Formationen der Condroz-Schichten. 2) Oberdevonische Proben aus dem Teufenintervall 1300 bis 1438 m (Famenne-Schiefer bis Esneux-Formation der Condroz-Schichten, undifferenziert). 3) Repräsentative unterdevonische Proben aus dem Teufenintervall 1438 bis 2000 m, nicht alle Daten aus Tabelle 2 dargestellt. 4) Durchschnittliche Zusammensetzungen äquivalenter Gesteine des rechtsrheinischen Rhenoherzynikums (Schulz-Dobrick & Wedepohl 1983). PF = durchschnittliche paläozoische felsische Vulkanite und phanerozoische Granite (Condie 1993), PrS = durchschnittliche proterozoische kratonische Sandsteine, PS = durchschnittliche phanerozoische kratonische Sandsteine, S = Proben, entnommen Oberflächenaufschlüssen der nördlichen Eifel, UC = durchschnittliche Oberkruste (Rudnick & Gao 2005, Wedepohl 1995).

rocks (Hassan et al. 1999, Rashid 2002) because several sedimentary sources are expected.

Coal seams observed in the Upper Carboniferous units were not analysed. In the Upper Carboniferous shales, most $C_{org}$ concentrations vary between 0.4 and 0.6 wt.-% (max 0.79 %; Tab. 2). Devonian rocks are characterized by lower abundance of organic carbon, predominantly < 0.16 %, which is identical to the average values for the Rhenohercynian east of Rhine River (Schulz-Dobrick & Wedepohl 1983). Only in the Lower Devonian shales of the first core section (1439–1510 m; Tab. 2) higher values (0.30–0.54 wt-%) are analysed.

Relatively high S concentrations up to 0.6 % are observed in Upper Carboniferous samples which also have relatively high amounts of $C_{org}$. The enhanced S concentrations in Upper Devonian relative to Lower Devonian rocks are in line with the presence of dispersed pyrite in the Upper Devonian.

Nitrogen concentration data are presented relative to organic carbon (Fig. 4) in order to account for the fact that organic matter generally hosts most nitrogen (Williams & Ferrell 1991, Mingram et al. 2005). High $N/C_{org}$ ratios thus point to samples with potential abundance of inorganic $NH_4^+$. In the RWTH-1 well and in surface samples, lowest $N/C_{org}$ ratios occur in the Upper Carboniferous units followed by the Upper Devonian strata which also exhibit little variation.

Peaks within the $N/C_{org}$ distribution are observed in the Lower Devonian at 1450–1484 m and 1936–1942 m followed by variable but partly enhanced ratios in the depth interval 2141–2270 m. The zone between 1450–1484 m is represented in the uppermost core section and characterised by intensive deformation, fracturing and hydrothermal mineralisation (Lögering et al. 2006, Sindern et al. 2007). In Lower and Upper Devonian units maxima in the $N/C_{org}$ distribution coincide with peaks in the shear wave anisotropy, i.e. maxima in the distribution of fracture abundance (Fig. 4). In the Upper Carboniferous units none of the shear wave anisotropy maxima which are related to fracture abundance (660–720 m, < 400 m) is characterized by high $N/C_{org}$.

The range of Cl concentrations in core and cutting samples is displayed in figure 5. One can see that the core samples tend to show higher values than the cuttings. This becomes most obvious if only samples from the Lower Devonian section are considered (Tab. 2). Destruction of fluid inclusions which probably host a significant amount of Cl was observed by Kolb (pers. comm.) in cutting samples. In addition, these samples were intensively cleaned in an ultrasonic bath (Chatziliadou et al. 2005) which may also contribute to a loss of Cl. Chlorine may also easily be mobilised during weathering from rocks exposed in the Inde and Wurm Synclines because they show similar Cl concentrations as the cutting samples (Fig. 5). In general, Cl is not discussed further due to such secondary effects.

Similar to the mineralogical and major element data, most trace element concentrations (Ba, Cr, Cu, Ni, Pb, Rb, Zn, Zr) show less variation in the Upper Carboniferous units compared to the Upper and Lower Devonian ones (Figs. 6a, b). Only V and Sr concentrations significantly scatter in the Upper Carboniferous (Figs. 6c, d). Arsenic rarely exceeds the lower limit of determination of the XRF (i.e. 20 ppm) in Lower Devonian samples and is not considered further. Most prominent is the step towards lower concentrations of V, Cr, Ni and Fe at the Upper Devonian/Upper Carboniferous contact at 1012 m. Relative to its predominant concentration range Cu has enhanced concentrations at depths of 1096.14, 1936.10 and 2275.89 m (Tab. 2). In addition to the Cu concentrations, samples from 1936.10 m are also characterized by enhanced Ba concentrations. The trace element concentrations of the surface samples are in the range as observed in the corresponding stratigraphic units in the RWTH-1 well, except for slightly elevated Zn values in the Upper Devonian surface samples (Tab. 2). It has to be noted that all Ni con-

Table 2: Major and trace element concentrations in samples from the RWTH-1 drill hole and surface samples

| | RWTH-1 drill hole | | | | | | | | | | | | | | | | | | | |
|---|---|---|---|---|---|---|---|---|---|---|---|---|---|---|---|---|---|---|---|---|
| | Upper Carboniferous | | | | | | | | | | | | | | | | | | | |
| Sample | 36 | 49 | 158 | 159 | 200 | 250 | 302 | 350 | 400 | 451 | 499 | 550 | 649 | 650 | 749 | 799 | 848 | 851 | 904 | 949 |
| depth (m) | 71.68 | 85.94 | 190.20 | 191.30 | 231.30 | 285.40 | 338.05 | 390.51 | 439.00 | 492.99 | 542.97 | 593.50 | 693.03 | 694.05 | 794.03 | 844.00 | 892.00 | 895.00 | 948.00 | 996.00 |
| | major and minor elements, wt-% | | | | | | | | | | | | | | | | | | | |
| $SiO_2$ | 66.1 | | | 58.3 | | 58.9 | 58.5 | | 52.9 | 54.4 | 53.7 | 53.1 | 53.6 | | 60.8 | 59.1 | 54.7 | | 62.8 | 64.7 |
| $Fe_2O_{3T}$ | 6.6 | | | 6.8 | | 7.4 | 6.3 | | 8.1 | 7.3 | 6.1 | 7.0 | 6.7 | | 6.9 | 6.6 | 7.4 | | 5.8 | 6.1 |
| $TiO_2$ | 0.9 | | | 1.2 | | 0.9 | 0.7 | | 0.9 | 0.9 | 0.7 | 0.8 | 0.8 | | 0.8 | 0.8 | 0.9 | | 0.8 | 0.8 |
| $Al_2O_3$ | 15.5 | | | 16.4 | | 19.4 | 17.1 | | 23.1 | 18.8 | 14.8 | 15.0 | 17.3 | | 17.1 | 17.4 | 19.6 | | 15.7 | 15.2 |
| MnO | 0.1 | | | 0.2 | | 0.1 | 0.1 | | 0.1 | 0.1 | 0.1 | 0.1 | 0.1 | | 0.1 | 0.1 | 0.1 | | 0.1 | 0.1 |
| MgO | 1.8 | | | 2.2 | | 2.0 | 2.0 | | 2.4 | 2.6 | 2.4 | 2.3 | 2.7 | | 2.2 | 2.2 | 2.5 | | 2.1 | 2.1 |
| CaO | <0.1 | | | 2.8 | | 0.6 | 2.7 | | < 0.1 | 2.5 | 7.5 | 7.2 | 4.8 | | 1.0 | 1.3 | 1.7 | | 1.0 | 0.6 |
| $Na_2O$ | 0.7 | | | 0.6 | | 1.0 | 0.5 | | 0.6 | 0.6 | 0.6 | 0.6 | 0.6 | | 0.1 | 0.6 | 0.1 | | 0.9 | 0.7 |
| $K_2O$ | 2.5 | | | 3.0 | | 3.1 | 3.2 | | 4.4 | 3.6 | 2.8 | 2.9 | 3.4 | | 3.1 | 3.3 | 3.8 | | 3.0 | 3.1 |
| $P_2O_5$ | 0.1 | | | 0.2 | | 0.2 | 0.1 | | 0.1 | 0.1 | 0.2 | 0.1 | 0.1 | | 0.1 | 0.1 | 0.1 | | 0.2 | 0.1 |
| $SO_3$[2] | 0.3 | | | 0.4 | | 0.4 | 0.6 | | 0.4 | 0.4 | 0.5 | 0.4 | 0.6 | | 0.5 | 0.5 | 0.6 | | 0.6 | 0.5 |
| Loi | 5.1 | | | 7.3 | | 6.2 | 7.0 | | 6.6 | 7.5 | 9.8 | 10.8 | 8.9 | | 5.7 | 6.7 | 7.0 | | 5.5 | 5.1 |
| Total | 99.8 | | | 99.4 | | 100.2 | 98.8 | | 99.6 | 98.7 | 99.3 | 100.3 | 99.7 | | 98.4 | 98.7 | 98.4 | | 98.5 | 99.3 |
| | | | | | | | | | | | | | | | | | | | | |
| N | 0.091 | 0.031 | | 0.102 | | | 0.105 | 0.088 | 0.139 | 0.106 | 0.100 | 0.097 | 0.094 | 0.090 | 0.093 | | 0.117 | | 0.089 | 0.075 |
| $C_{org}$ | 0.79 | 0.27 | | 0.55 | | | 0.56 | 0.53 | 0.62 | 0.49 | 0.49 | 0.51 | 0.36 | 0.42 | 0.54 | | 0.52 | | 0.47 | 0.39 |
| $C_{inorg}$ | 0.25 | 0.42 | | 1.01 | | | 0.93 | 1.80 | 0.38 | 0.84 | 1.68 | 1.80 | 1.57 | 1.59 | 0.57 | | 0.85 | | 0.84 | 0.84 |
| $S_T$[3] | 0.05 | 0.14 | | 0.11 | | | 0.03 | 0.03 | 0.24 | 0.05 | 0.02 | 0.02 | 0.02 | 0.05 | 0.39 | | 0.63 | | 0.14 | 0.18 |
| $N/C_{org}$ | 0.12 | 0.12 | | 0.18 | | | 0.19 | 0.17 | 0.22 | 0.22 | 0.20 | 0.19 | 0.26 | 0.22 | 0.17 | | 0.22 | | 0.19 | 0.19 |
| | trace elements, ppm | | | | | | | | | | | | | | | | | | | |
| V | 111 | 45 | 111 | 126 | 197 | 129 | 129 | 116 | 187 | 146 | 106 | 111 | 119 | 123 | 133 | 144 | 159 | 184 | | 105 |
| Cr | 141 | 54 | 124 | 142 | 139 | 116 | 129 | 110 | 156 | 128 | 128 | 112 | 138 | 119 | 120 | 139 | 131 | 157 | | 122 |
| Ni | 61 | 35 | 66 | 69 | 86 | 58 | 69 | 65 | 85 | 78 | 64 | 65 | 69 | 67 | 68 | 69 | 78 | 85 | | 55 |
| Cu | 31 | 13 | 28 | 27 | 38 | 36 | 28 | 31 | 42 | 30 | 28 | 27 | 29 | 41 | 30 | 30 | 33 | 41 | | 24 |
| Zn | 83 | 45 | 92 | 92 | 102 | 101 | 88 | 90 | 107 | 107 | 81 | 94 | 101 | 94 | 71 | 57 | 97 | 109 | | 48 |
| As | | | | | | | | | | | | | | | | | | | | |
| Rb | 106 | 40 | 135 | 137 | 192 | 133 | 150 | 133 | 205 | 165 | 131 | 126 | 150 | 148 | 140 | 148 | 177 | 183 | | 126 |
| Sr | 69 | 42 | 96 | 98 | 101 | 82 | 95 | 150 | 100 | 107 | 158 | 147 | 130 | 131 | 73 | 91 | 98 | 101 | | 74 |
| Zr | 368 | 241 | 208 | 208 | 140 | 210 | 160 | 183 | 132 | 164 | 191 | 182 | 168 | 169 | 206 | 206 | 162 | 152 | | 214 |
| Ba | 307 | 116 | 391 | 369 | 535 | 505 | 396 | 362 | 481 | 439 | 335 | 347 | 363 | 382 | 343 | 350 | 420 | 394 | | 318 |
| Pb | 20 | | | 20 | 20 | 21 | 21 | | 28 | | 20 | | 20 | 20 | | | | 23 | | |
| Cl | 110 | 106 | 121 | | 127 | 120 | 114 | 134 | 112 | 130 | 124 | 131 | 127 | 128 | 115 | 145 | 109 | | 125 | 112 |
| | | | | | | | | | | | | | | | | | | | | |
| $10^4$ K/Rb | 1.93 | | | 1.82 | | 1.92 | 1.78 | | 1.79 | 1.82 | 1.79 | 1.90 | 1.87 | | 1.84 | 1.82 | 1.77 | | | 2.04 |
| CIA[4] | 80 | | | 79 | | 76 | 80 | | 80 | 79 | 78 | 77 | 79 | | 83 | 72 | 82 | | 77 | 77 |

[1] Core samples;
[2] $SO_3$ analysed by XRF in fused disc after ignition;
[3] $S_T$ total sulfur analysed by total combustion;
[4] Chemical Index of Alteration, according to Nesbit and Young (1982), calculated on a carbonate and apatite-free basis

Table 2, continued

| | RWTH-1 drill hole | | | | | | | | | | | | | | | | | | | | | | | |
|---|---|---|---|---|---|---|---|---|---|---|---|---|---|---|---|---|---|---|---|---|---|---|---|---|
| | Upper Devonian | | | | | | | | | | | | | | | | | | | | | | | |
| Sample | 1041 | 1016 | 1048 | 1100 | 1120 | 1146 | 1152 | 1200 | 1250 | 1254 | 1306 | 1308 | 1312 | 1322 | 1324 | 1332 | 1339 | 1344 | 1345 | 1346 | 1347 | 10–9[10] |
| depth (m) | 1047.00 | 1061.37 | 1096.14 | 1146.98 | 1168.02 | 1193.95 | 1200.12 | 1247.99 | 1296.12 | 1300.10 | 1353.01 | 1353.01 | 1359.00 | 1369.16 | 1371.04 | 1379.19 | 1385.62 | 1390.00 | 1391.00 | 1392.00 | 1393.20 | 1410.00 |
| $SiO_2$ | | 56.6 | 57.3 | 61.4 | 66.0 | 62.1 | 63.5 | 61.4 | 64.4 | 63.4 | | 60.7 | | | | 99.5 | | 58.4 | | | 58.0 | 39.7 |
| $Fe_2O_{3T}$ | | 4.4 | 4.1 | 3.7 | 3.7 | 3.8 | 2.8 | 5.0 | 5.3 | 4.6 | | 6.2 | | | | 6.5 | | 6.4 | | | 6.7 | 3.8 |
| $TiO_2$ | | 0.7 | 0.6 | 0.6 | 0.7 | 0.6 | 0.6 | 0.7 | 0.7 | 0.7 | | 0.8 | | | | 0.8 | | 0.8 | | | 0.8 | 0.5 |
| $Al_2O_3$ | | 13.1 | 12.3 | 10.7 | 11.7 | 11.1 | 11.1 | 14.5 | 14.2 | 15.6 | | 17.4 | | | | 17.6 | | 17.7 | | | 18.9 | 8.5 |
| MnO | | 0.1 | 0.1 | <0.1 | <0.1 | 0.1 | 0.1 | 0.1 | 0.1 | 0.1 | | 0.1 | | | | 0.1 | | 0.1 | | | 0.1 | 0.2 |
| MgO | | 4.9 | 4.3 | 4.4 | 3.7 | 4.3 | 3.8 | 3.9 | 3.0 | 2.7 | | 3.1 | | | | 3.3 | | 3.2 | | | 3.2 | 8.3 |
| CaO | | 5.0 | 5.8 | 5.1 | 2.6 | 4.9 | 3.9 | 2.3 | 1.1 | 0.9 | | 1.1 | | | | 1.0 | | 1.0 | | | 0.6 | 13.7 |
| $Na_2O$ | | 0.6 | 0.3 | 0.4 | 1.0 | 0.5 | 1.1 | 1.1 | 1.5 | 1.2 | | 1.1 | | | | 1.1 | | 1.1 | | | 0.9 | 0.6 |
| $K_2O$ | | 5.1 | 4.7 | 4.5 | 4.7 | 4.5 | 4.3 | 5.2 | 4.6 | 4.7 | | 4.7 | | | | 4.7 | | 4.6 | | | 4.8 | 2.2 |
| $P_2O_5$ | | 0.2 | 0.1 | 0.1 | 0.1 | 0.1 | 0.1 | 0.1 | 0.2 | 0.2 | | 0.1 | | | | 0.2 | | 0.1 | | | 0.1 | 0.2 |
| $SO_3$[*2] | | 0.1 | 0.4 | 0.4 | 0.1 | 0.5 | 0.4 | 0.1 | 0.1 | 0.3 | | 0.5 | | | | 0.1 | | 0.4 | | | 0.5 | 0.4 |
| LoI | | 9.4 | 9.4 | 7.9 | 5.1 | 7.3 | 6.8 | 5.5 | 3.5 | 4.1 | | 4.6 | | | | 4.5 | | 4.5 | | | 4.6 | 20.6 |
| Total | | 100.1 | 99.4 | 99.3 | 99.4 | 99.8 | 98.3 | 99.9 | 98.6 | 98.5 | | 100.4 | | | | 99.4 | | 98.3 | | | 99.2 | 98.7 |
| N | | 0.031 | 0.074 | 0.015 | 0.015 | 0.015 | | 0.031 | 0.027 | | | 0.041 | | | | | | 0.046 | | | 0.044 | 0.028 |
| $C_{org}$ | | 0.11 | 0.16 | 0.10 | 0.03 | 0.07 | | 0.07 | 0.04 | | | 0.05 | | | | | | 0.03 | | | 0.10 | 0.11 |
| $C_{tot}$ | | 1.77 | 1.84 | 1.51 | 0.84 | 1.39 | | 0.74 | 0.31 | | | 0.34 | | | | | | 0.29 | | | 0.35 | 5.81 |
| ST[*3] | | 0.03 | 0.03 | 0.09 | 0.03 | 0.05 | | 0.05 | 0.08 | | | 0.16 | | | | | | 0.18 | | | 0.07 | 0.01 |
| $N/C_{org}$ | | 0.29 | 0.46 | 0.15 | 0.44 | 0.22 | | 0.46 | 0.72 | | | 0.91 | | | | | | 0.59 | | | 0.43 | 0.27 |
| V | 48 | 58 | 55 | 41 | 51 | 52 | 42 | 70 | 67 | 73 | 91 | 86 | 97 | 100 | 99 | 97 | 102 | 100 | 105 | 104 | 102 | |
| Cr | 69 | 75 | 81 | 73 | 79 | 76 | 79 | 91 | 96 | 112 | 101 | 107 | 126 | 128 | 123 | 124 | 129 | 125 | 130 | 132 | 112 | |
| Ni | 30 | 38 | 45 | 34 | 36 | 37 | 33 | 53 | 56 | 55 | 58 | 58 | 60 | 61 | 59 | 59 | 63 | 60 | 59 | 59 | 62 | |
| Cu | 35 | 19 | 100 | 13 | 10 | 16 | 12 | 23 | 29 | 23 | 25 | 25 | 23 | 23 | 23 | 30 | 26 | 27 | 24 | 23 | 25 | |
| Zn | 22 | 60 | 77 | 35 | 54 | 43 | 36 | 70 | 69 | 71 | 74 | 70 | 74 | 78 | 77 | 87 | 80 | 80 | 75 | 80 | 83 | |
| As | | | | | | | | | | | | | | | | | | | | | | |
| Rb | 106 | 131 | 116 | 93 | 94 | 97 | 92 | 138 | 129 | 138 | 162 | 164 | 170 | 171 | 170 | 163 | 172 | 168 | 176 | 177 | 175 | |
| Sr | 83 | 85 | 57 | 77 | 64 | 81 | 78 | 84 | 92 | 97 | 78 | 81 | 73 | 67 | 72 | 72 | 67 | 69 | 72 | 64 | 71 | |
| Zr | 216 | 212 | 179 | 289 | 318 | 263 | 271 | 186 | 221 | 211 | 198 | 195 | 196 | 174 | 171 | 179 | 167 | 177 | 181 | 172 | 155 | |
| Ba | 355 | 468 | 348 | 429 | 451 | 415 | 404 | 467 | 494 | 499 | 325 | 535 | 497 | 477 | 490 | 492 | 439 | 462 | 481 | 510 | 501 | |
| Pb | | | | | | | | | | | | | | | | | | | | | | |
| Cl | | | 182 | 141 | | 138 | | 135 | 138 | 128 | 127 | 133 | | | | | | | | | 129 | 128 |
| 100*K/Rb | | 3.34 | 3.37 | 4.03 | 4.17 | 3.82 | 3.88 | 3.12 | 3.00 | 2.85 | | 2.40 | | | | 2.41 | | 2.30 | | | 2.29 | |
| CIA[*4] | | 62 | 43 | 56 | 60 | 56 | 45 | 64 | 64 | 64 | | 70 | | | | 67 | | 71 | | | 74 | 70 |

Table 2, continued

| | RWTH-1 drill hole | | | | | | | | | | | | | | | | | | | | | | | |
|---|---|---|---|---|---|---|---|---|---|---|---|---|---|---|---|---|---|---|---|---|---|---|---|---|
| | Upper Devonian | | | | | | | | | | | | | | | | | | | | | | | |
| Sample | 18-3[1] | 20-3[1] | 22-2[1] | 25-16[1] | 35-3[1] | 38-2[1] | 46-1[1] | 46-2[1] | 1448 | 1477r | 1477g | 1555 | 1599 | 1652 | 1688g | 1688r | 1759 | 1779 | 1859 | 1860g | 1860r | 1864 | 1866 | 1868 | 1873 |
| depth (m) | 1439.20 | 1444.70 | 1450.00 | 1457.40 | 1484.00 | 1490.00 | 1510.00 | 1511.00 | 1524.01 | 1556.00 | 1556.00 | 1641.17 | 1684.50 | 1733.73 | 1774.00 | 1774.00 | 1844.09 | 1864.00 | 1935.15 | 1936.10 | 1936.10 | 1940.00 | 1941.90 | 1944.00 | 1949.00 |
| $SiO_2$ | 53.2 | 55.7 | 60.5 | 67.7 | 59.9 | 67.3 | 62.5 | 57.1 | 61.0 | | | 67.1 | 64.4 | 62.2 | | | 65.6 | | 60.7 | | 59.8 | 57.2 | 60.6 | 67.2 | |
| $Fe_2O_{3T}$ | 8.8 | 6.8 | 7.1 | 7.1 | 5.3 | 7.8 | 5.7 | 10.0 | 7.5 | | | 6.3 | 7.4 | 7.2 | | | 6.2 | | 7.8 | | 7.7 | 7.8 | 7.5 | 6.1 | |
| $TiO_2$ | 1.0 | 1.0 | 1.0 | 0.8 | 1.2 | 0.9 | 1.1 | 0.9 | 0.9 | | | 0.8 | 0.9 | 0.9 | | | 0.8 | | 0.9 | | 1.0 | 0.9 | 0.9 | 0.8 | |
| $Al_2O_3$ | 20.6 | 23.0 | 20.9 | 14.8 | 21.4 | 14.5 | 19.5 | 17.3 | 18.5 | | | 14.7 | 16.9 | 17.9 | | | 15.6 | | 18.7 | | 20.2 | 19.1 | 17.3 | 15.9 | |
| MnO | 1.2 | 0.3 | < 0.1 | < 0.1 | < 0.1 | 0.1 | 0.1 | 1.2 | 0.4 | | | 0.3 | 0.2 | 0.3 | | | 0.2 | | 0.2 | | 0.2 | 0.2 | 0.2 | 0.1 | |
| MgO | 1.7 | 1.5 | 0.8 | 0.7 | 1.2 | 1.3 | 1.3 | 1.6 | 1.5 | | | 1.4 | 1.5 | 1.5 | | | 1.9 | | 1.7 | | 1.8 | 2.3 | 2.4 | 1.9 | |
| CaO | 0.4 | 0.3 | 0.1 | 0.2 | 0.1 | 0.2 | 0.2 | 0.5 | 0.0 | | | 0.1 | 0.4 | < 0.1 | | | 0.5 | | < 0.1 | | < 0.1 | 1.1 | 0.9 | < 0.1 | |
| $Na_2O$ | 0.7 | 0.8 | 0.8 | 0.6 | 0.8 | 0.4 | 0.8 | 0.6 | 0.7 | | | 0.6 | 0.6 | 0.6 | | | 0.9 | | 0.6 | | 0.7 | 0.7 | 0.7 | 0.8 | |
| $K_2O$ | 4.1 | 4.5 | 4.1 | 2.8 | 4.1 | 2.5 | 3.5 | 2.9 | 3.0 | | | 2.5 | 2.9 | 3.2 | | | 2.4 | | 3.3 | | 3.8 | 3.9 | 3.4 | 2.8 | |
| $P_2O_5$ | 0.1 | 0.1 | < 0.1 | 0.1 | 0.1 | < 0.1 | 0.1 | 0.1 | 0.1 | | | 0.1 | 0.1 | 0.1 | | | 0.1 | | 0.1 | | 0.2 | 0.1 | < 0.1 | 0.1 | |
| $SO_3$[2] | 0.4 | 0.4 | 0.4 | 0.5 | 0.4 | 0.4 | 0.4 | 0.4 | 0.3 | | | 0.3 | 0.5 | 0.3 | | | 0.3 | | 0.3 | | 0.3 | 0.3 | 0.4 | 0.3 | |
| LoI | 6.9 | 5.4 | 3.4 | 2.6 | 3.7 | 3.2 | 3.8 | 6.2 | 4.7 | | | 4.9 | 4.0 | 4.2 | | | 4.4 | | 4.3 | | 4.2 | 5.3 | 4.9 | 3.6 | |
| Total | 99.1 | 99.8 | 99.3 | 97.9 | 98.3 | 98.8 | 98.8 | 98.8 | 98.6 | | | 99.1 | 99.9 | 98.5 | | | 99.0 | | 98.8 | | 99.8 | 99.0 | 99.2 | 99.5 | |
| N | 0.079 | 0.094 | 0.088 | 0.059 | 0.091 | 0.055 | 0.067 | 0.058 | | | | 0.031 | 0.060 | | 0.062 | 0.077 | 0.047 | 0.041 | | 0.071 | 0.089 | | 0.069 | | 0.036 |
| $C_{org}$ | 0.40 | 0.30 | 0.02 | 0.02 | 0.03 | 0.07 | 0.12 | 0.54 | | | | 0.07 | 0.07 | | 0.06 | 0.16 | 0.06 | 0.03 | | 0.03 | 0.03 | | 0.03 | | 0.03 |
| $C_{inorg}$ | 0.71 | 0.18 | 0.02 | 0.04 | 0.04 | 0.09 | 0.09 | 0.46 | | | | 0.21 | 0.20 | | 0.18 | 0.29 | 0.39 | 0.43 | | 0.11 | 0.09 | | 0.42 | | 0.11 |
| ST[3] | 0.01 | 0.01 | < 0.01 | < 0.01 | < 0.01 | < 0.01 | 0.01 | 0.01 | | | | 0.02 | 0.02 | | 0.01 | 0.02 | 0.03 | 0.01 | | 0.01 | < 0.01 | | 0.01 | | 0.01 |
| $N/C_{org}$ | 0.20 | 0.31 | 3.67 | 2.81 | 3.03 | 0.74 | 0.55 | 0.11 | | | | 0.48 | 0.86 | | 0.97 | 0.50 | 0.79 | 1.19 | | 2.43 | 3.18 | | 2.30 | | 1.13 |
| V | 128 | 164 | | 70 | 138 | 89 | | | 110 | 129 | 115 | 94 | 92 | 109 | 96 | 162 | 98 | 72 | 118 | 114 | 137 | 135 | 115 | | 61 |
| Cr | 112 | 115 | | 134 | 118 | 121 | | | 137 | 162 | 138 | 154 | 131 | 147 | 156 | 165 | 153 | 201 | 141 | 129 | 133 | 161 | 165 | 34 | 178 |
| Ni | 60 | 63 | | 46 | 50 | 55 | | | 64 | 69 | 68 | 64 | 60 | 68 | 72 | 85 | 76 | 57 | 66 | 71 | 72 | 86 | 82 | 73 | 59 |
| Cu | 47 | 36 | | 14 | 33 | 24 | | | 29 | 21 | 27 | 24 | 24 | 27 | 25 | 30 | 38 | 28 | 40 | 69 | 47 | 16 | 14 | 22 | 18 |
| Zn | 79 | 84 | | 45 | 65 | 75 | | | 86 | 84 | 90 | 70 | 80 | 86 | 89 | 100 | 77 | 67 | 85 | 94 | 84 | 86 | 77 | 67 | 54 |
| As | 35 | 56 | | | | | | | 34 | | | 24 | | | | 31 | 38 | | | | | | | | |
| Rb | 162 | 187 | | 126 | 180 | 110 | | | 132 | 155 | 156 | 108 | 131 | 138 | 120 | 143 | 102 | 77 | 143 | 163 | 195 | 175 | 157 | 123 | 71 |
| Sr | 78 | 97 | | 77 | 93 | 67 | | | 72 | 74 | 73 | 59 | 64 | 70 | 59 | 71 | 59 | 46 | 60 | 63 | 111 | 69 | 69 | 54 | 44 |
| Zr | 169 | 155 | | 433 | 315 | 351 | | | 222 | 224 | 208 | 254 | 244 | 224 | 272 | 192 | 231 | 320 | 217 | 193 | 171 | 185 | 214 | 246 | 350 |
| Ba | 602 | 593 | | 394 | 699 | 410 | | | 489 | 655 | 501 | 400 | 489 | 487 | 402 | 440 | 335 | 282 | 557 | 685 | 1050 | 657 | 555 | 409 | 248 |
| Pb | | | | | | | | | 46 | | | 20 | | 22 | | 29 | 35 | | | | | | | | |
| Cl | 144 | 155 | 119 | 134 | 136 | 159 | 148 | 193 | 127 | | | 117 | 111 | 127 | | | 123 | | | | 106 | | 127 | | |
| 100*K/Rb | 2.08 | 1.99 | | 1.86 | 1.91 | 1.90 | | | 1.87 | | | 1.91 | 1.85 | 1.90 | | | 1.99 | | 1.92 | | 1.61 | 1.87 | 1.80 | 1.88 | |
| CIA[4] | 79 | 79 | 78 | 78 | 79 | 81 | 79 | 81 | 81 | | | 80 | 80 | 80 | | | 79 | | 80 | | 80 | 73 | 78 | 79 | |

Table 2, continued

| | RWTH-1 drill hole | | | | | | | | | | | | | | | | | | | | | | | | | | | | | |
|---|---|---|---|---|---|---|---|---|---|---|---|---|---|---|---|---|---|---|---|---|---|---|---|---|---|---|---|---|---|---|
| | Upper Devonian | | | | | | | | | | | | | | | | | | | | Warm-Syncline | | | | Indo-Synclinc | | | | | |
| | | | | | | | | | | | | | | | | | | | | | UCarb. | | U.Dev. | | Upper Carbonaiferous | | | U.Dev. | | |
| Sample | 1897 | 1904g | 1904r | 1912g | 52-1[a] | 2087 | 2130 | 2136 | 2191 | 2206 | 2212g | 2212r | 2230r | 2306 | 2470 | 54-1[a] | 59-1[a] | EK1[a] | EK2[a] | YWT1 | YWT2 | YWT3 | IM5 | IM15 | IM17 | AK1 | | | | |
| depth (m) | 1973.03 | 1980.15 | 1980.15 | 1987.86 | 2141.40 | 2149.24 | 2194.03 | 2200.00 | 2253.95 | 2269.17 | 2275.79 | 2293.91 | 2302.03 | 2371.27 | 2536.01 | 2537.70 | 2542.00 | 2543.90 | 2544.00 | Surface outcrops | | | | | | | | | | |
| $SiO_2$ | 63.2 | | 62.6 | 64.7 | 62.6 | 81.0 | 81.6 | 74.3 | 70.1 | 63.5 | | 67.2 | | 68.6 | 73.9 | 57.6 | 75.4 | 63.6 | 48.1 | 78.4 | 62.2 | 67.8 | 83.3 | 69.7 | 65.2 | 56.2 | | | | |
| $Fe_2O_{3T}$ | 6.3 | | 7.9 | 6.4 | 7.6 | 3.4 | 3.0 | 5.0 | 4.9 | 7.6 | | 6.4 | | 5.8 | 5.0 | 7.7 | 4.0 | 6.3 | 7.1 | 4.1 | 6.9 | 3.7 | 2.0 | 5.9 | 5.8 | 5.8 | | | | |
| $TiO_2$ | 0.9 | | 0.9 | 0.9 | 0.9 | 0.6 | 0.5 | 0.7 | 0.8 | 0.9 | | 0.8 | | 0.8 | 0.6 | 0.9 | 0.6 | 0.9 | 1.3 | 0.6 | 1.0 | 0.8 | 0.7 | 1.0 | 0.9 | 0.9 | | | | |
| $Al_2O_3$ | 16.4 | | 17.7 | 15.9 | 16.7 | 8.4 | 8.6 | 12.1 | 14.1 | 17.0 | | 15.1 | | 14.0 | 11.7 | 18.4 | 10.7 | 17.8 | 26.8 | 9.7 | 17.5 | 13.9 | 8.8 | 16.4 | 15.9 | 20.3 | | | | |
| MnO | 0.2 | | 0.1 | 0.2 | 0.1 | < 0.1 | 0.1 | 0.1 | 0.1 | 0.1 | | < 0.1 | | 0.1 | 0.1 | 0.2 | 0.1 | 0.1 | 0.1 | < 0.1 | 0.1 | < 0.1 | < 0.1 | < 0.1 | 0.1 | 0.0 | | | | |
| MgO | 2.4 | | 2.1 | 1.9 | 2.8 | 1.1 | 1.0 | 1.8 | 1.6 | 2.6 | | 1.9 | | 2.0 | 1.6 | 3.1 | 1.6 | 2.7 | 3.2 | 0.9 | 1.5 | 2.7 | 0.6 | 1.7 | 1.7 | 3.7 | | | | |
| CaO | 0.7 | | 0.4 | 0.6 | 0.3 | 0.1 | 0.3 | 0.3 | 0.3 | 0.4 | | 0.2 | | 0.9 | 0.5 | 1.3 | 1.3 | 0.4 | 0.4 | 0.2 | 0.4 | 0.2 | 0.2 | 0.2 | 3.3 | 0.3 | | | | |
| $Na_2O$ | 1.0 | | 0.7 | 1.0 | 0.6 | 0.7 | 0.4 | < 0.1 | 0.6 | 0.6 | | 0.7 | | 0.6 | 1.1 | 1.2 | 1.3 | 1.4 | 1.1 | 0.9 | 1.2 | 0.5 | 0.2 | 0.2 | 0.2 | 0.2 | | | | |
| $K_2O$ | 2.8 | | 3.3 | 2.8 | 3.2 | 1.3 | 1.4 | 2.2 | 2.4 | 3.2 | | 2.8 | | 2.4 | 1.6 | 3.1 | 1.4 | 3.1 | 5.5 | 1.3 | 2.8 | 5.3 | 1.5 | 3.3 | 3.2 | 7.1 | | | | |
| $P_2O_5$ | 0.1 | | 0.1 | 0.1 | 0.1 | < 0.1 | 0.5 | 0.1 | 0.5 | < 0.1 | | < 0.1 | | < 0.1 | 0.1 | 0.1 | 0.1 | 0.2 | 0.2 | 0.2 | 0.2 | 0.1 | 0.1 | 0.1 | 0.1 | 0.1 | | | | |
| $SO_3$[b] | 0.5 | | 0.4 | 0.4 | 0.4 | 0.5 | 0.3 | 0.4 | 0.3 | 0.4 | | 0.5 | | 0.4 | 0.4 | 0.5 | 0.5 | 0.1 | 0.1 | 0.2 | 0.1 | 0.2 | 0.2 | 0.2 | 0.2 | 0.1 | | | | |
| LoI | 4.1 | | 4.0 | 3.9 | 3.9 | 1.7 | 2.0 | 2.8 | 3.2 | 3.8 | | 3.1 | | 3.7 | 3.1 | 5.0 | 3.0 | 3.7 | 5.3 | 2.9 | 5.2 | 3.4 | 0.6 | 1.2 | 2.8 | 4.5 | | | | |
| Total | 98.5 | | 100.3 | 98.7 | 99.3 | 98.7 | 99.6 | 99.7 | 98.8 | 100.1 | | 98.7 | | 99.2 | 99.8 | 99.0 | 99.9 | 100.2 | 99.2 | 99.4 | 98.8 | 98.6 | 100.1 | 99.8 | 99.5 | 99.1 | | | | |
| N | 0.061 | 0.072 | | 0.061 | 0.064 | 0.024 | 0.026 | 0.044 | | 0.058 | | 0.050 | 0.032 | 0.043 | 0.036 | 0.061 | 0.028 | | | 0.037 | 0.076 | 0.027 | 0.041 | 0.088 | 0.084 | 0.056 | | | | |
| $C_{org}$ | 0.09 | 0.04 | | 0.10 | 0.03 | 0.03 | 0.02 | 0.04 | | 0.03 | | 0.03 | 0.04 | 0.04 | 0.05 | 0.08 | 0.06 | | | 0.25 | 0.73 | 0.04 | 0.19 | 0.49 | 0.66 | 0.08 | | | | |
| $C_{inc}$ | 0.32 | 0.01 | | 0.23 | 0.08 | 0.03 | 0.07 | 0.01 | | 0.08 | | 0.04 | 0.16 | 0.22 | 0.21 | 0.45 | 0.26 | | | 0.02 | 0.06 | 0.06 | 0.02 | 0.15 | 1.06 | 0.03 | | | | |
| ST[b] | 0.04 | 0.01 | | 0.01 | 0.01 | 0.01 | 0.01 | 0.02 | | < 0.01 | | < 0.01 | 0.01 | < 0.01 | 0.03 | < 0.01 | 0.01 | | | 0.01 | 0.01 | 0.01 | < 0.01 | 0.01 | < 0.01 | 0.00 | | | | |
| $N/C_{org}$ | 0.66 | 1.89 | | 0.61 | 2.13 | 0.86 | 1.34 | 1.26 | | 2.05 | | 1.67 | 0.84 | 1.19 | 0.74 | 0.73 | 0.47 | | | 0.15 | 0.10 | 0.77 | 0.22 | 0.18 | 0.13 | 0.72 | | | | |
| V | 110 | 116 | 111 | 98 | 114 | 38 | 40 | 73 | 78 | 105 | 98 | 96 | 93 | 56 | 80 | 56 | 120 | 53 | 104 | 211 | 54 | 108 | 56 | 35 | 105 | 92 | 128 | | | | |
| Cr | 168 | 158 | 212 | 156 | 154 | 157 | 169 | 166 | 184 | 161 | 161 | 175 | 180 | 198 | 147 | 149 | 137 | 123 | 142 | 205 | 68 | 103 | 94 | 68 | 111 | 102 | 122 | | | | |
| Ni | 81 | 76 | 67 | 69 | 90 | 40 | 46 | 64 | 64 | 89 | 76 | 85 | 79 | 56 | 69 | 52 | 82 | 46 | 77 | 94 | 35 | 57 | 42 | 30 | 67 | 59 | 72 | | | | |
| Cu | 26 | 32 | 21 | 19 | | 11 | 16 | 17 | | | 68 | 13 | | | 30 | 16 | 33 | 13 | 25 | 11 | 15 | 32 | 16 | | 27 | 25 | 25 | | | | |
| Zn | 79 | 85 | 80 | 77 | 73 | 33 | 42 | 61 | 55 | 71 | 73 | 73 | 57 | 50 | 69 | 60 | 89 | 52 | 80 | 87 | 65 | 119 | 100 | 57 | 127 | 86 | 134 | | | | |
| As | | | | 27 | | | | | | | | | | | | | 25 | | 20 | 22 | | | | | | | | | | |
| Rb | 120 | 142 | 119 | 117 | 141 | 49 | 58 | 91 | 103 | 141 | 147 | 128 | 125 | 75 | 104 | 64 | 126 | 54 | 121 | 216 | 53 | 117 | 122 | 57 | 132 | 134 | 192 | | | | |
| Sr | 57 | 56 | 53 | 62 | 38 | 23 | 23 | 29 | 39 | 43 | 48 | 41 | 42 | 29 | 40 | 49 | 64 | 57 | 61 | 82 | 51 | 83 | 54 | 46 | 75 | 114 | 61 | | | | |
| Zr | 244 | 220 | 364 | 299 | 232 | 399 | 238 | 247 | 313 | 208 | 261 | 237 | 240 | 345 | 270 | 268 | 198 | 295 | 245 | 297 | 266 | 240 | 320 | 369 | 241 | 217 | 174 | | | | |
| Ba | 430 | 479 | 441 | 408 | 633 | 190 | 213 | 360 | 409 | 557 | 480 | 480 | 439 | 258 | 439 | 228 | 464 | 197 | 463 | 861 | 181 | 425 | 406 | 133 | 344 | 322 | 692 | | | | |
| Pb | | | | 27 | | | | | | | | | | | | | 35 | | | | | 21 | 30 | | 20 | 21 | 28 | | | | |
| Cl | 119 | | | 123 | 190 | | 118 | 118 | 108 | | | 124 | 119 | | 164 | 150 | 143 | 166 | 107 | 123 | 166 | 99 | 101 | 114 | | | | | | | |
| $10^4$K/Rb | 1.95 | | 2.28 | 1.96 | 1.89 | 2.20 | 1.99 | 1.96 | 1.92 | 1.87 | | 1.86 | | 1.92 | 2.11 | 2.05 | 2.17 | 2.10 | 2.13 | | | | | | | | | | | |
| CIA[b] | 78 | | 78 | 78 | 78 | 76 | 80 | 83 | 79 | 78 | | 78 | | 77 | 77 | 76 | 69 | 74 | 76 | 76 | 76 | 77 | 68 | 83 | 82 | 76 | 71 | | | |

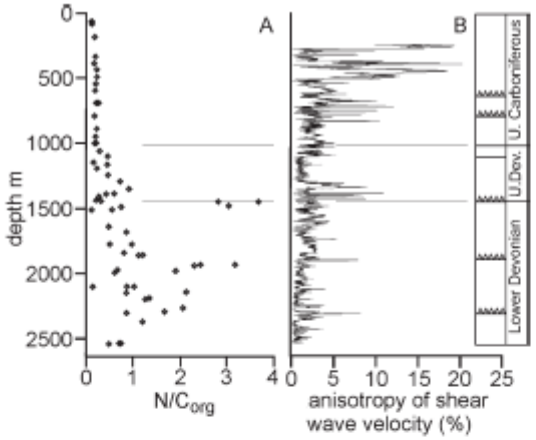


Fig. 4: $N/C_{org}$ (A) and anisotropy of shear wave velocity (B) versus depth in the RWTH-1 well. The degree of anisotropy (%) correlates with fracture intensity. Peaks in the anisotropy measurement are an indication of fault zones. Only at 400 to 535 m steeply inclined bedding planes are the main cause for the high anisotropy. Dividing lines between main stratigraphic units are drawn in the figures and indicated by the simplified profile to the right.

Abb. 4: $N/C_{org}$ (A) und Scherwellenanisotropie (B) gegen Teufe der Bohrung RWTH-1. Der Grad der Scherwellenanisotropie (%) korreliert mit der Bruchhäufigkeit. Maxima in der Anisotropiebestimmung zeigen Störungszonen an. Im Teufenbereich von 400 bis 535 m sind jedoch stark einfallende Schichtflächen der Hauptgrund für ein Maximum in der Scherwellenanisotropie. Trennlinien für die wichtigsten stratigrafischen Einheiten finden sich in der Grafik und können aus dem vereinfachten Profil auf der rechten Seite abgeleitet werden.

centrations detected in the RWTH-1 well are lower than the range of values (107–320 ppm) of Rhenohercynian rocks to the east of river Rhine (Schulz-Dobrick & Wedepohl 1983) while the concentrations of V, Cr, Zn, Rb, Ba and Pb are within the corresponding ranges of values. This will be addressed below.

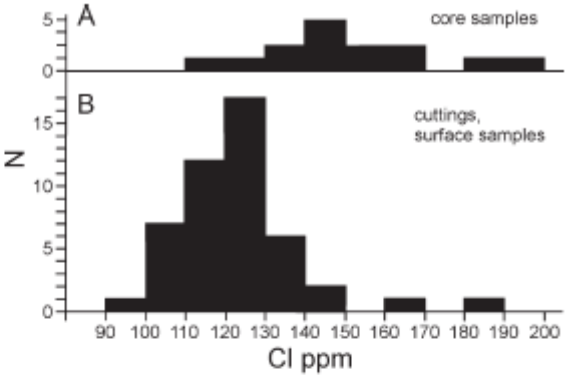


Fig. 5: Frequency distribution of Cl concentrations in (A) drill core samples and (B) cutting and surface samples.

Abb. 5: Häufigkeitsverteilung der Cl-Konzentration in (A) Bohrkernproben und (B) Bohrklein- und Oberflächenaufschluss-Proben.

## 6. Discussion

The controlling factor of trace element distribution prior to any hydrothermal overprint is either determined by specific heavy minerals (e.g. zircon, Zr; chromite, Cr; tourmaline, B) or by rock forming minerals (e.g. Cullers 1995) among which illite can be expected to be most effective among the rocks studied here due to its specific surface and modal abundance, followed by feldspars and chlorite. In addition, the role of sulfides and carbonates has to be considered. Thus element distribution is a mirror of the sources of sediments as well as of the sum of diagenetic and hydrothermal effects (Milliken 2003).

A control of trace element contents by clay minerals becomes obvious in the clear covariation of trace element concentration and clay mineral abundance. This can clearly be seen in the Upper Devonian units which are characterized by

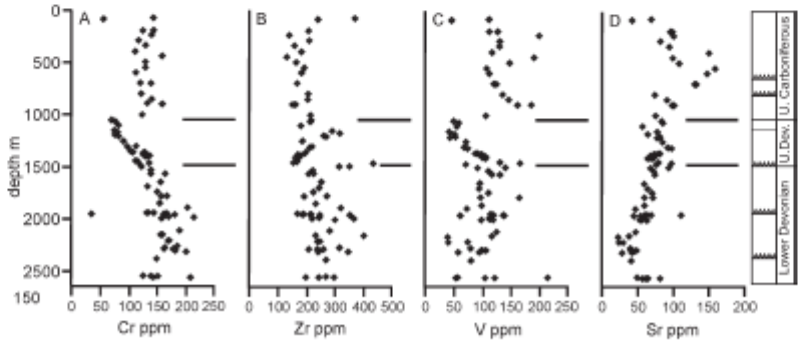


Fig. 6: Concentration of Cr (A), Zr (B), V (C) and Sr (D) in core and cutting samples of the RWTH-1 well. Dividing lines between main stratigraphic units are drawn in the figures and indicated by the simplified profile to the right.

Abb. 6: Konzentrationen von Cr (A), Zr (B), V (C) and Sr (D) in Bohrkern- und Bohrklein-Proben der Bohrung RWTH-1. Trennlinien für die wichtigsten stratigrafischen Einheiten finden sich in der Grafik und können aus dem vereinfachten Profil auf der rechten Seite abgeleitet werden.

both low concentrations of V, Cr, Ni and clay minerals (i.e. illite, also $V_{SH}$) and enhanced concentrations of these elements and clay minerals with increasing depth (Tabs. 1, 2, Fig. 6).

The Al concentration may serve as a suitable approximation for the clay mineral abundance (Press 1986) although in the Upper Devonian rocks Al occurs in feldspar to a significant amount. The volume of shale ($V_{SH}$) data displayed in table 1 correlate well (r = 0.90) with the $Al_2O_3$ values for the corresponding samples from table 2. Consequently, the correlation of concentration of an element with Al is an indication that this element is mainly bound to the clay minerals, which are dominated by illite in the rocks considered here.

A reasonable correlation with Al is detected for V, Rb and Ba in all of the three stratigraphic units of the Lower and Upper Devonian as well as Upper Carboniferous (Tab. 3). However, the deviating K/Rb ratio of all Upper Devonian rocks points to the role of K-feldspar for the Rb concentration in these rocks (Tab. 2).

Strontium is only roughly correlated with Al (Tab. 3). In the Upper Devonian and Upper Carboniferous highest Sr concentrations are observed in samples with high $C_i$. Here, Sr from carbonates contributes to the Sr bound to illite.

The exceptionally high concentrations of Cu at 1096.40, 1936.10, 2275.89 m and Ba at 1936.10 m all form high ratios with Al clearly exceeding the range of ratios within other sections of the RWTH-1 well. This points to a source of Cu and Ba which is not only of sedimentary origin or due to possible diagenetic remobilisation (Milliken 2003). The concentration peaks of Cu and Ba do neither correspond to $C_{org}$ or $C_i$ nor to S concentrations or sulphide mineralisation. Therefore it is concluded that the enhanced concentrations point to a secondary enrichment, most probably by a hydrothermal fluid. However, Cu and Ba are bound to the existing minerals, mainly illite, rather than specific sulphide or sulphate ore minerals.

Illite and feldspar may control Zn in the Upper Devonian rocks (Tab. 3), but not in Lower Devonian and Upper Carboniferous units. However, our data provide no evidence of any exclusive controlling factor. Possibly, Zn was mobilized during diagenetic and/or hydrothermal processes.

Like Zn, Cr and Ni show a good correlation with Al in the Upper Devonian rocks. Here, the Cr concentration is controlled by phases such as illite and feldspar in which it can substitute for Al at octahedral sites (Press 1986, Marshall & Fairbridge 1999). In the Lower Devonian and Upper Carboniferous the Cr concentrations reach higher values, are much more variable although there is no correlation of Cr with Al. This indicates that in these units chromite, which has variable abundances due to sedimentary processes, is the most significant Cr mineral phase. In a study of sand- and siltstones of the northern Eifel Mountains Haverkamp (1991) observed that chromite reaches portions of up to 42 % of the accessory heavy minerals in the Siegenian, the Lower Devonian unit represented in the RWTH-1 well. Nickel shows minor correlation with Al in the Lower Devonian and Upper Carboniferous sections. Thus, a significant amount of Ni may be controlled by an accessory mineral phase. However, our data give no further indication for this phase.

Zirconium is not or even negatively correlated to Al. Obviously zircon, also described by Haverkamp (1991) to reach abundances of 53 % in the heavy mineral fractions of sand-siltstones of the region, controls the concentration of this element. This also explains the tendency to negative correlation with Al (Tab. 3) because zircon has higher abundances in the mature sediments characterized by low amounts of sheet silicates and feldspar.

Nitrogen, mainly released by breakdown of organic matter (Mingram et al. 2005) during diagenetic and metamorphic events (Meyer & Ridgway 1991) becomes mobile in a hydrothermal fluid as $NH_3$ or $N_2$ at T > 200 °C whereas at T < 200 °C the dominant N species is $NH_4^+$ (Williams & Ferrell 1991, Williams et al. 1992, Mingram et al. 2005). Ammonium can be transported over long distances (Williams & Ferrell 1991) and finally be incorporated in rocks during hydrothermal fluid rock interaction. Mineral phases most susceptible for incorporation of ammonium – which due to charge and radius has similar chemical characteristics as $K^+$ – are K bearing phases such as clay mineral (e.g. illite) or K-feldspar (Wedepohl 1978, Meyer & Ridgway 1991). Increased concentration of ammonium bound to mineral phases may therefore be indicative of former fluid flow.

The high $N/C_{org}$ ratios in those parts of the well in which the Lower Devonian units are affected by most intensive fracturing, can be interpreted to indicate incorporation of $NH_4^+$ transported by a fluid phase and incorporated into authigenic minerals among which illite is the dominating K bearing mineral, especially in Lower Devonian units (Tab. 1; Haverkamp 1991, Sindern et al. 2007).

In the section 1936.10 to 1941.90 m the $NH_4^+$ bearing fluid may also account for the high concentrations of Cu and Ba. In the plot of $N/C_{org}$ vs. Al (Fig. 7b) Upper Carboniferous, Upper Devonian and some of the Lower Devonian sam-

Tab. 3: Pearsson correlation coefficient of trace elements and Al in Upper Carboniferous, Upper Devonian and Lower Devonian sections of the RWTH-1 drill hole.

| | V | Cr | Ni | Cu | Zn | Rb | Sr | Zr | Ba |
|---|---|---|---|---|---|---|---|---|---|
| Upper Carbonif. | 0.93 | 0.47 | 0.74 | 0.86 | 0.54 | 0.87 | – 0.23 | – 0.49 | 0.85 |
| Upper Devonian | 0.98 | 0.93 | 0.94 | 0.84[1)] | 0.85 | 0.98 | 0.05 | 0.80 | 0.80[1)] |
| Lower Devonian | 0.97 | 0.03 | 0.54 | 0.68[2)] | 0.78 | 0.94 | 0.77 | – 0.38 | 0.92[2)] |

[1)] without sample 1048
[2)] without sample 1860r

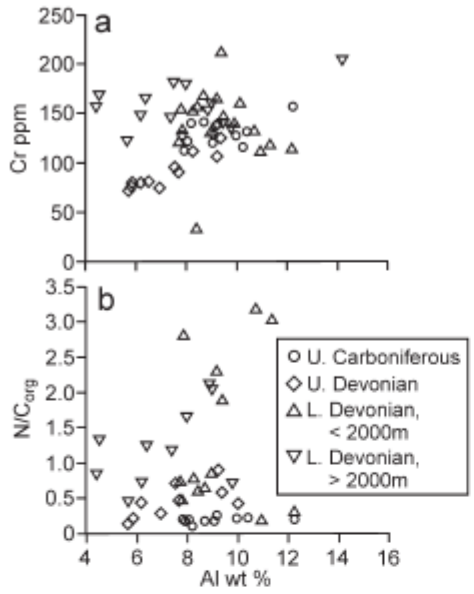


Fig. 7: Concentration of Cr in ppm (a) and $N/C_{org}$ (b) versus Al (wt.-%) in core and cutting samples of the RWTH-1 well.

Abb. 7: Konzentrationen von Cr in ppm (a) und $N/C_{org}$ (b) gegen Al (Gew.-%) in Bohrkern- und Bohrklein-Proben der Bohrung RWTH-1.

ples scatter within a limited range of values ($N/C_{org} < 1$) independent of the Al concentration. Here, N seems to be situated in organic matter and its abundance is thus not correlated with Al. Those samples with $N/C_{org} > 1$ show a clear covariation with Al, which suggests that in these samples $NH_4^+$ is fixed inorganically, mainly in illite but possibly also in feldspar.

The Upper Carboniferous rocks have low $N/C_{org}$ values. An explanation could be that the $NH_4^+$ transporting fluid did not reach these units, on the other hand, however, there is clear evidence for major faults and hydrothermal quartz-calcite veins in the cuttings. However, taking the relatively high amounts of organic matter in the Upper Carboniferous rocks into account, it is more likely that $NH_4^+$ added by a hydrothermal fluid is not reflected by the $N/C_{org}$ ratios.

The chemical data presented and discussed so far, reflect to the one hand sedimentary characteristics which point to the provenance of detrital components and, on the other hand, diagenetic and hydrothermal processes.

**Sedimentary characteristics**

The Lower Devonian and Upper Carboniferous rocks of the RWTH-1 well have similar mineralogical and geochemical characteristics. Both are characterised by high "Chemical Indices of Alteration" (CIA; Nesbitt & Young 1982) indicating intensively weathered source and/or intensive sedimentary recycling. This is in accordance with results of Schulz-Dobrick & Wedepohl (1983) for the Rhenohercynian to the east of Rhine River (Fig. 8). The similarity in CIA of the Upper Carboniferous to the Lower Devonian rocks may partly also reflect that the latter was exhumed and eroded during Upper Carboniferous times (Steingrobe 1990) and thus contributed to the sediments of that time.

As was underlined before, the Upper Devonian rocks are markedly different. Their composition mirrors a completely different source. Figure 3 shows that they plot around average composition of the upper crust (Wedepohl 1995) and trend towards felsic igneous compositions, especially in the Condroz Beds. The CIA are very low pointing to almost unweathered crust in the source area (Fig. 8). In contrast to this, the CIA calculated from the average composition of Upper Devonian rocks of the Rhenohercynian basin to the east of Rhine River (Schulz-Dobrick & Wedepohl 1983) is clearly higher, implying a more intensively weathered and reworked source. This difference in CIA in the western and eastern Rhenohercynian can be best explained assuming the Brabant Massif, situated in the basement immediately to the NW of the area studied here (Wrede 1985, Ribbert 1998), is the dominating source of detritus in the Upper Devonian of the northern Eifel region near Aachen, as was also stated for the Condroz Beds by Walter (1992) and Knapp (1980). The occurrence of mainly dacitic but also rhyolithic volcanic and intrusive rocks is described at the southern margin of the Brabant Massif (Dewaele & Muchez 2004). These rocks, formed during subduction in Ordovician times, may have

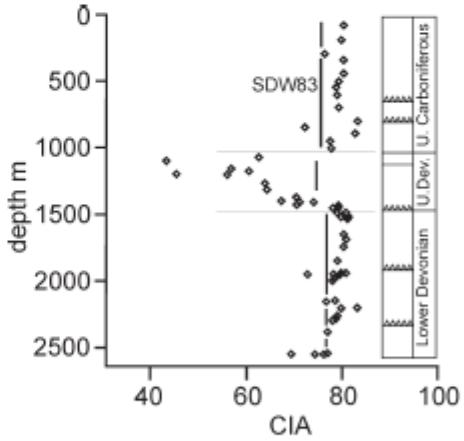


Fig. 8: Chemical Index of Alteration (CIA) according to Nesbitt & Young (1982). Dividing lines between main stratigraphic units are drawn in the figures and indicated by the simplified profile to the right. The vertical line marks the average CIA of equivalent rocks in the Rhenohercynian to the east of river Rhine (Schulz-Dobrick & Wedepohl 1983) calculated on a carbonate-free basis.

Abb. 8: Chemical index of alteration (CIA) nach Nesbitt & Young (1982). Trennlinien für die wichtigsten stratigrafischen Einheiten finden sich in der Grafik und können aus dem vereinfachten Profil auf der rechten Seite abgeleitet werden. Die vertikale Linie markiert den durchschnittlichen CIA äquivalenter Gesteine des rechtsrheinischen Rhenoherzynikums (Schulz-Dobrick & Wedepohl 1983), auf karbonatfreier Basis berechnet.

served as source rocks as well as rocks related to a large granitic batholith in the centre of the Brabant Massif (Van Grootel et al. 1997).

The observed low CIA (Fig. 8) points to limited intensity of chemical weathering (Nesbitt & Young 1982). This is in line with the statement of Thorez (2002) that the time of deposition of the Condroz Beds, especially the Montfort and Evieux times, are in general characterized by a warm and dry palaeoclimate with only short wet periods.

Abundance of Zr and Cr is most clearly controlled by accessory phases in Lower Devonian and Upper Carboniferous units of the RWTH-1 well pointing to zircon and chromite, also described as most abundant heavy minerals (Haverkamp 1991). On the basis of chromite analyses (Press 1986, Haverkamp 1991) the source of the chromite in the NW Rhenohercynian Basin is identified as alpinotype ophiolite. These have been transported into the basin from a northern to northeastern direction (Schulz-Dobrick & Wedepohl 1983, Haverkamp 1991) during the Lower Devonian and are reflected by higher relative abundance of chromite in the heavy mineral spectrum in eastern relative to western parts of the Rhenohercynian Basin (Haverkamp 1991). A lack of chromite input in the Upper Devonian, as shown in the chemical data of the RWTH-1 well, thus also underlines that the sedimentary input from other (northeastern) sources was suppressed relative to the Brabant Massif.

Nickel is an element which is also related to ultramafic sources. It was suggested that also Ni is partly controlled by an accessory phase. Chromite of the northern Eifel area has negligible amounts of Ni (Haverkamp 1991). The Ni concentrations of all rock units of the RWTH-1 well are close to the average crustal value (56 ppm; Wedepohl 1995) and thus markedly lower than the values (i.e. 107–320 ppm) observed to the east of Rhine River (Schulz-Dobrick & Wedepohl 1983). This is in line with the idea of ultramafic source rocks situated in a northeastern or eastern direction. Olivine forms a significant component of ultramafic rocks and it is generally characterized by high abundances of Ni (Wedepohl 1978). The parts of the Rhenohercynian Basin exposed to the east of Rhine River would be closer leading to higher abundances of olivine and its weathering products. In the part of the northern Eifel Mountains studied here olivine or Ni bound to its weathering products would be more dispersed due to the transport distance and more diluted due to the enhanced input from the Brabant Massif, especially in the Upper but also in the Lower Devonian.

**Hydrothermal processes**

Chemical evidence for fluid transport is given by enhanced values of mobile components (e.g. $NH_4$) or components which are in part considered to be added by a fluid phase (Ba and Cu). Thus a chemical record ($NH_4$) of fluid flux can be seen in the footwall (1450–1484 m) below the fault zone at 1440–1465 m (Tab. 2, Fig. 2). For this zone in the upper core section intensive veining is described and it is characterized by a high fracture density (Fig. 4) pointing to elevated palaeo-permeability in this region. The second core section also yields enhanced $NH_4$ values though there is less evidence for vein formation in thin sections (Sindern et al. 2007). However, this zone also shows peaks of shear wave anisotropy.

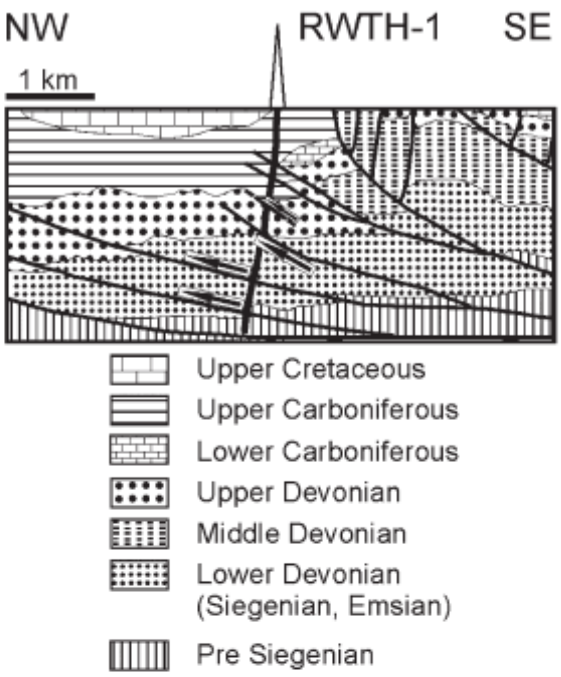


Fig. 9: Simplified section across the Aachen Thrust indicating position of the RWTH-1 well. Arrows indicate zones of focussed fluid flow, see text for discussion.

Abb. 9: Vereinfachte Profildarstellung quer zur Aachener Überschiebung und Position der Bohrung RWTH-1. Pfeile geben Zonen fokussierten Fluidflusses an, siehe Text für weitere Diskussion.

Marked chemical evidence for fluid flow (Ba, Cu, $NH_4$) is detected in cuttings at 1096 m, 1936 m and 2269–2275 m (Fig. 2). All three zones are indicated as fault zones by dipmeter and image data (Trautwein-Bruns, unpubl.). Although sample 1048 at 1096 m is taken from cuttings, it has a high Cl concentration possibly indicative of abundant fluid inclusions. The two lowermost zones which also show high fracture density (Fig. 4) are identified as larger scale thrust faults by seismic imaging within the footwall of the Aachen Thrust (Fig. 9).

Clear chemical evidence of hydrothermal fluid flow is neither observed in the surface samples nor in the Upper Carboniferous of the RWTH-1 well although fault zones representing potential pathways for fluids are obvious by dipmeter, shear wave anisotropy and seismic data (Fig. 4; Trautwein-Bruns, unpubl.).

It has to be noted that in contrast to the post-Variscan fluid inclusions, the Variscan ones are characterized by the occurrence of $N_2$ gas, assumed to be released from the pre-Variscan rocks during Variscan metamorphism (Behr et al. 1987). The incorporation of $NH_4^+$ in Devonian rocks observed here may thus serve as an indication that the fluid

flow was of Variscan age. This is in line with the statement of Lögering et al. (2006) and Sindern et al. (2007) that fluid flow in the first core section is Variscan. They derived this from fluid inclusion characteristics and indication of syndeformational chlorite. Applying these results to the whole sequence of the RWTH-1 well one can consequently assume hydrothermal fluid flow in the footwall of the Aachen Thrust during Variscan compression (Fig. 9) which mainly seems to be focussed along faults. This is in accordance with the ideas of Lünenschloss et al. (1997), Lünenschloss (1998), Teichmüller & Teichmüller (1979) and Winterfeld (1994) who assume significant fluid discharge in the footwall of the Aachen Thrust to explain vitrinite reflectance data in the Wurm Syncline.

## 7. Conclusions

This study contributes to the general aims of the RWTH-1 geoscientific research program. The geochemical data presented here provide information on the depositional history (Lower Devonian, Siegenian, to Upper Carboniferous, Namurian to Westphalian) of the NW Rhenohercynian Basin and set constraints on the mineralogical and hydrothermal control on trace element abundance in the northern Eifel region near Aachen (Germany) at the Variscan front close to the Aachen Thrust. The concentrations of V, Ni, Rb, Sr, Cu and Ba are mainly determined by the amount of illite and in part by feldspar. However, for Sr there are significant contributions from carbonates and Ni is controlled by a detrital component in the Lower Devonian rocks. The elements Cr and Zr are controlled by chromite and zircon. Chromite, however, is not significant in the Upper Devonian Condroz Beds.

Chlorine has been observed as most susceptible to weathering in surface samples and loss from cutting samples probably due to destruction of fluid inclusions.

Lower Devonian and Upper Carboniferous units have similar chemical characteristics indicating similar sources of detritus and in part resedimentation of Lower Devonian detritus in Upper Carboniferous times. The high CIA points to intensive weathering in the source area and/or recycling during transport, which was also described for the eastern part of the Rhenohercynian Basin (Schulz-Dobrick & Wedepohl 1983). The idea of an ophiolitic source of detritus situated in the NE of the Rhenohercynian Basin expressed by Schulz-Dobrick & Wedepohl (1983) and Haverkamp (1991) can be supported in this study by the abundance of Cr and Ni, mainly in the Lower Devonian. A marked change for the sedimentary input is recorded in the Upper Devonian (Famennian shales and Condroz Beds) in the mineralogical and chemical data. Here, chemically mainly unweathered rocks with felsic composition dominate. In line with literature data on the occurrence of the Condroz Beds the Brabant Massif to the NW which was affected by rapid uplift must have hosted this source.

Chemical evidence for fluid flow is detected around fault zones indicated in the RWTH-1 well. Input of Cu, Ba and $NH_4$ is attributed to this Variscan hydrothermal event for which no clear chemical evidence exists in the Upper Carboniferous rocks of the RWTH-1 well and in surface outcrops. Rather, fluid flow is focussed along larger thrust faults in the footwall of the Aachen Thrust.

## 8. Acknowledgements

This work was funded by the DFG through grant SI 810/2. M. Dohms and Prof. Dr. F. Lehmkuhl (Aachen) made N analyses available. We would like to thank A. Willner (Bochum) and R. Gaupp (Jena) for their reviews and R. Pechnig (Aachen) for advice to interpretation of log data. Assistance with analytical work by V. Havenith, M. Wiechert and R. Neef is greatfully acknowledged. P. Endres, S. Gehlen and S. Prantl are thanked for drawing figures.

## 9. References

Armstrong, P., Ireson, D., Chmela, B., Dodds, K., Esmersoy, C., Miller, D., Hornby, B., Sayers, C., Schoenberg, M., Leany, S. & Lynn, H. (1994): The promise of elastic anisotropy. – Oilfield Rev., 6: 36–47, Amsterdam (Elsevier).

Behr, H.J., Horn, E.E., Frentzel-Beyme, K. & Reutel, C. (1987): Fluid inclusion characteristics of the Variscan and post-Variscan mineralizing fluids in the Federal Republic of Germany. – Chem. Geol., 61: 273–285, Amsterdam (Elsevier).

Chatziliadou, M., Sindern, S., Hilgers, C. & Kramm, U. (2005): Spurenelementverteilung in Gesteinen der RWTH-1 Bohrung, Aachen. – Ber. Dt. Mineral. Ges.; Beih. Europ. J. Mineral., 17: 22, Stuttgart (Schweizerbart).

Condie, K.C. (1993): Chemical composition and evolution of the upper continental crust: contrasting results from surface samples and shales. – Chem. Geol., 104: 1–37, Amsterdam (Elsevier).

Cullers, R.L. (1994): The chemical signature of source rocks in size fractions of Holocene stream sediments derived from metamorphic rocks in the Wet Mountains region, Colorado, U.S.A. – Chem. Geol., 113: 327–343, Amsterdam (Elsevier).

Cullers, R.L. (1995): The controls on the major- and trace-element evolution of shales, siltstones and sandstones of Ordovician to Tertiary age in the Wet Mountains region, Colorado, U.S.A. – Chem. Geol., 123: 107–131, Amsterdam (Elsevier).

Dewaele, S. & Muchez, P. (2004): Alteration, mineralisation and fluid flow characteristics in the Bierghes Sill, Anglo-Brabant fold belt, Belgium. – Geologica Belgica, 7 (1–2): 55–69, Brussels.

Engel, W., Flehmig, W. & Franke, W. (1983): The mineral composition of Rhenohercynian flysch sediments and its tectonic significance. – In: Martin, H. & Eder, F.W. (eds.): Intracontinental fold belts: 171–184, Berlin (Springer).

Flehmig, W. (1983): Mineral composition of pelitic sediments in the Rhenohercynian zone. – In: Martin, H. & Eder, F.W. (eds.): Intracontinental fold belts: 257–265, Berlin (Springer).

Friedrich, G., Germann, A. & Jochum, J. (1993): Schichtgebundene Pb-Zn-Vorkommen in klastischen Sedimenten vom Typ Maubach-Mechernich – Lagerstättenbildung durch intraformationale Prozesse. – Mitt. österr. mineral. Ges., 138: 93–106, Wien (Österr. Mineral. Ges.).

Ganssloser, M. (2000): Schwermineralanalytische Dokumentation rhenoherzynischer Grauwacken – ein Beitrag zur Liefergebiets-

Interpretation. – Z. dt. geol. Ges., 151: 127–170, Stuttgart (Schweizerbart).

Gibbs, A.K., Montgomery, C.W., O'Day, P.A. & Erslev, E.A. (1986): The Archean-Proterozoic transition: Evidence from the geochemistry of metasedimentary rocks of Guyana and Montana. – Geochim. Cosmochim. Acta, 50: 2125–2141, Amsterdam (Elsevier).

Glasmacher, U.A., Tschernoster, R., Clauer, N. & Spaeth, G. (2001): K-Ar dating of magmatic sericite crystallites for determination of cooling paths of metamorphic overprints. – Chem. Geol., 175: 673–687, Amsterdam (Elsevier).

Grabert, H. (1998): Abriss der Geologie von Nordrhein-Westfalen: 351 p., Stuttgart (Schweizerbart).

Hassan, S., Ishaga, H., Roser, B.P., Dozen, K. & Naka, T. (1999): Geochemistry of Permian-Triassic shales in the Salt Range, Pakistan: implications for provenance and tectonism at the Gondwana margin. – Chem. Geol., 158: 293–314, Amsterdam (Elsevier).

Haverkamp, J. (1991): Detritusanalyse unterdevonischer Sandsteine des Rheinisch-Ardennischen Schiefergebirges und ihre Bedeutung für die Rekonstruktion der sedimentliefernden Hinterländer. – Diss. RWTH Aachen: 195 p., Aachen (unpubl.).

Haverkamp, J., Hoegen, J. von, Kramm, U. & Walter, R. (1991): Application of U-Pb-systems from detrital zircons for palaeogeographic reconstructions – a case-study from the Rhenohercynian. – Geodinamica Acta, 5 (1991, 1992): 69–82, Paris (Masson).

Herron, M.M. (1988): Geochemical classification of terrigenous sands and shales from core or log data. – J. Sed. Petrol., 58: 820–829, Tulsa (OK) (Soc. Sediment. Geol.).

Hollmann, E.G. (1997): Der Variszische Vorlandüberschiebungsgürtel der Ostbelgischen Ardennen – ein bilanziertes Modell. – Aachener geowiss. Beitr., 25: 1–235, Aachen (Wissenschaftsverl. Mainz).

Hollmann, G. & Winterfeld, C. von (1999): Laterale Strukturvariationen eines Vorlandüberschiebungsgürtels. – Z. dt. geol. Ges., 150: 431–450, Stuttgart (Schweizerbart).

Kasig, W. & Wilder, H. (1983): The sedimentary development of the western Rheinisches Schiefergebirge and the Ardennes (Germany/Belgium). – In: Martin, H. & Eder, F.W. (eds.): Intracontinental fold belts: 185–209, Berlin (Springer).

Knapp, G. (1980): Geologischen Karte der nördlichen Eifel 1 : 100 000, mit Erläuterungen; 2. Aufl. – Geol. L.-Amt Nordrhein Westfalen, Krefeld.

Krahn, L. & Baumann, A. (1996): Lead isotope systematics of epigenetic lead-zinc mineralization in the western part of the Rheinisches Schiefergebirge, Germany. – Mineral. Deposita, 31: 225–237, Berlin (Springer).

Larionov, V.V. (1969): Borehole radiometry: 326 p., Moscow (Nedra) (in Russian).

Lögering, M.J., Kolb, J., Meyer, F.M. & Schwarzbauer, J. (2006): Paläofluide in störungskontrollierten Bruchsystemen der Aachener Geothermie-Bohrung. – Abstract, TSK11, 11. Symposium Tektonik, Struktur und Kristallingeologie, 22.–24. März, Göttingen.

Lünenschloss, B. (1998): Modellierung der Temperatur- und Fluidgeschichte an der variszischen Front (Verviers-Synklinorium und Nordeifel). – Scientific Technical Report STR98/07: 132 p., Geoforschungszentrum Potsdam, Potsdam.

Lünenschloss, B., Bayer, U. & Muchez, P. (1997): Coalification anomalies induced by fluid flow at the Variscan thrust front: a numerical model of the palaeotemperature field. – Geol. Mijnbouw, 76: 271–275, Dordrecht (Springer).

Lundershausen, S., Oesterreich, B., Ribbert, K.H. & Wrede, V. (2005): Geothermal well "RWTH-1", Aachen – technical aspects and first geological results. – Abstracts of the Meuse-Rhine Euregio Geologists Meeting; Alden Biesen (Belgian Limbourg), 20–21 May 2005.

Marshall, C.P. & Fairbridge, R.W. (1999): Encyclopedia of geochemistry: 712 p., Dordrecht (Kluwer).

McLennan, S.M., Hemming, S.R., Taylor, S.R. & Eriksson, K.A. (1995): Early Proterozoic crustal evolution: geochemical and Nd-Pb isotopic evidence from metasedimentary rocks, southwestern North America. – Geochim. Cosmochim. Acta, 59: 1153–1177, Amsterdam (Elsevier).

Meyer, W. (1994): Geologie der Eifel; 3. Aufl.: 618 p., Stuttgart (Schweizerbart).

Meyer, F.M. & Ridgway, J. (1991): Ammonium in Witwatersrand reefs: a possible indicator of metamorphic fluid flow. – South African J. Geol., 94: 343–347, Johannesburg (Geol. Soc. South Africa).

Milliken, K.L. (2003): Late diagenesis and mass transfer in sandstone-shale sequences. – In: Mackenzie, F.T. (ed.): Sediments, diagenesis, and sedimentary rocks, 7. – In: Holland, H.D. & Turekian, K.K. (eds.): Treatise on geochemistry: 159–190, Oxford (Elsevier-Pergamon).

Mingram, B., Hoth, P., Lüders, V. & Harlov, D. (2005): The significance of fixed ammonium in Palaeozoic sediments for the generation of nitrogen-rich natural gases in the North German Basin. – Int. J. Earth Sci., 94: 1010–1022, Berlin (Springer).

Muchez, P., Slobodnik, M., Viaene, W. & Keppens, E. (1994): Mississippi Valley-type Pb-Zn mineralization in eastern Belgium: indications for gravity-driven flow. – Geology, 22: 1011–1014, Boulder (CO) (Geol. Soc. America).

Nesbitt, H.W. & Young, G.M. (1982): Early Proterozoic climates and plate motions inferred from major element chemistry of lutites. – Nature, 299: 715–717, London (Macmillan).

Nierhoff, R. (1994): Metamorphose-Entwicklung im Linksrheinischen Schiefergebirge: Metamorphosegrad und -verteilung sowie Metamorphosealter nach K-Ar-Datierungen. – Aachener geowiss. Beitr., 3: 1–159, Aachen (Wissenschaftsverl. Mainz).

Oesterreich, B. & Lundershausen, S. (2002): Erkundungsbohrung „SuperC" des Geologischen Dienstes NRW in Aachen. – Z. angew. Geol., 4: 40–41, Stuttgart (Schweizerbart).

Oesterreich, B., Ribbert, K.H. & Wrede, V. (2005): Erste Ergebnisse zur biostratigrafischen und tektonischen Einordnung der Bohrung RWTH-1. – Geol. Dienst NRW 2005 (unpubl. report).

Oncken, O., Winterfeld, C. von & Dittmar, U. (1999): Accretion of a passive margin: the late Paleozoic Rhenohercynian fold and thrust belt (Middle European Variscides). – Tectonics, 18: 75–91, Washington D. C. (American Geophys. Union).

Oncken, O., Plesch, A., Weber, J., Ricken, W. & Schrader, S. (2000): Passive margin detachment during arc-continent collision (Central European Variscides). – In: Franke, W., Haak, V., Oncken, O. & Tanner, D. (eds.): Orogenic processes: quantification and modelling in the Variscan Belt. – Geol. Soc. London, Spec. Publ., 179: 199–216, London (Geol. Soc. London).

Pechnig, R. (2005): Auswertung der bohrlochgeophysikalischen Messungen in der RWTH-1 – Möglichkeiten und Grenzen der Lithologierekonstruktion. – RWTH Aachen University, E.ON Energy Research Center, Applied Geophysics and Geothermal Energy (unpubl.).

Press, S. (1986): Detrital spinells from alpinotype source rocks in middle Devonian sediments of the Rhenish Massif. – Geol. Rdsch. 75: 333–340, Stuttgart (Enke).

Rashid, S.A. (2002): Geochemical characteristics of Mesoproterozoic clastic sedimentary rocks from the Chakrata Formation, Lesser Himalaya: implications for crustal evolution and weathering history in the Himalaya. – J. Asian Earth Sci., 21: 283–293, Oxford (Elsevier).

Redecke, P. (1992): Zur Geochemie und Genese variszischer und postvariszischer Buntmetallmineralisation in der Nordeifel und der Niederrheinischen Bucht. – Mitt. Mineral. Lagerst.-Kde., 41: 1–152, Aachen (Inst. Mineral. Lagerst.-Lehre).

Ribbert, K.H. (1998): Das Famenne im Untergrund der Niederrheinischen Bucht. – Fortschr. Geol. Rheinland Westfalen, 37: 81–107, Krefeld (Geol. L.-Amt Nordrhein-Westfalen).

Ribbert, K.H. (2006): Die Bohrung RWTH-1 – Regionalstratigraphische Einordnung und Deutung. – Geol. Dienst NRW (unpubl.).

Rottke, W. & Stroink, L. (1999): Die Genese devonischer Vorlandsedimente am NW-Rand des Rheinischen Massivs – Zement- und Porenraumentwicklung. –Z. dt. geol. Ges., 150: 471–491, Stuttgart (Schweizerbart).

Rudnick, R.L. & Gao, S. (2005): Composition of the continental crust. – In: Rudnick, R.L. (ed.): The Crust, 3: 1–64. – In: Holland, H.D. & Turekian, K.K. (eds.): Treatise on geochemistry, Oxford (Elsevier-Pergamon).

Schneider, J., Chatziliadou, M., Sindern, S., Hilgers, C. & Kramm, U. (2007): Multiple hydrothermal fluid flow in the NW Rhenohercynian. – Geochim. Cosmochim, Supplement, 71: 15 p., Abstr. 17th Annual V.M. Goldschmidt Conference, Cologne, Germany, 2007: A900.

Schulz-Dobrick, B. & Wedepohl, K.H. (1983): The chemical composition of sedimentary deposits in the Rhenohercynian Belt of central Europe. – In: Martin, H. & Eder, F.W. (eds.): Intracontinental fold belts: 211–229, Berlin (Springer).

Sindern, S., Stanjek, H., Hilgers, C. & Etoundi, Y. (2007): Short-term hydrothermal effects on the "crystallinities" of illite and chlorite in the footwall of the Aachen-Faille du Midi thrust fault – first results of the RWTH-1 drilling project. – Clays Clay Minerals, 55: 200–212, Oxford (Pergamon).

Steingrobe, B. (1990): Fazieseinheiten aus dem Aachen-Erkelenzer Oberkarbonvorkommen unter besonderer Berücksichtigung des Inde-Synklinoriums. – Diss. RWTH Aachen: 325 p., Aachen.

Stets, J. & Schäfer, A. (2004): Deltasedimentation im Nordabschnitt des Rhenoherzynischen Beckens (Unterdevon, Rheinisches Schiefergebirge). – In: Kukla, P., Littke, R., Stollhofen, H. & Schwarzer, D. (eds.): Sediment 2004 – Tagungsband, Schriftenr. Dt. Ges. Geowiss., 33: 256–273, Hannover (Dt. Ges. Geowiss.).

Stroetmann-Heinen, V. (1999): Simulation einer paläozoischen passiven Plattenrandentwicklung in den mitteleuropäischen Variziden – Das linksrheinische Schiefergebirge. – Z. dt. geol. Ges., 150: 451–470, Stuttgart (Schweizerbart).

Teichmüller, M. & Teichmüller, R. (1979): Ein Inkohlungsprofil entlang der linksrheinischen Geotraverse von Schleiden nach Aachen und die Inkohlung in der Nord-Süd-Zone der Eifel. – Fortschr. Geol. Rheinland Westfalen, 27: 323–355, Krefeld (Geol. L.-Amt Nordrhein-Westfalen).

Thorez, J. (2002): Palaeosols and inferred palaeoclimatology in the Condroz Sandstone (Upper Famennian, northeastern part of the Dinant Synclinorium, Belgium). – Aardkundige Meded., 12: 145–148, Leuven (Univ. Press).

Trautwein-Bruns, U., Kukla, P., Urai, J., Sindern, S., Lögering, M., Dijkshorn, L., Lünenschloss, B. & Chatziliadou, M. (2007): Aachens's geothermal well "RWTH-1" – the geoscientific research program. – 67. Jtag. Dt. Geophys. Ges., 26.–29. März 2007, Aachen.

Van Grootel, G., Verniers, J., Geerkens, B., Laduron, D., Verhaeren, M., Hertogen, J. & de Vos, W. (1997): Timing of magmatism, foreland basin development, metamorphism and inversion in the Anglo-Brabant fold belt. – Geol. Mag., 134: 607–616, Cambridge (Cambridge Univ. Press).

Veizer, J. & Mackenzie, F.T. (2003): Evolution of sedimentary rocks. – In: Mackenzie, F.T. (ed.): Sediments, diagenesis, and sedimentary rocks, 7: 369–407. – In: Holland, H.D. & Turekian, K.K. (eds.): Treatise on geochemistry, Oxford (Elsevier-Pergamon).

Walter, R. (1992): Geologie von Mitteleuropa; 5. Aufl.: 561 p., Stuttgart (Schweizerbart).

Wedepohl, K.H. (1978): Handbook of geochemistry: 442 p., Berlin (Springer).

Wedepohl, K.H. (1995): The composition of the continental crust. – Geochim. Cosmochim. Acta, 59: 1217–1232, Amsterdam (Elsevier).

Williams, L.B. & Ferrell, R.E. (1991): Ammonium substitution in illite during maturation of organic matter. – Clays Clay Minerals, 39: 400–408, Oxford (Pergamon).

Williams, L.B., Wilcoxon, B.R., Ferrell, R.E. & Sassen, R. (1992): Diagenesis of ammonium during hydrocarbon maturation and migration, Wilcox Group, Louisiana, U.S.A. – Appl. Geochem., 7: 123–134, Oxford (Pergamon).

Winterfeld, C.-H. von (1994): Variszische Deckentektonik und devonische Beckengeometrie der Nordeifel – ein quantitatives Modell. – Aachener geowiss. Beitr., 2: 1–319, Aachen (Wissenschaftsverl. Mainz).

Wrede, V. (1985): Tiefentektonik des Aachen-Erkelenzer Steinkohlengebietes. – In: Drozdzewski, G., Engel, H., Wolf, R. & Wrede, V. (eds.): Beiträge zur Tiefentektonik westdeutscher Steinkohlenlagerstätten: 9–103, Krefeld (Geol. L.-Amt Nordrhein-Westfalen).

Manuscript received: 02.02.2008
Accepted for publication: 07.06.2008

11.

Sindern, S., Meyer, F.M., Lögering, M.J., Kolb, J., Vennemann, T., Schwarzbauer, J. (2012b) Fluid evolution at the Variscan front in the vicinity of the Aachen thrust. International Journal of Earth Sciences (Geol Rundsch) 101, 87–108.

With permission of Springer.

Re-use in thesis granted by Springer, Rights and Permissions, Tiergartenstrasse 17, 69121 Heidelberg, Germany, permission letter 14th of October 2015.

Int J Earth Sci (Geol Rundsch) (2012) 101:87–108
DOI 10.1007/s00531-011-0662-2

ORIGINAL PAPER

# Fluid evolution at the Variscan front in the vicinity of the Aachen thrust

**S. Sindern · F. M. Meyer · M. J. Lögering · J. Kolb · T. Vennemann · J. Schwarzbauer**

Received: 12 July 2010 / Accepted: 7 April 2011 / Published online: 1 May 2011
© Springer-Verlag 2011

**Abstract** Quartz–carbonate–chlorite veins were studied in borehole samples of the RWTH-1 well in Aachen. Veins formed in Devonian rocks in the footwall of the Aachen thrust during Variscan deformation and associated fluid flow. Primary fluid inclusions indicate subsolvus unmixing of a homogenous $H_2O$–$CO_2$–$CH_4$–($N_2$)–Na–(K)–Cl fluid into a $H_2O$–Na–(K)–Cl solution and a vapour-rich $CO_2$–($H_2O$, $CH_4$, $N_2$) fluid. The aqueous end-member composition resembles that of metamorphic fluids of the Variscan front zone with salinities ranging from 4 to 7% NaCl equiv. and maximum homogenisation temperatures of close to 400°C. Pressure estimates indicate a burial depth between 4,500 and 8,000 m at geothermal gradients between 50 and 75°C/26 MPa, but pressure decrease to sublithostatic conditions is also indicated, probably as a consequence of fracture opening during episodic seismic activity. A second fluid system, mainly preserved in pseudo-secondary and secondary fluid inclusions, is characterised by fluid temperatures between 200 and 250°C and salinities of <5% NaCl equiv. Bulk stable isotope analyses of fluids released from vein quartz, calcite, and dolomite by decrepitation yielded $\delta D_{H2O}$ values from −89 to −113 ‰, $\delta^{13}C_{CH4}$ from −26.9 to −28.9‰ (VPDB) and $\delta^{13}C_{CO2}$ from −12.8 to −23.3‰ (VPDB). The low $\delta D$ and $\delta^{13}C$ range of the fluids is considered to be due to interaction with cracked hydrocarbons. The second fluid influx caused partial isotope exchange and disequilibrium. It is envisaged that an initial short lived flux of hot metamorphic fluids expelled from the epizonal metamorphic domains of the Stavelot–Venn massif. The metamorphic fluid was focused along major thrust faults of the Variscan front zone such as the Aachen thrust. A second fluid influx was introduced from formation waters in the footwall of the Aachen thrust as a consequence of progressive deformation. Mixing of the cooler and lower salinity formation water with the hot metamorphic fluid during episodic fluid trapping resulted in an evolving range of physicochemical fluid inclusion characteristics.

**Keywords** Aachen · Variscan front zone · Fluid inclusions · Palaeo-fluid flow · H–C–O isotopes

S. Sindern (✉) · F. M. Meyer · J. Kolb
Institute of Mineralogy and Economic Geology,
RWTH Aachen University, Wüllnerstr. 2,
52056 Aachen, Germany
e-mail: sindern@rwth-aachen.de

M. J. Lögering
Geoforschungszentrum Potsdam GFZ,
Albert-Einstein-Str. 48, 14473 Potsdam, Germany

J. Kolb
De Nationale Geologiske Undersoegelser for Danmark og
Groenland, Oester Voldgade 10, 1350 Kopenhagen K, Denmark

T. Vennemann
Institute for Mineralogy and Geochemistry,
University of Lausanne, BFSH-2, 1015 Lausanne, Switzerland

J. Schwarzbauer
Institute of Geology and Geochemistry of Petroleum
and Coal, RWTH-Aachen University, Lochnerstr. 24,
52056 Aachen, Germany

## Introduction

Thrusting and thrust loading in an orogenic wedge causes fluid expulsion into the foreland (Moore 1989; Oliver 1986), and fluid-overpressure formation above and below the thrust plane if the bulk rock is of intermediate permeability (Smith and Wiltschko 1996). Sibson (2001) showed

the important role of hydrothermal fluids in the thermal evolution, diagenesis, mineralisation, and rupture mechanics of faults in an orogenic front.

Fluid generation and expulsion is also to be expected in the frontal zone of the Variscan orogen that resulted from late Palaeozoic continent–continent collision between Laurussia and Gondwana to form the supercontinent of Pangaea. The Aachen thrust as NE extension of the Midi thrust represents the northern front of the Variscan orogen in central Europe (Oncken et al. 1999). Abundant indications of fluid flow are given by high coalification grades in the hanging wall and in the footwall close to the Aachen thrust (Babinecz 1962; Teichmüller and Teichmüller 1979; von Winterfeld 1994) that are interpreted to be the result of Carboniferous and thus Variscan (Knapp 1980) hydrothermal fluid flow. Similarly, Lünenschloss et al. (1997, 2008) concluded from the regional distribution of vitrinite reflectance that coalification anomalies resulted from significant fluid flow at the Variscan thrust front. Other valuable monitors of fluid flow are mineralised veins that are ubiquitous in many metamorphic settings. Veins may represent conduits for regionally migrating fluids or local crack-fill diffusional processes, or both. The evaluation of vein formation and associated metasomatic processes are generally considered to be very helpful for assessing fluid fluxes, flow paths and the chemical impact of fluids during metamorphism.

The RWTH-1 well was drilled in the city of Aachen in 2004 to generate geothermal energy. The borehole is situated approximately 500 m to the north of the Aachen thrust intersecting the footwall of this structure. Core samples are characterised by intensive veining and syntectonic hydrothermal formation of chlorite and white mica that indicate fluid flow of Variscan age (Sindern et al. 2007). Zones of intensive hydrothermal alteration resulting from fluid–rock reaction are ubiquitous around fault intersections (Sindern et al. 2008). To date, Variscan metamorphic fluids are fairly well studied in the Venn–Weser–Inde nappe, the Ardennes, the Variscan front zone in Belgium and northern France, and in the Rhenish massif, east of the Rhine river (Behr et al. 1987, 1993; Dewaele et al. 2004; Kenis et al. 2000, 2005; Muchez et al. 1998, 2000, 2002; Vogtmann–Becker 1990). However, a systematic fluid study close to the Aachen thrust is still lacking.

The aim of this study is analysing the physicochemical parameters and geochemical composition of palaeo-fluids in samples from the RWTH-1 well. For that purpose, we studied fluid inclusions in vein quartz and carbonates and stable isotope compositions (i.e. $\delta$D, $\delta^{18}$O and $\delta^{13}$C) of host rocks, vein minerals and fluid inclusions. The data permit identification and characterisation of fluid composition and fluid pulses, and provide information on the fluid origin and PT conditions of the hydrothermal event associated with the Variscan orogeny.

## Geological setting

### Regional geology and fluid evolution

The Rhenohercynian domain of the central European Variscan orogen comprises the Ardennes of western Germany and eastern Belgium and the Rhenish massif (Oncken et al. 2000; Walter 1995). The study area, i.e. the city of Aachen and environs, is situated in the Variscan front zone (Kenis et al. 2000; Muchez and Sintubin 1998) that is characterised by regional-scale synclines, anticlines and locally developed thrusts which strike NE–SW related to the Variscan deformation ($D_1$). In Aachen, the Variscan thrust front is represented by the Aachen thrust that connects to the west with the Midi thrust in eastern Belgium (Hollmann and von Winterfeld 1999; Oncken et al. 1999, 2000; Walter 1995; Fig. 1). Variscan NW–SE trending faults cross-cut the Variscan structures and host the Jurassic to Cretaceous post-Variscan Pb–Zn deposits known from the Aachen region, eastern Belgium and the NW Rhenohercynian (Dejonghe and Boni 2004; Franke 1989; Heijlen et al. 2001; Muchez et al. 2002; Schneider et al. 1999, 2007, 2008).

This study is based on borehole samples and cuttings from the RWTH-1 borehole that intersected lower and upper Devonian as well as upper Carboniferous rocks in the northern limb of the Aachen anticline (Becker 2008) (Fig. 1). The Wurm syncline follows north of the Aachen anticline and joins up in the west with the Verviers syncline in eastern Belgium. The basement is represented by the Brabant massif in the north and the Stavelot–Venn massif in the south. Devonian and Carboniferous cover rocks were thrusted onto the Brabant massif along the south dipping Variscan $D_1$ thrust faults.

Palaeozoic rocks in the study area are affected by compressive Variscan deformation which was dated by Nierhoff (1994) to have occurred between 336 and 300 Ma. Glasmacher et al. (2001) obtained an Ar–Ar age of 314 ± 7 Ma for Variscan cleavage formation and a minimum age of 300 ± 8 Ma for a hydrothermal fluid flow event.

Fluid inclusion thermometry, mineral assemblage studies, chlorite-thermometry and vitrinite data indicate peak temperatures of 330–400°C for Variscan metamorphism in the southern Venn–Weser–Inde nappe (Glasmacher 1995; Hilgers et al. 2006; Oncken et al. 1999; Vogtmann–Becker 1990; Zhang et al. 1997). For the Verviers syncline in eastern Belgium, the southern and eastern parts of the Stavelot–Venn massif, and the Rhenish massif to the east of the Rhine river the colour alteration index (CAI) of conodonts points to variable temperatures reaching epizonal values as high as 420°C (Fransolet and Kramm 1983; Helsen and Koenigshof 1994; Helsen 1995; Kramm 1982; Schreyer 1975).

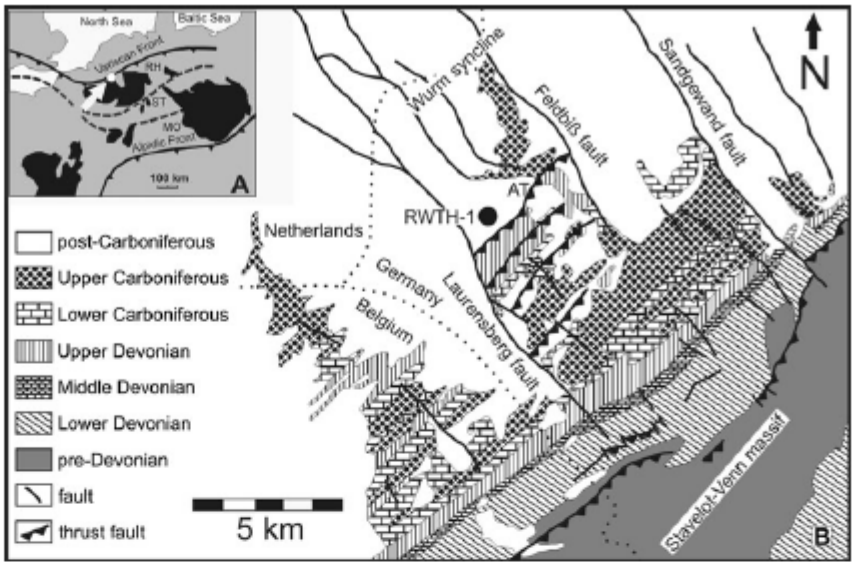


**Fig. 1** Geological sketch maps; *A* overview of the Middle European Variscan zones (according to Oncken et al. 2000), *MO* Moldanubian, *RH* Rhenohercynian, *ST* Saxothuringian, *white point* and *arrow* indicate study area. *B* area of the Variscan front zone in the region of Aachen (after Knapp 1980; Walter 1995). *Black spot* marks position of the RWTH-1 well close to the Aachen thrust (*AT*)

For the region north of the Venn–Weser–Inde nappe, Oncken et al. (1999) report lower, anchizonal (Merriman and Frey 1999) peak temperatures of 250–280°C. In the foreland of the Aachen thrust mineralogical, textural and vitrinite reflectance data from Carboniferous and Devonian rocks point to a maximum temperature overprint of 200°C (Hollmann 1997). The low metamorphic grade is in accordance with estimated burial depths of 4.5 km (Helsen 1995; Rottke and Stroink 1999) to 6 km in maximum (Sehrt et al., in prep.).

Temperature information for the Wurm syncline north of the Aachen thrust is derived from organic maturity data. Within the upper Carboniferous of the Wurm syncline vitrinite reflectance increases towards the south and the Aachen thrust (Babinecz 1962; Steingrobe 1990; Teichmüller and Teichmüller 1979; von Winterfeld 1994). Increased organic maturity in this area is explained by enhanced heat flow which was caused by fluid discharge in the footwall of the Aachen thrust (Knapp 1980; Lünenschloss et al. 1997, 2008; Lünenschloss 1998; Teichmüller and Teichmüller 1979). A similar thermal overprint in the temperature range of 210–310°C can also be assumed for the rock units of the RWTH-1 well. This is supported by microstructural considerations that indicate minimum temperatures of 200–250°C (Sindern et al. 2007).

Behr et al. (1993) investigated the regional fluid inventory in the Rhenohercynian domain of the Variscan orogeny and identified a synkinematic fluid system that they called 'tectonic brines'. The 'tectonic brines' represent a $H_2O$–Na–(K)–Cl-dominated metamorphic fluid with $CO_2$, $CH_4$, and $N_2$ that is characterised by salinities <15 wt% NaCl equiv. and homogenisation temperatures ≤350°C. Fluid inclusion studies carried out in the Anglo–Brabant fold belt, Ardennes and the Stavelot–Venn massif, and in the Variscan front zone in eastern Belgium recognised a syn-Variscan $H_2O$–$CO_2$–NaCl-dominated metamorphic fluid of low salinity and homogenisation temperatures ≤380°C (Table 1, Behr et al. 1987; Dewaele et al. 2004; Kenis et al. 2000, 2005; Muchez et al. 1998; Schroyen and Muchez 2000; Vogtmann–Becker 1990). The post-Variscan hydrothermal ore deposits of the Rhenohercynian domain are derived from 'basement brines' (Behr et al. 1993). The 'basement brines' are $H_2O$–Ca–Na–Cl-dominated fluids with high salinities up to halite saturation due to evaporation in a marine environment. Homogenisation temperatures of ≤200°C are distinctly lower as compared to the metamorphic Variscan fluids (Behr et al. 1987; Heijlen et al. 2001; Kucera et al. 2010).

## Stratigraphy, lithology and structural geology of the RWTH-1 well

Technical aspects of the RWTH-1 well are described by Lundershausen et al. (2005). Cores were cut at depth intervals 1,392–1,515, 2,128–2,143 and 2,536–2,544 m. From the end of hole at 2,544 m to a depth of 1,438 m, cores and cuttings contain lower Devonian siliciclastic sediments with root fragments, ooides and nodular calcrete horizons. Spore analysis indicates an upper Siegen sedimentation age for the rocks at 1,490 m (Wrede, personal communication).

The thinly bedded lower Devonian shales are red to grey and inter-bedded with fine-grained to coarse-grained, grey sandstones that contain rock fragments in an argillaceous

**Table 1** Characteristic features of pre-Variscan, Variscan and post-Variscan non-magmatic fluids in the Rhenohercynian between the Anglo Brabant fold belt and the eastern Bohemian massif

| Region | Event | Origin | Fluid type | Salinity % eq. NaCl | Temperature in °C | References |
|---|---|---|---|---|---|---|
| Anglo–Brabant fold belt | Late Silurian to early Devonian metamorphism, compressive veins | Core of Anglo–Brabant fold belt | $H_2O$–$CO_2$–($CH_4$)–NaCl–KCl | | ≤350 | Dewaele et al. (2004) |
| Stavelot–Venn massif | Caledonian | | $H_2O$–$CO_2$–NaCl | 0.6–5.7 | 200–299, $T_h$ | Schroyen and Muchez (2000) |
| Stavelot–Venn massif | Post Caledonian, pre-Variscan | | $CO_2$–$N_2$ | 1.3–3.7 | 400, Ttrap | Schroyen and Muchez (2000) |
| Anglo–Brabant fold belt | Secondary FI in compressive veins and post compressive | | $H_2O$–NaCl–KCl | 0.2–16.3 | 81–285, $T_h$ | Dewaele et al. (2004) |
| Ardennes | Burial/Variscan deformation, anchizonal metamorphism | | $H_2O$–NaCl–$CO_2$–($CH_4$–$N_2$) | 0–3.5 | 277–291, $T_h$ | Kenis et al. (2005) |
| Ardennes | Burial/Variscan deformation, epizonal metamorphism | Internal origin, closed system hydrolysis reactions | $H_2O$–NaCl–$CO_2$–($CH_4$–$N_2$) | 0.6–17.0 | 200–400, $T_h$ | Kenis et al. (2005) |
| Ardennes | Late Variscan retrograde anchizonal metamorphism | Affected by hydration reactions during retrograde metamorphism | $H_2O$–NaCl | 0–2.7 | 138–261 | Kenis et al. (2005) |
| Ardennes | Late Variscan retrograde epizonal metamoprhism | | $H_2O$–NaCl | 3–10.6 | 127–362 | Kenis et al. (2005) |
| Stavelot–Venn massif | Variscan metamorphism | | $H_2O$–NaCl–$CO_2$ | 4–6 | 100–420, $T_h$ | Vogtmann–Becker (1990) |
| Stavelot–Venn massif | Variscan metamorphism | | $H_2O$–NaCl | 7–11.5 | 100–420 | Vogtmann–Becker (1990) |
| Rhenish massif (east of Rhine River) | Variscan syn-metamorphic mineralization | | Na–K–(Ca)–Cl, abundant $CO_2$–($CH_4$–$N_2$) | Low | <50–380, Ttrap | Behr et al. (1987) |
| Rhenish massif (west of Rhine River)[a] | Variscan deformation | | | Low salinity | 293–350, $T_h$ | Germann and Friedrich (1999) |
| Variscan front zone | Variscan deformation | Limestone, rock-buffered | | 12–16 | 260 | Kenis et al. (2000) |
| Stavelot–Venn massif | Variscan | Metamorphic | $H_2O$–$CO_2$–NaCl | 0.7–6.9 | 385–435, Ttrap | Schroyen and Muchez (2000) |
| Anglo–Brabant fold belt | Post-Variscan, mesozoic | Basement brines | $H_2O$–NaCl–$CaCl_2$ | 9.5–21.2 | 98 – 169, $T_h$ | Dewaele et al. (2004) |
| Rhenish massif (east of Rhine River) | Post-Variscan permian to old mesozoic hydroth. min. | Deep basinal brines | Ca–Na–(K, Mg)–Cl, no $CO_2$, $N_2$ | >23 | 100–200, Trap | Behr et al. (1987) |
| Rhenish massif (west of Rhine River)[b] | Post-Variscan Pb–Zn mineralisation | Basement brines | $H_2O$–NaCl–$CaCl_2$ | 20–24 | 120–180 | German and Friedrich (1999)[c] |
| Rhenish massif (west of Rhine River)[d] | Post-Variscan Pb–Zn mineralisation | | $H_2O$–NaCl–$CaCl_2$ | | <250 | Redecke (1992) |
| Rhenish massif[e] | Post-Variscan Pb–Zn min | Basement brines | $H_2O$–NaCl–$CaCl_2$ | 16–23.1 | 68–120, $T_h$ | Heijlen et al. (2001) |

**Table 1** continued

| Region | Event | Origin | Fluid type | Salinity % eq. NaCl | Temperature in °C | References |
|---|---|---|---|---|---|---|
| Variscan front zone, Flône[f] | Post-Variscan calcite cements | | $H_2O$–NaCl–$CaCl_2$ | 18.1–25.3 Eq. $CaCl_2$ | 37–131, $T_h$ | Muchez and Sintubin (1998) |
| Variscan front zone, Flône[f] | Post-Jurassic uplift, post early cretaceous karstification | | $H_2O$–NaCl | 1.7–8.6 | <50 | Muchez and Sintubin (1998) |
| Stavelot–Venn massif | Post-Variscan | | $H_2O$–NaCl | 0.3–8.9 | 94–312, $T_h$ | Schroyen and Muchez (2000) |
| Eastern Bohemian massif | Post-Variscan Zn–Pb–Cu veins | Evaporated seawater, evolved by fluid rock interaction | $H_2O$–NaCl–$CaCl_2 \pm MgCl_2$ | 16.6–28.4 | 66–148, $T_h$ | Kucera et al. (2010) |

$T_h$ homogenisation temperature, *Ttrap* trapping temperature of fluid inclusions

[a] Backthrusts of Malsbenden and Schleiden

[b] Mechernich, Maubach, Albertsgrube, Rescheid, Lichtenhard

[c] Compiled from Strich (1991), Friedrich et al. (1989), Redecke (1992)

[d] Bleiberg, Plombières

[e] Bleiberg

[f] Meuse River Valley, Belgium

ground mass. These rocks contain micrite to microsparite cements. They are overlain by an alternation of upper Devonian siliciclastic rocks and shallow water carbonates from 1,438 to 1,012 m of the Frasnian to the Famennian stage. They consist of thinly bedded siliciclastic rocks and are intercalated with a dolomite bank, dolomite-marl and calcite-marl, and a nodular limestone (Fig. 2a) with a biorelic fabric. Hydrothermal dolomitisation is ubiquitous (Lögering 2008). Two thin carbonaceous layers at 1,408 m and 1,428–1,438 m are rich in fossils. Conodonts indicate the crepida zone of the upper Devonian Nehden stage (Becker 2008). These layers can be correlated with upper Devonian sedimentary profiles to the south of the Aachen thrust and Midi thrust in the Bolland and Soumagne wells (Lögering 2008). Lower Devonian silty shales are characterised by an irregular distribution of red, green and grey colours (Becker 2008) indicating differing redox conditions during diagenesis or later events.

Famennian to Givetian and lower Carboniferous units are missing (Fig. 3). Evidence of tectonic processes causing absence of strata is not observed (Becker 2008; Becker et al. 2011). Reasons for gaps in the stratigraphic column are sedimentary hiati that are also reported from other areas of the western Rhenohercynian (Ribbert 2006). This may be a result of the near shore position at the southern margin of the Brabant massif (Lögering 2008). From 1,012 m up to surface the upper Devonian is overlain by upper Carboniferous rocks of the Namurian and the Westphalian stages (Österreich et al. 2005).

Petrological examinations of core samples revealed a marked paucity of visible porosity in the Carboniferous to Devonian lithologies. This results from micrite and microsparite cementation and concomitant loss of primary depositional porosity. Voids and joints are sealed by quartz, carbonates and chlorite that precipitated from a hydrothermal fluid. Further information on various aspects of the RWTH-1 well are given in Becker (2008), Becker et al. (2011), Lögering (2008), Sindern et al. (2007, 2008), Trautwein–Bruns et al. (2007, 2010).

All rocks in the core section from 1,515 to 1,391 m are characterised by hydrothermal veins and several cataclastic deformation zones (Lögering 2008; Sindern et al. 2007, 2008; Fig. 3). A major $D_1$ thrust fault and shear zone was identified around 1,438 m. Late diagenetic textures are overprinted by the $D_1$ deformation forming a $S_1$ foliation in the argillaceous and silty rocks. In parts, a second cleavage $S_2$ is oriented oblique to $S_1$ indicating shear deformation (Sindern et al. 2007). The occurrence of pseudotachylite veins with thicknesses varying between 2 and 4 mm is indicative of major brittle deformation events (Lögering, 2008) (Fig. 2h).

The core intervals from 2,143 to 2,131 m, and from 2,542 to 2,537 m represent an undisturbed stratigraphic succession of lower Devonian rocks, which are unaffected or only weakly overprinted by Variscan $D_1$ deformation and veining.

However, $D_1$ faults with thrust character were also recognised in the depth intervals between 660 and 720 m,

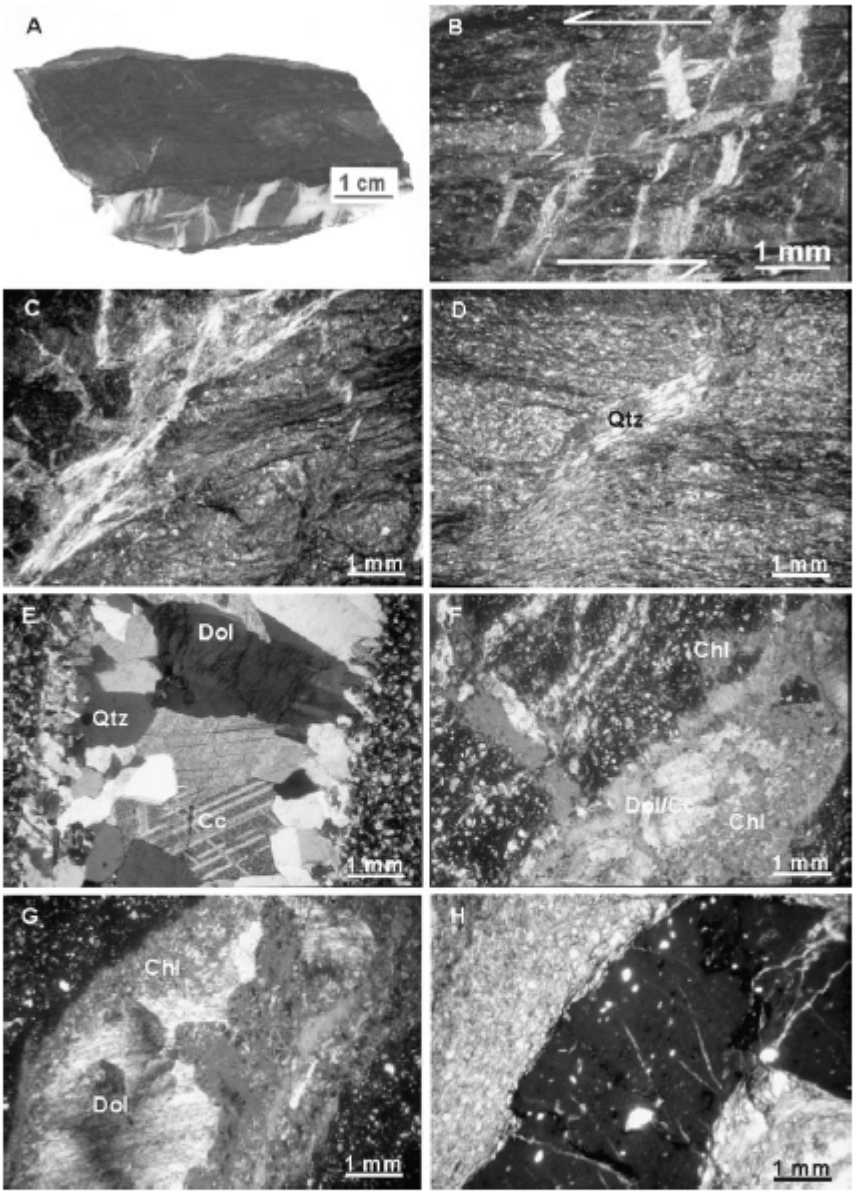


**Fig. 2** Rock and vein types in representative samples from the upper core section of the RWTH-1 well. **a** Nodular limestone, 1,433.33 m, **b** shale with tension gashes consisting of quartz and carbonate, 1,433.70 m, plane polarizers, **c** shale with shear veins (qtz, k-fsp, chl) cross-cutting foliation, 1,446.38 m, crossed polarizers, **d** shale with quartz grains grown in dilational jog, 1,402.42 m, crossed polarizers, **e** Quartz–carbonate (±chlorite) vein in sandstone, 1,402.60 m, crossed polarizers, **f** Carbonate–chlorite vein in shale, 1,503.02 m, plane polarizers, **g** Carbonate–chlorite vein in shale, 1,485.80 m, crossed polarizers, **h** Pseudotachylite vein with dark matrix enclosing angular to rounded fragments of the wall rock, 1,512.95 m, plane polarizers

900 and 960 m, 1,880 and 1,942 m and 2,220 and 2,310 m based on geophysical logging (Pechnig 2005; Trautwein–Bruns, unpublished data), seismic data (Becker 2008) and the discovery of vein material in cutting samples (Lögering 2008).

## Veins and host rock alteration

Veins in core sections are a few millimetres to centimetres thick and can add up to ±20 vol.% of the host rock in some parts. Veins cross-cut upper and lower Devonian

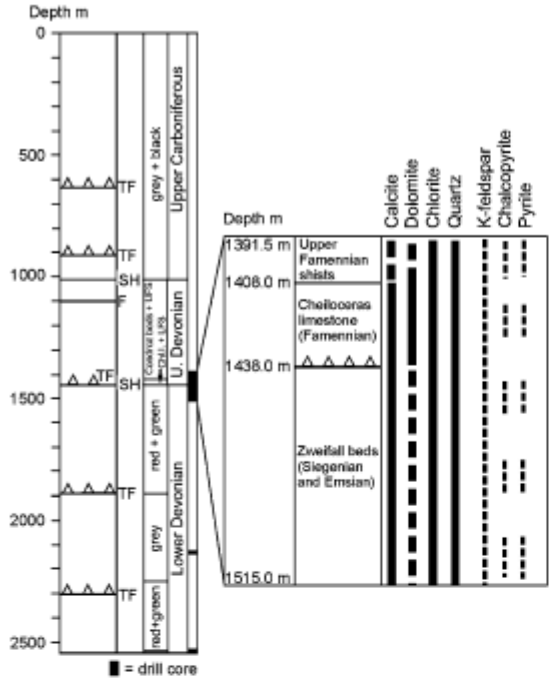


**Fig. 3** Schematic geological profile of the RWTH-1 well (according to Österreich et al. 2005; Ribbert 2006; Sindern et al. 2008; Trautwein–Bruns et al. 2010), *Ch.l.* cheiloceras limestone, *F* fault with uncertain character, *LFS* lower Famennian Shale, *SH* sedimentary hiatus, *TF* thrust fault, *UFS* upper Famennian Shale. The *enlarged diagram* to the *right* of the profile shows the distribution of minerals in veins in the first core section of the RWTH-1 well. Relative abundance is indicated by *solid* (high) and *dashed* (low) *lines*. Interrupted *dashed lines* show rare occurrence

lithologies and structures. Three different vein types are distinguished: (1) quartz–carbonate ± chlorite veins, (2) carbonate ± chlorite veins and (3) quartz ± chlorite veins (Fig. 2). Within the first two types, one can distinguish three different carbonate associations. Dolomite and calcite occur intergrown as coarse or finegrained aggregates (Fig. 2e, f), often only with quartz in direct contact to the host rocks. In addition, veins in which either only calcite or dolomite (Fig. 2g) occur are observed. Here, carbonates are frequently intensively intergrown with chlorite but are more abundant in the centre of the veins. In larger fractures, the vein mineral assemblages are accompanied by rare K-feldspar and chalcopyrite (Fig. 3).

The most abundant quartz–carbonate ± chlorite veins (1) vary in size from a few mm to >3 cm. Carbonate grains mainly occur in the centre of the vein as blocky, idiomorphic to hypidiomorphic crystals. Idiomorphic quartz grains mainly precipitated along the vein margins adjacent to the carbonate minerals. Quartz formed either as single elongated crystals or as patches of blocky minerals intergrown with carbonates. Undulatory extinction of quartz and carbonate grains, deformational twinning of carbonates, and an initial stage of subgrain development in some of the quartz crystals are indications of deformational overprint. Where fibrous to elongated chlorite occurs along the vein margins, quartz and carbonates are situated in the centre of the veins (Fig. 2g). However, chlorite can also be observed intergrown with quartz and/or carbonates in the centre of the veins (Fig. 2f) indicative of contemporaneous growth.

The carbonate ± chlorite veins (2) are slightly smaller than the quartz–carbonate ± chlorite veins described above. These veins vary in size from mm to >2 cm and are composed either of calcite or dolomite only or composite calcite/dolomite grains (Fig. 2f). The calcite and/or dolomite crystals have idiomorphic to hypidiomorphic textures but in places also form xenomorphic (saddle-type) textures with the typical curved grain margins. Again, deformational textures are ubiquitous such as undulatory extinction and deformational twinning.

The quartz ± chlorite veins (3) display similar cross-cutting relationships with the host rocks as the vein types mentioned before. They are slightly smaller than the quartz–carbonate ± chlorite veins and vary in size from mm scale to >2 cm wide. The veins are either composed of blocky crystals up to ~200 µm in size or of elongate, irregularly shaped 200–1,000 µm large grains. Smaller crystals <50 µm are also irregularly shaped. Subgrains mainly occur at the grain boundaries of the elongated quartz crystals or along fibrous micro-shears. Re-crystallised quartz grains have straight grain boundaries and show sub-grain rotation.

There is abundant textural evidence that quartz, carbonates and chlorite formed contemporaneously and that the veins were progressively deformed. Bent chlorite crystals indicate syntectonic growth (Sindern et al. 2007). Becker et al. (2011) describe cross-cutting veins from the upper section of the RWTH well with similar microstructures and mineralogy that formed at episodic microfracturing events during progressive shearing and vein formation in one single tectonic episode. Multiple reopening of fractures and episodic vein filling is documented by bands of rock fragment along vein margins (Lögering 2008). Other vein textures are indicative of crack-seal processes (Becker et al. 2011; Chatziliadou 2009; Lögering 2008).

The main alteration minerals adjacent to the veins are chlorite and dolomite but also K-feldspar and illite. Compositional data of chlorite, which is a Fe–Mg chlorite with chamosite (Bailey 1991) as predominant end-member, is given in Lögering (2008). Within the alteration halos crystal sizes are generally less than 5 µm. The alteration halo extends laterally a few millimetres into the host rock.

## Analytical methods

The nature of vein and alteration minerals, and their modal proportions were studied using X-ray diffraction (XRD), electron microprobe analyses (EMPA), microthermometry, cathodoluminescence microscopy and gas-chromatography at the RWTH–Aachen University. Stable isotope analyses ($\delta$D, $\delta^{13}$C and $\delta^{18}$O) of whole rock samples, vein minerals and fluid inclusions were carried out at the University of Lausanne.

Microthermometric measurements of fluid inclusions were performed on doubly polished 60–100 µm thick sections on a modified USGS cooling–heating stage with a Zeiss 50× long working-distance objective. The experimental approach is based on standard petrography and systematic statistical evaluation of fluid inclusion types and generations in veins. On samples only containing aqueous liquid–vapour inclusions, the homogenisation temperature [$T_h$] was first measured, followed by the eutectic temperatures [$T_e$], which are derived from the observation of first melting, and final melting temperatures [$T_m$]. The stage was calibrated by measuring the $T_h$ and $T_m$ in a synthetic $H_2O$ fluid inclusion standard ($T_h$ = 374.1°C), as well as $T_m$ of a synthetic $CO_2$ fluid inclusion standard ($T_m$ = −56.5°C). The reproducibility of the measurements was in the order of 1–2°C for $T_h$ and 0.1–0.2°C for $T_m$.

Gas bulk composition of trapped fluid inclusions in quartz and carbonates was analysed by pyrolysis–gas-chromatography–mass spectrometry (Py-GC/MS). A quadrupole mass spectrometer linked with a gas-chromatograph was online coupled with a Pyroprobe 1000 pyrolysis unit. Pyrolysis was performed on aliquots of approximately 0.5 mg at pyrolysis temperatures ranging from 500 to 700°C. The pyrolysis time was approximately 3.5 s. Gas-chromatographic separation was carried out on a Carboxen 1010 PLOT fused silica capillary column (30 m, 0.32 mm ID) with helium as carrier gas (35 m/s). The mass spectrometer was operated by scanning from 15 to 50 m/z at a scan rate of 1 s/decade (interscan time 0.1 s) with a source temperature of 200°. Fluid inclusion compositions were determined qualitatively and semi-quantitatively using an external one-point calibration generated from a reference gas mixture ($CO_2$, $CH_4$ and $N_2$; 1:1:1 v:v:v). Electron microprobe analysis was carried out on a JEOL JXA-8900R electron microprobe. The quantitative analyses were performed using wavelength dispersive spectrometers with an acceleration voltage of 15 kV, a beam current of 20 nA and a focused beam size. Natural and synthetic standards were used for calibration. Carbonates occurring in veins were quantitatively analysed for Mg, Ca, Mn, Fe, Sr and Ba (Table 2). Precisions are <1% for major and <10% for minor and trace elements. Lower limits of determination for the elements expressed as oxides are 0.03 wt% (Mn, Fe, Ba), 0.02 wt% (Ca, Sr) and 0.01 wt% (Mg).

The oxygen isotopes of the silicate mineral separates from various vein types and alteration zones, as well as powdered samples of siliciclastic rocks were analysed using the laser-based microanalytical method described by Rumble and Hoering (1994).

The analyses of carbonate samples of 100–200 µg for $\delta^{13}$C and $\delta^{18}$O were carried out in the Gas Bench II (Thermo–Finnigan) with a 100% orthophosphoric acid ($H_3PO_4$) digestion technique at 70°C (Spötl and Vennemann 2003). Precision for $\delta^{18}$O and $\delta^{13}$C determined by repeated analysis of an in-house Carrara marble standard is 1 and 4% (relative, 2 $\sigma$), respectively.

Measurements of the hydrogen isotope compositions of minerals were made using high-temperature (1,450°C) reduction methods with He-carrier gas and a TC–EA linked

**Table 2** Representative analyses of calcite (Cc) and associated dolomite (Dol) in quartz–carbonate–chlorite veins in nodular limestone (nls) and dolomite marl (dm)

| | 632* nls | | | | 633** nls | | 636*** dm | | | |
|---|---|---|---|---|---|---|---|---|---|---|
| | Cc1 | Cc2 | Dol1 | Dol2 | Cc1 | Dol1 | Cc1 | Cc2 | Dol1 | Dol2 |
| FeO | 0.12 | 0.22 | 1.85 | 1.94 | 0.14 | 1.83 | 1.15 | 1.12 | 2.34 | 1.52 |
| MnO | 0.03 | 0.07 | 0.14 | 0.16 | 0.03 | 0.16 | 0.10 | 0.10 | 0.16 | 0.15 |
| CaO | 54.00 | 53.60 | 31.23 | 31.38 | 54.41 | 31.13 | 56.49 | 54.55 | 32.33 | 32.34 |
| MgO | 0.81 | 0.61 | 16.93 | 16.59 | 0.18 | 16.64 | 0.54 | 0.44 | 17.54 | 17.87 |
| SrO | 0.07 | 0.06 | <0.02 | <0.02 | 0.08 | <0.02 | 0.14 | 0.10 | 0.05 | 0.04 |
| BaO | 0.03 | <0.03 | <0.03 | 0.04 | <0.03 | <0.03 | 0.04 | <0.03 | <0.03 | <0.03 |
| Sum | 55.05 | 54.57 | 50.16 | 50.11 | 54.86 | 49.75 | 58.47 | 56.31 | 52.41 | 51.92 |
| $T_{AE}$ (°C) | 358 | 303 | | | 280 | | 294 | 250 | | |

$T_{AE}$ indicates temperature derived from calcite composition applying the calcite–ferroan dolomite solvus thermometer (equation 31) of Anovitz and Essene (1987)

* Depth 1,430.84 m; ** depth 1,433.34 m; *** depth 1,436.90 m

to a Delta Plus XL mass spectrometer from Thermo–Finnigan on 2–4 mg sized samples according to a method adapted after Sharp et al. (2001). The precision of the in-house kaolinite standard and NBS-30 biotite for hydrogen isotope analyses was better than ±2‰ for the method used; all values were normalised using a value of −125‰ for the kaolinite standard and −65‰ for NBS-30 analysed during the same period as the samples.

Water contained in fluid inclusions of quartz, calcite and dolomite from various vein types was extracted by mechanical-crushing decrepitation in a vacuum extraction line. Released $H_2O$ and $CO_2$ were trapped under vacuum in a liquid nitrogen-cooled U-tube. Methane was separated from $H_2O$ and $CO_2$ by careful expansion into an isolated part of the vacuum line and in turn oxidised to $H_2O$ and $CO_2$. The procedure is described in Tarantola et al. (2007). Standards introduced into the vacuum line reproduced within 5‰. Isotopic compositions were normalised against the V-SMOW (hydrogen, oxygen) and V-PDB (carbon) standards using the $\delta$-notation in ‰.

## Results

### Fluid inclusion petrography

Vein quartz and carbonates host transparent (type I) as well as dark (type II) inclusions. The transparent (type I) inclusions which occur in all vein types are $H_2O$-rich two-phase liquid–vapour inclusions. The volume fraction of the vapour phase was estimated at ambient P–T conditions and varies between 15 and 50 vol.% with a mean around 35 vol.% (Table 3). The dark (type II) inclusions are associated with the aqueous type I inclusions. They are vapour-rich (i.e. low density) but further optical analysis was not possible due to their almost opaque appearance.

The transparent type I comprises primary, pseudo-secondary and secondary inclusions. Assemblages of primary inclusions occur in growth zones in carbonates and along grain boundaries in quartz grains. These fluid inclusions are dominant in the veins and have an irregular to negative crystal shape (Fig. 4). The pseudo-secondary inclusions show irregular to negative crystal shapes and are trapped as clusters and intra-granular trails within the minerals. Inclusions classified secondary occur in trans-granular trails in quartz showing irregular to oval shapes. Primary and/or pseudo-secondary fluid inclusions can locally be observed together with secondary inclusions. Most of the fluid inclusions are less than 15 µm in length; however, inclusions larger than 25 µm are also locally present. Evidence of post trapping modification such as necking down or leakage was not recognised in the inclusions studied.

### Microthermometry and gas-chromatography

The investigated two-phase liquid–vapour fluid inclusions homogenise to the liquid phase. They show no expansion during cooling.

$T_e$ from primary and pseudo-secondary inclusions in samples from the upper core section is consistently between −21 and −23°C, indicating their $H_2O$–Na–Cl or $H_2O$–Na–K–Cl composition. Deviations to $T_e = -24.2$°C in the first core section and −29.0°C in the second core section (Table 3) point to the minor presence of divalent cations. Most probably, these are Ca and Mg—as can also be deduced from the formation of calcite and dolomite in the veins.

The sporadic higher $T_e$ values (up to −10.2°C, Table 3) in mainly secondary inclusions are related to reduced visibility of the small amount of fluid formed at the eutectic point. Sodium can be considered as predominant cation followed by K. In the following, the fluid will be referred to as $H_2O$–Na–(K)–Cl fluid.

Analyses of the two-phase inclusions from various vein systems were recalculated using the $H_2O$–Na–(K)–Cl equation of Bowers and Helgeson (1985) implemented in the MacFlinCor software (Brown 1989).

Homogenisation temperatures (Fig. 5) recorded in primary fluid inclusions in quartz and dolomite are similar ranging from 389°C (qtz) and 398°C (dol) to 238°C (qtz) and 261°C (dol). $T_h$-values were found to be independent of vein host rock or position within the core. It is noteworthy, however, that the lowest maximum temperatures in quartz (i.e. 328°C) were determined in nodular limestones sampled from a shear zone at 1,438 m. Taking the late diagenetic to low anchizonal grade of the vein host rocks into consideration, these fluids clearly are hydrothermal.

Salinities in primary dolomite and quartz inclusions, in general, vary in the range from 1.82% (Qtz) and 1.98% (Dol) to 9.32% (Qtz) and 7.39% (Dol). The lowest values occur in veins in nodular limestone. Maximum $T_h$ and salinities in primary inclusions in calcite are lower than in dolomite and quartz and do not exceed 364°C and 7.68%, respectively. Secondary inclusions in quartz exhibit a narrow range in $T_h$-values from 179 to 211°C, independent of the host rock. Measured salinities of the majority of samples are <5% NaCl equiv, with a maximum value of 7.68 NaCl equiv.

Homogenisation temperatures and salinities determined in pseudo-secondary inclusions in quartz and calcite occupy an intermediate position between primary and secondary inclusions. This will be addressed later in the discussion.

A spatial variation of $T_h$ is obvious in some veins where higher temperatures are determined in grains close to the wall rock contact and lower temperatures in grains closer to

**Table 3** Fluid inclusion data from veins of the RWTH-1 well, mineral abbreviations according to Siivola and Schmidt (2007)

| Vein type | Host rock | *n* | TS | Depth (m) | HM | IT | Vol% | $T_{h\ L-V}$ °C | $T_{m\ ice}$ °C | $T_e$ °C | Mass-eq. % NaCl | Molar vol. $cm^3/mol$ |
|---|---|---|---|---|---|---|---|---|---|---|---|---|
| *Upper Devonian* | *1. core section* | | | | | | | | | | | |
| Qtz-Cb | Sandstone | 12 | 993, 994, 1,059 | 1,399.63–1,405.42 | Qtz | P | 10–50 | 270–380 | −2.7 to −4.2 | −21.4 to −22.4 | 4.39–6.67 | 22.85–30.95 |
| Qtz-Cb | Sandstone | 8 | 996, 997 | 1,402.60–1,403.17 | Qtz | PS | 15–30 | 225–246 | −2.6 to −4.2 | −20.2 to −22.4 | 4.23–6.67 | 20.75–21.66 |
| Qtz-Cb | Sandstone | 6 | 996, 997 | 1,402.60–1,403.17 | Qtz | S | 15–25 | 182–212 | −1.4 to −3.9 | −20.9 to −21.9 | 2.13–6.23 | 20.28–20.92 |
| Qtz-Cb | Sandstone | 10 | 994, 996 | 1,401.39–1,402.60 | Cc | PS | 20–35 | 229–310 | −3.1 to −4.4 | −21.7 to −22.9 | 5.01–6.96 | 21.31–25.27 |
| Qtz-Cb | Dolomite marl, dolostone | 18 | 981, 999, 1,040 | 1,408.77–1,420.70 | Qtz | P | 15–45 | 238–375 | −2.0 to −4.2 | −20.8 to −22.1 | 3.28–6.67 | 21.72–32.30 |
| Qtz-Cb | Dolomite marl, dolostone | 4 | 999, 1,040 | 1,408.77–1,418.40 | Dol | P | 15–60 | 299–307 | −3.9 to −5.3 | −24.9 to −25.1 | 6.23–8.24 | 23.74–24.20 |
| Qtz-Cb | Shale | 1 | 1,041 | 1,427.76 | Qtz | P | 20 | 310 | −3.9 | −21.7 | 6.23 | 24.6 |
| Qtz-Cb | Shale | 6 | 1,041 | 1,427.76 | Qtz | S | 15–20 | 189–207 | −1.2 to −1.9 | −10.3 to −10.9 | 1.98–3.12 | 20.49–21.05 |
| Qtz-Cb | Shale | 3 | 1,041 | 1,427.76 | Dol | P | 20–25 | 278–286 | −3.2 to −3.7 | −21.1 to −21.9 | 5.17–5.93 | 23.4–23.5 |
| Cb | Dolomite marl | 2 | 1,042 | 1,429.93 | Cc | P | 35–45 | 274–289 | −3.2 to −3.7 | −22.9 to −23.7 | 5.17–5.93 | 22.95–23.96 |
| Cb | Limestone | 6 | 1,077 | 1,431.08 | Dol | P | 10–40 | 261–362 | −2.5 to −3.6 | −21.4 to −24.1 | 3.44–5.78 | 22.56–29.27 |
| Cb | Nodular limestone | 10 | 985, 1,044, 1,046 | 1,433.78–1,435.84 | Dol | P | 20–50 | 297–339 | −1.2 to −3.7 | −12.1 to −23.4 | 1.98–5.93 | 24.92–27.50 |
| Cb | Nodular limestone | 6 | 1,044 | 1,433.78 | Cc | P | 10–30 | 263–274 | −2.1 to −2.3 | −21.3 to −22.6 | 3.44–3.76 | 22.79–22.85 |
| Qtz-Cb | Nodular limestone | 6 | 982, 984, 1,050 | 1,430.84–1,436.68 | Qtz | P | 25–40 | 247–328 | −1.1 to −4.2 | −21.3 to −24.1 | 1.82–6.52 | 21.98–26.58 |
| Qtz-Cb | Nodular limestone | 1 | 983 | 1,433.34 | Qtz | PS | 25 | 230 | −3.8 | −21.9 | 6.08 | 21.34 |
| Qtz-Cb | Nodular limestone | 11 | 983, 984 | 1,433.34–1,434.40 | Qtz | S | 10–30 | 179–202 | −2.3 to −3.7 | −21.3 to −24.1 | 3.76–5.93 | 19.92–20.81 |
| Qtz-Cb | Nodular limestone | 9 | 982, 1,043, 1,050 | 1,430.84–1,436.68 | Cc | P | 15–50 | 254–345 | −2.4 to −4.9 | −20.4 to −24.2 | 3.92–7.68 | 22.25–26.61 |
| Qtz-Cb | Dolomite marl | 9 | 986, 1,045 | 1,436.90–1,441.75 | Qtz | P | 20–40 | 312–389 | −2.7 to −6.1 | −20.4 to −24.1 | 4.39–9.32 | 25.16–39.72 |
| Qtz-Cb | Dolomite marl | 2 | 1,045 | 1,441.75 | Qtz | S | 15–20 | 179–182 | −1.1 to −1.2 | −21.5 to −21.7 | 1.82–1.98 | 20.35–20.39 |
| Qtz-Cb | Dolomite marl | 3 | 1,045 | 1,441.75 | Dol | P | 25–30 | 378–390 | −5.4 to −5.8 | −21.3 to −22.8 | 8.38–8.92 | 29.12–32.55 |
| *Lower Devonian* | *1. core section* | | | | | | | | | | | |
| Qtz | Siltstone | 8 | 1,057, 1,058 | 1,448.87–1,502.82 | Qtz | P | 20–35 | 341–391 | −2.8 to −3.8 | −20.1 to −22.5 | 4.55–6.08 | 27.12–32.52 |
| Qtz | Siltstone | 3 | 1,057 | 1,448.87 | Qtz | S | 15–20 | 204–211 | −3.7 to −4.9 | −21.7 to −22.1 | 5.93–7.68 | 20.54–20.69 |
| Qtz-Cb | Shale | 26 | 992, 989, 1,051, −2, −3, −5, 1,060 | 1,462.32–1,509.15 | Qtz | P | 20–45 | 292–389 | −3.1 to −4.3 | −20.7 to −23.8 | 5.17–6.81 | 23.73–31.93 |
| Qtz-Cb | Shale | 3 | 1,053 | 1,462.32 | Cc | P | 25–30 | 351–364 | −3.4 to −4.2 | −21.3 to −22.1 | 5.47–6.67 | 27.36–38.85 |
| Qtz-Cb | Shale | 2 | 1,051, 1,052 | 1,479.83–1,491.48 | Qtz | PS | 20–30 | 241–245 | −2.4 to −2.8 | −10.7 to −21.6 | 3.92–4.55 | 21.09–21.60 |
| Qtz-Cb | Shale | 5 | 1,051, 1,052 | 1,479.83–1,491.48 | Qtz | S | 15–25 | 193–209 | −1.3 to −2.7 | −10.2 to −22.1 | 2.14–4.39 | 20.25–21.04 |
| Qtz-Cb | Shale | 1 | 1,051 | 1,479.83 | Cc | PS | 25 | 247 | −2.5 | −22.2 | 4.07 | 20.40 |
| Qtz-Cb | Shale | 5 | 1,051, 1,055 | 1,479.83–1,486.85 | Dol | P | 30–40 | 380–398 | −3.4 to −4.2 | −21.4 to −23.9 | 5.47–7.39 | 29.81–32.81 |
| Qtz-Cb | Siltstone | 14 | 988, 1,048 | 1,483.30–1,485.80 | Qtz | P | 15–40 | 328–370 | −3.9 to −5.7 | −20.7 to −23.4 | 6.23–8.78 | 25.55–28.78 |
| Qtz-Cb | Siltstone | 8 | 1,048 | 1,483.30 | Qtz | S | 25–40 | 189–209 | −1.9 to −2.8 | −10.5 to −10.9 | 3.12–4.55 | 20.26–20.78 |
| Qtz | Shale | 7 | 987, 1,054 | 1,446.38–1,479.20 | Qtz | P | 15–30 | 344–361 | −2.7 to −3.8 | −20.9 to −22.2 | 4.39–6.08 | 27.16–29.40 |
| Qtz | Shale | 5 | 1,054 | 1,479.20 | Qtz | S | 15–25 | 189–205 | −1.4 to −2.1 | −10.2 to −11.1 | 2.31–3.44 | 20.52–20.86 |

**Table 3** continued

| Vein type | Host rock | *n* | TS | Depth (m) | HM | IT | Vol% | $T_{h\ LV}$ °C | $T_{m\ ice}$ °C | $T_e$ °C | Mass-eq % NaCl | Molar vol. $cm^3/mol$ |
|---|---|---|---|---|---|---|---|---|---|---|---|---|
| Qtz | Siltstone | 2 | 1,058 | 1,502.82 | Qtz | PS | 30 | 256–266 | −2.4 to −2.8 | | 3.92–4.55 | 22.16–22.77 |
| *Lower Devonian* | *2. core section* | | | | | | | | | | | |
| Qtz | Sandstone | 15 | 990 | 2,129.33 | Qtz | S | 10–30 | 177–210 | −2.3 to −4.2 | −21.1 to −24.2 | 3.76–6.67 | 19.92–20.96 |
| Cb | Sandstone | 9 | 991 | 2,131.64 | Dol | P | 20–50 | 295–364 | −1.3 to −3.3 | −20.2 to −26.1 | 2.14–5.32 | 24.77–30.09 |
| Cb | Sandstone | 18 | 991 | 2,131.64 | Cc | P | 10–30 | 200–303 | −0.1 to −2.9 | −21.1 to −29.0 | 0.17–4.70 | 20.54–26.05 |

*TS* thin section, *HM* host mineral, *IT* inclusion type (*P* primary, *PS* pseudo-secondary, *S* secondary), Vol% = volume-% of vapour bubble, $T_{hLV}$ homogenisation temperature (homogenisation to liquid), $T_{mice}$ final melting temperature of ice, $T_e$ eutectic temperature

Mass-equivalent in % NaCl and Molar volume of FI are calculated using the MacFlinCor software by Brown (1989)

the centre of the vein. The analyses of inclusions in samples from the lower core section (2,143–2,131 m) that is much less affected by deformation and vein formation are similar to those of the upper section, with salinities tending to be lower in the former sample suite (Table 3).

Gas bulk composition of trapped fluid inclusions in quartz and carbonates reveal that $H_2O$ is the main solution component together with smaller amounts of $CO_2$, $CH_4$ and $N_2$. It is assumed that the dark, vapour-rich type II inclusions contain the majority of these gases. The presence of $H_2O$–Na–(K)–Cl-fluids and gas-rich $CO_2$–($H_2O$, $CH_4$, $N_2$)-dominated fluid inclusions may indicate a process of fluid unmixing (Crawford and Hollister 1986).

Temperature calculations for vein calcite in compositional equilibrium with dolomite, using the calcite–ferroan dolomite solvus thermometer of Anovitz and Essene (1987), yield values between 250 and 358°C (Table 2). This range is similar to the range of $T_h$ in fluid inclusions and may correspond to conditions of vein formation. Solid-solution geothermometry on chlorite from various vein types, slickensides and alteration halos yields temperatures between 290 and 350°C clustering around 310°C (Lögering 2008).

## Stable isotope geochemistry

Hydrogen isotope signatures of siliciclastic and carbonate host rocks to hydrothermal veins vary between $\delta D = -49‰$ and $-57‰$. The lowest values within this range are from two grey shale samples that differ markedly from the other shales analysed (Table 4). Chlorite from veins tends to have lower $\delta D$ values between −52 and −66‰ (Fig. 6). Whole rock samples of altered vein margins dominated by chlorite are in the same range. Hydrogen isotope signatures of fluid inclusions are significantly lower than those of vein chlorites and host rocks. Fluid inclusions in quartz vary between $\delta D = -89‰$ and −99‰ whereas fluid inclusions in calcite and dolomite are even lower with $\delta D = -104‰$ and −113‰, respectively.

Carbonate rocks display the largest spread of $\delta^{18}O$ values (22.1–14.9‰), whereas siliciclastic rock samples record a $\delta^{18}O$ range between 15 and 14.4‰ (Table 4; Fig. 7). Most vein quartz samples show elevated $\delta^{18}O$ values (19.2–16.3 ‰) as compared to carbonates. Lowest $\delta^{18}O$ values (8.2–8.4‰) are observed in the alteration halos around veins. Oxygen isotope signatures of quartz and carbonate fractions occurring together in veins are displayed in Fig. 8. On the assumption that isotopic equilibrium was attained between the associated minerals, the data would indicate variable formation temperatures in the range from 260 to 400°C.

Carbon isotope data show a marked variation depending on the position relative to the thrust fault at 1,438 m

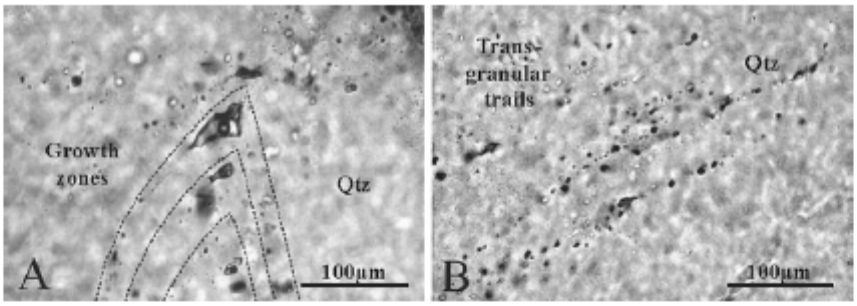


**Fig. 4** Fluid inclusions (type 1) of the RWTH-1 well, first core section. **a** Primary aqueous two-phase fluid inclusions in growth zones of quartz in a quartz–chlorite–vein (1,512.46 m). **b** Secondary aqueous type 1 two-phase inclusions along a trans-granular trail in quartz

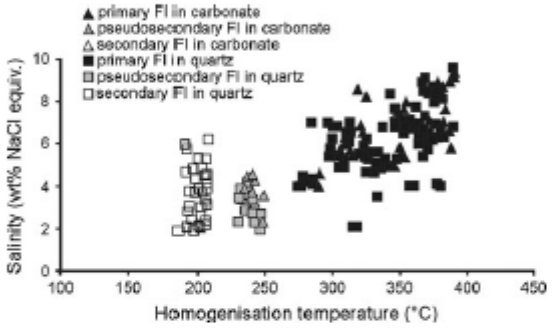


**Fig. 5** Salinity (wt% NaCl equiv.) versus homogenisation temperatures ($T_h$ in °C) in primary, pseudo-secondary and secondary fluid inclusions in vein quartz and carbonates of the first core section of the RWTH-1 well

(Table 4). Dolomite sampled from veins at depths >1,438 m have $\delta^{13}C$ (VPDB) values <−10‰ whereas vein calcite varies between $\delta^{13}C = -4.6‰$ and $-9.2‰$ and shows a significant decrease of $\delta^{13}C$ values with decreasing distance to the thrust fault at 1,438 m. In contrast, dolomite/calcite fractions from veins not affected by the thrust fault are characterised by little variation and relatively high values ($\delta^{13}C = -0.4‰$ to $-1.5‰$). The values are similar to the isotope signatures of the carbonate rocks ($\delta^{13}C = -0.1‰$ to $-1.0‰$) from the RWTH-1 well and the lower Carboniferous limestones (LCL in Fig. 7) exposed to the SE of Aachen (Chatziliadou 2009). However, RWTH-1 vein carbonates are isotopically distinct from post-Variscan vein carbonates from the Aachen region (Fig. 7, Chatziliadou 2009; Muchez et al. 1994).

As secondary inclusions are less abundant and only found in quartz it is conceivable that bulk decrepitation analysis predominantly reflects primary and pseudo-secondary inclusions in quartz and, particularly, in carbonates. Carbon will mainly be derived from dark, vapour-rich type II inclusions. As no or almost none of the other inclusion types carry $CO_2$, isotope analysis will be biased by the composition of the vapour-rich inclusions.

The carbon species $CO_2$ and $CH_4$ extracted from fluid inclusions are characterised by low $\delta^{13}C$ values. Carbondioxide $\delta^{13}C$ varies between −12.8 and −23.3‰, while $CH_4$ reveals $\delta^{13}C$ values from −26.9 to −28.9‰. The analyses are presented in Fig. 7 that plots $\delta^{13}C$ versus $\delta^{18}O$ values of $CO_2$ and $CH_4$ in fluid inclusions in carbonate and quartz host minerals, and from carbonate host rocks as well as vein calcite and dolomite. Temperature estimates based on equilibrium fractionation data (Horita 2001) for $\delta^{13}C$ of $CO_2$ and $CH_4$ in fluid inclusions yield high temperatures in excess of 500°C which are unlikely. This temperature is also inconsistent with values derived from fractionation of $\delta^{13}C$ between $CO_2$ in fluid inclusions and carbonate minerals. The $\Delta_{mineral\text{-}fluid\ inclusion}$ values between calcite or calcite/dolomite and $CO_2$ in fluid inclusions are >8. This could be the consequence of (partial) equilibration at unrealistically low $T < 10$°C (Ohmoto and Rye 1979). On the other hand, dolomite fractions and $CO_2$ from fluid inclusions have lower $\Delta_{mineral\text{-}fluid\ inclusion}$ values which could indicate temperatures in the range of 205–210°C (Ohmoto and Rye 1979). In general, the $\delta^{13}C$ data seem to indicate that carbonate minerals and carbon species in fluid inclusions are not in isotopic equilibrium.

## Discussion

### Trapping conditions

The presence of a $H_2O$–Na–(K)–Cl-fluid in type I inclusions and a vapour-rich $CO_2$–($H_2O$, $CH_4$, $N_2$) fluid in type II inclusions may indicate unmixing of a homogenous $H_2O$–$CO_2$–($CH_4$, $N_2$)–Na–(K)–Cl fluid. Experimental and theoretical studies have shown fluid immiscibility in various $H_2O$–NaCl–$CO_2$–$CH_4$-systems causing unmixing to a NaCl–$H_2O$-rich and a $CO_2$- or $CH_4$-rich phase at lower greenschist to anchizonal conditions (Crawford and Hollister 1986; Duan et al. 1995; Frantz et al. 1992; Lamb et al. 2002).

**Table 4** Stable isotope compositions for mineral fractions from veins, whole rock samples and fluid inclusions in quartz and carbonate fractions from veins

| Sample type | No. | Depth (m) | Mineral | Lithology, mineralogy | δD VSMOW ±5% | $\delta^{18}O$ VSMOW ±1% | $\delta^{13}C$ VPDB ±4% |
|---|---|---|---|---|---|---|---|
| Chlorite | 52a | 1,399.63 | Chl | Qtz-Cb ± Chl V. | −53 | 11.8 | |
| | 23a | 1,435.50 | Chl | Qtz ± Chl V. | −59 | 11.8 | |
| | 37a | 1,436.90 | Chl | Qtz-Cb ± Chl V. | −59 | 11.6 | |
| | 56 | 1,479.20 | Chl | Qtz ± Chl V. | −52 | 11.0 | |
| | 62a | 1,488.25 | Chl | Qtz ± Chl V. | −58 | 11.3 | |
| | 35a | 1,503.25 | Chl | Qtz-Cb ± Chl V. | −56 | 11.1 | |
| | 24a | 1,403.17 | Chl | Qtz-Cb ± Chl V. | −65 | 11.6 | |
| | 30a | 1,486.70 | Chl | Qtz-Cb ± Chl V. | −66 | 11.2 | |
| Quartz | 52b | 1,399.63 | Qtz | Qtz-Cb ± Chl V. | | 18.5 | |
| | 54 | 1,402.60 | Qtz | Qtz-Cb ± Chl V. | | 19.0 | |
| | 24b | 1,403.17 | Qtz | Qtz-Cb ± Chl V. | | 18.3 | |
| | 60 | 1,417.16 | Qtz | Qtz-Cb ± Chl V. | | 19.2 | |
| | 58 | 1,430.69 | Qtz | Qtz-Cb ± Chl V. | | 18.0 | |
| | 37 | 1,436.90 | Qtz | Qtz-Cb ± Chl V. | | 18.5 | |
| | 30b | 1,486.70 | Qtz | Qtz-Cb ± Chl V. | | 17.9 | |
| | 62b | 1,488.25 | Qtz | Qtz ± Chl V. | | 18.0 | |
| | 35b | 1,503.25 | Qtz | Qtz-Cb ± Chl V. | | 17.8 | |
| | 33 | 2,129.50 | Qtz | Qtz. V. | | 16.3 | |
| Carbonates | 52 | 1,399.63 | Cal | Qtz-Cb ± Chl V. | | 16.4 | −4.74 |
| | 54 | 1,402.60 | Cal/Dol | Qtz-Cb ± Chl V. | | 17.1 | −0.88 |
| | 24 | 1,403.17 | Cal | Qtz-Cb ± Chl V. | | 16.0 | −4.63 |
| | 26 | 1,408.77 | Cal/Dol | Qtz-Cb ± Chl V. | | 18.2 | −0.44 |
| | 60 | 1,417.16 | Cal/Dol | Qtz-Cb ± Chl V. | | 16.6 | −1.52 |
| | 58 | 1,430.69 | Cal/Dol | Qtz-Cb ± Chl V. | | 16.2 | −1.06 |
| | 22 | 1,435.17 | Cal | Qtz-Cb ± Chl V. | | 16.0 | −5.62 |
| | 40 | 1,436.68 | Cal | Qtz-Cb ± Chl V. | | 16.0 | −7.93 |
| | 37 | 1,436.90 | Cal | Qtz-Cb V. | | 16.0 | −9.18 |
| | 39 | 1,441.75 | Dol | Dol ± Chl V. | | 18.3 | −10.58 |
| | 50 | 1,459.24 | Dol | Qtz-Cb ± Chl V. | | 16.4 | −17.31 |
| | 30 | 1,486.70 | Dol | Qtz-Cb V. | | 16.0 | −19.86 |
| | 62 | 1,491.48 | Dol | Qtz-Cb ± Chl V. | | 16.0 | −19.98 |
| | 35 | 1,503.25 | Dol | Dol ± Qtz ± Chl V. | | 17.4 | −17.36 |
| Whole rock | 53 | 1,399.63 | Chl | Chl-alteration halo in ss. | −62 | 8.3 | |
| | 73 | 1,399.63 | WR | Fine grained ss | −51 | | |
| | PE3 | 1,408.65 | WR | Dol marl | | 22.1 | −0.05 |
| | PE2 | 1,411.30 | WR | Dol marl | | 22.1 | −0.06 |
| | 60b | 1,417.16 | WR | Dol marl | −49 | | |
| | PE1 | 1,434.40 | WR | Nodular ls | | 16.7 | −1.04 |
| | 23b | 1,435.50 | Chl | Chl-alteration halo in ls | −66 | | |
| | 71/37c | 1,436.90 | WR | Dol marl | −51 | 14.9 | |
| | PB2a | 1,446.36 | WR | Grey sh | −56 | | |
| | 51 | 1,459.24 | Chl | Chl-alteration halo in ss | −61 | 8.4 | |
| | 51b | 1,459.24 | WR | Fine grained ss | −50 | | |
| | 57 | 1,479.20 | Chl | Chl-alteration halo in sh | −64 | 8.4 | |
| | 57b | 1,479.20 | WR | sh | −51 | | |
| | 29 | 1,485.80 | Chl | Chl-alteration halo in sh | −60 | 8.2 | |
| | 32/30c | 1,486.70 | WR | Silt-ss | −50 | 15.0 | |
| | PB2b | 1,502.78 | WR | Grey sh | −57 | | |
| | 36 | 1,503.25 | WR | sh | | 14.9 | |
| | PB4 | 1,507.18 | WR | Red silt-ss | −53 | | |
| | 11 | 1,512.43 | WR | sh | −53 | | |
| | 70 | 2,142.70 | WR | Fine grained ss | | 14.4 | |

**Table 4** continued

| | No. | Depth m | Host mineral | Lithology, mineralogy | δD VSMOW ±5% | $\delta^{13}C$ $CH_4$ VPDB ±5% | $\delta^{13}C$ $CO_2$ VPDB ±5% |
|---|---|---|---|---|---|---|---|
| Fluid inclusion | P5 | 1,403.68 | Cal | Qtz-Cal ± Chl V. | −104 | | −22.3 |
| | P11 | 1,408.75 | Dol | Qtz-Dol ± Chl V. | | | −12.8 |
| | P8 | 1,417.03 | Qtz | Qtz-Cb ± Chl V. | −89 | −28.9 | −13.3 |
| | P9 | 1,430.69 | Qtz | Qtz-Cal ± Chl V. | −99 | | −13.0 |
| | P4 | 1,436.68 | Cal | Qtz-Cal ± Chl V. | | −28.5 | −19.9 |
| | P7 | 1,436.90 | Qtz | Qtz-Cb ± Chl V. | −94 | −26.9 | −17.4 |
| | P12 | 1,459.24 | Dol | Qtz-Dol ± Chl V. | | −28.3 | −17.8 |
| | P2 | 1,479.20 | Qtz | Qtz-Cb ± Chl V. | | | −21.0 |
| | P6 | 1,486.70 | Qtz | Qtz-Cb ± Chl V. | −98 | | −23.3 |
| | P3 | 1,503.25 | Dol | Qtz-Dol ± Chl V. | −113 | | −18.0 |

Uncertainty is given in ‰ (2 σ), mineral abbreviations are according to Siivola and Schmid (2007)

*Cal* calcite, *Cb* carbonate, *Chl* chlorite, *Dol* dolomite, *ls* limestone, *Qtz* quartz, *sh* shale, *ss* sandstone, *V* vein, *WR* whole rock

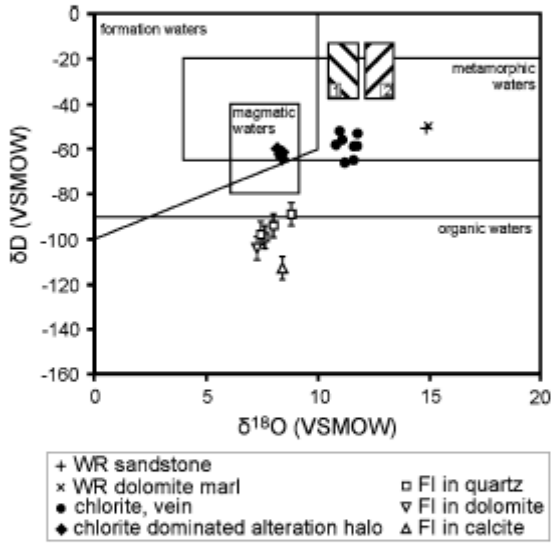


**Fig. 6** Plot of δD (VSMOW) versus $\delta^{18}O$ (VSMOW) for whole rock (WR) samples, vein chlorite, chlorite dominated alteration halos around veins and fluid inclusions (*FI*) from quartz, calcite and dolomite in veins. The $\delta^{18}O$ values of fluid inclusions were calculated assuming equilibration at 220°C as suggested by microthermometry of secondary fluid inclusions between $H_2O$ and the host minerals quartz (Matsuhisa et al. 1979), calcite and dolomite (Zheng 1999). The fields of magmatic, metamorphic and formation waters refer to Taylor (1974), the field of organic waters is shown in Tarantola et al. (2007). The cross-hatched fields denote hypothetic waters in equilibrium with chlorite in veins at $T = 350$°C as indicated by primary fluid inclusions. The value of δD in water in equilibrium with chlorite was calculated according to Graham et al. (1984). In field 1 $\delta^{18}O$ of $H_2O$ was calculated using chlorite–water equilibration (Savin and Lee 1988) whereas in field 2 equilibrium fractionation between vein quartz (see Table 4 for $\delta^{18}O$) and water was applied (Matsuhisa et al. 1979)

Primary and secondary Type I inclusions are characterised by variations in fluid salinity, bulk density and ionic composition. There is a noticeable transition from a moderate salinity $H_2O$–Na–(K)–Cl fluid at high temperatures (≤398°C) to a lower temperature (≤211°C) $H_2O$–Na–(K)–Cl fluid with lower salinities.

Isochores calculated with the MacFlinCor software (Brown 1989; Brown and Hagemann 1995) for a representative selection of primary, pseudo-secondary and secondary fluid inclusions from various veins and minerals are summarised in Fig. 9. The data show a significant variation in bulk density and homogenisation temperature of primary inclusions which trapped the high temperature fluid. Petrographic evidence of post trapping processes is not given.

Independent constraints on trapping conditions are provided by cc–dol–thermometry yielding temperatures <358°C (Table 2). Although post-crystallisation Ca–Mg-exchange cannot be ruled out, this temperature estimate is in good agreement with epizonal peak metamorphic conditions considered for the Venn–Weser–Inde nappe and Stavelot–Venn massif (Glasmacher 1995; Hilgers et al. 2006; Oncken et al. 1999; Vogtmann–Becker 1990; Zhang et al. 1997).

Thus, it may be assumed that trapping temperatures did not exceed 450°C. Even so, temperatures of around 400°C are still markedly higher than previously considered (i.e. late diagenetic to anchizonal grade, 200–310°C) for vein host rocks.

Upper pressure limits can be derived from thermobaric gradients (Fig. 9). According to Kenis et al. (2000), the geothermal gradient in the Variscan front zone was 50°C/26 MPa during Variscan compression. This would suggest that primary inclusions formed under lithostatic conditions at depths of c. 8 km. In contrast to that, Rottke and Stroink (1999) concluded that burial of lower Devonian rocks in the region did not exceed 4,500 m, and recent work by Sehrt et al. (in prep.) points to maximum burial depth of 6 km. If maximum burial was not deeper than 4,500 m a geothermal gradient of 75°C/26 MPa or higher than that would be needed to account for the thermobarometric data.

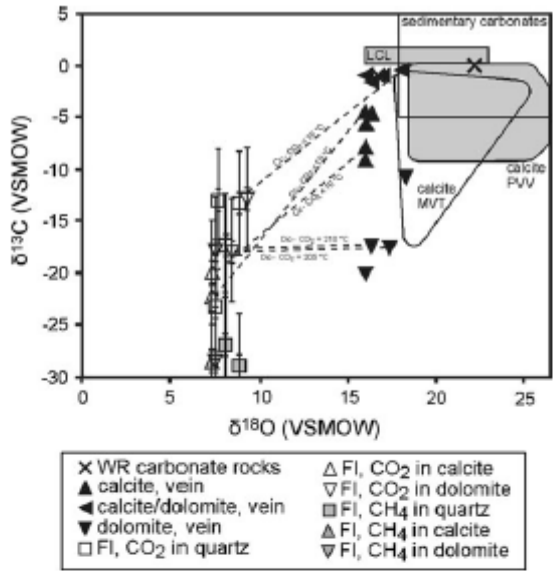


**Fig. 7** Plot of $\delta^{13}C$ (PDB) versus $\delta^{18}O$ (VSMOW) for whole rock (WR) carbonate samples, vein calcite, vein calcite/dolomite, vein dolomite, $CO_2$ from fluid inclusions (*FI*) in vein quartz, vein calcite, vein dolomite and $CH_4$ from fluid inclusions in vein quartz, vein calcite and vein dolomite. Chlorite dominated alteration halos around veins and fluid inclusions (*FI*) from quartz, calcite and dolomite in veins. Stippled lines indicate host calcite and dolomite and $CO_2$ from fluid inclusions, equilibrium temperatures of the respective carbonate-$CO_2$-pairs are calculated according to Ohmoto and Rye (1979). *LCL* denotes lower Carboniferous limestones occurring to the SE of Aachen (Chatziliadou 2009) and PVV indicates isotopic signatures of post-Variscan vein calcites from Hastenrath and Bleiberg situated only few kilometres to the SE and SW of Aachen (Chatziliadou 2009; Muchez et al. 1994). The field of sedimentary carbonates is from Hudson (1977) and Baker and Fallick (1989), the field (MVT) showing the isotope signatures of calcite from Mississippi–Valley-Type deposits is from Richardson et al. (1988)

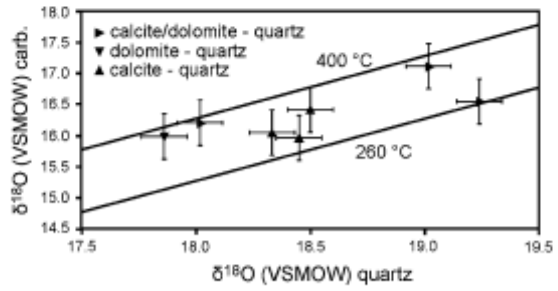


**Fig. 8** $\delta^{18}O_{quartz}$ versus $\delta^{18}O_{carbonate}$ values of coexisting quartz and carbonate fractions in veins of the first core section of the RWTH-1 well and equilibrium temperatures after Sharp and Kirschner (1994)

However, provided that all fluid inclusion properties are undisturbed by post-entrapment processes, the presence of primary fluid inclusions with the lowest bulk densities and

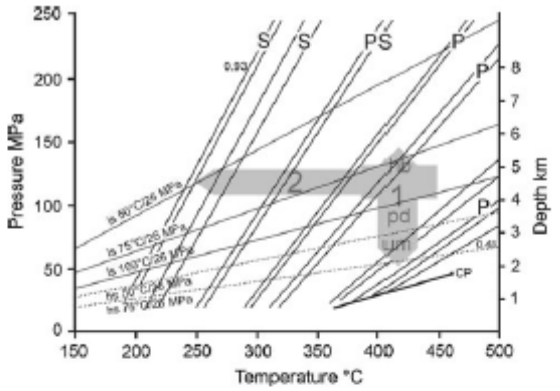


**Fig. 9** Pressure (MPa)–temperature (°C) diagram showing isochores (*solid lines*) of representative primary (*P*), pseudo-secondary (*PS*) and secondary (*S*) fluid inclusions. The *thick solid line* indicates the vapour saturation curve for a $H_2O$–NaCl (9 wt% NaCl) system, *CP* denotes the critical point. Maximum (0.93) and minimum (0.48) densities in g/cm$^3$ of fluid inclusions are shown. Stippled lines indicate geothermal gradients at different lithostatic (*ls*) and hydrostatic (*hs*) conditions. The shaded field illustrates the PT-range inferred for the palaeo-fluids of the RWTH-1 well reflected in the fluid inclusions. In a first pulse (*1*), a metamorphic fluid derived from the epizonal Stavelot–Venn massif enters fractures in part causing hydraulic brecciation (*hb*). Due to fracture opening in seismic events, fluid pressure drops (*pd*) lead to unmixing (*um*) and trapping of fluid inclusions with low density. For calculation, the equation of state for the $H_2O$–Na–(K)–Cl-system of Bowers and Helgeson (1985) implemented in the MacFlinCor software (Brown 1989) was applied

highest $T_h$ requires an even higher geothermal gradient of >100°C/26 MPa. Another possible scenario could involve release of fluids from a hot source and trapping at shallower crustal levels under sub-lithostatic pressure conditions.

## Fluid sources and migration

Comparing our micro-thermometric and petrographic data with previous fluid inclusion work (i.e. Table 1; Behr et al. 1987, 1993; Dewaele et al. 2004; Kenis et al. 2000; 2005; Muchez et al. 1998; Schroyen and Muchez 2000; Vogtmann–Becker 1990), we consider the primary fluid inclusions studied in the RWTH-1 well similar to Variscan hydrothermal fluids encountered along the entire Variscan front zone. The Stavelot–Venn massif records metamorphic fluids with similar temperatures and salinities (Schroyen and Muchez 2000; Vogtmann–Becker 1990) which makes this area a potential source for the fluids discussed here. There is a further line of evidence provided by Schroyen and Muchez (2000) and Muchez et al. (2002) who argue that the fluids in the Variscan front zone in Belgium were derived from the Ardennes area, several kilometres to the south and migrated along major thrust faults in a northerly direction. Fluid flow which was shown

to be syntectonic (Becker et al. 2011; Sindern et al. 2007) was driven by fault-valve action during Variscan thrusting and compression. The latter process involves fast fluid movement and little heat loss even over several tens of kilometres of distance (Clendenin and Duane 1990). Hot external fluid infiltration would account for fluid temperatures exceeding host rock temperatures as observed in this study. Further evidence is provided by the presence of syntectonic fault-fill veins, crack-seal processes and pseudotachylite formation as well as the general style of vein formation related to thrust faults. In this environment pressure cycling, i.e. repetition of pressurisation and rupturing cycles, accounts for multiple events of vein opening and filling. Pressure cycling as a result of seismic activity may be indicated by high-salinity and low-density fluid inclusions (Jin et al. 2008; Srivastava and Sahay 2003). Fault-failure during seismic events creates enhanced fracture permeability and fracture volume that acts as sink for fluids and triggers mineral deposition (Kolb et al. 2004; Petit et al. 1999; Sibson et al. 1988). Post-failure discharge causes drainage of 'geopressured' fluids (Sibson et al. 1988) and pressure drop towards or even to hydrostatic values, if the fault rupture reached the surface (Herrington and Wilkinson 1993; Sibson 2001). The above scenario invokes multiple episodes of fluid-pressure accumulation and discharge which may be indicated by variable bulk densities in fluid inclusions (Table 3). Isochores calculated for the primary inclusions with lowest bulk densities would be consistent with trapping under hydrostatic conditions. This would imply at least for a short period that fluid pathways allowed pressure equilibration with the surface.

In addition, unmixing of a homogeneous fluid in a $H_2O$–Na–(K)–Cl- and a $CO_2$- $H_2O$-rich fluid, evidenced by type I and type II inclusions, at 400°C can be expected at pressures between 30 and 50 MPa (Rusk et al. 2008) which also requires pressure drop to sublithostatic conditions.

## Fluid mixing

When considering a scenario involving fast metamorphic fluid flow, it becomes clear that temperatures of primary fluid inclusions in vein minerals do not necessarily reflect the regional thermal history of the rock section close to the Aachen thrust. In this case, it may be insufficient to explain the large temperature range indicated in the fluid inclusions by cooling solely as a result of tectonic transport and exhumation. The latter process was shown to account for temperature variation in a carbonate hosted fluid system in the western part of the Variscan front zone (Kenis et al. 2000). Another explanation may be to assume that mixing with a fluid of lower salinity and by temperatures buffered by host rocks caused the decrease in $T_h$ and salinity recorded in the variation of primary inclusion data, and even more in secondary and pseudo-secondary inclusions. In the context of active Variscan compression during the hydrothermal event, it is inferred that the cooler, low-salinity fluid was expelled from increasingly compressed late diagenetic to low anchizonal lower Palaeozoic sedimentary rocks of the footwall of the Aachen thrust. The process of admixture may also be enhanced due to fluid redistribution in the aftershock phase following seismic events (Sibson 2001). The variation in primary fluid inclusion data underlines that admixture of the cooler low-salinity fluid already occurred during vein formation and vein filling. This admixture continued through the formation of pseudo-secondary and secondary inclusions, and thus caused varying salinities and homogenisation temperatures (Fig. 5).

The influx of post-Variscan fluids is ruled out on the basis of salinity data (Table 1). Trapping of secondary inclusions could have happened under lithostatic conditions at a geothermal gradient of 50°C/26 MPa and assumed burial depth of c. 4,000–4,500 m (Rottke and Stroink 1999). In this case, trapping temperatures would be in the range of 200–250°C. This range is consistent with temperature estimates derived from textural evidence and illite 'crystallinity' for the host rocks (Sindern et al. 2007). Higher burial depths of 6 km (Sehrt et al. in prep.) would be consistent with lower geothermal gradients (e.g. 30°C/26 MPa) which cannot be excluded on the basis of data presented in this study.

## Isotope characteristics

In case of unmixing of a homogenous $H_2O$–$CO_2$–($CH_4$, $N_2$)–Na–(K)–Cl fluid, the resulting $H_2O$–Na–(K)–Cl and $CO_2$–($H_2O$, $CH_4$, $N_2$) fluids would in larger proportions be preserved in primary inclusions as these are predominant and characterised by less admixture of the low salinity fluid. In any case, the low salinity $H_2O$–Na–Cl fluid is considered to have less impact on the carbon isotope signature of the fluid inclusions.

If so, the bulk isotope analysis of fluid inclusions would mainly account for the composition of the Variscan hydrothermal fluid prior to unmixing. To investigate this further, a mean temperature of 350°C is used for following considerations.

A hydrothermal fluid in isotopic equilibrium with vein chlorite ($\delta$D values between −52 and −66‰) at a temperature of 350°C would have a $\delta$D range between −18.5 and −32.5‰ (Fig. 6). This range is rather typical for a metamorphic fluid (e.g. Sheppard 1986; Taylor 1974) and this would be in line with the interpretation of the microthermometry data of the primary fluid inclusions.

In contrast, fluids analysed after decrepitation from vein minerals have significantly lower $\delta$D-values which are not

consistent with chlorite–$H_2O$ fractionation at temperatures between 200 and 400°C (Fig. 6). This inconsistency can be explained by two different scenarios.

1. A first pulse of a fluid with metamorphic $\delta D$ and $\delta^{18}O$ isotope characteristics (fields 1, 2 in Fig. 6) that caused mineralisation of chlorite, associated quartz and carbonates was followed by a second fluid pulse that is now isotopically reflected in the inclusions. As mineralised vein textures do not indicate more than one syn-deformational hydrothermal event, both pulses would have occurred within a short period of time. The lack of an isotopic trace of the first pulse could be explained by an isotope exchange between fluid inclusions of the first pulse and the following pulse. Experiments by Bakker and Diamond (1999, 2003) and Bakker (2009) indicate D/H exchange by diffusion through quartz while $CO_2$ and NaCl are immobile. Nano-cracks, stacking faults and dislocations may enhance such transfer also at lower temperature conditions of sedimentary systems (Bakker 2009).

This scenario is considered as less probable as it requires a marked change in isotopic signatures within one event without leaving a trace in the fluid inclusions, which in turn requires a complete isotope exchange.

2. According to the second scenario, a Variscan fluid was responsible for vein mineralisation with isotope signatures equal or close to those represented in the fluid inclusions. In this case, the same range of $\delta D$ values of chlorite and host rocks would indicate that hydrogen was rock-buffered. This would require a low fluid-rock ratio which is in line with the observation of a short termed event shown by 'illite crystallinity' (Sindern et al. 2007).

Hydrogen ($\delta D$) isotope values of fluids (−89 to −113‰) can be derived from highly fractionated meteoric water (Mullis et al. 1994; Taylor 1974) but they are also characteristic of fluids strongly affected by the breakdown of organic matter (Sheppard 1986).

Assuming input from the breakdown of organic matter to the fluids would help to explain the low $\delta^{13}C$ signatures ($\delta^{13}C$ of $CO_2$: −12.8 to −23.3‰, $\delta^{13}C$ of $CH_4$: −26.9 to −28.9‰, Table 4) in the fluid inclusions (Fig. 7). Methane and $CO_2$ can be formed by biogenic decomposition of organic matter at $T \leq 80$°C leading to $\delta^{13}C$ as low as −110‰ (Whiticar 1999) while $CO_2$ keeps the C isotopic signature of the organic matter (Ohmoto and Goldhaber 1997).

Maturation and thermogenic cracking of higher hydrocarbons under anchizonal to epizonal conditions also produces $CH_4$ and $CO_2$ (Price 1997; Schoell 1980; Tocqué et al. 2005; Whiticar 1990). Carbon isotope signatures of these decomposition products ($\delta^{13}C$ of $CO_2$ predominantly −12 to −25‰ and $\delta^{13}C$ of $CH_4$ −30 to −50‰, Quanyou et al. 2007; Ohmoto and Goldhaber 1997; Whiticar 1990) are in the same range as $\delta^{13}C$ values determined in the fluid inclusions in the RWTH-1 well. It is thus plausible to assume that carbon in this fluid is predominantly derived from decomposition of organic matter. As the limit between 'organic' and 'metamorphic' waters in standard $\delta D$–$\delta^{18}O$ plots is a practical cut off (Sheppard 1986) within a continuum of isotopic signatures, the low $\delta D$ and also $\delta^{13}C$ values are not considered as contradiction to a classification as metamorphic fluids.

Genesis of $CH_4$ and $CO_2$ from reaction of graphite with $H_2O$ under metamorphic conditions cannot be ruled out. The $\delta^{13}C$ values of coexisting $CH_4$ and $CO_2$, however, point to unrealistically high temperatures in excess of 600°C (Ohmoto and Goldhaber 1997) irrespective of equilibrium between fluid and graphite or only between $CH_4$ and $CO_2$ in the fluid. Considering the temperature information from fluid inclusions and other studies of the RWTH-1 well (Sindern et al. 2007) as well as the presence of shales rich in organic carbon within the Devonian succession (Becker 2008) of the Wurm syncline, Palaeozoic to pre-Palaeozoic rocks of the Stavelot–Venn massif, and the Venn–Weser–Inde nappe (Glasmacher 1995; Wellens 1995) thermogenic decomposition of organic matter during Variscan peak metamorphic conditions is thus assumed as most probable dominant source for carbon and hydrogen in the fluid inclusions. Likewise, the presence of $CH_4$ in pre-Variscan and Variscan metamorphic fluids in the Anglo–Brabant fold belt and the Ardennes (Table 1) is similarly explained by fluid interaction with organic sedimentary matter (Dewaele et al. 2004; Kenis et al. 2005).

Fluids affected by decay of organic matter are likely to be reducing. It has to be noted that among all whole rock samples, the grey shales whose colour indicates reducing conditions are characterised by lowest $\delta D$ values (Table 4). This proves that the fluid was influenced by organic carbon with low $\delta D$ and low $\delta^{13}C$.

The variation in $\delta^{13}C$ of vein carbonates (i.e. calcite, dolomite and calcite/dolomite) shows that they contain carbon from various sources. The calcite/dolomite fraction has $\delta^{13}C$ similar to the carbonate rocks so that the carbon may mainly have been derived from the latter. This may indicate an early mineral formation event during which the isotopic composition is buffered by carbonates. Calcite partly re-equilibrated during the hydrothermal event as is reflected by the calcite data trend to lower $\delta^{13}C$. Carbon added to the system by the fluid at this stage was derived from breakdown of organic matter. However, the isotopic variation in the samples within short distances indicates that only partial or local equilibration on thin section scale was achieved.

Isotopic disequilibrium can also be observed for carbonates and their fluid inclusions. Tie-lines in Fig. 7 indicate that $\delta^{13}C$ values of host calcite, calcite/dolomite fractions and $CO_2$ in fluid inclusions from these fractions cannot reflect equilibrium conditions unless assuming unrealistically low temperatures of <10°C. Keeping in mind that the primary fluid inclusions with metamorphic water characteristics are found in dolomite and calcite one would expect $\delta^{13}C$ in calcite-$CO_2$ pairs to indicate higher temperatures.

In contrast, $\delta^{13}C$ of dolomite host minerals and associated fluid inclusion $CO_2$ are consistent with an equilibration temperature in the range of the microthermometry data (Fig. 7). The dolomite-$CO_2$ pairs sampled at depths 1,503.25 and 1,459.24 m yield temperatures of 210 and 205°C.

Isotopic heterogeneity may be caused by incomplete equilibration between host rock-derived and fluid-derived carbon consistent with the idea of low-fluid rock ratio and short episodic pulses in accordance with scenario II. The carbon isotope system in primary and pseudo-secondary fluid inclusions and host minerals may also be disturbed by fluid flow during formation of secondary inclusions.

The lowest $T_h$ and largest variation in $\delta^{13}C$ of carbonates was recorded in the nodular limestones at 1,438 m (Tables 3, 4). This section of the upper core section is cut by a thrust fault and represents a zone of higher permeability (Fig. 3; Sindern et al. 2008; Lögering 2008). Enhanced fluid flow at that level may serve as an explanation for the disturbance of fluid and isotope systems.

An initial formation of both quartz and carbonate under temperature conditions up to c. 400°C (as indicated by primary FI in quartz and carbonates) is also mirrored in $\delta^{18}O$ values of some quartz–calcite pairs (Fig. 8). However, lack of correlation among all quartz–calcite $\delta^{18}O$ data and tendency towards equilibration temperatures as low as 265°C may be the result of subsequent disturbance of the initial fluid system.

Alteration halos dominated by chlorite have lower $\delta^{18}O$ values than host rocks and vein minerals (Fig. 6, Table 4). Their oxygen isotope composition is similar to the composition of a fluid equilibrated at approximately 200°C with quartz in the host rock (Fig. 8). Such conditions can be assumed for the fluid trapped in secondary inclusions and it is suggested that alteration halos are the result of rock reaction with the secondary fluid. As the size of chlorite crystals in the alteration halos is significantly lower than in the veins, fluid–mineral isotope exchange with the secondary fluid will tend to go to completion in the alteration halos rather than in the veins.

## Conclusions

Quartz–carbonate–chlorite veins in lower to upper Devonian rocks studied in the RWTH-1 well result from Variscan deformation and fluid flow. Primary fluid inclusions of $H_2O$–Na–(K)–Cl-rich composition evolved through subsolvus

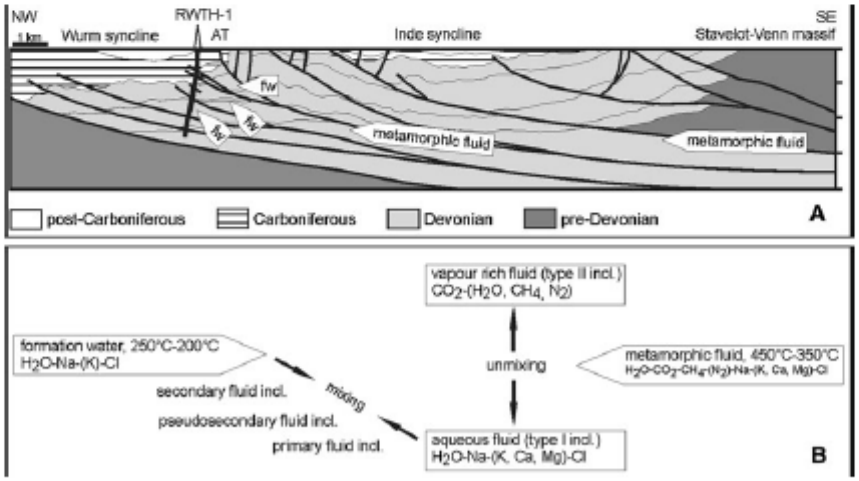


**Fig. 10** **a** Schematic cross section of the Variscan front zone near Aachen after Becker (2008) and Dewaele et al. (2004) showing pathways for a metamorphic fluid released in the Stavelot–Venn massif from Lower Palaeozoic or older units and underlying Devonian strata. Mixing of metamorphic fluid with formation water (*fw*) occurs in the footwall of the Aachen thrust (*AT*). **b** Scheme of fluid evolution showing unmixing of the metamorphic fluid to an aqueous (type I) and a vapour-rich (type II) fluid. Introduction of formation water and mixing with the aqueous metamorphic fluid causes the range of physicochemical fluid characteristics observed in primary, pseudo-secondary and secondary fluid inclusions

unmixing of an original homogeneous $H_2O$–$CO_2$–$CH_4$–($N_2$)–Na–Cl fluid with physico-chemical signatures similar to moderate salinity (chiefly 4–7% NaCl equiv.) metamorphic fluids of the Variscan front zone. Vapour-rich $CO_2$–($H_2O$, $CH_4$, $N_2$) fluids are considered concomitant subsolvus separation products. Maximum homogenisation temperatures of 398°C and vein cc-dolsolvus temperatures of 358°C are in excess of regional temperatures in the vein host rocks that are of late diagenetic to low anchizonal grade. Fluid temperatures point to an origin from the epizonal grade rocks of the Stavelot–Venn massif situated a few kilometres to the south (Fig. 10). Pseudo-secondary and secondary fluid inclusions with salinities <5% NaCl equiv. and temperatures of 200–250°C point to a second fluid system in thermal equilibrium with the footwall rocks of the Aachen thrust. This formation water mixed with the high-temperature metamorphic fluids (Fig. 10) during the course of Variscan deformation. Bulk fluid stable isotope analyses of vein quartz, calcite and dolomite reveal $\delta D_{H2O}$ values from −89 to −113‰, $\delta^{13}C_{CH4}$ values between −26.9 and 28.9‰ (VPDB) and $\delta^{13}C_{CO_2}$ values from −12.8 to −23.3‰ (VPDB).

To explain the low $\delta$D and $\delta^{13}$C range of the fluids, it is proposed that the stable isotope signature of metamorphic Variscan fluids was affected by interaction with cracked hydrocarbons. The hydrogen and oxygen isotope signatures further point to the fact that initial mineral precipitation occurred under rock-buffered conditions. A second fluid influx that caused partial isotope exchange and disequilibrium is thought to originate from lower Palaeozoic rocks in the footwall of the Aachen thrust. These Palaeozoic rocks, which are of late diagenetic to low anchizonal grade, could explain the temperatures of the secondary fluid.

Considering all information obtained from fluid inclusion petrography, microthermometry and stable isotope analyses, a scenario is proposed that envisages an initial short-lived flux of hot metamorphic fluids originating from the epizonal metamorphic domains of the Stavelot–Venn massif. The expelled fluid was focused along major thrust faults of the Variscan front zone such as the Aachen thrust. Subsequently, a second fluid influx was introduced from formation waters in the footwall of the Aachen thrust as a consequence of progressive deformation in the Variscan front zone. Fluid influx occurred in distinct pulses as is shown by the variation of bulk densities in primary fluid inclusions. Mixing of the cooler and lower salinity formation water with the hot metamorphic fluid during episodic fluid trapping resulted in an evolving range of physicochemical fluid inclusion characteristics, from primary to secondary fluid end-members.

**Acknowledgments** This study was supported by grant ME 1425/9-1, 2 of the German Science Foundation DFG to F. M. Meyer. The authors would like to thank P. Muchez and Chr. Hilgers for helpful discussions. The allocation of cores at the Geological Survey Brussels, Belgium, by M. Dusar is much appreciated. We want to thank S. Becker for his help during core work. We would like to thank T. Derichs for the preparation of the thin and thick sections and R. Klinghardt for his patience during EMPA work, A. Kronimus for his suggestions and advice on technical questions for gas-chromatographic work. J. Koester and A. Dziggel critically improved a previous version of the manuscript. Constructive criticism by the reviewers P. Muchez and A. Willner is gratefully acknowledged.

## References

Anovitz LM, Essene EJ (1987) Phase equilibria in the system $CaCO_3$–$MgCO_3$–$FeCO_3$. J Petrol 28:389–414

Babinecz W (1962) Das Inkohlungsbild des Aachener Steinkohlengebirges, dargestellt im Niveau des Flözes Großlangenberg. Fortschr Geol Rheinld U Westf 3(2):679–686

Bailey SW (1991) Chlorites: structures and crystal chemistry. In: Bailey SW (ed) Hydrous phyllosilicates. Reviews in mineralogy. Mineralogical Society of America, second printing, Washington, pp 347–403

Baker AJ, Fallick AE (1989) Evidence from Lewisian limestones for isotopically heavy carbon in two-thousand-million-year-old sea water. Nature 337:352–354

Bakker RJ (2009) Reequilibration of fluid inclusions: bulk-diffusion. Lithos. doi:10.1016/j.lithos.2009.03.006

Bakker RJ, Diamond LW (1999) Reequilibration of synthetic $CO_2$–$H_2O$ fluid inclusions in quartz: isofugacity experiments. Terra Nostra 99:20–21

Bakker RJ, Diamond LW (2003) Fluid inclusion re-equilibration experiments in quartz: chemical potential gradients. Acta Mineralogica-Petrographica Abstr Ser 2:95–96

Becker S (2008) The Aachen fold and thrust belt: an integration of surface geology, reflection seismics and new subsurface data of the well RWTH-1. Diploma thesis RWTH Aachen University, unpublished, Aachen, Germany, 182 p

Becker S, Hilgers Chr, Kukla P, Urai JL (2011) Crack-seal microstructure evolution in bi-mineralic quartz-chlorite veins in shales and siltstones from the RWTH-1 well, Aachen, Germany. J Struct Geol 33:676–689

Behr HJ, Horn EE, Frentzel-Beyme K, Reutel Chr (1987) Fluid inclusion characteristics of the Varsican and post-Variscan mineralizing fluids in the Federal Republic of Germany. Chem Geol 61:273–285

Behr HJ, Gerler J, Hein UF, Reutel CJ (1993) Tectonic brines und basement brines in den mitteleuropäischen Variszíden: Herkunft, metallogenetische Bedeutung und geologische Aktivität. Göttinger Arb Geol Paläont 58:3–28

Bowers TS, Helgeson HC (1985) Fortran programs for generating of fluid inclusions and fugazity coefficients for the system $H_2O$–$CO_2$–NaCl at high pressures and temperatures. Comput Geosci 11:203–213

Brown EB (1989) Flincor: a microcomputer program for the reduction and investigation of fluid inclusion data. Am Min 74:1390–1393

Brown PE, Hagemann SG (1995) MacFlinCor and its application to fluids in Archean lode-gold deposits. Geochim Cosmochim Acta 59:3943–3952

Chatziliadou MS (2009) Rb–Sr Alter und Sr–Pb Isotopencharakteristik von Gangmineralisationen in paläozoischen Gesteinen am Nordrand des linksrheinischen Schiefergebirges (Raum Stolberg-Aachen-Kelmis) und Vergleich mit den rezenten Thermalwässern in Aachen-Burtscheid. Dissertation RWTH Aachen University, pp 266

Clendenin CW, Duane MJ (1990) Focused fluid flow and Ozark Mississippi valley-type deposits. Geology 18:116–119
Crawford ML, Hollister LS (1986) Metamorphic fluids: the evidence from fluid inclusions. In: Walther JV, Wood BJ (eds) Fluid-rock interaction during metamorphism. Springer, New York, pp 1–35
Dejonghe L, Boni M (2004) The calamine-type zinc-lead deposits in Belgium and West-Germany: a product of mesozoic palaeoweathering processes. Geologica Belgica 8(3):3–14
Dewaele S, Muchez Ph, Banks D (2004) Fluid evolution along multistage composite fault systems at the southern margin of the lower palaeozoic Anglo-Brabant fold belt, Belgium. Geofluids 4:341–356
Duan Z, Møller N, Weare JH (1995) Equation of state fort he NaCl–$H_2O$–$CO_2$ system: prediction of phase equilibria and volumetric properties. Geochim Cosmochim Acta 59:2869–2882
Franke W (1989) Tectonostratigraphic units in the Variscan belt of central Europe. Geol Soc Am Spec Pap 230:67–90
Fransolet AM, Kramm U (1983) Mineralogie und Petrologie Mn-reicher Metapelite des Venn-Stavelot Massives, Ardennen, und die varistische Metamorphose im nordwestlichen Rheinischen Schild. Fortschr Min 61:31–69
Frantz JD, Popp RK, Hoering TC (1992) The compositional limits of fluid immiscibility in the system $H_2O$–NaCl–$CO_2$ as determined with the use of synthetic fluid inclusions in conjunction with mass spectrometry. Chem Geol 98:237–255
Friedrich G, Diedel R, Redecke P (1989) Postvariskische, intraformationale Stoffumsetzungen im Rheinischen Schiefergebirge und seinem nördlichen Vorland - Ansätze zur Quantifizierung lagerstättenbildender Prozesse.- 2. Zwischenbericht zum DFG-Forschungsvorhaben FR240/52-1, Aachen, pp 113
Germann A, Friedrich G (1999) Strukturkontrollierte, postvariskische Buntmetallmineralisation in paläozoischen und mesozoischen Sedimentgesteinen der nordwestlichen Eifel. Zeitschrift der deutschen Geologischen Gesellschaft 150:513–541
Glasmacher UA (1995) Variszische und postvariszische Fluidsysteme. In: Walter R, Glasmacher U, Wolf M (eds) KW-relevante Eigenschaften potentieller Mutter-und Speichergesteine am Nordrand des Linksrheinischen Schiefergebirges—RWTH Aachen, BMBF-Forschungsprojekt 032 6804 A 5, 01.04.1991–30.09.1994, Teil 5: 1–40
Glasmacher UA, Tschernoster R, Clauer N, Spaeth G (2001) K-Ar dating of magmatic sericite crystallites for determination of cooling paths of metamorphic overprints. Chem Geol 175:673–687
Graham CM, Atkinson J, Harmon RS (1984) Hydrogen isotope fractionation in the system chlorite-water. NERC 6th progress report of research 1981–1984, NERC publication series D 25:1–139
Heijlen W, Muchez Ph, Banks DA (2001) Origin and evolution of high-salinity, Zn–Pb mineralising fluids in the Variscides of Belgium. Mineralium Deposita 36:165–176
Helsen S (1995) Burial history of Palaeozoic strata in Belgium as revealed by conodont colour alteration data and thickness distributions. Geol Rundsch 84:738–747
Helsen S, Koenigshof P (1994) Conodont thermal alteration patterns in Palaeozoic rocks from eastern Belgium, northern France and western Germany. Geol Mag 131:369–386
Herrington RJ, Wilkinson JJ (1993) Colloidal gold and silica in mesothermal vein systems. Geology 21:539–542
Hilgers C, Büker C, Urai JL (2006) Fossil overpressures compartments? A case study from the Eifel area and some general aspects. In: Phillipp S, Leiss B, Vollbrecht A, Tanner D, Gudmundsson A (eds) 11. Symposium "Tektonik, Struktur- und Kristallingeologie", Zusammenfassung der Tagungsbeiträge, Göttingen, pp 87–89
Hollmann EG (1997) Der Variszische Vorlandüberschiebungsgürtel der Ostbelgischen Ardennen—Ein bilanziertes Modell. Aachener Geowissenschaftliche Beiträge, 25, pp 235
Hollmann G, von Winterfeld C (1999) Laterale Strukturvariationen eines Vorlandüberschiebungsgürtels. Zeitschrift der Deutschen Geologischen Gesellschaft 150:431–450
Horita J (2001) Carbon isotope exchange in the system $CO_2$–$CH_4$ at elevated temperatures. Geochim Cosmochim Acta 65:1907–1919
Hudson JD (1977) Stable isotopes and limestone lithification. J Geol Soc Lond 133:637–660
Jin Z, Cao J, Hu W, Zhang Y, Yao S, Wang X, Zhang Y, Tang Y, Shi X (2008) Episodic petroleum fluid migration in fault zones of the northwestern Junggar Basin (northwest China): evidence from hydrocarbon-bearing zoned calcite cement. AAPG Bull 92:1225–1243
Kenis I, Muchez Ph, Sintubin M, Mansy JL, Lacquement F (2000) The use of a combined structural, stable isotope and fluid inclusion study to constrain the kinematic history at the northern Variscan front zone (Bettrechies, northern France). J Struct Geol 22:589–602
Kenis I, Muchez Ph, Verhaert G, Boyce A, Sintubin M (2005) Fluid evolution during burial and Variscan deformation in the lower Devonian rocks of the High-Ardenne slate belt (Belgium): sources and causes of high-salinity and C-O–H–N fluids. Contrib Mineral Petrol 150:102–118
Knapp G (1980) Geologische Karte der nördlichen Eifel 1: 100000, mit Erläuterungen.-2. Auflage, Geologisches Landesamt Nordrhein Westfalen, Krefeld
Kolb J, Rogers A, Meyer FM, Vennemann TW (2004) Development of fluid conduits in the auriferous shear zones of the Hutti Gold Mine, India: evidence for spatially and temporally heterogeneous fluid flow. Tectonophysics 378:65–84
Kramm U (1982) Die Metamorphose des Venn-Stavelot-Massives, nordwestliches Rheinisches Schiefergebirge: Grad, Alter und Ursache. Decheniana 135:121–178
Kucera J, Muchez Ph, Slobodnik M, Prochaska W (2010) Geochemistry of highly saline fluids in siliciclastic sequences: genetic implications for post-Variscan fluid flow in the Moravosilesian Palaeozoic of the Czech Republic. Int J Earth Sci (Geologische Rundschau) 99:269–284
Lamb WM, Mcshane CJ, Popp RK (2002) Phase relations in the $CH_4$–$H_2O$–NaCl system at 2 kbar, 300 to 600°C as determined using synthetic fluid inclusions. Geochim Cosmochim Acta 66:3971–3986
Lögering MJ (2008) Fluid evolution, vein mineralization and alteration associated with a low angle shear zone at the northern Variscan fold- and-thrust belt in the vicinity of the Aachen Geothermic drilling, western Germany. Thesis, RWTH Aachen University, Aachen, Germany, pp 132
Lundershausen S, Oesterreich B, Ribbert KH, Wrede V (2005) Geothermal well "RWTH-1", Aachen—technical aspects and first geological results. Abstracts of the Meuse-Rhine Euregio Geologists Meeting: Alden Biesen (Belgian Limbourg), 20–21 May 2005
Lünenschloss B (1998) Modellierung der Temperatur- und Fluidgeschichte an der variszischen Front (Verviers-Synklinorium und Nordeifel). PhD Katholieke Universiteit Leuven (Belgium), 132 pp
Lünenschloss B, Bayer U, Muchez Ph (1997) Coalification anomalies induced by fluid flow at the Variscan thrust front: a numerical model of the palaeo-temperatures field. Geol Mijnbouw 76:271–275
Lünenschloss B, Muchez P, Bayer U (2008) Late-Variscan fluid migration at the Variscan thrust front of Eastern Belgium: numerical modelling of the palaeothermal and fluid flow field. Int J Earth Sci 97:1201–1212
Matsuhisa Y, Goldsmith JR, Clayton RN (1979) Oxygen isotopic fractionation in the system quartz-albite-anorthite-water. Geochim Cosmochim Acta 43:1131–1140

Merriman RJ, Frey M (1999) Patterns of very low-grade metamorphism in metapelitic rocks. In: Frey M, Robinson D (eds) Low-grade metamorphism. Blackwell, Oxford, pp 61–107

Moore JC (1989) Tectonics and hydrogeology of accretionary prisms: role of the décollement zone. J Struct Geol 11:95–106

Muchez Ph, Heijlen W, Dejonghe L, Sintubin M (2002) Tectonics and fluid flow at the northern Variscan front (Belgium). AAPG Hedberg Conference, Palermo, 14–18 May 2002, pp 1–4

Muchez Ph, Sintubin M (1998) Contrasting origin of palaeofluids in a strike-slip fault sytem. Chem Geol 145:105–114

Muchez Ph, Slobodnik M, Viaene W, Keppens E (1994) Mississippi valley-type Pb–Zn mineralization in eastern Belgium: indicators for gravity-driven flow. Geology 22:1011–1014

Muchez Ph, Zhang Y, Dejonghe L, Viaene W, Keppens E (1998) Evolution of palaeofluids at the Variscan thrust front in eastern Belgium. Geol Rundsch 87:373–380

Muchez Ph, Sintubin M, Swennen R (2000) Origin and migration pattern of paleofluids during orogeny: discussion on the Variscides of Belgium and northern France. J Geochem Explor 69–70:47–51

Mullis J, Dubessy J, Poty B, O'Neil J (1994) Fluid regimes during late stages of continental collision: physical, chemical, and stable isotope measurements of fluid inclusions in fissure quartz from a geotraverse through the Central Alps, Switzerland. Geochim Cosmochim Acta 58:2239–2267

Nierhoff R (1994) Metamorphose-Entwicklung im linksrheinischen Schiefergebirge: Metamorphosegrad und–verteilung sowie Metamorphosealter nach K-Ar-Datierungen. Aachener Geowissenschaftliche Beiträge 3, pp 159

Ohmoto H, Goldhaber MB (1997) Sulfur and carbon isotopes. In: Barnes HL (ed) Geochemistry of hydrothermal ore deposits, 3rd edn. Wiley, New York, pp 517–611

Ohmoto H, Rye RO (1979) Isotopes of sulfur and carbon. In: Barnes HL (ed) Geochemistry of hydrothermal ore deposits, 1st edn. Wiley, New York, pp 509–567

Oliver J (1986) Fluids expelled tectonically from orogenic belts: their role in hydrocarbon migration and other geological phenomena. Geology 14:99–102

Oncken O, von Winterfeld C, Dittmar U (1999) Accretion of a passive margin: the late Paleozoic Rhenohercynian fold and thrust belt (Middle European Variscides). Tectonics 18:75–91

Oncken O, Plesch A, Weber J, Ricken W, Schrader S (2000) Passive margin detachment during arc-continent collision (Central European Variscides). In: Franke W, Haak V, Oncken O, Tanner D (eds) Orogenic processes: quantification and modelling in the Variscan Belt, Geological Society, London, special publications 179:199–216, London (Geological Society)

Österreich B, Ribbert KH, Wrede V (2005) Erste Ergebnisse zur biostratigraphischen und tektonischen Einordnung der Bohrung RWTH-1, unpublished report, GD-NRW 2005

Pechnig R (2005) Auswertung der bohrlochgeophysikalischen Messungen in der RWTH-1—Möglichkeiten und Grenzen der Lithologierekonstruktion. RWTH Aachen University, E.ON Energy Research Center, Appl Geophys Geotherm Energy, unpublished

Petit J-P, Wibberley CAJ, Ruiz G (1999) 'Crack-seal', slip: a new fault valve mechanism? J Struct Geol 21:1199–1207

Price LC (1997) Minimum thermal stability levels and controlling parameters of methane, as determined by $C_{15+}$ hydrocarbon thermal stabilities. US Geological Survey Bulletin 2146-K, pp 139–176

Quanyou L, Wenhui L, Jinxing D (2007) Characterization of pyrolysates from maceral components of Tarim coals in closed system experiments and implications to natural gas generation. Org Geochem 38:921–934

Redecke P (1992) Zur Geochemie und Genese variszischer und postvariszischer Buntmetallmineralisation in der Nordeifel und der Niederrheinischen Bucht. RWTH Aachen, Dissertation, pp 159

Ribbert KH (2006) Die Bohrung RWTH-1—Regionalstratigraphische Einordnung und Deutung. Geologischer Dienst NRW, unpublished

Richardson CK, Rye RO, Wassermann MD (1988) The chemical and thermal evolution of the fluids in the Cave-in-rock fluorspar district, Illinois: stable isotope systematics at the Deardorff mine. Econ Geol 83:765–783

Rottke W, Stroink L (1999) Die Genese devonischer Vorlandsedimente am NW-Rand des Rheinischen Massivs—Zement-und Porenraumentwicklung. Zeitschrift der deutschen Geologischen Gesellschaft 150:471–491

Rumble D III, Hoering TC (1994) Analyses of oxygen and sulphur isotope ratios in oxide and sulphide minerals by spot heating with carbon dioxide laser in a fluorine atmosphere. Acc Chem Res 27:237–241

Rusk BG, Reed MH, Dilles JH (2008) Fluid inclusion evidence for magmatic-hydrothermal fluid evolution in the porphyry copper-molybdenum deposit at Butte, Montana. Econ Geol 103:307–334

Savin SM, Lee M (1988) Isotopic studies of phyllosilicates. In: Bailey SW (ed) Hydrous phyllosilicates, vol 19. Reviews in mineralogy. Washington, pp 189–223

Schneider J, Haack U, Hein UF, Germann A (1999) Direct Rb/Sr dating of sandstone-hosted sphalerites from stratabound Pb-Zn deposits in the northern Eifel, NW Rhenish Massif, Germany. In: Stanley CJ (ed) Mineral deposits: process to processing. In: Proceedings of 5th Bienn. SGA meeting and the 10th quadrennial IAGOD symposium, London, 22–25 Aug 1999, pp 1287–1290

Schneider J, Chatziliadou M, Sindern S, Hilgers Chr, Kramm U (2007) Multiple hydrothermal fluid flow in the NW Rhenohercynian. Geochimica Cosmochimica Acta Supplement 71, p. 15, Abstr. 17th annual V. M. Goldschmidt conference, Cologne, Germany, 2007, p A900

Schneider J, Sindern S, Hilgers Chr, Beiss V, Chatziliadou M, Wijbrans J, Kramm U, von Quadt A (2008) Timing of mineralizing fluid flow events in the NW Rhenohercynian belt. Schriftenreihe der Deutschen Gesellschaft für Geowissenschaften 60 (Abstracts, Geo2008 Resources and Risks in the Earth System), p 159

Schoell M (1980) The hydrogen and carbon isotopic composition of methane from natural gases of various origins. Geochim Cosmochim Acta 44:649–661

Schreyer W (1975) New petrologic evidence for Hercynian metamorphism in the Venn-Stavelot-Massif, Belgium. Geol Rundsch 64:819–830

Schroyen K, Muchez P (2000) Evolution of metamorphic fluids at the Variscan fold-and-thrust belt in eastern Belgium. Sed Geol 131:163–180

Sehrt M, Glasmacher UA, Wipf M, Stoeckli D, Kukla P Thermal and exhumation history at the Variscan front—an example from the RWTH-1 well (Germany), manuscript in preparation

Sharp ZD, Kirschner DL (1994) Quartz-calcite oxygen isotope thermometry: a calibration based on natural isotopic variations. Geochim Cosmochim Acta 58:4491–4501

Sharp ZD, Atudorei V, Durakiewicz T (2001) A rapid method for determining the hydrogen and oxygen isotope ratios from water and solid hydrous substances. Chem Geol 178:197–210

Sheppard SMF (1986) Characterization and isotopic variations in natural waters. In: Valley JW, Taylor HP, O'Neil JR (eds) Stable isotopes in high temperature geological processes, vol 16. Mineralogical Society of America, Washington, pp 165–183

Sibson RH (2001) Seismogenic framework for hydrothermal transport and ore deposition. In: Richards JP, Tosdal RM (eds) Structural controls on ore genesis, vol 14. Society of Economic Geologists, Reviews in Economic Geology, pp 25–50

Sibson RH, Robert F, Poulsen KH (1988) High-angle reverse faults, fluid-pressure cycling, and mesothermal gold-quartz deposits. Geology 16:551–555

Siivola J, Schmidt R (2007) List of mineral abbreviations. Recommendations by the IUGS Subcommission on the systematics of metamorphic rocks: Web version 01.02.07. http://www.bgs.ac.uk/scmr/home.html

Sindern S, Stanjek H, Hilgers C, Etoundi Y (2007) Short-term hydrothermal effects in the "crystallinities" of illite and chlorite in the footwall of the Aachen-Faille du Midi thrust fault—first results of the RWTH-1 drilling project. Clays Clay Min 55:200–212

Sindern S, Warnsloh JM, Trautwein-Bruns U, Chatziliadou M, Becker S, Yüceer S, Hilgers C, Kramm U (2008) Geochemical composition of sedimentary rocks and imprint of hydrothermal fluid flow at the Variscan front—an example from the RWTH-1 well (Germany). Zeitschrift der Deutschen Gesellschaft für Geowissenschaften 159:623–640

Smith RE, Wiltschko DV (1996) Generation and maintenance of abnormal fluid pressures beneath a ramping thrust sheet: isotropic permeability experiments. J Struct Geol 18:951–970

Spötl C, Vennemann T (2003) Continuous flow IRMS analysis of carbonate minerals. Rapid Commun Mass Spectrom 17:1004–1006

Srivastava DC, Sahay A (2003) Brittle tectonics and pore-fluid conditions in the evolution of the Great Boundary Fault around Chittaurgarh, Northwestern India. J Struct Geol 25:1713–1733

Steingrobe B (1990) Faziseinheiten aus dem Aachen-Erkelenzer Oberkarbonvorkommen unter besonderer Berücksichtigung des Inde-Synklinoriums. Dissertation RWTH-Aachen, Aachen, pp 325

Strich R (1991) Karbonatisierung von Sandsteinen und Konglomeraten im Bereich schichtgebundener Blei-Zink-Mineralisation, Lagerstätte Mechernich, Westfeld.- Diplomarbeit, Institut für Mineralogie und Lagerstättenlehre, RWTH Aachen, Aachen, pp 120 (unpublished)

Tarantola A, Mullis J, Vennemann T, Dubessy J, de Capitani C (2007) Oxidation of methane at the $CH_4/H_2O$-($CO_2$) transition zone in the external part of the Central Alps, Switzerland: evidence from stable isotope investigations. Chem Geol 237:329–357

Taylor HP (1974) The application of oxygen and hydrogen isotope studies to problems of hydrothermal alteration and ore deposition. Econ Geol 69:843–883

Teichmüller M, Teichmüller R (1979) Ein Inkohlungsprofil entlang der linksrheinischen Geotraverse von Schleiden nach Aachen und die Inkohlung in der Nord-Süd-Zone der Eifel. Fortschr Geol Rheinld u Westf 27:323–355

Tocqué E, Behar F, Budzinski H, Lorant F (2005) Carbon isotopic balance of kerogen pyrolysis effluents in a closed system. Org Geochem 36:893–905

Trautwein-Bruns U, Kukla PA, Urai J, Sindern S, Lögering M, Dijkshorn L, Lünenschloss B, Chatziliadou M (2007) Aachens's geothermal well "RWTH-1"—the geoscientific research program. 67. Jahrestagung der Deutschen Geophysikalischen Gesellschaft, Aachen, 26–29. März 2007

Trautwein-Bruns U, Schulze KC, Becker S, Kukla PA, Urai JL (2010) In situ stress variations at the Variscan deformation front—results from the deep Aachen geothermal well. Tectonophysics 493:196–211

Vogtmann-Becker J (1990) Mobilisation und Austausch von Elementen durch Regionalmetamorphose in kambro-ordovizischen Sedimentgesteinen des Stavelot-Venn-Massivs. Mitteilungen zur Mineralogie und Lagerstättenlehre 34:1–179

von Winterfeld CH (1994) Variszische Deckentektonik und devonische Beckengeometrie der Nordeifel—Ein quantitatives Modell. Aachener Geowissenschaftliche Beiträge 2:1–319

Walter R (1995) Geologie von Mitteleuropa. E. Schweizerbart'sche Verlagsbuchhandlung (Nägele u. Obermiller), Stuttgart, 6. Auflage, pp 566

Wellens M (1995) Charakterisierung der organischen Substanz in den potentiellen Muttergesteinen. In: Walter R, Glasmacher UA, Wolf M (eds) KW-relevante Eigenschaften potentieller Mutter- und Speichergesteine am Nordrand des Linksrheinischen Schiefergebirges. RWTH-Aachen, BMBF Forschungsprojekt 032 6804, pp 1–40

Whiticar MJ (1990) A geochemical perspective of natural gas and atmospheric methane. Org Geochem 16:531–547

Whiticar MJ (1999) Carbon and hydrogen isotope systematics of bacterial formation and oxidation of methane. Chem Geol 161:291–314

Zhang Y, Muchez P, Hein UF (1997) Chlorite geothermometry and the temperature conditions at the Variscan thrust front in eastern Belgium. Geol Mijnbouw 76:267–270

Zheng YF (1999) Oxygen isotope fractionation in carbonate and sulfate minerals. Geochem J 33:109–126

12.

Sindern, S., Stanjek, H., Hilgers, C., Etoundi, Y. (2007) Short-term hydrothermal effects on the „crystallinities“ of illite and chlorite in the footwall of the Aachen-Faille du Midi thrust fault – first results of the RWTH-1 drilling project. Clays and Clay Minerals, 55, 200 – 212.

With permission of the publisher Clays and Clay Minerals.

Re-use in thesis granted by The Clay Minerals Society, Editor-in-Chief of Clays and Clay Minerals, 3635 Concorde Pkwy Ste 500, Chantilly, VA 20151-1125 USA, permission letter 9th of December 2015.

*Clays and Clay Minerals*, Vol. 55, No. 2, 200–212, 2007.

# SHORT-TERM HYDROTHERMAL EFFECTS ON THE 'CRYSTALLINITIES' OF ILLITE AND CHLORITE IN THE FOOTWALL OF THE AACHEN-FAILLE DU MIDI THRUST FAULT – FIRST RESULTS OF THE RWTH-1 DRILLING PROJECT

SVEN SINDERN[1,*], HELGE STANJEK[2], CHRISTOPH HILGERS[3] AND YVONNE ETOUNDI[4]

[1] Institute of Mineralogy and Economic Geology, RWTH Aachen University, Wüllnerstrasse 2, 52056 Aachen, Germany
[2] Clay and Interface Mineralogy, RWTH Aachen University, Wüllnerstrasse 2, 52056 Aachen, Germany
[3] Lehr und Forschungsgebiet Geologie und Endogene Dynamik, RWTH Aachen University, 52056 Aachen, Germany
[4] Ministère de l'Industrie, des Mines et du Développment Technologie – CAPM – BP. 15620, Yaoundé, Cameroun

**Abstract**—Investigation of material from three core sections of the RWTH-1 drill-hole in the Wurm syncline of Aachen, Germany, shows mineralogical and structural evidence of intensive hydrothermal activity in the footwall of the Aachen thrust. Mineral and microstructural data indicate minimum temperatures of 200–250°C. $CIS_{illite\ 001}$ values of 0.45–0.61 (Δ°2θ) and insignificant amounts of smectite indicate a late diagenetic grade for illite pointing to temperatures <200°C. Chlorite, mainly formed in veins and cleavage planes, has $CIS_{chlorite\ 002}$ values between 0.35 and 0.26 (Δ°2θ) which only in part point to anchizonal grade. In contrast to these illite and chlorite data, maximum temperatures up to 370°C can be expected based on comparison with recently published fluid inclusion and mineral thermometric data. Illite is neither significantly affected by the hydrothermal event nor by deformation, and mirrors the burial history of the Wurm syncline.

Chlorite grew syntectonically as is shown by bent and predominantly stretched sheets which do not, however, have deformed structures. Syntectonic hydrothermal growth by incipient nucleation along crystal edges limited domain size and thus also the $CIS_{chlorite\ 002}$ values. The hydrothermal event did not last long enough to allow further crystal growth. The retarded $CIS_{illite}$ and $CIS_{chlorite}$ grades can be best explained by limited duration (probably <5000 y) of the hydrothermal event which for a short time reached epithermal temperatures. The hydrothermal fluid flow was caused by dewatering of sedimentary rocks during thrusting and tectonic thickening within the Variscan orogen and it was focused along the Aachen thrust which represents the frontal Variscan thrust.

**Key Words**—Aachen, Chlorite, CIS, Crystallinity, Fluid Flow, Hydrothermal, Illite, Integral Breadth, Variscan Orogeny, Wurm Syncline.

## INTRODUCTION

Clay minerals respond to increasing temperatures, pressures and changing fluid compositions by generating a reaction series, in which, *e.g.* smectites form mixed-layered phases, which, in turn increase in illite layers, until pure illite and finally muscovite is produced (Hower *et al.*, 1976). This reaction series is accompanied by a progressive increase in crystal thicknesses ('illite crystallinity'), which shows up not only as increasingly sharper peaks in X-ray diffraction (XRD) patterns, but was verified by transmission electron microscopy (TEM) observations (*e.g.* Środoń *et al.*, 1992; Árkai *et al.*, 1996). This peak sharpening of illites was first used by Weaver (1960) and Kübler (1964) to determine and define diagenetic and very low-grade metamorphic zones. Being a complex, sometimes strictly empirical parameter, the full width at half maximum height (FWHM) of the 001 peak of illite served long as the Kübler index (KI), but it became increasingly obvious that KI is influenced by many parameters and must not be overinterpreted (Guggenheim *et al.*, 2002; Jaboyedoff *et al.*, 2001; Kübler and Jaboyedoff, 2000). For example, small amounts of swelling layers (*e.g.* Eberl and Velde, 1989) increase the peak breadth as do interstratifications with other non-illitic layers, *e.g.* paragonite or margarite (Battaglia *et al.*, 2004). Apart from purely instrumental effects, which could be corrected by standards (Kisch, 1990; Warr, 1996), even the particle-size distribution itself influences the peak breadth (Langford *et al.*, 2000). Inclusion of other basal reflections in combination with fitting techniques (*e.g.* Lanson and Kübler, 1994) and/or simulations with Newmod (Eberl and Velde, 1989; Warr and Nieto, 1998) are therefore necessary to extract more information from the XRD patterns.

A quite different but related aspect of 'crystallinities' is the general question of whether we may interpret them in terms of thermodynamics or better in terms of kinetics. Merriman (2005) suggested that especially in low-*T* environments, sluggish reaction kinetics prevail over thermodynamic equilibrium (*e.g.* Robinson and Merriman, 1999; Essene and Peacor, 1995). Despite their attempt to minimize the free energy of the system, mineral assemblages and their properties reflect reaction

* E-mail address of corresponding author:
sindern@rwth-aachen.de
DOI: 10.1346/CCMN.2007.0550209

progress but not a thermodynamic equilibrium *sensu stricto*. As a consequence, it is not temperature itself which is mirrored in a mineral assemblage. Rather it is energy flux, which may comprise heat flow as well as tectonically induced strain energy – assuming that the chemical composition of a system stays relatively constant. In very high heat-flow geothermal systems, such as the Salton Sea geothermal field, clays reached the supermature stage during a heating event of only 10,000 y (Yau *et al.*, 1988; Velde and Lanson, 1993). In a study of the East Slovak Basin, Clauer *et al.* (2003) distinguished between illite growth either controlled by burial or by hydrothermal activity.

Little is known, however, for a geological situation like a thrust system, in which strain energy as well as both burial and hydrothermal heat flow contributed to the total energy flux. Such a system is represented by the Variscan Aachen-Midi thrust in Germany, the northernmost large-scale thrust fault of the Variscan orogeny (Oncken *et al.*, 1999) with a displacement of at least 17 km (von Winterfeld, 1994). Increased vitrinite reflectance data within a few km to the N and S of the Aachen thrust point to enhanced heat flow up to 0.15 W/m$^2$ along this structure in Carboniferous times (Lünenschloss, 1998; Teichmüller and Teichmüller, 1979; von Winterfeld, 1994; Oncken *et al.*, 1999) which exceeds the present-day value for this region of 0.07–0.08 W/m$^2$ (Lünenschloss, 1998). Evidence of hydrothermal activity in this region is found in veins within core material of the 2544 m deep RWTH-1 geothermal well (Chatziliadou *et al.*, 2005; Lögering *et al.*, 2005, 2006) which was drilled in 2004 only 500 m to the north of the Aachen thrust. The aim of this work was therefore to test whether energy flux by strain, burial or short-termed hydrothermal heat flow have left interpretable fingerprints on illites and chlorites.

## GEOLOGICAL SETTING

The site of the RWTH-1 drill-hole within the city of Aachen is located ~500 m to the north of the Aachen thrust which is the NE prolongation of the Faille de Midi (Oncken *et al.*, 1999). Along this south-dipping structure, Devonian to Carboniferous carbonaceous and siliciclastic units of the Aachen imbrication zone and the Venn-Weser-Inde nappe are thrust above the Wurm syncline (Figure 1). The upper 1000 m of the RWTH-1 drill-hole consists of Upper Carboniferous strata (Westfalian, Namurian, Österreich *et al.*, 2005). Marked by a characteristic change in lithofacies (Lundershausen *et al.*, 2005), these units are unconformably followed by Famennian shales and slates (in part equivalent to the Cheiloceras zone) up to 1448 m. The section from 1448 m to the end at 2544 m is predominantly composed of Lower Devonian sandstones and siltstones so far not described in detail. Cores were cut in the depth intervals 1392–1515 m, 2128–2143 m and 2536–2544 m. The first interval is characterized by intensive deformation and hydrothermal vein formation within a fault zone.

The compressive Variscan deformation and contemporaneous metamorphism in the Venn-Weser-Inde nappe was dated by Nierhoff (1994) at between 336 and 300 Ma on the basis of K-Ar analyses. Glasmacher *et al.* (2001) defined an age of 314±7 Ma for the Variscan cleavage deformation and a minimum age of 300±8 Ma for a late-stage hydrothermal fluid flow event using Ar-Ar dating. For the southern Venn-Weser-Inde nappe, peak temperatures of ~330ºC to 400ºC of the Variscan metamorphism are constrained by fluid-inclusion, mineral paragenesis, chlorite-thermometry and vitrinite data (Hilgers *et al.*, 2006; Vogtmann-Becker, 1990; Glasmacher, 1995; Oncken *et al.*, 1999; Zhang *et al.*, 1997) and Kübler index (epizonal grade, Tschernoster *et al.*, 1995). Based on vitrinite and fluid-inclusion data, Oncken *et al.* (1999) assumed that peak temperatures decrease to 250–280ºC in the northern part of the Venn-Weser-Inde nappe (Inde syncline).

In larger areas of the foreland of the Aachen thrust, lower temperatures can be expected. On the basis of mineralogical, textural and vitrinite reflectance data obtained in Carboniferous to Devonian rocks of the Liege syncline to the east of the Wurm syncline, Hollmann (1997) derived a temperature of 200ºC which is also consistent with maximum burial depths of 4.5 km (Rottke and Stroink, 1999). For the zone close to the Aachen thrust and especially for the Wurm syncline, detailed temperature information is mainly given by organic maturity data. Vitrinite reflectance, $R_{max}$, shows a correlation with stratigraphic position and ranges between 1.5 and 3.6% (Teichmüller and Teichmüller, 1979; von Winterfeld, 1994). For this region Fielitz and Mansy (1999) also reported temperatures of ~200ºC. Due to numerous vitrinite reflectance data within Carboniferous rocks (Babinecz, 1962; Teichmüller and Teichmüller, 1979; Steingrobe, 1990; von Winterfeld, 1994) it is well established that within the Upper Carboniferous of the Wurm syncline, vitrinite reflectance increases from north to south (Figure 1). One anomalously high $R_{max}$ value of 6.70% in Famennian rocks in the city of Aachen was reported by von Winterfeld (1994), and Oncken *et al.* (1999) pointed to epizonal peak $R_{max}$ values up to 7.3% at the Aachen-Midi thrust. Increased vitrinite reflectance is observed in the footwall of the Aachen-Midi thrust in a belt with a width of a few kilometres parallel to the Aachen-Midi thrust extending from the north of Aachen to Namur in Belgium (Knapp, 1980; von Winterfeld, 1994). Maturation of the organic material is older than deformation (Knapp, 1980) and therefore of Carboniferous age. The increased values of vitrinite reflectance along the Aachen thrust are explained by enhanced heat flow close to this structure during upper Carboniferous times (Teichmüller and Teichmüller, 1979; Knapp, 1980).

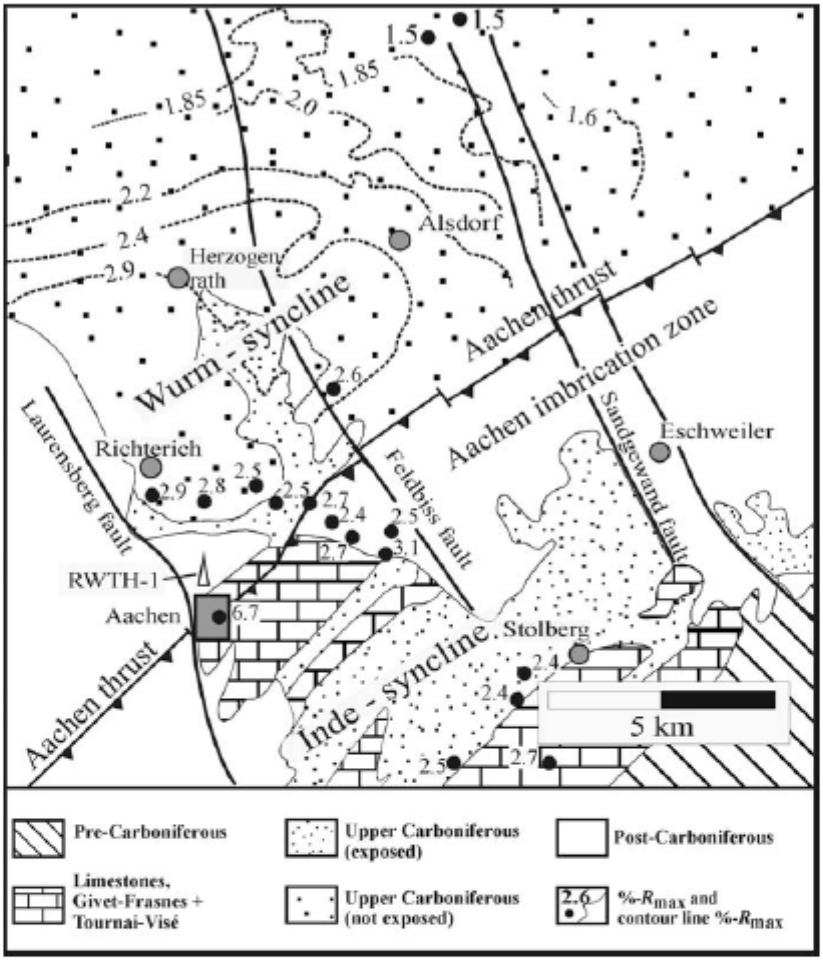


Figure 1. Geological sketch map of the RWTH-1 drill-hole location and the Aachen region, modified from Steingrobe (1990). Figures indicate the vitrinite reflectance (%-$R_{max}$) within Upper Carboniferous sediments except for the $R_{max}$ value within the city of Aachen that was derived from a Famennian rock outcrop which is too small to be shown on the map (Babinecz, 1962; Teichmüller and Teichmüller, 1979; von Winterfeld, 1994). The triangular symbol marks the position of the RWTH-1 drill-hole in the north of Aachen and to the north of the Aachen-Midi thrust which is here named Aachen thrust. The Aachen imbrication zone and the Inde syncline form the northernmost structures of the Venn-Weser-Inde nappe mentioned in the text.

Using numerical modeling, Lünenschloss *et al.* (1997) and Lünenschloss (1998) explained the regional distribution of vitrinite reflectance in the Wurm syncline and pointed out that under realistic burial depths of 4.5 km (Rottke and Stroink, 1999), significant fluid discharge in the footwall of the Aachen thrust is required. According to this model, paleotemperatures between 210 and 310ºC can be assumed for the rock units of the RWTH-1 drill-hole. A recent study of fluid inclusions, calcite-dolomite equilibria and chlorite composition of samples from the RWTH-1 drill core (Lögering *et al.*, 2006), indicates temperatures of 280–370ºC for minerals formed in the veins which are characteristic of the upper core section. High temperatures and low salinities of fluids (<9 wt.%) are considered similar to those of Variscan tectonic brines described by Behr *et al.* (1993) (Lögering *et al.*, 2006).

In post-Variscan times the region was affected by Pb-Zn mineralization at temperatures below 150ºC which was also controlled by major fracture zones (Muchez *et al.*, 1994; Friedrich *et al.*, 1993). For the Pb-Zn deposit of Mechernich (Germany) Schneider *et al.* (1999) derived a Jurassic age of 168±6 Ma.

## SAMPLES AND METHODS

### *Sample preparation*

Samples exclusively from drill-cores were used except for three samples from cuttings (Table 1), which were taken for testing methods and for compar-

Table 1. Description of RWTH-1 samples, mineral composition in the order of modal abundance in whole rock, and structural information for the <2 µm fraction.

| Sample | Depth (m) | Lithology | Mineral composition, wr | *d* value Il (005) Å | CIS (illite 001) | CIS (chlorite 002) | Wt.% of serpentine in chlorite* |
|---|---|---|---|---|---|---|---|
| 158 | 190.20 | shale | Qz, Chl, Wm, Fsp | 2.0010 | 0.61 | 0.33 | 7.3 |
| 18-2 | 1438.00 | slate | Qz, Wm, Chl | 2.0014 | 0.52 | 0.34 | 11.2 |
| 18-3 | 1439.40 | slate | Qz, Chl, Wm | n.d. | 0.50 | 0.33 | 10.2 |
| 20-3 | 1444.70 | slate | Qz, Chl, Wm, Cc | n.d. | 0.58 | 0.35 | 12.6 |
| 25-16 | 1457.40 | siltstone | Qz, Wm, Chl, Hm, Dol | 2.0036 | 0.50 | 0.31 | 9.5 |
| 1860red | 1936.10 | slate | Qz, Chl, Wm, Hm | 2.0014 | 0.59 | 0.31 | 5.4 |
| 1860grn | 1936.10 | slate | Qz, Chl, Wm | 2.0007 | 0.50 | 0.29 | 4.2 |
| 52-1 | 2141.40 | shale | Qz, Chl, Wm, Fsp | 2.0007 | 0.46 | 0.26 | 3.2 |
| 54-1 | 2537.70 | shale | Qz, Chl, Wm, Fsp, Cc | n.d. | 0.46 | 0.31 | 6.7 |
| 59-1 | 2542.00 | shale | Qz, Fsp, Chl, Wm, Cc | 2.0013 | 0.45 | 0.28 | 9.7 |

Abbreviations: Cc = calcite, Chl = chlorite, Dol = dolomite, Fsp = feldspar, Hm = hematite, Il = illite, Qz = quartz, Wm = white mica, wr = whole rock, n.d. = not determined.
Samples 158, 1860red and 1860grn are from cuttings.
Samples 18-2, 18-3, 20-3, 25-16 are from the first core interval.
Samples 52-1 represent the second and 54-1, 59-1 the third core intervals.
* Maximum abundance of serpentine in chlorite (wt.%) based on Newmod® calculation of $w(001_{chlorite}) - w(004_{chlorite})$

ison purposes. To prepare the <2 µm fraction, only rock pieces without macroscopically visible veins or chlorite-filled planes were selected.

Samples were washed and carefully crushed and ground under water in a mortar mill for 5 min under constant machine parameters thus minimizing and keeping constant, preparation effects on crystallinity (Krumm, 1992). The <2 µm fraction was obtained by settling after Sr saturation according to Eberl *et al.* (1987). From the clay fractions, ~200 mg were dispersed in 2 mL of $H_2O$ and transferred to glass slides measuring 28 mm × 48 mm. Preliminary measurements showed that the reproducibility at sample loadings of <10 mg/cm$^2$ were not satisfactory (Etoundi, 2006). Therefore, loading of 15 mg/cm$^2$ was chosen, which yields samples infinitely thick to the X-ray radiation.

### *X-ray diffraction and interpretation of peak-profile shapes*

The air-dried specimens were scanned from 2 to 35°2θ and from 47 to 61°2θ (for 005 illite) in steps of 0.015°2θ using filtered CoKα radiation. The Huber 423 goniometer ($r$ = 223 mm) was equipped with two Soller slits with an axial divergence of <0.5°. The divergence slits were set to values where beam overflow had no influence on the peak shape. Polytype determination of illite was performed on the randomly distributed material of the <2 µm fraction using a Guinier image plate camera (Huber G670). The scans were fitted with MacClayFit (Stanjek and Häusler, 2000).

Interpretations of peak parameters in terms of 'crystallinity', 'particle size' or 'strain' have to be done with caution because the observed profile, $h$, is actually the convolution of the pure diffraction profile, $f$, of the sample with the profile of the instrument, $g$. Although the extraction of $f$ is possible using Stoke's method (Klug and Alexander, 1974), the pure diffraction profile, $f$, is itself the fold of several diffraction effects. The most important contribution to the integral breadth ($w$) of the profile $f$ stems from an average coherence length, which is frequently identified as being similar or even equal to the apparent particle size perpendicular to the reflecting planes (*e.g.* Guinier, 1963). The profile shape of such a pure size-broadened sample has contributions from both Lorentzian and Gaussian profiles, which make up the Voigt profile (Langford and Wilson, 1978). In preliminary evaluations we used the numerical approximation to the Voigt profile as given by Thompson, Cox and Hastings (Thompson *et al.*, 1987) for extracting the Gaussian and Lorentzian contributions to the 00$l$ peaks. Non-systematic variations of both parameters rendered this approach inapplicable. Consequently, for the present study the Pseudo-Voigt function was used for illite and the integral peak breadths were interpreted without considering the profile shape.

The chlorite peaks were fitted with a Pseudo-Voigt function, whereas the two quartz peaks (which served as an internal standard) were modeled with a Thompson-Cox-Hastings function using the *X* (Scherrer broadening) and the *W* parameter (Gaussian component). The latter function couples the peak breadths of the 100 and the 101 peaks and enabled the separation of the illite 003 peak from the 101 of quartz. The goodness-of-fit ranged between 1.06 and 1.48.

Apart from a volume-averaged particle size, the kind and dispersion of the particle-size distribution affects the profile shape (Rao and Houska, 1986; Langford *et al.*, 2000) and the particle shape in turn changes the profile shape and may yield anisotropic peak broadening (Scherrer, 1918; Langford and Wilson, 1978). Further contributions to the profile shape come from mixed layering and from stacking faults which, however, would only affect *hk*0 reflections (Mering, 1949). The latter are not measured in textured samples used here. The contribution of strain to the profile shape can principally be assessed by the method of Bertaut (1950), but requires Fourier analyses and, hence, reference samples which yield the instrumental profile, *g*. Consequently, it is evident that for a study that is not based on Fourier deconvolution, even the evaluation of four to five 00*l* peaks does not allow us to quantify the contribution of strain. As the most important contribution to the peak breadth is given by the average coherence length, the integral breadths, *w*, of illite and chlorite are considered to primarily reflect crystal thickness (*i.e.* 'crystallinity').

Since glycolation of samples did not give peak widths significantly different from air-dried samples (Etoundi, 2006), we report here only results from air-dried specimens.

*Standardization procedures*

For standardization to the 'crystallinity' index standard (CIS) according to Warr and Rice (1994), repeated analyses of the standards SW1 to SW6 resulted in the conversion equations:

$$CIS_{illite\ 001} = w_{uncalibrated} * 1.147 + 0.050,\ R^2 = 0.92$$
$$CIS_{chlorite\ 002} = w_{uncalibrated} * 1.004 + 0.080,\ R^2 = 0.96$$

Thus, effects caused by sample and slide preparation and also by using Co instead of Cu radiation are eliminated. Four true replicates of sample 158 (including rock-sample preparation, glass-slide production and XRD analysis) yielded a precision for the $CIS_{illite\ 001}$ and $CIS_{chlorite\ 002}$ of 0.028° and 0.023° (1σ), respectively. For *d* values, a precision of 0.003° was obtained. For simplicity and in order to mark the standardized character of the data, the established abbreviation 'CIS' (crystallinity index standard, Warr and Rice, 1994) and the term 'crystallinity' are used here though the one-dimensional XRD data are not suitable to define the 'crystallinity' of a three-dimensional structure (Guggenheim *et al.*, 2002).

*Chemical analyses and IR spectrometry*

The K concentration of the <2 µm fraction was obtained using HF-$H_3BO_4$ dissolution in a microwave equipped with Teflon bombs and quantitative determination by inductively coupled plasma-optical emission spectroscopy (Perkin Elmer DV 2000). Nitrogen analysis of the <2 µm fraction was performed in the 'Zentralabteilung für Chemische Analysen', Forschungszentrum Jülich (analyst M. Michulitz) on a TC436Ar (Leco) analyzer with a thermal conductivity detector at $T_{max}$ = 2700°C with He as the carrier gas. Determination of $C_{org}$ was carried out using a RC-412 (Leco) analyzer at $T$ < 500°C with oxygen gas. $CO_2$ produced by combustion was detected by infrared (IR) absorption. The precision of both methods is better than 4%. The IR absorption spectra were measured with a resolution of 2 $cm^{-1}$ on a Perkin Elmer 1600 FTIR spectrometer using discs made of 200 mg NaCl and 1 mg of sample. The sample material was decarbonated with 0.5 N HCl and oxidized using $H_2O_2$ (15%) in order to eliminate organic matter.

## RESULTS

The samples are slates and shales mainly composed of quartz, illite, chlorite and in some cases also hematite and calcite or dolomite (Table 1, Figure 2). Feldspar is a minor constituent in samples 158, 52-1, 54-1 and 59-1 (Table 1). Based on the 002 reflections of microcline and albite in the whole-rock samples, one can assume that albite is more abundant than K-feldspar. This is in line with the results of Flehmig (1983) who found that in Upper Devonian shales and silty shales of the Rhenohercynian, albite is generally at least twice as abundant as K-feldspar. Calcareous microfossils show stylolite planes indicative of pressure solution (sample 20-3).

Quartz grains show pressure solution creep with quartz overgrowth in strain shadows. Samples 18-2, 18-3 and 20-3 are locally deformed by cataclasis with transgranular fractures and grain-size reduction, in which the quartz grains locally expose dislocation glide deformation as shown by undulose extinction (Figure 2b). The transgranular fractures are filled by calcite. Quartz veins are blocky to elongate blocky and partly recrystallized by subgrain rotation and grain-boundary migration recrystallization. These features point to intensive deformation within a fault zone in the upper core section (1392–1515 m). Samples 18-2, 18-3, 20-3 are strongly cleaved and, locally, the S1 cleavage is overprinted by a second set of cleavage planes (S2, Figure 2a). Cleavage S2 is oriented oblique to S1 indicating shear deformation. Chlorite which is characterized by greenish-blue anomalous interference colours indicative of an Fe-rich variety (Deer *et al.*, 1992) also occurs in fine sheets and veins. It is the dominant mineral in cleavage planes and veins where it

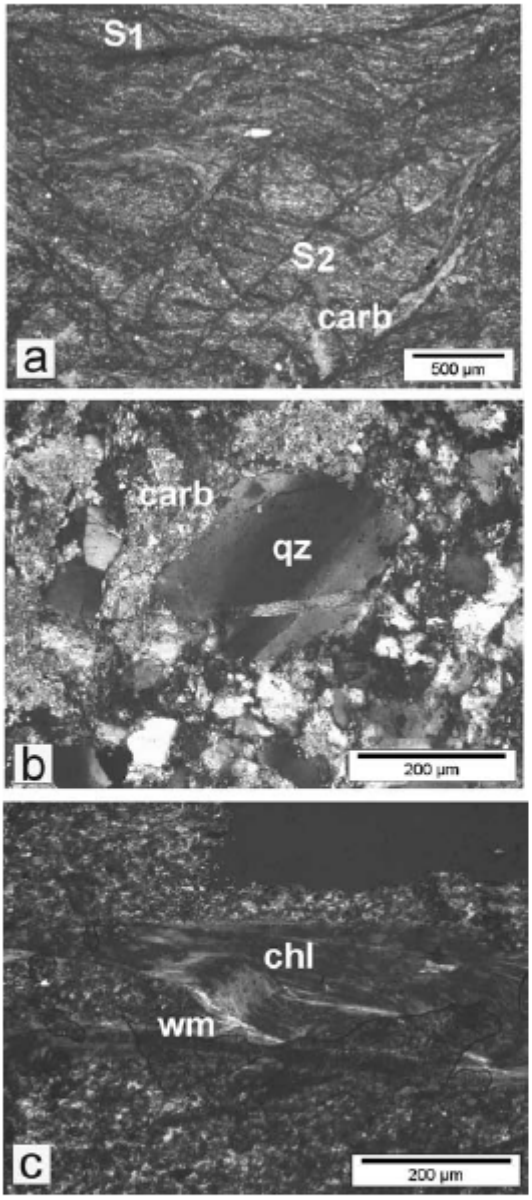


Figure 2. Thin-sections of representative samples from the upper core section of the RWTH-1 drill-hole, under crossed polars: (a) sample 18-2, S1 and S2 are cleavage planes with chlorite, carbonates (carb) form irregular patches which are sub-parallel to S2 as well as irregularly distributed; (b) sample 18-2, undulose extinction of detrital quartz (qz), carbonates are marked by carb, lower half of the photo predominantly shows detrital quartz; (c) sample 18-3, undulose extinction in folded platy chlorite (chl), light gray flakes are white micas (wm) formed in chlorite.

is associated with quartz giving evidence for a fluid and strain-controlled crystallization of chlorite. Chlorite overgrows calcite veins, implying formation after calcite-vein generation. Within cleavage planes, chlorite crystals are partly bent and show undulose extinction. White mica occurs in the matrix as detrital grains and sometimes formed in extension cracks between chlorite crystals in cleavage planes and chlorite veins (Figure 2c). These white micas which are only found in sample 20-3 crystallized during deformation along the cleavage planes with sizes up to 100 µm (Figure 2c).

Shaley rocks (*i.e.* samples 158, 52-1, 54-1, 59-1) and siltstone sample 25-16 contain chlorite veinlets associated with quartz veins. The presence of chlorite veins underlines the hydrothermal formation of chlorite in these rocks, too.

*Illite and chlorite, structural information*

The results of the XRD analyses on textured slides are presented in Table 1 and in Figures 3 and 4. Analysis of the randomly oriented samples (<2 µm fraction) indicates that illites belong to the $2M_1$ polytype. The $w(001_{illite})$ decreased only slightly when the samples were treated with ethylene glycol. This indicates that the number of swelling layers is very small or non-existent, though small amounts of smectite have to be expected in order to explain the variation of $w(00l_{illite})$ (Figure 3a). The $d$ values for the illite 005 reflection of all samples vary between 2.0007 and 2.0036 Å (Table 1).

Taking into consideration that a representative $d_{005}$ value for a $2M_1$ white mica is 2.00148 Å (Brindley, 1980) one can state that, within the precision of the method (here 0.003 Å), the $d_{005}$ values of illite in the samples are identical to this value. As $hk0$ reflections cannot be determined in oriented specimens, the data do not allow us to discuss possible stacking defects which may be caused by deformation (Merriman and Peacor, 1999). However, significant structural distortion would lead to a positive correlation of $w(00l_{illite})$ and $\tan(\theta)$ (*i.e.* increasing order of the reflection) which cannot be observed (Figure 3a).

The basal reflections of chlorite (<2 µm fraction) in all samples show a similar pattern (Figure 3b) to those of illite (Figure 3a). The $w(00l_{chlorite})$ values vary around a constant value and do not increase significantly with increasing order. This precludes significant structural distortion which could be expected considering the bent sheets of chlorite showing undulose extinction (Figure 2). The variation of the $w(00l_{chlorite})$ indicates the presence of serpentine layers within chlorite (Reynolds *et al.*, 1992). A Newmod® simulation (Table 1) on the basis of the ratios of $w(001_{chlorite})$ to $w(004_{chlorite})$ points to serpentine abundances of up to 12.6 wt.% within chlorite (Table 1).

*Illite and chlorite grades*

$CIS_{illite\ 001}$ ranges from 0.45 to 0.61 with the highest values (*i.e.* lowest grade) in the cuttings and the lowest values in the lowermost drill-core sample (Table 1,

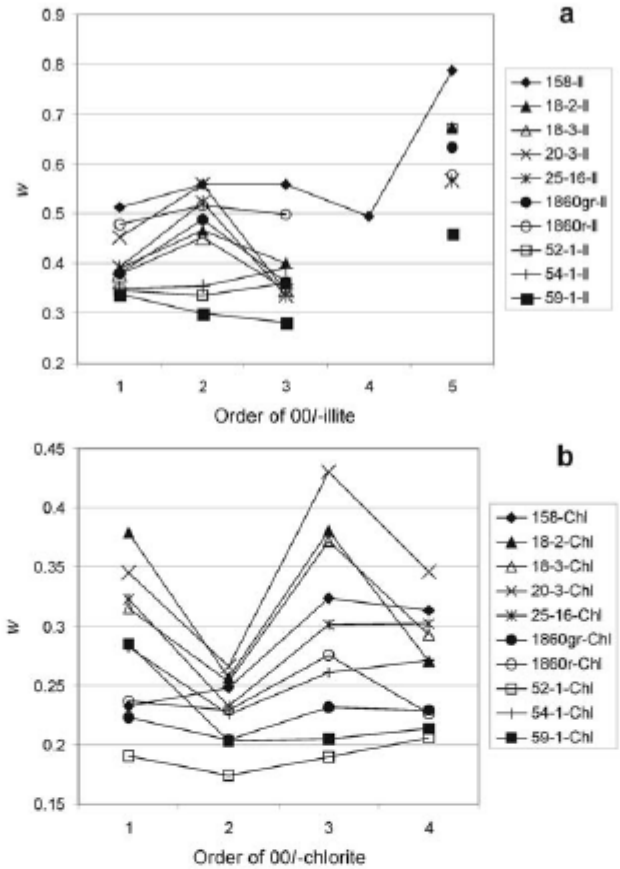


Figure 3. Integral breadth ($w$) in °2θ (CoKα) of basal reflections of illite (a) and chlorite (b) in <2 μm fractions. Integral breadths were multiplied by cos(θ) in order to account for Scherrer broadening.

Figure 4). The zone of the upper-core section, which is characterized by intensive deformation and vein formation, shows varying $CIS_{illite\ 001}$ values. However, within the limits of precision, all illite data overlap to a large extent. Taking the $CIS_{illite\ 001}$ values and the absence or presence of only small proportions of interlayered smectite into account, the illite data of all RWTH-1 samples would indicate late diagenetic grade (Merriman and Peacor, 1999) over the whole drill-core.

In contrast to the $CIS_{illite\ 001}$, the $CIS_{chlorite\ 002}$ of chlorite points to anchizonal grades in the lower-core sections (average of $CIS_{chlorite\ 002}$ = 0.28) whereas the upper-core section shows diagenetic grade for chlorite (average of $CIS_{chlorite\ 002}$ = 0.33, Figure 4). Most data show a large overlap within the limits of precision.

*Ammonium in illite*

Ammonium-rich clay minerals have often been described and are supposed to affect determination of illite 'crystallinity' (Árkai *et al.*, 2004, and references therein). In sedimentary settings, $NH_4$, probably derived from maturing organic matter, may be adsorbed on clay mineral surfaces or it substitutes for K in the interlayer position (*e.g.* Williams *et al.*, 1989; Šucha *et al.*, 1998). Nieto (2002) showed that either K or $NH_4$ predominate in distinct packets of dioctahedral illite clay minerals or white mica. The $NH_4$-rich illite component is called tobelite after the Tobe mine (Higashi, 1982 in Árkai *et al.*, 2004).

Krooss *et al.* (2005) pointed out that significant amounts of inorganic $NH_4$ exist in Carboniferous shales of the North German Basin and Mingram *et al.* (2005) found that 50–100% of N in this basin is fixed as $NH_4$ in inorganic phases. This and the potential role of $NH_4$ for illite 'crystallinity' necessitated $NH_4$ determination in the samples studied here in those cases in which enough of the limited drill core material was available. Nitrogen in the <2 μm fraction can be present in organic phases and as $NH_4$ in K-bearing minerals such as illite. In order to distinguish between organic and inorganic N the total organic carbon concentration (TOC) and the N/C ratio in the organic phases have to be known (Árkai *et al.*, 2004). Krooss *et al.* (2005) determined N/C ratios from kerogen of Paleozoic rocks of the North German Basin which range between 0.006 and 0.016 (by weight).

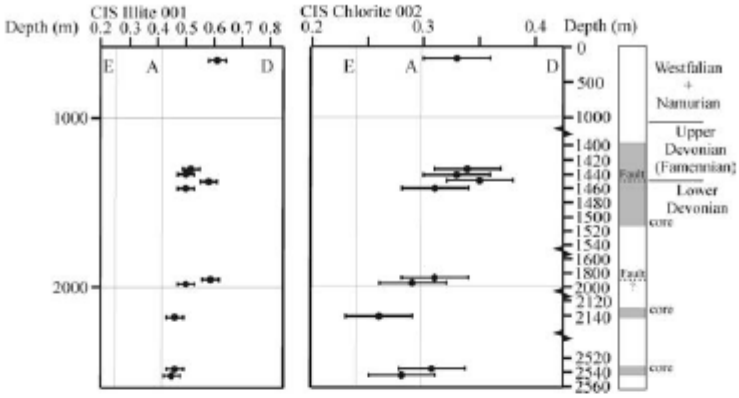


Figure 4. CIS values *vs.* depth of the RWTH-1 drill-hole. Gray fields on the right side mark core sections; depth not to scale. E, A and D denote epizone, anchizone and diagenetic zones, respectively. Limiting values for illite by Kübler (1968, 1990) and for chlorite by Árkai *et al.* (1996). Stratigraphic information according to Österreich *et al.* (2005).

The $K_2O$ concentration of the <2 µm fractions (Table 2, samples 158, 20-3, 25-16) which consist of illite, chlorite and quartz can be used to quantify the amount of illite (wt.%) because this is the predominant K-bearing phase. As K-feldspar, another K-bearing mineral, was detected by XRD as being only a minor constituent in the whole-rock fraction of sample 158 (Table 1), and even less common in the <2 µm fraction, K-feldspar is considered as insignificant here. For this calculation, a $K_2O$ concentration of 7.6% was assumed for the illite according to Środoń *et al.* (1986).

After assessment of the illite abundance and calculation of the minimum and maximum amounts of inorganic N derived from N/TOC ratios mentioned above (Krooss *et al.*, 2005), considered to be entirely incorporated in illite (not in chlorite or quartz), one can estimate the $NH_4$ amounts in illite (Table 2) which range between 0.19 and 0.44 wt.%. As the <2 µm fraction was Sr saturated, $NH_4$ is considered to be situated in interlayer position rather than being adsorbed on the surface. On the basis of the sum of N + K, the molar proportion of $NH_4$ in illite would range between 11.8 and 27.4%. However, such $NH_4$ concentrations should lead to a shift in the basal reflection towards higher *d* values (Árkai *et al.*, 2004; Drits *et al.*, 1997). Assuming a linear increase of the *d* value with increasing $NH_4$, at least for small amounts of $NH_4$ and independent of the distribution of $NH_4$ (Drits *et al.*, 1997), and that the pure $NH_4$-illite (*i.e.* tobelite) has a *d* value of 2.048 Å (Árkai *et al.*, 2004), a molar $NH_4$ abundance of 15% should result in a $d_{005}$ value of 2.0085 Å. This is beyond the limits of precision (0.003 Å) greater than the maximum *d* value of 2.0036 Å (Table 1) in the illites of the RWTH-1 drill core and thus points to $NH_4$ abundance in illite of <15%. Fourier transform infrared (FTIR) absorption spectra of the <2 µm fractions confirm this result. These show the characteristic absorption near 1430 $cm^{-1}$ indicative of $NH_4$ in phyllosilicates whereas absorption between 2800 and 3300 $cm^{-1}$ caused by N–H stretching (Wilson *et al.*, 1992; Pironon *et al.*, 2003) is not pronounced. If compared to absorption spectra of smectite saturated in solutions of various $NH_4$/K ratios, the sizes of the absorbance peaks near 1430 $cm^{-1}$ of the <2 µm fractions are consistent with $NH_4$ abundance in illite <15%. It is possible that the $NH_4$ concentrations in illite derived from the chemical analyses are too high as they are based on the assumption of N/TOC ratios in kerogen similar to characteristic ratios in the North German Basin (Krooss *et al.*, 2005). The N/TOC ratio in kerogen may be greater in the rocks of the RWTH-1 drill core.

Table 2. Total organic carbon (TOC), N and $K_2O$ concentrations in the <2 µm fractions of the RWTH-1 samples and calculated illite abundance* and $NH_4$ concentration in illite. All data in wt.%. See text for further explanation.

| Sample | Lithology | TOC | N | $K_2O$ | Illite* | $NH_4$ ** | $NH_4$ *** |
|---|---|---|---|---|---|---|---|
| 158 I | Shale | 1.55 | 0.144 | 3.04 | 40.0 | 0.36 | 0.44 |
| 20-3 | Slate | 0.36 | 0.101 | 3.75 | 49.0 | 0.19 | 0.21 |
| 25-16 | Siltstone | 0.38 | 0.31 | 3.71 | 48.8 | 0.25 | 0.26 |

* based on the assumption of 7.6 wt.% $K_2O$ in illite (Środoń *et al.*, 1986)
** based on N/TOC = 0.02
*** based on N/TOC = 0.005

## DISCUSSION

In the samples studied here, hydrothermal syntectonic crystallization of chlorite and white mica (sample 20-3) can be observed. Quartz in cataclastic fault zones exhibits discontinuous undulose extinction and quartz in veins shows grain boundary migration/sub grain rotation recrystallization. Such features point to minimum temperatures of 200–250ºC (Oncken, 1989) for the hydrothermal event represented in the RWTH-1 drill core. This is in agreement with homogenization temperatures of up to 370ºC in veins (Lögering *et al.*, 2006). The temperatures of the hydrothermal event are greater than those derived by paleogeothermometers of the host-rock in the foreland of the frontal Variscan thrust of ~200ºC (Hollmann, 1997; Rottke and Stroink, 1999). This supports previous assumptions that hydrothermal fluid flow was necessary to explain the high coalification grades close to the Aachen thrust (von Winterfeld, 1994; Lünenschloss *et al.*, 1997; Lünenschloss, 1998). As was indicated by Knapp (1980), maturation of organic material and therefore also the hydrothermal event discussed here is of Carboniferous and thus Variscan age. The fluids have characteristic features (*i.e.* temperature, salinity) of tectonic brines (Lögering *et al.*, 2006, Behr *et al.*, 1993) which also point to the Variscan event. The alternative – that the hydrothermal event is post-Variscan – is less plausible because post-Variscan mineralization occurred at temperatures predominantly <150ºC (Muchez *et al.*, 1994; Friedrich *et al.*, 1993; Redecke, 1992) and caused the formation of Pb-Zn-sulfides which are absent from the RWTH-1 drill core (Chatziliadou *et al.*, 2005; Lögering *et al.*, 2005).

Thrusting and thrust loading, as can be expected within the orogenic wedge to the south of the Aachen thrust during the Variscan orogeny, caused fluid expulsion into the foreland (Oliver, 1986; Moore, 1989; von Winterfeld, 1994) and fluid-overpressure formation above and below the thrust plane, if the bulk rock is of intermediate permeability (Smith and Wiltschko, 1996). In our field area, both hangingwall and footwall consist of shale-sandstone multilayers and thus have the potential to keep fluid pressures high over the time-interval of the events discussed here. Ge and Garven (1992) numerically simulated the fluid expulsion associated with thrust loading and calculated a disturbance of the fluid flow field. They proposed that fluid expulsion towards the foreland takes ~5000 y before returning to normal hydrological conditions. The injection of hot fluids would thus increase the temperature in the host-rock adjacent to the Aachen thrust during a period of 5000 y.

### *Illite*

In contrast to the thermal indicators (*i.e.* mineralogical observations of the RWTH-1 drill core, published vitrinite and fluid inclusion data) mentioned above, the $CIS_{illite}$ data reflect a late diagenetic grade and thus temperatures approaching <200ºC.

A lower grade of illite relative to chlorite and other grade indicators is common and discussed frequently (Árkai *et al.*, 2004; Maynard *et al.*, 2001; Wang *et al.*, 1996). It can be ascribed to a retarded reaction progress of illite which is due to isolation of phyllosilicates from porefluids (*i.e.* low water/rock ratio, Pollastro, 1993) caused by precipitation of secondary minerals (Árkai *et al.*, 2004). Also, low K activity and high $H_2O$ pressure slow down the smectite-illite reaction (Árkai *et al.*, 2004; Pollastro, 1993). The concentration of $K_2O$ in the rocks of RWTH-1 drill-hole varies between 1.38 and 4.81 wt.% depending on the amount of detrital white mica, clay minerals and minor detrital K-feldspar (Sindern, unpublished data). It is therefore assumed that K should have been present in a pore-fluid. Ammonium substitutes for K in the illite structure to <15% and is therefore also considered less significant as a reason for decreasing the growth rate of illite.

As was pointed out in the method section above, the XRD profile from textured samples mainly reflects crystallite size but cannot be used to quantify structural distortion unless extensive corrections are applied to the peak profiles. If deformation in the rocks of the RWTH-1 drill-hole had a significant impact on the illite structure leading to the high integral breadth *w*, as was described by Árkai *et al.* (1997) for rocks in the hangingwall of the Glarus thrust in Switzerland (Merriman and Frey, 1999), this should be reflected in our samples here because the different core intervals show different degrees of deformation. In this case one would expect that CIS values from the slate samples mainly of the first core interval would be greater than those of shale and siltstone samples. A comparison of the average $CIS_{illite\ 001}$ of the more intensively deformed samples (0.54±0.04 SD) with the average $CIS_{illite\ 001}$ of the less deformed samples (0.50 ± 0.07 SD) (Table 1, Figure 4) makes clear that deformation does not have a significant impact on the $CIS_{illite\ 001}$.

In the samples studied here, illite is almost entirely restricted to the rock matrix whereas chlorite occurs in veins, attesting to the role of fluids especially in the formation of chlorite. Crystal growth of chlorite was therefore probably faster than growth of illite within the less permeable matrix. This explains why in some cases $CIS_{chlorite}$ indicates higher grades than $CIS_{illite}$ (Figure 4). Transfer of elements during the (hydro-) thermal peak and thus illite growth was restricted because the duration of the event was too short for the permeability conditions in the rock. The late diagenetic grade reflected by illite is equivalent to the temperatures reported for the foreland of the Aachen thrust (200ºC, Hollmann, 1997; Rottke and Stroink, 1999, Fielitz and Mansy, 1999). As the illite of the RWTH-1 drill core seems unaffected by the hydrothermal event, it is therefore concluded that illite mirrors the burial history rather than hydrothermal fluid flow.

*Chlorite*

$CIS_{chlorite}$ data reflect a late diagenetic grade in the upper-core section and in part, anchizonal grade, in the lower-core sections (Figure 4). Chlorite which occurs in veins and cleavage planes should reflect the higher grade estimated for the hydrothermal event from the mineralogical observation. The deviation to lower $CIS_{chlorite}$ grades than expected could be explained by deformation of chlorite. However, the integral breadths, *w*, of the basal reflections do not increase with increasing order of $00l_{chlorite}$ and thus are not consistent with structure deformation being dominant (Figure 3b). This suggests that the XRD data do not reflect post-crystalline deformation. As the partly oriented structure and undulose extinction of chlorite indicate deformation effects, hydrothermal chlorite growth must have occurred syntectonically. Syntectonic hydrothermal growth of platy and fibrous chlorite occurred by incipient nucleation along the tips and edges of crystals. This probably limited domain size and thus also the integral breadth of the basal reflection. It would also explain why the chlorite precipitated at higher (up to epizonal) temperatures yields lower grades indicated by $CIS_{chlorite\ 002}$ values (*i.e.* diagenetic to anchizonal). Similar to the results derived from investigation of illite, one has to assume here, too, that the anchi- to epizonal peak thermal conditions did not last long, as otherwise one would expect domain growth under such conditions.

The finding of increased supermature $R_{max}$ values along the Aachen thrust supports the probability of a short-duration hydrothermal event. Vitrinite matures faster and its maturation is not as dependent on fluid-rock interaction as the growth of illite and chlorite (Velde and Lanson, 1993). Furthermore, in rocks in which chlorite and K-bearing phases such as illite next to detrital white mica and K-feldspar in some cases are as abundant, as in the samples studied here (Table 1), one would expect the formation of biotite (Inoue, 1995) if temperatures reached 300°C. As temperatures were as high as, or greater than 300°C, the lack of biotite points to a hydrothermal event which was too short for its growth.

## CONCLUSIONS

Investigation of material from three core sections of the RWTH-1 drill-hole in Aachen shows mineralogical and structural evidence of intensive Carboniferous (Variscan) hydrothermal activity in the footwall of the Aachen thrust. Mineral and microstructural data indicate minimum temperatures of 200–250°C, though maximum temperatures of the hydrothermal event up to 370°C can be expected taking recently published data for comparison. $CIS_{illite\ 001}$ values of 0.45–0.61 (Δ°2θ) and insignificant amounts of smectite indicate a late diagenetic grade for illite, pointing to temperatures of <200°C. Illite which contains minor amounts (<15 mole %) of $NH_4$ substituting for K is neither significantly affected by deformation nor by the hydrothermal impact but mirrors the burial history of the Wurm syncline. Chlorite, mainly formed in veins and cleavage planes, has $CIS_{chlorite\ 002}$ values between 0.35 and 0.26 (Δ°2θ) which only partly point to anchizonal grade. However, chlorite grew syntectonically as is shown by bent and predominantly stretched laths which do not have deformed structures. The evidence of syntectonic hydrothermal activity is in line with the idea that hydrothermal fluid flow was caused by fluid expulsion along the Aachen thrust due to thrusting and thrust loading during the Variscan orogeny. Syntectonic hydrothermal chlorite growth by incipient nucleation along crystal edges limited domain size and thus also the $CIS_{chlorite\ 002}$ values. The lack of larger chlorite domains indicates that the hydrothermal event, while probably reaching epizonal temperatures, did not last long enough to allow further crystal growth of chlorite and did not generate biotite. Based on numerical simulations in similar settings, one can assume a duration of ~5000 y for the expulsion of tectonic brines along the Aachen thrust which is part of the frontal Variscan front.

## ACKNOWLEDGMENTS

This study was funded by DFG grant SI 810/2-1. The work of S. Prantl who helped with the figures, of G. Siebel and J. Warnsloh who supported XRD analyses, and of Chr. Marchel and V. Havenith (all in Aachen), who assisted with FTIR spectroscopy and TOC analyses, respectively, is gratefully acknowledged. Lars Reuning (Aachen) helped to identify calcareous microfossils in one sample. We also thank R.J. Merriman, N. Liewig and R.E. Ferrell, Jr. for their constructive reviews which helped significantly to improve the manuscript.

## REFERENCES

Árkai, P., Merriman, R.J., Roberts, B., Peacor, D. and Tóth, M. (1996) Crystallinity, crystallite size and lattice strain of illite, muscovite and chlorite: comparison of XRD and TEM data for diagenetic to epizonal pelites. *European Journal of Mineralogy*, **8**, 1119–1137.

Árkai, P., Balogh, K. and Frey, M. (1997) The effects of tectonic strain on crystallinity, apparent mean crystallite size and lattice strain of phyllosilicates in low temperature metamorphic rocks. A case study from the Glarus overthrust, Sitzerland. *Schweizerische Mineralogische und Petrographische Mitteilungen*, **77**, 27–40.

Árkai, P., Livi, K.J.T., Frey, M., Brukner-Wein, A. and Sajgo, C. (2004) White micas with mixed interlayer occupancy: a possible cause of pitfalls in applying illite Kübler index ('crystallinity') for the determination of metamorphic grade. *European Journal of Mineralogy*, **16**, 469–482.

Babinecz, W. (1962) Das Inkohlungsbild des Aachener Steinkohlengebirges, dargestellt im Niveau des Flözes Großlangenberg. *Forschritte Geologie Rheinland und Westfalen*, **3**, 679–686.

Battaglia, S., Leoni, L. and Sartori, F. (2004) The Kübler index in late diagenetic to low-grade metamorphic pelites: A critical comparison of data from 10 Å and 5 Å peaks. *Clays and Clay Minerals*, **52**, 85–105.

Behr, H.J., Gerler, J., Hein, U.F. and Reutel, C.J. (1993)

Tectonic brines und basement brines in den mitteleuropäischen Variszіden: Herkunft, metallogenetische Bedeutung und geologische Aktivität. *Göttinger Arbeiten zur Geologie und Paläontologie*, **58**, 3–28.

Bertaut, E.F. (1950) Raies de Debye-Scherrer et répartition des dimensions des domaines de Bragg dans les poudres polycristallines. *Acta Crystallographica*, **3**, 14–18.

Brindley, G.W. (1980) Order-disorder in clay mineral structures. Pp. 125–196 in: *Crystal Structures of Clay Minerals and their X-ray Identification* (G.W. Brindley and G. Brown, editors). Monograph No. **5**, Mineralogical Society, London.

Chatziliadou, M., Sindern, S., Hilgers, C. and Kramm, U. (2005) Spurenelementverteilung in Gesteinen der RWTH-1 Bohrung, Aachen. *Berichte der Deutschen Mineralogischen Gesellschaft, Beih. Z. European Journal of Mineralogy*, **17**, 22.

Clauer, N., Liewig, N., Pierret, M.-C. and Toulkeridis, T. (2003) Crystallization conditions of fundamental particles from mixed-layer illite-smectite of bentonites based on isotopic data (K-Ar, Rb-Sr and $\delta^{18}O$. *Clays and Clay Minerals*, **51**, 664–674.

Deer, W.A., Howie, R.A. and Zussmann, J. (1992) *An Introduction to the Rock-forming Minerals*, 2nd edition. Longman, Essex, UK, 696 pp.

Drits, V.A., Lindgreen, H. and Salyn, A.L. (1997) Determination of the content and distribution of fixed ammonium in illite-smectite by X-ray diffraction: Application to North Sea illite-smectite. *American Mineralogist*, **82**, 79–87.

Eberl, D.D. and Velde, B. (1989) Beyond the Kübler index. *Clay Minerals*, **24**, 571–577.

Eberl, D.D., Środoń, J., Lee, M., Nadeau, P.H. and Northrop, H.R. (1987) Sericite from the Silverton caldera, Colorado: correlation among structure, composition, origin, and particle size. *American Mineralogist*, **72**, 914–934.

Essene, E.J. and Peacor, D.R. (1995) Clay mineral thermometry – a critical perspective. *Clays and Clay Minerals*, **43**, 540–553.

Etoundi, Y. (2006) Tonmineralogische Untersuchung an Material der RWTH-1 Bohrung. Diploma thesis, Institute of Mineralogy and Economic Geology, RWTH Aachen University, Germany, 61 pp.

Fielitz, W. and Mansy, J.L. (1999) Pre- and synorogenic burial metamorphism in the Ardenne and neighbouring areas (Rhenohercynian zone, central European Variscides). *Tectonophysics*, **309**, 227–256.

Flehmig, W. (1983) Mineral composition of pelitic sediments in the Rhenohercynian zone. Pp 257–265 in: *Intracontinental Fold Belts* (H. Martin and F.W. Eder, editors). Springer Verlag, Berlin, Heidelberg, New York.

Friedrich, G., Germann, A. and Jochum, J. (1993) Schichtgebundene Pb-Zn-Vorkommen in klastischen Sedimenten vom Typ Maubach-Mechernich – Lagerstättenbildung durch intraformationale Prozesse. *Mitteilungen der Österreichischen Mineralogischen Gesellschaft*, **138**, 93–106.

Ge, S. and Garven, G (1992) Hydromechanical modeling of tectonically driven groundwater flow with application to the Arkoma foreland basin. *Journal of Geophysical Research*, **97**, 9119–9144.

Glasmacher, U.A. (1995) Variszische und postvariszische Fluidsysteme. Pp 1–40 in: *KW-relevante Eigenschaften potentieller Mutter- und Speichergesteine am Nordrand des Linksrheinischen Schiefergebirges* (R. Walter, U. Glasmacher and M. Wolf, editors). RWTH-Aachen, BMBF Forschungsprojekt 032 6804 A 5, Teil 5.

Glasmacher, U.A., Tschernoster, R., Clauer, N. and Spaeth, G. (2001) K-Ar dating of magmatic sericite crystallites for determination of cooling paths of metamorphic overprints. *Chemical Geology*, **175**, 673–687.

Guggenheim, S., Bain, D.C., Bergaya, F., Brigatti, M.F., Drits, V.A., Eberl, D.D., Formoso, M.L.L., Galán, E., Merriman, R.J., Peacor, D.R., Stanjek, H. and Watanabe, T. (2002) Report of the Association Internationale pour l'Etude des Argiles (AIPEA) Nomenclature committee for 2001: Order, disorder and crystallinity in phyllosilicates and the use of the 'Crystallinity Index'. *Clay Minerals*, **37**, 389–393.

Guinier, A. (1963) *X-ray Diffraction in Crystals, Imperfect Crystals and Amorphous Bodies*. Freeman and Company, San Francisco, USA, 387 pp.

Higashi, S. (1982) Tobelite, a new ammonium dioctahedral mica. *Mineralogical Journal*, **11**, 138–146.

Hilgers, C., Büker, C. and Urai, J.L. (2006) Fossil overpressure compartments? A case study from the Eifel area and some general aspects. In: *TSK (Symposium Tektonik. Strukturgeologie Kristallingeologie) 11* (G. Gudmundsson, editor). Göttingen.

Hollmann, E.G. (1997) Der Variszische Vorlandüberschiebungsgürtel der Ostbelgischen Ardennen – Ein bilanziertes Modell. *Aachener Geowissenschaftliche Beiträge*, **25**, 235 pp.

Hower, J., Eslinger, E.V., Hower, M.E. and Perry, E.A. (1976) Mechanisms of burial metamorphism of argillaceous sediments: Mineralogical and chemical evidence. *Geological Society of America Bulletin*, **87**, 725–737.

Inoue, A. (1995) Formation of clay minerals in hydrothermal environments. Pp. 268–329 in: *Origin and Mineralogy of Clay – Clays and the Environment* (B. Velde, editor). Springer, Berlin.

Jaboyedoff, M., Bussy, F., Kübler, B. and Thelin, Ph. (2001) Illite 'crystallinity' revisited. *Clays and Clay Minerals*, **49**, 156–167.

Kisch, H.J. (1990) Calibration of the anchizone: A critical comparison of illite 'crystallinity' scales used for definition. *Journal of Metamorphic Geology*, **9**, 665–670.

Klug, H.P. and Alexander, L.E. (1974) *X-ray Diffraction Procedures for Polycrystalline and Amorphous Materials*. John Wiley and Sons, New York, 966 pp.

Knapp, G. (1980) *Erläuterungen zur Geologischen Karte der nördlichen Eifel, 1: 100000, 2. Auflage*. Geologisches Landesamt Nordrhein Westfalen, Krefeld, 152 pp.

Krooss, B.M., Friberg, L., Gensterblum, Y., Hollenstein, J., Prinz, D. and Littke, R. (2005) Investigation of the pyrolytic liberation of molecular nitrogen from Palaeozoic sedimentary rocks. *International Journal of Earth Sciences*, **94**, 1023–1038.

Krumm, S. (1992) Illitkristallinität als Indikator schwacher Metamorphose – Methodische Untersuchungen, regionale Anwendungen und Vergleiche mit anderen Parametern. *Erlanger Geologische Abhandlungen*, **120**, 1–75.

Kübler, B. (1964) Les argiles, indicateurs de métamorphisme. *Revue de l'Institut Francais du Petrole*, **19**, 1093–1112.

Kübler, B. (1968) Evaluation quantitative du métamorphisme par la cristallinité de l'illite. *Bulletin du Centre de Recherches de Pau-SNPA*, **2**, 385–397.

Kübler, B. (1990) "Cristallinité" de l'illite et mixed-layers: brève révision. *Schweizerische Mineralogische und Petrographische Mitteilungen*, **70**, 89–93.

Kübler, B. and Jaboyedoff, M. (2000) Illite crystallinity. *Comptes Rendu de l'Academie Scientifique de Paris, Science de la Terre et des Planètes*, **331**, 75–89.

Langford, J.I. and Wilson, A.J.C. (1978) Scherrer after sixty years: a survey and some new results in the determination of crystallite size. *Journal of Applied Crystallography*, **11**, 102–113

Langford, J.I., Louer, D. and Scardi, P. (2000) Effect of a crystallite size distribution on X-ray diffraction line profiles

and whole-powder-pattern fitting. *Journal of Applied Crystallography*, **33**, 964–974.

Lanson, B. and Kübler, B. (1994) Experimental determination of the coherent scattering domain size distribution of natural mica-like phases with the Warren-Averbach technique. *Clays and Clay Minerals*, **42**, 489–494.

Lögering, M.J., Kolb, J. and Meyer, F.M. (2005) Fluidsysteme in hydrothermalen Gängen der Aachener Geothermie-Bohrung. *Berichte der Deutschen Mineralogischen Gesellschaft, Beih. Z. European Journal of Mineralogy*, **17**, 84.

Lögering, M.J., Kolb, J., Meyer, F.M. and Schwarzbauer, J. (2006) Paläofluide in störungskontrollierten Bruchsystemen der Aachener Geothermie-Bohrung. *Abstract, TSK (Symposium Tektonik, Struktur und Kristallingeologie) 11*, pp. 22–24, März, Göttingen, Germany.

Lundershausen, S., Oesterreich, B., Ribbert, K.H. and Wrede, V. (2005) Geothermal well 'RWTH-1', Aachen – Technical aspects and first geological results. *Abstracts of the Meuse-Rhine Euregio Geologists Meeting: Alden Biesen (Belgian Limbourg)*, 20–21 May 2005.

Lünenschloss, B. (1998) *Modellierung der Temperatur- und Fluidgeschichte an der variszischen Front (Verviers-Synklinorium und Nordeifel)*. Scientific Technical Report STR98/07 Geoforschungszentrum Potsdam, 132 pp.

Lünenschloss, B., Bayer, U. and Muchez, Ph. (1997) Coalification anomalies induced by fluid flow at the Variscan thrust front: a numerical model of the palaeotemperature field. *Geologie en Mijnbouw*, **76**, 271–275.

Maynard, J.B., Elswick, E.R. and Hower, J.C. (2001) Reflectance of dispersed vitrinite in shales hosting Pb-Zn-Cu ore deposits in western Cuba: comparison with clay crystallinity. *International Journal of Coal Geology*, **47**, 161–170.

Mering, J. (1949) L'interférence de rayons X dans les systems a stratification désordonnée. *Acta Crystallographica*, **2**, 371–377.

Merriman, R.J. (2005) Clay minerals and sedimentary basin history. *European Journal of Mineralogy*, **17**, 7–20.

Merriman, R.J. and Frey, M. (1999) Patterns of very low-grade metamorphism in metapelitic rocks. Pp. 61–107 in: *Low-grade Metamorphism* (M. Frey and D. Robinson, editors). Blackwell Sciences, Oxford, UK.

Merriman, R.J. and Peacor, D.R. (1999) Very low-grade metapelites: mineralogy, microfabrics and measuring reaction progress. Pp. 10–60 in: *Low-grade Metamorphism* (M. Frey and D. Robinson, editors). Blackwell Sciences, Oxford, UK.

Mingram, B., Hoth, P., Lüders, V. and Halrov, D. (2005) The significance of fixed ammonium in Palaeozoic sediments for the generation of nitrogen-rich natural gases in the North German Basin. *International Journal of Earth Sciences*, **94**, 1010–1022.

Moore, J.C. (1989) Tectonics and hydrogeology of accretionary prisms: role of the décollement zone. *Journal of Structural Geology*, **11**, 95–106.

Muchez, Ph., Slobodnik, M., Viaene, W. and Keppens, E. (1994) Mississippi Valley-type Pb-Zn mineralization in eastern Belgium: Indications for gravity-driven flow. *Geology*, **22**, 1011–1014.

Nierhoff, R. (1994) Metamorphose-Entwicklung im Linksrheinischen Schiefergebirge: Metamorphosegrad und –verteilung sowie Metamorphosealter nach K-Ar-Datierungen. *Aachener Geowissenschaftliche Beiträge*, **3**, 1–159.

Nieto, F. (2002) Characterization of coexisting $NH_4$- and K-micas in very low-grade metapelites. *American Mineralogist*, **87**, 205–216.

Oliver, J. (1986) Fluids expelled tectonically from orogenic belts: Their role in hydrocarbon migration and other geological phenomena. *Geology*, **14**, 99–102.

Oncken, O. (1989) Geometrie, Deformationsmechanismen und Paläospannungsgeschichte großer Bewegungszonen in der höheren Kruste (Rheinisches Schiefergebirge). *Geotektonische Forschungen*, **73**, 1–215.

Oncken, O., von Winterfeld, C. and Dittmar, U. (1999) Accretion of a passive margin: The late Paleozoic Rhenohercynian fold and thrust belt (Middle European Variscides). *Tectonics*, **18**, 75–91.

Österreich, B., Ribbert, K.H. and Wrede, V. (2005) Erste Ergebnisse zur biostratigrafischen und tektonischen Einordnung der Bohrung RWTH-1. Unpublished report, GD-NRW, 2005.

Pironon, J., Pelletier, M., de Donato, P. and Mosser-Ruck, R. (2003) Characterization of smectite and illite by FTIR spectroscopy of interlayer $NH_4^+$ cations. *Clay Minerals*, **38**, 201–211.

Pollastro, R.M. (1993) Considerations of the illite-smectite geothermometer in hydrocarbon-bearing rocks of Miocene to Mississippian age. *Clays and Clay Minerals*, **41**, 119–133.

Rao, S. and Houska, C.R. (1986) X-ray diffraction profiles described by refined analytical functions. *Acta Crystallographica*, **A42**, 14–19.

Redecke, P. (1992) Zur Geochemie und Genese variszischer und postvariszischer Buntmetallmineralisation in der Nordeifel und der Niederrheinischen Bucht. *Mitteilungen zur Mineralogie und Lagerstättenkunde*, **41**, Aachen, 152 pp.

Reynolds, R.C. Jr., Distefano, M.P. and Lahann, R.W. (1992) Randomly interstratified serpentine/chlorite: Its detection and quantification by powder X-ray diffraction methods. *Clays and Clay Minerals*, **40**, 262–267.

Robinson, D. and Merriman, R.J. (1999) Low-temperature metamorphism: an overview. Pp. 1–9 in: *Low-grade Metamorphism* (M. Frey and D. Robinson, editors). Blackwell Sciences, Oxford.

Rottke, W. and Stroink, L. (1999) Die Genese devonischer Vorlandsedimente am NW-Rand des Rheinischen Massivs – Zement- und Porenraumentwicklung. *Zeitschrift der deutschen Gesellschaft für Geowissenschaften*, **150**, 471–491.

Scherrer, P. (1918) Bestimmung der Größe und der inneren Struktur von Kolloidteilchen mittels Röntgenstrahlen. *Göttinger Nachrichten*, **2**, 98–100.

Schneider, J., Haack, U., Hein, U.F. and Germann, A. (1999) Direct Rb/Sr dating of sandstone-hosted sphalerites from stratabound Pb-Zn deposits in the northern Eifel, NW Rhenish Massif, Germany. Pp. 1287–1290 in: *Mineral Deposits: Processes to Processing. Proceedings of the 5th Biennial. SGA Meeting and the 10th Quadrennial IAGOD Symposium* (C.J. Stanley, editor). London, 22–25 August, 1999.

Smith, R.E. and Wiltschko, D.V. (1996) Generation and maintenance of abnormal fluid pressures beneath a ramping thrust sheet: isotropic permeability experiments. *Journal of Structural Geology*, **18**, 951–970.

Środoń, J., Elsass, F., McHardy, W.J. and Morgan, D.J. (1992) Chemistry of illite-smectite inferred from TEM measurements of fundamental particles. *Clay Minerals*, **27**, 137–158.

Środoń, J., Morgan, D.J., Eslinger, E.V., Eberl, D.D. and Karlinger, M.R. (1986) Chemistry of illite/smectite and end member illite. *Clays and Clay Minerals*, **34**, 368–378.

Stanjek, H. and Häusler, W. (2000) Quantifizierung silikatischer Tonminerale im Textur- und Pulverpräparat mit MacClayFit. *Berichte der Deutschen Ton- und Tonmineralgruppe e.V.*, **7**, 256–265.

Steingrobe, B. (1990) Fazieseinheiten aus dem Aachen-Erkelenzer Oberkarbonvorkommen unter besonderer Berücksichtigung des Inde-Synklinoriums. Dissertation RWTH-Aachen, Germany, 325 pp.

Šucha, V., Elsass, F., Eberl, D.D., Kuchta, L., Madejová, J., Gates, W.P. and Komadel, P. (1998) Hydrothermal synthesis of ammonium illite. *American Mineralogist*, **83**, 58–67.

Teichmüller, M. and Teichmüller, R. (1979) Ein Inkohlungsprofil entlang der linksrheinischen Geotraverse von Schleiden nach Aachen und die Inkohlung in der Nord-Süd-Zone der Eifel. *Forschritte Geologie Rheinland und Westfalen*, **27**, 323–355.

Thompson, P., Cox, D.E. and Hastings, J.B. (1987) Rietveld refinement of Debye-Scherrer synchroton X-ray data of $Al_2O_3$. *Journal of Applied Crystallography*, **20**, 79–83.

Tschernoster, R., Glasmacher, U., Spaeth, G. and Clauer, N. (1995) K-Ar- Datierungen zur Abkühlungsgeschichte ausgewählter Magmatite und Metapelite aus dem Stavelot Venn Massiv. Pp. 1–20 in: *KW-relevante Eigenschaften potentieller Mutter- und Speichergesteine am Nordrand des Linksrheinischen Schiefergebirges* (R. Walter, U. Glasmacher and M. Wolf, editors). RWTH-Aachen, BMBF Forschungsprojekt 032 6804 A 5, Teil 4.

Velde, B. and Lanson, B. (1993) Comparison of I/S transformation and maturity of organic matter at elevated temperatures. *Clays and Clay Minerals*, **41**, 178–183.

Vogtmann-Becker, J. (1990) Mobilisation und Austausch von Elementen durch Regionalmetamorphose in kambro-ordovizischen Sedimentgesteinen des Stavelot-Venn-Massivs. *Mitteilungen zur Mineralogie und Lagerstättenlehre*, **34**, 1–179.

Von Winterfeld, C.-H. (1994) Variszische Deckentektonik und devonische Beckengeometrie der Nordeifel – Ein quantitatives Modell. *Aachener Geowissenschaftliche Beiträge*, **2**, 319 pp.

Wang, H., Frey, M. and Stern, W.B. (1996) Diagenesis and metamorphism of clay minerals in the Helvetic Alps of eastern Switzerland. *Clays and Clay Minerals*, **44**, 96–112.

Warr, L.N. (1996) Standardized clay mineral crystallinity data from the very low-grade metamorphic facies rocks of southern New Zealand. *European Journal of Mineralogy*, **8**, 115–127.

Warr, L.N. and Rice, A.H.N. (1994) Interlaboratory standardization and calibration of clay mineral crystallinity and crystallite size data. *Journal of Metamorphic Geology*, **12**, 141–152.

Warr, L.N. and Nieto, F. (1998) Crystallite thickness and defect density of phyllosilicates in low-temperature metamorphic pelites: A TEM and XRD study of clay-mineral crystallinity-index standards. *The Canadian Mineralogist*, **36**, 1453–1474.

Weaver, C.E. (1960) Possible uses of clay minerals in search for oil. *Bulletin of the American Association of Petroleum Geologists*, **44**, 1505–1518.

Williams, L.B., Ferrell, R.E., Chinn, E.W. and Sassen, R. (1989) Fixed-ammonium in clays associated with crude oils. *Applied Geochemistry*, **4**, 605–616.

Wilson, P.N., Parry, W.T. and Nash, W.P. (1992) Characterization of hydrothermal tobelitic veins from black shale, Oquirrh Mountains, Utah. *Clays and Clay Minerals*, **40**, 405–420.

Yau, Y.C., Peacor, D.R., Bearne, R.e., Essene, E.J. and McDowell, S.D. (1988) Microstructures, formation mechanisms, and depth-zoning of phyllosilicates in geothermally altered shales, Salton Sea, California. *Clays and Clay Minerals*, **36**, 1–10.

Zhang, Y., Muchez, Ph. and Hein, U.F. (1997) Chlorite geothermometry and the temperature conditions at the Variscan thrust front in eastern Belgium. *Geologie en Mijnbouw*, **76**, 267–270.

(*Received 25 July 2006; revised 11 December 2006; Ms. 1194; A.E. Ray E. Ferrell Jr.*)

## 13. Acknowledgements

Inspiring discussions and support by U. Kramm and F.M. Meyer in the last years are greatfully acknowledged. Valuable advice and help with analytical work was also provided by A. Dziggel, A. Hellmann, J. Kolb, T. Körner, J. Warnsloh, A. Wiechowski and T. Witzke. I also thank M. Brand, T. Derichs, D. Esser, R. Klinghardt, I. Knisch, R. Neef, M. Wiechert and P. Zimmermann for analytical and technical support of research work carried out in the last years. Heike Bostelmann, Y. Etoundi, P. Friedrichs, L. Gronen, V. Havenith, H.C. Oskierski, R. Schauerte are thanked for assistance in the laboratory and preparation of drawings. Financial support for work reported here was provided by the German Science Foundation (DFG Grants Kr 1195/4, Me 1425/2, Me 1425/9, Si 810/2) and the Institute of Mineralogy and Economic Geology, RWTH Aachen University. I wish to express special thanks to my wife Imke and my daughters Mariele and Nele for their support and understanding.